Hot corinos : the early organic molecular enrichment of the planet formation zones

Marta de Simone

To cite this version:

Marta de Simone. Hot corinos : the early organic molecular enrichment of the planet formation zones. Galactic Astrophysics [astro-ph.GA]. Université Grenoble Alpes [2020-..], 2022. English. NNT : 2022GRALY007 . tel-03791884

UGA
Université
Grenoble Alpes

THÈSE

Pour obtenir le grade de

DOCTEUR DE L'UNIVERSITÉ GRENOBLE ALPES

Spécialité : Astrophysique et Milieux dilues
Arrêté ministériel : 25 mai 2016

Présentée par

Marta DE SIMONE

Thèse dirigée par **Cecilia CECCARELLI,** Astronome, Université Grenoble Alpes,
et codirigée par **Claudio CODELLA,** INAF-Osservatorio Astrofisico di Arcetri

préparée au sein du **Laboratoire Institut de Planétologie et d'Astrophysique de Grenoble**
dans **l'École Doctorale Physique**

Hot Corinos: the early organic molecular enrichment of the planet formation zones

Hot Corinos: l'enrichissement précoce de molécules organiques des régions de formation planétaires

Thèse soutenue publiquement le **31 Janvier 2022**,
devant le jury composé de :

Monsieur Rafael BACHILLER
ASTRONOME, National Astronomical Observatory (OAN), Rapporteur
Monsieur Sergio MOLINARI
DIRECTEUR DE RECHERCHE, INAF-Istituto di Astrofisica e Planetologia Spaziali di Roma, Rapporteur
Monsieur Pierre BECK
PROFESSEUR DES UNIVERSITES, Université de Grenoble Alpes, President
Madame Claire CHANDLER
ASTRONOME, National Radio Astronomy Observatory, Examinatrice
Madame Linda PODIO
DOCTEUR EN SCIENCES, INAF-Osservatorio Astrofisico di Arcetri, Examinatrice
Monsieur Leonardo TESTI
DIRECTEUR DE RECHERCHE, European Southern Observatory, Membre invité
Madame Paola CASELLI
PROFESSEUR DES UNIVERSITES, Max Planck for Extraterrestrial Astrophysics, Membre invité

Contents

Abstract

So far Earth is the only known planet hosting life, which is based on organic chemistry. Interestingly, some of the chemical precursors of life, e.g. amino acid, have been found in Solar System objects (e.g., comets and meteorites). This finding supports the possibility that the first steps of organic chemistry started already during the early stages of the formation of our Solar System. However, is it actually true?

Planetary systems as the Solar System are formed continuously in the Milky Way so that it is possible to study them to recover what happened to our Solar System. The formation of Solar-type stars goes through different stages, starting from a collapsing molecular core that evolves into a protostar, a protoplanetary disk, and eventually a planetary system. Together with the physical evolution, a chemical evolution takes place. In particular, several relatively complex organic molecules have been detected in the early protostellar phase, i.e., hot corinos. Therefore, their chemical characterization is a crucial point in retrieving our origins. Nevertheless, after almost twenty year of studies, very few hot corinos have been discovered, and many of them show very different molecular spectra at millimeter wavelengths.

In this perspective, with this Thesis I aim to answer two main questions:
i) What is the origin and nature of hot corinos?
ii) How are interstellar complex organic molecules synthesized?

In order to answer these questions, I investigated the protostellar binary system NGC 1333 IRAS 4A and its surrounding environment. This system, extensively studied at millimeter wavelengths, is composed of two sources, IRAS 4A1 and IRAS 4A2, with very different millimeter molecular spectra. Additionally, the two protostars are ejecting two bipolar outflows that interact with the surrounding envelope.
I used i) VLA centimeter wavelengths observations toward the two protostars to investigate their chemical nature and history and ii) high-angular resolution observations with NOEMA, as part of the SOLIS (Seeds of Life in Space) Large Program, to study the chemical complexity of their molecular outflows.

This Thesis work is part of the project Dawn of Organic Chemistry (DOC), funded by the European Research Council (ERC) under the grant No 741002.

Abstract

Jusqu’à présent, la Terre est la seule planète connue accueillant la vie, qui est basée sur la chimie organique. Il est intéressant de noter que certains des précurseurs chimiques de la vie, comme les acides aminés, ont été découverts dans des objets du système solaire (comètes et météorites, par exemple). Cette découverte appuie la possibilité que les premières étapes de la chimie organique aient commencé dès les premiers stades de la formation de notre système solaire. Cependant, est-ce vraiment vrai ?

Des systèmes planétaires comme le Système solaire se forment continuellement dans la Voie Lactée, si bien qu’il est possible de les étudier pour retrouver ce qui est arrivé à notre Système solaire. La formation des étoiles de type solaire passe par différentes étapes, à commencer par l’effondrement d’un cœur moléculaire qui évolue en une protoétoile, un disque protoplanétaire et, finalement, un système planétaire. L’évolution physique s’accompagne d’une évolution chimique. En particulier, plusieurs molécules organiques relativement complexes ont été détectées dans la phase protostellaire précoce, c’est-à-dire dans les ”hot corinos”. Par conséquent, leur caractérisation chimique est un point crucial pour retrouver nos origines. Néanmoins, après presque vingt ans d’études, très peu de Hot corinos ont été découverts, et beaucoup d’entre eux montrent des spectres moléculaires très différents aux longueurs d’onde millimétriques.

Dans cette perspective, avec cette thèse, je cherche à répondre à deux questions principales:
i) Quelle est l’origine et la nature des hot corinos ?
ii) Comment sont synthétisées les molécules organiques complexes interstellaires ?

Afin de répondre à ces questions, j’ai étudié le système binaire protostellaire NGC 1333 IRAS 4A et son environnement. Ce système, largement étudié aux longueurs d’onde millimétriques, est composé de deux sources, IRAS 4A1 et IRAS 4A2, dont les spectres moléculaires millimétriques sont très différents. De plus, les deux proto-étoiles éjectent deux outflows bipolaires qui interagissent avec l’enveloppe environnante. J’ai utilisé i) des observations aux longueurs d’onde centimétriques du VLA vers les deux proto-étoiles pour étudier leur nature chimique et leur histoire et ii) des observations à haute résolution angulaire avec NOEMA, dans le cadre du grand programme SOLIS (Seeds of Life in Space), pour étudier la complexité chimique de leurs écoulements moléculaires.

Ce travail de thèse fait partie du projet Dawn of Organic Chemistry (DOC), financé par le Conseil européen de la recherche (ERC) sous la subvention n° 741002.

Abstract

Finora la Terra è l'unico pianeta conosciuto che ospita la vita, basata sulla chimica organica. È interessante notare che alcuni dei precursori chimici della vita, ad esempio gli aminoacidi, sono stati trovati in oggetti del sistema solare (ad esempio, comete e meteoriti). Questa scoperta supporta la possibilità che i primi passi della chimica organica siano iniziati già durante le prime fasi della formazione del nostro sistema solare. Tuttavia, è effettivamente vero?

I sistemi planetari come il Sistema Solare si formano continuamente nella Via Lattea, per cui è possibile studiarli per recuperare ciò che è successo al nostro Sistema Solare. La formazione delle stelle di tipo Solare passa attraverso diverse fasi, a partire da un nucleo molecolare in collasso che si evolve in una protostella, un disco protoplanetario e infine un sistema planetario. Insieme all'evoluzione fisica, ha luogo un'evoluzione chimica. In particolare, diverse molecole organiche relativamente complesse sono state rilevate nella prima fase protostellare, cioè negli "hot corinos". Pertanto, la loro caratterizzazione chimica è un punto cruciale per recuperare le nostre origini. Tuttavia, dopo quasi venti anni di studi, sono stati scoperti pochissimi hot corinos, e molti di essi mostrano spettri molecolari molto diversi a lunghezze d'onda millimetriche.

In questa prospettiva, con questa tesi mi propongo di rispondere a due domande principali:
i) Qual è l'origine e la natura degli hot corinos?
ii) Come vengono sintetizzate le molecole organiche complesse interstellari?

Per rispondere a queste domande, ho studiato il sistema binario protostellare NGC 1333 IRAS 4A e il suo ambiente circostante. Questo sistema, ampiamente studiato alle lunghezze d'onda millimetriche, è composto da due sorgenti, IRAS 4A1 e IRAS 4A2, con spettri molecolari millimetrici molto diversi. Inoltre, le due protostelle espellono due flussi bipolari che interagiscono con l'involucro circostante.

Ho usato i) osservazioni VLA a lunghezze d'onda centimetriche verso le due protostelle per indagare la loro natura chimica e la loro storia e ii) osservazioni ad alta risoluzione angolare con NOEMA, come parte del SOLIS (Seeds of Life in Space) Large Program, per studiare la complessità chimica dei loro deflussi molecolari.

Questo lavoro di tesi fa parte del progetto Dawn of Organic Chemistry (DOC), finanziato dall'European Research Council (ERC) sotto la sovvenzione n. 741002.

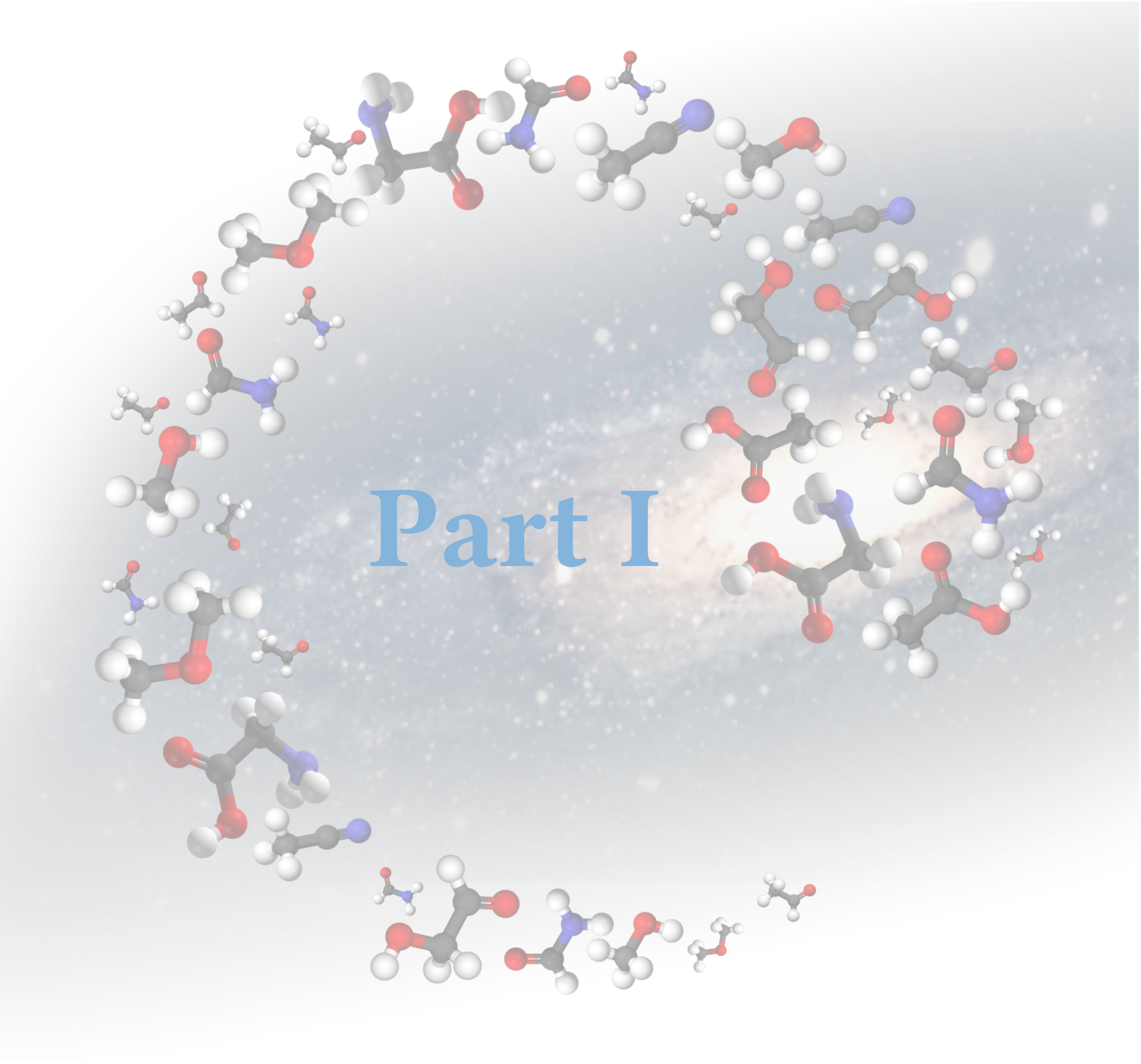

Part I

1

Introduction

In a clear moonless night, to our eyes, the sky is sprinkled by several thousand stars, each appearing as a bright shining dot of light. If the sky is clear enough and the light pollution is minimal, it is possible to distinguish a hazy band of light stretching all the way around the celestial sphere: our Galaxy, the Milky Way. Just as any galaxy in the Universe, the Milky Way is a complex system of billions of stars, gas, and dust particles that lie in a flattened spiral disk of $\sim$ 30 kpc across, with a central bulge of $\sim$3 kpc in radius (Stahler & Palla 2005). The mass of most galaxies is primarily in form of dark matter (material that cannot be seen directly whose nature is still unknown) while only the $\sim$5% represent the baryonic matter[1] which is responsible for almost all the energy emitted by the galaxies. The baryonic matter evolves with the galaxy: at early times it is almost constituted by gas, but as the galaxy evolves this gas is gradually converted to stars, and part of it can be ejected (e.g., in form of winds) or stripped away. Regarding the Milky Way, the baryonic matter is characterized mostly by stars and stellar remnants. However, $\sim$10% of the baryons are found in the matter between the stars, the so-called Interstellar Medium (Tielens 2005; Draine 2011). The black lanes and holes seen in optical images (e.g. see Figure 1.1) are one of the proof of the presence of the cold interstellar medium, being dense and cold material absorbing the light of the background stars of the Milky Way.

1.1 The Interstellar Medium

The importance of the Interstellar Medium (ISM) is not only its crucial role for the structure and morphology of the Galaxy but, in particular, its direct link with the stellar (and Galactic) formation and evolution. When a star dyes, all the products of its internal nucleosynthesis are ejected, thanks to winds or supernova explosions, into the ISM. This material will be then reused for the future generation of stars. Therefore, the actual composition of interstellar matter is the product of galactic evolution. To better understand how stars are formed, it is crucial to understand the characteristic of the ISM.

The interstellar medium is constituted for $\sim$ 99% by gas (ions, atoms, and molecules), while the remaining $\sim$ 1% is dust (small grains of solid material, silicates, and carbonaceous with sizes from 0.005 to 10μm). Additionally, the ISM is continuously stimulated by several pro-

---

[1] The baryonic matter is the matter composed of baryons, i.e. protons, neutrons and all the objects composed of them, as atomic nuclei. However, in this context also electrons are taken into account.

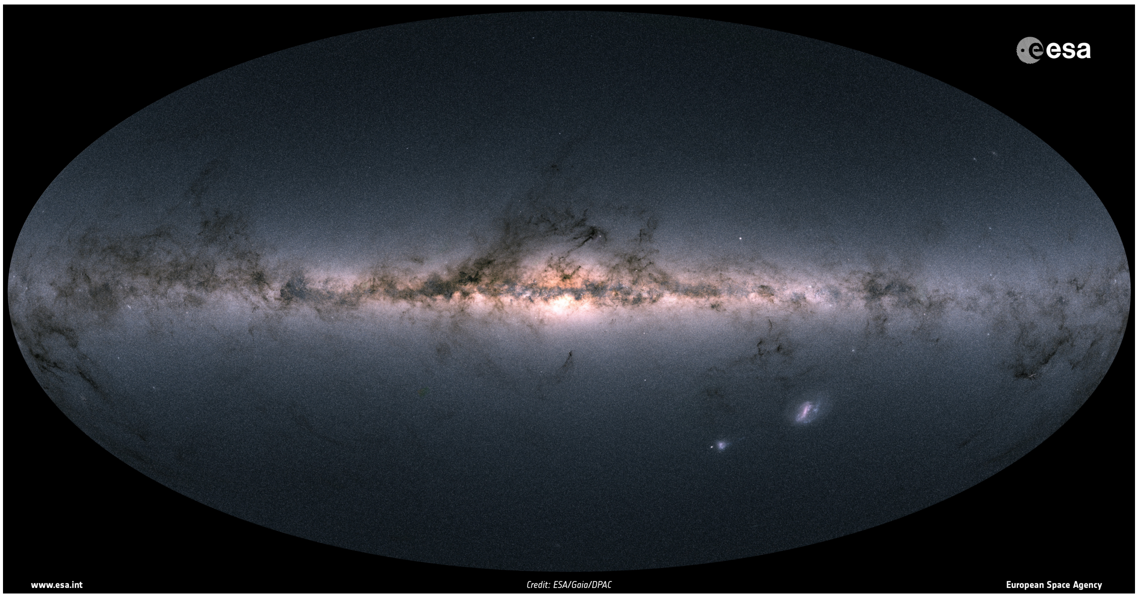

Figure 1.1: Gaia's all-sky view of the Milky Way (and the two neighboring galaxies, the Magellanic clouds) based on measurements of $\sim 10^9$ stars. The map shows the total brightness and color of stars observed by the ESA satellite in each portion of the sky between July 2014 and May 2016. Brighter regions indicate denser concentrations of bright stars, while darker regions correspond to foreground clouds of the interstellar gas and dust, which absorb the light of background stars. (Credit: ESA/Gaia/DPAC)

cesses which shape its status (Tielens 2005; Draine 2011). One of them is the electromagnetic radiation. It corresponds to the photons that pervade the ISM covering different wavelength ranges dominated by different types of sources (e.g., infrared radiation due to thermal emission of dust, atoms, and molecules, or optical and ultraviolet radiation due to stellar photospheres). In particular, the ultraviolet (UV) photons have a strong influence on the ISM being responsible for the ionization and the heating process of the gas through gas photo-ionization and photoelectric effect on dust grains. However, ultraviolet photons are efficiently absorbed by the dust, so they can ionize either tenuous (with low densities) or small (with low column density) clouds, or just the external layers of dense/large clouds. On the contrary, in dense or large clouds, where UV photons do not penetrate, cosmic rays are the major ionization agent. They are high-energetic particles (protons, atomic nuclei, and electrons for the 1%) probably produced by energetic supernova explosions or by O/B stars at different stages of their life. They have a low cross section, which means that they interact very little with the matter and, therefore, they can penetrate in very dense and large clouds, becoming the only source of gas heating and ionization. Then, we have interstellar magnetic fields and gravitational fields. The former constrain the movement of charged particles and control the propagation of cosmic rays influencing gas ionization. The latter act on all the matter in the Galaxy (as ISM, stars, stellar remnants, etc.) playing a major role in shaping all the structures in the Universe. The combined action of these two fields is crucial for the collapse of dense clouds and the formation of future newborn stars.

A comprehensive description of the above listed processes can be found in Tielens (2005) and Draine (2011).

Table 1.1: Phases of the gas in the interstellar medium, classified regarding temperature, density and the Hydrogen ionization fraction.

ISM Phase	Temperature [K]	Density [cm^{-3}]	Ionization Fraction [a]	Observational tracers
Hot Ionized Medium (HIM)	10^6	3×10^{-3}	1	UV; X-ray; Synchrotron
HII regions	10^4	10 (diffuse) -10^4 (compact)	1	Optical line & free-free
Warm Ionized Medium (WIM)	8×10^4	0.1	1	UV; Hα; free-free
Warm Neutral Medium (WNM)	8×10^4	0.5	~ 0.1	HI 21cm; CII 157μm
Cold Neutral Medium (CNM)	80	50	$\sim 10^{-4}$	HI 21cm
Molecular Clouds	≥ 10	≥ 200	$\leq 10^{-6}$	OI;CI;CO

[a] from Caselli et al. (1998); Wolfire et al. (2003); Jenkins (2013)

1.1.1 Interstellar Gas

The gas represents 99% of the interstellar medium. It is composed of hydrogen ($\sim$ 70% in mass), helium ($\sim$ 28% in mass), and few heavier atoms ($\sim$2% in mass) like oxygen, carbon, and nitrogen (called metals). It can be ionized, neutral, or molecular, depending on the status of the hydrogen atoms. In fact, it is possible to distinguish, even if with not a strict separation, different states of the ISM depending on the H ionization status, density, and temperature (Tielens 2005; Draine 2011; Klessen & Glover 2016; Snow & McCall 2006). The ISM phases and their main characteristics are summarized in Table 1.1.

- ⋆ Hot Ionized Medium (HIM): It is the warmest (T$\geq 10^6$ K) and diffuse ($\sim$ 0.003 cm^{-3}) phase of the ISM. This gas has been shock-heated by stellar winds from early-type stars and by supernova explosions and, consequently, it is collisionally ionized. It cools down on time scales of $\sim$Myr through adiabatic expansion or X-ray emission. Observational tracers are UV, X-ray, and radio synchrotron emission. The hot gas fills most of the volume of the Galaxy at a height of $\sim$ 3 Kpc, while the distribution in the disk is quite irregular.

- ⋆ HII regions: They are created when the ultraviolet radiation from very luminous and hot (O/B-type) stars ionizes and heats the surrounding gas. The best tools to study the properties of HII regions are the atomic recombination lines[2]. Beside hydrogen (and in part helium) recombination lines, HII regions also show metal lines as result of recombination of ionized atoms (such as NII - low ionization stage - or OIII - high ionization stage).

- ⋆ Warm Ionized Medium (WIM): Photo-ionized gas with low density ($\sim$ 0.01 cm^{-3}) and temperature of $\sim$8000 K. The source of ionization is not entirely clear even if the most likely candidates are ionizing photons from O/B stars. It cools down through the emission of the ionized hydrogen. Observational tracers are UV, Hα, and radio free-free emission. The volume filling factor is thought to be around 4 % in the disk midplane and

---

[2] The recombination lines are emission lines that follow recombination, the process by which the higher stage of ionization captures an electron (usually at low energies) into a high level of the ion. As the electron drops down through the energy levels of the atom, it emits recombination lines at wavelengths that depend on the difference in energy between the levels. The classical examples are the hydrogen Lyman, Balmer, Paschen, etc. series (Gordon & Sorochenko 2002).

to increase moving away, reaching a maximum of about 30 % at a height of $\sim$ 1.5 Kpc (Gaensler et al. 2008).

The neutral gas of the ISM is traced by the 21 cm line of atomic hydrogen, but can also be observed in optical and ultraviolet absorption lines of various elements towards bright background stars. It is organized in cold diffuse HI clouds (cold neutral medium) and warm intercloud gas (warm neutral medium).

- ⋆ Warm Neutral Medium (WNM): Gas with temperature and density of the same order of magnitude of the WIM, namely 8000 K and 0.5 cm^{-3}, but constituted mainly by neutral hydrogen. By definition, only photons with energies smaller than 13.6 eV (ionization energy of atomic hydrogen) can penetrate, as those with higher energy are absorbed by the ionized skin of the WNM cloud. Therefore, while H and O are neutral, C atoms can be ionized (as the C ionization energy is 11.3 eV) and, given their abundance they are the major positive charge carries. Additionally, the UV photons with energy lower than 13.6 eV can heat the gas directly by ionizing the C atoms and indirectly by ionizing the dust grains via photoelectric effect. Indeed, in both cases, the electrons liberated from the carbon atoms and the dust grains (if it is positively charged) are injected into the gas with a certain amount of energy that will be transferred to the electrons, H atoms or H_2 molecules of the gas through collisions. Based on the elemental abundances and the gas temperatures, hydrogen, oxigen and carbon lines are potentially the most important cooling lines. Given that, the temperature of the WNM gas is high $\sim 10^4$ K, the fine-structure lines are negligible in cooling the gas, while the H Lymanα line become the dominant coolant Indeed, these two emission lines are used as observational tracers for the WNM. It fills almost 30-40% of the volume of the galactic disk.

- ⋆ Cold Neutral Medium (CNM): In this case, the gas is constituted mainly by neutral hydrogen as for the WNM, but in contrast, it is cold (T$\sim$80 K) and denser ($\sim$ 50 cm^{-3}) and it fills only a few parts ($\sim$1%) of the galactic volume. The gas is heated as for the WNM gas, through C ionization and photoelectric effect on the dust grains. Considering that carbon is mostly ionized, the cooling from the fine-structure lines of the neutral carbon is negligible. Therefore, considering that the CNM temperature is about 80 K, the dominant coolant are the fine-structure lines from oxygen (63μm) and/or C^+ (157μm) .

- ⋆ Molecular Clouds: They are clouds of the ISM where the hydrogen in mainly molecular (H_2), as photons with energies larger than 4.5 eV (the dissociation potential of H_2) are shielded or absorbed by the dust. In particular we can distinguish:

  i) Diffuse molecular clouds have a substantial fraction of hydrogen in molecular form ($\sim$ 10 %). However, enough photons are still present to photo-ionize any atomic carbon, or to photo-dissociate CO, such that carbon is still ionized (in form of C^+). They have to be surrounded by diffuse atomic gas that provide a shielding for the radiation. These clouds have density of 100-500 cm^{-3}, temperature of 30-100 K and visual extinction $A_V \sim 0.2$;

  ii) Translucent clouds where carbon begins to transition from ionized atomic C^+, that is no longer the dominant form, into neutral atomic (C) or molecular (CO) form. These clouds must be surrounded by diffuse molecular cloud material to shield enough radiation to reach visual extinction $A_V \geq 1$;

iii) Dense molecular clouds where carbon is almost completely in molecular CO. The electron abundance is very low and the cosmic-rays are the dominant source of ionization as the visual extinction is $A_V \geq 4$. Therefore, the two main source of gas heating are the ionisation of H and He by cosmic rays, and the collisions between the dust grains and the gas particles. On the other hand, the gas in molecular clouds is cooled down by line emission and in particular, given its abundance and spectroscopic properties, CO is the major coolant. Molecular clouds contain other molecules in addition to CO and H_2 and, actually they were discovered at the end of 1930s through the detection of simple diatomic molecules (e.g., CH and CN; Dunham 1937; Swings & Rosenfeld 1937) using optical absorption observations, while the H_2 detection came much later (Carruthers 1970). Other molecules, such as OH, NH_3, H_2O, H_2CO, were later discovered usually via their rotational lines (Weinreb et al. 1963; Rank et al. 1971).

Molecular clouds are important as they represent about 50% in mass of the ISM and are the sites of active star formation. Indeed, inside these clouds clumps of material can be dense and cold enough to collapse under their own gravity to form the future stars.

1.1.2 Interstellar Dust

The influence of the interstellar dust can be detected looking up to the Milky Way with naked eyes. In fact, it is clear how the visual appearance of the Galaxy is dominated by dark regions all along the galactic plane, and beyond (e.g., Figure 1.1). The origin of these dark lanes is not due to the absence of stars, rather to the absorption of the background stars by the foreground dust. In fact, despite their small contribution to the total mass of the galaxy, interstellar dust particles are very efficient (more than the gas) in absorbing, scattering, and re-radiating photons (Whittet 2003; Tielens 2005; Draine 2011).

The absorption of starlight from interstellar dust is the most visible effect of the dust presence, indeed it was the first process to be investigated (Barnard 1907, 1910; Trumpler 1930). Additionally, another involved process is the scattering of photons. While an absorbed photon is completely removed from the light beam and its energy is converted into internal energy of the dust particle, a scattered photon is deflected from the line of sight. Both absorption and scattering contribute to the extinction of the emitted light and the spectral dependence of the extinction is a function of the composition, structure, and size distribution of the dust particles. In this way, by studying the extinction from astronomical observations, it is possible to retrieve the dust properties. Considering an average grain size of $\sim 0.1\mu$m, the optical and ultraviolet wavelengths are efficiently scattered and absorbed by the dust particles. In particular, photons at longer wavelengths (the 'red' ones) are predominant in the transmitted component while the scattered component is predominantly at short wavelengths (the 'blue' ones). This process produces some among the most spectacular astronomical images in the sky, such as the reflection nebulae, visible thanks to the light from embedded or nearby bright stars scattered by diffuse dust particles, that often show a blue shading. On the other hand, as all the bodies in the Universe, dust grains emit photons approximately as a Black Body at the dust temperature. Considering the average temperature of the dust in the Galaxy (from 10 K to 1500 K), the dust emission is mainly from the Near Infrared to millimeter (mm). The cold (15-20 K) component, emitting in the far-IR, is due to large ($\sim 0.1\mu$m) grains in radiative equilibrium with the interstellar radiation field. The hot ($\sim$ 500 K) component, dominating the near- and mid-IR is strong evidence for very small grains (0.1-10 nm) in the ISM (Desert et al. 1990), plus large carbon-chain molecules, formed by more than 50 carbon atoms, called Poly-Aromatic-Hydrocarbons (PAHs) (Tielens 2013). Beyond 1500 K, depending on their composition, dust grains are vaporized. Additionally, dust can have an important role in light polarization. Indeed, linear polarization is due to the propagation of light in a medium where the grains are elongated (the cross-section is larger in one direction than in the other) and (partially) aligned. It appears that the grains are aligned with their shortest axes tending to be parallel to the magnetic field direction, even if the mechanism responsible for the grain alignment remains uncertain (e.g., Andersson et al. 2015). The circular polarization is due to the propagation of light through a medium of aligned grains whose alignment angle changes position. Scattering of light by dust grains generally also leads to polarization and, for single scattering the polarization vector is perpendicular to the direction between the light source and the scattering grain (Whittet 2003; Andersson et al. 2015).

Generally, with very few exceptions, dust and gas are well mixed in the ISM. Indeed, several studies using multiple independent methods have found a good correlation between the dust extinction with the column density of the total hydrogen nuclei (e.g., Bohlin et al. 1978; Shull & van Steenberg 1985; Nguyen et al. 2018a), and a gas to dust mass ratio of $\sim$ 100 for regions dominated by diffuse interstellar matter. Even if the dust represents only $\sim$1% in mass of the ISM, it provides the dominant opacity source in the ISM and dominates the heating of the largest portion of the gas in the Galaxy. Additionally, dust grains lock up a substantial fraction of heavy elements and provide a surface on which species (atoms and molecules) can accrete, meet and synthesize new molecules. This has important consequences on the formation of rocky planets and the life appearance (as the elements locked on dust grains will govern the available elements for biotic chemistry) (Tielens 2005, 2013). The abundance estimate, in the ISM, of heavy elements (such as C, O, Mg, Si, S, and Fe) in atomic form with respect to hydrogen started with the *Copernicus* satellite in the early 70s (Rogerson et al. 1973) through observations of UV atomic lines in absorption against bright stars background. From these observations, it came out that these abundances were below the solar abundance ratios, which are supposed to approximate the true total element abundances for the ISM in our surroundings in the Galaxy. This difference was thought to represent the loss of atoms into solid form within dust grains (Tielens 2005; Jenkins 2009). However, estimating the amount of each element depleted into the dust grain is a very difficult task. Jenkins (2009) reports a range of possible abundances that can be compared with the solar values, showing that only half of C and O, and a fraction of N are trapped into dust grains, while almost all of Mg, Si, and Fe are depleted. Hence, one would expect dust grains to be composed of such elements. Indeed, the main dust components are silicates, graphite, or amorphous carbon that form what is called the refractory core (Tielens 2005).

In the dense molecular cloud, dust grains are covered by iced molecules that form the so-called *grain mantles*. These coatings are tick ices containing molecular species in solid form. The species can be formed by the accretion of gas-phase species (e.g. CO) and by the formation of new species by surface reactions (e.g., water and other hydrogenated species) (see Section 1.3). The main components of the grain mantles have been investigated through the molecular vibrational transition in the near- to far- IR (Boogert et al. 2015). Indeed, most ice features are detected as pure absorption bands against IR continuum point sources (e.g., Murakawa et al. 2000; Pontoppidan et al. 2004; Pontoppidan 2006). From these observations, we know that the major components in interstellar ices in dense molecular clouds are water (H_2O), CO, CO_2, methane (CH_4), ammonia (NH_3), formaldehyde (H_2CO) and methanol (CH_3OH). The spectra profile of the ice bands, namely peak position, widths, and shapes, are influenced by the composition and structure of the ices (crystallinity, density, and homogeneity) as a result of the interactions between neighboring molecules, and by the properties of the dust grains (size, shape, relative mantle/core volumes). Additionally, they are quite sensitive to the physical conditions, age, and elemental abundances (Boogert et al. 2015). Therefore, despite their low fraction in the ISM, interstellar dust grains have a crucial role in the physics and chemistry of the ISM.

1.1.3 Life cycle of interstellar matter

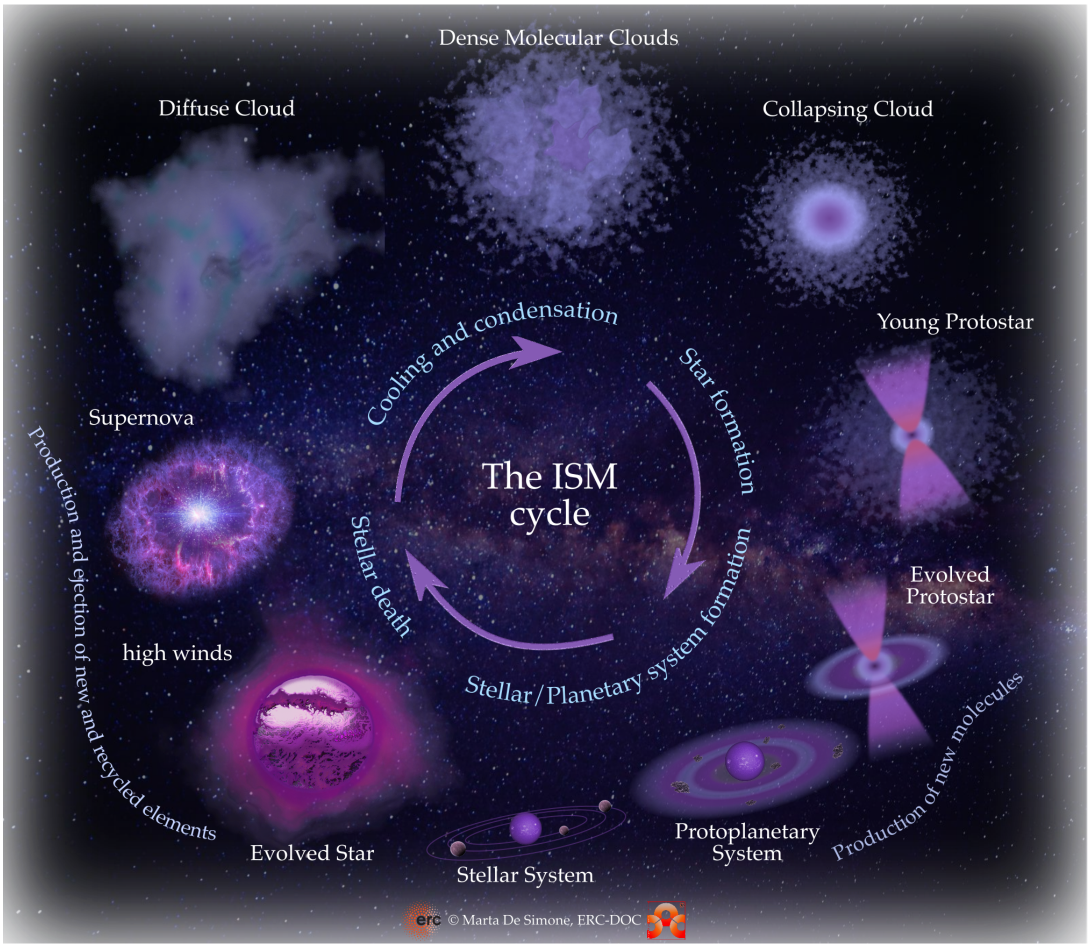

Figure 1.2: Artistic representation of the life cycle of galactic matter. The material injected into the surrounding gas, thanks to stellar winds and supernova explosions, is recycled inside the new-formed molecular clouds.

The stellar and interstellar components are continuously interacting and exchanging material. In fact, between the stellar evolution and the interstellar medium, there is a complex feedback that determines the structure, composition, and chemical evolution of the ISM in the Galaxy (Tielens 2005; Molinari et al. 2014). A representative illustration is reported in Figure 1.2.

Once a star approaches the end of its life, its death could be more or less violent depending on its mass. During the latest stages of its life, the star expels large amounts of matter in strong winds. If the star is massive enough its life could end in a spectacular and powerful explosion, called supernova. This energetic process results in the ejection of stellar material (i.e., all the products of the nucleosynthesis built up over the star's lifetime) at high velocities toward the surrounding medium, and new heavy elements (heavier than iron) can be formed (Johnson 2019). In this way, a significant fraction of the matter that constitutes the star is returned to the ISM, which is then enriched in heavy elements (compared to its state when the star was born). Supernova explosions and stellar winds provide a significant input of mechanical and radiative energy into the interstellar medium, driving interstellar turbulence, injecting nuclear-processed material, and generating dust (that is an important opacity source, see Section 1.1.2. Furthermore, they carve and shape the ISM creating large structures, like hot bubbles and dense shells, that move and interact with the surrounding gas. This gas could eventually cool down, aggregate in the local concentration of matter, denser clouds, that can collapse and form new stars. After successive generations of stars, the galactic matter is progressively enriched in heavy elements (heavier than hydrogen and helium), with the consequence that younger stars have a higher chemical diversity than older stars (Tielens 2005).

On the other hand, during the formation of a star, the molecular complexity increases in its surroundings. Indeed, the formation of more complex molecules through reactions occurring in the gas phase and/or icy grains is enhanced. These molecules containing carbon and at least six atoms are called interstellar Complex Organic Molecules (iCOMs, see Section 1.3). Although they are extremely small molecules when compared to the biotic ones, iCOMs may have provided the bricks to build them, and they might be then delivered to planets by comets, interplanetary dust particles, and meteorites (Caselli & Ceccarelli 2012).

1.2 Low Mass Star Formation

1.2.1 From a quiet cloud to a planetary system

Solar-type stars are formed in the dense and dark molecular clouds in the ISM where the gas is characterized by high density and relatively low temperatures (see Table 1.1). The process of gas condensation is mainly driven by the action of the gravitational force, while other effects, as gas pressure, turbulence, rotation, and magnetic field, tend to contrast the aggregating action of gravity. However, both the magnetic field and the turbulent motions can play a double role: they can help star formation collecting material into small regions favoring the instability or can contrast the collapse generating a pressure that acts against the gravitational force (Stahler & Palla 2005; Klessen & Glover 2016).

Recently studies done with the ESA Hershel[3] space telescope revealed an intricate network of filamentary structures in the interstellar clouds. These interstellar filaments are ubiquitously present in our Galaxy and are thought to be the first key step in the star formation process (e.g., Molinari et al. 2010; André et al. 2014; Schisano et al. 2020). However, the exact process ruling the formation of these filamentary structures and their specific role in triggering star formation is still debated (e.g., Hennebelle & Inutsuka 2019; Robitaille et al. 2020). A major

---

[3] https://sci.esa.int/web/herschel

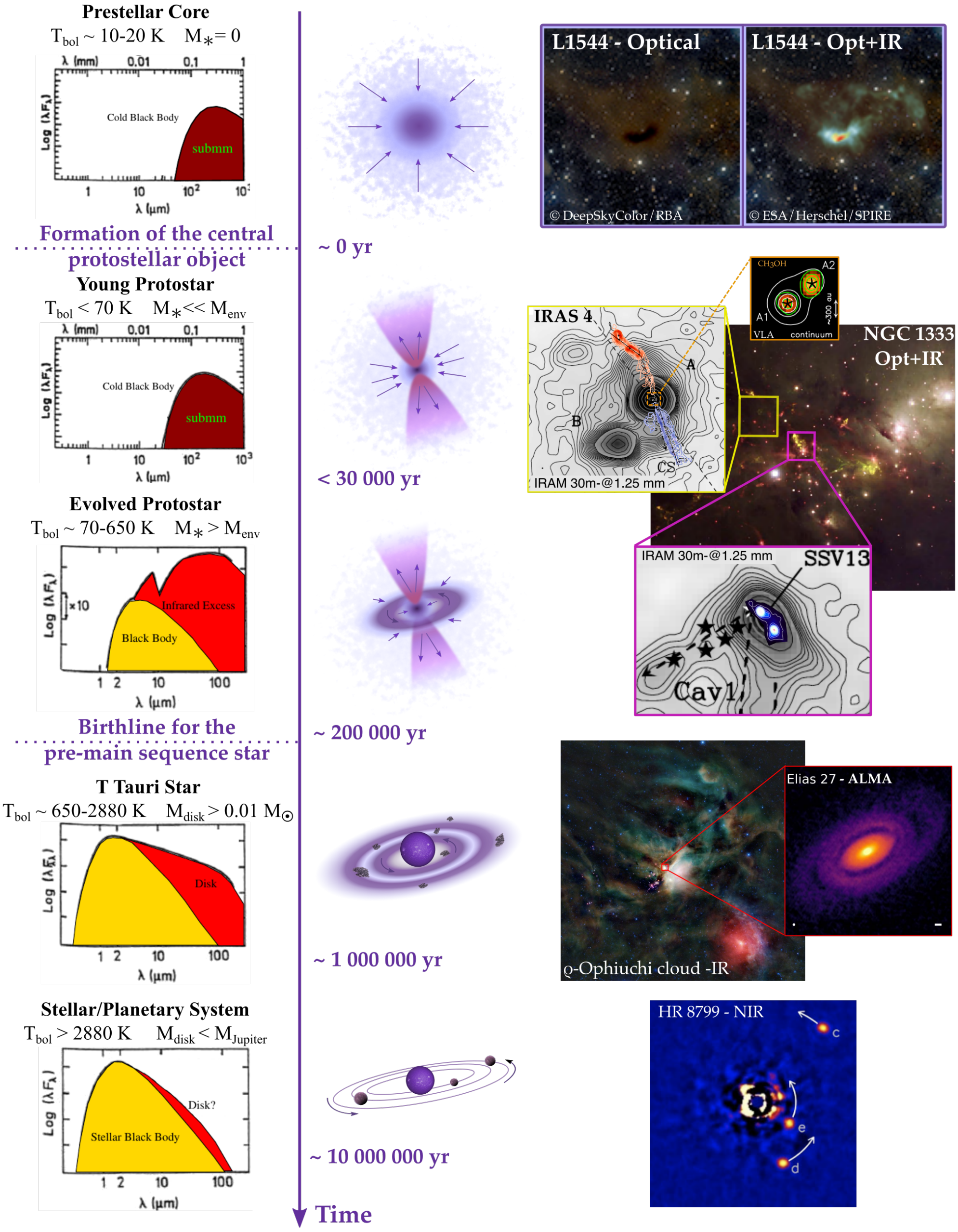

Figure 1.3: *Left panels:* Evolutionary sequence for the formation of a single low mass star based on the shape of the dust continuum Spectral Energy Distribution (SED). The bolometric temperature and the mass of the circumstellar material are indicated on the top of each panel. The violet arrow shows the temporal direction, with the typical expected time for each phase (adapted from André 2002). *Middle panels:* Schematic structure of objects in each phase. *Right panels*: Real observations of the different evolutionary stages taken with different instruments. The prestellar core is the L1544 object shown as a superposition of optical image (credits: DeepSkyColor/RBA) with Infrared observations done by Hershel (Punanova et al. 2018). The protostars Class 0 and I are IRAS 4A and SVS13 A, shown with the IRAM 30m millimeter observations (Lefloch et al. 1998a) located in the NGC1333 region (shown with optical +IR image; Walawender et al. 2008). For IRAS 4A is also shown its large bipolar outflow traced by SiO (Choi 2005) and a zoom towards the two central protostars with VLA observations at cm wavelengths (De Simone et al. 2020a), for SVS13 the two central protostars are shown with NOEMA observation (Bianchi et al. 2019a). The Class II is an ALMA view of the protoplanetary disk surrounding the young star Elias 27 (credits: NASA/JPL/WISE Team; Andrews et al. 2018). The Class III object is the image of the system HR 8799 with three orbiting planets, observed in the near IR with the Keck II telescope (Marois et al. 2010, https://www.eso.org/public/videos/eso1905b/ to see the orbital motion).

process in their shaping, in addition to the presence of magnetic fields, is the compression of the molecular gas by external triggers, such as shock fronts, large colliding flows, turbulence, and (magneto-) hydro-dynamical gravitational instabilities (Padoan et al. 2001; Hennebelle 2013; Vázquez-Semadeni et al. 2019; Federrath et al. 2021).

Once the filament is formed, the gravitational force becomes dominant leading to the fragmentation of the filament in overdensity regions, identified as dense cores. If the dense core is both starless (with no associated central hydrostatic protostellar object) and gravitationally bound with evidence of contraction motion (Lee & Myers 2011; Keto et al. 2015), it can be identified as *prestellar core*. Known prestellar cores have roundish and not very elongated shapes with a density structure similar to a Bonnor-Ebert isothermal spheroids bounded by the external pressure from the parent cloud. Therefore, the density profile is flat at the center, reaching about 10^7 cm^{-3}, and falls off with r^{-2} outside (e.g., Andre et al. 1996; Ward-Thompson et al. 1999; Alves et al. 2001; Tafalla et al. 2004). Being a self-gravitating condensation of gas and dust, the prestellar core evolves towards higher degrees of central condensation and might form an individual star, or system, through gravitational collapse.

It is possible to identify, in the formation of Solar-like stars, a series of different evolutionary stages leading from a dense core to a main sequence star (e.g., Shu et al. 1987; Lada 1987; Andre et al. 2000; Dunham et al. 2014, see also Figure 1.3). Historically, these stages were classified from an observational point of view backward in time, starting from the most evolved, optically visible young stars, and going toward less evolved, heavily obscured objects. In the near-mid infrared wavelengths, three main classes of Young Stellar Objects (YSOs) can be distinguished based on the slope ($\alpha_{\rm IR}$) of the Spectral Energy Distribution (SED, λF$_\lambda$) between 2.2 μm and 10-25 μm (André 2002). Going backward in time we have, Class III ($\alpha_{\rm IR} < -1.5$) and Class II ($-1.5 < \alpha_{\rm IR} < 0$) sources that correspond to the Pre-Main Sequence (PMS) stars, and the youngest YSO Class 0 and I sources with $\alpha_{\rm IR} > 0$ and typical ages of 10^{4-5} yr. Let see them in detail.

Once the dense core becomes gravitationally unstable, it undergoes a phase of free-fall collapse and a central hydrostatic stellar embryo begins to build up its mass through the addition of material from the infalling envelope. The center of the core is then characterized by a compact radio continuum emission while a centrally peaked but extended sub-millimeter continuum emission is tracing the spheroidal infalling dusty envelope (André 2002). This stage is identified as Class 0 and represents the youngest known YSO. The central object starts to accrete material from the envelope and through an accretion disk. However, the angular momentum in the circumstellar disk prevents material from directly falling into the central stellar core. Therefore, a mechanism is necessary to remove angular momentum (Frank et al. 2014). Mass ejection through protostellar jets/winds may be the solution. Indeed, at low velocity (1-30 km s^{-1}) rotating extended winds coming out the disk down to $\sim$ 10 au scales have been observed (Greenhill et al. 1998; Bjerkeli et al. 2016). Thus, they can remove angular momentum from the outer part of the disks allowing the disk material in the wind-launching region to accrete. The protostellar jets are much more collimated and dense with much higher velocity $\geq$ 100 km s^{-1}, and they are ejected along the rotational axis from the innermost part of the disk ($\lesssim$1 au) allowing the disk material to fall onto the central protostars (Lee et al. 2017a). Additionally, the ejected material interacts with the surrounding medium generating shocks that heat the gas and induce several processes such as chemical reactions, grain sputtering, and shuttering (see Section 1.4.2).

After about 10^5 yr, the protostar reaches an evolved stage of accretion in which the large scale envelope is partially dissipated, where the material continues to accrete on the central object through a rotating disk. The evolved protostar is now identified as Class I source. Its emission is characterized by an infrared excess due to the reprocessing of the radiation from the surrounding dust, either in the envelope or in the disk (Lada 1987; Andre et al. 1993). There is not a sharp transition between Class 0 and Class I sources. Often a bolometric temperature (T_{bol}) of 70 K or a luminosity ratio $L_{bol}/L_{submm} < 0.005$ has been adopted as a division between the two classes (Myers & Ladd 1993; Dunham et al. 2014). Thanks to recent high-resolution (sub-arcseconds) observations, many Class 0 and I protostars turned out to be multiple systems sharing a common envelope and a circumbinary disk (Maury et al. 2014b; Tobin et al. 2016).

With time the central object evolves towards the Class II stage, with a typical age of 10^{6-7} yr, in which the envelope has mostly vanished and the central pre-main sequence star, which becomes optically visible, is surrounded by an accretion disk known as *protoplanetary disk*. Indeed, this is the stage in which the planet formation has long been thought to occur as the circumstellar disk is still very massive and very dense in both dust and gas (Testi et al. 2014; Helled & Morbidelli 2021). Indeed, at this stage the disk carry the imprints of the planetary systems that they hosts (e.g., dust and rings; see e.g., Isella et al. 2016; Andrews et al. 2018; Fedele et al. 2018; Long et al. 2019) However, submillimeter surveys show that the mass reservoir available in Class II disks is much lower than the masses needed to explain the formation of the observed exoplanetary systems (e.g., Andrews & Williams 2007; Greaves & Rice 2011; Najita & Kenyon 2014; Testi et al. 2016; Manara et al. 2018; Sanchis et al. 2020). Indeed, recent studies suggest that planet formation occurs in young disks (less than 1 Myr, Class 0/I phase; e.g., Harsono et al. 2018; Podio et al. 2020; Tychoniec et al. 2020; Sheehan et al. 2020; Segura-Cox et al. 2020).

The solid disk component changes in time as grains grow, drift with respect to the gas toward the star, are trapped in winds and accretion flows. In addition, on the one hand, grains are lost into rocky planets and planetesimals, and on the other hand they collide and fragment, replenishing the grain population (e.g., Johansen et al. 2014; Turner et al. 2014). At this stage, the disks are called *debris disks* and, in contrast to protoplanetary disks, they are usually optically thin with low mm-sized dust masses ($< 0.1 M_\oplus$) and very little evidence for gas. However, there is not a net boundary between the two classes (e.g., Wyatt 2018).

Finally, once the temperature inside the core is high enough to switch on the nuclear fusion of the hydrogen nuclei the central object becomes a star that reaches the main sequence, and the planetesimals could eventually turn out as planets and small objects, such as asteroids and comets, forming the stellar system.

1.2.2 Chemical evolution: from simple molecules to the bricks of life

As the primordial cloud evolves into a protostar, a protoplanetary disk, and finally a planetary system, different molecules are formed, destroyed, and passed to later stages. Thus, the chemical composition of the gas becomes more and more complex (Caselli & Ceccarelli 2012; Öberg & Bergin 2021). Indeed, molecular complexity builds up at each step of the star formation process, starting from simple and complex molecules, ending up in large polyatomic species. Figure 1.4 shows an artistic representation of this chemical evolution from a prestellar core to a planetary system.

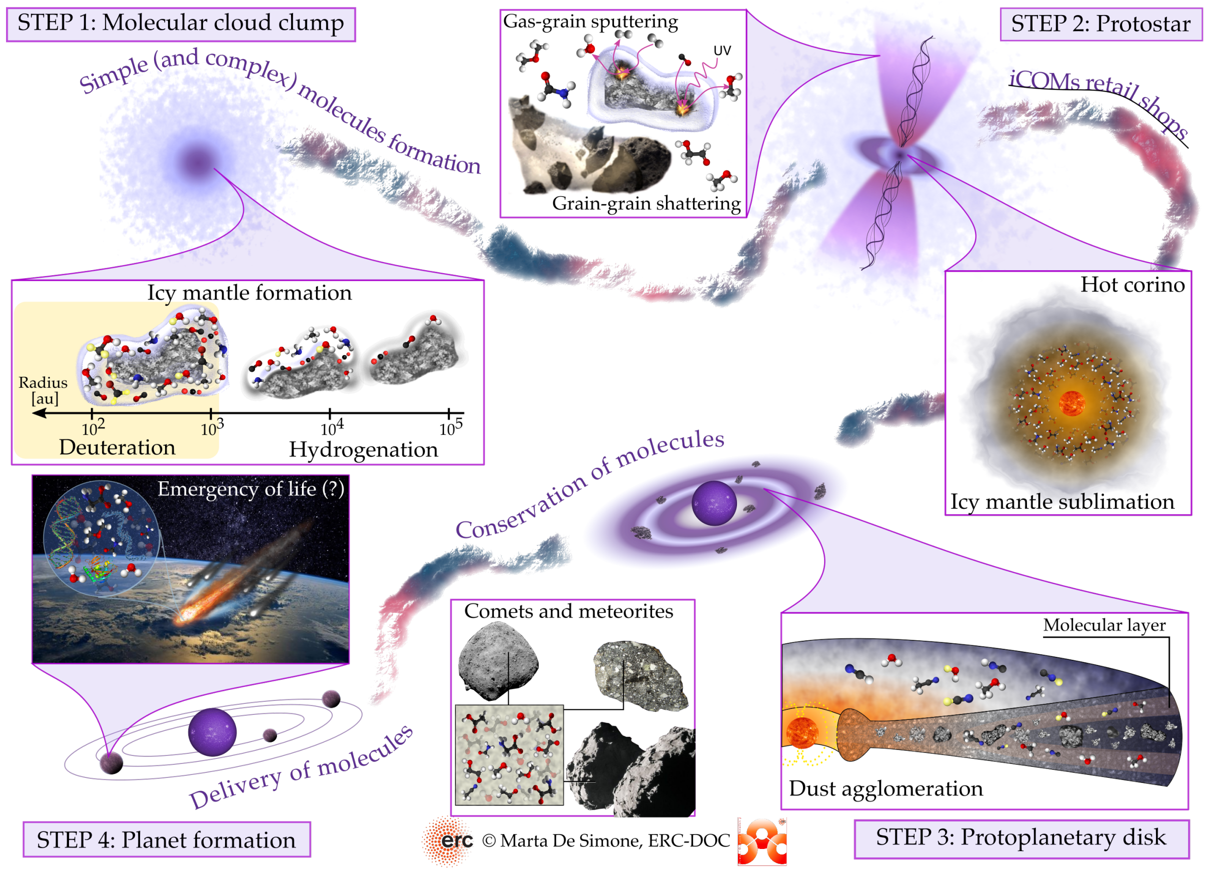

Figure 1.4: Representation of the chemical evolution during the early stages of star formation. Inspired from Caselli & Ceccarelli (2012); Ceccarelli et al. (2014).

Prestellar Core Phase:

While matter slowly accumulates toward the center of the prestellar core, the central density increases reaching values above 10^5 cm^{-3} (Keto & Caselli 2010), and the temperature decreases, reaching values less than 7 K (Crapsi et al. 2007; Bergin & Tafalla 2007). The conditions of the matter in these objects are crucial for their chemical composition. Indeed, the gas temperature and density constrain the various processes at play.

One of the main process working at the prestellar core temperature and density is the so called *freeze-out* (Caselli et al. 1999; Bergin & Tafalla 2007; Ceccarelli et al. 2007). Indeed, at temperatures lower than 10 K, species heavier than Helium (He) tend to disappear from the gas phase due to their adsorption onto the dust grain surfaces. Once a species lands on a grain surface, it cannot thermally evaporate[4] due to the low dust temperatures, and it cannot be photo-desorbed as interstellar photons cannot penetrate inside the prestellar core. Therefore, at this stage, dust grains are expected to build thick icy mantles (e.g.; Tielens & Hagen 1982).

As an example, CO has been measured in starless and prestellar cores to be freeze-out at 80-90% (Caselli et al. 1999; Bacmann et al. 2002; Redman et al. 2002), while the depletion of N-bearing species (such as N_2H^+ and NH_3) is occurring but in a lower percentage with respect the CO one (Bergin et al. 2002; Pagani et al. 2005; Tafalla et al. 2006). At first, this segregation

---

[4] The desorption rate depends on the dust temperature T_{dust} and the species binding energy E_B as $\exp^{E_B/kT_{dust}}$.

was assumed to be due to the lower binding energy of N_2 (the precursor molecule for both N_2H^+ and NH_3) with respect to CO (Bergin & Langer 1997). However, N_2 and CO seem to actually have similar binding energies (Öberg et al. 2005; Bisschop et al. 2006), although these values depend on both composition and local characteristics of the ice surfaces (Nguyen et al. 2018b). Nevertheless, notice that the two binding energies are not equal. Indeed Ferrero et al. (2020) found 1109–1869 K and 760–1458 K for CO and N_2 adsorbed on amorphous water ice, respectively. Only a small fraction of the adsorbed species can desorb into the gas phase (becoming detectable) thanks to non-thermal desorption mechanisms mainly driven by cosmic rays (e.g., Leger et al. 1985; Wakelam et al. 2021) and Far-UV photons produced by the interaction of the cosmic rays with H_2 molecules (Gredel et al. 1989; Shen et al. 2004; Caselli et al. 2012).

The increased abundance of CO in the ices has two main implications:
i) the frozen CO can be hydrogenated and deuterated, thanks to the high mobility of H and D atoms despite the low temperatures. Indeed species as formaldehyde (H_2CO), methanol (CH_3OH) and their deuterated forms, are thought to be formed by successive hydrogenation of CO (Hiraoka et al. 2002; Taquet et al. 2012a; Rimola et al. 2014). Interestingly, radicals are thought to be formed at this stage by the effect of UV photons and cosmic rays (Garrod & Herbst 2006; Öberg et al. 2009), or by partial hydrogenation of frozen species (Taquet et al. 2012b).
ii) CO is the second most abundant species in the gas phase (after H_2), so its disappearance from the gas phase opens the way to new chemical gas phase paths. In particular, the deuterium fractionation is enhanced (e.g., Roberts et al. 2002; Bacmann et al. 2002; Caselli et al. 2003; Ceccarelli et al. 2014). Indeed, the low temperatures of the region favor the exothermic reaction between H_3^+ and HD with respect to the inverse one ($H_3^+ + HD \rightarrow H_2D^+ + H_2$; Watson 1974), and the absence of gaseous CO (and other neutrals, as oxygen, that are frozen-out onto the grain mantles) will cut out competitive reactions with H_3^+ (Roberts et al. 2003; Walmsley et al. 2004). In this way, the atomic D/H ratio increases. This induce an efficient deuteration of surface species, such as CO, producing the (simply or doubly) deuterated form of, for example, methanol and formaldehyde, both detected in prestellar cores (Bacmann et al. 2003; Parise et al. 2002, 2004, 2006b; Bizzocchi et al. 2014).

Moreover, despite their cold and CO-depleted nature, prestellar cores are also sites in which interstellar Complex Organic molecules (iCOMs; see Section 1.3) have been detected (Bacmann et al. 2012; Cernicharo et al. 2012; Vastel et al. 2014; Jiménez-Serra et al. 2016, 2021; Punanova et al. 2018; Scibelli & Shirley 2020; Scibelli et al. 2021). It is worth notice that, recently, also in starless cores a rich complex chemistry has been discovered (see e.g., the case of TMC-1; McGuire et al. 2020; Agúndez et al. 2021; Cernicharo et al. 2021b,a). The origin of these complex molecules in these cold environments is still debated. Indeed, it is not easy to address how these molecules (if formed on the grain surfaces) or their precursor (if formed in the gas phase by grain surface precursor) are released into the gas phase (see Section 1.3 for more details).

Protostellar phase:

Once the collapse starts and the material falls towards the center ‘feeding’ the central object, the gravitational energy is converted into radiation, and the envelope around the central object starts to warm up. Both density and temperature increase toward the center so that the central region can reach gas temperatures > 100 K and densities $> 10^7$cm^{-}3.

When the dust temperature exceeds about 100 K, the grain icy mantles sublimate, and the species trapped in them are released in the gas phase. The molecules released from the grain mantles in the gas phase, the so-called *first generation* species, can react between each other giving rise to a *second generation* of more complex molecules through gas-phase reactions with no or small activation energy barrier (e.g., Charnley et al. 1992; Barone et al. 2015; Taquet et al. 2016; Skouteris et al. 2017, 2018, 2019; Vazart et al. 2020). The abundance of complex species dramatically increases giving rise to a rich chemistry. On the one hand we can find protostars that are rich in complex organic molecules, the so-called called *Hot Corino* (Ceccarelli 2004; Bottinelli et al. 2004a; Ceccarelli et al. 2007). A detailed review of these regions, which can be considered iCOMs retail shops, is given in section 1.4.1. On the other hand, there are the Warm Carbon Chain Chemistry (WCCC) sources that are protostars deficient in iCOMs but rich in unsaturated carbon chain molecules and hydrocarbons (Sakai et al. 2008; Sakai & Yamamoto 2013). However, there are few exceptions where the protostar shows both the properties of a hot corino region and a WCCC source (Imai et al. 2016; Oya et al. 2017).

At the same time as the collapse proceeds, the material starts to be ejected from the central object in the form of jets and winds, interacting with the surrounding medium, creating different types of shocks. These shocks can heat the gas up to hundreds/thousands of K and trigger several processes such as chemical reactions with relatively high activation barriers, and gas grain sputtering or grain-grain shattering (Flower & Pineau des Forets 1994; Caselli et al. 1997; Schilke et al. 1997; Gusdorf et al. 2008b; Guillet et al. 2011), which enhance the abundance of several species in the gas phase (e.g., Bachiller & Pérez Gutiérrez 1997; Bachiller et al. 2001; Maret et al. 2004; Codella et al. 2005). A detailed review of outflows and shocked regions, unique astrochemical laboratories, is given in section 1.4.2.

Protoplanetary Disk phase:

Besides jets and outflows, the collapse of the prestellar core leads to the formation of a circumstellar accretion disk which, initially, is embedded in the thick envelope surrounding a Class 0/I object and little by little starts to appear when the envelope is dissipated. Gas and dust in the disk are physically and chemically interacting in the disk which evolves with time. Initially, small dust grains are dynamically well coupled with the gas. Later on, they start to coagulate in bigger particles that settle down toward the disk midplane (e.g., Duchêne et al. 2004; Natta et al. 2007; Birnstiel et al. 2012; Testi et al. 2014). The gas phase or grain surface chemistry that occurs in protoplanetary disks reflects the diversity and inhomogeneity of these objects (Aikawa & Nomura 2006; Vasyunin et al. 2011; Akimkin et al. 2013; Fedele & Favre 2020). Broadly speaking, it is possible to divide the disk in three different chemical regions (Dullemond et al. 2007; Dutrey et al. 2014; Walsh et al. 2014):

i) The disk midplane, which is well shielded by the UV radiation from the central star and is heated indirectly via infrared emission from the upper layers. It is characterized by low-ionization degree and low temperatures, close to the prestellar ones (Bergin et al. 2007; Cleeves et al. 2015; Aikawa et al. 2021). Their density reaches values up to 10^{11}cm^{-3}, higher than the prestellar core ones, so that, in addition to the low temperatures, dust coagulation, freeze-out and deuterium fractionation processes are expected to proceed faster (Dullemond & Dominik 2004; Ceccarelli et al. 2005; Ceccarelli & Dominik 2006; Qi et al. 2008; Cleeves et al. 2014; Ceccarelli et al. 2014; Cataldi et al. 2021). Therefore, many gaseous molecules freeze onto dust grain mantles and, as in the prestellar phase, the icy mantles grow again. Each molecule has its binding energy distribution that corresponds to a specific freeze-out temperature range. Therefore, each molecule will deplete in a different region of the disk according to the physical conditions. Moving away from the midplane, the temperature increases vertically, and radially toward the central object (Dutrey et al. 2014).

ii) In the intermediate layer of the disk, also called the *molecular layer*, the temperature is high enough to sublimate various ice species (Aikawa et al. 2002; Markwick et al. 2002; Bergin et al. 2007). The radius where a given molecule is sublimated from the ice grain mantles and released in gas-phase, called *snow line*, depends on the species. Therefore, the snow lines for given species appear at a different radii. As example, the CO snowline has been images at a radius of about 30-45 au (e.g., Qi et al. 2015; Guidi et al. 2016), while the water snowline is though to be closer to the center (few au, as the temperature needed to sublimate water is about 100 K; Kennedy & Kenyon 2008). The latter has been imaged at about 40 au in a Fu-Ori disk, V380 Ori. This object is undergoing a burst in its luminosity that consequently moved out the snow line making it resolvable with ALMA (Cieza et al. 2016). Finally, within these species gaseous zones, sublimated molecules can undergo through several gas-phase reactions and new molecules can be formed. The chemistry can be considered similar to the hot corinos one (Bergin et al. 2007; Walsh et al. 2014).

iii) The ionised atmosphere, where the disk surface is heavily irradiated by stellar and interstellar UV photons as well as stellar X-rays (e.g., Ercolano et al. 2009; Aresu et al. 2012; Franz et al. 2020). Therefore, only simple atoms, ions, radicals, and polycyclic aromatic hydrocarbons (PAHs) are present (Dutrey et al. 2014).

The molecular content in the protoplanetary disks is still not well known. So far, only about twenty molecules have been detected. Most of them are small molecules of few atoms (such as CO, CO_2, OH, CS, SO, CN, HCN, HNC, H_2O, H_2S, H_2CS; e.g., Bergin et al. 2010; Hogerheijde et al. 2011; Dutrey et al. 2011; Guilloteau et al. 2012, 2016; Chapillon et al. 2012b; Phuong et al. 2018; Le Gal et al. 2019; Codella et al. 2020b), and some are carbon chains (CCH, C_2H_2, c-C_3H_2, HC_3N, CCS; e.g., Henning et al. 2010; Chapillon et al. 2012a; Ilee et al. 2021; Phuong et al. 2021). Only few interstellar complex organic molecules has been detected, i.e. formaldehyde (H_2CO; Dutrey et al. 1997; Aikawa et al. 2003; Qi et al. 2013; Öberg et al. 2017; Podio et al. 2020), methanol (CH_3OH; Walsh et al. 2016; van 't Hoff et al. 2018; Lee et al. 2019b; Podio et al. 2020; Booth et al. 2021), methyl cyanide (CH_3CN; Öberg et al. 2015; Bergner et al. 2018; Ilee et al. 2021), fomic acid (HCOOH; Favre et al. 2018). Interestingly, protoplanetary disks surrounding FU Orionis (or Fu Ori) stars are precious laboratories where to study the disk chemical composition. Indeed, the Fu Ori stars are undergoing a burst in their luminosity so to illuminate the surrounding disk by about 2-3 orders of magnitude larger than usual. Therefore, the sublimation of ices occurs outer in the disk and thus the observations of species released from the grains, become feasible. A particular example, is the Fu Ori V883 disk, where species more complex than methanol, such as methyl formate and acetaldehyde (CH_3OCHO, CH_3CHO; Lee et al. 2019b) were detected.

Therefore, iCOMs detections in protoplanetary disks around stars that are not experiencing Fu Ori-type bursts have been rare. The explanation for the few detections of larger molecules has to be addressed primarily to an observational limitation. Indeed, the detection of iCOMs in disks is very challenging as the dust along the line of sight might heavily absorb the lines, and the most chemically active regions are expected to be small and close (few au) to the central object (Walsh et al. 2014).

Evolved Pre-Main Sequence Star:

The small dust grains in the protoplanetary disk coagulate into larger rocks, known as planetesimals, the bricks of future planets. The chemical history inherited from the previous stages could have been recorded into the icy mantles that will later form residual bodies (as comets and asteroids). Later on, this material could be delivered to a potentially habitable young planet and contribute to the emergence of life. Indeed, all molecules detected in comets are also observed in star-forming regions, even if the measured abundances are not exactly the same (Walsh et al. 2014; Bianchi et al. 2019b; Drozdovskaya et al. 2018, 2019). The chemical link between the earliest and the latest stages of star formation is still an open question. Recent studies report the comparison of the chemical content between the different phases of a planetary system formation with bodies in the Solar system (such as comets). The abundances of some iCOMs in young Class 0/I protostars and comets, such as methyl formate ($HCOOCH_3$) and ethanol (CH_3CH_2OH), are similar within a factor of 10. On the other hand, for other iCOMs, as formamide (NH_2CHO) and acetaldehyde (CH_3CHO), the difference can be larger than a factor 30. In summary, it is not yet possible to address a general trend for all the iCOMs abundances between the first stages of star formation (Class 0 and I objects) and comets. However, the composition of volatile species in comets and planetesimals is suggested to be partially inherited from the prestellar and protostellar phases (Bianchi et al. 2019b; Drozdovskaya et al. 2019).

Another way to try to connect chemically and physically the various phases is through the deuterium fractionation process, metaphorically called *Ariadne's thread* by Ceccarelli et al. (2014). Indeed, enhanced deuterium fractionation is observed from prestellar cores (Bacmann et al. 2003; Vastel et al. 2003, 2006; Bizzocchi et al. 2014; Chacón-Tanarro et al. 2019) to protostellar envelopes, hot corinos (Parise et al. 2004; Ceccarelli et al. 2001; Parise et al. 2002, 2006b; Manigand et al. 2019), and protoplanetary disks (van Dishoeck et al. 2003; Guilloteau et al. 2006; Öberg et al. 2012; Huang et al. 2017; Salinas et al. 2017) and can be witnessed today in comets, carbonaceous chondrites, and interplanetary dust particles.

1.3 Interstellar Complex Organic Molecules

The first molecules detected in the interstellar medium were methylidyne (CH), methylidyne cation (CH^+) and cyano radical (CN) (Dunham 1937; Swings & Rosenfeld 1937; McKellar 1940). Since then, a large number of species have been detected and from the 1960s, starting with the first detection of OH (Weinreb et al. 1963), the advent of radio telescopes contributed to a boom in the detection of more complex molecules (e.g., Yamamoto 2017; McGuire 2021). As late of May 2021, about 250 species, from simple diatomic up to 13-atoms molecules, plus fullerenes C_{60} and C_{70}, have been detected in the interstellar medium or circumstellar shells (from Cologne Database for Molecular Spectroscopy, CDMS; Müller et al. 2005) through (sub-)mm and radio observations of their rotational spectral lines or by optical and infrared observations of their electronic or vibration-rotation spectra. A recent summary of the detected molecules in the ISM with relative references and history can be found in McGuire (2018, 2021).

Among the detected species, a lot of organic compounds are present. Indeed, more than

80% of them are C-bearing species. In 2009, Herbst & van Dishoeck defined the Complex Organic Molecules (or COMs) as C-bearing molecules with more than six atoms. Later on, in 2017, Ceccarelli et al. completed the definition considering that these molecules are only complex in the interstellar context, in contrast to what chemists would consider complex in the terrestrial context. Therefore the *i* letter was added to the COMs acronym in order to refer to *interstellar* Complex Organic Molecules (or iCOMs). It is possible to make a further distinction: the detected organic species can be saturated or unsaturated (Herbst & van Dishoeck 2009; Yamamoto 2017). Saturated species are rich in hydrogen atoms so that the C atoms are usually bonded with other atomic elements by single bonds; for example, CH_3OCH_3 or CH_3OH. Unsaturated species, on the other hand, miss some of these hydrogen atoms, so that their structure contains multiple double/triple bonds, for example, carbon-chain molecules (e.g., C_nH_x) or cyanopolyynes (with chemical formula HC_nN, n=3,5,7,...). Therefore, considering that most common terrestrial organic molecules tend to be fully saturated or near-saturated, we can consider the iCOMs complex saturated molecules. However, with this definition, fully saturated species with only C and H, such as CH_3CH_2, are usually not considered to be iCOMs, but hydrocarbons. Therefore, the presence of heteroatoms[5] is needed in the definition.

In this thesis, I refer to iCOMs as interstellar Complex Organic Molecules that are "saturated C-bearing molecules with more than six atoms and containing heteroatoms".

The first iCOMs have been observed in massive star formation regions (Rubin et al. 1971), while in 1987 was performed one of the first unbiased spectral surveys, at mm wavelengths, of a prototype massive star-forming region, the Orion Molecular Cloud (Blake et al. 1987). iCOMs are very abundant at the center of the core of a forming star where the protostellar radiation heats the surroundings leading to the sublimation of the icy grain mantles forming a hot and dense region in which the iCOMs abundance is enhanced. This region, defined as compact ($\leq$ 0.1 pc), with high density ($\geq 10^6$ cm^{-3}), and high temperature ($\geq$ 100 K), is called *hot core* (e.g., Blake et al. 1987; Kurtz et al. 2000; van der Tak 2004). The detection of these species in low mass star-forming regions, which will eventually form Solar-like planetary systems, came much later. In 2003, Cazaux et al. detected the spectral lines of several iCOMs, such as $HCOOCH_3$ and $(CH_3)_2O$, towards the low mass protostar IRAS 16293-2422. For the first time, complex chemistry was discovered in a Solar-like protostar, showing that it was not a peculiarity of high mass protostars, setting a direct link between the organic chemistry of the ISM with the Solar system one. For the analogy to the hot core of massive protostars, this hot ($\geq$ 100 K), dense ($\geq 10^7$cm^{-3}) and compact ($<$ 100 au) region surrounding low mass protostars is called *hot corino* (Ceccarelli 2004; Ceccarelli et al. 2007) and since then, more hot corinos have been discovered (see Section 1.4.1).

More recently, iCOMs have been detected also in starless core (e.g., McGuire et al. 2020; Agúndez et al. 2021; Cernicharo et al. 2021a,b) and prestellar cores (e.g., Bacmann et al. 2012; Cernicharo et al. 2012; Vastel et al. 2014; Jiménez-Serra et al. 2016; Punanova et al. 2018; Scibelli & Shirley 2020; Scibelli et al. 2021) and in low-mass jet driven outflow shocks (e.g, Bachiller et al. 2001; Arce et al. 2008; Codella et al. 2009, 2015a, 2017, 2020a; Lefloch et al. 2017).

iCOMs are important for three main reasons: i) they represent the dawn of organic chemistry in space; ii) they may perhaps be linked (through the different phases of star and planet formation) to the emergence of life acting as building blocks for prebiotic molecules; iii) their formation and destruction in the interstellar environment is a crucial point in order to assess

---

[5] A heteroatom is, strictly, any atom that is not carbon or hydrogen

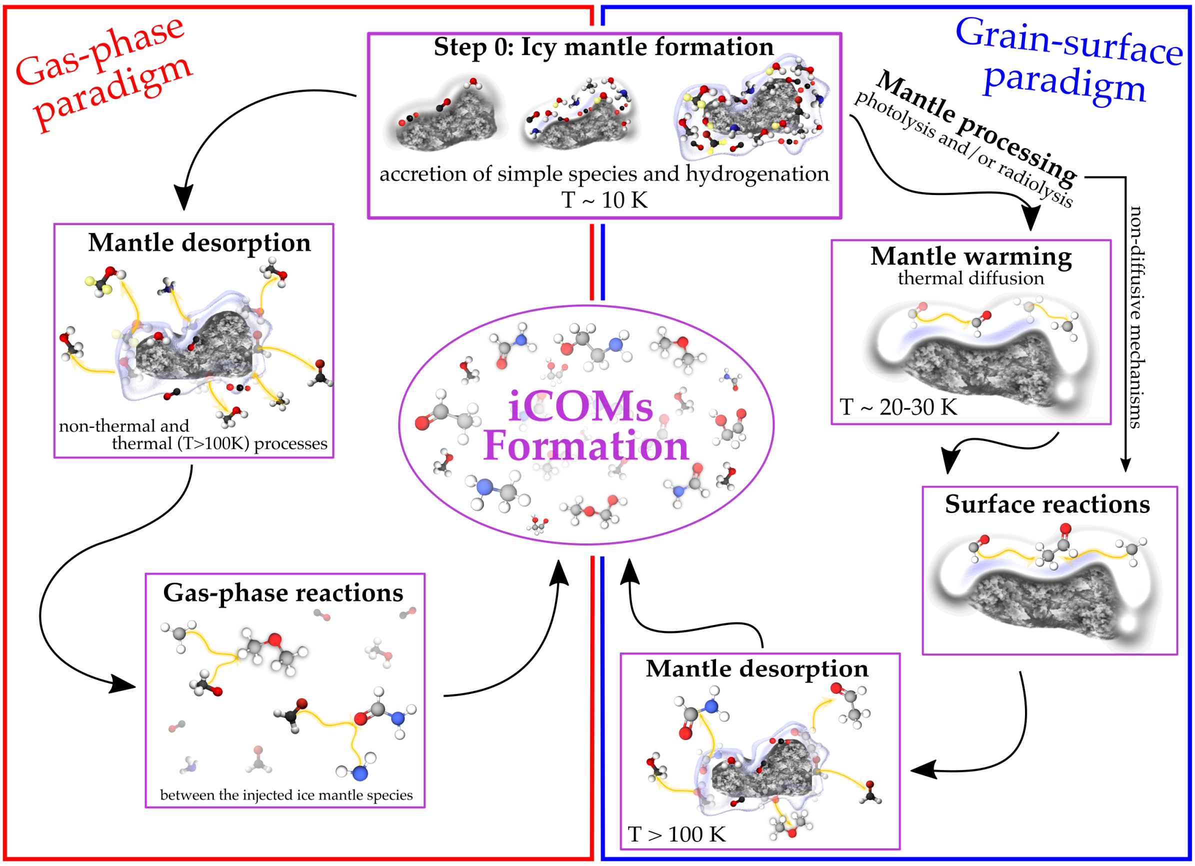

Figure 1.5: Scheme of the two main paradigms for the formation of iCOMs in warm sources as hot corinos.

the ultimate complexity of the ISM, and it is a real challenge for astrochemists (e.g., De Duve 2011; Caselli & Ceccarelli 2012; Öberg & Bergin 2021).

1.3.1 iCOMs formation: gas phase vs grain surface chemistry

Although the presence of iCOMs in the ISM is known since the 1970s (Rubin et al. 1971), still there is not a reliable theory that can fully explain the observed abundances in the various environments. Several models and theories have been then developed to explain the observed iCOMs abundances and, nowadays, two main paradigms are invoked (see e.g. Herbst 2017): iCOMs could be either synthesized on the grain surfaces (e.g. Garrod & Herbst 2006; Garrod 2008) or in the gas phase (e.g. Millar et al. 1991; Charnley et al. 1992; Balucani et al. 2015; Skouteris et al. 2017).

Figure 1.5 shows the two pathways, that have the same starting point, i.e. the formation of simple hydrogenated molecules, like H_2O, H_2CO, CH_3OH and NH_3, and oxidized (e.g., CO_2) on dust grain mantles during the cold ($\leq$ 20 K) prestellar phase (e.g. Tielens & Hagen 1982; Ioppolo et al. 2011). Then, in the gas phase paradigm, the chemical content of these ices is sublimated in the warm region (T>100 K), and the molecules released into the gas undergo hot gas-phase reactions leading to iCOMs (Charnley et al. 1992; Caselli et al. 1993). On the other hand, the grain surface paradigm assumes that, as the temperature slowly rises (T>20–30 K), the radical species frozen in the ice start to diffuse, and if they meet, they could react to form iCOMs that sublimate in the gas once the temperature is high enough (e.g. Garrod & Herbst 2006; Garrod 2008).

Until about 2003, the (warm) gas-phase chemistry was the most accredited paradigm for the iCOMs formation in hot cores/corinos (with temperatures of 100-300 K). This paradigm lasted for about two decades until new laboratory experiments and theoretical computations challenged it. For example, the formation of methyl formate (CH_3OCHO), through a gas phase reaction involving methanol (CH_3OH) and formaldehyde (H_2CO), both species sublimated from grain mantles, has an activation barrier that makes the reaction too slow to produce the observed abundances (Horn et al. 2004). Additionally, laboratory experiments showed that large molecules are broken up into small pieces through dissociative recombination instead of forming new iCOMs. For example, the recombination of protonated methanol, CH_3OH^+, with an electron is not leading to the methanol formation but rather to a three-body break-up producing CH_3, OH, and H due to the fragmentation of the C–O bond (Geppert et al. 2005, 2006). The same happens with the recombination of CH_3CHO^+ that does not lead to the formation of acetaldehyde (Vigren et al. 2007).

As a result, a new paradigm was proposed in 2006, which assumes that iCOMs form on the icy dust grain mantles, through a direct combination of radicals (Garrod & Herbst 2006). This paradigm is supported by laboratory studies that have been able to produce iCOMs through energetic processing of interstellar ice analogs (e.g., Hagen et al. 1979; Strazzulla et al. 1983; Tielens & Allamandola 1987; Linnartz et al. 2015; Öberg et al. 2009; Mart´ın-Doménech et al. 2020). However, models based on this paradigm are still not able to reproduce the observations in hot corinos and molecular shocks (e.g., Coutens et al. 2016; Müller et al. 2016; Ligterink et al. 2018b). Additionally, the reactions between radicals are not simply barrierless and straightforward as previously thought. Indeed, surface radical-radical reactions have activation energy barriers (e.g., due to the interaction of the radical to the ice), and competitive reactions other than the formation of iCOMs exist, such as direct H-abstraction. The possibility that an iCOM is formed, or the competitive H-abstraction reaction takes place, may as well depend on the relative orientation of the radicals (e.g, Enrique-Romero et al. 2016, 2019, 2020). Furthermore, surface reactions depend on the local surface conditions and its composition. For example, Lamberts et al. (2019) found barrierless reactions between HCO and CH_3 on CO surfaces to form acetaldehyde (CH_3CHO), while Enrique-Romero et al. (2019, 2021) found clear differences on the reactivity of radicals happening inside a cavity or on a flat surface.

As said in the previous paragraph, several iCOMs were also detected in prestellar cores and cold envelopes of low-mass protostar (Öberg et al. 2010; Cernicharo et al. 2012; Jaber et al. 2014) where the dust temperature is less than 30 K. In these cold environments, radicals cannot move and scan the surface of the dust mantles with the consequence that the radical-radical coupling reactions cannot take place. Additionally, if iCOMs form for whatever other mechanism on the grain ice mantles, the way they are ejected into the gas phase (where they are detected) must be non-thermal. One possible non-thermal mechanism is chemical desorption. Based on this mechanism, the product of a strongly exothermic surface chemical reaction can be injected into the gas phase thanks to the energy released by the reaction itself. The idea is that, part of this energy could be used to break the interaction of the product with the surface (Duley & Williams 1993; Garrod et al. 2007; Minissale & Dulieu 2014; Minissale et al. 2016). Recently, Pantaleone et al. (2020) studied the H + CO reaction on crystalline model ice using molecular dynamics simulation. They found that the HCO product does not undergo chemical desorption, and instead, it remains attached at the ice surface as a consequence of fast and very efficient energy absorption by the ice. Molecules with much weaker binding energies, formed after a strongly exothermic reaction, such as H_2 formed from the coupling of two H atoms, could easily be released into the gas phase. Indeed, a part of the released chemical reaction energy can be absorbed by the ice locally heating the surface for a short time. Then, weakly bound species, like CO, could be released into the gas phase (Pantaleone et al. 2021).

In conclusion, grain-surface chemistry cannot be the only pathway for the formation of all iCOMs. Gas-phase reactions must play a key role (Vasyunin & Herbst 2013; Balucani et al. 2015; Ruaud et al. 2015).

Once the precursor molecules, formed in the icy mantle of interstellar grains, are thermally or non-thermally desorbed, gas-phase reactions can occur. These reactions will regulate the formation and destruction routes of various species. Understanding the possible routes is a crucial point for astrochemical modeling. The gas-phase chemistry includes ion-neutral and neutral-neutral reactions. The former are important for the destruction of various species in the gas phase, and they are studied using both experimental and theoretical methodologies (e.g., Ascenzi et al. 2019; Skouteris et al. 2019; Ayouz et al. 2019). The latter, which were once considered to be much less important, have regained interest in the last decade thanks to the combination of experimental evidence and computational chemistry (e.g., Shannon et al. 2014; Barone et al. 2015). Many of the molecular processes included in the chemical networks used in astrochemical models (such as KIDA or UMIST Wakelam et al. 2015; McElroy et al. 2013) have either never been investigated in laboratory experiments or studied under conditions that do not reproduce the interstellar ones (for the temperature or pressure). Recently, thanks to the CRESU (Cinétique de Réaction en Ecoulement Supersonique Uniforme; Sims et al. 1994; Smith et al. 2004; Canosa et al. 2008) technique it is possible to explore these reactions at the very low temperatures of the interstellar clouds (11.7 K; Smith & Rowe 2000; Jiménez et al. 2015; Ocaña et al. 2019), and with the crossed molecular beam (Schreel et al. 1993; Ter Meulen 1997) technique at the very low densities of interstellar clouds (e.g., Casavecchia et al. 2009; Balucani et al. 2011). However, experimental techniques can either reproduce low temperature or low number density conditions. Therefore, theoretical calculations are essential to support the interpretation of the experimental results, to assist their extrapolation, and to provide a realistic estimate of the reaction rate coefficients and product branching ratios when no experimental data are available (e.g., Shannon et al. 2014; Sleiman et al. 2018). Important examples of neutral-neutral gas phase reactions estimated theoretically, with consequent astrochemical implications, are provided in Balucani et al. (2015, 2018); Vazart et al. (2015); Skouteris et al. (2017, 2018); Vazart et al. (2020).

In summary, both gas phase and grain surface chemistry are crucial in the iCOMs formation (and destruction), and still, there is no clear pathway leading to one or the other. Both processes have to be investigated and studied in detail using the combination of theoretical computations, laboratory experiments, and astronomical observations in order to constrain the formation of each detected species.

1.4 Protostellar Environments

1.4.1 The warm heart of protostars: Hot corinos, iCOMs retail shops

As explained in Section 1.2, Class 0 sources represent a stage where a thick envelope obscures the central object even at the near-infrared wavelengths. The outer envelope, dominating the (sub-)mm continuum emission, is cold (T$\sim$20 K) so that the molecules containing heavier elements (as C, N, O) are at least partially frozen onto the icy grain mantles. On the other hand, at the center of the envelope, the core warms up the surroundings creating an inner region of relatively warm dust and gas. Indeed, Ceccarelli et al. (1996) predicted that a source of 65 $L_\odot$ possesses a region of about 300 au in diameter with dust temperatures greater than 100 K. At these temperatures, the water ice grain mantles evaporate so that the components of the grain mantles are injected into the gas phase. Therefore, the abundance of the corresponding molecules increases with respect to the one in the cold envelope.

The first observations that support this hypothesis were performed by Ceccarelli et al. (2000a) and Maret et al. (2002) toward two Class 0 sources, IRAS 16293-2422 and NGC1333 IRAS 4, tracing water line emission. However, the interpretation of their data was difficult, as the observations performed with ISO (Infrared Space Observatory) had relatively poor spatial and spectral resolution. On the other hand, Ceccarelli et al. (1998, 2000b); Loinard et al. (2000), and Cazaux et al. (2003) observed IRAS 16293-2422 at mm and sub-mm wavelengths, using the single dish JCMT (James Clerk Maxwell Telescope) and IRAM 30m telescopes, with a spectral and spatial resolution of orders of magnitude higher than those obtained with ISO. These observations highlighted an extremely rich organic inventory at the center of the IRAS 16293-2422 source with abundant amounts of complex O- and N-bearing molecules such as formaldehyde H_2CO, methanol, CH_3OH, formic acid, HCOOH, acetaldehyde, CH_3CHO, methyl formate, CH_3OCHO, dimethyl ether, CH_3OCH_3, acetic acid, CH_3COOH, methyl cyanide, CH_3CN, ethyl cyanide, C_2H_5CN, and propyne, CH_3CCH. These type of molecules, iCOMs (see Section 1.3), were also detected in the hot regions of massive protostars, hot cores, but with lower abundances. That suggests that, in low-mass protostars, the hot region surrounding the central object is smaller and chemical different with respect to the massive hot core. For that reason, Ceccarelli (2004) proposed to call these regions *hot corinos*, as small hot cores, being compact ($<$ 100 au), hot ($>$ 100 K), and dense ($>10^7$ cm^{-3}) regions. Being the chemistry dominated by the sublimation of the icy mantles they are perfect iCOMs retail shops.

After IRAS 16293-2422, the hunt of hot corino regions around low mass protostars started. In 2004, Maret et al. presented a first survey of the formaldehyde emission in a sample of eight Class 0 protostars obtained with the IRAM 30m and JCMT millimeter telescopes. With their analysis, the authors noticed that, in some sources, the formaldehyde abundance has a jump in the central region. For that reason, they proposed the presence of a hot corino region in seven additional sources. In particular, NGC 1333 IRAS 4A (Bottinelli et al. 2004a), NGC 1333 IRAS 2A and IRAS 4B (Bottinelli et al. 2007) were confirmed later on to be hot corino sources. In the same year, Bottinelli et al. (2004b); Kuan et al. (2004) performed the first interferometric observations of two complex molecules, CH_3CN and $HCOOCH_3$, toward the IRAS 16293-2422 binary system imaging, for the first time, the two hot corinos. With the advent of ALMA, IRAS 16293-2422 was targeted by the first unbiased sub-millimeter line survey, PILS (Protostellar Interferometric Line Survey; Jørgensen et al. 2016), in order to extensively study the binary

Table 1.2: Low- and intermediate- mass Class 0 and I protostars that possess a hot corino region with more than one iCOM.

Source[a]	RA [h:m:s]	DEC [° :′:″]	Cloud	Distance [pc]	$L_{\rm bol}$ [$L_\odot$]	References
Low-mass Class 0						
IRAS 19347+0727 (B335)	19:37:00.93	+07:34:09.90	Barnard 335	∼ 100	∼ 1	[15]
IRAS16293-2422 A	16:32:22.88	−24:28:36.50	ρ-Ophiucus	∼ 140	∼ 21	[19],[10],[7],[18],[23]
IRAS16293-2422 B	16:32:22.62	−24:28:32.49	ρ-Ophiucus	∼ 140	∼ 21	[19],[10],[7],[18],[23]
IRAS 18148-0440 (L483)	18:17:29.95	-04:39:39.55	Aquila Rift	∼ 200	∼ 13	[30], [16]
∗*BHR71-IRS1*	12:01:36.49	-65:08:49.38	Coalsack	∼ 200	∼ 13	[34]
NGC1333 IRAS 4A2	03:29:10.43	+31:13:32.12	Perseus	∼ 300	∼ 6	[6],[32],[13],[22],[31]
NGC1333 IRAS 4B	03:29:12.02	+31:13:08.02	Perseus	∼ 300	∼ 6	[8],[13]
NGC1333 IRAS 2A1	03:28:55.57	+31:14:37.07	Perseus	∼ 300	∼ 16	[17],[8],[27],[13]
Barnard1b-S	03:33:21.35	+31:07:26.37	Perseus	∼ 300	∼ 0.3	[24]
∗*L1448-C*	03:25:38.87	+30:44:05.33	Perseus	∼ 300	∼ 9	[2], [35]
∗*L1455 IRS 1 (Per-emb 17)*	03:27:39.11	+30:13:02.96	Perseus	∼ 300	∼ 4	[35]
∗*NGC1333 IRAS 1A (Per-emb 35 A)*	03:28:37.10	+31:13:30.77	Perseus	∼ 300	∼ 13	[35]
∗*B1-c (Peremb 29)*	03:33:17.88	+31:09:31.74	Perseus	∼ 300	∼ 5	[35]
∗*IC 348 MMS (Per-emb 11A)*	03:43:57.07	+32:03:04.76	Perseus	∼ 300	∼ 0.1	[35]
∗*Ser-emb 1*	18:29:09.10	+00:31:30.90	Serpens	∼ 440	∼ 4	[1],[25]
∗*Ser-emb 8*	18:29:48.10	+1:16:43.70	Serpens	∼ 440	∼ 6	[1]
∗*OMC-2 FIR4 (HOPS-108)*	05:35:27.07	+05:10:00.37	Orion	∼ 450	∼ 38	[33], [11]
∗*MMS5 (HOPS-88)*	05:35:22.47	+05:01:14.34	Orion	∼ 450	∼16	[9]
∗*MMS9-a (HOPS-78A)*	05:35:25.97	+05:05:43.34	Orion	∼ 450	∼9	[9]
HH 212	05:43:51.41	-01:02:53.10	Orion	∼ 450	∼ 9	[12], [3], [20], [21]
Low-mass Class I						
∗*L1551-IRS5*	04:31:34.14	+18:08:05.10	Taurus	∼ 141	∼ 35	[5]
NGC1333 SVS13A	03:29:03.76	+31:16:03.80	Perseus	∼ 300	∼ 32	[13],[4]
Barnard1-a	03:33:16.67	+31:07:55.10	Perseus	∼ 300	∼ 1	[28]
∗*Ser-emb 11*	18:29:06.76	+00:30:34.30	Serpens	∼ 440	∼ 2	[26]
∗*Ser-emb 17*	18:29:06.20	+00:30:43.10	Serpens	∼ 440	∼ 4	[1]
Intermediate-mass Class 0						
Cep E-B	23:03:13.10	+61:42:26	Cepheus	∼800	∼ 75	[29]

[a] All the hot corinos in *italic* with the symbol ∗ have been discovered during the PhD thesis.

[b] References: [1] Bergner et al. (2019), [2] Belloche et al. (2020) [3] Bianchi et al. (2017), [4] Bianchi et al. (2019a), [5] Bianchi et al. (2020), [6] Bottinelli et al. (2004a), [7] Bottinelli et al. (2004b), [8] Bottinelli et al. (2007), [9] Bouvier et al. (2022), [10] Cazaux et al. (2003), [11] Chahine, L. et al. (2022), [12] Codella et al. (2016b), [13] De Simone et al. (2017), [14] Hsu et al. (2020), [15] Imai et al. (2016), [16] Jacobsen et al. (2019), [17] Jørgensen et al. (2005), [18] Jørgensen et al. (2016), [19] Kurtz et al. (2000), [20] Lee et al. (2017b), [21] Lee et al. (2019a), [22] López-Sepulcre et al. (2017), [23] Manigand et al. (2020), [24] Marcelino et al. (2018), [25] Martin-Domenech et al. (2019), [26] Mart´ın-Doménech et al. (2021) [27] Maury et al. (2014b), [28] Öberg et al. (2014), [29] Ospina-Zamudio et al. (2018) [30] Oya et al. (2017), [31] Sahu et al. (2019), [32] Taquet et al. (2015), [33] Tobin et al. (2019), [34] Yang et al. (2020), [35] Yang et al. (2021).

system and to understand the origin of the detected iCOMs (Coutens et al. 2016; Ligterink et al. 2018a; Jørgensen et al. 2018; Manigand et al. 2019, 2020, see e.g.,). Then, in 2014, the first interferometric line survey, CALYPSO (Continuum And Line Young ProtoStellar Object Maury et al. 2014a), was performed in the Perseus cloud with the IRAM Plateau de Bure interferometer (PdBi). Observing 17 low-mass Class 0 and I sources, they concluded that ∼30% of the sample shows emission from at least three iCOMs (Maury et al. 2014b; De Simone et al. 2017; Belloche et al. 2020).

Recently, new, large, and unbiased line surveys, PEACHES (Perseus ALMA Chemistry Survey; Yang et al. 2021) and ORANGES (ORion Alma New GEneration Survey; Bouvier et al. 2021, 2021b) were performed. The main results are that ∼50% of the sample shows iCOM emission in the case of Perseus and ∼30% in Orion. The comparison of these two surveys suggests that environmental properties can influence the formation of hot corinos. Yet, after almost twenty years of hunting using mm observations, only about 20 hot corinos showing emission of more than one iCOM are known (see Table 1.2), including not only Class 0 sources but the more evolved Class I. If considering the sources where only hot and compact methanol emission is detected, the number of hot corinos doubles up to about 40 (see Table 1.3)

Many of the hot corinos listed in Table 1.2 are part of binary systems, revealed thanks to high angular resolution observations. Indeed, recent continuum surveys found that 40–60% of protostars are multiple systems (Maury et al. 2014b; Tobin et al. 2016). Interestingly, with the first hot corino maps (obtained mainly thanks to high resolutions interferometric observations), it became clear that the two objects in a given binary system can substantially differ in molecular spectra. Typical examples are IRAS 16293-2422, NGC 1333 IRAS 4A, and CepE-mm. The first is a binary system composed of two sources separated by $5''$ ($\sim$ 720 au): source A is weaker in the mm continuum emission and brighter in the iCOMs lines than source B (Cazaux et al. 2003; Pineda et al. 2012; Jørgensen et al. 2016; Manigand et al. 2020). NGC 1333 IRAS 4A is composed of IRAS 4A1 and IRAS 4A2, separated by $1.''8$ (∼540 au); while the former dominates the mm continuum emission, only the latter shows bright iCOMs lines at mm wavelengths (Taquet et al. 2015; López-Sepulcre et al. 2017; De Simone et al. 2017). Unlike IRAS 4A and IRAS 16293-2422, the CepE-mm intermediate-mass binary system shows a different behavior. Indeed, the source that dominates the mm continuum emission, CepE-A, is the one that shows a rich chemical content, while the companion CepE-B lacks iCOMs emission (Ospina-Zamudio et al. 2018). This leaves open the question on why coeval objects are so different in millimeter molecular spectra.

1.4.2 Outflows and shocks: unique astrochemical laboratories

Outflows from young protostars are a spectacular manifestation of stars being born. They are ubiquitous and energetic phenomena emanating from young protostellar objects, covering a wide range of wavelengths from UV to radio (Bachiller 1996; Frank et al. 2014). The first observed outflow dates back to the early 1950s when Herbig (1951) and Haro (1952) discovered some nebulous patches in Orion, with peculiar emission line spectra. In the beginning, their nature was not so obvious; first, they were associated with stellar winds (Osterbrock 1958) and much later with an outflow from a young star interacting with the surrounding material (Schwartz 1975). With the emergence of cm-mm astronomy, the profiles of CO rotational lines revealed high-velocity outflowing molecular gas from young protostars, characterized

Table 1.3: Low- and intermediate- mass Class 0 and I protostars where only hot and compact CH$_3$OH is detected. Please note that all these studies were performed after the thesis start.

Source	RA [h:m:s]	DEC [$^\circ$:$'$:$''$]	Cloud	Distance [pc]	L^a_{bol} [$L_\odot$]	References
Low-mass Class 0						
L1448-2A (Per-emb 22A)	03:25:22.41	+30:45:13.26	Perseus	∼300	∼ 3	Yang et al. (2021)
L1448-2B (Per-emb 22B)	03:25:22.35	+30:45:13.11	Perseus	∼300	∼ 3	Yang et al. (2021)
L1448 IRS 3A	03:25:36.50	+30:45:21.90	Perseus	∼300	∼ 9	Yang et al. (2021)
Per-emb 33A	03:25:36.38	+30:45:14.72	Perseus	∼300	∼ 4	Yang et al. (2021)
NGC 1333 IRAS 7 SM1 (Per-emb 18)	03:29:11.27	+31:18:31.09	Perseus	∼300	∼ 4	Yang et al. (2021)
NGC 1333 IRAS 7 SM2 (Per-emb 21)	03:29:10.67	+31:18:20.16	Perseus	∼300	∼ 60	Yang et al. (2021)
L1455 IRS 4 (Per-emb 20)	03:27:43.28	+30:12:28.88	Perseus	∼300	∼ 2	Yang et al. (2021)
Per-emb 42	03:25:39.14	+30:43:57.90	Perseus	∼300	∼ 1	Yang et al. (2021)
Per-emb 2	03:32:17.92	+30:49:47.81	Perseus	∼300	∼ 2	Yang et al. (2021)
Per-emb 5	03:31:20.94	+30:45:30.24	Perseus	∼300	∼ 2	Yang et al. (2021)
B1-d (Per-emb 10)	03:33:16.43	+31:06:52.01	Perseus	∼300	∼ 1	Yang et al. (2021)
HH 211 MMS (Per-emb 1)	03:43:56.81	+32:00:50.16	Perseus	∼300	∼ 2	Yang et al. (2021)
B5 IRS 1 (Per-emb 53)	03:47:41.59	+32:51:43.62	Perseus	∼300	∼ 5	Yang et al. (2021)
IC 348 MMS (Per-emb 11c)	03:43:57.70	+32:03:09.82	Perseus	∼300	∼ 1	Yang et al. (2021)
G211.47−19.27S (HOPS-288)	05:39:56.097	−07:30:28.403	Orion	∼ 450	∼ 130	Hsu et al. (2020)
G210.49−19.79W (HOPS-168)	05:36:18.860	−06:45:28.035	Orion	∼ 450	∼ 50	Hsu et al. (2020)
G192.12−11.10	05:32:19.540	+12:49:40.190	Orion	∼ 450	–	Hsu et al. (2020)
CSO33-b-a (HOPS-56-B)	05:35:19.41	+05:15:38.41	Orion	∼ 450	∼ 23	Bouvier et al. (2022)
FIR6c-a (HOPS-409)	05:35:21.36	+05:13:17.85	Orion	∼ 450	∼8	Bouvier et al. (2022)
SIMBA-a (HOPS-96)	05:35:29.72	+ 04:58:48.60	Orion	∼ 450	∼6	Bouvier et al. (2022)
Intermediate-mass Class 0						
OMC-2 FIR3 (HOPS-370)	05:35:27.633	-05:09:34.40	Orion	∼450	∼ 360	Tobin et al. (2019)
G208.68−19.20N (HOPS-87)	05:35:23.486	−05:01:31.583	Orion	∼ 450	∼ 40	Hsu et al. (2020)

[a] Values from Enoch et al. (2009), Sadavoy et al. (2014), Young et al. (2015), (Furlan et al. 2016), Tobin et al. (2019), Bouvier et al. (2021).

by a bipolar structure (Snell et al. 1980). The first performed surveys revealed that outflows are common around young protostars (Lada 1985; Fukui et al. 1993; Wu et al. 2004). Since then, the number of reported molecular outflows has dramatically increased to more than a hundred. Although it is not yet clear the physical mechanism that produces the outflows, it is now believed that all young stellar objects undergo periods of copious mass loss, with the flow coming from a stellar or circumstellar region.

The observed ejections from young protostars can be identified as outflowing material in form of collimated jets and wide-angle winds (Bachiller 1996; Arce et al. 2007; Bally et al. 2007; Frank et al. 2014; Lee 2020). On the one hand, at low-velocity (1–30 km s^{-1}), rotating extended winds come out from the accretion disk down to $\sim$ 10 au scales (Konigl & Pudritz 2000; Lee et al. 2000, 2001, 2018). On the other hand, protostellar jets are highly collimated structures and usually episodic. They propagate away from the protostar at high-velocity ($\sim$100km s^{-1}) creating bow shocks when impacting with the surrounding medium. They are thought to be launched from the innermost part ($\leq$1 au) of the accretion disk (Lee et al. 2017a). Both jets and winds are expected to play a key role in facilitating the accretion process. As the central source evolves from Class 0 to I, the outflow power declines, and the primary winds tend to become increasingly atomic, and less molecular (e.g., Bontemps et al. 1996; Arce & Sargent 2006; Seale & Looney 2008; Mottram et al. 2017).

When the ejected material propagates into the ISM, it pushes and swept-up the surrounding material, forming molecular outflows around the jet axis (Bachiller 1996; Lee et al. 2000; Arce et al. 2007). The surrounding medium is perturbed via shock waves that heat and compress the gas triggering several processes (that do not occur in quiescent environments), such as molecular dissociation, warm gas chemical reactions, disruptions of grain mantles, and grain cores. Therefore, outflows can contribute to the chemical enrichment of the gas surrounding young stars (e.g., Bachiller & Pérez Gutiérrez 1997; Bachiller et al. 2001). Indeed, the action of bipolar outflows on the surrounding gas can enhance some molecular abundances. In particular, one of the most extreme examples is SiO, whose abundance is enhanced up to six orders of magnitude at the heads and along the axes of some molecular outflows (Bachiller et al. 1991; Martin-Pintado et al. 1992; Bachiller et al. 1998b; Codella et al. 1999; Nisini et al. 2007; Tafalla et al. 2015). The SiO enhanced abundance is due to the sputtering (gas-grain collisions) of the grain mantles and shattering (grain-grain collision) of the grain refractory cores, both processes releasing SiO and Si (which is quickly oxidized in SiO) into the gas-phase (e.g., Flower & Pineau des Forets 1994; Caselli et al. 1997; Schilke et al. 1997; Gusdorf et al. 2008a,b; Guillet et al. 2011).

The first observational evidence of iCOMs in protostellar outflows dates back to the late 90s. Indeed, CH_3OH and H_2CO have been observed to be enhanced in several outflows by a factor $\sim$100 (e.g., Bachiller et al. 1995; Bachiller & Pérez Gutiérrez 1997; Bachiller et al. 1998a, 2001; Maret et al. 2004; Jørgensen et al. 2004; Parise et al. 2006a). They were found tracing material at high density and high temperature, namely shocked regions. Later on, Arce et al. (2008) and Codella et al. (2009) reported the first detection in the B1 shock of the L1157 outflow (hereafter L1157-B1) of heavier iCOMs, such as CH_3OCHO, CH_3CN and C_2H_5OH. Successively, more and more complex species were detected in this shock region (Sugimura et al. 2011; Yamaguchi et al. 2012; Lefloch et al. 2017, 2018). These results converted the shock region L1157-B1 into the prototype for studies on shock chemical complexity. Besides L1157-B1, there are very few observations of iCOMs in other low-mass protostellar outflows. So far, iCOMs other than methanol have been detected toward a handful of object with single-dish facilities: formamide (NH_2CHO) toward L1157-B2 (Mendoza et al. 2014), acetaldehyde (CH_3CHO) toward IRAS 2A and IRAS 4A (Holdship et al. 2019) and acetaldehyde and dimethyl ether (CH_3OCH_3) toward SMM4-W (Öberg et al. 2011b). However, it is worth noting that all these works refer to single-dish observations at relatively low spatial angular resolution and are, by definition, unable to disentangle the different spatial distribution of iCOMs

With the first interferometric observations of L1157-B1, it was possible to image single species, discovering the presence of a spatial chemical segregation among several iCOMs (e.g., methanol, formamide and acetaldehyde; Codella et al. 2015a, 2017, 2020a). The comparison between observations and astrochemical models allows characterizing the dominant formation routes of the detected iCOMs. Indeed, the observations provide the chemical stratification in a time-dependent structure, while the model provides the evolution of the molecular abundances in the post-shocked gas. The iCOMs could have been released into the gas phase as a result of sputtering/shattering, or the result of post-shocked gas-phase reactions between precursor species released from the grain mantles. In particular, Codella et al. (2017) could constrain the dominant path for the formation of NH_2CHO (formamide) as the gas-phase reaction between H_2CO and NH_2 (Barone et al. 2015; Vazart et al. 2016; Skouteris et al. 2017). The same conclusion was reached later on by Burkhardt et al. (2019).

In summary, the shocked gas along outflows driven by low-mass protostars is a unique environment to study how the iCOMs can be formed.

1.5 Context and Thesis goals

1.5.1 The DOC Project

This thesis is part of the DOC (Dawn of Organic Chemistry) project (P.I. Cecilia Ceccarelli), funded by the ERC (European Research Council) under grant No 741002. The main objective of the project is to understand the dawn of organic chemistry, namely the start and the evolution of organic chemistry in Solar-type systems, to understand whether the chemical seeds of life are universal and to what extent. In other words, the goal of DOC is to build a reliable theory for organic chemistry in nascent Solar type systems.

In order to achieve this goal, the project is organized into three interconnected Work Packages (WPs), each having specific tasks and objectives (see Figure 1.6). The WPs are briefly summarized below.

The first WP (WP1) is based on astronomical observations obtained by state-of-the-art facilities, such as IRAM-30m, NOEMA, VLA, and ALMA. The objective is to obtain iCOMs abundance and their distribution in a large sample of prestellar cores, hot corinos, and outflow shocks. The WP1 work is organized in four interacting tasks: i) build a systematic inventory of the organic and molecular content of the selected sample; ii) identify the different chemical classes of Solar type protostars and whether/how the diversity is affected by the protostar environment and past history, namely the prestellar phase; iii) understand whether and how the organic complexity evolves from the large collapsing envelope to the planet-formation scales ($\leq$100 au); iv) provide constraints on the gas ionization, its value, and spatial distribution, in prestellar and protostellar sources.

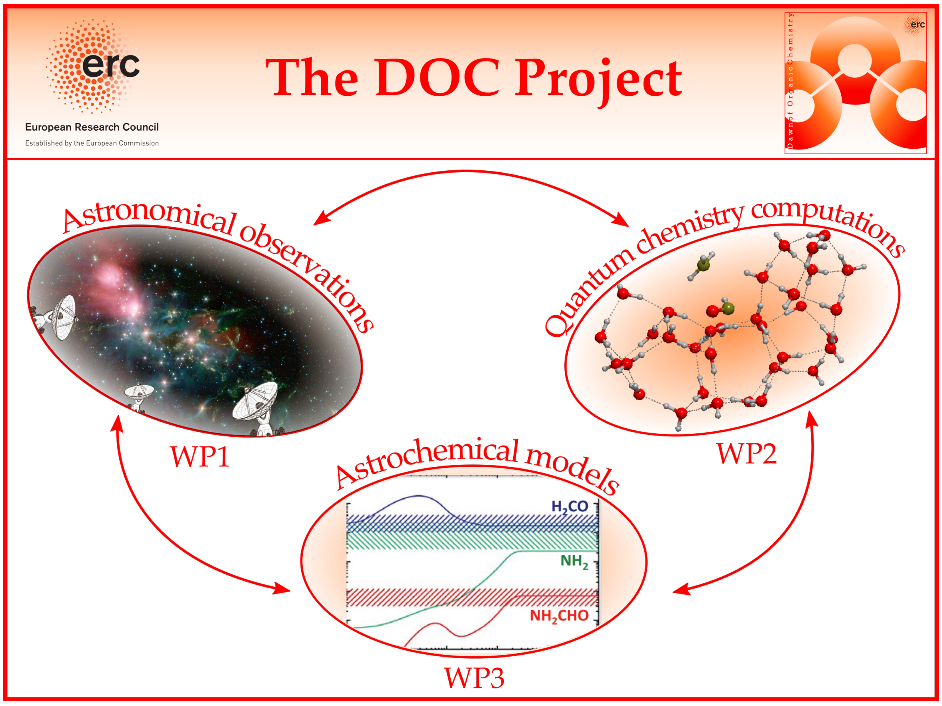

Figure 1.6: Scheme of the DOC projects and its work packages: i) WP1 on astronomical observations obtained with IRAM-30m, NOEMA, and ALMA; ii) WP2 on quantum chemical computations; iii) WP3 on astrochemical models and tools.

The second WP (WP2) is based on theoretical quantum chemistry computations with the objective to obtain systematic unprecedented state-of-the-art computations on reactions occurring on amorphous water ice surfaces and in the gas phase, in addition to having a systematic review of the gas-phase reactions involving COMs. The work is divided into four tasks. The first two tasks focus on key grain-surfaces processes, specifically hydrogenation and radical combination. The last two tasks focus on gas-phase reactions, namely computations of reaction energetics and kinetics, and search for new overlooked reactions.

The third WP (WP3) is based on astrochemical/physical models and tools to compare observations with model predictions. The objectives are i) to include micro-and macro- physics processes in the model, and ii) to develop new methods and tools, using up-to-date statistical methods to analyze and compare large data sets.

The interaction between the three work packages is a key element of the DOC project. Indeed, the information from the observations (WP1), namely iCOMs abundance and distribution, is used by the quantum chemical computations (WP2) to define the kind of computation to carry out. In the meantime, important reactants or products, resulting from the computations, can be targeted by future observations. The output from the observations and the computations (WP1 and WP2) is then used by astrochemical models (WP3). Indeed, the models will use the results from the computations to run model predictions that can be compared with observations.

My thesis work is based on astronomical observations of hot corinos, using (sub-)mm and cm facilities as, IRAM-NOEMA, ALMA, and VLA. It belongs to the DOC WP1, with the aim to shed light and give insight on the organic molecular complexity of Solar-type hot corinos.

The main goals of the thesis are explained with more details in the next section.

1.5.2 Thesis objectives: The early organic molecular enrichment of planet-formation zones

The Earth is the only known planet hosting life, which is based on organic chemistry. Additionally, some of the bricks of life, i.e., amino acids, are found in Solar System objects, namely comets and meteorites. That can let us think that it could be possible that the first steps of the organic chemistry that led to terrestrial life started during the formation of our Solar System.

As shown in Section 1.2, the formation of Sun-like stars goes through different stages, starting from a collapsing molecular core that evolves into a protostar, a protoplanetary disk, and eventually a planetary system. Together with the physical evolution, a chemical evolution takes place (see Figure 1.4). The discovery of iCOMs (see Section 1.3) in the youngest phase of the formation of Solar-type stars, i.e., hot corinos (see Section 1.4.1), raises a main important question: Is there a direct link between the first stages of Solar-like star formation and the latest ones? In other words, is the chemical complexity inherited from one stage to the other?

In order to answer this question, it is crucial to fully characterize, from a chemical point of view, the early stages of the formation of Sun-like stars, in particular the chemically rich hot corino phase. In my thesis, I aim to address two main questions:
Q1: What is the origin and the nature of hot corinos?
Q2: How these complex organic molecules are synthesized?

Q1: On the hot corino chemical origin and nature

As explained in Section 1.4.1, not every protostar possesses a hot corino region. Indeed, before the start of this thesis, only about ten hot corinos were known, all discovered using (sub-)millimeter observations. Therefore, after twenty years of studies, the nature and origin of hot corinos was still unclear. The first determinant factor for this situation is that observing hot corinos is not an easy task. Indeed, being compact objects ($\leq 1''$), high-resolution and high sensitivity facilities are required. With the advent of NOEMA and ALMA interferometers, the first hot corinos have been mapped, and the first line surveys were performed. Surprisingly, several hot corinos in binary systems show very different millimeter molecular spectra. What is the reason for this spectral diversity at mm wavelengths? It could reflect a real intrinsic molecular diversity, or it can be simply due to observational biases. This is, however, a crucial issue to solve to understand the hot corino nature and origin.

There are two complementary strategies to unveil the hot corino nature: i) to use a statistical approach studying a large number of objects or ii) to extensively characterize the chemistry of a single object. In this thesis, I used the second approach, focusing on the Class 0 binary system NGC 1333 IRAS 4A, that is described in detail in Section 3.1.3. Briefly, the two companions, IRAS 4A1 and IRAS 4A2, show very different millimeter molecular spectra. To understand the origin of the observed spectral differentiation, I used a novel approach: observations at centimeter wavelengths with the VLA interferometer. Complementing the new observations in the centimeter with the existing ones in the millimeter, I wanted to investigate the contribution of the dust opacity as a major observational bias.

Q2: On the synthesis of complex organic molecules

As explained in Section 1.3, the formation of iCOMs is still a matter of hot debate. There are two main paradigms: i) the formation of iCOMs exclusively on the interstellar ices and ii) iCOMs formation via gas-phase chemical reactions of sublimated grain mantle species. Constraining which paradigm is more efficient in forming iCOMs and where is not an easy task. Indeed, in the past years, to constrain their formation routes, astrochemical model predictions have been compared with observed iCOMs abundances in two regions: hot corinos and low-mass jet-driven outflow shocked regions. In particular, the latter approach has been proven to be very efficient, as it provides the time dependence as an additional constraint. Indeed, once the shock has passed, the chemistry of the shocked gas evolves with time.

In this thesis, I followed the second approach observing the outflowing gas from the binary system IRAS 4A. At the beginning of the thesis, very few observations of iCOMs in low-mass protostellar shocks have been performed with single dish facilities. However, being single dish observations, the spatial distribution, and consequently the detailed information on the emitting region, is missing. In contrast, high-angular interferometric observations provide the possibility to map the iCOMs emission toward shocked regions. The spatial information, together with the time dependence, can be used to constrain the iCOMs formation route. Indeed, as done by Codella et al. (2017) to constrain the formation route of formamide.

Within the IRAM/NOEMA SOLIS observational Large Program, my goal was to explore the molecular complexity of the IRAS 4A outflows and study the possible spatial differentiation between iCOMs and the implication obtained by comparing the iCOMs abundances with astrochemical model predictions, in close contact with chemists and modelers of the DOC team.

Collateral effects: the large scale view

Working on the IRAS 4A outflows with the NOEMA observations, I ran into some interesting molecular features in the surrounding region of IRAS 4A that were not showing evidence of being connected with the outflows. The star forming region hosting IRAS 4A is known to be associated with filamentary structures and to have been heavily shaped by external triggers, such as the explosion of one or more supernovae and other forms of stellar feedback activity, and by the dynamical interaction of internal outflows and external bubbles with the quiescent molecular cloud (e.g., Sandell & Knee 2001; Dhabal et al. 2018, 2019).

The thesis structure

The thesis is organized in four main parts:

- ⋆ Part I: It contains this introductory section (Chapter 1). It gives a scientific background and context, together with the goal of the thesis;
- ⋆ Part II: It contains the methodology used to achieve the goal of the thesis (Chapter 2). In particular, Section 2.1 describes the interferometric, the aperture synthesis, and the data reduction techniques. The state-of-the-art interferometric facilities, mainly used in this thesis, are described in Section 2.2. Part of the data used for this thesis work belongs to the IRAM/NOEMA observational Large Program SOLIS, described in Section

2.3. Finally, Section 2.4 gives an overview of the molecular lines analysis techniques used in this thesis;

- Part III: It consists of the scientific results of this thesis work that have been published (or submitted) in refereed journals, or in the process of being submitted. Additionally, future planned works are described.
  In particular, Chapter 3 gives an overview of the system studied in this work, NGC 1333 IRAS 4A (or IRAS 4A).
  Chapter 4 aims to answer the first question of the thesis (Q1). It presents the results of the VLA observations toward the IRAS 4A protostars and the future works planned to complete the frame.
  Chapter 5 aims to answer the second question of the thesis (Q2). It presents the results of the NOEMA observations toward the outflows of IRAS 4A, and the future works planned in the framework of the ALMA Large Program FAUST.
  Finally, Chapter 6 describes the *collateral effects* of the thesis, namely the works that were not initially planned but that are naturally part of this thesis. In particular, there are the results of the NOEMA observations toward the region surrounding IRAS 4A and the future planned observations with the SOFIA telescope toward SVS13 A, sibling of IRAS 4A in the NGC 1333 region.

- Part IV: It summarizes the main conclusions of this thesis and the future perspectives traced by this thesis work (Chapter 7 and 8).

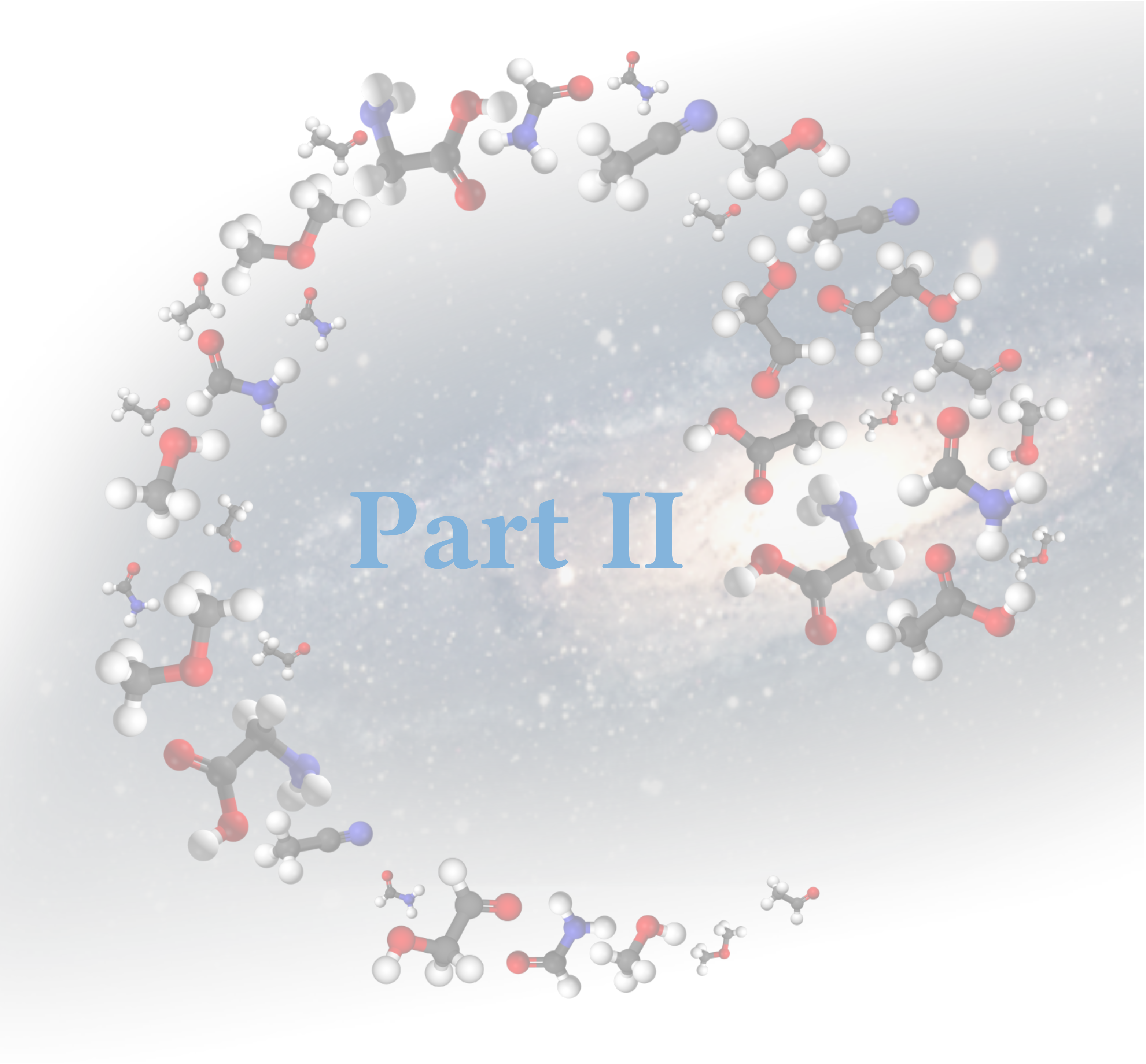

Part II

2 Methodology

My thesis work is mainly based on the analysis of interferometric observations in the (sub-) millimeter and centimeter range, using the spectral lines as diagnostic tools.

2.1 RadioAstronomy: Interferometry basic concepts

2.1.1 The need of interferometric observations

A central issue in observational astronomy is the quest for angular resolution: the theoretical resolution of a perfect circular optical system depends on the system aperture and the observed wavelength according to the Rayleigh criterion (Rayleigh 1879; Born & Wolf 1999): According to the Rayleigh criterion:

$$\theta = \frac{1.22\lambda}{\mathrm{D}} \tag{2.1}$$

where λ is the wavelength observed, D is the diameter of the optical system, and θ is the minimum angle (in radians) under which two distinct sources can be distinguished. The ability of an optical system to distinguish two separate point sources depends on the overlap of their Airy disks (central luminous disk surrounded by concentric rings less luminous) produced by diffraction (see Figure 2.1). In particular, two points are distinguishable if the central maximum of the first diffraction figure corresponds to the first minimum of the second diffraction figure. In order to achieve higher resolution, it can be possible to either decrease the observing wavelength or increase the diameter of the telescope The first option leads to operating on longer

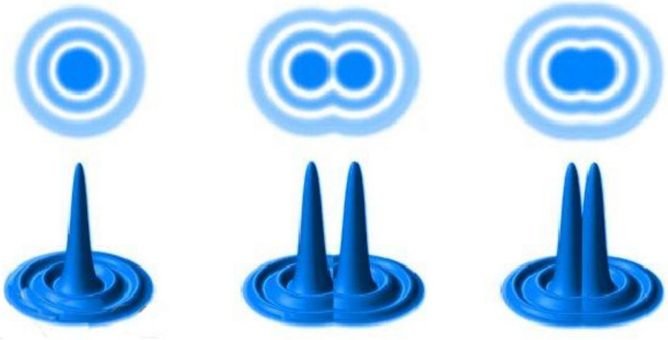

Figure 2.1: Diffraction model from an uniformly illuminated circular aperture.

wavelengths, still, the choice of the observation waveband is deeply linked to the investigated phenomena; the second option leads to building a telescope with very large apertures. Indeed, to observe very low spatial scales (such us 50-100 au, which corresponds to $\sim 0.3 - 0.7''$ at 150 pc, typical distance for a nearby star forming region), the telescope needs to have an aperture of 400-800 m in diameter. These small scales are typical for protostellar/protoplanetary regions. Actual telescopes do not have this aperture, and it is very difficult to build one of these huge dimensions, for both economical and structural reasons.

To solve this problem, it is possible to use observing techniques based on the principle of interferometry. It combines the signal from different receivers which observe the same source at the same time together; in that way, an array of separate telescopes, mirror segments, or radio antennas can work together as a single instrument in order to provide (theoretically) the angular resolution of a huge telescope with an aperture equal to the separation between the components. Some limitations of this instrument can be that it does not collect as much light as the complete single instrument mirror and the maximum angular size of a detectable emission source is limited by the minimum gap between the detectors of the array.

In order to create high-resolution observations combining signals from separate telescopes (or antennae), it is necessary to keep the light coherent within a fraction of a wavelength over long optical paths. The interferometric approach is based on the Young double-slit experiment with monochromatic light. Indeed, to make it works, the light coming from the same wavefront has to be correlated. The atmosphere can affect the coherence of the signal creating variable delays on the traveling light that depends on the wavelength observed (e.g., at centimeter wavelengths the effect comes principally from high atmospheric altitudes). Unlike optical and infrared spectral regions, radio waves are not strongly affected by atmospheric turbulence as the wavelengths are larger than the typical turbulence cells. Therefore, interferometry can be better exploited in radio rather than in the optical range as the wavefronts' coherence can be preserved even for wide separations between single telescopes.

2.1.2 Two-element interferometer

Figure 2.2 shows the simplest radio interferometer that consists of two antennas A1 and A2 separated by a *baseline* vector $\tilde{\mathbf{b}}$. Defining $\mathbf{s}$ the unit vector in the direction of a distant source, $\mathbf{b} \cdot \mathbf{s}$ is the difference of optical path to reach the two antennas that causes a geometrical delay τ_g. Indeed, the geometrical delay depends on the relative orientation of the baseline respect to the waves propagation: $\tau_g = \mathbf{b} \cdot \mathbf{s}/c$, where c is the speed of light.

A plane electromagnetic wave (with frequency $\nu = \omega/2\pi$) induce the voltage $V_1 \propto Ee^{i\omega t}$ at the outputs of the antenna A_1, while at the outputs of A_2 we have $V_2 \propto Ee^{i\omega(t-t_g)}$. The signals from the two antennas are then multiplied and coherently integrated in time by the correlator, taking into account the delay.

$$R(\tau) \propto \frac{E^2}{T} \int_0^T e^{i\omega t} e^{-i\omega(t-\tau_g)} \tag{2.2}$$

If T >> $2\pi/\omega$ (the time average is much longer than the time of a single full oscillation), the average over time T will not differ much from the average over a single full period. Then,

$$R(\tau) \propto \frac{\omega}{2\pi} E^2 \int_0^{1\pi/\omega} e^{i\omega\tau_g} \propto \frac{E^2}{2} e^{i\omega\tau_g} \quad . \tag{2.3}$$

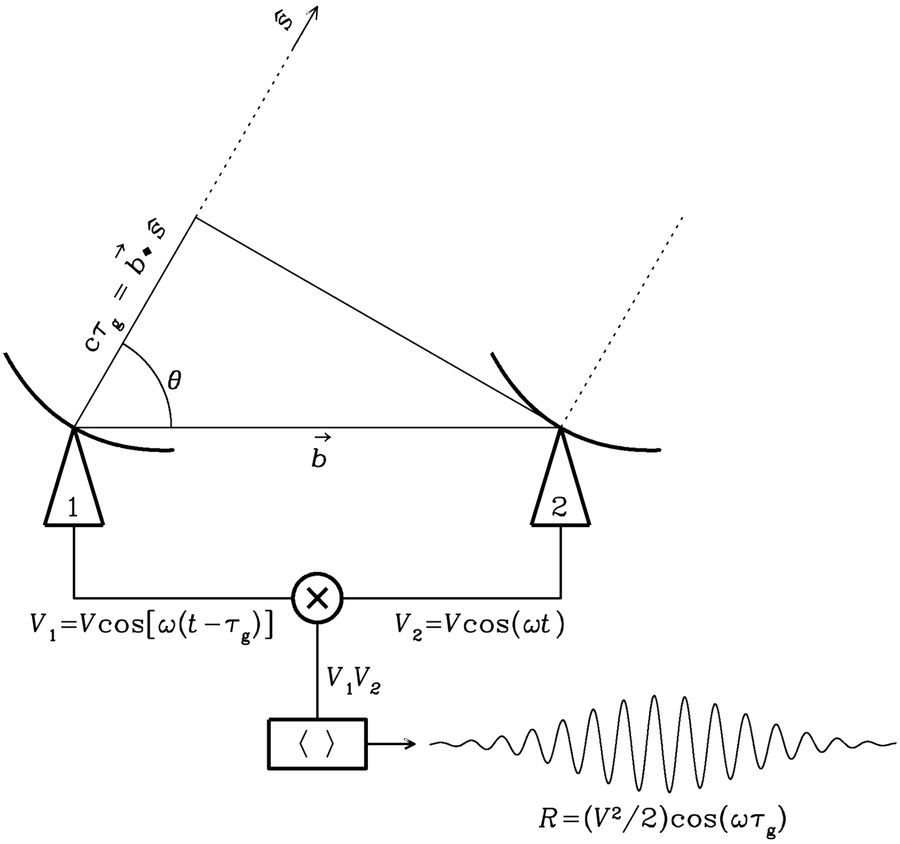

Figure 2.2: Schematic diagram of a two-element correlation interferometer. The antenna output voltages are V1 and V2, the geometrical delay is τ_g. Credits: NRAO

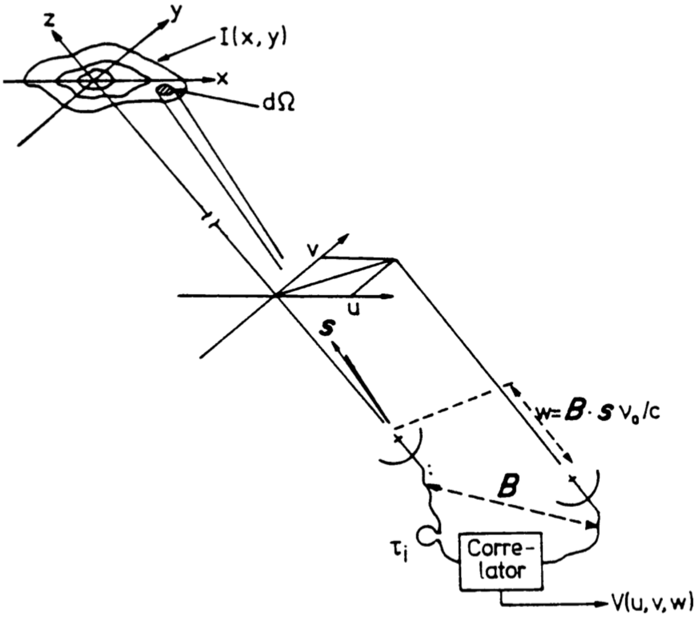

Figure 2.3: A representation of the geometry and coordinates for interferometric observations. (Wilson et al. 2009)

Therefore, the output of the interferometer correlator R varies with τ_g; Since **s** is slowly changing due to the rotation of the earth, τ_g will vary, and we will measure interference fringes as a function of time.

If the size of the source is bigger than the distance between two adjacent positive or negative fringes, it becomes resolved out and the response of the interferometer remains the same as the source moves across the sky. Therefore, for imaging large structures short baselines are required; on the other hand, long baselines are necessary to measure small-sized sources.

For a source of brightness $I_\nu(s)$ the power received per bandwidth $d\nu$ from the solid angle $d\Omega$ is $A(s)I_\nu(s)d\Omega d\nu$, where A is the effective collecting area in the direction s. Therefore, the total response of the interferometer is the so-called *visibility function*:

$$R(\mathbf{b}) = \int_\Omega \int A(s)I_\nu(s)e^{i\omega\tau_g}d\Omega d\nu \quad . \tag{2.4}$$

The main challenge of interferometry is to retrieve the best representation of $I_\nu(s)$ from the Visibility function $R(\mathbf{b})$.

2.1.3 Coordinate system

The first step to determine the source brightness I_ν from the Visibility function is to choose a convenient coordinate system. Let consider a far, incoherent, extended region, whose position is located by the vector s_0 such that the unit vector **s** is equal to $s_0 + \boldsymbol{\sigma}$ with $|\sigma| = 1$. $\sigma = (x, y, z)$ is defined in the Cartesian coordinates where the plane xy is the projection of the celestial sphere on the tangent plane with tangent point and origin defined by s_0 (see Figure 2.3). Therefore:

$$R(\mathbf{b}) = e^{i\omega(\mathbf{b}\cdot\mathbf{s}/c)}d\nu \int \int_S A(\boldsymbol{\sigma})I_\nu(\boldsymbol{\sigma})e^{i\omega\mathbf{b}\cdot\boldsymbol{\sigma}/c}d\boldsymbol{\sigma} \tag{2.5}$$

where the first exponential is defining the phase in the center of the image, and the integral is the *Visibility*

$$V(\mathbf{b}) = \int \int_S A(\boldsymbol{\sigma})I_\nu(\boldsymbol{\sigma})e^{i\omega\mathbf{b}\cdot\boldsymbol{\sigma}/c}d\boldsymbol{\sigma} \quad . \tag{2.6}$$

The baseline vector **b** can be specified in a new coordinate system, such that $\omega\mathbf{b}/(2\pi c) = (u, v, w)$, where (u, v, w) are measured in units of the wavelength $\lambda = 2\pi c/\omega$, and w is chosen in the direction of the source s_0, v point in the north direction, and u in the local east. The two set of coordinates, (x, y, z) and (u, v, w) are related as $\nu\mathbf{b} \cdot \mathbf{s}/c = ux + vy + wz$ and $\nu\mathbf{b} \cdot \mathbf{s_0}/c = w$. Therefore, the equation of Visibility in the new coordinate system become:

$$V(u, v, w)e^{-i2\pi w} \simeq V(u, v, 0) = \int_{-\infty}^{+\infty} \int_{-\infty}^{+\infty} A(x, y)I(x, y)e^{i2\pi(ux+vy)}dxdy \tag{2.7}$$

having considered that, i) the factor $e^{-i2\pi w}$ is the phase correction to apply to the observed V to measure the visibility in the uv plane (w = 0); ii) outside the primary beam[1] of the telescope A(x,y)=0; iii) the mapped region of the sky sufficiently small so that $z = \sqrt(1 - x^2 - y^2) \sim$ const ~ 1.

---

[1] the Primary Beam is the Full Width High Power of the individual antenna that gives also the Field of View (FoV) $\sim \lambda/d$.

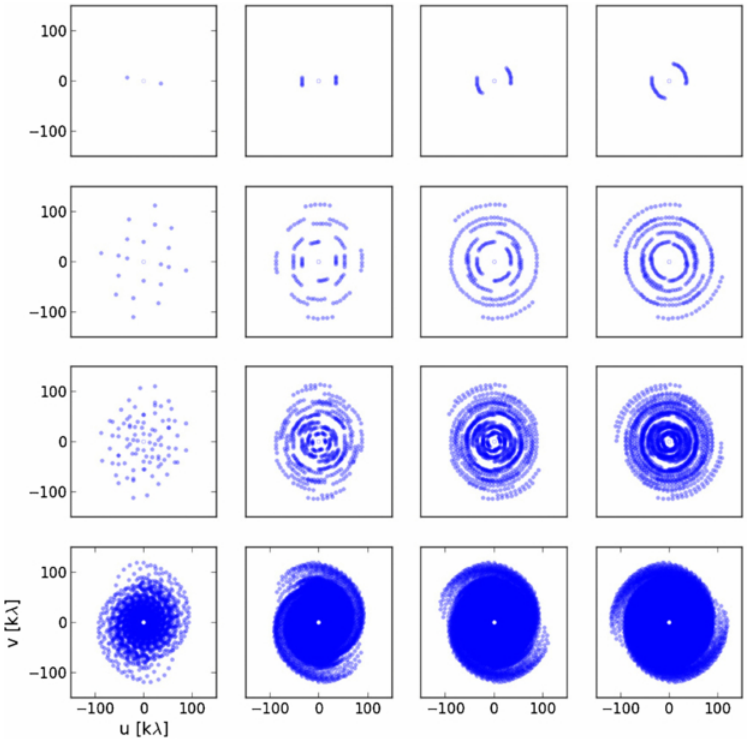

Figure 2.4: uv coverage of an interferometer os 2,5,10 and 50 antennas (top to bottom), and observing for 10s , 2hr, 4hr, 6hr (left to right) (Avison & George 2012).

Performing the inverse Fourier transform it is possible to derive the intensity I', that is the intensity modified by the primary beam shape $A(x, y)$:

$$I'(x, y) = I(x, y)A(x, y) = \int_{-\infty}^{+\infty} V(u, v, 0)e^{i2\pi(ux+vy)}dudv \quad . \tag{2.8}$$

It is clear that interferometric observations and brightness distribution of the sky are linked by the Fourier Transform. For this reason, the (u, v) plane is the *Fourier plane* referred to the *image plane* (x, y).

2.1.4 Synthesis imaging

The spacing and the orientation of two antennas at a given time can be then described in terms of fringe visibilities, i.e. Fourier transforms of the brightness distribution in the sky, and can be identified as a single point on the uv plane. Accordingly, performing the inverse Fourier Transform of the fringe visibilities, it is possible to obtain a map of the sky. This technique is called *synthesis or aperture imaging*.

A crucial parameter in interferometric observations is the *uv coverage*. It shows where, on the Fourier plane, the image has been sampled. A good image quality requires a good coverage of the uv plane and It is possible to take advantage of the Earth rotation to improve the uv coverage. Indeed, when the antennas are pointing a target in the sky, they measure the visibility function in a point (u, v) of the plane; as the Earth rotates and the telescope keeps tracking the source, the projected baseline changes, and after 24 hours of observations it draws an ellipse in the uv plane. If the interferometer is made by more than two elements at different mutual distances, the uv coverage is improved, as different baselines correspond to different *uv-distances*. A simplified scheme is shown in Figure 2.4. Actually, the visibility $\mathrm{V(u, v)}$ is equal to its complex conjugate $\mathrm{V^*(u, v)}$. This translates into the fact that the orientation of the baseline formed by two antennas repeats (with the phase reversed) after half rotation of the Earth, i.e. after 12 hours observations, no new information is obtained keeping tracking the source. We then call *Visibilities* the measurements collected scanning portions of the $\mathrm{(u, v)}$ plane, and they consist of the values of amplitude and phase of the correlator output for each baseline at a given time.

Retrieving the sky brightness distribution $\mathrm{I(x, y)}$ is not a straightforward process considering that the interferometer is affected by some limitations: i) the angular resolution is limited by the maximum values of $\mathrm{(u, v)}$ and ii) the minimum spacing between two antennas will set a minimum $\mathrm{u, v}$ distance in the map, iii) the missing $\mathrm{(u, v)}$ components, due to the limited uv coverage, make the image worse. Additionally, the instrumental noise and the atmospheric variations affect the measured visibilities, therefore, they need to be *calibrated* in order to retrieve their real values.

In order to retrieve $\mathrm{I(x, y)}$, Fast Fourier Transform (FFT) procedures are used. In order to use the FFT in an efficient way, the visibility function must be placed on a regular grid with total sizes that are powers of 2 of the sampling interval. Since the observations, do not usually lie in a regular pattern, an interpolation scheme is used through a convolution procedure.

Dirty image and dirty beam

The transfer function usually generates side-lobes; accordingly Fourier components are generally added with a weighting procedure to reduce the unwanted components. Even with this handling, the response of the system to a point source still presents perceptible side-lobes. This is called *dirty beam* and it is the equivalent of the Point Spread Function, PSF, typically used in optical observations, and can be considered as a transfer function that distorts the image.

Indeed, instead of getting the true brightness distribution of the sky (Eq. 2.8) a *dirty image* is obtained at this stage:

$$\mathrm{I_D(x, y)A(x, y)} = \int \mathrm{V(u, v)S(u, v)e^{i2\pi(ux+vy)}dudv} \tag{2.9}$$

where $\mathrm{S(u, v)}$ is the sampling function, that is equal to 1 when the uv plane is sampled, and 0 elsewhere. The equation (2.9) can be considered as the Fourier transform of the product of the two functions V and S, so we can apply the convolution theorem[2] to obtain

$$\mathrm{I_D(x, y)A(x, y) = I(x, y)A(x, y) * D(x, y)} \tag{2.10}$$

where $\mathrm{D(x, y)} = \int \mathrm{S(u, v)e^{i2\pi(ux+vy)}dudv}$ is the *dirty beam*. Since $\mathrm{S(u, v)}$ can be deduced knowing the geometry of the array and the location of the source in the sky, the form of the dirty beam can be obtained, and, consequently, the brightness $\mathrm{I(u, v)}$ can be derived by deconvolution methods. Deconvolution is always a non-linear process, and it is necessary to formulate a series of hypotheses and constraints to help to select plausible solutions.

---

[2] The convolution theorem states that a Fourier transform of a product of functions is the convolution of their Fourier transforms

Cleaning algorithms

The CLEAN algorithm (Högbom 1974) is the standard deconvolution method used, most commonly in the image plane, in order to retrieve the brightness I(u, v). It is based on the assumption that the radio source we want to image is an ensemble of a finite number of point sources in an empty background. The position and intensity of these point sources are found with an iterative approach, and the final deconvolved image results in a sum of these point components convolved with a CLEAN beam, usually Gaussian. The main steps (see Figure 2.5) are:

1 Create the dirty map and find the intensity and position of the brightest point;

2 Subtract from the dirty image, at the peak position, a fraction of the dirty beam and store the position and the intensity in a model as "CLEAN component";

3 From the residual map, find the brightest point intensity and position unless the peak is below the threshold specified by the user;

4 Repeat points 2 and 3 until the number of iteration set by the user is reached (unless no other bright peak is found in the residual map). The goal is to have a residual map with only noise;

5 Take all the CLEAN components, add the residual noise, and convolve them with a properly chosen CLEAN beam (usually a Gaussian fitted to the central lobe of the dirty beam).

Several modification to the original algorithm have been made (e.g. Clark, Cotton and Shwab; Clark 1980; Schwab & Cotton 1983) to reduce the computed time under certain conditions. However, there are still some concerns about the uniqueness and stability of the produces solutions due to the non-linearity of the operation.

A critical factor in the cleaning process is the *weighting* to be applied to the gridded data, as the recorded data are not uniformly distributed across the uv plane but are usually concentrated towards the center. The first and most common is the *natural weighting* which favors the signal-to-noise (S/N) ratio to the resolution. Indeed, in this case, each cell is given a weight proportional to the number of visibility points in it. A second option is the *uniform weighting* that applies equal weights to each sample (the gridded data in a cell), increasing the resolution but decreasing the signal-to-noise ratio. Indeed, equal weights are given to the cell regardless of the number of measurements in each cell. A third, and intermediate option, is the *Briggs or Robust weighting* that smoothly varies between natural and uniform weighting based on the signal-to-noise ratio of the measurements and a tunable parameter (called *robust*) that defines a noise threshold. High signal-to-noise samples are weighted by sample density to optimize for the shape of the point spread function, and low signal-to-noise data are naturally weighted to optimize for sensitivity. If the robust parameter is equal to 2 we retrieve the natural weighting, while if it is -2 we have the uniform. Please not the the given description applies to the CASA package and it can be package dependent.

Calibration

The calibration is the first step in data reduction. It is the process that determines the complex correction factors that must be applied to each visibility in order to make them as

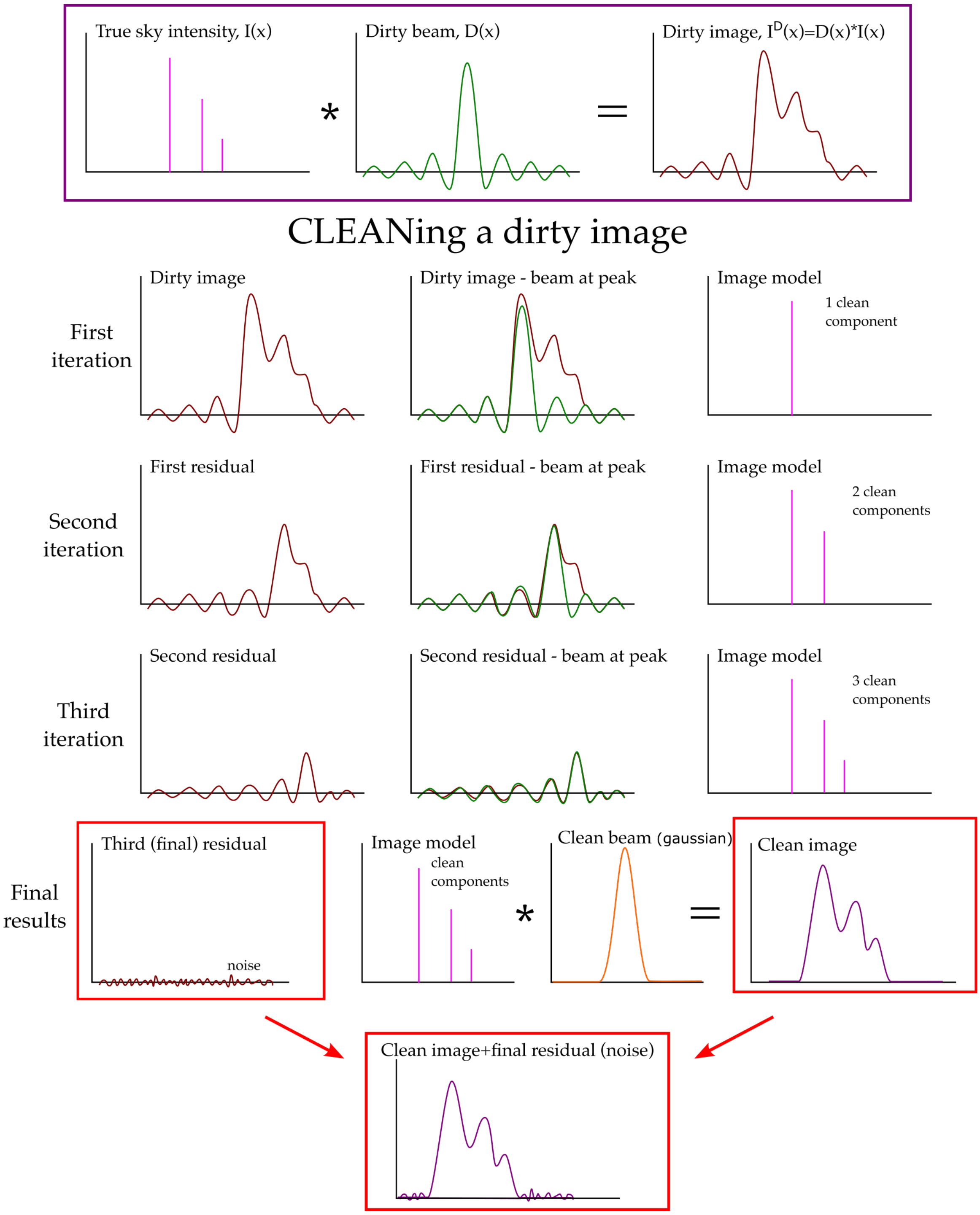

Figure 2.5: Schematically explanation of the steps of the CLEAN procedure to deconvolve a dirty image. Please note that only a *fraction* of the dirty beam is subtracted from the dirty image. The Figure adapted from López-Sepulcre A. slides in the context of the ITN/ACO school (https://aco-itn.oapd.inaf.it/events/aco-schools/aco-year-1-school).

close as possible to what an idealized interferometer would measure. In this way, when the data is imaged an accurate picture of the sky is obtained. In order to determine the correction factors, some references well known sources must be chosen: they are called *calibrators*.

Band-pass gain calibrator: It is used to correct the different responses across the band-pass, therefore it is largely used for spectral line observations. It needs to be a very bright, flat-spectrum source (usually a quasar), to have a good signal-to-noise for each channel used for the observations. Good bandpass calibration is a key to the detection and accurate measurement of spectral weak and broad features. Additionally, it can also be the limiting factor in the dynamic range of continuum observation. It is usually observed at least once every observing session, for a time interval that depends on its brightness.

Flux calibrator: It is used to correct the value of the absolute amplitude of the source in order to compensate for atmospheric opacity and loss of signal within the interferometer. It is crucial to use a very bright and point-like source with a well-known flux. If the source is resolved or has spectral lines, it must be very well modeled.

Time gain or phase calibrator: It is used to compensate temporal variations of the phase of the correlated signal on different antennas or baselines. These time-dependent variations are mainly due to: i) weather conditions; ii) different atmospheric opacity; iii) heating of the receivers structures during the observations; iv) in some cases, deformation of the antennas due to gravity.

It is important to choose accurately the time gain calibrator. It must be a point-like source, in order to have zero phase, quite close to the science target (usually within 10°), and must be observed frequently (e.g., typically in time intervals of 10 minutes, the calibrator is observed for 2 minutes and the source for the remaining 8 minutes). Note that the cycle time between target and calibrator depends on the telescope, configuration, and wavelength. This provides a model of atmospheric phase changes along the line of sight toward the science target, that can then be compensated for in the data.

Self-calibration The actual state-of-the-art interferometers, such as NOEMA, JVLA, and ALMA, have so high sensitivity that the image is often limited by residual calibration errors. Therefore, the noise of the image can be higher than the thermal noise as amplitude and phase errors scatter power across the image. To surpass this, if the targeted source has enough signal-to-noise (S/N) ratio, it is possible to calibrate the instrument on the source itself to obtain a better image. This is the *self-calibration* method.

The self-calibration is carried out in the uv plane, and it is possible to restrict it to an improvement of phase alone or to both phase and amplitude. If properly used, this method leads to a great improvement in interferometer images of compact intense sources. On the contrary, if it is used on objects with low S/N, it may give very wrong results by concentrating random noise into one part of the interferometer image. Therefore, it has to be used with caution.

The recommended signal to noise to perform self-calibration depends on the number of antennas. Indeed, in the case of phase-only self-calibration, the target source needs to be detected with a S/N$>$ 3 (or 10) in a solution time less than the time for significant phase (or

Figure 2.6: The IRAM–NOEMA observatory and its 11-antenna array scanning the Sky. Credits: IRAM

amplitude) variations for all baselines to a single antenna. For example, a rough estimation can be done on the image: for an array of 25 antennas, a $S/N \geq 20$ in the image is needed to attempt phase-only self-calibration. However, the S/N in the image can depend on the integration time. Therefore, the best approach is to consider the S/N ratio obtained by averaging the visibility data going into the gain solution.

Self-calibration is an iterative process. It starts with the generation of the model of the targeted source (it can be a first image generated using the CLEAN algorithm). Then this model is used to determine the gains as a function of time. The gain solutions are then applied to the data and re-imaged. These steps are repeated until the model is satisfying or the solution interval is too short to reach the necessary signal-to-noise. In general, the first attempt is done with phase-only self-calibration and the amplitude calibration is done at the end of the process only if there are amplitude-based gain artifacts in the data. Amplitude calibration should be used with caution as it can change the fluxes of both the sources and the noise in the data.

2.2 Interferometric facilities

The instruments used in the framework of my PhD Thesis for this work are three state-of-the arte interferometric facilities: NOEMA, VLA, and ALMA.

2.2.1 IRAM–NOEMA

The IRAM NOEMA (NOrthern Extended Millimeter Array, Figure 2.6) is the successor to the Plateau de Bure (PdB) observatory located in the French Alps on the wide and isolated Plateau de Bure at an elevation of 2550 meters. The construction started in 1985 and the first observations were performed with only three antennas in 1988. In 2002 the PdB interferometer was equipped with 6 antennas moving on two tracks, extending on a north-south and east-west axis, up to a maximum separation of 760 meters. In 2014, with the inauguration of the seventh antenna, the PdB interferometer passed the baton to NOEMA, with the commitment

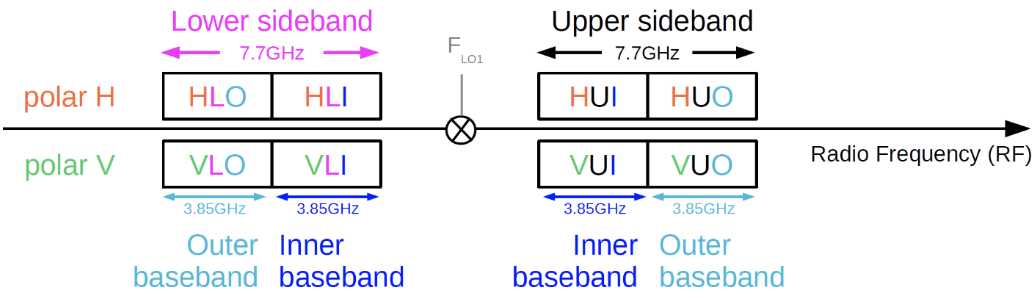

Figure 2.7: IRAM–NOEMA baseband fed to the correlator. Credits: https://www.iram.fr/.

to reach 12 antennas and increase the baseline to reach a maximum separation up to 1700 meters. NOEMA currently consists of eleven antennas, each 15 meters in diameter, that can be located up to a maximum separation of 760 m in the E-W direction and 368 m in the N-S direction. The last twelfth antenna has been commissioned, and the extension of the baseline are expected to be finished by 2022.

The antennas are equipped with three receiver bands observing in dual polarization in two side-bands (upper side-band, USB, and lower, LSB) in the 3 mm, 2 mm, and 1.3 mm atmospheric windows. The 3 mm receiver band (Band 1) covers sky frequencies between 71 and 119 GHz, the 2 mm receiver band (Band 2) covers sky frequencies between 127 to 182 GHz, and the 1.3 mm receiver band (Band 3) covers sky frequencies between 197 and 276 GHz. The receivers provide two orthogonal linear polarization that delivers a bandwidth of 7.744 GHz, in both USB and LSB simultaneously. The wide-band correlator PolyFIX can process a total instantaneous bandwidth of ∼31 GHz for up to twelve antennas that are split into two polarization in each of the two available side-bands. The centers of the two 7.744 GHz wide side-bands are separated by 15.488 GHz. Each side-band is composed of two adjacent base-bands of ∼3.9GHz width, called inner and outer baseband (see Fig. 2.7). The channel spacing is 2MHz throughout the 15.488 GHz effective bandwidth per polarization. Additionally, up to sixteen high-resolution chunks can be selected in each of the eight base-bands (i.e. up to 128 chunks in total). Each of these has a width of 64 MHz and a fixed channel spacing of 62.5 kHz.

Three primary ten-antenna configurations are available that can be combined to produce maps with different angular resolutions. These three configurations are usually scheduled during the course of a year. The most compact configuration is the D-array that allows reaching the maximum sensitivity and the lowest phase noise with a resolution of ∼ 4" at 100 GHz. The most extended configuration is the A-array that is well suited for mapping compact and strong sources providing a resolution of $\sim 1''$ at 100 GHz. The intermediate configuration is the C-array that provides fairly complete coverage of the uv plane with ∼ 2" at 100GHz. The three configurations can be used in different combinations to achieve complementary sampling of the uv plane, and to improve on angular resolution and sensitivity. The antenna half-power beam size is $50''$ at 100 GHz and the shortest possible antenna spacing is 24 m to avoid collisions between two antennas. The limitation in the short spacing can be overcome by combining additional short-spacing observations using the single-dish IRAM 30 m telescope.

In conclusion, NOEMA is the most powerful millimeter radiotelescope of the Northern Hemisphere, and one of the most advanced facilities existing today for radio astronomy.

Figure 2.8: The Jansky VLA observatory. Credits: NRAO

2.2.2 Jansky VLA

The Karl G. Jansky Very Large Array (VLA, Figure 2.8) is a centimeter-wavelength radio astronomy observatory located in central New Mexico on the Plains of San Agustin, ∼80 km west of Socorro, at an elevation of 2120 m. It is a component of the National Radio Astronomy Observatory (NRAO[3]). The array is composed of 28 antennas of 25 m in size (27 effective antennas plus one spared for maintenance) that are distributed along three arms (each 21 km long) of a track shaped in a Y-configuration. The Very Large Array project was approved in 1972, in 1975 the first antenna has been put in place, and the first interferometric observations started in 1976. In 1979 the final and 28th antenna had been delivered. In 2012, the 1970s-era electronics were replaced with state-of-the-art equipment, expanding the VLA technical capacities by a factor up to 8000, and the telescope was renamed into*Karl G. Jansky Very Large Array*.

All VLA antennas are provided with eight receivers providing continuous frequency coverage from 1 to 50 GHz. These receivers cover the frequency ranges of 1–2 GHz (L-band), 2–4 GHz (S-band), 4–8 GHz (C-band), 8–12 GHz (X-band), 12–18 GHz (Ku-band), 18–26.5 GHz (K-band), 26.5–40 GHz (Ka-band), and 40–50 GHz (Q-band). Additionally, all antennas of the VLA have receivers for lower frequencies, enabling observations at P-band (200–500 MHz), and 4-band (54–86 MHz). The correlator used is the WIDAR correlator that provides three basic modes: wideband, spectral line, and subarrays. The wideband setups available for all observing bands are: i) the 8-bit sampler, which provides 2 GHz (1GHz at L-band and 256 MHz

---

[3] NRAO is a facility of the National Science Foundation operated under cooperative agreement by Associated Universities, Inc

Figure 2.9: Panoramic view of the ALMA antennas on the Chajnantor Plateau. Credits: ESO

at P-band) total bandwidth per polarization, and ii) the 3-bit sampler that provides total bandwidths per polarization of 4 GHz (C/X-bands), 6 GHz (Ku-band), or 8 GHz (K/Ka/Q-bands). The WIDAR bandwidths are typically divided into subbands 128 MHz (64 MHz at L-band, 16MHz for P-band) wide for continuum. For spectral line observations, the correlator configuration is very flexible, allowing the use of narrower subbands (for a total of 64) in both samplers (3-bit or 8-bit). Additionally, it is possible to split the 8-bit correlator resources into multiple (up to 3) subarrays with setups completely independent in terms of observing frequency, polarization products, and integration times, but with some restrictions on the number of antennas used in each subarray.

The antennas are moved, using a big transporter, into four different arrangements, called configurations. They are denoted A, B, C, and D, from the most extended to the most compact, corresponding to a maximum antenna separation of 36.4 Km, 11.1 Km, 3.4 Km, and 1 Km respectively. The telescopes are switched between these configurations approximately every four months. The VLA resolution depends on the array configuration and the observed frequency; for the maximum available frequency (Q-band) it is possible to reach angular resolutions of $0.04''$ with A configuration.

In conclusion, VLA is the most advanced and powerful centimeter interferometer facility existing today for radio astronomy.

2.2.3 ALMA

ALMA (Atacama Large Millimeter/Submillimeter Array, Figure 2.9) is the largest ground-based international astronomical interferometer located on the Atacama Desert of northern Chile at an altitude of 5000m. The construction of the observatory goes back to 2004. North America, Eastern Asia, and Europe started to work independently to propose a telescope working at mm and sub-mm wavelengths in large magnitudes. The National Radio Astronomy Observatory (NRAO) in the United States planned a project called MilliMeter Array (MMA) with 40 8m antennas operating at 30-350 GHz. In parallel, the European Southern Observatory (ESO) planned the Large Southern Array (LSA) with 50 16m antennas operating < 350GHz. Finally, the National Astronomical Observatory of Japan (NAOJ) proposed the construction of a Large Millimeter/Submillimeter Array (LMSA) with 50 10m antennas operating at sub-mm wavelengths. However, such ambitious projects could not be developed by a single community, therefore they decided to join forces placing, in 2003, the first stone for the ALMA development. In 2011 ALMA started the first cycle of observations with 16 antennas, and in 2013 the ALMA inauguration took place.

The array is made of 66 high-precision antennas of which 54 are 12m antennas and 12 are antennas of 7m diameter. The 7m antennas plus four 12m antennas are the so-called ACA (ALMA Compact Array) designed to observe extended structures. The antennas can be moved by big and heavy transporters along the plateau to change the baseline distribution, obtaining a more extended or more compact array configuration. In the more compact configuration, the maximum baseline is 160 m, while in the most extended the maximum baseline is 16 km. The top spatial resolution reached by ALMA is 5 milli-arcseconds (mas) at 900 GHz and about 40 mas at 100 GHz in the most extended configuration. In order to recover the missing short spacing, ACA observations can be performed.

The ALMA front end can accommodate up to 10 receiver bands covering most of the wavelength range from 35–950 GHz. Each band is designed to cover a tuning range that is approximately tailored to the atmospheric transmission windows. So far, the available bands are from Band 3 to Band 10, starting at 84 GHz. Two additional bands are planned: Band 2 from 67 to 90 GHz, in development, and Band 1 from 35 to 50 GHz, in production. The receivers for Bands 3 to 8 are two-sideband (2SB) receivers, where both the upper and lower side-bands are provided separately and simultaneously for each polarization, with a bandwidth of 3.75 GHz. Bands 9 and 10 use a double side-band (DSB) receiver with two outputs, one per polarization, with an effective bandwidth of 7.5 GHz. Therefore, the effective system bandwidth available in Bands 9 and 10 is double that of the 2SB receivers (15 GHz). The data cubes can be produced up to 7680 frequency channels. The total bandwidth cannot exceed 8 GHz and the channel width can be between 3.8 kHz and 15.6 MHz.

In conclusion, ALMA is the largest ground-based (sub-)millimeter astronomical and international project existing today.

2.3 The NOEMA SOLIS Large Program

Part of the data used in this thesis are part of the international observational large programs: IRAM-NOEMA SOLIS, briefly described below. Other data, specifically those at centimeter wavelengths with the VLA, were acquired by my supervisors prior to my thesis.

Seed Of Life In Space

SOLIS (Seed of life in Space) is an IRAM-NOEMA Large Program (PIs. Cecilia Ceccarelli and Paola Caselli, 345.6 hrs), that involves an international and interdisciplinary team, with two main complementary goals (Ceccarelli et al. 2017): 1) understanding the origin of organic chemistry in space and 2) how it evolves during the formation of Solar-type systems. The project aims to systematically study a set of crucial iCOMs in a sample of seven sources (Table 2 in Ceccarelli et al. 2017), with well-known physical structure, that covers the various phases of Solar-type star formation: the prestellar cores L1544, L1521F, the Class 0 IRAS 4A, SVS13A, and CepE, the protostellar cluster OMC2-FIR4, CepE, and the shocked region L1157-B1. In particular, in the zoo of the detected iCOMs, five species have been selected as they are abundant and have the ability to discriminate between the principal mechanisms at work (Table 3 in Ceccarelli et al. 2017): methoxy (CH_3O), methanol (CH_3OH), dimethyl ether (CH_3OCH_3), methyl formate (CH_3OCHO), and formamide (NH_2CHO). The immediate goal is to pin down

Table 2.1: List of the Frequency Setups of SOLIS for the IRAS 4A source.

Setup	Angular resolution		Frequency range [GHz]		Velocity resolution [km s^{-1}]	
	[$''$]	[au]	WideX	Narrow Bands	WideX	Narrow Bands
1	∼4	∼1200	80.80−84.40	81.60−82.60	∼7	∼0.6
3	∼2	∼600	95.85−99.45	96.65−97.65	∼6	∼0.5
5	∼0.9	∼270	204.0−207.6	204.8−205.8	∼3	∼0.9

the location of iCOMs within each source, to estimate the iCOM abundances and their sensitivity to evolutionary and environmental factors. The location, extent and distribution of iCOMs and how they evolve from the early stages of the Solar-like star formation process (prestellar phase) to the more evolved ones (Class 0/I/II stage) is essential to establish not only how iCOMs form, but also whether they survive during protostellar evolution. This information will make it possible to link the initial stages of iCOM chemistry with their final delivery onto planetary systems and, consequently, to shed light on what happened to the Solar System.

The NOEMA interferometer provides the high sensitivity and spatial resolution observations in the Northern hemisphere needed for the objectives of SOLIS. Indeed iCOMs lines are generally weak (40-50 mJy/beam; e.g, Maury et al. 2014b; Taquet et al. 2015), and originate in small ($\leq 1''$) and complicated regions.

Among the targeted sources there is the protostellar binary system IRAS 4A (see Section 3.1.3), that is the source subject of my thesis study. The observations performed towards IRAS 4A are obtained via three (out of five) spectral setups listed in Table 2.1.

2.4 Spectral lines as diagnostic tools of ISM molecular gas

The work of this thesis is based on the analysis of molecular transitions lines. They are the results of photon emission and absorption of photons at specific frequencies. This section reports the basics of the radiative transfer and the main methods used in this thesis to derive the physical properties of the gas emitting a molecular species.

2.4.1 Radiative transfer equation

The propagation of the radiation through a medium is described by the equation of radiative transfer (see e.g., a classical books as: Rybicki & Lightman 1986; Elitzur 1992; Draine 2003; Tielens 2005; Wilson et al. 2009). When a light beam travels through a medium, energy can be added or subtracted by emission or absorption, and, generally, the specific intensity I_ν[4] will not remain constant. In the FIR to radio wavelength range, the scattering of photons is not a dominant source of radiation, so it can be neglected. Lets now define the coefficients that describe the emission and the absorption of photons.

The emission coefficient ϵ_ν is the energy emitted at a frequency ν per unit of time, solid angle, and volume. Therefore:

$$dE = \epsilon_\nu d\nu dt d\Omega dV \, . \tag{2.11}$$

---

[4] The specific intensity Iν is the energy flux at a frequency ν in one direction per unit of area, solid angle and frequency: $dE = I_\nu d\nu dA d\Omega dt$

Then, the intensity added to the light beam when it travels a distance ds is

$$\mathrm{dI}_\nu = \epsilon_\nu \mathrm{ds}\ . \tag{2.12}$$

The absorption coefficient k_ν represents the loss of intensity in a beam as it travels a distance ds. Therefore:

$$\mathrm{dI}_\nu = -\mathrm{k}_\nu \mathrm{I}_\nu \mathrm{ds}\ . \tag{2.13}$$

By convention, k_ν is positive for energy taken out of the light beam.

The variation of specific intensity in the direction of the beam propagation, incorporating the effects of emission and absorption, can be described by the radiative transfer equation:

$$\frac{\mathrm{dI}_\nu}{\mathrm{ds}} = -\mathrm{k}_\nu \mathrm{I}_\nu + \epsilon_\nu\ . \tag{2.14}$$

It gives a useful formalism for calculating the intensity in an emitting and absorbing medium, combining most of the macroscopic aspects of radiation into one equation, relating them to two coefficient k_ν and ϵ_ν.

The radiative transfer equation takes a particularly simple form if, instead of the distance s, another variable is used. Let's define the optical depth τ_ν that describes how much absorption occurs when the radiation travels through an absorbing medium. It depends on the properties of the absorbing material and of the quantity of material the radiation has to go through:

$$\mathrm{d}\tau_\nu = \mathrm{k}_\nu \mathrm{ds}\ . \tag{2.15}$$

If $\tau_\nu \gg 1$ the medium is optically thick, it absorbs all the emission and the observer sees where photons get their last interaction before being absorbed. If $\tau_\nu \ll 1$ the medium is optically thin, it is transparent and the photons can pass through it entirely.

The radiative transfer equation (Eq. 2.14) can be written, after dividing by k_ν, as:

$$\frac{\mathrm{dI}_\nu}{\mathrm{d}\tau_\nu} = -\mathrm{I}_\nu + \mathrm{S}_\nu\ , \tag{2.16}$$

where S_ν is the *source function* defined as the ratio between the emission and the absorption coefficient

$$\mathrm{S}_\nu = \frac{\epsilon_\nu}{\mathrm{k}_\nu}\ , \tag{2.17}$$

and it is a measure of how many photons in a light beam are removed and replaced by new ones when it passes through a medium.

The formal solution of the radiative transfer equation (Eq. 2.16) is then:

$$\mathrm{I}_\nu(\tau_\nu) = \mathrm{I}_\nu(0)\mathrm{e}^{-\tau_\nu} + \int_0^{\tau_\nu} \mathrm{S}_\nu \mathrm{e}^{(\tau_\nu - \tau'_\nu)} \mathrm{d}\tau'_\nu\ . \tag{2.18}$$

This equation can be interpreted as the sum of two terms: the initial intensity ($I_\nu(0)$) attenuated by absorption, plus the integrated source function attenuated by the absorption along the pathway.

In case of a constant source function, the solution becomes

$$\mathrm{I}_\nu(\tau_\nu) = \mathrm{I}_\nu(0)\mathrm{e}^{-\tau_\nu} + \mathrm{S}_\nu(1 - \mathrm{e}^{-\tau_\nu})\ . \tag{2.19}$$

In the optical thick case, $\tau_\nu \rightarrow \infty$

$$I_\nu = S_\nu \,, \tag{2.20}$$

which means that only the fraction of photons emitted in the medium and that are not absorbed can reach the border of the cloud.
In the optically thin case, $\tau_\nu \ll 1$

$$I_\nu(\tau_\nu) = I_\nu(0) + \tau_\nu(S_\nu - I_\nu(0)) \,, \tag{2.21}$$

so that most of photons can reach the border of the cloud. The source function is the quantity that the specific intensity tries to approach, and does approach if given sufficient optical depth.

In case of Local Thermodynamic Equilibrium (LTE[5]), the source function is governed by the gas kinetic temperature T through the Planck function. This is the *Kirchhoff law* for which:

$$B_\nu(T) = \frac{\epsilon_\nu}{k_\nu} = S_\nu \quad . \tag{2.22}$$

Therefore, the general solution of the radiative tranfer (eq. 2.18) becomes:

$$I_\nu(\tau_\nu) = I_\nu(0)e^{-\tau_\nu} + B_\nu(T)(1 - e^{-\tau_\nu}) \quad . \tag{2.23}$$

It is important to distinct between blackbody radiation, where $I_\nu = B_\nu(T)$, and thermal radiation, where $S_\nu = B_\nu(T)$. Thermal radiation becomes blackbody radiation only for optically thick media.

One way of characterizing the specific intensity (or brightness) at a certain frequency is to give the temperature of the blackbody having the same brightness at that frequency. Therefore, for any value I_ν, it is possible to define T_B by the relation:

$$I_\nu = B_\nu(T_B) \tag{2.24}$$

where T_B is the brightness temperature. In this way the intensity can be closely connected with the physical properties of the emitter, and can be characterized by the simple unit Kelvin [K] instead of [erg $cm^{-2}s^{-1}Hz^{-1}ster^{-1-}$]. This definition is usually used in radio astronomy, where the Rayleigh-Jeans law is usually applicable, so that

$$B_\nu(T_B) \simeq \frac{2\nu^2}{c^2} kT_B \,, \tag{2.25}$$

that translates into

$$T_B = \frac{c^2}{2k\nu^2} I_\nu \,. \tag{2.26}$$

The general solution of the radiative tranfer (eq. 2.19), in terms of brightness temperature, and in the Rayleigh-Jeans regime, becomes:

$$T_B = T_{bg}e^{-\tau_\nu} + T(1 - e^{-\tau_\nu}) \,, \tag{2.27}$$

where, T_B is the brightness temperature, T is the temperature of the source, and T_{bg} is the background temperature. If the optical depth is large, the brightness temperature of the radiation approaches the temperature of the medium.

---

[5] The LTE condition holds when the species collide so frequently with the collisor that the level populations are thermalized and, therefore, follow the Boltzmann distribution, which only depends on the gas temperature T.

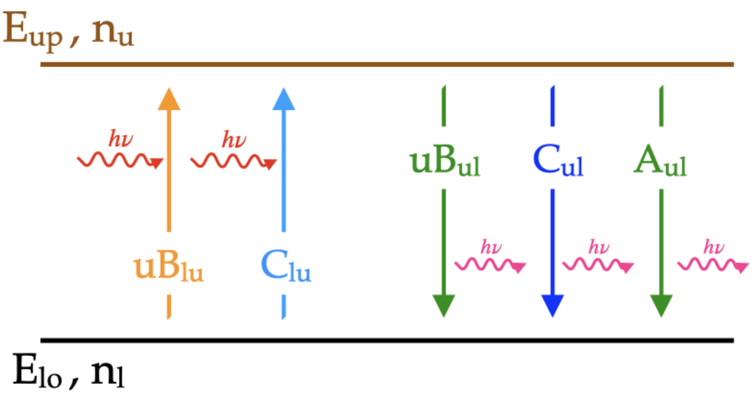

Figure 2.10: Sketch of two energy levels in a molecules. One photon, of energy $h\nu$, can be absorbed by an electron inducing a transition from a lower energy state E_{lo} to an upper level with energy E_{up}. The transition from E_{up} to E_{lo} can occur with a photon emission. A_{ul}, B_{ul} and B_{lu} are the Einstein coefficient for spontaneous emission, absorption, and stimulated emission, respectively. C_{ul} and C_{lu} are the collision coefficients.

2.4.2 Spectral lines fundamentals

Einstein coefficients

The Kirchhoff's law ($\epsilon_\nu = k_\nu B_\nu(T)$), which relates thermal emitter emission to absorption, must imply a microscopic link between emission and absorption. This relationship was first discovered by Einstein in a simple analysis of the interaction of radiation with an atomic system (Einstein 1916).

Consider a two-level system with a lower energy state E_{lo} with particle number density n_l and an upper level energy E_{up} with particle number density n_u, as illustrated in Fig 2.10. A system can move from the excited level E_{up} to the lower state E_{lo} and viceversa, through few processes:

∗ Excitation of the lower energy level:

- Absorption of a photon at frequency ν_{ul}. The probability of spontaneous absorption is related to the B_{lu} Einstein coefficient:

$$W_{lu} = -\frac{dn_l}{dt}\bigg|_{abs} = \frac{dn_u}{dt}\bigg|_{abs} = n_l B_{lu} u(\nu_{ul}) \tag{2.28}$$

  where ν_{ul} is the frequency associated to the energy difference of the two levels ($h\nu_{ul} = (E_u - E_l)$), and $u(\nu_{ul})$ is the average energy density of the radiation field.

- Collisions with other, more energetic molecules/atoms. The probability of excitation for collision is related to the C_{lu} coefficient:

$$W^c_{lu} = -\frac{dn_l}{dt}\bigg|_{coll.} = \frac{dn_u}{dt}\bigg|_{coll.} = n_l C_{lu} \quad . \tag{2.29}$$

∗ De-Excitation of the upper energy level:

- Emission of a photon at frequency ν_{ul}, either by spontaneous or stimulated emission. The probability of spontaneous and stimulated emission is related to the A_{ul} and B_{ul} Einstein coefficients, respectively:

$$W^{s}_{ul} = \left.\frac{dn_l}{dt}\right|_{spont.emiss.} = -\left.\frac{dn_u}{dt}\right|_{spont.emiss.} = n_u A_{ul} \quad , \tag{2.30}$$

$$W_{ul} = \left.\frac{dn_l}{dt}\right|_{stim.emiss.} = -\left.\frac{dn_u}{dt}\right|_{stim.emiss.} = n_u B_{ul} u(\nu_{ul}) \quad . \tag{2.31}$$

- Collision with other, less energetic molecules/atoms. The probability of de-excitation for collision is related to the C_{ul} coefficient:

$$W^{c}_{ul} = \left.\frac{dn_l}{dt}\right|_{coll.} = -\left.\frac{dn_u}{dt}\right|_{coll.} = n_u C_{ul} \quad . \tag{2.32}$$

The collision rate C_{ul} (or C_{lu}) depends on the number density of the collision partner n_{coll} as $C_{ul} = \gamma_{ul} \times n_{coll}$, where γ_{ul} is the velocity integrated collision cross section. In principle, collisions with any of the many different chemical species present in the ISM will contribute towards C_{ul}, but in practice, the main contributors are few key species like H_2, He, and free electrons.

Statistical equilibrium equation

If the system is in a stationary state, the number of absorbed and emitted photons must be equal. This is formulated by the statistical equilibrium equation:

$$n_u B_{ul} u(\nu_{ul}) + n_u C_{ul} + n_u A_{ul} = n_l B_{lu} u(\nu_{ul}) + n_l C_{lu} \quad . \tag{2.33}$$

This equation can then be generalized to a multi-level system, obtaining a system of levels N_{lev}(number of levels) equations:

$$n_u \sum_{l \neq u} (B_{ul} u(\nu_{ul}) + C_{ul} + A_{ul}) = \sum_{l \neq u} (n_l B_{lu} u(\nu_{ul}) + n_l C_{lu}). \tag{2.34}$$

with $u = 1, \cdots, N_{lev}$.

However, solving this equation can be a difficult task.

Detailed balance

Supposing that the collisions dominate both the excitation and the de-excitation of the levels, the statistical equilibrium equation (Eq. 2.33) becomes:

$$n_u C_{ul} = n_l C_{lu} \tag{2.35}$$

and being the levels thermalized by collisions, they follow the Boltzmann distribution

$$\frac{n_u}{n_l} = \frac{g_u}{g_l} e^{-h\nu_{ul}/kT} \tag{2.36}$$

where g_u and g_l are the statistical weights of the u and the l level, respectively. Therefore:

$$\frac{C_{lu}}{C_{ul}} = \frac{n_u}{n_l} = \frac{g_u}{g_l} e^{-h\nu_{ul}/kT} \tag{2.37}$$

that is called the *detailed balance* of the collision rate coefficients.

Critical density

If the collisions between atoms/molecules are not frequent enough to reach LTE, their energy level population will depend on the number of collisions and on the collisional coefficients. Let suppose that the radiation field $u(\nu_{ul})$ is negligible, the equation 2.33 becomes:

$$n_u C_{ul} + n_u A_{ul} = n_l C_{lu} \quad . \tag{2.38}$$

Therefore, using the equation of the detailed balance (Eq. 2.37), and that $C_{ul} = \gamma_{ul} \times n_{coll}$

$$\frac{n_u}{n_l} = \frac{g_u}{g_l} e^{-h\nu_{ul}/kT} \left(1 + \frac{n_{cr}}{n_{coll}}\right)^{-1} \tag{2.39}$$

where n_{cr} is the *critical density* defined as

$$n_{cr} = \frac{A_{ul}}{\gamma_{ul}} \ . \tag{2.40}$$

The critical density represents the minimum density needed to de-excite a transition faster than the emission of a photon. In other words, if the density is larger than the critical density ($n \gg n_{cr}$), the de-excitation is dominated by collision rather than photon emission. Consequently, the collisions totally govern the level populations (i.e., the LTE condition) that, therefore, follow the Boltzmann law. On the contrary, if the gas density is smaller than the critical density $n \ll n_{cr}$, the photon emission dominates the de-excitation of the upper level. In this case, the n_u/n_l ratio depends on the gas temperature but also on the density of the colliders. The levels are *sub-thermally populated.*

In case of a multi-level system, the critical density can be generalized as:

$$n_{cr} = \frac{\sum_0^{N_{lev}} A_{ul}}{\sum_0^{N_{lev}} \gamma_{ul}} \ . \tag{2.41}$$

Relations between Einstein Coefficients

Let consider the case where the radiation field $u(\nu_{ul})$ dominates the excitation and the de-excitation of the levels (the collisions are negligible). A typical case can be a low density gas illuminated by a strong radiation field. The statistical equilibrium equation (eq. 2.33) becomes:

$$n_u B_{ul} u(\nu_{ul}) + n_u A_{ul} = n_l B_{lu} u(\nu_{ul}) \ , \tag{2.42}$$

and can be written as

$$u(\nu_{ul}) = A_{ul} \frac{n_u}{n_l B_{lu} - n_u B_{ul}} \ . \tag{2.43}$$

If $u(\nu_{ul})$ is a black body at temperature T_{rad},

$$u(\nu_{ul}) = \frac{8\pi h \nu_{ul}^3}{c^3} \frac{1}{e^{h\nu_{ul}/kT_{rad}} - 1} \ . \tag{2.44}$$

Combining this two equations, with the Boltzmann distribution (Eq. 2.36), we find the following correlation between the Einstein coefficients:

$$g_l B_{lu} = g_u B_{ul} \quad , \qquad B_{ul} = \frac{c^2}{2h\nu_{ul}^3} A_{ul} \ . \tag{2.45}$$

It is possible to notice that A_{ul}/B_{ul} is independent on the temperature, as the Einstein coefficients are inherent to the system, and only depends on the energy difference of the two levels ($\nu_{ul} = E_u - E_l$). Additionally, increasing ν_{ul} it is more likely to have spontaneous emission than stimulated one; indeed maser emission, dominated by stimulated emission, is naturally occurring typically in the microwave range.

Excitation Temperature

In the ISM, levels are generally not in LTE. It is useful to define the *excitation temperature* T_{ex} as the temperature of the gas if the two levels were thermally populated. Therefore, if the levels are thermally populated, they follow the Boltzmann distribution (Eq. 2.36). Inverting the Boltzmann equation, it is possible to write T_{ex} as:

$$T_{ex} = \frac{-h\nu_{ul}}{k}\left(\ln\left(\frac{n_u g_l}{n_l g_u}\right)\right)^{-1} \quad . \tag{2.46}$$

Using the definition of critical density (Eq 2.40) and assuming that the radiation field ($u(\nu_{ul})$) is negligible, it holds:

$$T_{ex} = T\left(\frac{kT}{h\nu_{ul}}\ln\left(1+\frac{n_{cr}}{n_{coll}}\right)+1\right)^{-1} \quad . \tag{2.47}$$

Therefore, for densities larger than the critical density (i.e., LTE conditions) $T_{ex} \sim T$, namely T_{ex} is exactly the kinetic temperature of the gas. On the contrary, for densities lower than the critical density, $T_{ex} < T$.

The definition of T_{ex} only holds for a two-level system. In a multi-level system, each transition has its own T_{ex}. However, when all levels are in LTE, the excitation temperature is the same for all transitions and it is called rotational temperature T_{rot}. When the gas is in LTE, both the excitation temperature (T_{ex}) and the rotational temperature (T_{rot}) are the same and equal to the gas kinetic temperature ($T_{ex} = T_{rot} = T$).

Emission and absorption coefficients in terms of Einstein coefficients

Spectral lines are not infinitely narrow but are broadened by different processes which give them an absorption profile $\phi(\nu)$ and an emission profile $\psi(\nu)$. These profiles describe the transmission probability for photons of frequency ν, and are normalized to 1 ($\int \phi(\nu)d\nu = 1$ and $\int \psi(\nu)d\nu = 1$). The absorption and emission profiles are identical if between both processes no change in frequency occurs or if, on the contrary, there is a complete frequency redistribution. Therefore, the probability of absorption and of spontaneous and stimulated emission of a photon in a frequency interval $d\nu$ becomes, respectively,

$$W^{abs} = n_l B_{lu} I_\nu \phi(\nu) d\nu \ , \tag{2.48}$$

$$W^{em}_{spont} = n_u A_{ul} \psi(\nu) d\nu \ , \tag{2.49}$$

$$W^{em}_{stim} = n_u B_{ul} I_\nu \phi(\nu) d\nu \ . \tag{2.50}$$

Considering the stimulated emission as negative absorption, and since each atom contributes an energy $h\nu$, distributed over 4π solid angle for each transition, the amount of energy absorbed and emitted per unit of time, solid angle, and volume is, respectively:

$$\mathrm{dE^{abs}} = \frac{h\nu}{4\pi}\mathrm{dVd\Omega dt(W^{abs} - W^{em}_{stim})} \quad , \tag{2.51}$$

$$\mathrm{dE^{em}} = \frac{h\nu}{4\pi}\mathrm{W^{em}_{spont}dVd\Omega dt} \quad . \tag{2.52}$$

Using the definition of intensity (see Section 2.4.1), it is possible to link the emission and absorption line coefficients, ϵ_ν and k_ν, to the Einstein coefficients. The amount of energy dE emitted and absorbed per unit of time, solid angle, volume and frequency is, by definition (see Section 2.4.1):

$$\mathrm{dE^{em}} = \epsilon_\nu \mathrm{dVd\Omega d\nu dt} \, , \tag{2.53}$$

$$\mathrm{dE^{abs}} = I_\nu k_\nu \mathrm{dVd\Omega d\nu dt} \, . \tag{2.54}$$

Combining the previous equations (2.51 and 2.54, 2.52 and 2.53), the emission and absorption coefficients can be expressed in terms of Einstein coefficients, as:

$$\epsilon_\nu = \frac{h\nu}{4\pi} n_u A_{ul} \psi(\nu) \, , \tag{2.55}$$

$$k_\nu = \frac{h\nu}{4\pi}(n_l B_{lu} - n_u B_{ul})\phi(\nu) \, . \tag{2.56}$$

The latter, using the correlation between the Einstein coefficients (eq. 2.45), can also be written as:

$$k_\nu = \frac{c^2}{8\pi\nu^2} n_u A_{ul}\left(\frac{g_u n_l}{g_l n_u} - 1\right)\phi(\nu) \quad . \tag{2.57}$$

Assuming that the line profiles of absorption and emission are the same, we can write the source function S_ν in terms of the Einstein coefficients as

$$S_\nu = \frac{\epsilon_\nu}{k_\nu} = \frac{n_u A_{ul}}{n_l B_{lu} - n_u B_{ul}} \, . \tag{2.58}$$

Line broadening mechanisms in the ISM molecular gas

As said before, atomic and molecular levels are not infinitely sharp. Besides the intrinsic width of the atomic/molecular levels that arises from the Heisenberg uncertainty principle (*natural* broadening), there are several mechanisms that determine the shape of the line but only one is relevant in the ISM: the thermal (or Doppler) broadening.

Any species (atoms or molecules) is in thermal motion, so that the frequency of emission or absorption in its own frame corresponds to a different frequency for an observer. Each species has its own Doppler shift, and as the atoms/molecules follow the Maxwell distribution, the line is spread over a range in frequency. Therefore, combining the Maxwell distribution with the Doppler shift formula, we have that the line profile is a Gaussian:

$$\phi(\nu) = \frac{1}{\Delta\nu_D\sqrt{\pi}} e^{-\frac{(\nu-\nu_0)^2}{\Delta\nu_D^2}} \tag{2.59}$$

where the Doppler full width half maximum (in frequency), $\Delta\nu_{\rm FWHM}$ is:

$$\Delta\nu_{\rm FWHM} = 2\sqrt{\ln 2}\Delta\nu_{\rm D} = 2\sqrt{\ln 2}\frac{\nu_0}{\rm c}{\rm b} \tag{2.60}$$

and b, the Doppler parameter, is linked to the temperature T of the gas:

$$\rm b = \sqrt{\frac{2kT}{m_x}} = 0.129\sqrt{\frac{T}{A_x}} km\ s^{-1} \tag{2.61}$$

with $\rm m_x$ the mass of the species x and $\rm A_x$ its atomic number.

As example, the $\rm CH_3OH$ transition at 96.755 GHz, emitted from a molecular gas at 100 K would have a Doppler FWHM linewidth of $\sim$0.4 km $\rm s^{-1}$, while at 300 K the FWHM linewidth is $\sim$0.7 km $\rm s^{-1}$. Analogously, the SiO (2-1) transition at 86.846 GHz emitted from a gas at 100 K is $\sim$ 0.2 km $\rm s^{-1}$.

2.5 Solving the radiative transfer equation

Finding a solution of the radiative transfer equation (eq. 2.33) is not an easy task due to the coupling between the level populations and the intensity of radiation in the medium to model. In general, a complete solution of the radiative transfer requires powerful numerical techniques and still the solution may be difficult to obtain, because the iterative process may not converge. Additionally, when it involves multi-level systems the problem becomes even more challenging, if not prohibitive. Therefore, a possibility is to identify some cases where some assumptions can be made and a solution can be more easily found. In the following, I present the two main line spectra analysis methods used in this thesis: the LTE Rotational Diagram (RD) and the non-LTE Large Velocity Gradient (LVG) methods.

2.5.1 LTE Rotational Diagrams method

When several lines from the same molecules are detected, it is possible to interpret them using the Rotational Diagram analysis. It is the *step 0* analysis that provides an approximate and a rough estimate of the average temperature of the emitting gas as well as the column density of the species emitting the lines. Two main assumptions are made: LTE conditions and optically thin lines.

In LTE conditions, the radiative transfer equation for a constant source function (Eq. 2.23), and in absence of an external source $\rm I_\nu(0)$ is:

$$\rm I_\nu(\tau_\nu) = B_\nu(T)(1 - e^{-\tau_\nu})\ . \tag{2.62}$$

The line opacity τ can be related to measurable parameters. Indeed, recalling that $\rm d\tau = k_\nu ds$, and using the absorption coefficient relation with the Einstein emission coefficient $\rm A_{ul}$ (Eq 2.57), we have:

$$\tau = \int \tau_\nu {\rm d}\nu = \frac{\rm c^2}{8\pi\nu^2}\int \rm n_u A_{ul}\left(\frac{g_u n_l}{g_l n_u} - 1\right) ds \int \phi(\nu) d\nu\ . \tag{2.63}$$

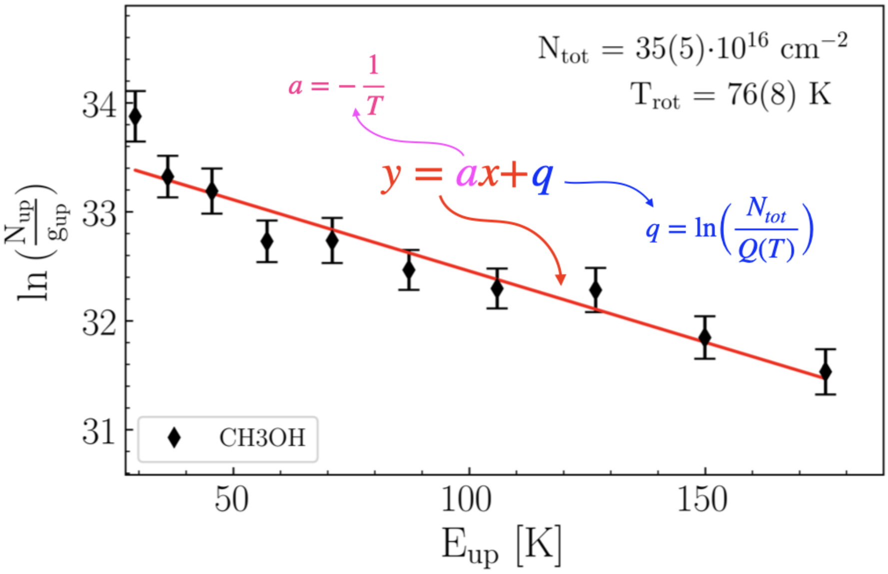

Figure 2.11: Example of a Rotational Diagram of CH_3OH lines. The rotational temperature is the inverse of the slope of the fitted line (in red), and the total column density can be derived from the intercept. The deviation of the observed points from the fitted line are due to non-LTE effects and/or optically thick lines (see text).

Considering a Gaussian line profile with a FWHM linewidth $\Delta\nu$, the expression of τ becomes:

$$\tau = \frac{c^2}{8\pi\nu^2\Delta\nu}\int n_u ds A_{ul}\left(\frac{g_u n_l}{g_l n_u} - 1\right) . \tag{2.64}$$

As we are under the LTE conditions, we can use the Boltzmann distribution (Eq. 2.36) to rewrite the optical depth as:

$$\tau_\nu = \frac{c^2}{8\pi\nu^2\Delta\nu}\int n_u ds A_{ul}(e^{h\nu/kT} - 1) . \tag{2.65}$$

Using the Rayleigh-Jeans approximation for the blackbody emission ($h\nu \ll kT$) and the definition of Brightness temperature T_B (eq. 2.26), we can write:

$$T_B = \frac{hc^3}{8\pi k\nu^2\Delta\nu}A_{ul}\int n_u ds\left(\frac{1 - e^{-\tau}}{\tau}\right) \quad . \tag{2.66}$$

Defining the velocity-integrated intensity $W = \int T_B d\nu \sim T_B\Delta\nu$, it is possible to express the column density of the upper state, $N_u = \int n_u ds$, in terms of the observed quantity T_B, inverting the equation above. Assuming optically thin lines:

$$N_u = \frac{8\pi k\nu^2}{hc^3}\frac{W}{A_{ul}} . \tag{2.67}$$

At this point we have a basic equation for the number of molecules in the upper energy state u of the two-level system. Now, it is important to relate the number of molecules in the upper energy level u (N_u) to the total population of all energy levels in the molecule N_{tot}. In LTE conditions, if we consider *all* the energy levels and that $h\nu_{ul} = (E_{up} - E_{lo})$, the Boltzmann distribution becomes:

$$\frac{n_u}{g_u} = \frac{n_{tot}}{Q(T)} e^{-E_{up}/kT} \tag{2.68}$$

where $n_{tot} = \sum n_l$, and Q(T) is the partition function at a given temperature, that represents a statistical sum over all rotational energy levels in the molecule:

$$Q(T) = \sum g_l e^{-E_{lo}/kT} \quad . \tag{2.69}$$

Considering an isothermal cloud and integrating along the line of sight, so that $N_u = \int n_u ds$ and $N_{tot} = \int n_{tot} ds$, the equation 2.68 becomes, in logarithmic scale:

$$\ln\left(\frac{N_u}{g_u}\right) = \ln\left(\frac{N_{tot}}{Q(T)}\right) - \frac{E_{up}}{kT} \tag{2.70}$$

where N_{tot} is the total column density of the species, i.e. the total number of molecules of a species per unit area integrated along the line of sight.

Therefore, with several observed line transitions, it is possible to construct the *Rotational Diagrams* (or Boltzmann plots). The Rotational Diagram is a plot of the column density per statistical weight of a number of molecular energy levels, $y = \ln(N_u/g_u)$, as a function of their upper level energy, $x = E_{up}/kT$ (see Figure 2.11). Fitting the data points with a straight line it is possible to derive two quantities (see eq. 2.70): the rotational temperature, T_{rot}, that corresponds to the inverse of the slope of the fitted line, and the total column density, N_{tot}, from the intercept ($y = \ln(N_{tot}/Q(T))$).

If the assumptions of LTE conditions and optically thin lines are fully satisfied, the fitted points should follow a perfect straight line. In this case, T_{rot} gives a good estimate of the kinetic gas temperature (so, only if *all* levels are thermally populated). However, in real life this is not always the case, and the points are scattered along the line. This means that non-LTE effects and/or optically thick lines are present. In this case, the Rotational Diagram analysis will provide only an approximate value of the average gas temperature and the species column density.

Finally, the column density of the upper energy level N_u (and derived by the velocity-integrated intensity from eq. 2.67) is averaged over the telescope beam. If the emitting source (θ_{source}) is smaller than the telescope beam (θ_{beam}), in order to have the correct value of the column density N_{tot} it is important to correct for the beam dilution, applying the so-called *filling factor*.

$$ff = \frac{\theta^2_{source}}{\theta^2_{beam} + \theta^2_{source}} \quad . \tag{2.71}$$

If the lines falls in a small range of frequencies, this corresponds to a factor to apply to N_{tot} only. However, if the lines cover a large range of frequencies, the filling factor will be different for different lines leading to a wrong rotational temperature too, if not duely corrected.

2.5.2 Non-LTE Large Velocity Gradient method

The escape probability formalism

The radiative transfer equation is non-linearly coupled with the statistical equilibrium equation, so that a complete solution of the radiative transfer is difficult to obtain. The situation gets simpler if the different regions of the medium are not coupled *radiatively*, or, in other words, if the absorption of the photons is local. This happens when either the emitted photon is absorbed close to the point of emission or it escapes the medium. When in the medium there is a large velocity gradient, the Doppler shift moves the frequency of the photons emitted in a point outside the line profile. In this case, the statistical equilibrium equations can be decoupled from the radiative transfer ones, simplifying the problem.

A very popular and powerful method to approach the solution of radiative transfer in spectral lines in a medium with large velocity gradients is the *escape probability formalism*. It was first introduced by Sobolev (1957, 1960) for the treatment of the radiative transfer in expanding envelopes and later extended to other physical problems. The basic idea is the introduction of a local multiplicative factor describing the probability that a photon will escape the medium after it is generated.

In this approximation, we can write that the net absorption, corrected for stimulated emission, is equal to the photons that do not escape, i.e.:

$$(\mathrm{n_l B_{lu}} - \mathrm{n_l B_{ul}})\mathrm{u}(\nu_{\mathrm{ul}}) = \mathrm{n_u A_{ul}}(1 - \beta(\tau)) \tag{2.72}$$

where $\beta(\tau)$ is the *escape probability* factor that is the probability that a photon formed at optical depth τ escapes through the front surface. $\beta(\tau)$ only depends on the source geometry and on the optical depth, and it can be expressed as:

$$\beta = \frac{1}{4\pi}\int\int \mathrm{e}^{-\tau}\phi(\nu)\mathrm{d}\nu\mathrm{d}\Omega\ . \tag{2.73}$$

Considering the expression of the source function in terms of the Einstein coefficients (eq. 2.58), from eq. 2.72, the average radiation field u_ν in the level population calculation can be expressed in terms of the source function S_ν as:

$$\mathrm{u}(\nu) = \mathrm{S}_\nu(1 - \beta) \quad . \tag{2.74}$$

If no photons escape from the cloud (optically thick source) then $\mathrm{u}(\nu)$ is the source function S_ν. Therefore, the statistical equilibrium equation (eq 2.33) becomes:

$$\mathrm{n_l C_{lu}} = \mathrm{n_u C_{ul}} + \mathrm{n_u}\beta(\tau)\mathrm{A_{ul}}\ . \tag{2.75}$$

Considering the detailed balance equation (eq. 2.37) we have:

$$\frac{\mathrm{n_u}}{\mathrm{n_l}} = \frac{\mathrm{g_u}}{\mathrm{g_l}}\mathrm{e}^{-\mathrm{h}\nu/\mathrm{kT}}\left(1 + \beta\frac{\mathrm{n_{cr}}}{\mathrm{n_{coll}}}\right)^{-1}\ . \tag{2.76}$$

Comparing this solution with the escape probability approximation to the eq. 2.39 it is possible to notice that the trapping of the photons reduces the critical density. Another way to see it is that the photon trapping has the effect to reduce the the spontaneous emission rate, which physically corresponds to the fact that a photon is *emitted* only if it escapes the absorption.

How to express the escape probability factor β?

The escape probability $\beta(\tau)$ depends on the geometry and velocity structure of the region, and several forms have been proposed.
For radiation with intensity I_ν entering a slab whose optical depth normal to its face is τ, the intensity at exit is $I_\nu e^{-\tau}$. Therefore, the probability for radiation to escape from an optical depth τ is $e^{-\tau}$, also known as the *escape factor*. If the radiation is generated inside the source, we do not know the precise point of production, and an average over optical depth is needed. The mean escape probability is then:

$$\beta = \frac{1}{\tau}\int_0^\tau e^{-\tau'} d\tau' = \frac{1 - e^{-\tau}}{\tau} \quad . \tag{2.77}$$

This is the expression of β used in the LVG approximation (see e.g., Sobolev 1960; Mihalas 1978; De Jong et al. 1980; Elitzur 1992), and it is a rough approximation for a radially expanding sphere. Even if it is a very crude and inexact derivation, it conveys the essence of more precise treatments. Indeed, every model based on the escape probability approach employs some tipe of averaging of the escape factor, and ends up with an expression for β that is similar to the one above (eq. 2.77) and changes based on the averaging method used by the particular model. The behavior of the mean escape probability in the limits of small and large optical depths is:

$$\beta \simeq \begin{cases} 1 & \tau \ll 1 \\ \tau^{-1} & \tau \gg 1 \end{cases} \quad . \tag{2.78}$$

Indeed, in the optically thin case ($\tau \ll 1$) the medium is transparent and each photon escapes the source without interaction, so $\beta = 1$. In the optically thick case ($\tau \gg 1$) the source can be divided into τ zones of optical depth unity. A photon can escape, on the average, if and only if it is produced in the outermost zone, and the probability for that is τ^{-1}.

In a optically thick source, the photon is random walking in the frequency space due to the repeated effect of absorption and re-emission, and can escape when it reaches the line wings where $\tau \leq 1$. Considering $\phi(\nu)$ the line profile, the corresponding frequency shift from the line center, ν_1, at which the line becomes optically thin, follows

$$\phi(\nu_1)\tau = 1 \tag{2.79}$$

that, for a Doppler line profile has as solution

$$\nu_1 = \sqrt{\ln\left(\frac{\tau}{\sqrt{\pi}}\right)} \quad . \tag{2.80}$$

The probability that a photon reaches the frequency value ν_1 above which the medium becomes optically thin and escapes the cloud is the corresponding fractional area under the profile wings:

$$\beta \approx 2\int_{\nu_1}^{\infty} \phi(\nu) d\nu \quad , \tag{2.81}$$

that at large ν_1, for a Doppler line profile is (Mihalas 1978; Elitzur 1992):

$$\beta \approx \frac{e^{-\nu_1^2}}{2\sqrt{\pi}\nu_1} = \frac{1}{\tau\sqrt{\ln(\tau/\sqrt{\pi})}} \quad . \tag{2.82}$$

Let consider now the case of an homogeneous semi-infinite slab, where the physical conditions are assumed to be uniform (i.e., the temperature and the overall density are the same at every point). In a plane parallel geometry, when we can consider an axial symmetry (i.e. only variations in the z direction), the escape probability becomes (Scoville & Solomon 1974; De Jong et al. 1975):

$$\beta = \frac{1 - e^{-3\tau}}{3\tau} \quad . \tag{2.83}$$

On the other hand, for a uniform sphere, the escape probability is (Osterbrock 1974):

$$\beta = \frac{1.5}{\tau}\left(1 - \frac{2}{\tau^2} + e^{-\tau}\left(\frac{2}{\tau} + \frac{2}{\tau^2}\right)\right) \quad . \tag{2.84}$$

The Large Velocity gradient approximation

The application of the escape probability method to the problem of a gas with a systematic Large Velocity Gradient was first introduced by Sobolev (1960) for a expanding stellar atmosphere and it is called *Sobolev* or *Large Velocity Gradient* (LVG) method. The basic idea is that a photon emitted to a position P with velocity v_P cannot be absorbed at the point P′ with velocity v_P, because the photon frequency is Doppler-shifted outside the $h\nu + \Delta\nu_D$ interval, where $\Delta\nu_D$ is the thermal width of the line. Therefore, either the photon is absorbed close where it is emitted, or it escapes the medium.

The simplest example of a velocity gradient is that of a linear velocity dependence, $v(r) = rV/R$, that is appropriate to a uniform spherical cloud of radius R and maximum expanding velocity V. The line optical depth ($d\tau = k_\nu ds$), considering eq. 2.56, and the rectangular line profile ($\phi(\nu) \sim 1/\Delta\nu$ for $\nu < \Delta\nu$ and 0 otherwise) will then be (Takahashi et al. 1983):

$$\tau = \int_0^L ds(n_l B_{lu} - n_u B_{ul})\frac{hc}{4\pi}\frac{R}{V} \, . \tag{2.85}$$

Therefore, the line opacity τ is inversely proportional to the velocity gradient V/R, so that the larger is the gradient the smaller is the line opacity. Using the formalism of the escape probability, the flux F of a line emitted by a source at a distance d, by definition, is:

$$F = \frac{d1}{4\pi d^2}\int_V dVh\nu A_{ul} n_u \beta(\tau) \, . \tag{2.86}$$

Therefore, the line flux depends on the line opacity τ, the line frequency ν, the spontaneous emission coefficient A_{ul}, and the upper level state population n_u (that can be known solving the statistical equilibrium equation, eq. 2.75).

In summary, the LVG method allows to calculate the flux from a cloud of gas with a systematic gradient of velocity, constant density and constant temperature, for a given geometry. It depends on four parameters: the gas density and temperatures (needed to compute n_u/n_l and τ), the column density of the molecule, and the size of the emitting region.

Thanks to its relatively simple application, the LVG method is extensively used in interpreting the molecular spectra. The collisional rate coefficients, needed in order to compute the critical density (in eq. 2.75), can be found in spectroscopic catalogs such as LAMDA (https://home.strw.leidenuniv.nl/~moldata/) and BASECOL (https://basecol.vamdc.eu/). So far, these coefficients are available for several diatomic and triatomic molecules, but only for a set of larger molecules (such as C_3H_2, HC_3N, H_2CO, H_2CS, HNCO, NH_3, CH_3OH, and CH_3CN). Therefore, the LVG method cannot be applied to molecules more complex than methanol (CH_3OH).

The LVG code used for this thesis is that developed by Ceccarelli et al. (2003).

Part III

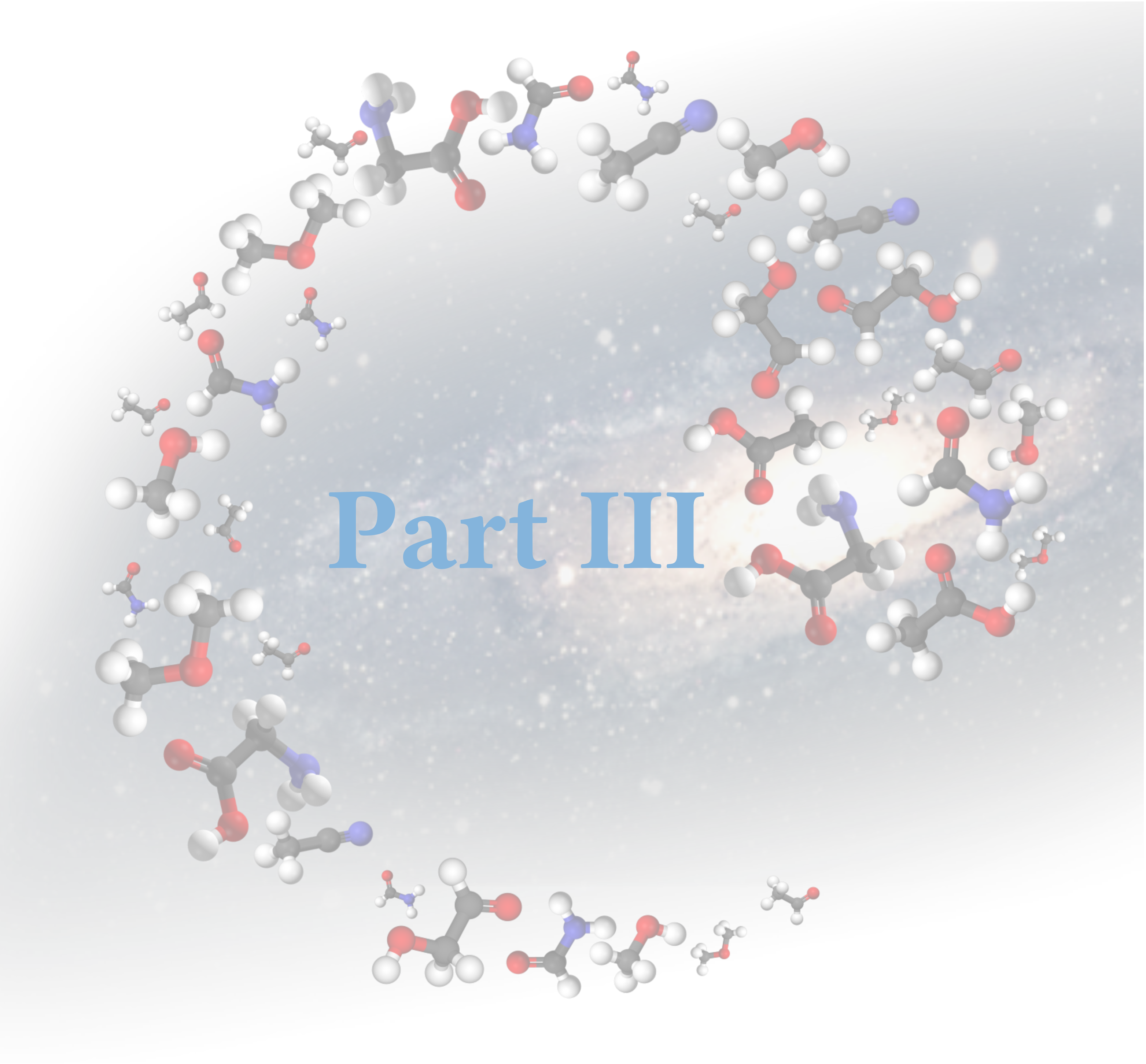

3

Source background

3.1 The Perseus molecular complex

3.1.1 Perseus molecular cloud

The Perseus molecular cloud is a nearby (orders of 300-400 pc; Zucker et al. 2018) giant molecular cloud in the constellation of Perseus with coordinates α(J2000) = $03^{\mathrm{h}}35^{\mathrm{m}}$, δ(J2000) = $+31^{\circ}13'$ (Kirk et al. 2006). It is part of the Perseus OB2 association, that is one of the major OB association[1] in the Solar vicinity and it is about 6 Myr old (Kirk et al. 2006, 2007; Bally et al. 2008). This association has blown a shell of atomic hydrogen of about 100 pc in diameter (20°) into the ISM, probably due to the combined effects of ionizing radiation, winds, and supernovae, and the Perseus molecular cloud appears to be embedded into the western rim of the shell (see Figure 1 in Bally et al. 2008). The Perseus molecular cloud has a mass of about $10^{4}\mathrm{M}_{\odot}$ and an angular extent of about $1.5^{\circ} \times 5^{\circ}$ (Bachiller & Cernicharo 1986; Kirk et al. 2006).

Like most molecular clouds, it consists of a complex and chaotic structure consisting of dense cloud cores, that appear as dark patches in the optical image in Figure 3.1, surrounded by an interconnected network of filaments. The entire Perseus cloud has been mapped in dust continuum at 850 μm with the Sub-millimeter Common User Bolometric Array (SCUBA) on the 15m James Clerk Maxwell Telescope (JCMT) (Hatchell et al. 2005; Kirk et al. 2006), at 1.1 mm with the Calthech Sub-mm Telescope (CST) (Enoch et al. 2006), and with the infrared cameras on Spitzer (Jørgensen et al. 2006). Additionally, it has been surveyed in narrow-band Hα and SII emission (Walawender et al. 2005, 2008). All these surveys reveal a large population of low-mass pre-main sequence stars, embedded protostars, and starless cores (e.g., Ladd et al. 1993; Lada & Lada 1995; Hatchell et al. 2005; Enoch et al. 2006; Kirk et al. 2006; Evans et al. 2009). Jørgensen et al. (2006), using a Spitzer survey, identified about 400 Young Stellar Objects (YSOs) in Perseus, of which about two-thirds are associated with the two major clusters IC 348 and NGC 1333. Of the remaining one-third, over half are parts of the smaller aggregates in B1, L1448, and L1455. About two-thirds of these identified YSOs have been classified as Class II objects, and the remaining as Class I. However, these 400 sources are a lower bound to the actual number. For example, Muench et al. (2007) found about 420 YSOs in IC 348 only. Indeed, it is important to notice that Spitzer observations tend to select YSOs in either their Class I or II stages of evolution, while the Class 0 sources tend not to be visible, and the older Class

---

[1] High-mass stellar clusters containing large groups of O-type (>18 $\mathrm{M}_{\odot}$) and B-type (∼4-18 $\mathrm{M}_{\odot}$) stars.

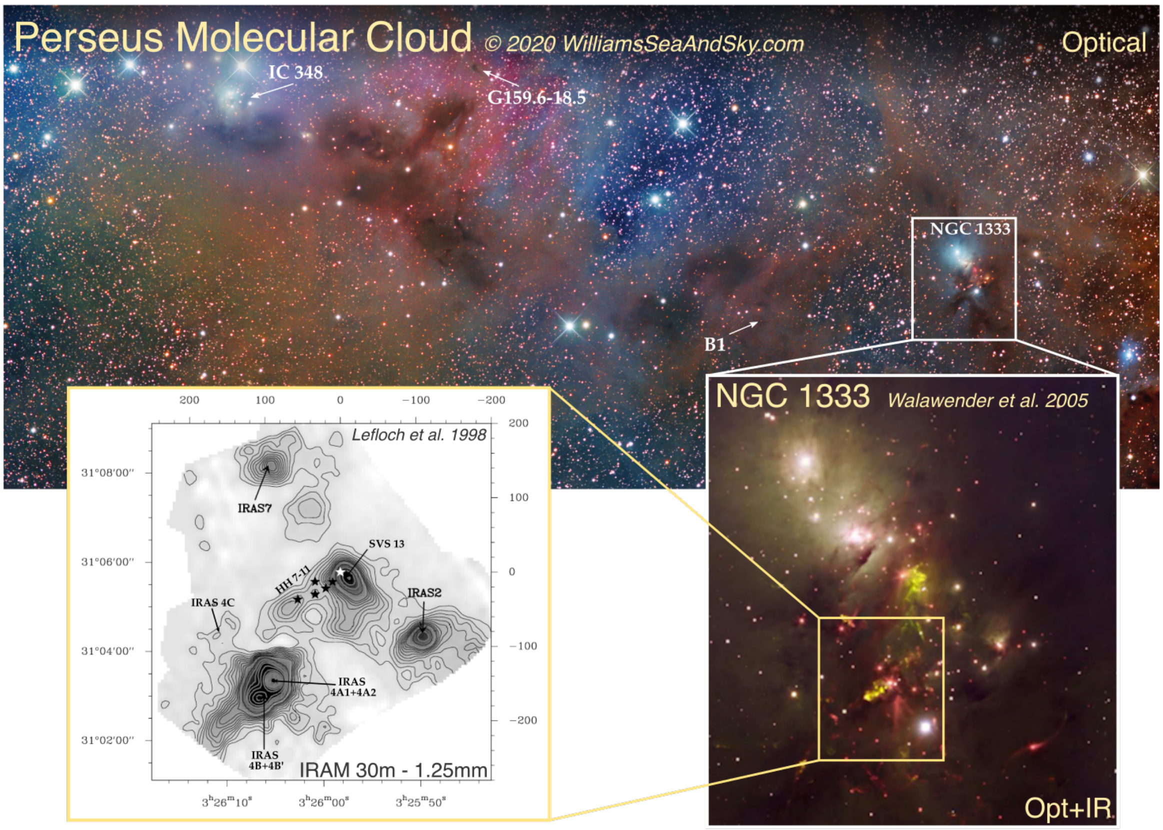

Figure 3.1: *Upper:* Optical image of the Perseus molecular cloud located at 300 pc (Zucker et al. 2018) from the Sun. *Lower right:* Zoom-in of the star forming region NGC 1333 with a composite of optical and infrared images (Walawender et al. 2008). The optical component is from the Mosaic camera on the Mayall 4 meter telescope at Kitt Peak with the broadband i' filter mapped to blue, the Hα to green, and the SII to orange. The infrared component (mapped to the red channel) is from the Spitzer Space Telescope 4.6 μm image. *Lower-left:* Zoom-in inside the NGC 1333 star forming region. It shows the continuum emission at 1.25mm obtained with the IRAM 30m radiotelescope (Lefloch et al. 1998a). The main cores are reported (IRAS 4, SVS13, IRAS 2, IRAS 7).

III sources tend to be hard to distinguish from the hundreds of main-sequence stars along the line of sight.

Currently the most active site of on-going star formation in Perseus is NGC 1333 (Bally et al. 1996; Lada et al. 1996).

3.1.2 The NGC 1333 stellar nursery

NGC 1333 is a bright reflection nebula, illuminated by two late-type B stars, located in the western portion of the Perseus molecular cloud (van den Bergh 1966; Racine 1968; Strom et al. 1974; Cernis 1990), at a distance of 299 ± 17pc (Zucker et al. 2018)(see Figure 3.1). Nowadays, the term NGC 1333 is used to denote the young stellar cluster associated with the reflection nebula.

The NGC 1333 cluster contains about 150 young stars with a median age of about 10^6 years and a total mass of about 100 $M_\odot$, and its star formation rate averaged over the last million years, is estimated to be close to 10^{-4} $M_\odot$ yr^{-1} (Walsh et al. 2006, 2007).

The NGC 1333 cluster was first mapped at infrared wavelengths by Strom et al. (1976), who identified 25 sources, all likely YSOs. Later on, Jennings et al. (1987) identified nine distinct far-infrared sources, using data from the Infrared Astronomical Satellite (IRAS). In particular, two of them, IRAS 1 and IRAS 4, were obscured by their infalling envelope of gas and dust, so they were identified as protostars. With the Spitzer infrared surveys (Jørgensen et al. 2006; Rebull et al. 2007), 137 YSOs were found to be associated with NGC 1333, of which 39 protostellar objects and 98 pre-main-sequence stars with disks (Gutermuth et al. 2008). NGC 1333 is the most active star-forming region in protostellar activity in Perseus. Indeed, it contains a large number of Class 0/I objects, denoting its current star-formation activity (Jørgensen et al. 2008).

As pointed out by different studies (Lada et al. 1996; Gutermuth et al. 2008), the stellar population in NGC 1333 is segregated into two groups: the north subcluster is located at the surroundings of SVS3, and it is dominated by a large population of Class II/III objects; the south subcluster contains most of the young sources found in this region, like IRAS 2, IRAS 4, and SVS13[2](see Figure 3.1). Most of the high column density material is located in the middle and southern parts of the NGC 1333 region (Warin et al. 1996; Hacar et al. 2017). It is characterized by cavities, that can be traced to the action of current outflows or can be the remnants of past outflow activity (Lefloch et al. 1998a; Sandell & Knee 2001; Quillen et al. 2005), forming an intricate network of cores and filamentary structures, some of which are collections of velocity-coherent fibers (Hacar et al. 2017; Chen et al. 2020).

Evidences of the interaction between the protostars and the circumstellar environment as Herbig-Haro (HH) objects have been reported. Indeed, NGC 1333 is peculiar for the large number of Herbig-Haro objects, with a covering factor greater than 50% in the central region (Walawender et al. 2008). Bally et al. (1996) found over 30 groups of HH objects associated with more than a dozen of currently active outflows. In particular, the HH 7-11 is one of most evident chains of HH objects propagating from the vicinity of SVS13 that has been extensively studied at different wavelengths (e.g., Hartigan et al. 1989; Reipurth et al. 1993; Gredel 1996;

---

[2] SVS 13 was listed as source number 13 by Strom et al. (1976), which led to the SVS designation. Herbig & Jones (1983), however, chose to use SSV 13 because"the designation SVS has been pre-empted". Subsequently both SVS and SSV have been used in the literature when referring to this source. I use the SVS designation to match the majority of the literature.

Molinari et al. 1999; Bachiller et al. 1998b; Codella et al. 1999; Molinari et al. 2000; Bachiller et al. 2000; Noriega-Crespo et al. 2002; Neufeld et al. 2006).

It is possible to identify three main filaments in NGC 1333 (Dhabal et al. 2018): one in the southeast part (SE), and two in the north (NE and NW) (see Figure 3.2). The NE filament shows a velocity gradient along its length ($\sim$ 0.7 km s^{-1}) and across its width ($\sim$0.5 km s^{-1}) with a mean systemic velocity of 8.5 km s^{-1}. The NW filament has a systemic velocity $\sim$ 8 km s^{-1}and it is populated by a sequence of five Class II sources. The region between these two filaments is clear of dust and gas, and many evolved YSOs and main-sequence stars are present here. Therefore, past outflows from these sources could have played an important role in the formation of the two filaments by clearing out the cloud (Knee & Sandell 2000; Quillen et al. 2005; Dhabal et al. 2019). On the other hand, the SE filament is characterized by two substructures running parallel to each other with two distinct systemic velocities, +7.5 km s^{-1} and +8.2 km s^{-1}, respectively, with the western one blue-shifted with respect to the eastern one. An arch-like structure with a velocity of 6.5 km s^{-1}, west to the SE filament, traces the borders of a large cavity. The protostellar systems of IRAS2, SVS13, and IRAS4 lie northwest of this cavity, and the SK1 system is to the south of it. Dhabal et al. (2019) suggested that this region represents the gas compressed by a *turbulent cell* moving from the south and clashing against the NGC 1333 cloud. This clash could have formed the SE filament and triggered the formation of the IRAS 2, SVS13, and IRAS 4 protostars.

3.1.3 NGC 1333 IRAS4 system

The NGC 1333 IRAS 4 was first identified by its H_2O maser emission detected by Haschick et al. (1980), and later on, it was detected in the IRAS maps by Jennings et al. (1987). Additionally, the latter suggested that IRAS 4 could have been binary based on its association with two maser sources. This suggestion was later confirmed by sub-millimeter and radio observations that resolved IRAS 4 into two sources separated by $\sim$ 30$''$, IRAS 4A with a mass of $\sim$ 9M$_\odot$ and IRAS 4B with a mass of $\sim$ 4M$_\odot$ (Sandell et al. 1991; Mundy et al. 1993). In 1995, Lay et al. revealed IRAS 4A to be a binary itself composed of two sources separated by 1.$''$8, and IRAS 4B containing more than two components. Later on, the system has been imaged at mm and radio wavelengths, and it was possible to disentangle the two components in IRAS 4A, 4A1 and 4A2, and two components in IRAS 4B, 4B and 4B$'$ separated by 10$''$ (Choi et al. 1999; Smith et al. 2000; Looney et al. 2000; Di Francesco et al. 2001; Reipurth et al. 2002). Several nomenclature were used for these sources in the various studies[3], but I refer here to the one used by Di Francesco et al. (2001).

At millimeter wavelengths, 4A1 is three times brighter than 4A2. However, their respective luminosity is unknown since they are not resolved in the sub-mm – IR wavelengths range where the luminosity peak lies. The bolometric luminosity of the whole IRAS 4A system is 9.1 L$_\odot$ (Kristensen et al. 2012; Karska et al. 2013). IRAS 4A is the second hot corino ever discovered (Bottinelli et al. 2004a), after IRAS 16293-2422 (Cazaux et al. 2003). Interferometric IRAM/PdBI (Plateau de Bure Interferometer, now evolved into NOEMA) observations later suggested that

---

[3] 4B$'$ is the southeastern source, $\sim$10$''$ away from 4B, that is $\sim$ 20$''$ southeast of IRAS 4A. 4B$'$ has been called *4C* by Choi et al. (1999) and Looney et al. (2000), but that name had already been given to a third IRAS 4 source detected $\sim$ 45$''$ northeast of IRAS 4A by Sandell et al. (1991); Rodriguez et al. (1999); Smith et al. (2000); Sandell & Knee (2001). Instead, Sandell & Knee (2001) called it *4BE*, and Smith et al. (2000) called it *4BII*.

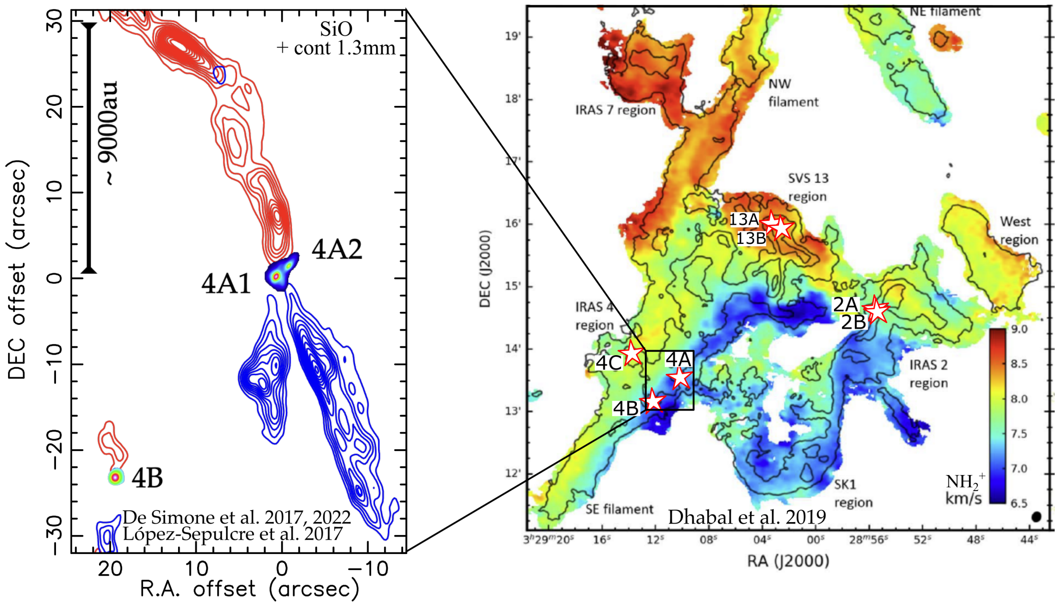

Figure 3.2: *Right:* N_2H^+ (1-0) line-of-sight velocity map of the southern-east part of NGC 1333 from CARMA observations (Dhabal et al. 2019). The main protostellar cores of the region are marked with white stars. *Left:* Overlap of the continuum at 1.3 mm of the IRAS 4A binary system as observed with ALMA (López-Sepulcre et al. 2017) and IRAS 4B (De Simone et al. 2017), with their outflows as traced by SiO observed with NOEMA (De Simone et al. 2022). In red and blue contours the red- and blue-shifted component with respect to the systemic velocity.

iCOM emission originates from 4A2 rather than 4A1 (Taquet et al. 2015; De Simone et al. 2017; López-Sepulcre et al. 2017). Also IRAS 4B is known to possess a hot corino region (Bottinelli et al. 2007; De Simone et al. 2017).

As for many Class 0 protostars, IRAS 4A is associated with a spectacular large-scale (a few arcminutes) bipolar outflow (see Figure 3.2) observed with several tracers, such as CO, SiO, SO, HCN (Blake et al. 1995; Lefloch et al. 1998a; Choi 2005; Choi et al. 2011). Choi (2005) clearly traced the high-velocity component with SiO emission using VLA observations at 2″ angular resolution. From its map, it is possible to distinguish two different blue-shifted lobes toward the south and only one northern redshifted lobe with a peculiar bending toward the northeast at 20″ from the protostars. Using IRAM/PdBI high spatial resolution observations (<1″), Santangelo et al. (2015) mapped the outflows at lower scale (∼30″) with respect to the SiO map from Choi (2005), using CO, SiO and SO as tracers. They were able to disentangle the two southern lobes, revealing a fast collimated jet associated with bright H_2 emission and driven by 4A1 (southeast lobe) and a slower and precessing jet driven by 4A2 (southwest lobe). Furthermore, the jets present different morphologies: the 4A2 jet shows a large spatial extent and an S-shaped pattern on small scales, probably due to jet precession; the 4A1 jet is faster, covers a smaller extent (∼15″), and presents as C-shaped tilted toward the east of 4A1. Thanks to a detailed study on sulfur species using interferometric observations, for the first time Taquet et al. (2020) were able to distinguish the outflow driven by 4A1 from the one driven by 4A2 also in the northern lobe.

4

Molecular Richness of young protostars

4.1 Unveiling the hot corino's chemical nature

The first studies I carried out in my thesis were on the chemical nature of the IRAS 4A hot corinos. At the time of these studies, after almost twenty years of hunting, less than a dozen hot corinos were known. Most of these studies were performed at mm wavelengths with single-dish facilities as IRAM-30m. With the advent of facilities with high sensitivity and high angular resolution, as NOEMA and ALMA, many more hot corinos have been detected and many of them were discovered to be part of close ($\leq 1''$) binary systems. At the time of the thesis writing, new surveys suggest that $\leq$ 50% of protostars develop a hot corino (e.g., Belloche et al. 2020; Yang et al. 2021). Additionally, several hot corinos in binary systems show very different millimeter molecular spectra (e.g., López-Sepulcre et al. 2017; Ospina-Zamudio et al. 2018; Manigand et al. 2020; Yang et al. 2021).

Two possibilities may explain why hot corinos are so difficult to find and why the millimeter spectra of coeval objects are so different:

i) If the dust is optically thick enough to absorb the millimeter molecular lines, it may hide hot corinos and there may not be a real chemical diversity in the hot corinos of binary systems. Several indirect evidences point that, at mm wavelengths, the dusty envelopes wrapping Class 0/I hot corinos could be optically thick (e.g., Miotello et al. 2014; Galván-Madrid et al. 2018; Galametz et al. 2019).

ii) Hot corinos are rare and the millimeter spectra reflect an intrinsic chemical diversity likely caused by a different history of the object.

This said, it is of paramount importance to measure the chemical composition of the ice mantles formed in the previous prestellar core phase to understand the origin and nature of hot corinos.

However, the direct study of the ice mantle composition in young embedded sources is challenging, as a strong infrared background continuum is needed to obtain the absorption spectra from which the mantles composition is derived. A possibility is to retrieve it indirectly by observing the ice mantle species when they are released in the gas phase in hot corinos. Indeed, the protostar chemical appearance depends on the mantle composition, as showed by various theoretical studies (Aikawa et al. 2020; Kalvāns 2021). In turn, the mantle chemical content is sensitive to environmental conditions and to the ice formation timescale (e.g., Taquet et al. 2012a; Cuppen et al. 2017). Among the major ice mantle species (Boogert et al. 2015), the critical tracers in the gas phase are NH_3 and CH_3OH, as CO is often optically thick and confused with the envelope, CO_2 and CH_4 do not have observable transitions in the gas phase, and H_2O is hampered by the Earth's atmosphere.

Therefore, to investigate these two possibilities and to retrieve the protostars ice mantle history, I observed, with the VLA interferometer at centimeter wavelengths, the Class 0 NGC 1333 IRAS 4A binary system. This system was extensively studied at mm wavelengths, with IRAM-NOEMA and ALMA, providing an exhaustive chemical census and highlighting the chemical difference of the two components, IRAS 4A1 and IRAS 4A2. Indeed, IRAS 4A1 is the brightest mm continuum source that lacks in iCOM emission, while IRAS 4A2 is a well known hot corino enriched in iCOMs (De Simone et al. 2017; Taquet et al. 2015; López-Sepulcre et al. 2017).

The research presented in this section has resulted in two scientific papers:

- "*Hot corinos chemical diversity: myth or reality*"
  De Simone M., Ceccarelli C., Codella C., Svoboda B.E., Chandler C. ,Bouvier M., Yamamoto S., Sakai N., Caselli P., Favre C., Loinard L., Lefloch B., Baobab Liu H., López-Sepulcre A., Pineda J.E., Taquet V., and Testi L.
  Published in the *Astrophysical Journal Letters, 2020, 896, L3*.

  It was associated with a *press release* from NRAO (National Radio Astronomy Observatory) in USA, INAF (Istituto Nazionale Astrofisica Italiana) in Italy, and CNRS (Centre National de la Recherche Scientifique) in France.
  CNRS_PressLink, UGA_PressLink NRAO_PressLink, INAF_PressLink,

- "*Tracking the ice mantle history in the NGC 1333 IRAS 4 protostars*".
  De Simone M., Ceccarelli C., Codella C., Svoboda B.E., Chandler C. ,Bouvier M., Yamamoto S., Sakai N., Caselli P., Favre C., Loinard L., Lefloch B., Baobab Liu H., López-Sepulcre A., Pineda J.E., and Testi L.
  The paper is in finalization and it will be submitted to the *Astrophysical Journal Letters.*

4.2 Hot corinos chemical diversity: myth or reality

4.2.1 Introduction

Interstellar Complex Organic Molecules (iCOMs) are molecules detected in the interstellar medium containing carbon and at least six atoms (Herbst & van Dishoeck 2009; Ceccarelli et al. 2017). These molecules are of particular interest because they carry a substantial fraction of carbon usable for prebiotic chemistry (e.g., Caselli & Ceccarelli 2012).

In Solar-like young Class 0 protostars, iCOMs are found in relatively large quantities toward the so-called hot corinos, which are compact ($\lesssim$100 au), hot ($\gtrsim$100 K) and dense ($\geq 10^7$ cm^{-3}) regions enriched in iCOMs at the center of the envelopes accreting the future star (Ceccarelli 2004; Ceccarelli et al. 2007; Caselli & Ceccarelli 2012).

The first hot corino was discovered in 2003 toward the Class 0 source IRAS 16293−2422 (e.g., Cazaux et al. 2003; Jørgensen et al. 2016; Manigand et al. 2020). Since then other Class 0 hot corinos have been discovered: NGC 1333 IRAS 4A (hereafter IRAS 4A; e.g. Bottinelli et al. 2004a; Taquet et al. 2015; López-Sepulcre et al. 2017; De Simone et al. 2017; Sahu et al. 2019), NGC 1333 IRAS2A, NGC 1333 IRAS4B (e.g., Jørgensen et al. 2005; Bottinelli et al. 2007; Maury et al. 2014b; De Simone et al. 2017), HH212 (Codella et al. 2016b; Bianchi et al. 2017; Lee et al. 2017b, 2019a), B335 (Imai et al. 2016), L483 (Oya et al. 2017; Jacobsen et al. 2019), Barnard1b-S (Marcelino et al. 2018), Ser-emb 1 (Martin-Domenech et al. 2019), BHR71-IRS1 (Yang et al. 2020). Lately, few more evolved Class I hot corinos were also discovered: NGC 1333 SVS13A (De Simone et al. 2017; Bianchi et al. 2019b), B1a (Öberg et al. 2014) and Ser-emb 17 (Bergner et al. 2019). Therefore, after almost twenty years, only about a dozen hot corinos are known. Recent surveys concluded that ∼30% of low-mass Class 0/I protostars show emission from at least three iCOMs (De Simone et al. 2017; Belloche et al. 2020).

Most of the hot corinos cited above turn out to be binary systems when imaged at high angular resolution. This is in agreement with previous surveys that found that 40-60% of protostars are multiple systems (Maury et al. 2014b; Tobin et al. 2016). Interestingly, with the first hot corino maps it became clear that the two objects in a given binary system can substantially differ in molecular complexity. Illustrative examples are provided by IRAS 16293−2422 and IRAS 4A (Jørgensen et al. 2016; López-Sepulcre et al. 2017). IRAS 16293−2422 is composed by two sources, A and B, separated by $5\farcs1$ (∼ 720 au), where source A, weaker in millimeter continuum emission, is brighter in iCOMs lines than source B (e.g., Caux et al. 2011; Pineda et al. 2012; Jørgensen et al. 2016; Manigand et al. 2020). IRAS 4A, located in the NGC1333 region in the Perseus cloud at (299 ± 15) pc of distance (Zucker et al. 2018), is also a binary system composed by IRAS 4A1 and IRAS 4A2 (hereafter 4A1 and 4A2), separated by $1\farcs8$ (∼540 au): while 4A1 is brighter in the mm continuum than 4A2, only 4A2 shows bright iCOMs lines (Taquet et al. 2015; López-Sepulcre et al. 2017; De Simone et al. 2017). However, not always the brightest millimeter continuum source in a binary system is the one weak in iCOMs emission (see e.g. Ospina-Zamudio et al. 2018).

In summary, despite two decades of hunting, only a dozen hot corinos are known so far. Of them, many are binary systems with the two components showing drastically different molecular spectra. Two related questions arise: (1) Why are hot corinos so difficult to find? While it is known that not all Class 0/I sources possess hot corinos (e.g., Sakai & Yamamoto 2013; Higuchi et al. 2018; Bouvier et al. 2020), observational biases might hamper their detection.

(2) Why do coeval objects seem drastically differ in their chemical composition? Is this a real difference or is it only/mostly due to observational biases?

A major observational bias could be caused by the dust opacity, that could be very high in Class 0/I sources, due to their high densities and, consequently, column densities (e.g., Miotello et al. 2014; Galván-Madrid et al. 2018; Galametz et al. 2019). If the effect of dust absorption is not negligible, there are three major consequences: (1) hot corinos may be difficult to detect in the millimeter (also) because of the high dust absorption of the iCOMs lines; (2) the molecular complexity diversity observed in binary systems objects may reflect a difference in the front dust column density rather than a real chemical difference of the two objects; (3) the iCOMs abundances in hot corinos could have been so far underestimated. In order to test this hypothesis, we targeted the IRAS 4A binary system, where the two objects show extremely different iCOMs line spectra at mm wavelengths (see above), and carried out observations of several methanol lines, one of the simplest iCOMS, at centimeter wavelengths where the dust is optically thin.

4.2.2 Observations

The IRAS 4A system was observed at 1.3 cm using K–band receivers (18-26.5 GHz) of the Karl G. Jansky Very Large Array (VLA) in C-configuration (35–3400 m) on December 10, 2018 (project ID: VLA/18B-166). We targeted ten CH_3OH lines, with frequencies from 24.9 to 26.4 GHz, upper level energies E_{up} from 36 to 175 K and Einstein coefficients A_{ij} in the range (0.5 – 1.1) $\times 10^{-7}$ s^{-1} (Table 4.1). The observed spectra were divided into eight spectral windows with $\sim$0.017 MHz (0.2 km s^{-1}) spectral resolution and $\sim 1''$ ($\sim$300 au at the distance of IRAS 4A) angular resolution. The observations were centered on 4A2, at α(J2000) = $03^h29^m10^s.43$, δ(J2000) = $31^\circ13'32''.1$. The flux calibrators were J0137+3309 and J0521+1638, while the bandpass and the gain ones were J0319+4130, and J0336+3218, respectively. The absolute flux calibration error is $\leq$15%[1].

Data reduction and cleaning process were performed using the CASA[2] package while data analysis and images were performed using the GILDAS[3] package. We obtained a continuum image by averaging line-free channels from all the spectral windows (Figure 4.1). We self-calibrated, in phase amplitude, using the line-free continuum channels and applied the solutions to both the continuum and molecular lines. The dynamic range, as defined by peak source flux over RMS noise, was improved by 20% by the self-calibration. The final RMS noise in the continuum image, 3μJy beam^{-1}, is consistent with that reported by the VLA Exposure Time Calculator for a line-free continuum bandwidth of 4.5GHz, 26 antennas, and an on-source integration time of 3 hours. The cube were subsequently continuum subtracted, smoothed to 1 km s^{-1} ($\sim$ 0.08 MHz) and cleaned in CASA using a multiscale deconvolution[4] (scales=[0,5,15,18,25]) with natural weighting. The synthesized beams for each spectral window are reported in Table 4.1. The half power primary beam is $\sim 80''$.

---

[1] https://science.nrao.edu/facilities/vla/docs/manuals/oss/performance/fdscale

[2] https://www.casa.nrao.edu/

[3] http://www.iram.fr/IRAMFR/GILDAS

[4] This technique is a scale-sensitive deconvolution algorithm efficient for images with complicated and extended spatial structures. In fact, it allows to model the sky brightness as a linear combination of flux components of different scale sizes. The scale sizes are chosen following approximately the sizes of the dominant structures in the image and including the ‘0’ scale to model the unresolved ones (see casadocs-deconvolution-algorithms).

Table 4.1: Spectral parameters, synthesized beams and Gaussian fit results of the CH_3OH lines extracted toward the 4A1 and 4A2 continuum peaks.

Transition	Frequency$^{(a)}$ [GHz]	$E_{up}^{(a)}$ [K]	$\log A_{ij}^{(a)}$	Synthesized Beam maj × min (PA) [$'' \times ''$ (°)]	IRAS 4A1 $\int T_B dV^b$ [K km s^{-1}]	IRAS 4A1 V_{peak}^b [km s^{-1}]	IRAS 4A1 FWHM^b [km s^{-1}]	IRAS 4A1 RMS^c [K]	IRAS 4A2 $\int T_B dV^b$ [K km s^{-1}]	IRAS 4A2 V_{peak}^b [km s^{-1}]	IRAS 4A2 FWHM^b [km s^{-1}]	IRAS 4A2 RMS^c [K]
3(2,1)-3(1,2) E	24.92871	36	-7.2	0.97 × 0.95 (−12)	17(4)	6.5(0.2)	2.7(1.2)	1.0	34(3)	6.8(0.2)	3.1(0.3)	0.9
4(2,2)-4(1,3) E	24.93347	45	-7.1	0.97 × 0.95 (−12)	23(3)	6.5(0.2)	3.7(0.5)	1.0	32(3)	6.9(0.2)	3.1(0.3)	0.9
2(2,0)-2(1,1) E	24.93438	29	-7.2	0.97 × 0.95 (−12)	19(3)	6.5(0.2)	3.3(0.6)	1.0	27(3)	6.9(0.2)	2.9(0.3)	0.9
5(2,3)-5(1,4) E	24.95908	57	-7.1	0.97 × 0.95 (−12)	19(3)	6.1(0.3)	4.2(0.9)	0.9	32(3)	6.8(0.2)	3.1(0.3)	0.9
6(2,4)-6(1,5) E	25.01812	71	-7.1	0.97 × 0.95 (−19)	19(3)	6.3(0.3)	3.5(0.6)	1.0	31(3)	6.7(0.1)	2.5(0.2)	1.0
7(2,5)-7(1,6) E	25.12487	87	-7.1	0.98 × 0.95 (−21)	20(2)	7.0(0.2)	3.2(0.5)	0.9	35(3)	6.8(0.2)	2.9(0.3)	1.2
8(2,6)-8(1,7) E	25.29442	106	-7.0	0.96 × 0.94 (−11)	13(3)	6.8(0.3)	3.4(0.9)	0.9	32(2)	6.8(0.1)	2.8(0.3)	0.9
9(2,7)-9(1,8) E	25.54140	127	-7.0	0.96 × 0.92 (−50)	18(2)	6.5(0.2)	2.7(0.5)	0.8	31(2)	6.9(0.1)	2.6(0.2)	0.9
10(2,8)-10(1,9) E	25.87827	150	-7.0	0.97 × 0.93 (−35)	20(2)	6.4(0.2)	3.2(0.5)	0.8	32(2)	6.9(0.1)	2.6(0.2)	0.8
11(2,9)-11(1,10) E	26.31312	175	-6.9	0.94 × 0.91 (−35)	24(4)	6.0(0.4)	4.9(0.9)	1.1	31(3)	6.8(0.1)	2.9(0.3)	0.9

[a] Spectroscopic parameters by Xu et al. (2008) are from the CDMS (Cologne Database for Molecular Spectroscopy; Müller et al. 2005) molecular database.
[b] Results of the Gaussian fit algorithm.
[c] The RMS is computed over each spectral window.

4.2.3 Results

Continuum emission map

Figure 4.1 reports the map of the continuum emission at 25 GHz. The two continuum peaks mark the two protostars, whose coordinates (α(J2000) = $03^h29^m10\overset{s}{.}536$, δ(J2000) = $31^\circ13'31\overset{''}{.}07$ for 4A1, and α(J2000) = $03^h29^m10\overset{s}{.}43$, δ(J2000) = $31^\circ13'32\overset{''}{.}1$ for 4A2) are consistent with those derived by Tobin et al. (2016) and López-Sepulcre et al. (2017) with higher angular resolution observations. Since the angular resolution of our observations ($\sim 1''$) is smaller than the separation between 4A1 and 4A2 ($1.8''$), they are clearly disentangled in our images, even if individually unresolved with the current resolution.

At cm wavelengths, 4A1 shows a brighter continuum emission (due to dust or free-free) than 4A2. The peak fluxes are (2.1 $\pm$ 0.3) mJy beam^{-1} and (0.47 $\pm$ 0.07) mJy beam^{-1} toward 4A1 and 4A2, respectively. Taking into account the slightly different wavelength (1.05 cm) and angular resolution ($\sim 0\overset{''}{.}1$), these values are consistent with the ones measured by Tobin et al. (2016): (1.3 $\pm$ 0.2) mJy beam^{-1} for 4A1 and (0.38 $\pm$ 0.04) mJy beam^{-1} for 4A2.

Methanol lines

All the targeted methanol lines are detected with a signal-to-noise ratio larger than 3 (Table 4.1). Their velocity-integrated spatial distribution is shown in Fig. 4.1. The methanol emission peaks exactly toward the 4A1 and 4A2 continuum peaks, and it is well disentangled, even if unresolved at the current angular resolution, around the two protostars.

Figure 4.2 shows the ten methanol line spectra, isolated and not contaminated by other species, extracted toward the 4A1 and 4A2 continuum peaks. The lines are slightly brighter toward 4A2 than 4A1, whereas the linewidths are very similar (see also Tab. 4.1). We derived the velocity-integrated line intensities for each detected CH_3OH transition using a Gaussian fit, being the profile Gaussian-like. The fit results for both sources, namely the integrated emission ($\int T_b dV$), the linewidth (FWHM), the peak velocities (V_{peak}) and the RMS computed for each spectral window, are reported in Table 4.1. The velocity peaks are consistent with the systemic velocity of the molecular envelope surrounding IRAS 4A ($\sim$ 6.7 km s^{-1}; Choi 2001). The linewidths are between 3 and 4 km s^{-1} in agreement with those found by Taquet et al. (2015) and López-Sepulcre et al. (2017) toward 4A2 at mm wavelength.

In summary, our new VLA observations show a first clear important result: the detection

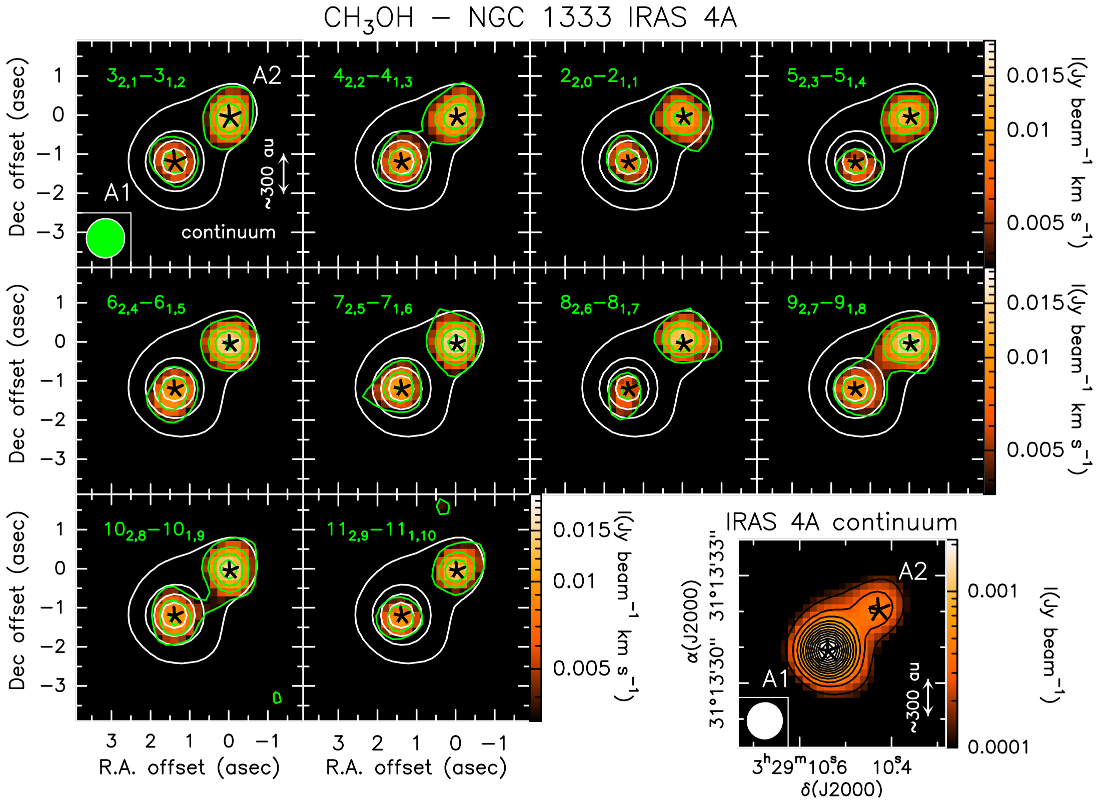

Figure 4.1: *Bottom right panel:* IRAS 4A continuum emission map at 25 GHz. First contour and steps correspond to 50σ_C (σ_C = 3μJy beam^{-1}). *Other panels:* CH_3OH velocity-integrated maps toward IRAS 4A in color scale overlapped with the continuum (white) contours (from 50σ_C with steps of 170σ_C). The emission is integrated from -2 km s^{-1} to 2 km s^{-1} with respect to the v_{sys} ($\sim$ 6.7 km s^{-1}). Methanol first contour (green) and steps correspond to 3σ (σ=1.2 mJy beam^{-1} km s^{-1}). The transition of the imaged line is reported in each panel. The black stars show the 4A1 and 4A2 positions. Synthesised beams for continuum (white) and lines (green) are in the lower left corner.

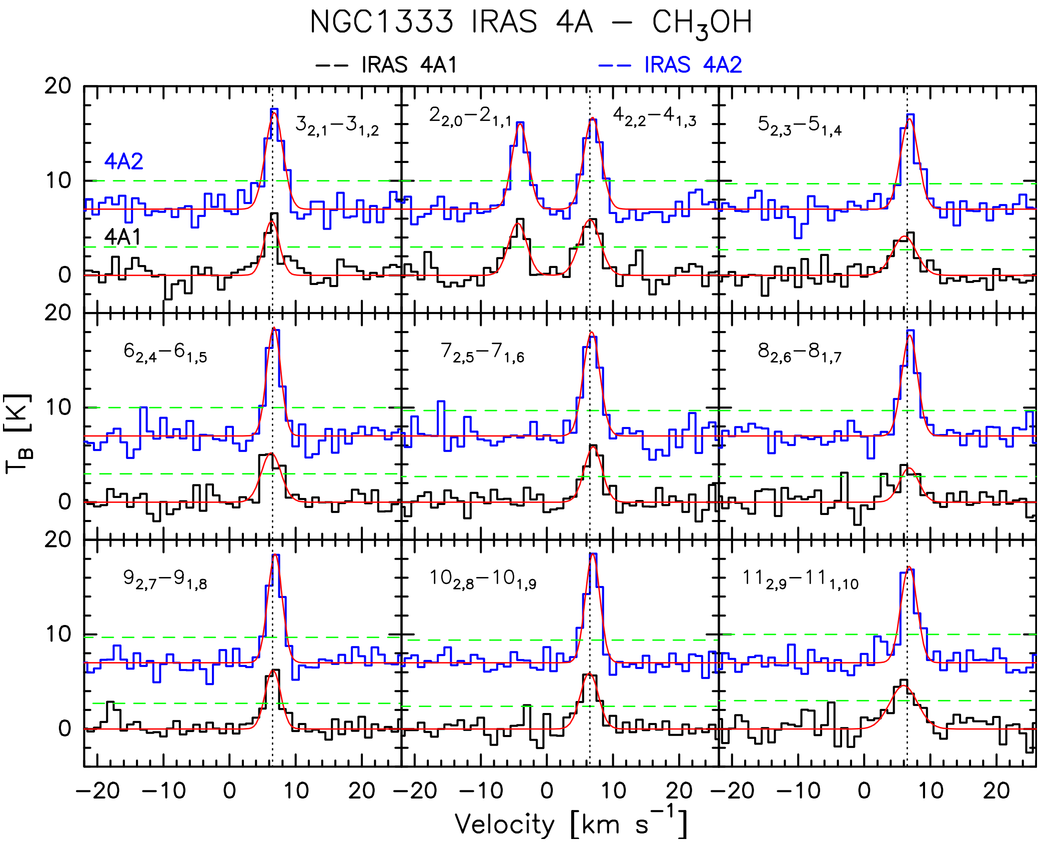

Figure 4.2: The methanol lines (marked in each panel) detected in the VLA K–band toward 4A1 (black) and 4A2 (blue). The horizontal green dashed lines show the 3σ level. The vertical dotted black lines report the v_{sys} (6.7 km s^{-1}). The red and magenta curves show the best Gaussian fits (see Table 4.1).

of methanol emission toward 4A1, the protostar where previous mm observations showed no iCOMs emission (López-Sepulcre et al. 2017).

4.2.4 Centimeter vs millimeter observations: dust absorption derivation

We compared our new cm observations of methanol lines with previous ones at 143–146 GHz in order to understand whether the dust absorption, more important at mm than at cm wavelengths, may explain the absence of iCOMs mm line emission in 4A1 (López-Sepulcre et al. 2017). We first carried out a non-LTE analysis of the cm methanol lines from which we derived the gas temperature, density and CH_3OH column density toward 4A1 and 4A2. Then, using the same parameters, we predicted the methanol line intensities at 143–146 GHz, the frequency of the observations by Taquet et al. (2015). Finally, we compared the predicted and measured mm line intensities and we attributed the difference to the absorption of the dust between us and the gas emitting methanol, via the usual equation:

$$I_{\nu}^{obs} = I_{\nu}^{pred} e^{-\tau_{\nu}} \tag{4.1}$$

in order to derive the dust optical depth toward 4A1 and 4A2, respectively.Please note that the foreground dust opacity obtained by Eq. 4.1 assumes that the absorbing dust fully covers the emitting gas area, which may not be necessarily the case. Yet, the derived attenuation of the methanol line intensities is still valid, even though it is only an average over the emitting gas area.

non-LTE analysis of the cm methanol lines

To derive the physical properties of the gas emitting CH_3OH, namely gas temperature, density and methanol column density, we performed a non-LTE analysis using a Large Velocity Gradient (LVG) code Ceccarelli et al. (2003). CH_3OH can be identified in A- and E-type due to the total spin (I) state of the hydrogen nuclei in the CH_3 group: A-type if the total spin function is symmetric (I=3/2), E-type if asymmetric (I=1/2) (Rabli & Flower 2010). We used the collisional coefficients of both types of CH_3OH with para-H_2, computed by Rabli & Flower (2010) between 10 and 200 K for the first 256 levels and provided by the BASECOL database (Dubernet et al. 2013). We assumed a spherical geometry to compute the line escape probability (De Jong et al. 1980), the CH_3OH-A/CH_3OH-E ratio equal to 1, the H_2 ortho-to-para ratio equal to 3, and that the levels are populated by collisions and not by the absorption of the dust background photons whose contribution is very likely negligible due to the low values of the CH_3OH Einstein coefficients A_{ij}. Please note that the present LVG analysis only accounts for the line optical depth (to have also the dust τ in the methanol emitting region would require information on the structure of the region which we do not have, as the emission is unresolved).

We ran a large grid of models (≥10000) covering the frequency of the observed lines, a total (CH_3OH-A plus CH_3OH-E) column density N_{CH_3OH} from 2×10^{16} to 8×10^{19} cm^{-2}, a gas density n_{H_2} from 1×10^6 to 2×10^8 cm^{-3}, and a temperature T from 80 to 200 K. We then simultaneously fitted the measured CH_3OH-A and CH_3OH-E line intensities via comparison with those simulated by the LVG model, leaving N_{CH_3OH}, n_{H_2}, T, and the emitting size θ as free parameters. Following the observations, we assumed the linewidths equal to 3.5 km s^{-1} and 3.0 km s^{-1} for 4A1 and 4A2, respectively, and we included the calibration uncertainty (15%) in the observed intensities.

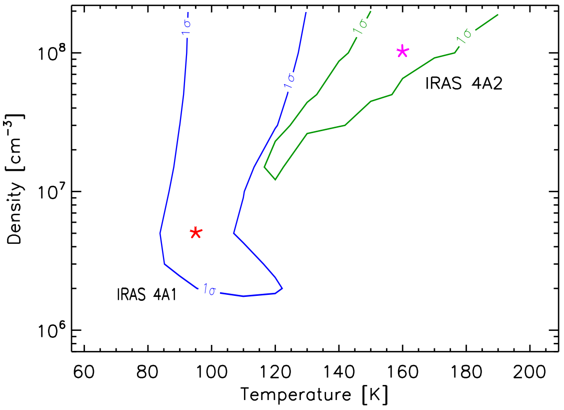

Figure 4.3: Density-Temperature χ^2 contour plots. The contours represent 1σ confidence level contours for 4A1 (blue) and 4A2 (green), respectively, assuming the best fit values of N_{CH_3OH} and θ in Table 4.2. The best fit solutions are marked by the red (4A1) and magenta (4A2) asterisks.

The best fit is obtained for a total CH_3OH column density N_{CH_3OH} = 2.8×10^{19} cm^{-2} with reduced chi-square χ^2_R = 0.6 for 4A1 and N_{CH_3OH} = 1×10^{19} cm^{-2} with χ^2_R = 0.1 for 4A2. All the observed lines are predicted to be optically thick and emitted by a source of $0\farcs22$ for 4A1 and $0\farcs24$ for 4A2 (~70 au) in diameter. Solutions with $N_{CH_3OH} \geq 1 \times 10^{18}$ cm^{-2} for 4A2 and $\geq 1 \times 10^{19}$ cm^{-2} for 4A1 are within 1σ of confidence level. Increasing the methanol column density, the χ^2_R decreases until it reaches a constant value for $N_{CH_3OH} \geq 1 \times 10^{19}$ cm^{-2} for 4A1 and $N_{CH_3OH} \geq 3 \times 10^{19}$ cm^{-2} for 4A2; this is because all the observed lines become optically thick ($\tau \sim 10-30$ for 4A1,$\tau \sim 2-6$ for

4A2) and, consequently, the emission becomes that of a black body. The results do not change assuming a linewidth ±0.5 km s^{-1} with respect to the chosen one.

Figure 4.3 shows, for both sources, the density-temperature χ^2 surface of the N_{CH_3OH} best fit. The gas temperature is (90–130) K for 4A1 and (120–190) K for 4A2, while for the gas density we obtained a lower limit of 2×10^6 cm^{-3} for 4A1 and 1.5×10^7 cm^{-3} for 4A2, which implies that the levels are LTE populated. The fit results are reported in Table 4.2. The derived n_{H_2} and T are consistent with those computed with the model summarised in Su et al. (2019) using our sizes.

Predictions of mm methanol line intensities

Adopting the 1σ range of gas temperature and density derived for 4A1 and 4A2 (Table 4.2), we ran a new grid of LVG models with the CH_3OH column density from 1×10^{18} to 8×10^{19} cm^{-2} at 143–146 GHz to predict the methanol line intensities observed by Taquet et al. (2015). We then used the CH_3OH $3_1 - 2_1$ A^+ line at 143.866 GHz, which provides the most stringent constraint to the dust optical depth, to compare the predicted intensity with that observed by Taquet et al. (2015). In the comparison, we took into account our LVG-derived source size and the angular resolution of the Taquet et al. (2015) observations. While for 4A2 we considered the line intensity quoted by Taquet et al. (2015), for 4A1, not having CH_3OH detection, we used the 3σ level of the Taquet et al. (2015) observations integrated over 3 km s^{-1} (average linewidth toward 4A1: see Section 4.2.3).

The 4A1 and 4A2 CH_3OH predicted and observed values are reported in Table 4.2. While the two intensities are similar toward 4A2, they differ by about a factor five toward 4A1.

Dust absorption toward 4A1 and 4A2

Assuming that the difference between the predicted and observed intensities is due to the (foreground) dust absorption and using Eq. 4.1, we derived the dust optical depth at 143 GHz (τ_{dust}^{143GHz}; Table 4.2). While τ_{dust}^{143GHz} toward 4A2 is small ($\sim$ 0.3), that toward 4A1 is large ($\geq$ 1.6) enough to attenuate the methanol line intensity by a factor $\geq$5. Therefore, the dust is affecting the mm line emission differently in the two sources.

4.2.5 Discussion

Is IRAS 4A1 a hot corino?

So far, only about a dozen hot corinos have been detected (Section 4.2.1) and the question arises whether this is because they are rare or because the searches have always been carried out at mm wavelengths, where dust could heavily absorb the lines emission.

Our first result is that a source that was supposed not to be a hot corino based on mm observations, IRAS 4A1 (López-Sepulcre et al. 2017), indeed possesses a region with temperature $\geq$ 100 K (Section 4.3), namely the icy mantle sublimation one, and shows methanol emission (Section 4.2.3), the simplest of the iCOMs, when observed at cm wavelengths. According to its definition (Ceccarelli 2004), thus, IRAS 4A1 is a hot corino.

Although we cannot affirm that hot corinos are ubiquitous, it is clear that the searches at

Table 4.2: *Top:* Best-fit results and 1σ confidence level (range) from the non-LTE LVG analysis of the CH_3OH lines toward 4A1 and 4A2. *Bottom:* Comparison of the LVG model predictions with the Taquet et al. (2015) millimeter observations (see text).

		IRAS 4A1		IRAS 4A2	
		LVG Results			
		Best Fit	Range	Best Fit	Range
n(H_2)	[cm^{-3}]	5×10^6	$\geq 2\times10^6$	1×10^8	$\geq1\times10^7$
T_{kin}	[K]	100	90-130	160	120-190
N_{CH_3OH}	[cm^{-2}]	2.4×10^{19}	$\geq1\times10^{19}$	1×10^{19}	$\geq1\times10^{18}$
Source size	[$''$]	0.22	0.20-0.24	0.24	0.22-0.30
		Predictions vs mm observations			
$T_b dV_{pred}$	[K km s^{-1}]	4.7(0.8)		9.1(1.2)	
$T_b dV_{obs}$	[K km s^{-1}]	$\leq$ 0.9		6.5(1.9)	
τ_{dust}^{143GHz}		$\geq$1.6		0.3	

mm wavelengths may be heavily biased and that complementary cm observations are necessary to account for dust opacity and understand the occurrence of hot corinos.

4A2 versus 4A1: are they chemically different?

Unlike 4A2, no sign of iCOMs mm emission was revealed toward 4A1 (Taquet et al. 2015; López-Sepulcre et al. 2017). Using ALMA observations at 250 GHz, López-Sepulcre et al. (2017) found that the iCOMs abundances toward 4A2 and 4A1 differ by more than a factor 17, with the largest values ($\sim$100) for $HCOOCH_3$ and CH_3CN.

The first question to answer is whether the chemical difference between the two coeval objects is real or due to a different absorption by the surrounding dust.

We found that τ_{dust} at 143 GHz toward 4A1 and 4A2 is $\geq$1.6 and 0.3, respectively (see Table 4.2). Using the dependence of τ_{dust} from the frequency ($\tau_{\nu_2}/\tau_{\nu_1} = (\nu_2/\nu_1)^{\beta}$) and assuming $\beta = 2$ (ISM value), the optical depth scaled at 250 GHz (frequency at which López-Sepulcre et al. 2017, derived the above iCOMs abundance ratios) is $\geq$4.9 for 4A1 and 0.9 for 4A2. Therefore, the different dust absorption toward 4A1 and 4A2 provides us, as lower limit, a factor 55 difference in their line intensities (I^{A2}/I^{A1}), comparable to the 4A2/4A1 iCOMs abundance ratios derived by López-Sepulcre et al. (2017). A large dust absorption was also suggested by the anomalous flattened continuum spectral index at 100-230 GHz (Li et al. 2017) and the 90° flipping of the linear polarization position angles observed at above and below 100 GHz frequencies (Ko et al. 2020).

Although we cannot exclude that a real chemical difference exists between 4A1 and 4A2, the observations so far available cannot support that hypothesis. Centimeter observations of other iCOMs than methanol are necessary to settle this issue. This conclusion may apply to other binary systems where an apparent chemical difference is observed using mm observations.

Are the iCOMs abundances in hot corinos underestimated?

The dust absorption also affects the iCOMs line intensities in 4A2. At 143 GHz $\tau_{\rm dust}$ is 0.3, which leads to underestimate the iCOMs abundances by about 30%. At higher frequencies, this factor becomes more important; e.g., at 250 GHz, where several hot corinos studies are carried out (see references in Section 4.2.1), the absorption factor would be 2.5, and at 350 GHz, frequency where the most sensitive iCOMs search has been carried out (e.g., Jørgensen et al. 2016), the absorption factor would be 6. This behaviour also agrees with what already found in massive hot cores (e.g., Rivilla et al. 2017). Therefore, in order to derive reliable iCOMs abundances complementary cm observations are needed to estimate the dust absorption.

4.2.6 Conclusion

We carried out observations of methanol lines at cm wavelengths with the VLA interferometer toward the binary system IRAS 4A, where previous mm observations showed a possible chemical differentiation between the two objects. Specifically, while 4A2 showed iCOMs line emission, 4A1 did not.

Our new observations detected ten methanol lines in 4A1 and 4A2 with similar intensities. Using a non-LTE analysis and comparing with previous methanol mm observations, we showed that (1) 4A1 is a hot corino, (2) the lack of iCOMs detection toward 4A1 at mm wavelengths is caused by a large dust optical depth, and (3) the determination of the iCOMs abundances toward 4A2 via mm observations is slightly underestimated by the dust absorption.

Therefore, the difficulty in discovering new hot corinos could be because the searches have been carried out at (sub)mm wavelengths, where the dust absorption might be not negligible. The suspected different chemical nature of coeval objects of the same binary system needs also to be verified at cm wavelengths, as well as the iCOMs abundances estimated from mm observations.

We conclude that centimeter observations of hot corinos are of paramount importance for their correct study. In the future, next generation instruments in the centimeter wavelenght regime, such as ngVLA (McGuire et al. 2018) and SKA (Codella et al. 2015b), could be even the most efficient way to identify hot corinos and certainly the most appropriate facilities to study them.

4.3 Investigating the ice mantle history of the IRAS 4 protostars

4.3.1 Introduction

The thousands exoplanets discovered so far (e.g., http://exoplanet.eu/) provide clear evidence of the incredible variety of planetary systems, different from each other and from our Solar System. In order to understand the origin of such diversity, it is crucial to characterize the early stages (Class 0/I protostellar objects, $10^4 - 10^5$ yr; Andre et al. 2000) of the formation of a planetary system. To study the diversity of these early stages , a powerful observational diagnostic tool is their chemical composition (Ceccarelli et al. 2007; Sakai & Yamamoto 2013). Indeed, the chemical complexity in star-forming regions starts at the very beginning of the process, during the pre-collapse phase. At this stage, icy mantles form on interstellar grains and grow rich of hydrogenated species. Then, during the warm protostellar phase, the ice mantle species are released in the gas phase through ice mantle sublimation (forming the so-called hot corinos[5]) (e.g., Caselli & Ceccarelli 2012; Öberg & Bergin 2021). Therefore, the composition of the icy mantles is crucial in establishing the observed chemical diversity.

Infrared (IR) absorption observations towards Solar-type protostars have shown that the icy mantles major components are H_2O, CO, CO_2, CH_4, NH_3, CH_3OH and other species with lower abundances (Bottinelli et al. 2010; Öberg et al. 2011a; Boogert et al. 2015). However, these observations can only be obtained toward sources with enough bright IR continuum emission, making it very difficult to characterize the ice mantles of deeply embedded protostars, and even more of prestellar cores. Another possibility is to observe the icy mantles major components once they are released into the gas phase during the hot corino phase. In this context, NH_3 and CH_3OH are the best, if not the only, major components of the mantle composition that can be studied with ground-based telescopes. Indeed, they are the only easily observable tracers as CO is often optically thick and confused with the surrounding cloud, CO_2 and CH_4 do not have dipole moments, and H_2O observations are hampered by the terrestrial atmosphere. Since NH_3 and CH_3OH are grain surface products (Watanabe & Kouchi 2002; Fuchs et al. 2009; Rimola et al. 2014; Song & Kästner 2017), their abundance ratio only depends on the mantle formation history (e.g., time, density, and temperature of the pre-collapse clump; Taquet et al. 2012b; Cuppen et al. 2017; Aikawa et al. 2020). Additionally, both molecules are key participants in the formation of more complex N- and O-bearing molecules

In this Letter we investigate the icy mantle composition, through the relative abundance of NH_3 and CH_3OH, of a set of Class 0 hot corinos in the inner 300 au region where planets will eventually form. In particular we targeted three sources in the Perseus NGC 1333 region (distant (299 ± 15) pc Zucker et al. 2018): the Class 0 protobinary system IRAS 4A, composed by IRAS 4A1 and IRAS 4A2 (hereafter 4A1 and 4A2) separated by $1.8''$ ($\sim$540 au), and IRAS 4B (hereafter 4B) located $\sim 30''$ south-east of IRAS 4A. All the three sources have a hot corino region (Taquet et al. 2015; López-Sepulcre et al. 2017; De Simone et al. 2017, 2020a; Sakai et al. 2006; Bottinelli et al. 2007; De Simone et al. 2017).

---

[5] Hot corinos are compact ($<$100 au), hot ($\geq$100 K) and dense ($n_{H_2} \geq 10^7$ cm^{-3}) regions (e.g., Ceccarelli 2004), enriched in interstellar Complex Organic Molecules (iCOMs; Herbst & van Dishoeck 2009; Ceccarelli et al. 2017).

4.3.2 Observations

The data used for this work are the VLA observations in K-band described in De Simone et al. (2020a) (project ID: 18B-166). In summary, we targeted ten CH_3OH and five NH_3 lines, with frequencies from 23.8 to 26.4 GHz and upper level energies ($E_{\rm up}$) from 36 to 175 K for CH_3OH and from 24 to 640 K for NH_3 (see Table 4.3). The observed lines were associated to 13 spectral windows with $\sim$0.017 MHz ($\sim$0.2 km s^{-1}) spectral resolution and $1''$ ($\sim$ 300 au at the distance of IRAS 4A; Zucker et al. 2018) angular resolution. The absolute flux calibration error is $\leq$15%[6]. Data reduction and cleaning process were performed using the CASA[7] package while data analysis and images were performed using the GILDAS[8] package. Further details can be found in De Simone et al. (2020a). The cubes, self-calibrated and continuum subtracted, were smoothed to 1 km s^{-1} ($\sim$0.08 MHz). The synthesized beams for each spectral window are reported in Table 4.3. The half power primary beam is $\sim 80''$.

4.3.3 Results

Maps and Spectra

Figure 4.4 reports the velocity-integrated map of the five NH_3 lines, for the three targeted sources (4A1, 4A2, and 4B), and of ten CH_3OH lines for 4B (as the CH_3OH maps for 4A1 and 4A2 are reported in De Simone et al. 2020a), overlapped with the 25 GHz continuum emission. The emission of both species peaks at the continuum position of the sources, with coordinates $\alpha(\mathrm{J2000}) = 03^{\mathrm{h}}29^{\mathrm{m}}10\overset{\mathrm{s}}{.}536$, $\delta(\mathrm{J2000}) = 31^{\circ}13'31\overset{''}{.}07$ for 4A1, $03^{\mathrm{h}}29^{\mathrm{m}}10\overset{\mathrm{s}}{.}43$, $31^{\circ}13'32\overset{''}{.}1$ for 4A2, and $03^{\mathrm{h}}29^{\mathrm{m}}12\overset{\mathrm{s}}{.}02$, $31^{\circ}13'07\overset{''}{.}9$ for 4B. Additionally, even if unresolved at the current angular resolution, the emission of NH_3 around the binaries 4A1 and 4A2 is well disentangled around the two protostars.

Figure 4.5 shows the spectra of all the targeted lines extracted at the continuum peak of the sources (the CH_3OH spectra for 4A1 and 4A2 are reported in De Simone et al. 2020a). We derived the velocity-integrated line intensities for each transition using for CH_3OH a Gaussian fit, while for NH_3 we used a Hyperfine fit since we were able to spectrally resolve the hyperfine structure. The Hyperfine fit is taking into account the hyperfine structure of ammonia assuming: i) the same excitation temperature for all the components of the multiplet, ii) Gaussian distribution of velocity, iii) the lines have the same width, and iv) the multiplet components do not overlap. The fits results are reported in Table 4.3. In the case of NH_3, the integrated emission is computed as the sum of the integrated area of the main and the satellite hyperfine components. The velocity peaks are consistent with the systemic velocity of the cloud hosting IRAS 4A1, 4A2 and 4B ($\sim$ 6.7 km s^{-1}; Choi 2001). In summary, we detected multiple lines of ammonia and methanol in the three Class 0 hot corinos, IRAS 4A1, 4A2 and 4B, at small scale ($\sim 1''$) around the central region.

---

[6] https://science.nrao.edu/facilities/vla/docs/manuals/oss/performance/fdscale

[7] https://www.casa.nrao.edu/

[8] http://www.iram.fr/IRAMFR/GILDAS

Table 4.3: Spectral parameters, synthesized beams and the Gaussian and Hyperfine fit results for the CH_3OH and NH_3 lines, respectively, extracted toward the IRAS 41A, 4A2 and 4B continuum peak.

Transition	Frequency$^{(a)}$ [GHz]	$E_{up}^{(a)}$ [K]	$\log A_{ij}^{(a)}$	Synthesized Beam maj × min (PA) [$'' \times ''$ (°)]	Source $\int T_B dV$ [K km s^{-1}]	V_{peak}^{b} [km s^{-1}]	FWHM^{b} [km s^{-1}]	RMS [K]
		CH_3OH				IRAS 4B		
3(2,1)-3(1,2) E	24.92871	36	-7.2	0.97 × 0.95 (−12)	17(2)	+6.9(0.1)	1.5(0.2)	1.2
4(2,2)-4(1,3) E	24.93347	45	-7.1	0.97 × 0.95 (−12)	21(3)	+6.9(0.2)	2.2(0.4)	1.2
2(2,0)-2(1,1) E	24.93438	29	-7.2	0.97 × 0.95 (−12)	17(3)	+6.9(0.2)	2.3(0.4)	1.2
5(2,3)-5(1,4) E	24.95908	57	-7.1	0.97 × 0.95 (−12)	17(2)	+6.8(0.1)	1.5(0.2)	1.2
6(2,4)-6(1,5) E	25.01812	71	-7.1	0.97 × 0.95 (−19)	21(3)	+6.9(0.2)	2.3(0.5)	1.4
7(2,5)-7(1,6) E	25.12487	87	-7.1	0.98 × 0.95 (−21)	19(2)	+6.8(0.1)	1.7(0.2)	1.5
8(2,6)-8(1,7) E	25.29442	106	-7.0	0.96 × 0.94 (−11)	19(2)	+6.9(0.1)	1.9(0.3)	1.2
9(2,7)-9(1,8) E	25.54140	127	-7.0	0.96 × 0.92 (−50)	22(3)	+6.8(0.1)	1.8(0.3)	1.4
10(2,8)-10(1,9) E	25.87827	150	-7.0	0.97 × 0.93 (−35)	16(2)	+7.1(0.1)	1.9(0.3)	1.1
11(2,9)-11(1,10) E	26.31312	175	-6.9	0.94 × 0.91 (−35)	14(2)	+6.6(0.2)	1.4(0.5)	1.4
		NH_3				IRAS 4B		
3-3	23.87013	124	-6.6	1.00 × 0.95 (+6)	64(8)	7.2(0.2)	1.7(0.5)	1.5
4-4	24.13942	201	-6.5	0.99 × 0.94 (−2)	41(7)	7.1(0.1)	1.7(0.1)	1.4
5-5	24.53299	296	-6.5	0.99 × 0.95 (−3)	39(7)	6.6(0.4)	2.5(0.7)	1.4
6-6	25.05602	409	-6.5	0.97 × 0.95 (−18)	37(7)	6.1(0.2)	1.7(0.4)	1.4
7-7	25.71518	639	-6.4	0.96 × 0.92 (−45)	27(7)	6.9(0.3)	1.7(0.1)	1.4
		NH_3				IRAS 4A2		
3-3	23.87013	124	-6.6	1.00 × 0.95 (+6)	169(20)	+6.9(0.1)	2.3(0.1)	1.3
4-4	24.13942	201	-6.5	0.99 × 0.94 (−2)	89(14)	+6.9(0.1)	1.8(0.1)	1.2
5-5	24.53299	296	-6.5	0.99 × 0.95 (−3)	54(14)	+6.9(0.1)	1.7(0.2)	1.2
6-6	25.05602	409	-6.5	0.97 × 0.95 (−18)	62(11)	+6.5(0.1)	2.3(0.1)	1.1
7-7	25.71518	639	-6.4	0.96 × 0.92 (−45)	40(8)	+7.1(0.1)	1.8(0.1)	1.0
		NH_3				IRAS 4A1		
3-3	23.87013	124	-6.6	1.00 × 0.95 (+6)	121(16)	+6.4(0.1)	2.7(0.2)	1.3
4-4	24.13942	201	-6.5	0.99 × 0.94 (−2)	90(13)	+6.5(0.1)	1.9(0.1)	1.0
5-5	24.53299	296	-6.5	0.99 × 0.95 (−3)	87(12)	+6.4(0.1)	2.5(001	1.0
6-6	25.05602	409	-6.5	0.97 × 0.95 (−18)	87(11)	+6.7(0.1)	2.9(0.2)	1.1
7-7	25.71518	639	-6.4	0.96 × 0.92 (−45)	46(9)	+6.4(0.1)	1.9(0.2)	1.1

[a] Spectroscopic parameters are by Xu et al. (2008) from the CDMS (Cologne Database for Molecular Spectroscopy; Müller et al. 2005) molecular database for CH_3OH and Yu et al. (2010) from the JPL (Pickett et al. 1998, Jet Propulsion Laboratory) catalog for NH_3.

[b] The spectral resolution is 1 km s^{-1}.

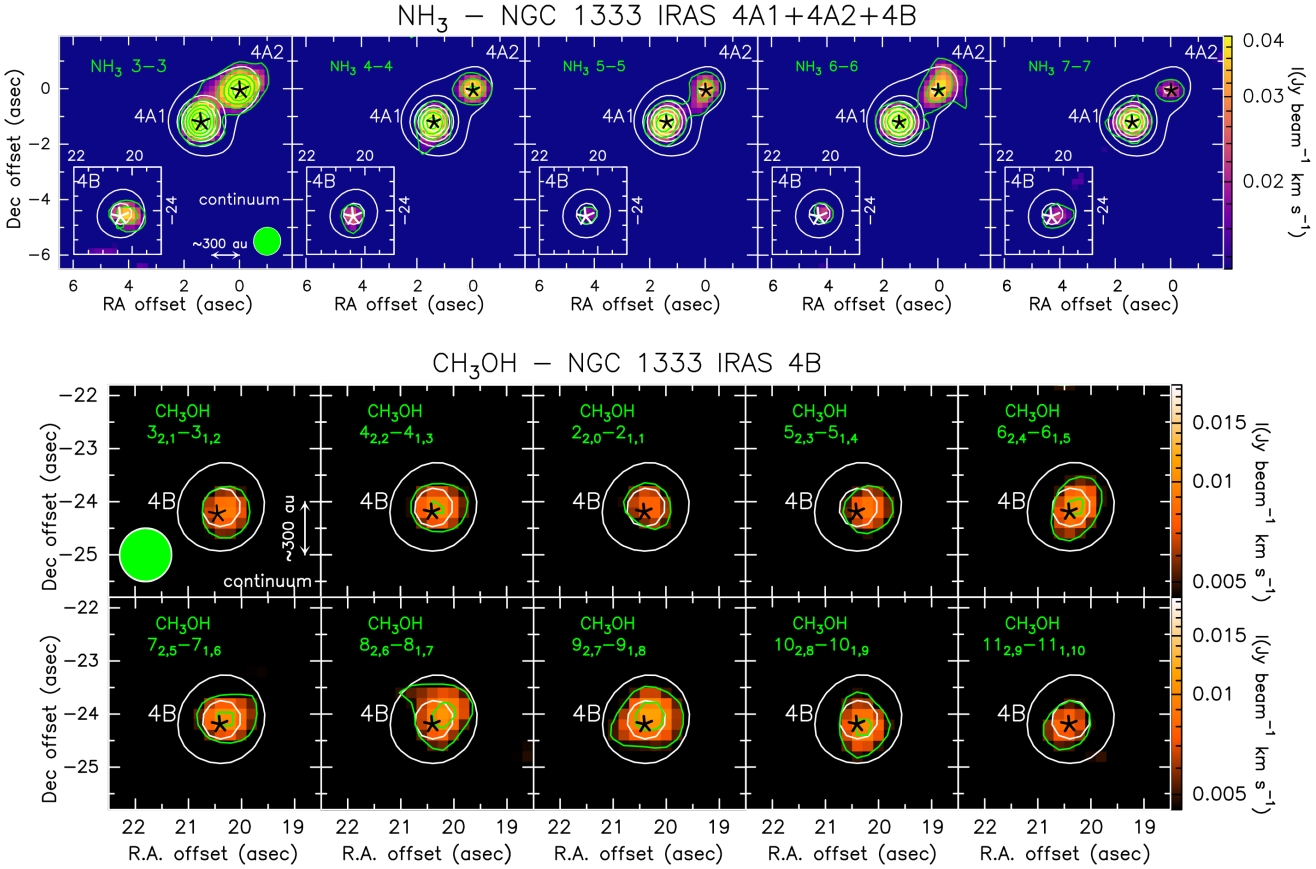

Figure 4.4: *Top panels*: NH$_3$ velocity-integrated maps toward IRAS 4A1, 4A2, and 4B in color scale, overlapped with the continuum white contours (from 50σ with steps of 100σ). The emission is integrated from −30 to −11 km s^{-1}, −3 to +15 km s^{-1}, and +25 to +43 km s^{-1}, in order to include the main and the satellite hyperfine components. NH$_3$ first contour and steps (in green) correspond to 3σ (σ=4.4 mJy beam^{-1}). *Bottom panels:* CH$_3$OH velocity-integrated maps toward IRAS 4B in color scale overlapped with the continuum white contours (from 50σ with steps of 100σ). The emission is integrated from −2 to +2 km s^{-1} with respect to the v$_{\rm sys}$ ($\sim$ +6.7 km s^{-1} Choi 2001). Methanol first contour and steps (in green) correspond to 3σ (σ=1.6 mJy beam^{-1} km s^{-1}). The CH$_3$OH maps for IRAS 4A1 and IRAS 4A2 are reported in De Simone et al. (2020a). The transition of the imaged line is reported in each panel. The black stars show protostars positions. Synthesised beams for continuum (white) and lines (green) are in the lower left corner.

Column density estimation

Thanks to the detection of several lines of NH_3 and CH_3OH covering a large range of upper level energies (see Table 4.3) we could perform a multi-line analysis to derive the abundance ratio of these two species. More specifically, we performed a non-LTE analysis via our in-home Large Velocity Gradient (LVG) code `grelvg` originally developed by Ceccarelli et al. (2003). The collisional coefficients of CH_3OH (both A-type and E-type; Rabli & Flower 2010) and NH_3 with para-H_2 are taken from the BASECOL database (Dubernet et al. 2013). They are computed between 10 and 200 K by Rabli & Flower (2010) for the first 256 levels of CH_3OH and by Bouhafs et al. (2017) for the lowest 17 and 34 rotation-inversion levels of ortho- and para-NH_3. We assumed the CH_3OH A-type/E-type ratio equal to 1 and the NH_3 ortho-to-para ratio equal to 2. For both NH_3 and CH_3OH we assumed a semi-infinite slab geometry to compute the line escape probability as a function of the line optical depth, and the H_2 ortho-to-para ratio equal to 3.

Methodology: We first performed the LVG analysis to the methanol lines, in order to better constrain the gas conditions, namely gas density and temperature, and to derive the CH_3OH column density and emitting size. Assuming that NH_3 is tracing the same gas as CH_3OH, we performed the LVG analysis to the NH_3 lines in order to derive the NH_3 column density considering the source size, the gas density and temperature ranges derived for CH_3OH. Finally, we computed the NH_3/CH_3OH abundance ratio.

Methanol line analysis: The methanol line analysis for IRAS 4A1 and IRAS 4A2 is reported in De Simone et al. (2020a). We carried out a similar analysis for IRAS 4B. Indeed, we ran a large grid of models ($\sim$ 70000) covering the frequency of the observed CH_3OH lines, a total (A-type plus E-type) column density N_{CH_3OH} from 2×10^{16} to 16×10^{19} cm^{-2}, a gas density n_{H_2} from 1×10^7 to 1×10^9 cm^{-3}, and a temperature T from 60 to 200 K. We simultaneously fit the measured CH_3OH line intensities, for IRAS 4B, via comparison with those simulated by the LVG model, leaving N_{CH_3OH}, n_{H_2}, T and the emitting size θ as free parameters. Following the observations, we assumed a linewidth equal to 2 km s^{-1} and we included the calibration uncertainty (15%) in the observed intensities. The best fit is obtained for a total CH_3OH column density N_{CH_3OH}=1.4×10^{18} cm^{-2}, with a reduced chi-square χ^2_R=0.4, emitted by a source of $0''.24 - 0''.40$. Solutions with $N_{CH_3OH} \geq 1 \times 10^{18}$ cm^{-2} are within 1σ of confidence level. The χ^2_R decreases, increasing the CH_3OH column density, until a constant value, as all the observed lines become optically thick ($\tau = 1.5 - 3$) and, consequently, the emission is that of a black body. The gas density and temperature, the CH_3OH column density and emitting size for IRAS 4A1, 4A2 and 4B are reported in Table 4.4.

Ammonia line analysis: We then considered the source size, the gas density and temperature derived by the methanol line analysis and ran a grid of models ($\sim$ 5000) with these parameters to fit the observed ammonia lines for the three sources, leaving as free parameter the ammonia column density.

Following the observations we assumed a linewidth of 12, 10, 9 km s^{-1}, for 4A1, 4A2, and 4B, respectively. The assumed linewidth is computed as the one derived from the Hyperfine fitting (Table 4.3) multiplied by the number of components (main plus satellites). The best fit

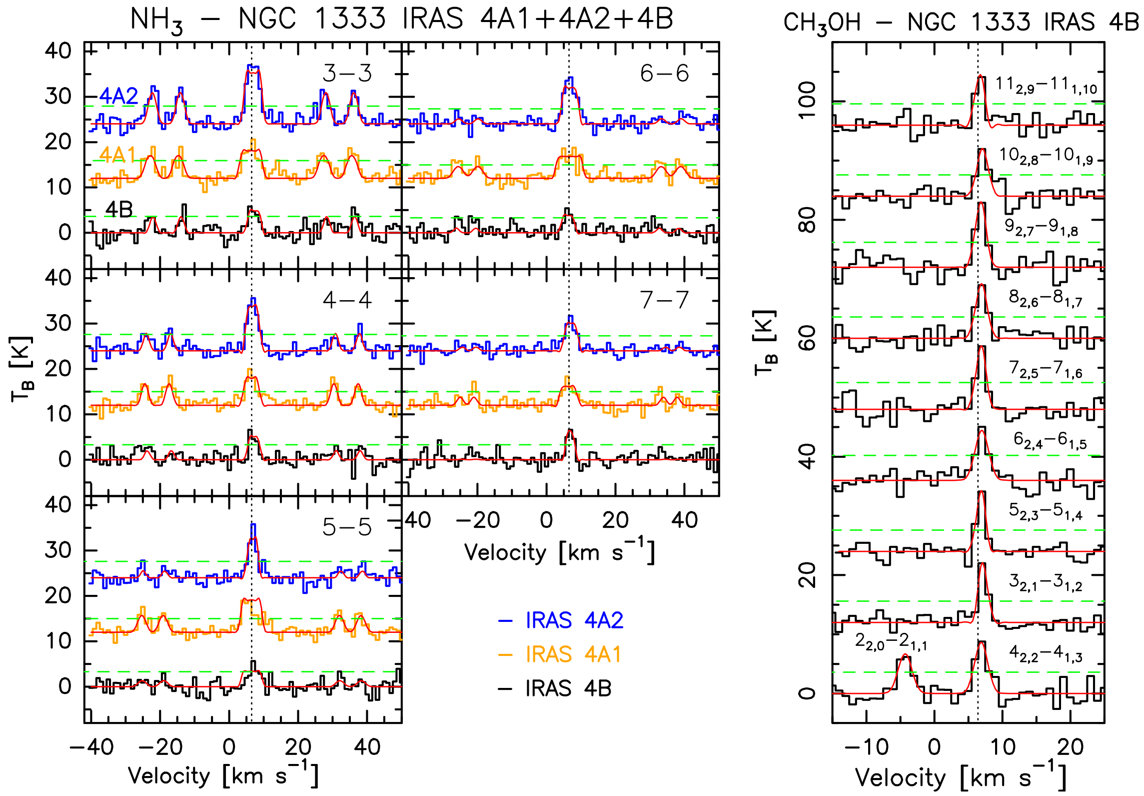

Figure 4.5: *Left panels:* NH_3 lines (marked in each panel) detected toward the continuum peak of IRAS 4B (black), 4A1 (orange), 4A2 (blue). The red curves show the best hyperfine fits. Each spectrum is shifted on 12 K from the previous one. *Right panel:* CH_3OH lines (marked on each spectrum) detected in the VLA K-band toward 4B. The red curves show the best Gaussian fits. Each spectrum is shifted on 12 K from the previous one. The vertical dotted black lines report the v_{sys} (6.7 km s^{-1}) and the horizontal green dashed lines show the 3σ level.

is obtained for N_{NH_3} = 1.4×10^{18} cm^{-2} with χ^2_R=0.4 for 4A1, 2×10^{18} cm^{-2} with χ^2_R=1.1 for 4A2, and 1.6×10^{18} cm^{-2} with χ^2_R=1.4 for 4B. The N_{NH_3} 1σ confidence level range is reported in Table 4.4. Some of the observed lines are quite optically thick (~20-40), while the majority of the NH_3 lines have opacity between 0.4 and 4. The lines that are optically thin ($\leq$1) allowed us to constrain the column density.

Abundance ratios: Finally, we computed the NH_3/CH_3OH abundance ratio, using the column densities derived from the LVG analysis described above. The derived values are ≥ 0.5, ≥ 3, and ≥ 15, for 4A1, 4A2 and 4B (Table 4.4). They are all upper limits as the derived CH_3OH column density is a lower limit.

4.3.4 Discussion

Astrochemical modelling

We used the astrochemical model GRAINOBLE (Taquet et al. 2012b, 2013). Briefly, this is a time-dependent grain-gas chemistry code that computes the layered grain mantles structure. The model adopted here follows the one used in Ceccarelli et al. (2018). For further details on the processes included in the model (such us accretion, diffusion, surface, and desorption)

Table 4.4: Results of the non-LTE LVG analysis of the CH_3OH and NH_3 lines toward IRAS 4A1, 4A2 and 4B using the `grelvg` code. The reported values for gas density (n_{H_2}) and temperature (T_{kin}), source size, species column densities and their abundance ratio, are the 1σ confidence level.

		IRAS 4A1	IRAS 4A2	IRAS 4B
n_{H_2}	[cm^{-3}]	$\geq 2\times10^6$	$\geq 10^7$	$\geq 2\times10^7$
T_{kin}	[K]	100-120	130-160	110-130
N_{CH_3OH}	[cm^{-2}]	$\geq 10^{19}$	$\geq 10^{18}$	$\geq 10^{18}$
N_{NH_3}	[cm^{-2}]	$(1.2\text{-}5)\times10^{18}$	$(0.6\text{-}3)\times10^{18}$	$(0.3\text{-}15)\times10^{18}$
size[a]	["]	0.20-0.24	0.22-0.24	0.24-0.26
NH_3/CH_3OH	-	≤ 0.5	≤ 3	≤ 15

[a] The reported range for the source size is constrained from both CH_3OH and NH_3 analysis.

please refer to Ceccarelli et al. (2018). For the reactions occurring in the gas phase, we used the KIDA 2014 network; (http://kida.obs.u-bordeaux1.fr; Wakelam et al. 2015), updated with the reactions described in Loison et al. (2014); Balucani et al. (2015); Skouteris et al. (2017, 2018); Codella et al. (2020a). The reactions on the grain surface leading to formaldehyde, methanol and water are described in Taquet et al. (2013). The hydrogenation of C and N that leads to methane (CH_4), ammonia (NH_3), respectively, have been added.

We assumed that the H number density of the molecular cloud, n_H is constant, and an average grain radius of 0.1 μm^2, typical of the galactic ISM grains (e.g., Jones et al. 2013). The gas and dust are assumed to be thermally coupled, and the abundances of the elements in the gas phase are the one reported in Table 2 by Ceccarelli et al. (2018).

We started with a partially atomic cloud, i.e. all the elements are in atomic form except for hydrogen that is assumed to be in molecular form. The cloud chemical composition is left to evolve with time for 10^7 yr. The GRAINOBLE code follows the chemical evolution of each grain mantle layer, therefore it provides the composition of each layer as the mantle grows. The mantle is formed of approximately 100 layers.

Observations vs model predictions

The NH_3 and CH_3OH relative abundance depends on the pre-collapse clump temperature and density, and the ice mantle formation timescale. Figure 4.6 reports the theoretical predictions of the abundance ratio between ammonia and methanol as a function of time for several temperatures (8,9,12,15,18,20 K) and H density ((0.2, 2, 20)$\times10^5$ cm^{-3}).

The NH_3/CH_3OH abundance ratio decreases with time, as methanol starts to form after ammonia. The first layers of the grain mantle are mostly composed of the hydrogenated forms of C and N, namely methane and ammonia. When the C and N atoms land on the grain, they undergo hydrogenation, which is a fast process since it does not have energy barriers. Then, the gaseous abundance of both C and N drops and CO and N_2 form. Later on, the gaseous CO freezes out into the mantles, and the methanol is efficiently formed through its hydrogenation.

Increasing the cloud temperature, the mantle growth is slower and the mantles have less layers becoming thinner (see Figure 1 in Ceccarelli et al. 2018). As a consequence of the increasing temperature, the hydrogenation processes are reduced as the residence time in the mantle of H and O atoms, as well as of CO molecules, decreases, so that the hydrogenation and

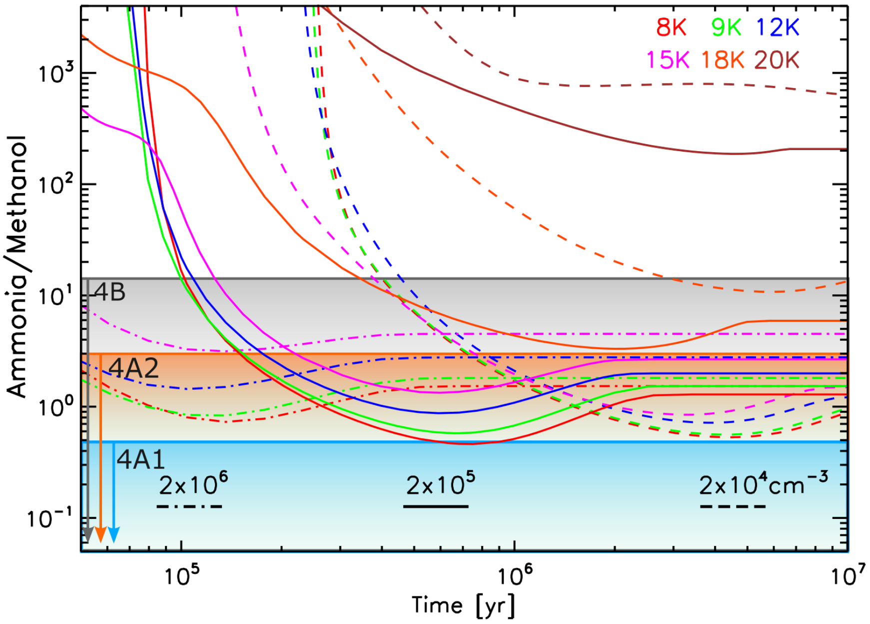

Figure 4.6: Theoretical predictions of NH_3/CH_3OH versus time for several temperatures (8, 9, 12, 15, 18, 20 K) and H density ((0.2, 2, 20)$\times10^5$ cm^{-3}), obtained with the GRAINOBLE code, following the model described in Ceccarelli et al. (2018). The grey, orange and blue bands represent the NH_3/CH_3OH values derived in 4B, 4A2 and 4A1, respectively.

oxidation processes are reduced. Additionally, if the dust temperature becomes larger than its sublimation temperature (approximately 20–30 K) CO cannot remain frozen on the surface. Therefore, increasing the temperature, the methanol abundance decreases and consequently the NH_3/CH_3OH ratio increases (see Figure 4.6).

On the other hand, increasing the n_H density, the species accretion on the grain mantles is faster, as the accretion rate is directly proportional to the grain number density [9]. Therefore, the formation of hydrogenated species occurs earlier and, consequently, the predicted curves move towards shorter timescales when the gas density increases.

Figure 4.6 reports also, as colored bands, the observed gas-phase abundance ratio NH_3/CH_3OH toward the prostostars 4A1, 4A2, and 4B. Comparing the observed values with the model predictions we can constrain the pre-collapse clump conditions.

The main results are: i) we can exclude pre-collapse clump temperature higher than 18 K, as they cannot reproduce the observed values; ii) More precisely, the upper limits are $T\leq18$ K for IRAS 4B, $T\leq12$–15 K for IRAS 4A2, and $T\leq8$ K for IRAS 4A1; iii) The stringent upper limit on the abundance ratio computed toward IRAS 4A1 allows us to constrain, besides the pre-collapse clump temperature ($T\leq8$ K), the gas density (around 10^5 cm^{-3}) and the ice mantle formation timescale (5–9$\times10^5$ yr).

In summary, we could retrieve information on the early stages of the formation of the three protostars. In particular, we showed which conditions of the pre-collapse clump would lead to a different ice mantle history.

---

[9] A species x with mass m_x can accrete from the gas to the grain surfaces with an accretion rate $k_{acc} = S_x \pi a^2 n_{grain} v_x$, where S_x is the species sticking probability, a the (average) grain radius, n_{grain} the grain number density, and v_x the velocity of the gaseous species ($v_x = (2k_b T_{gas}/m_x)^{1/2}$).

4.3.5 Conclusions

We carried out observations of ammonia and methanol lines at cm wavelengths with the VLA interferometer toward three protostars in the NGC 1333 region (IRAS 4A1, IRAS 4A2, and IRAS 4B), in order to retrieve the ice mantle history of these objects.

We detected 10 methanol lines and 5 ammonia lines with compact emission around the targeted protostars. Using a non-LTE LVG analysis we could retrieve the NH_3/CH_3OH abundance ratio. We compared the observed abundance ratio with astrochemical models that predict the evolution of NH_3/CH_3OH with varying the pre-collapse clump conditions, namely gas density and temperature, and ice mantle formation timescale. We could constrain the gas temperature for all the three protostars, and the gas density and formation timescale for IRAS 4A1.

These results show how powerful is this method in retrieving the ice mantle history of Solar-type protostars without being biased by the dust opacity. Indeed, following the conclusion by De Simone et al. (2020a), centimeter-wave observations are crucial for the correct study of hot corinos, and more in general for protostars. Indeed, with interferometric observations at centimeter wavelengths it is possible to get rid of the dust contribution (that can be important in the embedded protostellar phase) and to observe simultaneously and at planet formation scales the two major grain components NH_3 and CH_3OH, whose relative abundance, being grain surface species, will mainly depend on the gas conditions during their formation in the prestellar phase.

This is just a first step, and more observations are needed, in particular towards other star forming regions, possibly associated with different initial conditions. Additionally, these observations are an important testbed for future results that can be obtained with the next generation instruments in the centimeter wavelength regime such as ngVLA (McGuire et al. 2018) and SKA (Codella et al. 2015b).

4.4 Future project

4.4.1 Constrain the dust opacity spectral index β in the IRAS 4A protostars

The variation of the dust optical depth with frequency, in the NIR-millimeter wavelength range, can be approximated by a power law (e.g., Hildebrand 1983):

$$\tau_\nu \propto \nu^\beta \tag{4.2}$$

where β is the so-called dust opacity spectral index, and it is related to dust properties. β depends on dust grain sizes, chemical composition, porosity, geometry and on the grain size distribution (e.g., Pollack et al. 1994; Draine 2006; Natta et al. 2007). In particular, it is largely sensitive to grain sizes, i.e. larger grains give smaller β values. For example, regardless of all the uncertainties on the dust model, dust grains with sizes of the order of 1 mm or larger lead to β values lower than 1 (Natta & Testi 2004).

Therefore, the dust opacity spectral index changes with the evolutionary stage of the sources: the highest values have been measured towards pre-stellar cores with $1 < \beta < 2.7$ (e.g., Shirley et al. 2011; Schnee et al. 2010; Sadavoy et al. 2013; Bracco et al. 2017), while the lowest values have been measured towards Class II protostars, hosts of protoplanetary disks, with $0 < \beta < 1$ (e.g., Ricci et al. 2010a,b; Bracco et al. 2017; Tazzari et al. 2021). Early studies of Class 0 and I protostars found intermediate values $\beta \sim 1.7 - 2$ (Natta et al. 2007).

However, more recent studies toward Class 0 protostars have often found β values lower than 1, suggesting that grain growth could already be at work at these early stages (e.g., Jørgensen et al. 2007; Li et al. 2017; Galametz et al. 2019; Bouvier et al. 2021).

Typically, the method used to derive the dust spectral index is by fitting the SED (Spectral Energy Distribution) at different wavelengths (from sub-mm to radio). Using Eq. 4.2 and knowing that the flux density F_ν is given by

$$F_\nu = B_\nu(T)(1 - e^{-\tau_\nu}) \,, \tag{4.3}$$

it is possible to relate the spectral index β to the flux density:

$$\nu^\beta \propto \ln(1 - F_\nu/B_\nu(T)) \,, \tag{4.4}$$

where $B_\nu(T)$ is the blackbody of the dust at the temperature T.

In general, a good sampling of SED from the centimeter to the submillimeter bands allows simultaneously fitting the dust temperature, dust opacity and β.

In the case where dust emission is optically thin (i.e. $\tau \ll 1$), and in the Rayleigh-Jeans limit ($h\nu/kT \ll 1$) equation 4.3 can be simplied as $F_\nu \propto \nu^\alpha$ where $\alpha = 2 + \beta$. Based on these assumptions, it is possible to derive β from observations at two frequency bands. However, when using only two frequency bands, the small separation in the frequency range and uncertainties from flux measurements would yield a large uncertainty in the derivation of β. Additionally, the assumptions of low optical depth and Rayleigh-Jeans regime cannot be always applied. For example, Class 0 sources tend to be highly obscured even at (sub-)millimeter wavelengths, so that the optically thin assumption breaks down. Additionally, at longer wavelengths there can be contamination to the dust continuum emission, such as the free-free emission. All of these effects could lead to the underestimation of β, and hence give incorrect predictions on grain sizes (see, e.g., the discussion in Bouvier et al. 2021).

Regarding the source target of my thesis, IRAS 4A, the spectral index beta has been measured in IRAS 4A2 to be $\sim 1.2 - 1.7$, using the SED fitting method (Jørgensen et al. 2007; Cox et al. 2015; Li et al. 2017). I propose here another method to derive the dust spectral index β toward the Class 0 IRAS 4A1 and IRAS 4A2: the use of the CH_3OH line emission at three different wavelengths ($\sim$25, $\sim$143, and $\sim$206 GHz). As shown in Section 4.2, using the VLA observations of methanol lines toward the IRAS 4A system, I could derive the dust opacity at mm wavelengths. Specifically, using the VLA observations at $\sim$ 25 GHz, I was able to derive the gas density and temperature, methanol column density and emitting size, via a non-LTE LVG analysis on the several methanol lines. Using the derived gas conditions I predicted the theoretical intensity of the methanol lines at $\sim$143 GHz, where previous observations were performed by Taquet et al. (2015). Comparing the predicted intensity at $\sim$143 GHz with the observed value, I obtained the dust opacity τ_ν in both IRAS 4A1 and IRAS 4A2 via the standard radiative transfer equation:

$$\mathrm{I}_\nu^{\mathrm{obs}} = \mathrm{I}_\nu^{\mathrm{pred}} \mathrm{e}^{-\tau_\nu}. \tag{4.5}$$

I found $\tau_{143\mathrm{GHz}} \sim 0.3$ for IRAS 4A2 and $\tau_{143\mathrm{GHz}} > 1.6$ for IRAS 4A1.

Within the SOLIS Large Program, methanol lines are also detected toward IRAS 4A2 at $\sim$ 206 GHz. Therefore, using the same method, it is possible to derive the opacity of the foreground dust at 206 GHz. Considering ν_1 = 143 GHz and ν_2 = 206 GHz it is then possible to derive the dust spectral index β as:

$$\ln\left(\frac{\tau_{\nu_1}}{\tau_{\nu_1}}\right) = \beta \ln\left(\frac{\nu_1}{\nu_1}\right). \tag{4.6}$$

The β value derived in this way will be a rather straightforward measurement of β, which will not depend on the Rayleigh-Jeans approximation or the free-free emission.

4.4.2 VLA proposals

I. Hot Corinos chemical diversity: myth or reality?

As explained in Section 4.2, among the few detected hot corinos, several are binary system with very different millimeter molecular spectra. Illustrative examples are IRAS 16293-2422 in ρ-Oph, IRAS 4A in Perseus, and CepE-mm in Cepheus. IRAS 16293-2422 is composed of two sources separated by $\sim 5''$ ($\sim$720 au): the source A is weaker in mm continuum emission and brighter in iCOMs lines than the source B (e.g., Caux et al. 2011; Pineda et al. 2012; Jørgensen et al. 2016; Manigand et al. 2020). IRAS 4A is also a binary system composed of IRAS 4A1 and IRAS 4A2, separated by $\sim 1.''8$ ($\sim$540 au); while the former dominates the mm continuum, only the latter shows bright iCOMs lines at mm wavelengths (Taquet et al. 2015; López-Sepulcre et al. 2017; De Simone et al. 2017). In contrast, the CepE-mm intermediate mass binary system shows a different behavior with respect to IRAS 4A and IRAS 16293-2422. Indeed, the source that dominates the mm continuum emission, CepE-A, is the one that shows a rich chemical content, while the companion CepE-B (separated by $\sim 1.''7$) lacks iCOMs emission (Ospina-Zamudio et al. 2018, 2019).

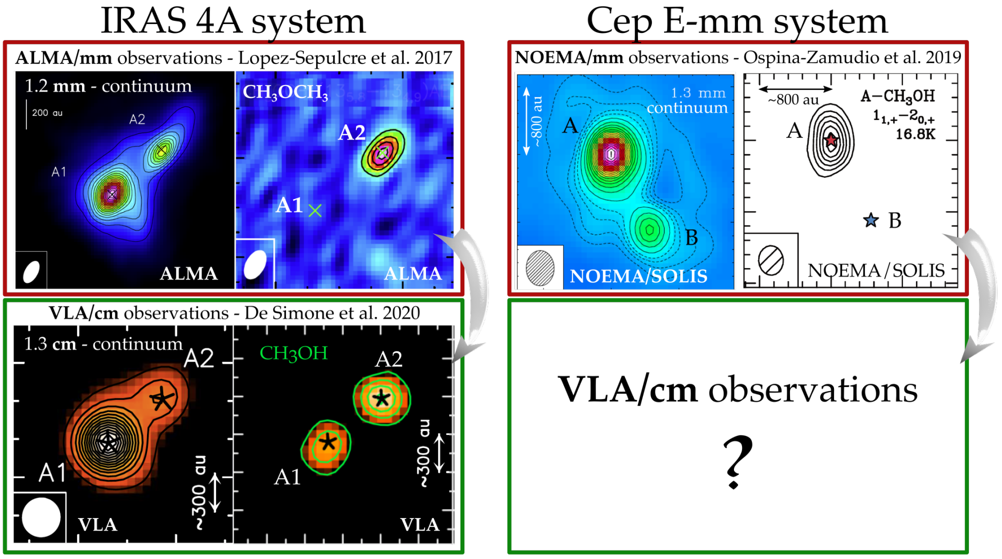

Figure 4.7: ***IRAS 4A binary system vs Cep-E binary system***. *Left: IRAS 4A system observed at mm wavelengts (red upper box) showing that the line emission comes from the source weaker in mm continuum emission, and at cm wavelengths (lower green box) showing that the line emission is actually coming from both sources: the dust was obscuring the hot corino in IRAS 4A1. Right: CepE-mm binary system at mm wavelengths (red upper box) showing that the line contribution is from the sources brighter in mm continuum emission. What will CepE look like at cm wavelengths?*

Why do coeval objects seem drastically different in their chemical composition? A major observational bias could be caused by the dust opacity which could be very high in Class 0/I sources and absorb the iCOMs line emission. Alternatively, if the dust contribution is negligible, the source could have a hot corino region that is small enough to be beam-diluted. In both cases, the two components of the binary system are not necessarily chemically different. A last possibility is that the source actually does not possess a hot corino region, and thus, the difference in the chemical composition of the two sources is real.

With the VLA observations at centimeter wavelengths, where the dust is more likely optically thin, (De Simone et al. 2020a) I could reveal a new hot corino, hidden by the dust, toward IRAS 4A1 (see Section 4.2). Is the case of IRAS 4A one of a kind? Are we missing hot corinos around other Class 0 protostars due to the dust opacity contribution?

In the case of IRAS 4A (and probably in IRAS 16293) the dust is responsible for the chemical difference observed at mm wavelengths. However, the case of the CepE-mm binary system is even more puzzling. Indeed, in CepE-mm, contrary to IRAS 4A, the protostar that dominates the continuum emission possesses a hot corino region detectable at mm wavelengths, while the fainter protostar does not show any iCOM emission. Therefore, is the chemical differentiation in the CepE binary systems a myth or a reality? First of all, it is needed to absolutely exclude the dust opacity effect going to centimeter high angular resolution observations with the VLA.

To this end, I proposed to observe the Cep-E binary system following the same observations performed toward IRAS 4A in (De Simone et al. 2020a) with the VLA in C configuration ($\sim 1''$ of angular resolution). I targeted several methanol lines in K-band with the VLA, to assess whether a hot corino is present in both Cep-E components, and several NH_3 lines to constrain the gas temperature. Indeed the ammonia lines can be useful in case of methanol

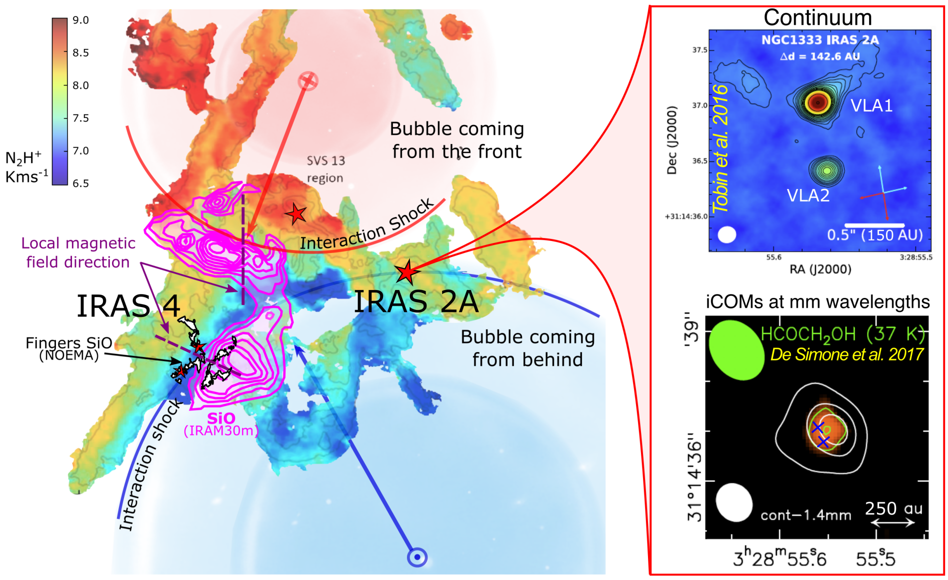

Figure 4.8: ***IRAS 2 and IRAS 4 in the NGC 1333 filament shaped by two incoming bubbles*** *(the red coming from the front and the blue from behind). Left: Overlap of* N_2H^+ *velocity map (Dhabal et al. 2019) in color scale with IRAM-30m SiO large scale ambient emission (Lefloch et al. 1998b) in magenta, and SOLIS/NOEMA SiO finger-like emission in black. Right: Zoom-in in the IRAS 2 system, as observed in the 0.9 cm continuum, showing the two sources, VLA1 and VLA2 separated by* $0.''6$ *(upper-right panel), and in the mm-wave* $HCOCH_2OH$ *line emission tracing the hot corino toward the whole IRAS 2A system (lower-right panel). The system was never imaged in complex organic molecules lines with enough angular resolution to disentangle the two protostars.*

non-detection, as they could help to explain the absence of a hot corino region if the derived temperature is lower than the expected 100 K.

- This proposal has been submitted in the VLA 2021A semester. It was approved with *22 observing hours*. The observations have been performed in August-September 2021.

II. Tracking the ice mantle history of baby stars

As explained in Section 4.3, the composition of the icy grain mantles is crucial in establishing the chemical diversity observed in Class 0/I hot corinos.

Using JVLA observations toward the IRAS4A protobinary system, I detected several transitions of CH_3OH and NH_3. Performing a non-LTE multiline analysis via the LVG code `grelvg` (Ceccarelli et al. 2003) I could derive the NH_3/CH_3OH abundance ratio. Comparing the observed values with the theoretical predictions from the astrochemical model GRAINOBLE (Taquet et al. 2012b; Ceccarelli et al. 2018), I could constrain the pre-collapse clump conditions on a scale of ~70 au (see Section 4.3).

In order to make a step further, I propose to obtain the same observations toward another Class 0 binary system, IRAS 2A, with the JVLA B configuration (~ $0\overset{''}{.}3$ angular resolution). Both IRAS 4A and IRAS 2A are part of the NGC 1333 region that is one of the most active sites of ongoing star formation in the vicinity of the Sun and it is known to be heavily shaped by external events that could have triggered the star formation (e.g. Sandell & Knee 2001; Dhabal et al. 2018). In a recent work, evidence of the clash of an expanding bubble with the southern filament of NGC 1333, where IRAS 4A and IRAS 2A belong, has been reported (Dhabal et al. 2019). This clash could have triggered the collapse and, consequently, the formation of both protostars. If connected by the same fate, both IRAS 4A and IRAS 2A should have a similar grain mantle history. In order to verify this scenario we propose to measure the NH_3/CH_3OH abundance ratio in IRAS 2A and compare it with that measured toward the IRAS 4A sources.

The system IRAS 2A was initially observed with both single-dish and interferometric mm observations (with angular resolution $\geq 0.''8$) revealing the presence of a hot corino with an estimated deconvolved size of $0.''4$ (Bottinelli et al. 2007; Maury et al. 2014b; Taquet et al. 2015; Coutens et al. 2015; De Simone et al. 2017). Only in 2015, Tobin et al. imaged the cm continuum emission of IRAS 2A with JVLA, revealing the two binary sources, VLA1 and VLA2 separated by $\sim 0.''6$ ($\sim$180 au, see Figure 4.8). However, the chemical complexity of the individual sources is still uknown as, so far, no observations of complex molecules as been done with enough angular resolution to disentangle the two protostars. In this perspective, future ALMA or NOEMA observations with angular resolution $\leq 0.''5$, targeting several complex organic molecules with a large spectral coverage, will be ideal to fully characterize the chemical composition of the system. Here I propose to start their characterization with the observation of methanol, the simplest of iCOMS.

- I plan to submit this proposal, for 20 observing hours, in the VLA 2023A semester using B configuration ($0.''3$ angular resolution).

5 Synthesis of complex organic molecules

5.1 Constraining iCOMs formation routes

Since the discovery of interstellar complex organic molecules (iCOMs, C-bearing saturated molecules containing heteroatoms and at least six atoms; Herbst & van Dishoeck 2009; Ceccarelli et al. 2017) in Solar-type protostars (Cazaux et al. 2003), the question of whether they had a role in the appearance of life on Earth (and elsewhere in the Universe) has been raised. In particular, iCOMs may have provided the bricks to build pre-biotic molecules.

So far, about 250 species have been detected in the interstellar medium or circumstellar shells (CDMS; Müller et al. 2005; McGuire 2018, 2021). Still, there is not a reliable theory that can fully explain the observed abundance in the various environments where these iCOMs are detected. Nowadays, two main paradigms are invoked (e.g., Herbst 2017) that argue that iCOMs are either synthesized on the grain surfaces (e.g., Garrod & Herbst 2006; Garrod 2008; Jin & Garrod 2020) or in the gas phase (e.g., Millar et al. 1991; Balucani et al. 2015; Skouteris et al. 2018). As a starting point, both pathways have the formation of simple hydrogenated molecules on dust grain mantles during the prestellar phase. Constraining which of the two pathways to synthesize iCOMs is more efficient and where iCOMs form is not a simple task. Many methods have been used, from the comparison of the iCOM measured abundances in hot cores/corinos with model predictions to their measured deuterium fractionation (Turner 1990; Ceccarelli et al. 1998; Coutens et al. 2016; Skouteris et al. 2017, 2018; Jørgensen et al. 2018; Vazart et al. 2020).

Another method, that turned out to be very efficient, is to compare the iCOMs abundances toward low-mass jet-driven outflow regions with model predictions (Codella et al. 2017, 2020a). This method has the advantage that the outflow shocked regions provide as an additional constraint the time dependence. Indeed, thanks to interferometric high angular resolution observations, it is possible to localize the iCOM emission in a particular region, and in that region, it is possible to identify a shock event that corresponds naturally to a precise kinematical age (Gueth et al. 1996; Podio et al. 2016).

Once the shock has passed, the chemistry of the shocked gas evolves with time. Thus, depending on the mechanism of formation of iCOMs, their observed abundance in the gas phase differs. If iCOMs form on the grain surfaces, they are injected into the gas phase right after the shock passage so that their abundance in the gas phase will jump-step increase and then decrease being destroyed by gas-phase reactions or frozen onto the grain mantles. On the contrary, if iCOMs are a gas-phase product, they form from precursor ice-mantle species ejected into the gas phase, and their synthesis takes some time. This means that their abundances will increase in a few tens/thousands yrs (depending on the species) after the shock passage, and then decrease because of reactions or freeze-out, as above. Therefore, the comparison of observed iCOM abundances with model predictions provides strong constraints on the formation routes because it is possible to make the comparison at a precise kinematical shock age.

This method was successfully applied to the L1157–B1 outflow shock to constrain the formation route of formamide by Codella et al. (2017). Indeed, thanks to interferometric high spatial resolution observations, the authors found a difference in the spatial distribution between acetaldehyde and formamide emission, and consequently, they were able to constrain the formamide formation as being due to gas-phase reactions. These conclusions apply to L1157-B1 only. However, given its power, it is important to apply the same method to other iCOMs and other protostellar shocks.

The detection of iCOMs in low-mass interstellar outflows started with single-dish observation toward a handful of objects: several iCOMs toward L1157-B1 (Arce et al. 2008; Lefloch et al. 2017), formamide toward L1157-B2 (Mendoza et al. 2014), acetaldehyde toward IRAS 2A and IRAS 4A (Holdship et al. 2019), and acetaldehyde and dimethyl ether toward SMM4-W (Öberg et al. 2011b). However, these studies could not disentangle the spatial distribution of the iCOMS.

In order to apply the method explained above, interferometric observations are needed and, so far, only the L1157-B1 outflow was observed at enough angular resolution to disentangle the iCOMs emission. To this end, I used high angular resolution ($\sim 2''$) observations of the IRAS 4A system, as part of the Seed Of Life (SOLIS) NOEMA Large Program, to explore the molecular content of its outflows.

The research presented in this section has resulted in one scientific paper:

- "Seeds of Life in Space (SOLIS) X. Interstellar Complex Organic Molecules in the NGC 1333 IRAS 4A outflows "
  De Simone M., Codella C., Ceccarelli C., López-Sepulcre A., Witzel A., Neri R., Balucani N., Caselli P., Favre C., Fontani F., Lefloch B., Ospina-Zamudio J., Pineda J. E., and Taquet V.
  Published in *Astronomy and Astrophysics, 2020, 640, A75*.

5.2 Interstellar Complex Organic Molecules in the NGC 1333 IRAS 4A outflows

5.2.1 Introduction

Since the discovery of interstellar Complex Organic Molecules (iCOMs[1], molecules containing carbon and at least six atoms: Herbst & van Dishoeck 2009; Ceccarelli et al. 2017) in Solar-type protostars (Cazaux et al. 2003), the question whether they had a role in the appearance of life on Earth (and elsewhere in the Universe) has been raised. Although they are extremely small molecules when compared to the biotic ones, iCOMs may have provided the bricks to build them. The presence of amino acids in meteorites and comets has certainly revived this possibility (e.g. Pizzarello et al. 2006; Elsila et al. 2009; Altwegg et al. 2016).

In addition to their possible role in the emergence of life, iCOMs have represented a challenge for astrochemistry, as their synthesis is all but obvious. Nowadays, two main paradigms are invoked (see e.g. Herbst 2017), that argue that iCOMs are either synthesized on the grain surfaces (e.g. Garrod & Herbst 2006; Garrod 2008) or in the gas phase (e.g. Millar et al. 1991; Balucani et al. 2015; Skouteris et al. 2018). As a starting point, both pathways have the formation of simple hydrogenated molecules on dust grain mantles during the prestellar phase. Constraining which of the two ways to synthesize iCOMs is efficient and where the iCOMs formation happen, is not a simple task. Many methods have been used, from the comparison of the iCOMs measured abundances in hot cores/corinos with model predictions to their measured deuterium fractionation (Turner 1990; Ceccarelli et al. 1998; Coutens et al. 2016; Skouteris et al. 2017; Jørgensen et al. 2018).

One method that turned out to be very efficient is to compare observations towards low-mass outflow shocks with model predictions (Codella et al. 2017). The advantage of this method is that the outflow shocks provide the time dependence as additional constraint. In fact, once localized the iCOMs emission in a precise region (thanks to high spatial resolution observations), it is possible to identify in that region a shock event that corresponds naturally to a precise kinematical age (e.g. Gueth et al. 1996; Podio et al. 2016). After the passage of the shock, the chemistry in the shocked region evolves with time. Therefore, the comparison of observed iCOMs abundances with model predictions provides strong constraints on the formation routes because it is possible to do the comparison at the precise kinematical shock age. This method was successfully applied in the L1157−B1 outflow shock to constrain the formation route of formamide. In fact, thanks to interferometric high spatial resolution observations, Codella et al. (2017) found a difference in the spatial distribution between acetaldehyde and formamide emission, and consequently, they could constrain the formamide formation as due to gas-phase reactions. Of course, those conclusions apply to L1157-B1 only. Given its power, it is important to apply the same method to other iCOMs and other protostellar shocks.

Unfortunately, observations of iCOMs in low-mass protostellar shocks are very few. To our knowledge, iCOMs other than methanol have been detected only towards a handful of objects: several iCOMs towards L1157-B1 (Arce et al. 2008; Lefloch et al. 2017), formamide towards

---

[1] Please note that we added “i” to the commonly used COMs acronym in order to be clear that these molecules are only complex in the interstellar context, contrary to what chemists would consider complex in the terrestrial context.

L1157-B2 (Mendoza et al. 2014), acetaldehyde towards IRAS 2A and IRAS 4A (Holdship et al. 2019) and acetaldehyde and dimethyl ether towards SMM4-W (Öberg et al. 2011b). However, it is worth noticing that all these works refer to (relatively low spatial angular resolution) single-dish observations and are, by definition, unable to disentangle the different spatial distribution of iCOMs caused by the age of the shocks, so that the method described above cannot be used.

In this work, we present new high spatial observations towards the two outflows from IRAS 4A. This source is one of the target of the Large Program SOLIS (Seeds Of Life In Space: Ceccarelli et al. 2017), at the IRAM/NOEMA (NOrthern Extended Millimeter Array) interferometer, whose goal is to investigate the iCOM chemistry during the earliest formation phases of Solar–type stellar systems. The observations targeted three iCOMs in addition to methanol (CH_3OH): acetaldehyde (CH_3CHO), dimethyl ether (CH_3OCH_3) and formamide (NH_2CHO). All these iCOMs were detected in our data set. The detection of different iCOMs in the outflowing gas of IRAS 4A with high spatial resolution observations allows us to apply the method of model-observations comparison described above.

The article is organized as follows: we first give the IRAS 4A source background in Section 5.2.2, then present the observations in Section 5.2.3 and the results in Section 5.2.4; we derive the abundance ratios of the detected iCOMs in different positions of the IRAS 4A outflows (Section 5.2.5), and the model predictions to interpret them (Section 5.2.6); in Section 5.2.7 we discuss what our new observations imply and finally, Section 5.2.8 summarizes our work.

5.2.2 IRAS 4A: Source Background

IRAS 4A is part of the multiple system IRAS 4, located at a distance of 299±15 pc in the NGC 1333 region of the Perseus complex (Zucker et al. 2018). The system IRAS 4A is constituted by four objects: 4A, 4B, 4B$'$ and 4C (Lay et al. 1995; Looney et al. 2000; Smith et al. 2000; Di Francesco et al. 2001; Choi 2001). IRAS 4A is itself a binary system with two Class 0 objects, 4A1 and 4A2, separated by $1''.8$ ($\sim$ 540 au; Looney et al. 2000; Santangelo et al. 2015; López-Sepulcre et al. 2017; Maury et al. 2019). In the millimeter wavelengths, 4A1 is three times brighter than 4A2. However, their respective luminosity is unknown since they are not resolved in the sub-millimeter to IR wavelengths where the luminosity peak lies. The bolometric luminosity of the whole IRAS 4A system is 9.1 $L_\odot$ (Kristensen et al. 2012; Karska et al. 2013).

IRAS 4A is the second ever discovered hot corino (Bottinelli et al. 2004a), after IRAS 16293-2422 (Cazaux et al. 2003). Interferometric IRAM/PdBI (Plateau de Bure Interferometer, now evolved into NOEMA) observations have later suggested that iCOMs emission originates rather from 4A2 than 4A1 (Taquet et al. 2015; De Simone et al. 2017). More recently, López-Sepulcre et al. (2017) obtained high resolution ($\sim 0''.5$) ALMA images of IRAS 4A and confirmed the huge contrast between 4A1 and 4A2: while 4A2 shows a hot corino activity with enriched iCOMs emission, no sign of iCOMs is detected in 4A1. López-Sepulcre et al. (2017) suggest that either 4A1 does not host any hot corino or, alternatively, the hot corino size is less than $\sim$15 au (after scaling to 299 pc the distance adopted by López-Sepulcre et al. 2017), namely six times smaller than the 4A2 one.

As for many Class 0 protostars, IRAS 4A is associated with a spectacular large–scale (few arcminutes) bipolar outflow observed with several tracers, such as CO, SiO, SO, HCN (Blake et al. 1995; Lefloch et al. 1998a; Choi 2005; Choi et al. 2011). Choi (2005) well traced the high

Table 5.1: List of the characteristics of the SOLIS WideX backend setups.

Setup	Frequency Range (GHZ) [GHz]	Spectral resolution [km s^{-1}]	[MHz]	Spatial resolution [$''$]	[au]^a	Synthesized Beam [$'' \times ''$ ($^\circ$)]	Primary Beam [$''$]	[au]^a
1	80.8-84.4	7	2	4	$\sim$1200	4.5×3.5 (27)	61.″4	$\sim 2\times10^4$
3	95.5-99.5	6	2	4	$\sim$1200	2.2×1.9 (96)	59.″2	$\sim 2\times10^4$

[a] computed at the distance of the NGC 1333 region ($\sim$299 pc; Zucker et al. 2018).

velocity component with SiO emission using VLA observations at 2$''$ spatial resolution. From their map, it is possible to distinguish two different blue–shifted lobes towards south and only one northern red–shifted lobe with a peculiar bending toward north–east at 20$''$ from the protostars. Using IRAM/PdBI high spatial resolution observations ($<$ 1$''$), Santangelo et al. (2015) mapped the outflows at lower scale ($\sim$30$''$) with respect to the SiO map from Choi (2005). They traced different velocity component (from $\sim$10 km s $^{-1}$ to $\sim$ 60 km s $^{-1}$) using CO, SiO and SO as tracers. With their study, Santangelo et al. (2015) were able to clearly disentangle the two southern lobes revealing a fast collimated jet associated with bright H_2 emission and driven by 4A1 (south–east lobe) and a slower and precessing jet driven by 4A2 (south–west lobe). Furthermore, the jets present different morphologies: the 4A2 jet shows a large spatial extent and a S–shape pattern on small scales, probably due to jet precession; the 4A1 jet is faster than the 4A2 one, covers a smaller extent ($\sim$ 15$''$) and presents a C-shape tilted towards east of 4A1.

Thanks to a detailed study on sulfur species using interferometric observations, for the first time, Taquet et al. (2020) were able to distinguish the outflow driven by 4A1 from the one driven by 4A2 also in the northern lobe.

The left panel of figure 5.1 summarizes the situation: it shows the distribution of the dust cores at large scale, trace by the continuum at 1.3 mm using the IRAM 30m (Lefloch et al. 1998a), together with large scale high velocity outflow traced by the SiO (1-0) line using the VLA interferometer (Choi 2005).

5.2.3 Observations

IRAS 4A was observed with the IRAM/NOEMA interferometer during several tracks in June and September 2016. Two frequency setups were used, called 1 and 3 in Ceccarelli et al. (2017, Table 4), centered at $\sim$82 and $\sim$97 GHz, respectively. The array was used in configurations D and C with baselines from 15 m to 304 m for Setup 3 and from 16 m to 240 m for Setup 1. Here, we present the data obtained using the WideX backend, whose characteristics are summarized in Table 5.1

The phase center is on the IRAS 4A1 source, whose coordinates are listed in Table 5.2. The bandpass was calibrated on 3C454.3 and 3C84, while the flux was calibrated using MWC349 and LKHA101. The calibration of phase and amplitude was done observing 0333+321. The system temperatures ranged typically between 50 and 200 K. The calibration error associated to the absolute flux is $\leq$ 15%. The data were reduced using the packages CLIC and MAPPING of the GILDAS[2] software collection. The data were self-calibrated in phase only; the self-calibration solutions were applied to the data spectral cube, which was then cleaned.

---

[2] http://www.iram.fr/IRAMFR/GILDAS

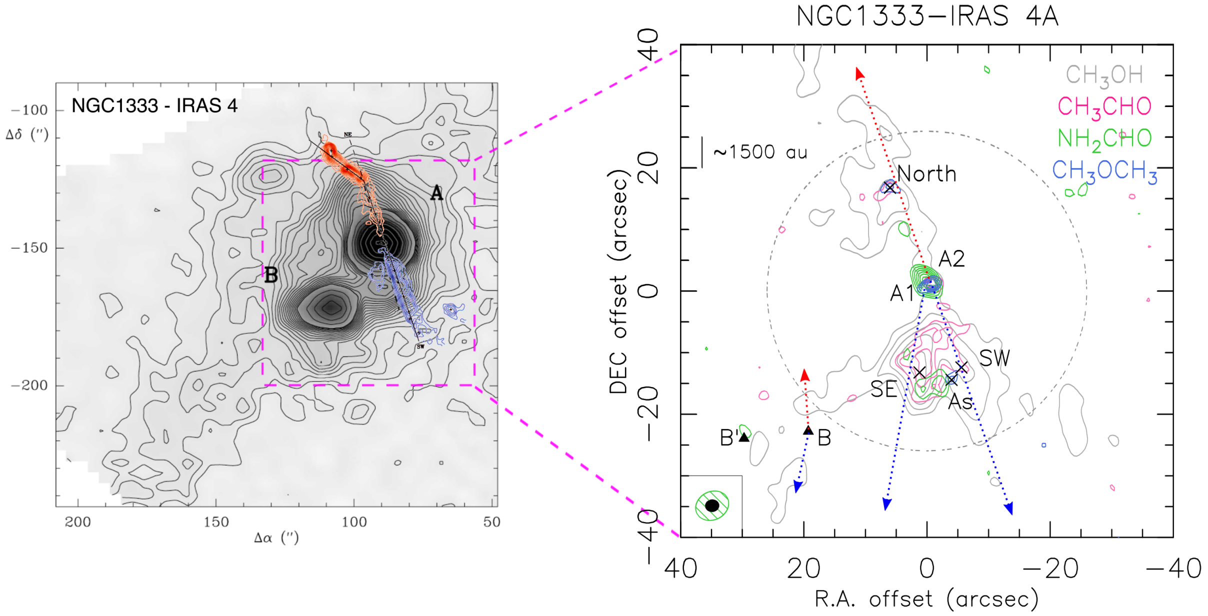

Figure 5.1: *Left:* Overlap of the contour map of the 1.25 mm continuum emission from NGC 1333 IRAS 4 region in Perseus, observed with the IRAM 30m antenna (Lefloch et al. 1998a), with the map of SiO line (VLA observations; Choi 2005). Axes offsets are in arcseconds from SVS 13 ($\alpha(2000) = 03^{\rm h}29^{\rm m}3^{\rm s}.9$ and $\delta(2000) = 31^{\circ}16'8''$). *Right:* Zoom in in the IRAS 4A system with NOEMA-SOLIS observations. Axes offsets are in arcseconds from IRAS 4A. A spatial separation of $5''$ correspond to $\sim$ 1500 au at a distance of 299 pc (Zucker et al. 2018). The white triangles mark the position of the sources 4A1 and 4A2, while the black triangles mark the position of the sources 4B and 4B′ (coordinates in Table 5.2). The black crosses mark the analyzed positions in the outflows (SE, SW, North and As; coordinates in Table 5.2). The dashed blue and red arrows indicate the direction of the blue– and red–shifted 4B outflow (from the HCN observations of Choi 2001) and of the 4A ones. The contour map represents the iCOMs emission at 3 mm in the IRAS 4A outflows (this work). For all the iCOMs the contours start at 3σ with steps of 1σ, except for methanol whose contours have steps of 20σ. The emission distribution is the following: 1) methanol (CH_3OH in grey), integrated over the transitions $2_{0,2}-1_{0,1}$ A, $2_{0,2}-1_{0,1}$ E and $2_{-1,2}-1_{-1,1}$ E with σ = 75 mJy/beam km/s; 2) acetaldehyde (CH_3CHO, in magenta), here in the $5_{0,5}-4_{0,4}$ A emission with σ = 11mJy/beam km/s; 3) formamide (NH_2CHO, in green), $4_{1,4}-3_{1,3}$ emission with σ = 10 mJy/beam km/s; dimethyl ether (CH_3OCH_3, in blue), $4_{1,4}-3_{0,3}$ emission with σ = 9 mJy/beam km/s. The synthesized beams for the formamide line (green, $\sim 4''$) and for the other species (black, $\sim 2''$) are indicated in the lower left corner. The primary beam ($\sim 52''$) is shown with a dashed grey circle.

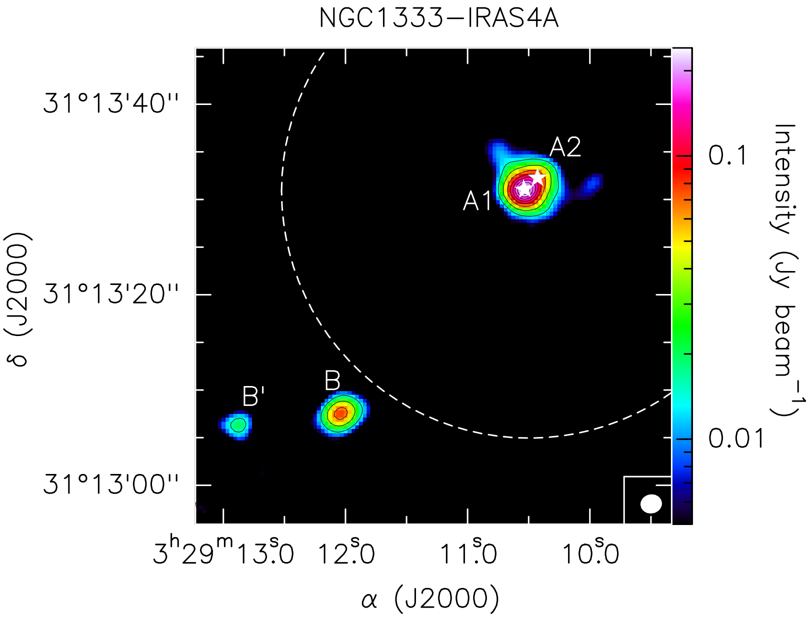

Figure 5.2: Dust continuum emission maps of IRAS 4A at 95.85-99.45 GHz (Setup 3, see Table 5.1). Contours start at 3σ and increase by steps of 20σ, with σ = 1.5mJy/beam. The synthesized beam (∼ 2″) is represented in white in the lower right corner of the panel, the primary beam (∼ 52″) is shown with a dashed white circle. The millimeter continuum sources in the field are labeled following the nomenclature used by Choi (2001) for 4A1 and 4A2 and Di Francesco et al. (2001) for B and B′.

A continuum map (see Figure 5.2) was obtained by averaging line-free channels from the self–calibrated data. The resulting synthesized beam is 2.″2×1.″9 (P.A.=96°), for Setup 3, and 4.″5×3.″5 (P.A.=27°) for Setup 1. The half power primary beam is 59.″2 and 61.″4 for Setup 3 and Setup 1 respectively.

5.2.4 Results

Dust continuum emission

Figure 5.2 shows the map of the dust continuum emission at 3 mm, whose emission peaks at the position of 4A1 and 4A2. As expected, the two sources are not disentangled as the angular resolution of ∼ 2″ is too close to their angular separation (∼ 1.″8; Section 5.2.3). In addition, the two protostars IRAS 4B and IRAS 4B′ (e.g. Looney et al. 2000; Choi 2001; Di Francesco et al. 2001; Maury et al. 2019) were detected, even if they were located outside the primary beam of our observations (∼ 52″). The coordinates of all the four protostars are reported in Table 5.2.

The root mean square (RMS) noise level is 1.5 mJy/beam and the peak flux towards IRAS 4A1+4A2 is 240±40 mJy/beam. Taking the error on the measured flux into account and considering the slightly different wavelength (2.7 mm) and angular resolution (∼ 1.″2) of the observations, this flux value is consistent with the one found by López-Sepulcre et al. (2017). The uncertainties in the flux measurements include the amplitude calibration error (∼ 15%) that dominates the RMS.

Line emission: maps

The present observations allow us to image both 4A1 and 4A2 and their molecular outflows. The study of the molecular content around 4A1 and 4A2 protostars is out of the scope of the present paper. Instead, we focus here on the molecular composition of the outflows.

Several lines from methanol (CH_3OH), acetaldehyde (CH_3CHO), dimethyl ether (CH_3OCH_3) and formamide (NH_2CHO) were detected along the outflows with a signal to noise ratio (S/N) larger than 3. Table 5.3 lists the detected lines with their spectroscopic properties. In Setup 3, we detected six lines of methanol which cover a range of upper level energy (E_{up}) from 7 to 28 K, eight lines of acetaldehyde with E_{up} between 13 and 23 K, and four lines of dimethyl ether, blended together and all with E_{up}=10 K. In Setup 1, we detected one line of formamide with E_{up} of 28 K.

Figure 5.1 shows the distribution of the line emission of the four detected iCOMs. To obtain the methanol map we integrated from -36 km s^{-1} to 36 km s^{-1} with respect to the systematic velocity of the source ($\sim$ 6.5 km s^{-1}), for acetaldehyde between -15 km s^{-1} to 15 km s^{-1}, while for formamide and dimethyl ether we integrated from -9 km s^{-1} to 9 km s^{-1}. First, the methanol emission is extended ($\sim$ 1$'$) and covers the lobes of the two outflows from the two protostars: north (North) and south-west (SW) lobes of the outflow from 4A2, and the south-east (SE) lobe from 4A1. Second, acetaldehyde emission is less extended than the methanol one($\sim$ 15$''$) and it is bright towards the southern lobes, especially towards the SE one. The dimethyl ether emission is not resolved being less than the beam size (2$''$) in two positions, in the North lobe and in the region As (named by Ceccarelli et al. 2017) where SE and SW lobes seem to cross. Finally, formamide emission is also compact ($\sim$ 6$''$) and is located around the As position (see also Ceccarelli et al. 2017). The same iCOMs are also detected in the central protostars (4A1+4A2): please note that the methanol and acetaldehyde emission is not visible in Figure 5.1 because hidden by the dimethyl ether and formamide contours. Figure 5.1 clearly shows a first important result: the evidence of a spatial segregation between the different iCOMs due to the fact that their emission covers different outflow regions.

Table 5.2: Coordinates of the protostars, (see also: Choi 2001; Di Francesco et al. 2001; López-Sepulcre et al. 2017; Maury et al. 2019), and the analyzed emission peaks (chosen from methanol and dimethyl ether emission, see text) in the outflows.

Position	$\alpha(2000)$	$\delta(2000)$
4A1	$03^{h}29^{m}10^{s}.536$	$31^{\circ}13'31''.07$
4A2	$03^{h}29^{m}10^{s}.428$	$31^{\circ}13'32''.27$
4B	$03^{h}29^{m}12^{s}.000$	$31^{\circ}13'08''.10$
4B$'$	$03^{h}29^{m}12^{s}.813$	$31^{\circ}13'06''.97$
SE peak	$03^{h}29^{m}10^{s}.591$	$31^{\circ}13'17''.53$
SW peak	$03^{h}29^{m}10^{s}.061$	$31^{\circ}13'18''.61$
North peak	$03^{h}29^{m}10^{s}.966$	$31^{\circ}13'47''.87$
As region	$03^{h}29^{m}10^{s}.184$	$31^{\circ}13'16''.62$

Line emission: spectra and intensities

In order to do a quantitative analysis, we extracted the spectra from different positions of the three lobes, where both methanol and acetaldehyde emit. The first two selected positions correspond to the emission peaks of methanol in the two southern lobes, named SE and SW, while the last selected position corresponds to the emission peak of dimethyl ether in the north lobe, named North (Figure 5.1). A fourth position is the one where formamide and dimethyl

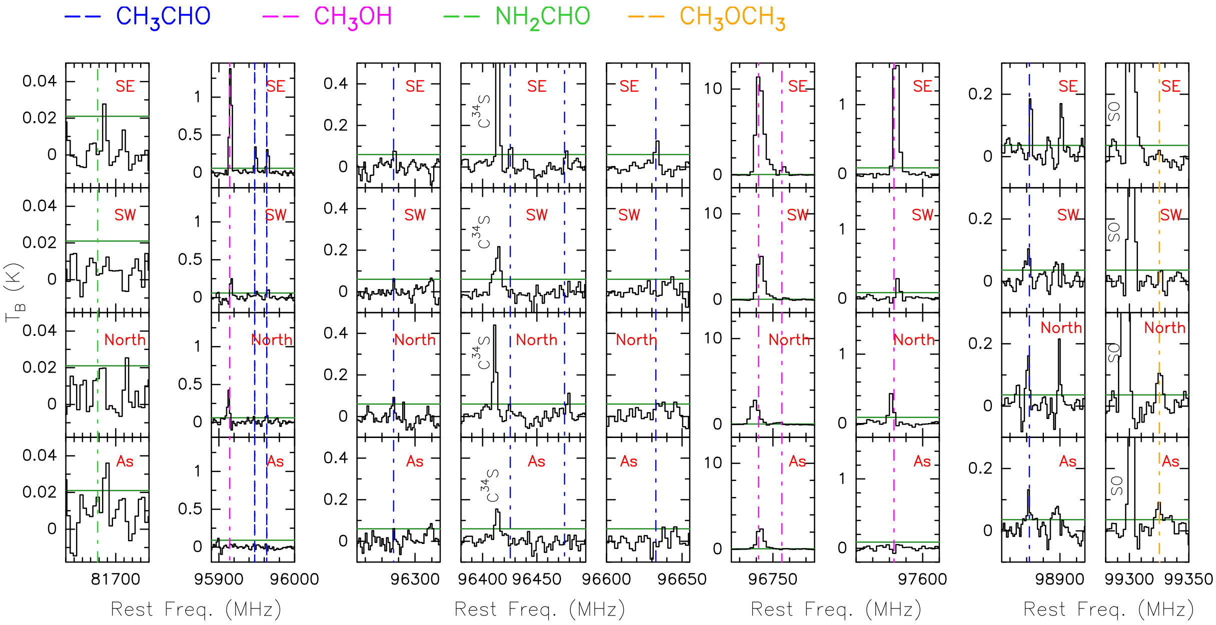

Figure 5.3: Spectra towards the four positions along the outflows of IRAS 4A, listed in Table 5.2. The horizontal green lines represent the 3σ levels (reported in Table 5.3); the vertical dashed lines in blue and magenta represent the rest frequency of acetaldehyde and methanol lines, respectively. The rest frequency corresponds to the protostar LSR velocity (6.5 km s^{-1}).

ether emit, named As. The spectra extracted at the pixels corresponding to the four positions are shown in Fig. 5.3. It is immediately evident that the SE position is richer and brighter in iCOMs when compared to the other ones (SW, North and As).

We then derived the velocity-integrated line intensities of each detected transition using a Gaussian fit, obtained with the CLASS package of the GILDAS software. All the lines used for the analysis are not contaminated by other species and are well isolated. For instance, three of the six detected methanol lines, namely $2_{-1,2}$−$1_{-1,1}$ E (E$_{up}$=13 K), $2_{0,2}$−$1_{0,1}$ A (E$_{up}$=7 K), $2_{0,2}$−$1_{0,1}$ E (E$_{up}$=21 K), are blended together at the WideX resolution (∼2 MHz): therefore they were not used in the analysis described in the next section. Table 5.3 reports the fit results; in case of non-detection, is reported the 3σ limit.

5.2.5 Derivation of the column densities and abundance ratios

Methanol and acetaldehyde

We used the detected lines of methanol and acetaldehyde to estimate their column densities in the four positions of Table 5.2. We used the standard rotational diagram method (Goldsmith & Langer 1999), which assumes local thermodynamic equilibrium (LTE) and optically thin line emission. Note that we checked a posteriori that the latter assumption is valid. Also, because the map shown in Figure 5.1 shows that the emission is more extended with respect to the observation beam, we did not apply any dilution factor. The used error bar of each data point includes the spectral RMS and the calibration error (∼15%).

Figure 5.4 shows the rotational diagrams of methanol and acetaldehyde in SE, SW and North positions (Table 5.2) and Table 5.4 lists the fitted values. In the As position, we could

Table 5.3: Spectral parameters and fit results of the detected iCOMs emission lines observed using the NOEMA WideX backend towards the IRAS 4A outflow peaks (see text and Table 5.2).

Transition	Spectral Parameters			Outflow SE			Outflow SW			Outflow North			Region As $^{(a)}$		
	Frequency$^{(b)}$ [GHz]	$E_{up}^{(b)}$ [K]	$\log A_{ij}^{(b)}$	Area$^{(c)}$ [K km s^{-1}]	T_{peak} [K]	RMS$^{(d)}$ [mK]	Area$^{(c)}$ [K km s^{-1}]	T_{peak} [K]	RMS$^{(d)}$ [mK]	Area$^{(c)}$ [K km s^{-1}]	T_{peak} [K]	RMS$^{(d)}$ [mK]	Area$^{(c)}$ [K km s^{-1}]	T_{peak} [K]	RMS$^{(d)}$ [mK]
CH_3OH															
$2_{1,2}-1_{1,1}$ A	95.91431	21.4	-5.6	17.1(0.9)	1.4	20	2.7(0.3)	0.4	20	5.1(0.5)	0.4	20	≤ 0.5	≤ 0.05	30
$2_{-1,2}-1_{-1,1}$ E $^{(e)}$	96.73936	12.5	-4.6												
$2_{0,2}-1_{0,1}$ A $^{(e)}$	96.74138	6.9	-5.6	199 (4)	12	20	69(4)	5	30	48(4)	3	20	37(1)	2.5	30
$2_{0,2}-1_{0,1}$ E $^{(e)}$	96.74454	20.1	-5.5												
$2_{1,1}-1_{1,0}$ E	96.75550	28.0	-5.5	11.2(0.3)	0.9	20	2.0(0.2)	0.3	30	3.2(0.3)	0.2	20			
$2_{1,1}-1_{1,0}$ A	97.58280	21.6	-5.6	21.5(0.2)	1.9	20	2.5(0.3)	0.3	30	4.4(0.3)	0.4	30	≤ 0.5	≤ 0.05	30
CH_3CHO															
$5_{0,5}-4_{0,4}$ E	95.94744	13.9	-4.5	3.9(0.2)	0.4	20	≤ 0.6	≤ 0.06	20	0.8(0.4)	0.1	20	≤ 0.5	≤ 0.05	30
$5_{0,5}$ - $4_{0,4}$ A	95.96346	13.8	-4.5	3.7(0.3)	0.4	20	1.7(0.4)	0.1	20	1.3(0.5)	0.1	20	≤ 0.5	≤ 0.05	30
$5_{2,4}$ - $4_{2,3}$ A	96.27425	22.9	-4.6	1.1(0.4)	0.1	30	0.7(0.3)	0.07	20	1.0(0.2)	0.1	30	0.5(0.3)	0.1	20
$5_{2,4}$ - $4_{2,3}$ E	96.42561	22.9	-4.6	1.1(0.2)	0.2	30	≤ 0.7	≤ 0.07	20	0.8(0.3)	0.06	30	≤ 0.3	≤ 0.03	20
$5_{2,3}$ - $4_{2,2}$ E	96.47552	23.0	-4.6	0.8(0.2)	0.1	20	≤ 0.7	≤ 0.07	20	≤ 0.8	≤ 0.08	30	≤ 0.3	≤ 0.03	20
$5_{2,3}$ - $4_{2,2}$ A	96.63266	23.0	-4.6	1.5(0.3)	0.1	20	≤ 0.7	≤ 0.07	20	≤ 0.8	≤ 0.08	30	≤ 0.3	≤ 0.03	20
$5_{1,4}$ - $4_{1,3}$ E	98.86331	16.7	-4.5	2.3(0.4)	0.2	20	1.6(0.8)	0.1	20	2.1(0.5)	0.2	30	2.8(0.6)	0.1	20
$5_{1,4}$ - $4_{1,3}$ A	98.90094	16.5	-4.5	2.5(0.5)	0.2	20	≤ 0.6	≤ 0.06	20	1.9(0.3)	0.2	30	2.0 (0.3)	0.1	20
CH_3OCH_3															
$4_{1,4}$ - $3_{0,3}$ EA $^{(e)}$	99.32443	10.2	-5.3	≤ 0.2	≤ 0.02	15	≤ 0.3	≤ 0.03	15	2.1(0.3)	0.12	15	1.8(0.5)	0.09	15
$4_{1,4}$ - $3_{0,3}$ AE $^{(e)}$	99.32443	10.2	-5.3												
$4_{1,4}$ - $3_{0,3}$ EE $^{(e)}$	99.32521	10.2	-5.3												
$4_{1,4}$ - $3_{0,3}$ AA $^{(e)}$	99.32607	10.2	-5.3												
$NH_2CHO^{(f)}$															
$4_{1,4}$ - $3_{1,3}$	81.69354	12.8	-4.5	≤ 0.2	≤ 0.02	7	≤ 0.1	≤ 0.01	7	≤ 0.06	≤ 0.006	7	0.4(0.1)	0.04	10

[a] Region where formamide and dimethyl ether emits (Ceccarelli et al. 2017);

[b] Frequencies and spectroscopic parameters are retrieved from the JPL (Jet Propulsion Laboratory; Pickett et al. 1998) molecular database and from the CDMS (Cologne Database for Molecular Spectroscopy; Müller et al. 2005): for CH_3OH by Xu et al. (2008), for CH_3CHO by Kleiner et al. (1996), for CH_3CHO_3 by Neustock et al. (1990), for NH_2CHO by Kirchhoff et al. (1973). Upper level energies refer to the ground state of each symmetry.

[c] Mean velocity–integrated line flux over the whole velocity emission range from the spectra extracted at the CH_3CHO and CH_3OH transitions at each outflow peaks (see Table 5.2). In case of non–detection we report the 3σ limit. The lines are centered at $\sim$ 3 km s^{-1}, $\sim$ 1 km s^{-1}, $\sim$ 11 km s^{-1} for outflow SE, SW and North respectively, in agreement with the expected outflow velocity (Santangelo et al. 2015) given the WideX channel resolution ($\sim$ 6 km s^{-1}).

[d] The rms is computed over a 200 km s^{-1} band around each line.

[e] These lines are blended together at the WideX resolution ($\sim$2 MHz), therefore they are not used for the non-LTE analysis.

[f] From Setup 1.

not build a rotational diagram for either of the two species, as not enough lines were detected. In this case, we obtained an estimate of their column density, by assuming a rotational temperature ranging from 10 to 30 K (range that includes the temperatures found in the other positions, SE, SW and North). If no line was detected we used the 3σ limit.

To compute the methanol over acetaldehyde abundance ratios, quoted in Table 5.4, we adopted the assumptions that the lines emitted by the two species come from the same region and, therefore, possess the same rotational temperature T_{rot}. Under these two assumptions, the column density ratio R between the two species is obtained by taking the column density N_x of each species at the same rotational temperature T_{rot}, namely $R=N_1(T_{rot})/N_2(T_{rot})$. The error bar δR is then obtained by computing R at the smallest and largest T_{rot} of the two species. For example, in the Outflow SE the derived T_{rot} is equal to (11±3) K and (9±2) K in methanol and acetaldehyde, respectively; therefore, to estimate the error δR we computed $R(T_{rot})$ at 7 and 14 K. Note that the method described above allows to reduce the error bar in the abundance ratio because the calibration uncertainty, which enters in the column density estimate of each species, cancels out when considering the column density of two species derived with the same observation data set.

For methanol, we obtain a column density $N_{CH_3OH} \simeq 9 - 50 \times 10^{14}$ cm^{-2} and a rotational temperature T_{CH_3OH} between 11 K and 23 K. For acetaldehyde, we obtain $N_{CH_3CHO} \simeq 0.6 - 1.3 \times 10^{14}$ cm^{-2} and T_{CH_3CHO} between 9 K and 23 K. Their abundance ratio varies from 10–20 to ∼44 in the three lobes; more precisely, the SE lobe is the one with the largest CH_3OH/CH_3CHO abundance ratio. In As, we only derive a lower limit to the CH_3OH/CH_3CHO abundance ratio, $\geq$20. Note that our observations provide different values of the CH_3OH/CH_3CHO abundance ratio compared to those previously derived by Holdship et al. (2019, ∼300) towards the south and north lobes of the IRAS 4A outflows via single-dish observations. We attribute this difference to the fact that the single-dish observations of IRAS 4A by Holdship et al. (2019) include emission from a much larger region (including also some from the central protostars) with respect to that probed by the present SOLIS observations. Moreover Holdship et al. (2019) do not explicitly derive the emitting size, even though they minimize with respect to this parameter: since the maximization is done independently for each species, their column density ratio has a relatively large intrinsic uncertainty. Therefore the interferometric images allow us to minimize the risk of mixing different gas components (indeed typical of shocked regions).

The abundance ratio analysis confirms what we could see from the emission maps (Figure 5.1), namely that the methanol and acetaldehyde emission (and their relative abundance) is quite different in the SE lobe with respect to the SW and Northern lobes. We emphasize that the difference cannot be attributed to excitation effects, having the methanol and acetaldehyde lines with similar upper level energies (E_{up} from 7 K to 28 K), similar Einstein coefficients ($A_{ij} \sim 10^{-5}$ s^{-1}) and comparable derived temperature, within the measurement errors.

To summarize, the southern–west and northern lobes have a relatively low CH_3OH/CH_3CHO abundance ratio (8–20), whereas the southern–east lobe presents a ratio at least twice larger (∼ 44). Since the SW and North lobes belong to the same outflow emanating from 4A2 and the SE lobe traces the outflow emanating from 4A1, it seems reasonable to attribute the observed difference to an intrinsic difference in the two outflows. We will explore this hypothesis in the next section with the help of an astrochemical model.

Dimethyl ether and formamide

Regarding formamide and dimethyl ether, we detected only one line at most of the latter and four lines (blended at the WideX resolution, ∼2 MHz) of the former in any position (see Table 5.3. For this reason, we did not carry out the rotational diagram analysis as we did for the other iCOMs. Furthermore, while formamide is marginally resolved at the As position, dimethyl ether is not resolved in any outflow peaks (see Figure 5.1). In presence of detection, we derived the column densities using the integrated area of the $4_{1,4} - 3_{1,3}$ line for formamide and the blended ones for dimethyl ether, assuming fixed rotational temperatures. As for methanol and acetaldehyde, we used 11, 16 and 19 K for SE, SW and North, respectively and 10–30 for As. In case of non detection, an upper limit on the column density is derived considering the 3σ limit of the spectra and using the above rotational temperatures. The derived values are reported in Table 5.4.

5.2.6 Astrochemical modelling

We ran our model GRAINOBLE+ in order to reproduce the observations and understand what could be the cause of the observed difference in the CH_3OH/CH_3CHO abundance ratio in the different lobes of the IRAS 4A outflows.

There is solid (observational, theoretical and from laboratory experiments) evidence that methanol is synthesized on the grain surfaces via the hydrogenation of iced CO by successive addition of H atoms (Boogert et al. 2015; Tielens & Hagen 1982; Watanabe & Kouchi 2002). On the contrary, the acetaldehyde formation route is less clear, and the two paths, formation

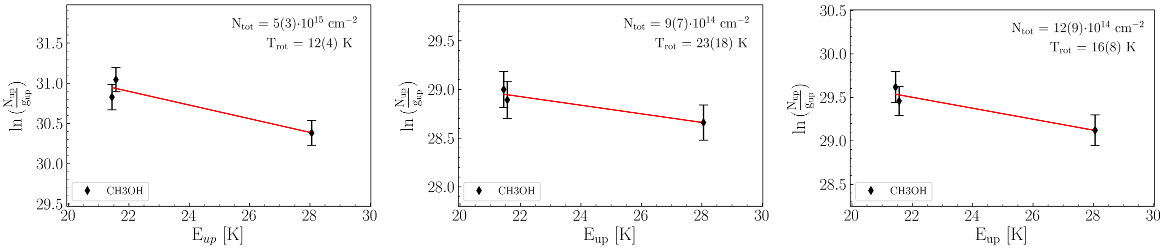

Outflow SE Outflow SW Outflow North

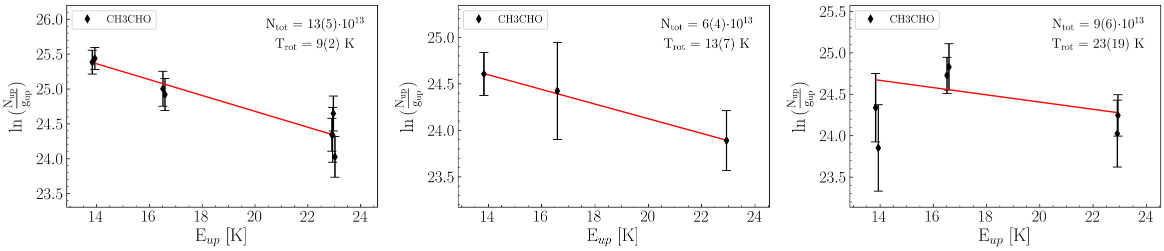

Figure 5.4: *Upper panels:* Rotational Diagrams of methanol (CH_3OH) in outflow SE, SW and North from left to right; *Lower panels:* Rotational Diagrams of acetaldehyde (CH_3CHO) in outflow SE, SW and North. The parameters N_{up}, g_{up}, and E_{up} are the column density, the degeneracy, and the energy of the upper level. The error bars on $\ln(N_{up}/g_{up})$ are computed by taking the calibration error on the integrated flux (15%) into account. The red lines represent the best fits.

Table 5.4: Results of the LTE analysis with the Rotational diagrams, for each outflow peaks, using the observation with the NOEMA WideX backend. In the last row are shown the values of the abundance ratio between methanol and acetaldehyde for each outflow peak.

Molecule			Outflow SE	Outflow SW	Outflow North	Region As[(a)]	L1157-B1[(b)]
CH_3OH	N_{tot}	[10^{14} cm^{-2}]	50(30)	9(7)	12(9)	5-15	130(30)
	T_{rot}	[K]	11(3)	23(18)	18(8)	10-30[(c)]	10.0(1.1)
CH_3CHO	N_{tot}	[10^{14} cm^{-2}]	1.3(0.5)	0.6(0.4)	0.9(0.6)	$\leq$ (0.25-0.5)	0.7(0.3)
	T_{rot}	[K]	9(2)	13(7)	23(19)	10-30[(c)]	8(1)
CH_3OCH_3	N_{tot}	[10^{14} cm^{-2}]	$\leq$ 0.5	$\leq$ 0.7	1.6(0.7)	1.0(0.4)	3
	T_{rot}	[K]	11	16	19	10-30[(c)]	9
NH_2CHO	N_{tot}	[10^{14} cm^{-2}]	$\leq$ 0.02	$\leq$ 0.02	$\leq$ 0.02	0.03(0.02)	–
	T_{rot}	[K]	11	16	19	10-30[(c)]	–
$\frac{CH_3OH}{CH_3CHO}$ [(d)]			44(5)	11(3)	17(3)	$\geq$ 20	190(60)

[a] Region where formamide and dimethyl ether emits (Ceccarelli et al. 2017);

[b] From Codella et al. (2020a) based on interferometric observations;

[c] Fixed rotational temperature used to derive a range of possible N_{tot};

[d] Abundance Ratio computed dividing the best fit column densities derived assuming that the two species are tracing the same gas with the same properties (see text).

in the gas phase or on the grain surfaces, are still debated. Specifically, grain surface models predict that CH_3CHO could be formed through the combination of the two radicals CH_3 and HCO (previously formed by photodissociation of methanol and formaldehyde, respectively) on the surface of the grains (Garrod & Herbst 2006). However, recent quantum chemistry computation by Enrique-Romero et al. (2016, 2019) show that alternative channels leading back to the two simple species CH_4 and CO are competitive. Conversely, gas phase models claims that acetaldehyde formation could occur by the oxidation of hydrocarbons (formed previously on the grain mantles as hydrogenation of carbon chains; Charnley et al. 1992; Charnley 2004). In particular, the injection from grain mantles of ethane (C_2H_6) is expected to drive CH_3CH_2 that will then react in the gas phase with atomic oxygen, giving CH_3CHO (Charnley 2004). The crucial reaction is, therefore:

$$CH_3CH_2 + O \rightarrow CH_3CHO + H \tag{5.1}$$

Following these two possibilities, we ran a grid of astrochemical models in order to reproduce our observations and to understand the possible cause of the difference in the observed CH_3OH/CH_3CHO values in the two IRAS 4A outflows.

Model description

GRAINOBLE+ is a gas–grain model simulating the chemical evolution of gas and ices. It is the upgraded version of GRAINOBLE, initially developed by Taquet et al. (2012b); in particular it is re-coded and improved in terms of computational efficiency and treatment of processes. The GRAINOBLE+ version[3] allows an easy incorporation of many complicated processes that occur in the gas and on the grain surfaces. The code can carry out an easy implementation of evolution of physical conditions of a cloud with a given time dependent physical profile. Additionally, the new code allows a distribution of size for the grains, multilayer formation of the grain ice mantle, growth and depletion of the ice, and desorption.

Table 5.5: The injected abundances (with respect to H-nuclei) into the gas phase at the second step of the model. These values are based on previous observations towards L1157-B1 (Codella et al. 2017).

molecules	injected abundances (/H)
CO_2	3×10^{-5}
H_2O	2×10^{-4}
OCS	2×10^{-6}
H_2CO	1×10^{-6}
NH_3	2×10^{-5}

In this work, we used a chemical network of 522 species and 7785 reactions based on the KIDA database[4] which has been updated from various recent works (e.g. Loison et al. 2014; Balucani et al. 2015; Skouteris et al. 2017, 2018).

In order to simulate the passage of a shock in IRAS 4A, we employed the gas–phase mode of GRAINOBLE+. The simulation follows two steps: (1) a cold molecular gas phase at 10 K and $2 \times 10^4 cm^{-3}$ H–nuclei density (n_H); (2) a post–shock gas phase where density and temperature suddenly jump to $2 \times 10^6 cm^{-3}$ and 70 K.

In other words, the second phase inherits the evolved chemical composition of the cloud

---

[3] A detailed description of the GRAINOBLE+ model will be reported in a forthcoming dedicated article.

[4] http://kida.obs.u-bordeaux1.fr

from the cold phase[5]. Additionally, the gas is infused by species that were formerly synthesized in ice mantles due to the grain sputtering caused by the shock passage.

It is possible that, before reaching the temperature of 70 K, the shocked gas passes through a short initial phase with high temperature. However, this phase unlikely affects the results reported in Fig. 5.6 because there are not known gas–phase reactions with activation barrier forming acetaldehyde. This is confirmed by models taking into account the temperature evolution in the shocked gas (e.g. Nesterenok 2018; Burkhardt et al. 2019).

We do not have precise estimates of the density and temperature in the positions where we derived the CH_3OH/CH_3CHO abundance ratio. However, the values derived at positions close to the ones selected here, via a non-LTE analysis of observed SO_2 lines, (Taquet et al. 2020) are similar to those adopted in our modelling. We assumed that the cosmic ray ionization rate is the same than towards L1157-B1 ($\zeta = 3 \times 10^{-16}$ s^{-1}, Podio et al. 2014) and that the abundance of the injected species are also similar to the ones adopted for L1157–B1 (see Table B1 of Codella et al. 2017), listed in Table 5.5.

We ran series of models to compare the observed CH_3OH/CH_3CHO abundance ratio with the predicted one and to understand what the ratio depends on. We start exploring the gas phase formation route of acetaldehyde assuming that its formation is dominated by reaction 5.1 in the passage of shock. Oxygen is much more abundant than the injected ethyl radical in the post–shock phase; therefore, CH_3CH_2 is the bottleneck of the rate of the reaction 5.1. First, we ran a grid of 169 models with different injected abundances in the beginning of the shocked phase for ethyl radical (CH_3CH_2), and methanol from $[4 \times 10^{-9}, 4 \times 10^{-7}]$ and $[4 \times 10^{-8}, 4 \times 10^{-6}]$ ranges respectively. The methanol abundance range is chosen in order to include the observed values in the hot corinos and in the protostellar shocks (the L1157-B1 outflow in particular); the ethyl radical one is chosen in order to match our observed CH_3OH/CH_3CHO abundance ratio. The results are shown in Figure 5.5 and described in the next section.

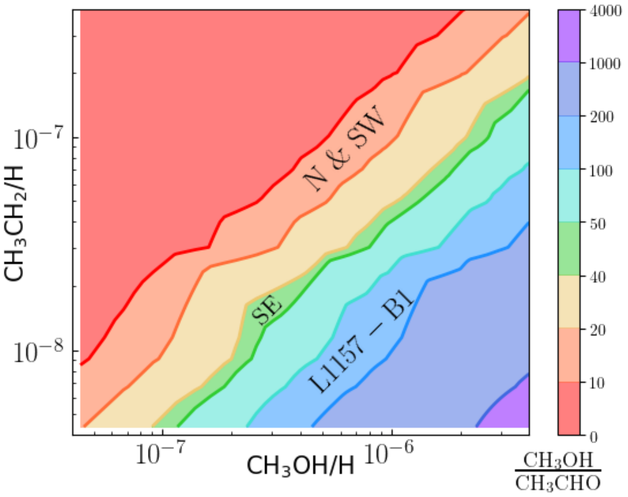

Figure 5.5: Contour map of the CH_3OH/CH_3CHO abundance ratio at 1000 year after the start of the shock passage. The x and y axis are the injected abundances of methanol $[4 \times 10^{-8}, 4 \times 10^{-6}]$ and the parent molecule of acetaldehyde, ethyl radical CH_3CH_2 $[4 \times 10^{-9}, 4 \times 10^{-7}]$, respectively. The measured methanol to acetaldehyde abundance ratio of North and SW outflows (8 – 20) fall in the orange band and the SE one (38 – 50) in the green band; L1157-B1 value (130 – 250) is covered by the blue band (Codella et al. 2020a).

Second, we studied the influence of the density and cosmic ray ionization rate ζ, on the chemical evolution and how the CH_3OH and CH_3CHO abundances and their relative ratio depend on the time, after the shock passage. Note in fact that protostellar shocks could be local accelerators of cosmic ray protons (Padovani et al. 2016) and therefore, in this work ζ is an unknown parameter. We ran then two additional models. In the first one, we lower down the chosen n_H density

---

[5] Note that we do not compute the grain mantle composition as this is treated as a parameter in the following analysis.

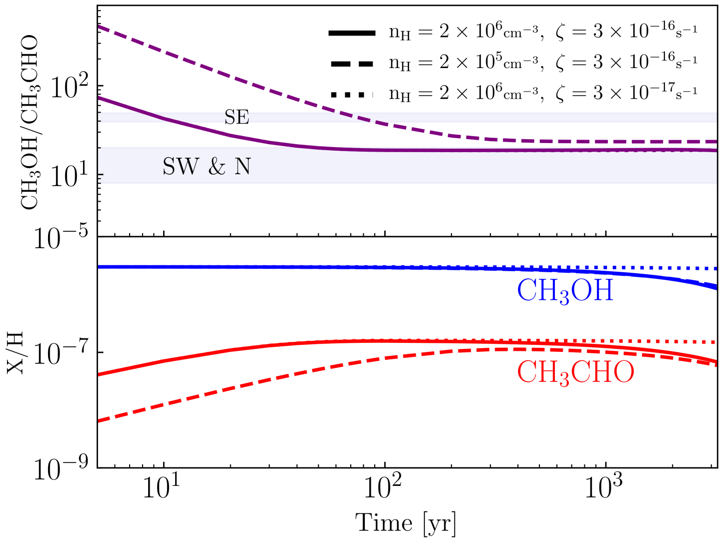

Figure 5.6: Time evolution of abundances of methanol in blue and acetaldehyde in red (bottom) and their ratios in purple (top) for the same injected methanol abundance, 3×10^{-6}, and ethyl radical one, 3×10^{-7}. The different line styles correspond to models run with different conditions, as reported in the upper panel legend. Please note that the CH_3OH/CH_3CHO abundance ratio is constant if both species are directly injected from the grain mantles (see text).

value up to 2×10^5 cm^{-3}; in the second one, we lower down the chosen cosmic ray ionization rate value up to $\zeta = 3 \times 10^{-17}$ s^{-1} for the post–shock phase. The injected abundances of methanol is 3×10^{-6} and for ethyl radical it is 3×10^{-7} in both cases. These values are chosen such that the models reproduce the observed CH_3OH/CH_3CHO abundance ratios for the SW and North lobes (8-20) at 1000 yr (orange band of Figure 5.5) and for the SE one as well. The results are shown in Figure 5.6 and described in the next section.

Finally, we ran a model with the assumption that acetaldehyde is synthesized on the ice mantles and injected directly into the gas phase at the passage of the shock.

Model results

Figure 5.5 shows the contour map of the CH_3OH/CH_3CHO abundance ratio at 1000 years after the shock passage, as a function of the injected methanol and ethyl radical, assuming that acetaldehyde is entirely synthesized in the gas phase. Note that the chosen age (1000 yr) is in the order of magnitude of the kinematical age of L1157-B1 (Podio et al. 2016; Codella et al. 2017) and, likely, IRAS 4A outflows.First, the figure shows that there is a linear dependence of the CH_3OH/CH_3CHO abundance ratio both on the injected methanol and ethyl radical abundance, in the range explored in our simulations. Second, reasonable values of methanol and ethyl radical abundance can reproduce the observed values in the four IRAS 4A outflow positions that we studied (Table 5.2).

In Figure 5.6, we show the evolution of methanol and acetaldehyde abundance as a function of the time after the shock passage, for different densities n_H and cosmic ray ionization rates ζ. Given that methanol is a grain surface product, even by varying n_H or ζ, the injected abundance remains constant in the early stages of the shock up to $\sim 2 \times 10^3$ years. The time evolution of acetaldehyde in the early stages is different from the one of methanol; while the latter remains constant, acetaldehyde abundance increases soon after the shock passage. This is expected, since we assumed that acetaldehyde is a gas phase product and its evolution is dominated by the formation through ethyl radical reaction (5.1). Furthermore, the time evolution of acetaldehyde in the post–shock phase is influenced by variation of n_H or ζ. Lower density slows down the formation rate of acetaldehyde in the early stages; this is due the fact that in lower density gas the ion abundance is higher. Therefore, the contribution of destruction rates is higher in the evolution. Similar to methanol, a lower cosmic ray ionization rate does not affect the early stages.

Finally, we ran a model in which acetaldehyde is synthesized on the icy dust surfaces and injected directly into the gas phase. Therefore, in the model, the species injected into the gas phase right after the shock, is not anymore the ethyl radical but the acetaldehyde, whose abundance is chosen to be equal to the observed one. Therefore, the gas–phase production of acetaldehyde is, in this case, negligible. As for methanol, the abundance of acetaldehyde, now injected from grains, remains constant up to $\sim 2{\times}10^3$ yr when the destruction by ions (H_3O^+ in this specific case) becomes dominant. Therefore, the difference in the abundance of acetaldehyde between the gas– and grain– synthesized is only within the first 200 years of the shocked phase, when acetaldehyde takes time to be formed by the reactions between ethyl radical with atomic oxygen.

5.2.7 Discussion

The two IRAS 4A outflows

Our new SOLIS observations show that the two outflows emanating from 4A1 and 4A2, previously identified by Choi (2005) and Santangelo et al. (2015) via simple molecules (SiO, CO and SO), are enriched with methanol all across the three (visible) lobes. Conversely, acetaldehyde is spread only over the southern lobes and is concentrated in a compact spot in the northern one. Therefore, a first conclusion of this work is that, in the protostellar post–shock regions there is the release in gas phase of methanol, previously formed on the grain surfaces, and the production of acetaldehyde. The statistic is very poor for the moment, with the two IRAS 4A outflows and the L1157–B1 one in which acetaldehyde is detected with interferometric observations (Codella et al. 2015a, 2017, 2020a).

Regarding the IRAS 4A outflows, the SE lobe is richer in both methanol and acetaldehyde, namely the outflow emanating from 4A1. We notice that this is an opposite behavior with respect to the SiO emission, which is instead brighter along the 4A2 outflow (Choi 2005). This anti-correlation with SiO is also seen in other (simple) molecules, such as NH_3, H_2CO and HCN by Choi et al. (2011). As Choi et al. suggested, it could be due to a different strength of the shock (the sputtering of Si could require different shock velocities with respect to the other molecules) or because the SiO traces different physical conditions with respect to the other molecules. For example, SiO could trace the jet while the other molecules could be originated in the gas entrained by the jet (e.g. Bachiller et al. 1998b; Ospina-Zamudio et al. 2018, 2019). Linked with this, the different spatial distribution between SiO and other species, could be due to time-evolution effects, namely different ages of the shocks, as previously observed in other outflows (e.g. Castets et al. 2001). We will discuss more this point in the next section.

Finally, it is not clear what is the origin of the iCOMs emission in the As position. It does not seem to be clearly associated with any of the two southern lobes but rather with a point where they intersect. That would imply that additional shocks can occur at the interface of the swept-up cavities opened up by the jets. Higher spatial resolution observations are needed to confirm or reject this hypothesis.

The CH_3OH/CH_3CHO abundance in IRAS 4A1 and 4A2 outflows

In Section 5.2.5, we measured the methanol over acetaldehyde abundance ratio towards the three positions of the two IRAS 4A outflows, in the North, SW and SE lobes, respectively (Table 5.4). While the North and SW lobes have a similar values, between 8 and 20 (considering the error bars), the SE lobe has larger CH_3OH/CH_3CHO, 38–50. In other words, the methanol over acetaldehyde abundance ratio is about twice larger in the outflow emanating from 4A1 with respect to the one from 4A2. In this section, we try to understand the origin of this difference, having in mind that, while methanol is a past grain-surface product, acetaldehyde can either be itself a past grain-surface or a gas-phase product.

One easy possible explanation, then, of the CH_3OH/CH_3CHO difference is that the grain mantle composition is different in the two outflows. However, this seems unlikely, because, on one hand, no gradient in the ratio is seen between the North and SW lobes of the 4A2 outflow; moreover, the SW and SE lobes are very close in space, closer than the two 4A2 outflow positions where we estimated the CH_3OH/CH_3CHO abundance ratio. Therefore, although we cannot totally exclude it, it seems to us that the different grain composition is an improbable explanation.

If acetaldehyde is synthesized by the gas-phase reaction (5.1), there are more possibilities other than a different grain mantle composition. As shown by the modelling of section 5.2.6, a smaller density or a younger age of the 4A1 outflow with respect to the 4A2 one would explain the observed CH_3OH/CH_3CHO difference. Specifically, if the two outflows are very young and 4A1 is younger than about 200 yr, then this would explain why its ratio is larger than the 4A2 one (see Figure 5.6).

Unfortunately, our observations did not have enough methanol lines to allow a meaningful non-LTE analysis to derive the volume density, so we do not know if the density in the 4A1 outflow is lower than in the 4A2 outflow. With a non-LTE analysis on SO_2, Taquet et al. (2020) suggest that there is no significant difference in density between the outflow driven by 4A1 and the one from 4A2. On the other hand, assuming a typical shock velocity of 100 km/s, we estimate a kinematical age of $\sim$200 yr for the 4A1 outflow which has a very short extent; this seems to support the younger age of 4A1 hypothesis. Furthermore, Santangelo et al. (2015), using high spatial resolution observations of CO, SiO and SO, showed that the 4A1 jet is faster than the 4A2 one; this, combined with the smaller spatial extension again support the hypothesis that 4A1 outflow is younger than the 4A2 one. In favor of a different age of the two outflows there is also the observed chemical differentiation between the two driving sources, 4A1 and 4A2: the former is bright in the continuum but lacks iCOMs line emission, exactly the opposite of 4A2 (e.g. López-Sepulcre et al. 2017). One of the possible explanation for this situation is the smaller hot corino size, which could also imply a younger age of 4A1, and this agrees with the younger age of its outflow too.

In summary,the different CH_3OH/CH_3CHO abundance ratio measured in the 4A1 and 4A2 outflows is unlikely caused by a different grain mantle composition of the two outflows, because the more extended 4A2 outflow shows no significant variation of this ratio over a scale of about 6000 au. On the contrary, the observed CH_3OH/CH_3CHO abundance ratio is consistent with the scenario in which (i) the 4A1 outflow is younger (and, consequently, faster) than the 4A2 one and (ii) in both outflows acetaldehyde is synthesized in the gas phase. The major reaction is that between atomic oxygen and ethyl radical. The gas-phase synthesis hypothesis also agrees with theoretical quantum chemistry studies (Enrique-Romero et al. 2016, 2019). Thus, although terrestrial laboratory experiments show that acetaldehyde can be formed on the surfaces of dust grains (e.g Bennett et al. 2005a,b; Öberg et al. 2009), our results provide evidence that the gas phase formation route cannot be neglected and actually appears to be the dominant one in the IRAS 4A outflows. We emphasize that these conclusions are robust, as they very little depend on the details of the modeling being based on known reactions in the gas-phase.

Comparison with other Solar-type objects

Figure 5.7 shows the methanol over acetaldehyde abundance ratio in the IRAS 4A outflows, compared with the values measured in other low/intermediate star forming regions for which the emitting size has been estimated via interferometric observations: the L1157-B1 molecular shock and seven hot corinos.

First, the IRAS 4A outflows have a definitively lower CH_3OH/CH_3CHO with respect to the L1157–B1 value (130-250), reliably measured by Codella et al. (2020a). Following the discussion of the previous section, this could be due to a difference in the composition of the grain mantles, to a lower density or to a younger age of the 4A outflows with respect to the L1157-B1 one. At present, the information in our hands is not enough to be able to support or rule out any of these three possibilities; a more accurate analysis of the IRAS 4A outflows is needed. Obviously, having more information of one key actor, the abundance of ethyl radical in these outflows, could shed more light on why the two outflow systems are different.

Finally, the same difference observed between the IRAS 4A and L1157 outflows, if not larger, is observed with respect to the values measured in Class 0 and I hot corinos (Marcelino et al. 2018; Bianchi et al. 2017; Taquet et al. 2015; López-Sepulcre et al. 2017; Jacobsen et al. 2019; Jørgensen et al. 2016; Bianchi et al. 2019b; Ospina-Zamudio et al. 2018; Codella et al. 2020a).

In Figure 5.7, we ordered the hot corinos according their (increasing) bolometric luminosity L_{bol}, keeping in mind that the measure of L_{bol} is relatively uncertain. It is possible to notice an interesting trend: in the Class 0 hot corinos,the CH_3OH/CH_3CHO abundance ratio decreases with increasing L_{bol}. Our modeling, (Section 5.2.6), is not directly applicable to the hot corino case for two main reasons: 1) the hot corinos density (n_H $\sim 10^7 cm^{-3}$) is larger than those used in our model (Figure 5.6, and 2) there is continuous injection of the infalling material towards the center. Having said that, it seems improbable that the behavior shown in Figure5.7 has something to do with a time effect. In the hot corino conditions (higher density and low cosmic ionization rate) the synthesis in the gas phase is fast during the first decades while the destruction by molecular ions is slow in the latest stages($\geq 10^5$ yr), leading to a CH_3OH/CH_3CHO abundance ratio almost constant.

On the contrary, a possible interpretation is that larger luminosity correspond to larger hot corino sizes (namely larger regions with a dust temperature $\geq$100 K; Ceccarelli et al. 2007) and, assuming a central peaked density distribution, regions with lower densities. Since methanol

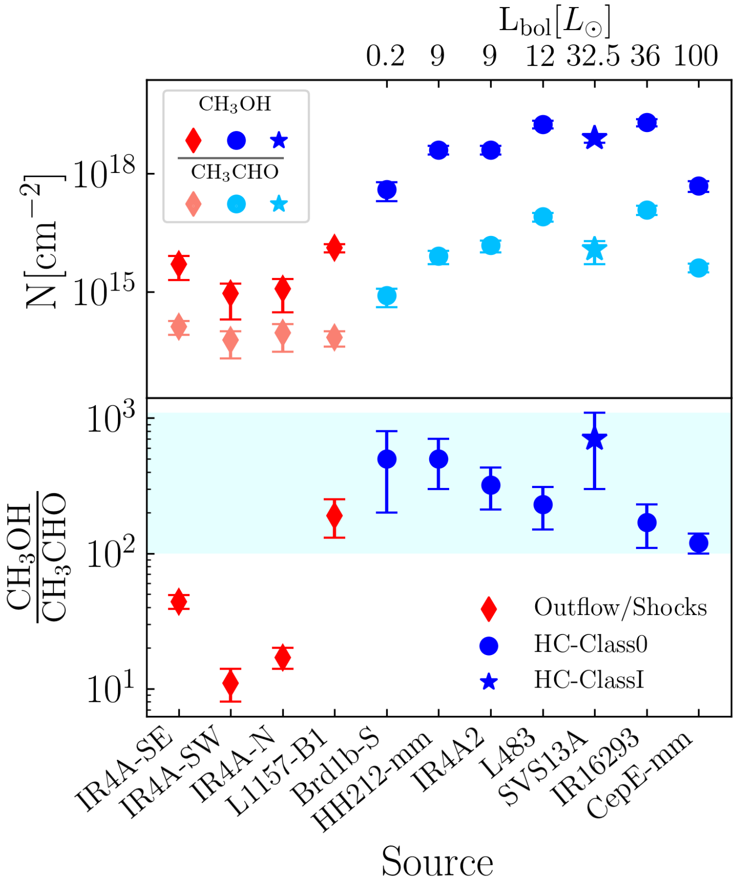

Figure 5.7: Abundance ratios between CH_3OH and CH_3CHO (*Bottom panel*), CH_3OH and CH_3CHO column density (*Upper panel*) compared to different sources for which the emitting size has been estimated via interferometric observations: the values in the outflows of IRAS 4A (this paper), in the outflow of L1157-B1 (Codella et al. 2020a), the Class I source SVS 13A (Bianchi et al. 2019b), and the Class 0 sources, in decreasing order of bolometric luminosity, Barnard1b-S (Marcelino et al. 2018), HH212-mm (Bianchi et al. 2017; Codella et al. 2020a), IRAS 4A2 (Taquet et al. 2015; López-Sepulcre et al. 2017), L483 (Jacobsen et al. 2019), IRAS 16293-2422B (Jørgensen et al. 2016), CepE-mm (Ospina-Zamudio et al. 2018). The outflow values are shown with red (pink for CH_3CHO) markers, the hot corinos in blue (cyan for CH_3CHO), using diamonds for the outflows, dots for Class 0 and star for the Class I source. The cyan band represents the area in which the the hot corinos values fall.

is produced during the prestellar phase by hydrogenation of frozen CO (Taquet et al. 2012a; Vasyunin et al. 2017), a larger density will bring a larger methanol abundance; acetaldehyde, on the other hand, could be either a past grain-surface or a present-day gas-phase product (see Section 5.2.6). Therefore, the decreasing CH_3OH/CH_3CHO abundance ratio could indicate that, while methanol abundance decreases with density, acetaldehyde or its gas-phase precursors do not. We emphasize that these conclusions have to be taken with caution as the errors on the hot corinos bolometric luminosity are relatively large, but they are worth a deeper study.

5.2.8 Conclusions

In this work we reported new observations using the IRAM/NOEMA interferometer in the context of the SOLIS large program, and the detection of several iCOMs in the two outflows emanating from IRAS 4A1 and 4A2, respectively: methanol, acetaldehyde, dimethyl ether and formamide. This is the second ever outflow system, after the Solar-type protostellar L1157 outflow, where multiple iCOMs have been detected using interferometers. Our main conclusions are the following:

- As in the case of L1157-B1 (Codella et al. 2017), iCOMs are not homogeneously distributed across the IRAS 4A outflows: methanol is more widespread over the two outflows, while acetaldehyde emission is only bright in the southern lobes, and dimethyl ether and formamide are concentrated in a spot at the (apparent) interface between the south lobes of the 4A1 and 4A2 outflows. We, therefore, forewarn that derivation of iCOMs abundance ratios from single-dish observations could be hazardous.

- The measured methanol over acetaldehyde abundance ratio is twice larger in the 4A1 outflow with respect to that in the 4A2 one; the comparison between these results with model predictions suggests that: 1) the 4A1 outflow is younger than the 4A2 one and 2) acetaldehyde is synthesized in the gas phase by the reaction of atomic oxygen with ethyl radical. Alternatively, the grain mantle distribution should vary widely on small scale, which seems unlikely since the larger scale 4A2 outflow shows a similar CH_3OH/CH_3CHO in two distant points of the southern and northern lobes.

- Considering the CH_3OH/CH_3CHO abundance ratio, the two IRAS 4A outflows show a sharp difference with respect to the L1157-B1 one. This may indicate that either the grain mantles or the gas volume densities are very different in the two regions. Additional observations are necessary to better constrain the reason of the observed difference.

- The methanol over acetaldehyde abundance ratio in the Solar-type hot corinos is at least ten times larger than in the IRAS 4A outflows, again pointing to different grain mantles composition or densities. Interestingly, we noticed that CH_3OH/CH_3CHO tentatively decreases with increasing bolometric luminosity of the Class 0 hot corino; a possible reason could be the larger sizes of the hot corinos.

5.3 Future projects

5.3.1 The ALMA FAUST Large Program

FAUST (Fifty AU STudy of the chemistry in the disk/envelope system of Solar-like protostars) is a ALMA Large Program (2018.1.01205.L; PI: Satoshi Yamamoto, 151.8 hr), that involves an international team with the goal to reveal and quantify the chemical diversity observed in the envelope/disk system of young Solar-like systems at planet-formation scales. Indeed, the chemical differentiation seen in Solar-type protostars is present at scales between 100 au and 3000 au but it is not yet clear if such diversity is also seen in the inner regions ($\leq$50 au) where planets are supposed to form. Additionally, one of the FAUST goal is to understand what molecules are passed from the large scale envelope to the disk scale, as it will help to characterize the chemical content available for future forming planetary systems.

To address these points, FAUST is designed to survey the chemical composition of a sample of 13 Class 0/I protostars, probing regions from about 1000 to 50 au (all have a distance $\leq$250 pc). The targeted sources are chosen to be a representative sample known to exhibit a wide chemical composition diversity (based on the available large-scale observations). In particular, they show very different molecular spectra: one the one side, there are sources with a spectra dominated by iCOMs, and, on the other, by carbon-chain molecules and hydrocarbons. Each source will be imaged in about 100 lines, so that the final dataset will consist of thousands of images, constituting a key legacy for astrochemistry. All the targeted lines will be used as a powerful diagnostic tool, together with the kinematics, as they are differential enhanced in the different zones of the envelope/disk system (envelope, barrier, disk).

Finally, the FAUST survey provides a uniform sample in terms of frequency setting, angular resolution and sensitivity, summarized in Table 5.6.

I am involved in the FAUST project mainly to study the chemical complexity of the Class 0 IRAS 4A (the source target of this thesis), plus other two sources, the Class I L1551 IRS5, and the Class 0 NGC 1333 IRAS 4C. Additionally, I will have the occasion to tackle other kind of studies, such as gas ionization and deuteration.

5.3.2 Formamide and acetaldehyde formation routes

Formamide and acetaldehyde are two iCOMs largely detected in interstellar environments, such as hot corinos and shocked regions (e.g., Cazaux et al. 2003; López-Sepulcre et al. 2015,

Table 5.6: List of the spectral setups of FAUST and the list of targeted molecular lines.

Setup	Angular resolution		Frequency range	Velocity resolution [km/s]	
	[″]	[au]	[GHz]	Low Res	High Res
1	0.21–0.37	50	214.0–219.0 229.0–234.0	∼ 1.3	∼ 0.2
2	0.21–0.37	50	242.5–247.5 257.5–262.5	∼1.2	∼ 0.2
3	0.21–0.37	50	85.0–89.0 97.0 – 101.0	∼0.2	∼1.5

2017; Lefloch et al. 2017; López-Sepulcre et al. 2019; De Simone et al. 2020b; Codella et al. 2015a, 2017, 2020a). However, their formation route is still matter of debate (e.g., Skouteris et al. 2017; Codella et al. 2017, 2020a; Rimola et al. 2018; Enrique-Romero et al. 2019, 2021).

A possible reaction route for formamide involves the reaction in gas phase between formaldehyde (H_2CO) and the amidogen radical (NH_2), which can be formed starting from ammonia or by the partial protonation/hydrogenation of atomic nitrogen (e.g., Barone et al. 2015; Vazart et al. 2016; Skouteris et al. 2017). On the other hand, astronomical observations show a good linear correlation between isocyanic acid (HNCO) and formamide (NH_2CHO), which might suggest HNCO hydrogenation on ice as a plausible formation route for formamide. However, it has been shown that the hydrogenation of HNCO on an amorphous solid water surface is a very slow process (Noble et al. 2015; Song & Kästner 2016). Alternatively, formamide has been thought to form on grain surfaces by the NH_2 + HCO radical-radical reaction (e.g., Garrod 2008). However, this reaction competes with the formation of NH_3 and CO, the product of the direct H-abstraction from HCO and NH_2. The occurrence of one channel or the other depends on the relative orientation of the reacting radicals and the morphology of the water ice (Rimola et al. 2018; Enrique-Romero et al. 2019, 2021, 2021b). Another possibility is the reaction between a gas-phase CN radical with water molecules belonging to the ice mantle as the former lands on them. This is a multi-step reaction that can lead to formamide thanks to the initial formation of a hemibond[6] between CN and water, assuming that there are no significant energy losses throughout the ice mantle after each reaction step (Rimola et al. 2018).

The formation of acetaldehyde in the gas phase can occur through two possible reactions: i) the reaction between ethyl radical (CH_3CH_2) with atomic oxygen (Charnley 2004; Vastel et al. 2014; Vazart et al. 2020) that can form also formaldehyde (H_2CO) and ethylene (CH_2CH_2), and iii) the reaction between ethanol (CH_3CH_3OH) with OH and Cl and lead to the formation of acetaldehyde, formic acid and acetic acid (the so-called genealogical ethanol tree; Skouteris et al. 2018; Vazart et al. 2020). Additionally, the reaction between methanol (CH_3OH and CH (Vasyunin et al. 2017) has been studied. However, it forms mainly formaldehyde and ethylene and only a negligible fraction of acetaldehyde (Vazart et al. 2020). On the other hand, acetaldehyde can be formed on the interstellar grain through the radical-radical reaction between CH_3 and HCO. As in the case of formamide, this reaction competes with the formation of CH_4 and CO through direct H-abstraction (Enrique-Romero et al. 2019, 2020). In addition, a recent study shows that the reaction may not occur at all, depending on the ice surface characteristics (Enrique-Romero et al. 2021).

A method that turned out to be efficient in constraining the iCOMs formation route is to compare theoretical predictions with iCOMs abundances measured in hot corinos. In particular, the iCOMs deuteration ratio has been successfully used (Skouteris et al. 2017). Indeed, the deuteration ratio in different molecules might provide the temporal sequence of their formation and, possibly, information on their synthetic route (e.g., Caselli & Ceccarelli 2012; Ceccarelli et al. 2014). So far, deuterated formamide has only been detected toward one source, the hot corino of IRAS16293-2422 B by Coutens et al. (2016). They found similar NH_2DCO/NH_2CHO and $NHDCHO/NH_2CHO$ abundance ratios around 0.02 – 0.05 and suggested a grain-surface formation of NH_2CHO. Indeed, considering the relatively small percentage of deuterated formamide with respect to formaldehyde, they suggested a preference for synthesis on ice, as gas-phase routes should mostly retain the deuteration ratio of par-

---

[6] The hemibond is a non-classical type of chemical bond that relates two nuclear centers and three electrons.

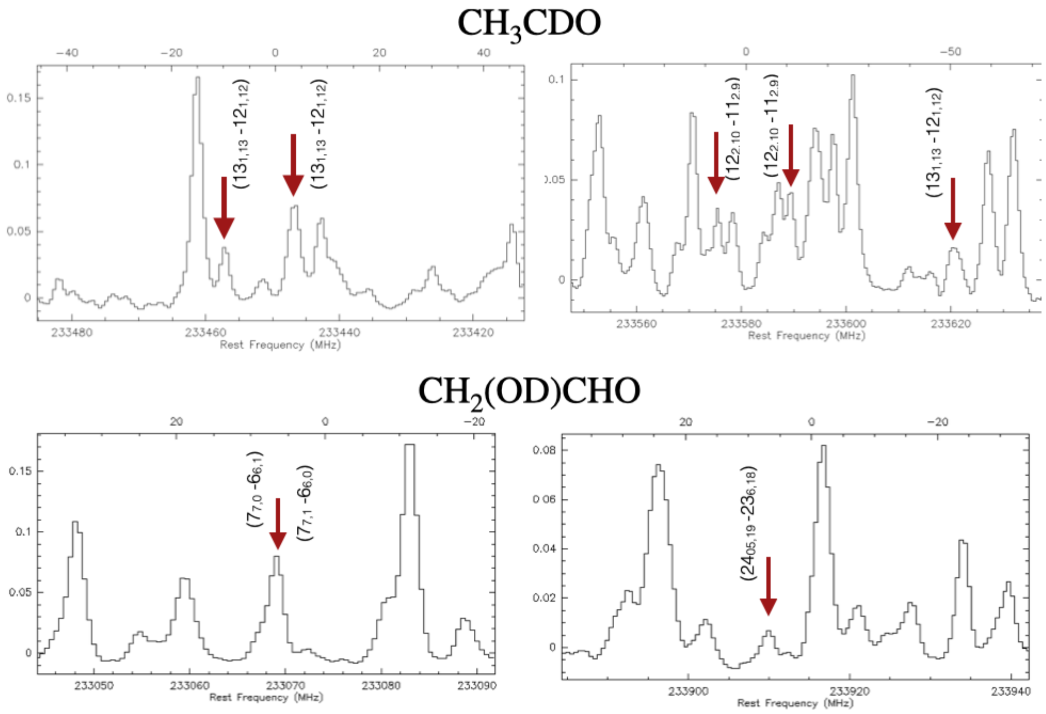

Figure 5.8: Deuterated acetaldehyde (CH_3CDO, top panels) and deuterated glycolaldehyde ($CH_3(OD)CHO$, bottom panels) transitions detected toward the IRAS 4A2 hot corino using ALMA/FAUST observations. The shown spectra are preliminary.

ent molecules (NH_3 and H_2CO). However, Skouteris et al. (2017) later performed quantum chemical computations showing that the precursors and formamide deuteration are in perfect agreement with the observations by Coutens et al. (2016), supporting the gas phase channel.

The same approach used by Skouteris et al. (2017) to constrain the formation route of formamide can be used to investigate the formation route of other iCOMs. To this end, I propose to observe the deuterated forms of both acetaldehyde and formamide in the IRAS 4A2 hot corino, using the data of the ALMA FAUST Large Program. Indeed, recently, the gas-phase chemical reactions leading to acetaldehyde, and its deuterated forms, have been investigated with quantum chemical computations (Vazart et al. 2020, 2021). Additionally, the first preliminary ALMA spectra toward IRAS 4A2 shows that the CH_3CDO is well detected (see Figure 5.8).

Finally, the same approach could be performed for glycolaldehyde once the computational results will be available (Vazart et al. in preparation for the formation in the gas phase, Enrique-Romero et al. in preparation for the formation on the grain surface).

6

Collateral effects

Molecular clouds forming Solar-type stars are dominated by an intricate net of filaments which are widely accepted to play an important role in the star formation process. Indeed, most of the young stars and cores are embedded in these filaments (e.g., Schneider & Elmegreen 1979; Goldsmith et al. 2008). This characteristic is shown to be ubiquitous by large scale maps of the Herchel Space Observaory and Planck satellites (e.g., Molinari et al. 2010; Zari et al. 2016). However, the exact process ruling the formation of these filamentary structures and their specific role in triggering star formation are still debated (e.g., Hennebelle & Inutsuka 2019; Robitaille et al. 2020). A major process in their shaping, in addition to the presence of magnetic fields, is the compression of the molecular gas by external triggers, such as stellar winds or supernovae remnants, cloud-cloud collisions, and (magneto-)hydro-dynamical gravitational instabilities (e.g., Padoan et al. 2001; Hennebelle 2013; Vázquez-Semadeni et al. 2019; Federrath et al. 2021).

The NGC 1333 molecular cloud hosts a large number of young protostars associated with filamentary structures, probably shaped by external triggers (e.g., Dhabal et al. 2019). The southern filament is composed of multiple structures with distinct systemic velocities and velocity gradients (e.g., Sandell & Knee 2001; Dhabal et al. 2018, 2019). The IRAS 4A system is located on the west side of this filament. Dhabal et al. (2019) hypothesized that the entire southwest part of NGC 1333, encompassing the filament where IRAS 4A lie, is due to a colliding "turbulent cell", a clash that could have triggered the birth of the protostars. However, no specific signatures of a clash, namely shocks, have been reported so far, leaving unanswered how and where the energy of this clash, if real, is dispersed.

Within the Seed Of Life (SOLIS) NOEMA Large Program, observations at high angular resolution ($\sim 2''$) of the large scale ($\sim 60''$; $\sim$18000 au) region surrounding the IRAS 4A system were performed targeting both methanol and SiO. These two species are traditionally considered among, if not the best, tracers of shocks, where their abundance is observed to drastically increase by several orders of magnitude (e.g., Bachiller et al. 1998b, 2001; Arce et al. 2008; Codella et al. 2012; Lefloch et al. 2017; Codella et al. 2020a). The SiO enhanced abundance is due to the sputtering of the grain mantles and shattering of the grain refractory cores, both processes releasing SiO and Si (which is quickly oxidized in SiO) into the gas-phase (e.g., Caselli et al. 1997; Schilke et al. 1997; Gusdorf et al. 2008a,b; Guillet et al. 2011). Likewise, CH_3OH is believed to be mainly formed on the cold grain surfaces (e.g., Watanabe & Kouchi 2002; Rimola et al. 2014) and released into the gas-phase by the grain mantle sputtering (e.g., Flower et al. 2010).

Using the SOLIS observations, I imaged the SiO and the CH_3OH emission in the IRAS 4A region, discovering the presence of peculiar features in the southern part of the map. Indeed, besides the emission coming from the two IRAS 4A outflows, three elongated filamentary structures have been detected south of the protostar center. They show very narrow spectral profile peaked at the systemic velocity of the cloud, and they do not seem to be connected to the outflows.

Analyzing the emission in these structures I wanted to understand: i) what is the origin of these structures, ii) what caused the release of CH_3OH and SiO from the grains, and iii) if they are the signature of the clash hypothesized by Dhabal et al. (2019).

The research presented in this section has resulted in one scientific paper:

- “A train of shocks at 3000 au scale? Exploring the clash of an expanding bubble into the NGC 1333 IRAS 4 region. SOLIS XVI”
  De Simone M., Codella C., Ceccarelli C., López-Sepulcre A., Neri R., Rivera Ortiz P.R., Busquet G., Caselli P., Bianchi E., Fontani F., Lefloch B., Oya Y., and Pineda J.E.
  Accepted in *Monthly Notices of the Royal Astronomical Society.*

6.1 A train of shocks at 3000 au scale? Exploring the clash of an expanding bubble into the NGC 1333 IRAS 4 region. SOLIS XVI

6.1.1 Introduction

Molecular clouds forming Solar-type stars are characterized by an intricate net of filaments which are widely accepted to play an important role in the star formation process. Indeed most of the young stars and cores in low-mass star forming regions are embedded in filaments of gas and dust which dominate the cloud structure (e.g., Schneider & Elmegreen 1979; Ungerechts & Thaddeus 1987; Goldsmith et al. 2008), a characteristic shown to be ubiquitous by the large scale maps of the Herschel Space Observatory and Planck satellites (e.g., Molinari et al. 2010; André et al. 2010, 2014; Zari et al. 2016). Some of the most prominent cloud filaments actually are collections of velocity-coherent fibers that can become gravitationally unstable and fragment into chains of cores (Hacar et al. 2013, 2017; Tafalla & Hacar 2015; Henshaw et al. 2016, 2017; Sokolov et al. 2019, 2020; Chen et al. 2020). However, the exact process ruling the formation of these filamentary structures and their specific role in triggering star formation are still debated (e.g., Hennebelle & Inutsuka 2019; Robitaille et al. 2020). A major process in their shaping, in addition to the presence of magnetic fields, is the compression of the molecular gas by external triggers, such as ionization/shock fronts around OB stars or supernovae remnants, cloud-cloud collisions, and (magneto-)hydro-dynamical gravitational instabilities (e.g., Padoan et al. 2001; Hennebelle 2013; Vázquez-Semadeni et al. 2019; Federrath et al. 2021).

All these external triggers leave signatures at different scales, from parsec to sub-parsec, observed with specific molecular shocks tracers (e.g., Jiménez-Serra et al. 2010; Berné et al. 2010; Dumas et al. 2014; Cosentino et al. 2018, 2019, 2020). SiO and CH_3OH are traditionally considered among the best tracers of such shocks, where their abundance is observed to drastically increase by several orders of magnitude (e.g., Bachiller et al. 1998b, 2001; Arce et al. 2008; Codella et al. 2012; Lefloch et al. 2017; Codella et al. 2020a). The SiO enhanced abundance is due to the sputtering of the grain mantles and shattering of the grain refractory cores, both processes releasing SiO and Si (which is quickly oxidized in SiO) into the gas-phase (e.g., Caselli et al. 1997; Schilke et al. 1997; Gusdorf et al. 2008a,b; Guillet et al. 2011). Likewise, CH_3OH is believed to be prevalently formed on the cold grain surfaces (e.g., Watanabe & Kouchi 2002; Rimola et al. 2014) and released into the gas-phase by the grain mantle sputtering (e.g., Flower et al. 2010).

Perseus is one of the molecular clouds in the vicinity of our Sun that is believed to have been formed and shaped by external triggers, such as the explosion of one or more supernovae and other forms of stellar feedback activity. For example, new 3D dust extinction maps obtained by GAIA support this hypothesis (see e.g., Zucker et al. 2021; Bialy et al. 2021). One of the most active sites of ongoing star formation in Perseus is NGC 1333 in the Perseus molecular cloud complex (∼300 pc; Zucker et al. 2018). This region hosts a large number of young stars and protostars associated with filamentary structures, and it displays a complex network of fibers characterized by a high degree of internal fragmentation with typically three to four cores per fiber (Hacar et al. 2017).

Recent observations produced large scale maps of the magnetic field in NGC 1333, helping in understanding their role in the star formation process (e.g., Doi et al. 2020). For all these reasons, NGC 1333 is one of the best regions to study the connection between filaments, magnetic fields, external triggers, and star formation.

More specifically, this article focuses on the southern filament of NGC 1333, which is composed of multiple structures with distinct systemic velocities and velocity gradients (e.g., Sandell & Knee 2001; Dhabal et al. 2018, 2019). The famous IRAS 4A system, a protostellar binary which drives two large-scale molecular outflows, is located on the west side of the filament (Choi 2005; Santangelo et al. 2015; De Simone et al. 2020b; Taquet et al. 2020; Chuang et al. 2021). The filament joins an arc-like structure on the west which hosts other young protostars (the SVS13 and IRAS 2 systems). In a recent study, Dhabal et al. (2019) hypothesized that the entire southwest region of NGC 1333, encompassing the filament where IRAS 4A lies, is due to a colliding "turbulent cell", a clash that triggered the birth of the above-mentioned protostars. However, no specific signatures of a clash, namely shocks, have been reported so far, leaving unanswered how and where the energy of this clash, if real, is dispersed.

To answer this question, we analyzed new high spatial resolution ($\sim$ 600 au) observations of CH_3OH and SiO toward IRAS 4A, obtained in the context of the IRAM-NOEMA Large Program SOLIS[1] (Seeds Of Life In Space; Ceccarelli et al. 2017). Our goal is to search for specific signatures of the clash event and to gain a more detailed insight into what happened and why.

The article is organized as follows. In Sects. 6.1.2 and 6.1.3, we described the observations and the results, respectively. In Sect. 6.1.4, we analyze the physical and chemical properties of the observed structures. In Sect. 6.1.5, we discuss the implication of our analysis and in Sect. 6.1.6 we summarise our conclusions.

6.1.2 Observations

The IRAS 4A system was observed at 3mm with the IRAM NOEMA (NOrthern Extended Millimeter Array) interferometer[2] within the SOLIS project[1]. Part of the data was already published in De Simone et al. (2020b). For the present study, we used the observations obtained with two setups, hereinafter called 3 and 6, during several tracks (18.6 hrs for setup 3 in June, September, and October 2016 and 6.8 hrs for setup 6 in March 2018).

Setup 3 was observed with the WideX correlator at 95.5-99.5 GHz and with $\sim$2 MHz ($\sim$6 km s^{-1}) spectral resolution, plus four narrow spectral windows with $\sim$0.16 MHz ($\sim$0.5 km s^{-1}) spectral resolution. Setup 6 was observed using the PolyFiX correlator[3] at 80.4-88.1 GHz (lower sideband, LSB) and 95.9-103.6 GHz (upper sideband, USB) with $\sim$2 MHz ($\sim$6 km s^{-1}) spectral resolution, plus 64 narrow spectral windows with $\sim$0.06 MHz ($\sim$0.2 km s^{-1}) spectral resolution.

The NOEMA array was used in configurations DC (baselines 15-304 m) and AC (64-704 m) for setup 3 and 6, respectively. The phase center was on IRAS 4A1, at coordinates α(J2000) = $03^h29^m10\overset{s}{.}5$, δ(J2000) = $+31^\circ\ 13'\ 30\overset{''}{.}9$.

The bandpass was calibrated on 3C454.3 and 3C84, the absolute flux was fixed by observing MWC349, LKHA101, and the gains in phase and amplitude were set on 0333+321. The final

---

[1] https://solis.osug.fr/

[2] https://www.iram-institute.org/EN/noema-project.php

[3] https://www.iram.fr/IRAMFR/GILDAS/doc/html/noema-intro-html/node6.html

Table 6.1: Spectroscopic parameters and line Gaussian-fit results of CH_3OH and SiO lines observed toward the selected positions (1a, 1b and 2) on the IRAS 4A fingers shown in Fig. 6.2).

	Spectroscopic parameters					Gaussian-fit results				
Setup$^{(a)}$	Transition	Frequency$^{(b)}$ [GHz]	$E_{up}^{(b)}$ [K]	$\log A_{ul}^{(b)}$ [s^{-1}]	Finger^{c} position	Integrated Area [K km s^{-1}]	v_{peak} [km s^{-1}]	FWHM [km s^{-1}]	T_{peak} [K]	rms [mK]
					CH_3OH					
6-HR	$5_{1,5}-4_{0,4}$ E	84.5212	40	-5.7	1a	25.6(0.3)	6.50(0.01)	1.37(0.02)	17.6	300
					1b	35.3(0.2)	6.30(0.01)	1.40(0.01)	23.7	300
					2a	-	-	-	$\leq$0.9^{d}	300
3-HR	$2_{-1,2}-1_{-1,1}$ E	96.7394	13	-5.6	1a	4.8(0.1)	6.40(0.02)	1.60(0.03)	2.8	60
					1b	8.0(0.1)	6.30(0.01)	1.60(0.02)	4.7	60
					2a	-	-	-	$\leq$0.2^{d}	60
3-HR	$2_{0,2}-1_{0,1}$ A	96.7414	7	-5.5	1a	4.8(0.1)	6.20(0.02)	1.46(0.03)	3.1	60
					1b	8.8(0.1)	6.10(0.01)	1.60(0.02)	5.2	60
					2a	-	-	-	$\leq$0.2^{d}	60
3-HR	$2_{0,2}-1_{0,1}$ E	96.7445	21	-5.5	1a	3.5(0.1)	6.10(0.02)	1.66(0.05)	1.9	60
					1b	4.6(0.1)	6.00(0.03)	1.70(0.02)	2.6	60
					2a	-	-	-	$\leq$0.2^{d}	60
3-HR	$2_{1,1}-1_{1,0}$ E	96.7555	28	-5.6	1a	1.9(0.1)	6.40(0.03)	1.55(0.08)	1.2	60
					1b	1.8(0.1)	6.20(0.03)	1.6(0.1)	1.1	60
					2a	-	-	-	$\leq$0.2^{d}	60
					SiO					
6-LR	2-1	86.8469	6	-4.5	1a	5.6(0.4)	7.3(0.5)	6.9(0.3)	0.8	40
					1b	5.7(0.4)	8.6(0.4)	6.9(0.2)	0.8	40
					2a	6.4(0.3)	8.3(0.5)	6.9(0.8)	0.9	40

[a] HR: High resolution ($\Delta v\sim$0.5 and 0.2 km s^{-1} for setup 3 and 6, respectively); LR: Low resolution ($\Delta v\sim$6 km s^{-1} in both setups).

[b] Frequencies and spectroscopic parameters are taken from Xu et al. (2008) and Müller et al. (2013) and retrieved from the CDMS (Cologne Database for Molecular Spectroscopy: Müller et al. 2005) database. Upper level energies E_{up} refer to the ground state of each symmetry. $\log A_{ul}$ are the logarithmic spontaneous emission coefficients.

[c] Selected position on the IRAS 4A fingers (see text and Fig. 6.2).

[d] 3σ limit for non-detection.

uncertainty on the absolute flux scale is $\leq$ 15%. The phase rms was $\leq 50^\circ$ and $\sim$ 10-20° and the typical precipitable water vapor (pwv) was 4-15 mm and 1-30 mm for setup 3 and 6, respectively. The system temperature was 50-200 K for both setups.

The data were reduced using the GILDAS[4] software collection. The continuum map was obtained by averaging line-free channels and self-calibrating the data. The self-calibration solutions were then applied to the spectral cubes, which were subsequently cleaned using natural weighting. The resulting synthesised beams are $2\farcs2\times1\farcs9$ (P.A.=96°) and $2\farcs05\times1\farcs12$ (P.A.=11°) and the half power primary beams are $59\farcs2$ and $61\farcs2$ for setups 3 and 6, respectively.

6.1.3 Results

We detected five CH_3OH and one SiO lines, listed in Table 6.1 with their spectroscopic parameters. Figure 6.1 shows the spatial distribution of the CH_3OH and SiO line emission in two different velocity ranges: around the systemic velocity V_{sys} ($\sim$ 6.7 km s^{-1}) and at High-Velocity (HV), at about $\pm$7 km s^{-1} from the systemic velocity and over a velocity interval of about $\Delta v \sim$ 6 km s^{-1} (see caption for details). Two major components appear in the figure: the two outflows associated with A1 and A2, especially visible in the HV maps, and two filamentary structures at the systemic velocity, which we will refer to as ”fingers” in the following.

Outflows emission

The emission from the IRAS 4A outflows detected by SOLIS in different molecular lines has been presented already and discussed by Taquet et al. (2020) (S-bearing species) and De Simone et al. (2020b) (interstellar Complex Organic Molecules). The Fig. 6.1 methanol emission map is in general agreement with those two studies and, being not the focus of this paper, will not be discussed further.

Fingers emission

The high resolution spectra of the five methanol lines (Fig. 6.1) show that the elongated structures are characterized by narrow lines (FWHM$\sim$1.5 km s^{-1}) centered at the systemic velocity V_{sys} (see below). Their filamentary morphology is better highlighted in Fig. 6.2, where the CH_3OH and SiO narrow-line emission is shown over a larger field of view. Based on Fig. 6.2 and the spectral profile described above, we identified three fingers:
Finger1, traced by CH_3OH and SiO, is the northern one;
Finger2, traced only by SiO, is 10″ south and parallel to Finger1;
Finger3, traced only by SiO, is an additional 10″ south and, again parallel to Finger1.
While Finger2 and Finger3, detected only in SiO (2-1), are perfectly in agreement with the SiO (1-0) VLA observations by Choi (2005), Finger1 was never detected before and it is traced by both CH_3OH and SiO. It is worth emphasizing that the three fingers are each separated by about 10″ ($\sim$ 3000 au) and are parallel to each other.

In order to understand the nature of the three fingers, we selected three positions along Finger1 and Finger2 to carry out a non-LTE analysis to derive the gas temperature and density and the column density of CH_3OH and SiO, respectively (see Section 6.1.4)[5]. The three posi-

---

[4] http://www.iram.fr/IRAMFR/GILDAS

[5] Note that since Finger3 is outside the primary beam we did not carry the analysis there.

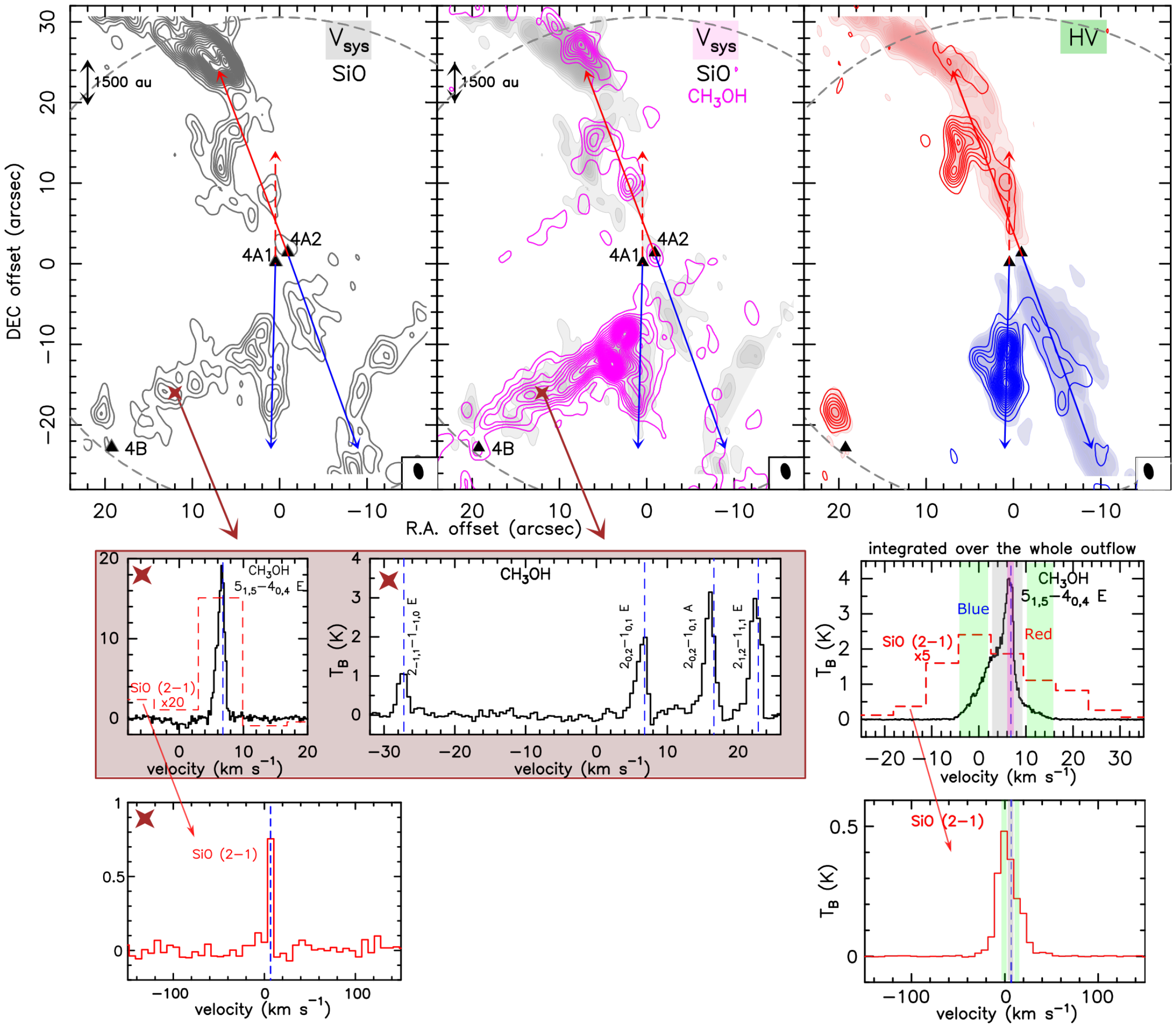

Figure 6.1: *Upper panels:* Velocity-integrated maps of CH$_3$OH $5_{1,5}$-$4_{0,4}$ E (coloured contours) and SiO 2-1 (gray contours and shaded colors) of the NGC 1333 IRAS 4 system. The three protostellar sources in the field are marked by black triangles. Jet directions are indicated by blue and red arrows following Choi (2005) and Santangelo et al. (2015). The primary beam ($\sim 62''$) is shown by the grey dashed circle and the synthesized beam ($\sim 1\farcs5$) is shown in the lower right corner of the panels. Upper left panel: SiO emission at the systemic velocity channel, with first contours and steps of 3σ (σ=1 mJy beam^{-1} km s^{-1}). Upper middle panel: CH$_3$OH Emission integrated from 5.8 to 7.8 km s^{-1} around the systemic velocity, with first contours and steps of 3σ (σ=15 mJy beam^{-1} km s^{-1}). Upper right panel: CH$_3$OH Blue- and red-shifted high velocity (HV) emission integrated from -4 to 2.4 km s^{-1} (blue) and 9.6 to 16 km s^{-1} (red) with first contours and steps of 3σ ($\sigma_{\rm blue}$=35 mJy beam^{-1} km s^{-1} and $\sigma_{\rm red}$=13 mJy beam^{-1} km s^{-1}). *Lower panels:* CH$_3$OH (in black) and SiO (in red) spectra extracted at the Finger1a position with offset ($-12''$, $+16''$) marked by a brown cross (see text). To compare with CH$_3$OH the SiO spectra is overlapped in dashed red magnified by a factor of 20. The map integrated ranges are shown as colored bands on the spectra of SiO (in red) and CH$_3$OH (in black overlapped, for comparison, with SiO in dashed red magnified by a factor of 5) integrated over the whole outflow in the lower right panels.

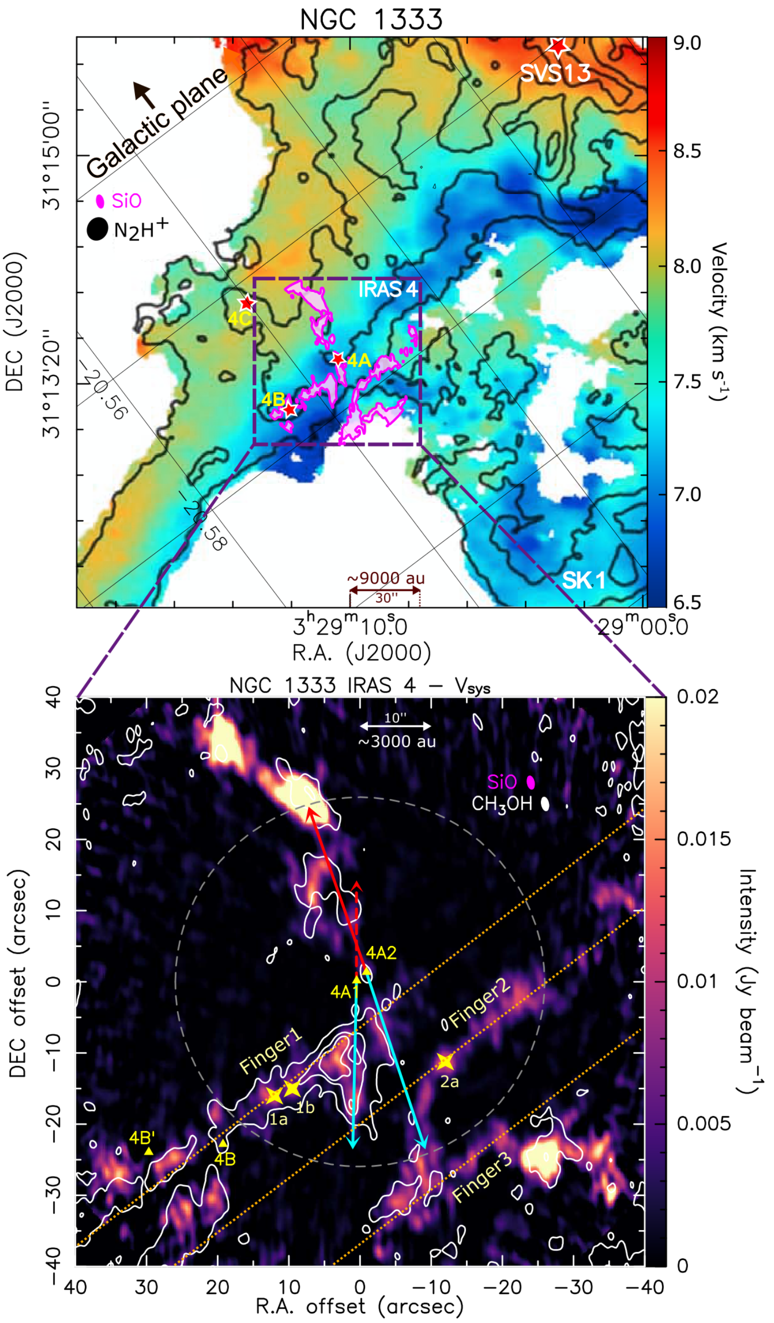

Figure 6.2: Emission of the fingers detected by NOEMA-SOLIS in the CH_3OH and SiO shown at a large scale. *Upper panel*: Overlap of the N_2H^+ (1-0) line-of-sight velocity map of the southern-east part of NGC 1333 from CARMA observations (adapted from Fig. 17 of Dhabal et al. 2019) with the SiO emission from NOEMA-SOLIS observations (this work) shown as 3σ contours. The internal grid is in Galactic coordinates. The red stars mark the position of IRAS 4A, 4B, 4C, and SVS13. The synthesized beams ($\sim 1''.5$ for SiO and $\sim 3''.5$ for N_2H^+) are in the upper left corner. *Bottom panel*: Zoomed-in map of the IRAS 4A system with SiO (colour scale, 3σ= 3 mJy beam^{-1}) and CH_3OH (white contours starting at 3σ with steps of 15σ, σ=30 mJy beam^{-1}) emission integrated in a range of $\sim$6 km s^{-1} around the v_{lsr} ($\sim$ 6.7 km s^{-1}). The yellow triangles indicate the sources 4A1, 4A2, 4B and 4B$'$. The synthesized beams ($\sim 1''.5$) are in the upper right corner, while the primary beam ($\sim 61''$) is a dashed white circle. The yellow crosses mark the fingers positions where we carried out a non-LTE analysis of the methanol lines. Orange lines show the direction of the three fingers (Finger1, traced by CH_3OH and SiO; Finger2 and Finger3 traced by SiO only) and are parallel to the Galactic plane.

Table 6.2: 1σ Confidence Level (range) from the Non-LTE LVG Analysis of the CH_3OH lines toward the three selected positions in the Fingers (marked as yellow crosses in Fig. 6.2).

Species	N(X) [cm^{-2}]	n_{H_2} [cm^{-3}]	T_{gas} [K]	size [arcsec]
	Finger1a -offset (+12″, -16″)			
CH_3OH	(8-30)$\times 10^{15}$	(5-20)$\times 10^5$	80-160	0.6-1.5
SiO	(5-10)$\times 10^{13}$	″	″	″
[CH_3OH]/[SiO]	160-300			
	Finger1b - offset (+9.5″, -15″)			
CH_3OH	(4-12)$\times 10^{15}$	(2-3)$\times 10^5$	130-210	1.5-2.5
SiO	(2-5)$\times 10^{13}$	″	″	″
[CH_3OH]/[SiO]	200-240			
	Finger2a - offset (-12″, -11.2″)			
CH_3OH^a	$\leq 1.6\times 10^{15}$	(5-20)$\times 10^5$ ^{a}	80-210 ^{a}	1-2 ^{a}
SiO	(4-15)$\times 10^{13}$	″	″	″
[CH_3OH]/[SiO]	$\leq$40			

[a] Assumed the same gas condition (n_{H_2} and T_{gas}) of the Finger1.

tions (two -1a and 1b- toward Finger1 and one -2a- toward Finger2), are shown in Fig. 6.2 and their coordinates are reported in Table 6.2. These positions were selected because they show the brightest CH_3OH and SiO emission in the fingers and are outside the outflows emission region in order to minimize the contamination from the latter. Figure 6.1 shows the CH_3OH and SiO spectra extracted from Finger1a, as an example.

In each of the three selected positions, we extracted the spectra of CH_3OH and SiO and derived the velocity-integrated line intensities of each detected transition using a Gaussian fit with the GILDAS-CLASS package. The fit results, namely the integrated emission ($\int T_b dV$), the linewidth (FWHM), the peak velocities (V_{peak}), and the rms computed for each spectral window, are reported in Table 6.1. As mentioned above, the methanol lines observed with the high resolution narrow bands have an average linewidth of about 1.5 km s^{-1}. Unfortunately, for SiO we are limited by the PolyFiX low spectral resolution ($\sim$ 6 km s^{-1}). However, from the VLA observations, Choi (2005) estimated a similar linewidth ($\sim$1.5 km s^{-1}) for the SiO narrow component. It is worth noticing that, while the methanol emission drastically changes from one finger to another, the integrated SiO emission derived at points Finger1a, Finger1b, and Finger2a is almost constant. We will comment the implications of this characteristics in Sect. 6.1.4.

Finally, we searched for the presence of other molecules in the fingers' positions and only found faint emission of HC_3N (11-10), which appears to be associated with Finger1.

6.1.4 Physical and chemical properties of the Fingers

Physical properties

The detection of five CH_3OH transitions allowed us to perform a non-LTE analysis via our in-home Large Velocity Gradient (LVG) code `grelvg` adapted from Ceccarelli et al. (2003).

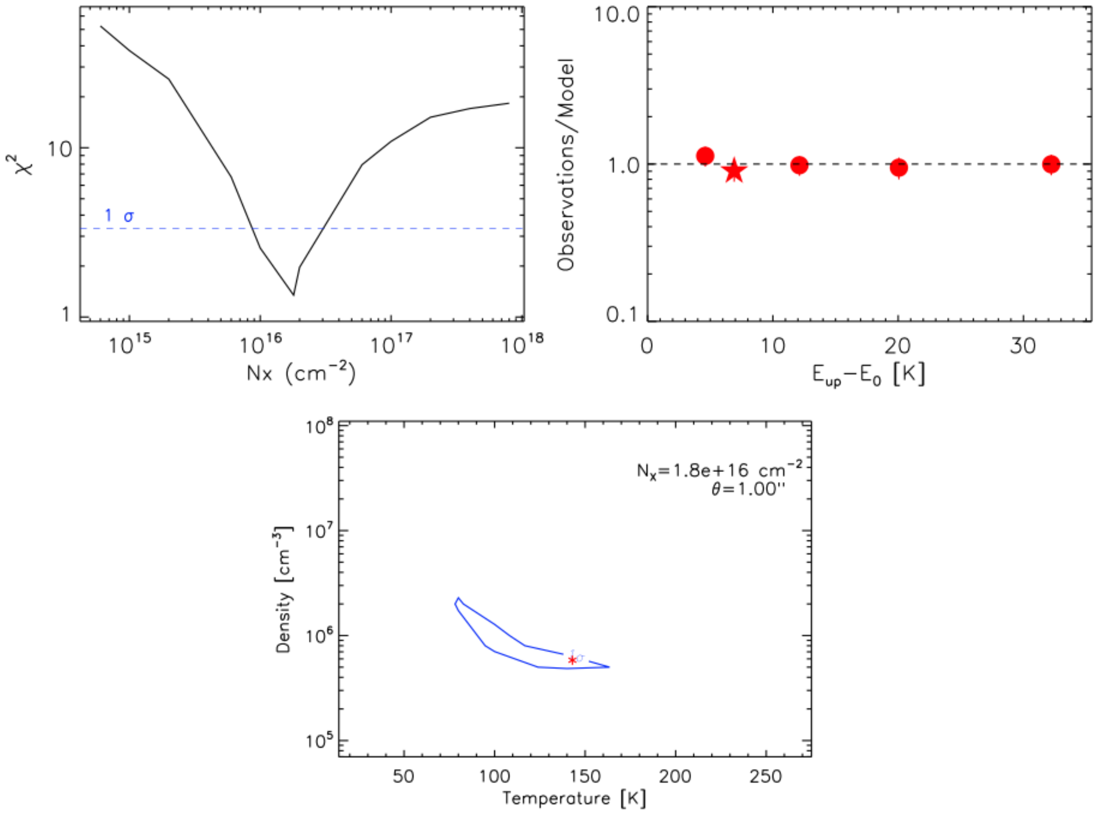

Figure 6.3: Results of the non-LTE analysis of CH_3OH at the Finger1a position using the `grelvg` code. *Top-left*: χ^2-column density N(CH_3OH) plot. The dashed blue line represent the 1σ confidence level. *Top-right*: Ratio between the observed line intensities (circle for E-type and star for A-type) with those predicted by the best fit model as a function of line upper-level energy E_{up}. *Bottom*: Density-Temperature χ^2 contour plot. The contour represents 1σ confidence level, assuming the best fit values of N(CH_3OH) and θ (upper right corner). The best fit solution is marked by the red asterisk.

CH_3OH has two nuclear-spin isomers, A-type (symmetric) and E-type (asymmetric), differentiated by the total spin state of the hydrogen nuclei in the CH_3 group (Rabli & Flower 2010). We used the collisional coefficients of both CH_3OH isomers with para-H_2, computed by Rabli & Flower (2010) between 10 and 200 K for the first 256 levels and provided by the BASECOL database (Dubernet et al. 2013). We assumed the CH_3OH-A/CH_3OH-E ratio equal to 1. A semi-infinite slab geometry was used to compute the line escape probability as a function of the line optical depth.

We ran a large grid of models ($\geq$ 5000) covering a total methanol (A-type plus E-type) column density N(CH_3OH) from 6×10^{14} to 8×10^{17} cm^{-2}, a gas H_2 density n_{H_2} from 3×10^5 to 6×10^6 cm^{-3}, sampled in logarithmic scale, and a gas temperature T from 20 to 200 K. We then simultaneously fitted the measured CH_3OH-A and CH_3OH-E line intensities by comparing them with those predicted by the `grelvg` model, leaving N(CH_3OH), n_{H_2}, T, and the emitting size θ as free parameters. Following the observations, we assumed the linewidth equal to 1.5 km s^{-1} (see Table 6.1), and we included the flux calibration uncertainty (15%) to the observed intensities errors.

The best fit in the Finger1a position is obtained for a total column density N(CH_3OH) = $1.8 \times 10^{16}cm^{-2}$, gas density n_{H_2}=5×10^5 cm^{-3}, gas temperature T=140 K and emitting size of $\sim$ 1$''$ with reduced χ^2_R=1.3 (see Figure 6.3). The values within the 1σ confidence level are reported in Table 6.2. To explore the gas conditions along the Finger1, we repeated the analysis described above in position 1b still finding high gas temperature and density (see Table 6.2). The derived emitting sizes represent the best-fit 2D-Gaussian FWHM[6], and suggest that the fingers may have a clumpy structure, not resolved by our $\sim$600 au spatial resolution.

To derive the SiO column density in the three positions we run `grelvg` for a range of N(SiO) from 5×10^{12} to 1×10^{15} cm^{-2} assuming the same gas temperature, density and emitting size as those found in Finger1a (Table 6.2). We then best fitted the measured SiO line intensities via comparison with those simulated by `grelvg` leaving only N(SiO) as a free parameter. The same procedure was adopted to estimate the upper limit of the CH_3OH column density in Finger2a. The results of the non-LTE analysis carried out toward the three positions are summarised in Table 6.2.

In order to assess the impact of assuming that the gas conditions derived for CH_3OH are also valid for SiO, we estimated the SiO column density by combining our NOEMA observations with the VLA observation by Choi (2005). We performed a LTE analysis using the SiO 2-1 and SiO 1-0 integrated emission in Finger2a deriving a SiO column density of $(30 \pm 7) \times 10^{12}$ cm^{-2}, which is consistent with the SiO column density derived above following our assumption (see Table 6.2). In other words, even if the gas conditions in Finger1 and Finger2 are not exactly the same, the observed abundance ratio of the two species is consistent, within the error bars, with what we computed. Additionally, in order to investigate the non detection of SiO in Finger1 in the maps of Choi (2005), we computed the predicted intensity ratio of the SiO 2-1 (target of our NOEMA observations) with respect to the SiO 1-0 (target of the VLA observations of Choi 2005) using the non-LTE LVG `grelvg` code. We found that the predicted SiO 2-1/1-0 line ratio varies from 6.5 to 13 in the range of gas density and temperature derived

---

[6] In fitting the observations with the LVG theoretical predictions, we considered three possibilities for the filling factor, depending on the shape of the emitting region: i) a 2D circular Gaussian shape, ii) an infinite finger-like shape with a resolved transverse size, and iii) emitting size larger than the synthesised beam. The best fit by far was obtained with the 2D circular Gaussian shape.

in Finger1 with our analysis (Table 6.2). Considering the various uncertainties, in particular on the column density in Finger1 and Finger2 (which are assumed to be the same but can be also a factor $\sim$2 different), there is no contradiction with the fact that there is no SiO detection in Finger1 with the VLA observations by Choi (2005).

Chemical properties

From the computations of the previous subsection, we can estimate the CH_3OH and SiO abundances in Finger1 as follows. In Finger1, assuming that the finger depth is equal to the linear diameter of the methanol emitting region ($\sim 0.6 - 1.5''$ equivalent to $\sim 180 - 450$ au: see Tab. 6.2) and considering the derived gas density range ($\sim 5 - 20 \times 10^5$ cm^{-3}: see Tab. 6.2), we obtained the H_2 column density N(H_2) range equal to $\sim 1.4 - 14 \times 10^{21}$ cm^{-2}. Using the derived CH_3OH column density range ($\sim 8 - 30 \times 10^{15}$ cm^{-2}: Tab. 6.2), we then estimate a methanol abundance [CH_3OH]/[H_2] range of $0.6 - 22 \times 10^{-6}$. Likewise, the SiO abundance [SiO]/[H_2] range is estimated to be $0.4–7.4 \times 10^{-8}$. The SiO abundance is then lower than that measured in the IRAS4A jets, $3–4 \times 10^{-7}$ by Santangelo et al. (2015).

From the derivation of the CH_3OH and SiO column densities in Finger1 and Finger2 of the previous subsection, the [CH_3OH]/[SiO] ratio is 160–300 in Finger1 and $\leq$40 in Finger2 (see Tab. 6.2). There seems to be a difference in the chemical composition of Finger1 and Finger2, at least regarding CH_3OH and SiO, with Finger1 enriched in methanol with respect to Finger2.

6.1.5 Discussion

Summary of the fingers properties

In the previous sections, we have shown that the new SOLIS maps, coupled with older VLA maps, reveal the presence of three filamentary structures, extended more than about 6000 au in the major axis (i.e. $\geq 20''$) and unresolved in the minor one, namely $\leq$450 au (Fig. 6.2 and Tab. 6.2). These structures, which we named "fingers", are approximately aligned in the direction of the galactic plane and to the large scale magnetic field observed by Planck (Collaboration et al. 2020), but approximately perpendicular to the local magnetic field (e.g. Doi et al. 2020, ; see their Fig. 4) and the SE filament where IRAS 4A lies. The three fingers are regularly spaced by about $\sim$ 3000 au (i.e. $\sim 10''$). Finally, they are almost perpendicular (certainly not parallel) to the outflows emanating from IRAS 4A1 and 4A2, even though they seem connected with them in some way: Finger1 starts midway at the edge of the south lobe of the 4A1 outflow and extends east of it, Finger2 starts midway at the edge of the south lobe of the 4A2 outflow and extends west of it, and Finger3 starts at the visible south end of the 4A2 outflow and extends west of it.

Using the detected multiple methanol lines, we carried out a non-LTE analysis that provided stringent constraints to the temperature and density of the gas in Finger1 (Section 6.1.4; Tab. 6.2). The derived temperature, 80–160 K, is definitively larger than that in the surrounding envelope gas, estimated to be smaller than $\sim$12 K (Jørgensen et al. 2002; Maret et al. 2005). In other words, Finger1 is too far away from the IRAS 4A for its gas to be heated by the protostar radiation, so that a non-thermal process must be responsible for the observed large temperature.

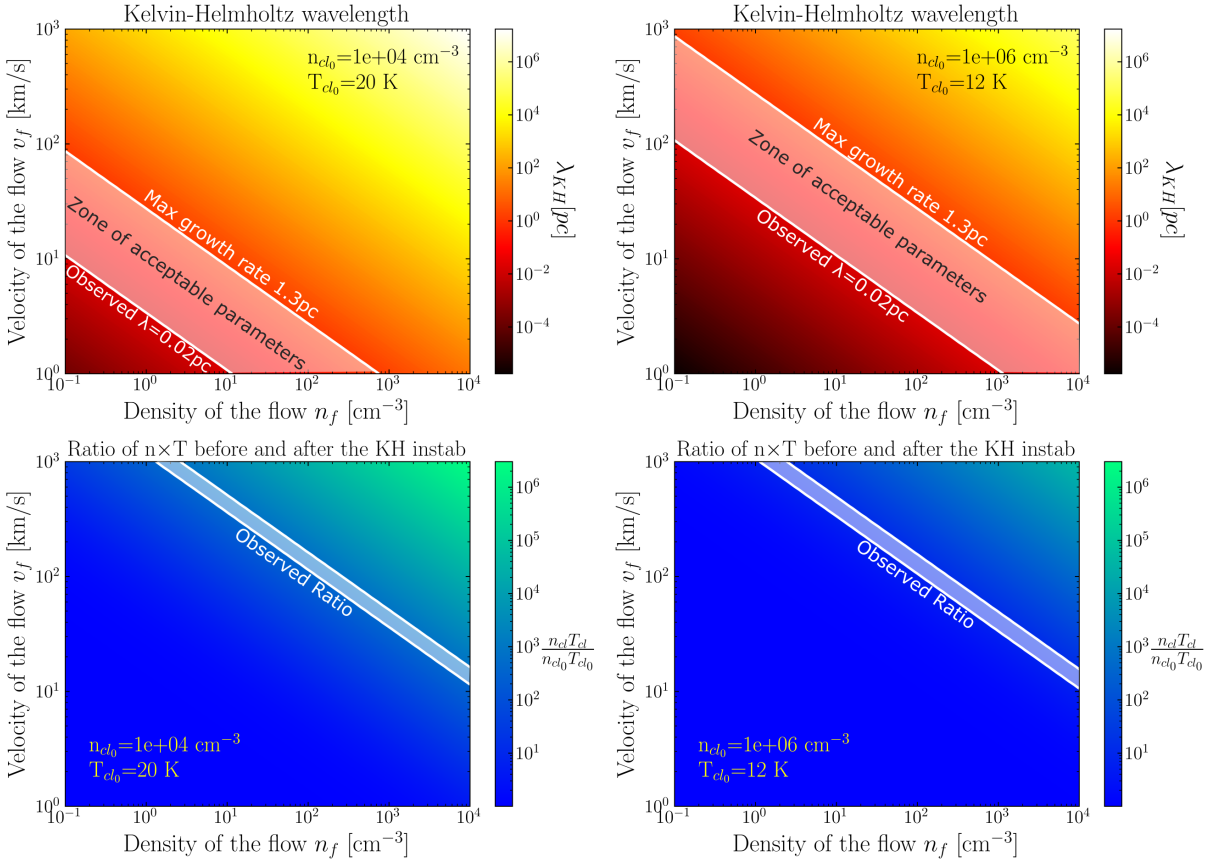

Figure 6.4: *Top:* Evolution of the Kelvin-Helmholtz wavelength for the observed molecular cloud as a function of density (n_f) and velocity of the flowing gas (v_f). The white continuous lines represent the observational constraints that set the zone (shadowed white) of physically acceptable values for n_f and v_f that allow a Kelvin-Helmholtz instability to exist. The condition assumed for the cloud before the interaction are reported in the upper right corner. *Bottom:* Ratio of the density Temperature product before and after the KH instability as a function of density (n_f) and velocity of the flowing gas (v_f). The shadowed white zone represents the observed ratio. The conditions assumed for the cloud before the interaction are given in the lower left corner.

In the same vein, the measured SiO enhanced abundance $4-7.4\times10^{-8}$ (Section 6.1.4) points to a non-thermal process capable of extracting silicon from the grains (see Introduction and Section 6.1.5). Likewise, methanol in Finger1, with an abundance of $0.6 - 22 \times 10^{-6}$, suggests a similar non-thermal process capable to extract it from the grain mantles.

There are not many possible non-thermal processes capable to create the observed linear and almost periodic structures with enhanced gas temperature and capable to increase the SiO and methanol abundances. To our best knowledge, only two processes could a priori reproduce the observed properties of the fingers in NGC 1333 IRAS 4A: hydro-dynamical Kelvin-Helmholtz instabilities and shocks. In the following, we will discuss in detail these two possibilities.

Do the IRAS 4A fingers trace Kelvin-Helmholtz instabilities?

Hydro-dynamical instabilities (HDI) are known to play a major role in shaping the morphology of the ISM, in particular in modifying the superficial structure of molecular clouds via Rayleigh-Taylor, Kelvin-Helmholtz, and self-gravity instabilities. All these processes can generate long and narrow streams of material (Hunter et al. 1997; Coughlin & Nixon 2020). Among them, the Kelvin-Helmholtz instability (KHI) occurs at the interface of two fluids of different densities in relative shear motion and it is characterized by a wavelike periodic structure. Such instabilities have been invoked to explain the periodic filamentary structures observed in Orion (Berné et al. 2010; Berné & Matsumoto 2012) and Taurus (Heyer et al. 2016). Following the approach by Berné et al. (2010), we explored if the development of a KHI is possible and in what conditions, and if it can reproduce the gas properties of the IRAS 4A fingers, assuming that the insulating layer (i.e., the interface between the two fluids) is infinitely thin.

Method: First, the spatial wavelength $\lambda_{\rm KH}$ of the KHI is connected to the physical conditions in which the instability occurs. Specifically, the value of $\lambda_{\rm KH}$ depends on the acceleration due to self-gravity $g_{\rm cl}$ and density $n_{\rm cl}$ of the first cloud, and the relative velocity $v_{\rm f}$ and density $n_{\rm f}$ of the second cloud, which we will call “flowing cloud”, as follows:

$$\lambda_{\rm KH} = \frac{2\pi}{g_{\rm cl}} v_{\rm f}^2 \frac{n_{\rm f}}{n_{\rm cl}} \tag{6.1}$$

where we used $g_{\rm cl}=\pi\ G\mu\ m_{\rm H}\ N_{\rm H}$ and which gives 1×10^{-11}m s^{-2} assuming $N_{\rm H}$ equal to 1.2×10^{21} cm^{-2} (from our analysis, see Section 6.1.4). On the other hand, the growth rate $\omega_{\rm KH}$ for a Kelvin Helmholtz instability depends on the velocity $v_{\rm f}$ and density $n_{\rm f}$ of the flowing cloud as follows:

$$\omega_{\rm KH}^2 = \frac{k^2 v_{\rm f}^2 n_{\rm f} n_{\rm cl}}{(n_{\rm f} + n_{\rm cl})^2} \tag{6.2}$$

where k is the spatial wavenumber. If the KHI is responsible for the IRAS 4A fingers, their spatial separation sets a lower limit to $\lambda_{\rm KH}$ equal to $\sim$0.02 pc at the distance of NGC 1333 (and assuming a face-on orientation). Likewise, the widths of the lines that trace the fingers set an upper limit to $\omega_{\rm KH}$ of about 8×10^5 yr^{-1}.

Second, we estimated how the temperature and density of the cloud would change in the region of KHI growth. As the first assumption, we considered the two interacting fluids in hydrostatic equilibrium so that the pressure of the flow and the cloud before the interaction is the same ($P_{\rm f_0}=P_{\rm cl_0}$). This is a standard assumption since the fluids previously were not mixed.

When the instability starts to grow, the thermal pressure and the ram pressure of the flow interact with the instability so that it holds:

$$P_{cl} = P_{cl_0} + \mu m_H n_f (v_f \cos\theta)^2 \tag{6.3}$$

where θ is the angle between the flow and the instability. Assuming that the vertical amplitude is unlikely to be larger than λ, the angle between the instability interface and the flow is at most θ=45°, and considering the ideal equation of state (P=nk_BT, where k_B is the Boltzmann's constant) we can rewrite Eq. 6.3 to link the density and temperature before (n_{cl_0} and T_{cl_0}) and after (n_{cl} and T_{cl}) the KHI emergence, respectively, as follows:

$$\frac{n_{cl}T_{cl}}{n_{cl_0}T_{cl_0}} = \frac{m_H n_f v_f^2}{2n_{cl_0}k_B T_{cl_0}} + 1 \tag{6.4}$$

We considered two cases: i) the interaction occurs in the cloud, where the gas density is 10^4 cm^{-3} and the temperature is 20 K (i.e. the same assumptions of Berné et al. 2010); ii) the interaction takes place inside the IRAS 4A envelope, at $\geq$3000 au from the center (where the first finger is located in the 2D projection), where the gas temperature and density are estimated to be $\leq$ 12 K and $\leq 10^6$ cm^{-3} (Jørgensen et al. 2002; Maret et al. 2005).

Results: Figure 6.4 shows the results of our calculations. Specifically, it displays the evolution of the KHI wavelength (Eq. 6.1) and the density-temperature ratio before and after the KHI (Eq. 6.4), using a grid of possible values for the velocity and density of the flowing cloud (v_f from 1 to 10^3 km s^{-1}and n_f from 0.1 to 10^4 cm^{-3}), and for the two cases described above (KHI occurring in the cloud or IRAS 4A envelope). Whatever are the conditions of the flowing gas, Fig. 6.4 demonstrates that KHI can not explain at the same time the observed fingers separation and the observed local increase of density and temperature in the cloud.

Finally, in addition to the difficulty to reproduce the observed fingers separation and enhanced gas density and temperature, KHI can not explain the presence of CH_3OH and SiO in the gas. Since no sputtering or shattering are expected to play a major role in KHI, the only way for them to release CH_3OH and SiO from the grains is via thermal evaporation of their volatile mantles. However, although the gas cools down slowly via line emission, the dust would cool down very rapidly and probably would never reach the temperature necessary for the grain mantle to sublimate.

In summary, KHI does not seem able to explain the observed properties of the IRAS 4A fingers.

Do the IRAS 4A fingers trace a train of shocks?

Shocks are omnipresent in the ISM, at various scales and in various objects, playing a major role in its thermal and physical structure. In particular, for decades young forming stars have been known to have energetic ejections of material which causes shocks when they encounter the quiescent surrounding matter (e.g., Lada 1985). In these shocks, the gas and density temperature, as well as both SiO and methanol abundances are enhanced (e.g., Bachiller et al. 1998b, 2001; Arce et al. 2008; Codella et al. 2012; Lefloch et al. 2017; Codella et al. 2020a). The quantitative details depend on the type of shock, jump (J) or continuous (C) when it is in presence of a magnetic field, the pre-shocked gas properties and velocity of the shock (e.g., Hollenbach & McKee 1979; Draine & McKee 1993). In the following, we discuss whether the observed properties of the fingers can be accounted for by shocks.

The shock hypothesis: The analysis of the relative abundances of CH_3OH and SiO shows a clear difference in the chemical composition of Finger1 and Finger2, with Finger1 enriched in methanol with respect to Finger2 by more than a factor four. As mentioned in the Introduction, methanol can not be produced by gas-phase reactions in the measured quantity (Geppert et al. 2006), while it is easily formed on the grain mantle surfaces by the hydrogenation of frozen CO (e.g., Tielens & Hagen 1982; Watanabe & Kouchi 2002; Rimola et al. 2014) during the prestellar cold phase (e.g., Caselli & Ceccarelli 2012). Therefore, the gaseous methanol observed in Finger1 must have been extracted from the grain mantles and injected into the gas phase. A similar argument applies to the observed gaseous SiO. The abundance of Si is extremely low in molecular clouds ($\leq 10^{-12}$; Ziurys et al. 1989; Requena-Torres et al. 2007) because it is trapped in the refractory and, to a lesser extent, in the volatile components of interstellar grains (Jenkins 2009), but it becomes very abundant in the gas where it is extracted from the grains, such as in shocks. In summary, the gaseous SiO and CH_3OH observed toward the three fingers must originate by their injection from the interstellar grains. This implies two possible explanations of the observed different $[CH_3OH]/[SiO]$ abundance ratio: either (1) the two species are injected from the grains with a different abundance ratio in the different fingers or (2) they are injected from the grains with the same abundance ratio but the latter changes in time because of chemical processes occurring in the gas phase. In the following, we investigate whether the relative and absolute abundances can be reproduced by "reasonable" shocks, where the reasonable meaning will become clear at the end of this discussion.

Chemical modelling of CH_3OH/SiO ratio - constraining timescale: To quantify the SiO and methanol abundance evolution after their injection into the gas phase and whether it could explain the measured $[CH_3OH]/[SiO]$ ratio, we ran an astrochemical model and compared the predictions with the observations in the three fingers. To this end, we used the time-dependent gas-phase code MyNahoon, which is a modified version of the publicly available code Nahoon[7] (Wakelam et al. 2012), in which we added the accretion of gaseous species into the grain mantles (but no chemistry is computed on the grain surfaces). To describe the injection of SiO and CH_3OH in the gas-phase, we adopted a two-step procedure, as follows (see also Codella et al. 2017, 2020a; De Simone et al. 2020b).

Step 1: We first compute the chemical composition of the gas during the phase preceding the ejection phenomenon. For this, we assumed the steady-state composition of a molecular cloud at 10 K with a H_2 density of 2×10^4 cm^{-3}, cosmic ray ionization rate of 3×10^{-17} s^{-1}, visual extinction of 20 mag, and initial elemental abundances as those adopted by Agúndez & Wakelam (2013, their Table 3).

Step 2: We increase the gas temperature, density, and gaseous abundance of the major components of the grain mantle to simulate their injection into the gas-phase due to the passage of the shock, while the other species abundance results from Step 1. The gas temperature and H_2 density are those found by the non-LTE LVG modeling in the Finger1a (Table 6.2). The abundances of the species injected into the gas phase are assumed to be those measured by IR observations of the interstellar dust ices in similar regions (Boogert et al. 2015): 2×10^{-4} for

---

[7] http://kida.astrophy.u-bordeaux.fr/codes.html

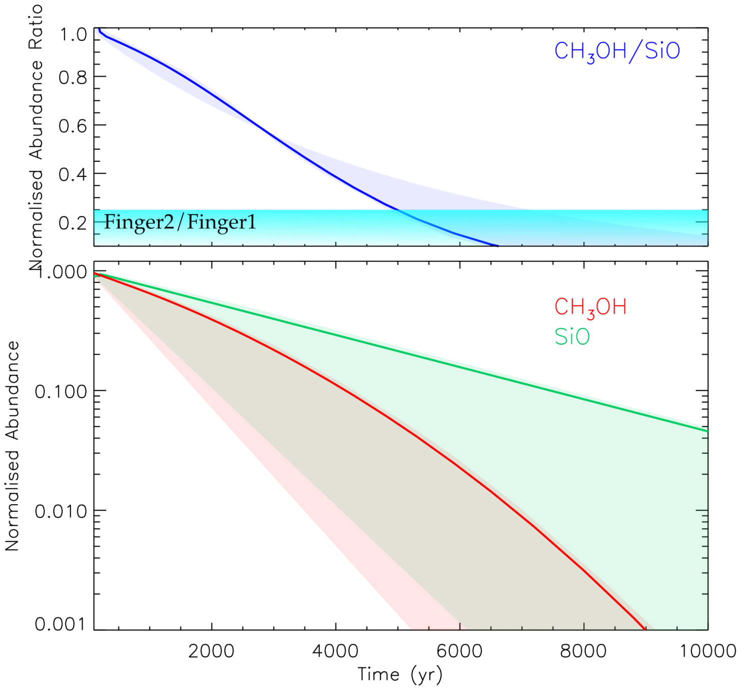

Figure 6.5: Predicted chemical evolution of methanol (red lines) and SiO (green lines) once injected into the gas phase by the passage of a shock. The solid lines show the predictions using the non-LTE best fit (Section 6.1.4), namely ~ 140 K and $\sim 5 \times 10^5$ cm^{-3}. The shadowed area represents the range of predictions obtained using the limits on the gas density and temperature derived by the non-LTE analysis and listed in Table 6.2. *Bottom panel:* Abundances normalized to 1 as a function of time. *Top panel:* Normalised [CH_3OH]/[SiO] abundance ratio as a function of time. The horizontal band represents the range of normalized abundance ratio observed in Finger2 with respect to that observed in Finger1.

H_2O; 3×10^{-5} for CO_2, CO and CH_4; 2×10^{-5} for CH_3OH and NH_3, where the abundances are with respect to the H-nuclei. The SiO abundance is assumed to be 200 times smaller than CH_3OH, namely 1×10^{-7}.

Results: The evolution of the SiO and CH_3OH abundances and their ratio are shown in Fig. 6.5. Using the best fit of the non-LTE analysis (Section 6.1.4 and Tab. 6.2), namely $\sim$ 140 K and $\sim 5 \times 10^5$ cm^{-3}, once methanol is ejected into the gas phase, its abundance decreases by a factor of 10 after more than 4000 yr mainly due to the reaction with OH (Shannon et al. 2013), while SiO remains in the gas phase longer (decreasing by a factor of 10 in abundance around 7000 yr because of the freeze-out into the grains). This basic result holds also for relatively different abundances of SiO and CH_3OH, with a ten times abundance decrease of methanol in 2000 yr or more and of SiO in 3000 yr or more. More important in the context of understanding what happened, for their normalized ratio being as that observed in Finger1 and Finger2 the difference in age of the two shocks should be larger than about 5000 yr (Fig. 6.5, top panel). In other words, if the same relative quantity of CH_3OH and SiO has been injected into the gas phase by the passage of two shocks, at Finger1 and Finger2 respectively, the shock in Finger1 is younger more than 5000 yr than that in Finger2. However, if the relative initial abundance ratio is different by a factor two, then the the time between two shocks can be different, namely 2000 yr if Finger2 has an initial abundance ratio higher than Finger1 and 10^4 yr in the opposite case.

Shock modelling of the SiO injection - constraining shock velocity: Since more than two decades models have predicted that the SiO abundance is highly enhanced in high velocity ($\geq$ 25 km/s) shocks, where the grains are shattered and silicon is liberated into the gas-phase where it undergoes reactions leading to the SiO formation (e.g. Draine & McKee 1993; Flower & Pineau des Forets 1994; Caselli et al. 1997; Schilke et al. 1997). In lower velocity shocks, Si or SiO previously frozen into the grain mantles are predicted to be injected into the gas-phase by the sputtering of the mantles because of the ions-neutral drift velocity (Gusdorf et al. 2008b; Lesaffre et al. 2013; Nguyen-Luong et al. 2013). Relevant for the case of the Fingers, the above models predict that shocks with velocities lower than about 10 km s^{-1} are not enough to liberate Si or SiO from the frozen mantles (see, e.g. Nguyen-Luong et al. 2013).

Nonetheless, it is worth emphasizing that these conclusions critically depend on the assumed frozen-SiO sputtering threshold energy, a parameter which is poorly constrained and which enters as an exponential factor in the equations (e.g. Barlow 1978; Flower & Pineau des Forets 1994). For example, Nguyen-Luong et al. (2013) used the **Paris-Durham shock code**[8] where the SiO sputtering threshold energy is 1900 K (in the original version of the code it was instead assumed to be 2500 K: Barlow 1978; Flower & Pineau des Forets 1994). We ran the Paris-Durham shock code to simulate the conditions found in the Fingers, described above. If the SiO sputtering threshold energy is 1200 K instead of 1900 K, SiO is predicted to be injected from the mantles into the gas-phase already at 7 km s^{-1} with a predicted SiO column density consistent with what we observe in the Fingers.

However, it is important to emphasize that the above constraints have to be taken with a grain of salt and not at face value. Therefore, giving the large uncertainty linked to the SiO sputtering threshold, which enters in an exponential term in the equations, one may speculate that shocks with velocities larger than about 7 km s^{-1} can reproduce the observations.

---

[8] The Paris-Durham shock code is publicly available at https://ism.obspm.fr/shock.html

Shock velocity and inclination angle: Using the time between Finger 1 and 2 shock passage derived using the chemical modelling, we can provide constraints to the shock velocity. The two quantities are linked by the following equation:

$$v_{shock} = \frac{s_{\perp}}{\sin\theta}\frac{1}{time} \tag{6.5}$$

where $s_{\perp}$ is the projected separation among the fingers and it is about 3000 au and θ is the angle of the shock propagation with respect to the line of sight.

The lower limit to the shock velocity so to be able to release enough SiO into the gas-phase, provided in the previous paragraph, provides an upper limit to the inclination angle, which depends on the shock passage time. Taking $v_{shock} \geq 10$ km s^{-1} gives $\theta \leq$15, 25 and 45 degrees for 10^4, 5000 and 2000 yr, respectively. In the case of lower SiO sputtering threshold, $v_{shock} \geq 7$ km s^{-1} corresponds to $\theta \leq$15, 25 and 90 degrees for 10^4, 5000 and 2000 yr, respectively. Note that,if the time is 2000 yr, no solutions exist for v_{shock} lower then 7 km s^{-1}, for any θ.

IRAS 4A fingers: the signature of the clash of an expanding bubble

As briefly mentioned in the Introduction, at a large scale, the NGC 1333 region is constituted by several filaments, of which the southeast one (SE) runs parallel to our Fingers (Dhabal et al. 2019). This SE filament is characterized by two substructures running parallel to each other with two distinct systemic velocities, +7.5 km s^{-1} and +8.2 km s^{-1}, respectively, with the western one blue-shifted with respect to the eastern (Dhabal et al. 2018). The gas in the arch-like structure west of the SE filament has approximately the same velocity as the western substructure of the SE filament, namely +6.5 km s^{-1}. This arch-like structure traces the borders of a large cavity (see Fig. 6.2), to the north and west of which lie the protostellar systems of IRAS2, SVS13, and IRAS4 and to the south the SK1 system. Dhabal et al. (2019) suggested that this region represents the gas compressed by a “turbulent cell” moving from the south and clashing against the NGC 1333 cloud. Always according to Dhabal et al. (2019), this clash could have formed the SE filament and triggered the formation of the IRAS2, SVS13, and IRAS4 protostars.

The new detection of the train of shocks in the IRAS 4A region allows us to put some constraints to this hypothesis.

First, the presence of a train of three shocks in IRAS 4A suggests that the turbulent cell is the result of an expanding bubble, which caused three different shock events, as schematically shown in Fig. 6.6. If the proposed bubble, coming from the southeast and moving toward the IRAS 4A main cloud from behind, continuously expands, it can create a series of shocks as the ones described in Section 6.1.5.

Following the discussion done in Section 6.1.5 to explain the observed SiO column density we propose that the expanding velocity of the bubble has to be at least 7 km s^{-1}.

Incidentally, this would not be the first case reported in the literature of a train of shocks caused by the clashing of an expanding bubble into a quiescent dense molecular cloud. It has been observed, for example, in at least two other cases, both associated with supernova remnants (SNR). Dumas et al. (2014) detected two parallel filamentary structures in SiO toward a cloud next to the SNR W51C and attributed them to the passage of the SNR primary shock. Similarly, Cosentino et al. (2019) reported the presence of two parallel shocks, probed by SiO, toward SNR W44, caused by the interaction of the expanding SNR bubble into the infrared dark cloud G034.77-00.55.

On the contrary, the origin of the expanding bubble clashing toward NGC 1333 is not obvious. As Dhabal et al. (2019) already pointed out, there are no known nearby ionizing stars, SNRs, or HII regions that could be responsible for it. Using CO isotopologues, Arce et al. (2011) presented a complete mapping of shells and bubbles in the Perseus molecular cloud. Among them, southeast of IRAS 4A, there is the so-called CPS 2 shell with $\sim 6'$ of radius and whose origin is unknown. However, CPS2 is located $24'$ away from the IRAS 4A fingers, so it does not seem to be a good candidate. On the other hand, our Galaxy is populated with very large (tens of degrees) loops, arcs, spurs, and filaments visible at different wavelengths (e.g., X-rays, microwaves, synchrotron emission). The most famous are the so-called Loop I, II, III, and IV, probably old ($\sim 10^5$ – 10^6 yr) nearby supernova (SN) remnants (Berkhuijsen et al. 1971; Vidal et al. 2015; Dickinson 2018). The NGC 1333 molecular complex lies at the edge of Loop II (called also Cetus arc; Large et al. 1962), an expanding bubble of $\sim 90^\circ$ of diameter and centered at galactic longitude -100° and latitude 30°. Hence, Loop II could be a possible candidate for the proposed expanding bubble.

Traces of other clashes in NGC 1333

Previous single-dish observations have shown the presence of extended SiO emission, with a narrow (FWHM<1.5 km s^{-1}) line profile at ambient velocity, in the region encompassing SVS13 and IRAS 4A (Lefloch et al. 1998b; Codella et al. 1999). The origin of this emission was debated but no clear consensus was reached. For example, the hypothesis of fossil shocks connected with the outflows from the protostars was evoked, although no definite answer was found. The three fingers discovered by SOLIS can help to elucidate the origin of this large-scale SiO narrow emission.

Figure 6.7 shows the overlap of the line-of-sight N_2H^+ line-of-sight velocity map by Dhabal et al. (2019) of the southern NGC 1333 filaments with the large-scale SiO narrow emission by Lefloch et al. (1998b) and the three fingers discovered by SOLIS in the present work. The large-scale SiO narrow emission extends from southeast of SVS13A to southwest of IRAS 4A, and it seems to be composed of two parts, or lobes, that have different orientations. In the northern lobe, the SiO emission is elongated in the direction northeast-west while, in the southern lobe, the emission runs in the direction northwest-southeast. The SOLIS fingers lie at the northern limit of the southern lobe and they are pretty much parallel to the observed large-scale SiO emission. As discussed in Sect. 6.1.5, we propose that the SOLIS fingers are due to shocks caused by the interaction of an expanding bubble coming from southeast behind the NGC 1333 SE filament, where IRAS 4A lies. It is tempting to hypothesize that the southern lobe of the SiO emission observed by Lefloch et al. (1998b) is an ensemble of small-scale shocks, like the ones traced by the SOLIS fingers, caused by older bubble expansion events. Our prediction, therefore, is that the SiO emission of the southern lobe will break up in multiple parallel small-scale shocks if observed with interferometers like NOEMA. If this is true, the frequency and chemical composition of these hypothetical shocks may add stringent constraints on the phenomenon and expansion velocity of the bubble clashing against NGC 1333 from the southeast.

A similar possibility could apply to the northern SiO lobe: it could be an ensemble of

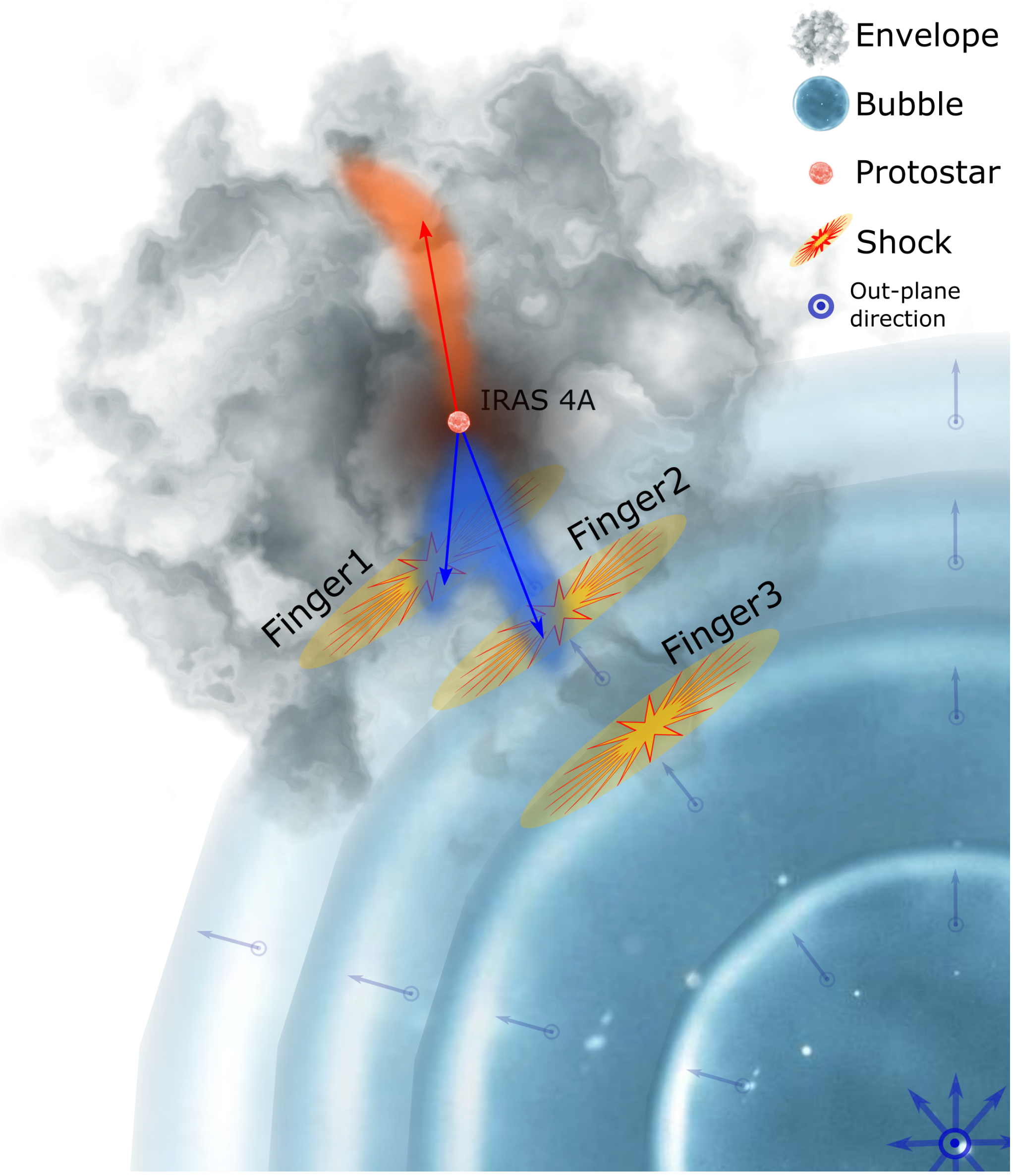

Figure 6.6: Cartoon model of the IRAS 4A region, illustrating the outflowing system inside the envelope and the proposed expanding bubble. The size of the bubble increases with time, and each circle in the figure represents the bubble at subsequent times: the largest circle represents the last expansion that caused the shock at the origin of Finger1. In the cartoon, the bubble is farther from us in the line of sight than the IRAS 4A main cloud and it is moving toward it. The three orange regions represent the collision zones, in which the observed three fingers are formed.

multiple parallel small-scale shocks unresolved by the single-dish observations of Lefloch et al. (1998b) and Codella et al. (1999). However, in this case, since the SiO emission orientation is almost perpendicular to that of the southern lobe, the shocks would be caused by another bubble clashing from the northwest and expanding toward the region encompassing SVS13-A from the front (being that region red-shifted in the N_2H^+ velocity map). We searched for SiO and methanol fingers around SVS13-A using the SOLIS observations toward this source, but we could not find any. Interestingly, however, the region encompassed by the SOLIS observations, in this case, lies in an area where Lefloch et al. (1998b) and Codella et al. (1999) did not detect the SiO narrow emission, slightly north to where it appears.

Finally, the comparison of the large-scale SiO narrow emission map and the local magnetic field (Figure 4 and 6 in Doi et al. 2020) presents an intriguing feature. The change in orientation observed in the two SiO lobes seems to be correlated with a change in the orientation of the magnetic field. Specifically, in both cases, the magnetic field is almost parallel to the direction of the shocks (and almost perpendicular to the fingers/filamentary emission).

6.1.6 Conclusions

We report new IRAM-NOEMA high spatial resolution ($\sim 1\farcs5$, $\sim$ 450 au) observations in the direction of NGC 1333 IRAS 4A, obtained in the context of the Large Program SOLIS.

The observations reveal the presence of three elongated filamentary structures traced by SiO and CH_3OH $\sim 10''$ ($\sim$3000 au) south from the protostar center. They are characterized by narrow (FWHM$\sim$1.5 km s^{-1}) lines peaked at the systemic velocity of the cloud. These structures, which we called fingers, are parallel to each other, extended for more than about 6000 au, approximately equispaced by about 3000 au, and almost perpendicular to the two outflows arising from IRAS 4A and the SE filament where IRAS 4A lies.

The non-LTE analysis of the methanol lines in the northern finger indicates that the gas has a high density (5–20 $\times 10^5$ cm^{-3}) and large temperature (80–160 K), much larger than that expected if the gas was heated by the central protostar. The three detected fingers are chemically different, with the northern one traced by both SiO and CH_3OH and the southern two only by SiO. The CH_3OH over SiO abundance ratio is 160–300 in the northern finger, while it is $\leq$ 40 in the southern one. Both the measured large temperature and enhanced SiO and CH_3OH abundances point to a non-thermal process responsible for them.

Given their quasi-periodicity and morphology, we considered the possibility that the fingers trace a Kelvin-Helmholtz instability occurring at the interface of the NGC 1333 IRAS4 region and a less dense cloud sliding from south to north. However, this hypothesis can not reproduce the observed properties of the fingers.

We then considered the possibility that the three fingers represent a train of three shocks. This hypothesis agrees with the observed physical and chemical properties of the fingers, and provides constraints on when the shocks occurred, with an interval of at least 5000 yr between the youngest northern finger and the next southern one.

Previous studies had already shown that the NGC 1333 is a region heavily shaped by the dynamical interaction of internal outflows and external bubbles with the quiescent molecular cloud. In particular, previous large-scale maps of gas distribution and velocities in the IRAS 4A region already suggested the presence of a "turbulent cell" pushing toward the NGC 1333 IRAS4 from behind and coming from the south. The newly detected fingers provide support to

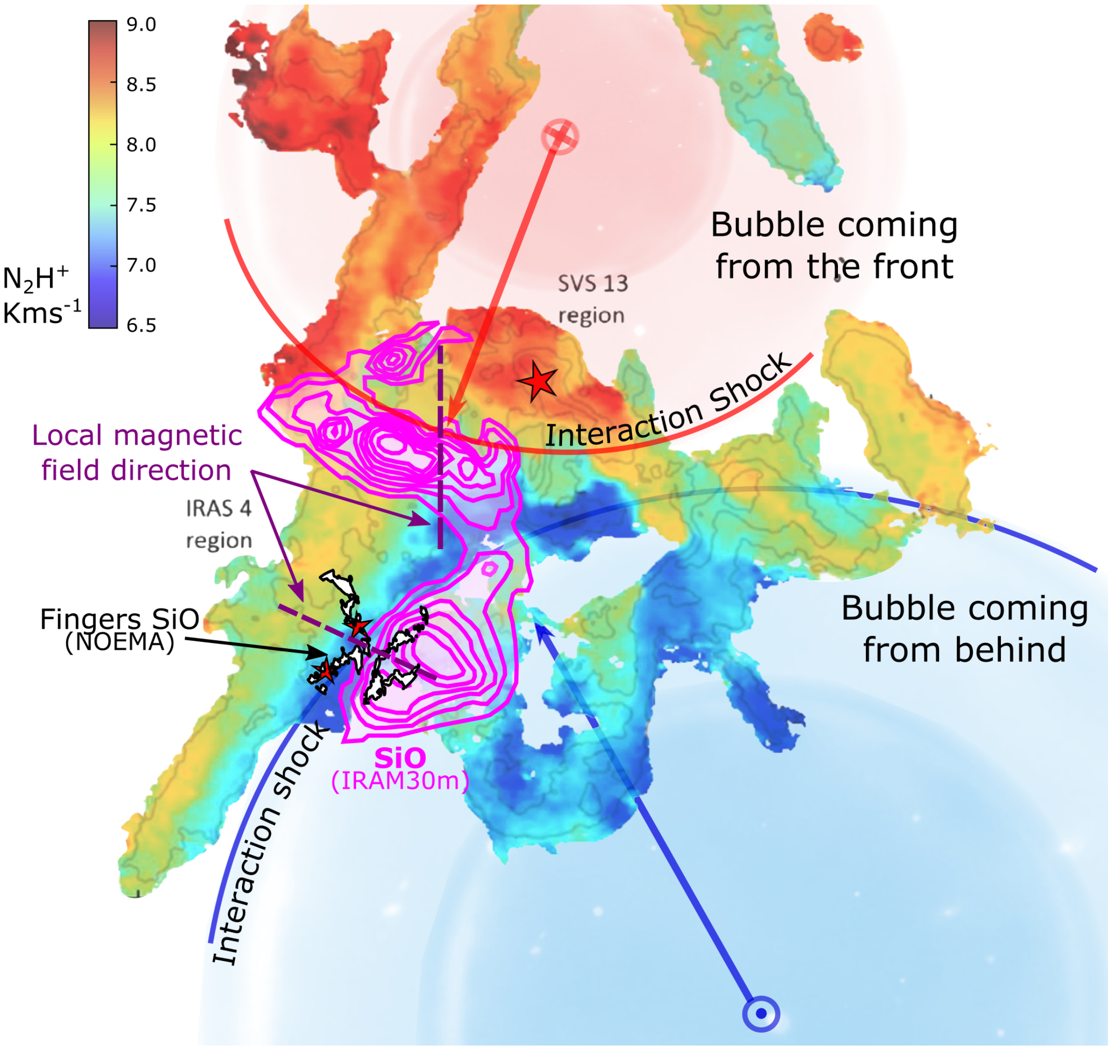

Figure 6.7: Large-scale view of the NGC 1333 filament. Overlap of the N$_2$H$^+$ line-of-sight velocity map by Dhabal et al. (2019) in color scale with the IRAM-30m SiO large scale ambient component emission by Lefloch et al. (1998b) in magenta contours and the IRAS 4A fingers detected in SiO with the SOLIS/NOEMA observations of the present work in black contours. The purple dashed lines represent the local magnetic field direction from Doi et al. (2020). The red stars mark the SVS13, IRAS 4A, and IRAS 4B protostars. The solid blue and red lines represent the interaction of the expanding bubbles: the red one is expanding from the northwest direction toward the SVS13 cloud from the front, and the blue one is expanding from the southwest direction toward the IRAS 4A cloud from behind.

this hypothesis, considering that the turbulent cell is the result of an expanding bubble, which caused three different shock events, with an expanding velocity of at least 7 km s^{-1}.

Finally, we suggest that the widespread narrow SiO emission observed toward the NGC 1333 IRAS 4 and SVS 13 region with single-dish observations in the late 90s is due to unresolved trains of shocks like the SOLIS fingers. These shocks would be the signature of the interaction of the bubble giving rise to the IRAS 4A fingers in the south and of another bubble pushing from the north toward SVS 13. We predict, therefore, that large-scale high-spatial resolution mosaics of SiO and other shock-related species can help to fully reconstruct the dynamical history of NGC 1333 and, consequently, provide precious constraints to the relevant theories and models.

6.2 Future projects

6.2.1 SOFIA proposal

In the course of my PhD and my research activity, I had the possibility to interact with researchers from the NASA Ames Reseach Center in the context of an international conference. In this occasion, their interest in my studies on hot corinos and the following discussions led to an interesting collaborative project, and a proposal submitted to the SOFIA airborne observatory, described below.

Water content in the early stages of planet-forming regions

The presence of water on an extraterrestrial planet is a crucial condition for its habitability (Güdel et al. 2014). This small molecule also plays an important role in the star formation process allowing clouds to collapse into stars acting as a major gas coolant and helping the coagulation of icy dust grains in planetesimals and, eventually, planets. Measuring the water content in astronomical sources is a very difficult task, because of the terrestrial atmosphere. Observations with several instruments, such as ISO, Spitzer and Herschel, showed that water in star forming regions is very abundant ($\sim10^{-4}$ with respect to H_2 Whittet & Duley 1991; van Dishoeck et al. 2014; Boogert et al. 2015; van Dishoeck et al. 2021). However, it is largely frozen into the dust icy mantles (e.g., Boogert et al. 2015), except in the warm regions where the water ices sublimate (Ceccarelli et al. 2000a; Helmich et al. 1996; Coutens et al. 2014) or in shocked regions where they are sputtered (Liseau et al. 1996; Snell et al. 2000; Nisini et al. 2010).

In Solar-type protostars the water-ice-sublimated regions are the hot ($\geq$100 K), dense ($\geq 10^7$ cm^{-3}) and compact ($\leq$100 au) hot corinos (Ceccarelli 2004). They are found around Class 0/I protostars (10^{4-5} yr; Andre et al. 2000; De Simone et al. 2017; Bianchi et al. 2019b; Belloche et al. 2020). Recent studies in Solar-type forming systems show that planet formation begins relatively early, already at the Class I stage (e.g., Harsono et al. 2018; Podio et al. 2020; Tychoniec et al. 2020; Sheehan et al. 2020; Segura-Cox et al. 2020). Gaps and rings structures observed towards protoplanetary disks embedded in Class I protostars have been interpreted as due to the presence of young planets or to their imminent formation (e.g., Isella et al. 2016; Andrews et al. 2018; Fedele et al. 2018; Long et al. 2019).

However, the abundance of water in these regions is unfortunately poorly known. Indeed, the few measurements performed with ISO and Herschel in hot corinos has been been mostly limited to Class 0 protostars, finding low water abundances ($\sim 10^{-6}$) with respect to the expected value ($\sim 10^{-4}$) estimated in the ices (Ceccarelli et al. 1999, 2000a; Kristensen et al. 2010, 2012; Coutens et al. 2012; Visser et al. 2012). It is important to exclude that the low measured water abundance is not due to an observational bias. Indeed, ISO observations suffer from the relatively large beam size, so that only the brightest water lines could be detected and are very likely optically thick so that they are poor probes of water abundances larger than 10^{-6} (Ceccarelli et al. 2000a). Similarly, HERSCHEL could only observe low lying water lines, which suffer of the same problem. On the contrary, large amount of deuterated water (N(HDO)$\sim 4 \cdot 10^{17}$cm^{-2}) has been detected in the Class I SVS13-A hot corino (see Figure 6.8), using single-dish IRAM 30m and interferometric IRAM/NOEMA observations in the ASAI and

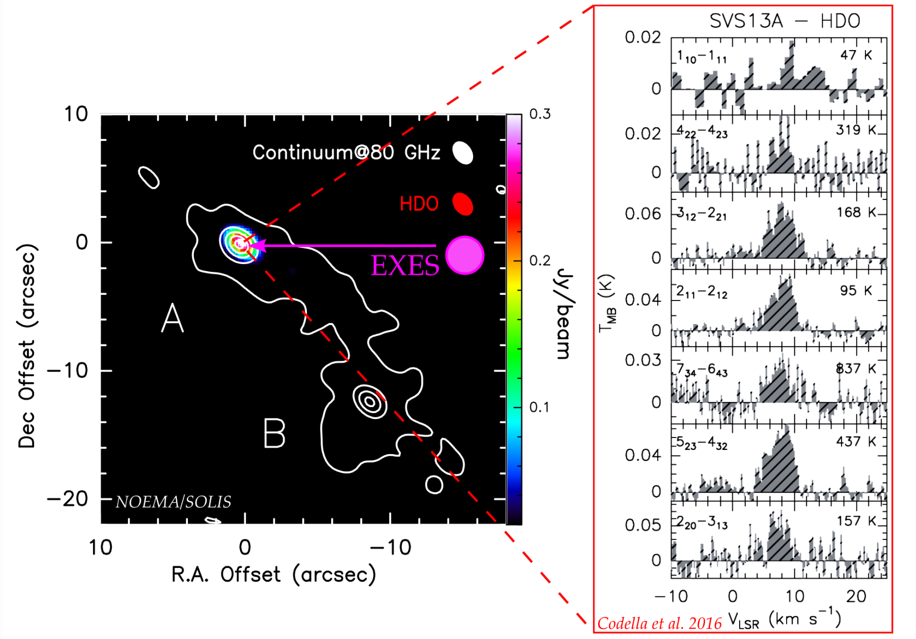

Figure 6.8: ***HDO in the Class I hot corino SVS13-A.*** *Left: The SVS13A system at mm wavelengths as seen by NOEMA/SOLIS (Ceccarelli et al. 2017) with the continuum emission in white contours and the unresolved HDO emission in color scale. Right: HDO line profiles observed with the IRAM 30m antenna towards SVS13-A (Codella et al. 2016a). The SOFIA/EXES width of 3.2 arcseconds is reported by the magenta circle, while the arrow point the selected observing position (SVS13-A).*

SOLIS Large Programs, suggesting abundant ($\sim 10^{-4}$) water there (Codella et al. 2016a).

SOFIA/EXES is currently the only available facility that provides sufficient spatial and spectral resolution to detect water line emission originated in hot corinos, at few arcseconds scales, with $\sim$5 km s^{-1} spectral resolution, and to measure its abundance. Following *ad hoc* model predictions, I propose to observe several rotational water lines at 22.5-26.5 μm toward the only Class I hot corino where evidence of water presence is so far known, NGC 1333 SVS13-A. The requested observations will allow to perform a multi-line analysis, using sophisticated radiative transfer models, in order to derive the SVS13-A hot corino properties, and the water abundance. In other words, it will be possible to measure how much water is available in regions where planets start to form. Additionally, combining these observations with previous HDO observations toward the same source, it will be possible to derive the deuteration ratio and compare it with the one measured in Solar System bodies (such as comets and meteorites).

In summary, the proposal focuses on the water content measurement in the planet formation zone when the process starts. This is a pilot project that will provide precious hints to understand the water journey from protostars to planets, and will be a guide to future similar James Webb Space Telescope (JWST) observations.

- This proposal has been submitted in the SOFIA Cycle 9. It was approved with *for 4.6 hours of observing time and Very Good grade.* The observations will be likely performed in January-February 2022.

Part IV

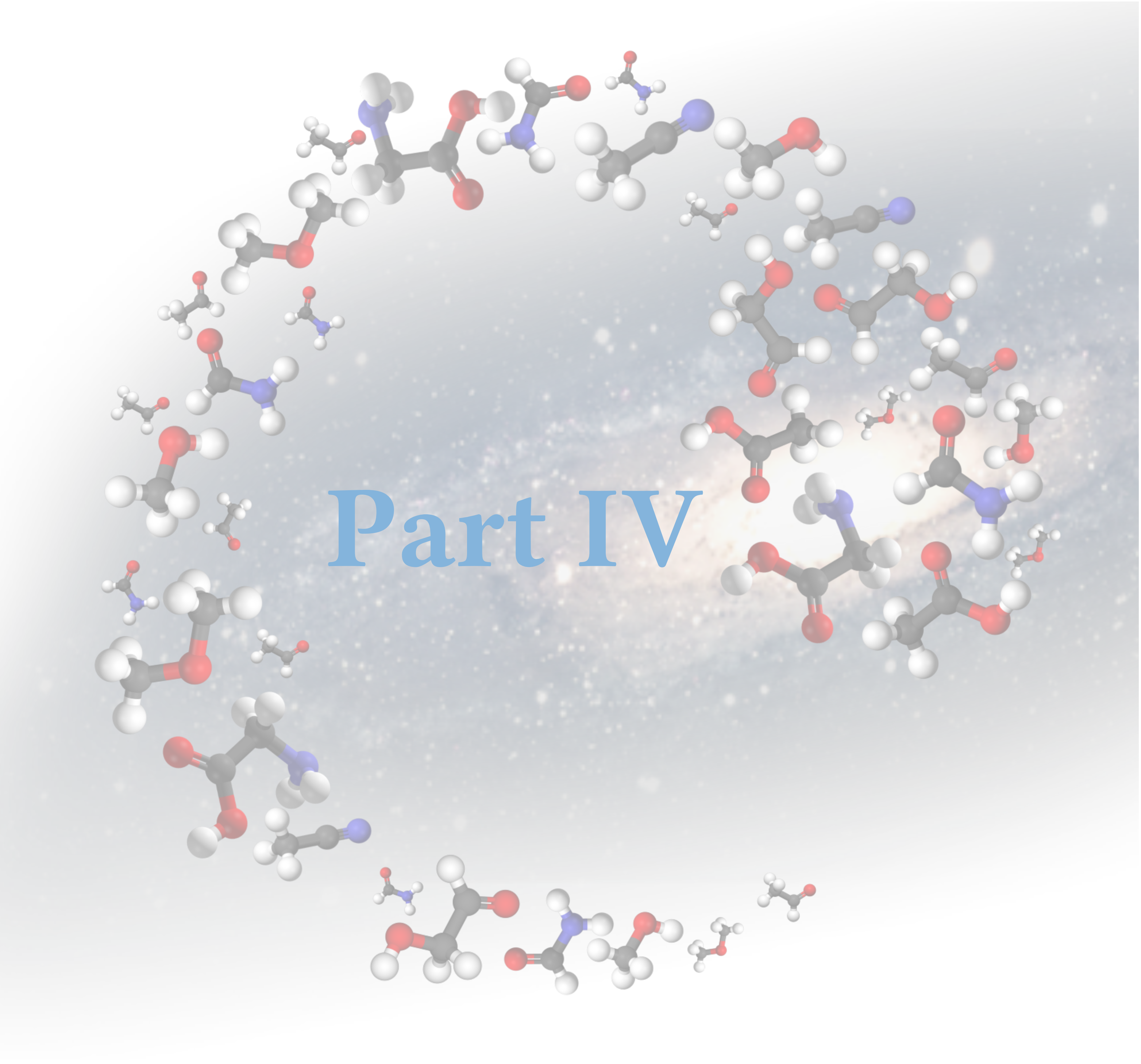

7 Conclusions

7.1 The main conclusions of an unexpected journey

The ultimate goal of this thesis was to characterize the early organic molecular enrichment of planet formation zones in Solar-like star forming regions. In particular, I aimed to answer two main questions, those reported in Section 1.5.2:

Q1: What is the origin and the nature of hot corinos?

Q2: How are these complex organic molecules synthesized?

In order to answer the proposed questions, I have studied the IRAS 4A binary system and its outflows using (sub-)mm and cm interferometric observations with state-of-the-art facilities, such as IRAM-NOEMA and VLA, and performed the molecular line analysis.

When I started my thesis, the fact that IRAS 4A is a binary system with very different millimeter molecular spectra have been known for a few years, and the origin of this spectral differentiation was still puzzling. Indeed, since the two protostars originate from the same molecular cloud and are supposed to be coeval, it was intriguing that only one of the two is surrounded by a dense region of complex organic molecules.

Therefore, I started to exploit the new NOEMA data from the SOLIS Large Program toward IRAS 4A. In particular, the first step was to investigate the nature and the origin of the spectral differentiation between 4A1 and 4A2. I started to search for new iCOMs to complete the census of the molecular complexity of the known hot corino IRAS 4A2 and to serendipitous search for possible iCOMs emission in the surrounding of IRAS 4A1. However, the trip did not follow a straight and clean path but was full of unexpected and intriguing ramifications that resulted in this thesis.

7.1.1 Constraining the formation route of acetaldehyde

During the exploitation of the NOEMA-SOLIS data in the IRAS 4A binary system, I noticed that the emission of some iCOMs is not only compact around the hot corino IRAS 4A2, but it also traces the two bipolar outflows coming from the two central protostars. This large-scale emission caught my attention, and I decided to focus on the chemical characterization of the molecular outflows. Recent interferometric studies on the molecular complexity of L1157-B1 highlighted the role of jet-driven shocked regions in low-mass protostars as perfect astrochemical laboratories where to constrain the iCOMs formation route (e.g., Codella et al. 2017).

Indeed, the imaging of iCOMs in shocked regions allows to spatially differentiate the emission from different iCOMs and to use the time dependence as constraint to retrieve the formation path of the iCOMs. However, this methodology was tested only in L1157-B1, therefore, I employed it on the IRAS 4A outflows.

Thanks to the new high-resolution NOEMA-SOLIS observations, I could image the emission of several iCOMs in the outflows emanating from IRAS 4A1 and 4A2: methanol, acetaldehyde, dimethyl ether, and formamide. The detected iCOMs are not homogeneously distributed across the outflows: methanol is widespread over the two outflows, acetaldehyde is only bright in the southern lobes, and dimethyl ether and formamide are concentrated in some compact spots along the outflows. The molecular richness of the IRAS 4A outflows was intriguing, being the second outflow where the iCOMs emission was imaged at high angular resolution, after L1157-B1. Additionally, the observed spatial segregation in the iCOMs emission deserved further investigation. Therefore, collaborating with the chemists and modelers of the DOC team, I could compare the observed iCOMs abundances in different positions of the two IRAS 4A outflows with theoretical predictions from astrochemical models. Finally, I was able to constrain the formation route of the acetaldehyde in the outflows as a gas-phase product, formed by the reaction between an ethyl radical with an oxygen atom. Notice that, at that time, the gas-phase reaction between ethanol and OH leading to acetaldehyde (from the ethanol tree Skouteris et al. 2018) was not taken into account, as it was not clear its relevance (Vazart et al. 2020).

This work showed the strengths of this method in constraining iCOM formation routes and highlighted that the derivation of iCOM abundance ratios from single-dish observations could be hazardous, as they are unable to disentangle the spatial distribution of the different iCOMs.

7.1.2 An unpredicted clash animating the journey

Investigating the methanol emission in the outflowing gas of the IRAS 4A system with the NOEMA-SOLIS data, I discovered the presence of a peculiar feature. There is a filamentary structure almost perpendicular to the IRAS 4A1 outflow and $10''$ away from the central protostars. It shows a very narrow spectral profile peaked at the systemic velocity of the cloud. There was no evidence for this feature, which I called *finger*, to be connected to the outflow. So I tried to figure out its origin.

Given that methanol is a grain surface species, it has to be released into the gas phase through a non-thermal process (such as a shock) given that there are no hot sources in the finger's close surroundings to drive thermal desorption. The NOEMA-SOLIS setup also covered one of the transitions of SiO, the best-known shock tracer. Therefore, I imaged the SiO line, and I noticed the presence of three equispaced and parallel fingers: the northern one is the finger traced by methanol, and the other two, detected only in SiO, had already been observed with the VLA by Choi (2005), even if the author did not find a clear explanation for their origin.

I explored various possibilities that could have led to the formation of the fingers, and the most plausible one, supported by the observed abundances of methanol and SiO and the fingers chemical differentiation, was a train of shocks.

The NGC 1333 star-forming region which hosts IRAS 4A is known to be heavily shaped by external triggers, such as the explosion of one or more supernovae in the vicinity and other forms of stellar activity. In particular, it has been suggested that the filament where IRAS 4A lies has been the result of the clash of an external expanding bubble (Dhabal et al. 2019). The presence of the fingers along with the methanol and SiO emission analysis supports this scenario. Therefore, I concluded that the observed fingers are the signature of the clash of an expanding bubble against the IRAS 4A envelope.

This work highlighted the importance of high arcsec angular resolution observations of shock tracers in helping to reconstruct the dynamical history of star-forming regions as NGC 1333.

7.1.3 IRAS 4A1 and IRAS 4A2: two apparently different companions

During my PhD, I had the opportunity to visit the NRAO Socorro site to reduce the VLA data of a proposal that was a pilot project aimed at retrieving the ice mantle history of two sources representative of two different classes of objects, hot corinos and warm carbon chain objects. The targeted molecules were ammonia and methanol, as they are the major gas-phase tracers of the ice mantle composition. One of the two representative sources was the IRAS 4A system.

Reducing the data, I created preliminary images of the methanol emission toward IRAS 4A. I immediately recognized that the emission was compact and well detected on both protostars with similar intensities, contrary to what was found so far at mm wavelengths in previous studies. Moved by this incredible discovery, I focused my attention on the methanol emission toward the two protostars in order to understand if the dust was the culprit of absorbing the emission at millimeter wavelengths and preventing the iCOMs detection toward IRAS 4A1. Indeed, methanol is one of the simplest iCOMs and precursors of many more complex molecules, so its detection toward IRAS 4A1 is a sign of the presence of a chemical complexity yet unknown. I analyzed the methanol emission via a non LTE code, confirming that it traces the warm and dense gas typical of hot corinos, and I compared theoretical predictions at millimeter wavelengths with previous observations.

As a result, I reported the first detection of a hot corino region around IRAS 4A1 and I confirmed the initial guess: the dust is the culprit in hiding the hot corino toward IRAS 4A1 and the observations at centimeter wavelengths allow to see through the thick veil of dust. Additionally, I estimated the effect of dust opacity on the known hot corino IRAS 4A2. Indeed, the dust affects the millimeter line emission differently in the two sources, with complete absorption in the case of IRAS 4A1 and a partial absorption in IRAS 4A2. This raises an important warning: iCOMs abundances derived at millimeter wavelengths can be heavily underestimated by the dust absorption.

The discovery, the novelty of the methodology used, and the importance of centimeter observations in the correct study of hot corinos led to a press release in France through the CNRS, in the USA through NRAO, and in Italy through INAF.

The VLA methanol observations highlighted the presence of a hot corino around IRAS 4A1 but they cannot support the hypothesis that a real chemical difference exists between 4A1 and 4A2. To this end, I went back to the original purpose of the VLA proposal, and I used the VLA observations of ammonia together with the methanol ones to retrieve the ice mantle history of the two protostars. Indeed, the relative abundance of these two molecules, being grain surface species, would mainly depend on the pre-collapse clump gas conditions during their formation in the prestellar phase. If a real chemical differentiation exists, it can reflect a difference in the ice mantle composition.

I detected compact ammonia emission toward both protostars. Then I compared the ammonia over methanol abundance ratio with astrochemical model predictions in which the pre-collapse clump conditions are varied, namely gas density and temperature, and ice mantle formation timescale. The idea is that the observed abundance ratio reflects the one in the grain mantles at the moment of the ice sublimation. With this method, I was able to constrain the gas conditions of the pre-collapse clump of the two protostars and to highlight the possible differences that could have led to different chemical compositions.

In summary, these studies highlighted the great, and previously unrecognized, importance of centimeter observations in the correct study of hot corinos and in understanding their origin and nature.

7.1.4 Final remarks

At the end of this journey, it is important to understand what has been my contribution to the questions I aimed to answer (Q1 and Q2 in 7.1).

Q1: Regarding the open question of the nature and origin of the hot corinos, I raised an important warning with my studies. The observational biases play a huge role in the characterization of hot corinos. Indeed, the role of the dust in hiding hot corinos is more important than what thought so far. With this work, I opened the *Pandora's box*. Indeed, I showed how the iCOMs abundances estimated at mm wavelengths can be highly underestimated due to the dust absorption. To face this problem, I used centimeter observations to the study molecular lines, in order to i) estimate the dust opacity contribution at millimeter wavelengths, and ii) retrieve the ice mantle history of Solar-type protostar in an indirect way. This work paves the way to new observations with future centimeter wavelengths facilities (see Section 8.1.1).

Q2: Regarding the open question of the iCOMs formation, I demonstrated how important is the close collaboration between observers, chemists, and modelers. Indeed, thanks to the different expertise, it was possible to efficiently exploit the observational data to constrain the formation route of acetaldehyde as a gas phase product in shocked regions. This is just a first step toward the full comprehension of the general problem, and future works will help in completing the scenario (see Section 8.1.2).

8 Perspectives

With my thesis work, I explored some of the main open questions related to the chemical enrichment of hot corinos, early-stage planet-forming regions. I provided the first pieces of the big puzzle that is the hot corino picture. However, a lot need still be done to fill the missing holes and to reach a complete characterization.

In the following, I propose some follow-up studies to continue the trip I started three years ago, divided in a short and long-term view.

8.1 Short-term perspectives

8.1.1 The chemical differentiation of hot corino binaries

Part of the work I carried out in the last three years is focused on the origin of the chemical differentiation observed in the IRAS 4A binary system (see Section 4.2). I used centimeter observations to i) understand the role of the dust in absorbing millimeter iCOMs lines and ii) to retrieve the ice mantle history of the two coeval protostars. In particular, I showed that, in the case of IRAS 4A, the dust is the protagonist hiding the hot corino toward the brightest millimeter continuum source. However, one may wonder if the case of IRAS 4A is one of a kind or if other hot corinos around Class 0 protostars are missing as their iCOMs lines are absorbed by the dust. I propose to further investigate if the dust is responsible for the chemical differentiation observed in the millimeter-wave spectra of other binary systems.

- Among all the various binary systems, the Class 0 CepE-mm is a peculiar one. The brightest millimeter continuum source hosts a hot corino region, while the fainter companion lacks iCOMs emission. What is the role of dust in this case? Is the chemical difference between the two protostars in the CepE-mm system apparent or real? To this end, I made an observational proposal targeting methanol and ammonia lines at cm wavelengths toward the CepE-mm system with the VLA interferometer. The proposal has been accepted, and the data have been observed in September 2021. Therefore, I aim to reduce and analyze these data and to combine them with the millimeter observations obtained within the SOLIS Large program to investigate if the chemical differentiation in CepE is real or not (see Section 4.4.2).
- Another binary system is NGC 1333 IRAS 2A. It is part of the southern filament of the Perseus NGC 1333 star-forming region together with IRAS 4A. In my PhD work, I reported evidence for the clash of an expanding bubble with this filament that could have triggered

the collapse and, consequently, the formation of both protostellar systems. If connected by the same fate, both IRAS 4A and IRAS 2A should have a similar grain mantle history. Therefore, I plan to observe methanol and ammonia lines with the VLA at high angular resolutions to resolve the binary system of IRAS 2A, in order to i) retrieve the ice mantle history of the two protostars and compare it with the IRAS 4A one, and ii) to make a first chemical characterization of the two IRAS 2A companions using methanol, the simplest iCOM. Indeed, no observations of iCOMs lines have been carried out so far toward IRAS 2A with enough angular resolution to resolve the two companions (see Section 4.4.2).

- As a follow-up of these proposals, I would like to build a first large survey of tens Solar-type hot corinos observed at planet-forming scales to characterize the chemical diversity of hot corinos and to provide their real chemical composition. I would use centimeter and millimeter observations, combining VLA, ALMA, and IRAM/NOEMA observations already in my hand with public archival data and dedicated follow-up proposals.
- All the methanol observations performed at centimeter wavelengths can be combined with previous ones at millimeter wavelengths to constrain the dust spectral index β. This factor is largely sensitive to grain sizes, i.e., larger grains give small β values. As a consequence, it is usually used to trace the growth of grains. Typically, it is derived fitting the Spectral Energy distribution at different wavelengths (from sub-mm to radio). However, this method depends on several assumptions. Using methanol observations at different wavelengths (e.g., 25 GHz, 143 GHz, 206 GHz), and considering that at centimeter wavelengths the dust is likely optically thin, I propose to retrieve the dust spectral index in Class 0 sources in a more straightforward manner (see Section 4.4.1).
- If the planet formation starts early, in the Class 0/I phase, it is important to assess the abundance of water at this stage. However, it is unfortunately poorly constrained, mainly due to observational biases. SOFIA/EXES is the only available facility that provides sufficient spatial and spectral resolution to detect water line emission in hot corinos and to measure its abundance. Therefore, I made a SOFIA observational proposal to observe water emission lines at 22.5-26.5 μm toward the only Class I hot corino where evidence of the presence of water is so far known, SVS13-A. Indeed deuterated water (HDO) has been detected with compact emission toward the Class I SVS13-A hot corino with single dish facilities and with the NOEMA/SOLIS data (see Section 6.2.1).

8.1.2 The iCOMs formation routes

In my thesis work, I showed that the comparison of iCOMs abundances towards low-mass jet-driven shocked regions with model predictions is a powerful method to constrain iCOMs formation routes (see Section 5.1). Another method consists of comparing iCOMs abundances in hot corinos with theoretical predictions. In particular, the iCOMs deuteration ratio has been successfully used to this end thanks to new quantum chemical computation results (Skouteris et al. 2017). The deuteration ratio in different molecules might provide the temporal sequence of their formation and, possibly, information on their synthetic route.

However, very few deuterated complex organic molecules have been detected, and only in one target, the hot corino IRAS 16293-2422 (Coutens et al. 2016; Manigand et al. 2020). I propose to observe the deuterated form of formamide and acetaldehyde in the hot corino IRAS 4A2, using the data obtained in the ALMA/FAUST Large Program (see Section 5.3.2). Using the computational results for formamide by Skouteris et al. (2017) and acetaldehyde by Vazart et al. (2020), I can constrain their formation route in IRAS 4A2 and compare the results with the ones obtained in IRAS 16293-2422. Additionally, the same methodology can be applied to the glycolaldehyde once the computational results will be available (Vazart et al. and Enrique-Romero et al. in preparation, both being part of the DOC group).

8.2 Long-term perspectives

8.2.1 A multiwavelength approach to unveil the hot corino nature

One of the main conclusions of my thesis is the importance of centimeter observations in the correct study and characterization of hot corinos. In particular, I showed how to quantify the contribution of dust opacity in absorbing the iCOMs emission lines in hot corinos and how to indirectly investigate the ice mantle composition by observing the major ice components once released to the gas phase.

Historically, the study of hot corinos has mainly been carried out at (sub-)millimeter wavelengths. That is because the most intense rotational emission lines of prebiotic complex organic molecules fall in this range. Cutting-edge interferometric facilities as ALMA and IRAM-NOEMA are used thanks to their high sensitivity and angular resolution.

However, hot corinos can be rich in different iCOMs, more or less complex, whose emission populates spectrum, appearing as a *forest* of lines. The line-rich (sub-)mm spectra at millimeter wavelengths will then be affected by two main problems:

i) *The dust opacity.* It has a higher impact moving to higher frequencies, and it can absorb iCOMs emission lines leading to an underestimation of their column density. Eventually, it can completely absorb iCOMs emission lines hiding hot corinos.

ii) *Line confusion.* Indeed, the high sensitivity of cutting-edge facilities allows the detection of less abundant species with low-intensity transitions. Therefore, there is a high probability that the observed lines will be blended, considering that, in hot corinos, the line profiles are usually of $\sim$3 km s^{-1}. Therefore, below a certain confusion limit threshold, it will be impossible to identify the lines and to retrieve information from the spectra.

To overcome these issues, a possibility is to observe hot corinos at centimeter wavelengths, since:

i) Dust is more likely optically thin so that hidden hot corinos can be revealed, as in the case of IRAS 4A1. Additionally, the dust opacity can be estimated, and the iCOMs abundances derived at millimeter wavelengths can be corrected.

ii) It is possible to study the ice mantle history of Solar-type protostars thanks to the simultaneous observations of the critical gas-phase tracers of the major ice mantle species (NH_3 and CH_3OH).

iii) Line confusion is less significant as the spectrum is less populated by the rotational transition of lighter and smaller molecules.

iv) It is possible to observe heavier and larger molecules as their rotational spectrum is shifted toward lower frequencies.

The current state-of-the-art interferometric centimeter facility is the Very Large Array

(VLA). The high angular resolution provided by interferometers is crucial to resolve hot corinos, map their distribution and study their kinematics.

As I showed in this PhD thesis, the VLA is currently the most powerful instrument to study and characterize hot corinos at centimeter wavelengths. Indeed, I was able to detect methanol emission in the cm with enough sensitivity (S/N∼10) using a reasonable amount of integration time. However, I could not detect more complex molecules, i.e., formamide, glycolaldehyde, methyl formate). That is because their emission lines, given their low abundances, lie below the detection threshold. Therefore, detecting more complex and less abundant molecules with respect to methanol and performing an unbiased spectral survey with enough spectral resolution and large bandwidth is still challenging in terms of sensitivity.

To overcome the sensitivity issues, two new centimeter interferometric facilities are in development: ngVLA and SKA. They will provide unprecedented sensitivity and angular resolution. Additionally, the upgrade of ALMA is planned with the upcoming Band1 (see section 8.2.2).

In summary, I believe that complementary millimeter and centimeter observations are needed to characterize the hot corinos nature.

At millimeter wavelengths, it is possible to detect small iCOMS and to study through them the kinematic of the source.
At centimeter wavelengths, it is possible to search for larger and heavier iCOMs and to study their distribution.
Complement millimeter with centimeter observations, it is possible to quantify the dust opacity contribution and correct the iCOMs abundances estimated at millimeter wavelengths by the opacity factor. Finally, it will be possible to detect several transitions of the same iCOM in a wide range of excitation energies to obtain a complete picture of the emission and to firmly derive the gas conditions with a multi-line radiative transfer analysis.

8.2.2 Future facilities for hot corinos studies

To overcome the sensitivity issues new future centimeter facilities are planned:

- The new generation Very Large Array (ngVLA; https://ngvla.nrao.edu/) interferometer will be constituted of 244 antennas each 18m in diameter, supplemented with a short baseline array of 19 antennas each 6m in diameter to deliver the shortest baselines. Each antenna is equipped with receivers spanning the frequency range of 1.2 − 50 GHz (21-0.6cm) and 70 − 116 GHz (4–2.6mm). The array will be located near the current VLA site in New Mexico, with an additional mid-baseline station spread over Arizona, Texas, and Mexico, and a long baseline array in Washington, West Virginia, California, Iowa, New Hampshire, Hawaii, Puerto Rico, US Virgin Islands, and Canada. The extended baselines will be of at least hundreds of kilometers, providing angular scales down to milliarcsecond. Using the longer baselines, separately or together with the main array, it will be possible to reach 0.1 milliarcsecond resolution. ngVLA will be ∼10 times more sensitive than VLA and ALMA for spectral line and continuum observations.
  In 2023 the first antenna prototype will be delivered to the VLA site, while the ngVLA construction is planned to start in 2025, and the ngVLA Early Science should start in 2029.

- The Square Kilometer Array (SKA; https://www.skatelescope.org/) will consist of two interferometers, one in South Africa (Mid) and one in Australia (Low), complementing each other. SKA-Low will cover the frequency range 50–350 MHz, and it consists of an array of 131072 Christmas tree-shaped antennas grouped in 512 stations that can reach $0\farcs3$ angular resolution. SKA-Mid will cover the frequency range 350 MHz –15.4 GHz (with a goal of 24 GHz, and perhaps 50 GHz), and it consists of 197 dish antennas that can reach $3''$ of angular resolution.
  SKA will provide angular resolution of 40–2 milliarcseconds at 0.5-10 GHz. It will have a point-source sensitivity of 4–20 times the current state-of-the-art facilities and a survey speed 10–100 times higher. The end of the construction is planned for 2029.

- The ALMA Band 1 receiver covers the 35–50 GHz frequency band (https://www.eso.org/public/usa/announcements/ann16044/). It will allow ALMA to bridge the gap between the mm/sub-mm and cm range and, given the large ratio of available bandwidth, it allows to study large range of energy regimes.
  Please note that this spectral frequency band is also covered by the VLA Ka/Q band. In terms of angular resolution and sensitivity, the two facilities will be comparable in this frequency range, but while VLA is very good for northern sources, ALMA will be crucial for southern ones allowing also to combine Band 1 with bands at a higher frequency. Therefore, the two facilities are highly complementary depending on the target and the scientific project goal.

Finally, the upcoming IR facilities with unprecedented sensitivity, such as JWST and ELT, will probe the ice mantles at more evolved stages, such as in protoplanetary disks. It will then be possible to compare the ice mantle composition of Class 0 hot corinos with the one in later stages.

I believe that these future facilities, combined with the current ones, will be a breakthrough in the study of the chemical complexity of hot corinos. Indeed their unprecedented sensitivity and angular resolution will allow targeting more complex iCOMs in a spectral range less affected by the dust opacity. Additionally, it will be possible to build large surveys of objects with different characteristics (e.g., evolutionary stage, hosting environment, etc.) using a large bandwidth.

We are moving toward an outstanding observational era. I believe that it will be a bright future for astrochemistry, full of new discoveries and new intriguing mysteries to be solved, of which I aim to be part.

French Summary

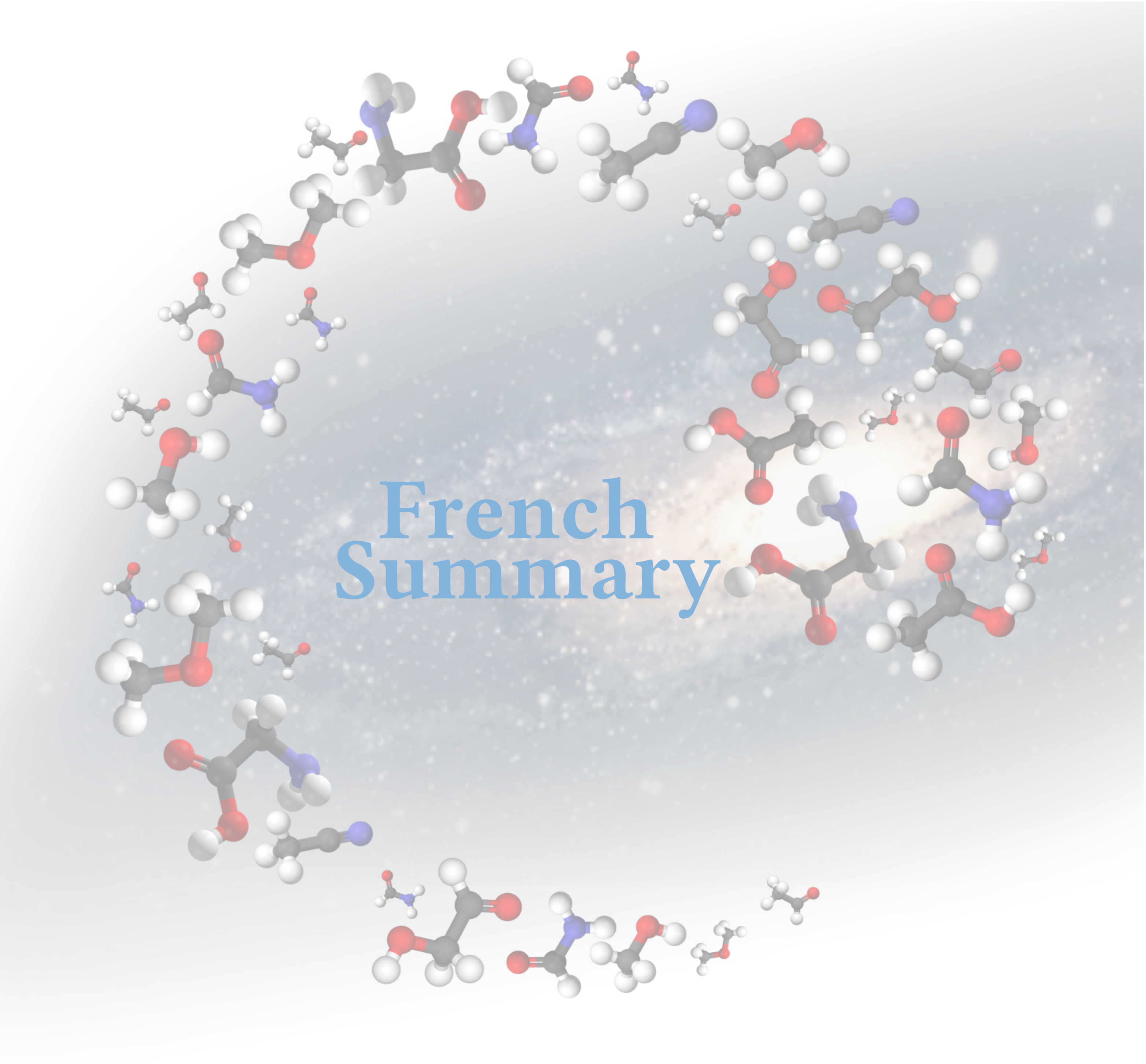

A

Contexte et objectifs de la thèse

A.1 Objectifs de la thèse : L'enrichissement moléculaire organique précoce des zones de formation des planètes.

La Terre est la seule planète connue abritant la vie, qui est basée sur la chimie organique. De plus, certaines des briques de la vie, c'est-à-dire les acides aminés, se trouvent dans des objets du système solaire, à savoir les comètes et les météorites. Cela nous laisse penser qu'il est possible que les premières étapes de la chimie organique qui a conduit à la vie terrestre aient commencé pendant la formation de notre système solaire.

La formation des étoiles semblables au Soleil passe par différentes étapes, à partir d'un noyau moléculaire qui s'effondre et évolue en une protoétoile, un disque protoplanétaire, et finalement un système planétaire. Parallèlement à l'évolution physique, une évolution chimique se produit (voir la figure 1.4). La découverte d'iCOMs dans la phase la plus jeune de la formation des étoiles de type solaire, c'est-à-dire les hot corinos, soulève une question importante : Existe-t-il un lien direct entre les premières étapes de la formation des étoiles de type solaire et les plus récentes ? En d'autres termes, la complexité chimique est-elle héritée d'un stade à l'autre ?

Afin de répondre à cette question, il est crucial de caractériser pleinement, d'un point de vue chimique, les premières étapes de la formation des étoiles semblables au Soleil, en particulier la phase de hot corino, chimiquement riche. Dans ma thèse, je vise à répondre à deux questions principales :
Q1 : Quelle est l'origine et la nature des hot corinos? Q2 : Comment ces molécules organiques complexes sont-elles synthétisées?

Q1: Sur l'origine chimique et la nature des hot corinos

Toutes les proto-étoiles ne possèdent pas une région de hot corino. En effet, avant le début de cette thèse, seulement une dizaine des hot corinos étaient connus, tous découverts à l'aide d'observations (sub-)millimétriques. Par conséquent, après vingt ans d'études, la nature et l'origine des hot corinos n'étaient toujours pas claires. Le premier facteur déterminant pour cette situation est que l'observation des hot corinos n'est pas une tâche facile. En effet, étant des objets compacts ($\leq 1''$), des installations à haute résolution et haute sensibilité sont nécessaires. Avec l'arrivée des interféromètres NOEMA et ALMA, les premiers hot corinos ont été imagé et les premiers relevés de lignes ont été effectués. De manière surprenante, plusieurs hot corinos dans des systèmes binaires présentent des spectres moléculaires millimétriques très différents. Quelle est la raison de cette diversité spectrale aux longueurs d'onde millimétriques ? Elle pourrait refléter une réelle diversité moléculaire intrinsèque, ou être simplement due à des biais d'observation. Il s'agit cependant d'une question cruciale à résoudre pour comprendre la nature et l'origine des hot corinos.

Il existe deux stratégies complémentaires pour dévoiler la nature des hot corinos : i) utiliser une approche statistique étudiant un grand nombre d'objets ou ii) caractériser de manière extensive la chimie d'un seul objet. Dans cette thèse, j'ai utilisé la deuxième approche, en me concentrant sur le système binaire de classe 0 NGC 1333 IRAS 4A, qui est décrit en détail dans la section 3.1.3. En bref, les deux compagnons, IRAS 4A1 et IRAS 4A2, présentent des spectres moléculaires millimétriques très différents. Pour comprendre l'origine de la différenciation spectrale observée, j'ai utilisé une nouvelle approche : des observations aux longueurs d'onde centimétriques avec l'interféromètre VLA. En complétant les nouvelles observations dans le centimètre avec les observations existantes dans le millimètre, j'ai voulu étudier la contribution de l'opacité de la poussière comme un biais observationnel majeur.

Q2: Sur la synthèse de molécules organiques complexes

La formation des iCOMs fait toujours l'objet d'un débat animé. Il existe deux paradigmes principaux : i) la formation d'iCOMs exclusivement sur les glaces interstellaires et ii) la formation d'iCOMs via des réactions chimiques en phase gazeuse d'espèces sublimées du manteau de grains. Déterminer quel paradigme est le plus efficace pour former des iCOMs et où n'est pas une tâche facile. En effet, au cours des dernières années, afin de contraindre leurs voies de formation, les prédictions des modèles astrochimiques ont été comparées aux abondances observées des iCOMs dans deux régions : les hot corinos et les régions choquées par le jet de faible masse. En particulier, cette dernière approche s'est avérée très efficace, car elle fournit la dépendance temporelle comme une contrainte supplémentaire. En effet, une fois le choc passé, la chimie du gaz choqué évolue avec le temps.

Dans cette thèse, j'ai suivi la seconde approche en observant le gaz s'échappant du système binaire IRAS 4A. Au début de la thèse, très peu d'observations des iCOMs dans les chocs protostellaires de faible masse ont été réalisées avec des single-dish antenna. Cependant, étant donné qu'il s'agit de single-dish observations, la distribution spatiale, et par conséquent les informations détaillées sur la région émettrice, sont manquantes. En revanche, les observations interférométriques à haute résolution angulaire offrent la possibilité de cartographier l'émission des iCOMs vers les régions choquées. L'information spatiale, ainsi que la dépendance temporelle, peuvent être utilisées pour contraindre la route de formation des iCOMs. En effet, comme l'a fait Codella et al. (2017) pour contraindre la voie de formation du formamide.

Dans le cadre du grand programme d'observation SOLIS de IRAM/NOEMA, mon objectif était d'explorer la complexité moléculaire des outflows de IRAS 4A et d'étudier la possible différenciation spatiale entre les iCOMs et l'implication obtenue en comparant les abondances des iCOMs avec les prédictions des modèles astrochimiques, en contact étroit avec les chimistes et les modélisateurs de l'équipe DOC.

Effets collatéraux : la vision à grande échelle

En travaillant sur les outflows de IRAS 4A avec les observations NOEMA, j'ai découvert des caractéristiques moléculaires intéressantes dans la région environnante de IRAS 4A qui ne semblaient pas être liées aux outflows. La région de formation d'étoiles qui abrite IRAS 4A est connue pour être associée à des structures filamentaires et pour avoir été fortement façonnée par des déclencheurs externes, tels que l'explosion d'une ou plusieurs supernovae et d'autres formes d'activité de rétroaction stellaire, et par l'interaction dynamique des outflows internes et des bulles externes avec le nuage moléculaire quiescent: (e.g., Sandell & Knee 2001; Dhabal et al. 2018, 2019).

B Richesse moléculaire des jeunes proto-étoiles

B.1 Dévoiler la nature chimique des hot corinos

Les premières études que j'ai menées dans le cadre de ma thèse ont porté sur la nature chimique des hot corinos de IRAS 4A. Au moment de ces études, après presque vingt ans de chasse, moins d'une douzaine de hot corinos étaient connus. La plupart de ces études ont été réalisées à des longueurs d'onde mm avec des single-dish installations comme l'IRAM-30m. Avec l'avènement des installations à haute sensibilité et haute résolution angulaire, comme NOEMA et ALMA, beaucoup plus des hot corinos ont été détectés et beaucoup d'entre eux ont été découverts comme faisant partie de systèmes binaires proches ($\leq 1''$). Au moment de la rédaction de la thèse, de nouveaux relevés suggèrent que $\leq 50\%$ des proto-étoiles développent un hot corino (e.g., Belloche et al. 2020; Yang et al. 2021). De plus, plusieurs hot corinos dans des systèmes binaires présentent des spectres moléculaires millimétriques très différents: (e.g., López-Sepulcre et al. 2017; Ospina-Zamudio et al. 2018; Manigand et al. 2020; Yang et al. 2021).

Deux possibilités peuvent expliquer pourquoi les hot corinos sont si difficiles à trouver et pourquoi les spectres millimétriques des objets coexistants sont si différents :

i) Si la poussière est optiquement assez épaisse pour absorber les raies moléculaires millimétriques, elle peut cacher les hot corinos et il se peut qu'il n'y ait pas de réelle diversité chimique dans les hot corinos des systèmes binaires. Plusieurs preuves indirectes indiquent que, aux longueurs d'onde millimétriques, les enveloppes de poussière enveloppant les hot corinos de classe 0/I pourraient être optiquement épaisses (e.g., Miotello et al. 2014; Galván-Madrid et al. 2018; Galametz et al. 2019).

ii) Les hot corinos sont rares et les spectres millimétriques reflètent une diversité chimique intrinsèque probablement due à une histoire différente de l'objet.

Ceci dit, il est primordial de mesurer la composition chimique des manteaux de glace formés lors de la phase précédente du noyau préstellaire pour comprendre l'origine et la nature des hot corinos.

Cependant, l'étude directe de la composition du manteau de glace dans les jeunes sources encastrées est difficile, car un fort continuum infrarouge de fond est nécessaire pour obtenir les spectres d'absorption à partir desquels la composition du manteau est dérivée. Une possibilité est de la récupérer indirectement en observant les espèces du manteau de glace lorsqu'elles sont libérées en phase gazeuse dans les hot corinos. En effet, l'apparence chimique de la proto-étoile dépend de la composition du manteau, comme le montrent diverses études théoriques: (Aikawa et al. 2020; Kalvāns 2021). À son tour, le contenu chimique du manteau est sensible aux conditions environnementales et à l'échelle de temps de la formation de la glace (e.g., Taquet et al. 2012a; Cuppen et al. 2017). Parmi les principales espèces du manteau de glace (Boogert et al. 2015), les traceurs critiques en phase gazeuse sont NH_3 et CH_3OH, car CO est souvent optiquement épais et confondu avec l'enveloppe, CO_2 et CH_4 n'ont pas de transitions observables en phase gazeuse, et H_2O est gêné par l'atmosphère terrestre.

Par conséquent, pour étudier ces deux possibilités et retrouver l'histoire du manteau de glace des proto-étoiles, j'ai observé, avec l'interféromètre VLA aux longueurs d'onde centimétriques, le système binaire de classe 0 NGC 1333 IRAS 4A. Ce système a été largement étudié aux longueurs d'onde mm, avec IRAM-NOEMA et ALMA, fournissant un recensement chimique exhaustif et mettant en évidence la différence chimique des deux composants, IRAS 4A1 et IRAS 4A2. En effet, IRAS 4A1 est la source de continuum mm la plus brillante qui manque d'émission d'iCOMs, alors que IRAS 4A2 est un hot corino bien connu enrichi en iCOMs (De Simone et al. 2017; Taquet et al. 2015; López-Sepulcre et al. 2017).

Les recherches présentées dans cette section ont donné lieu à deux articles scientifiques :

- "*Hot corinos chemical diversity: myth or reality*"
  De Simone M., Ceccarelli C., Codella C., Svoboda B.E., Chandler C. ,Bouvier M., Yamamoto S., Sakai N., Caselli P., Favre C., Loinard L., Lefloch B., Baobab Liu H., López-Sepulcre A., Pineda J.E., Taquet V., and Testi L.
  Publié dans le *Astrophysical Journal Letters, 2020, 896, L3*.

  Il a été associé à un *communiqué de presse* de NRAO (National Radio Astronomy Observatory) in USA, INAF (Istituto Nazionale Astrofisica Italiana) in Italy, and CNRS (Centre National de la Recherche Scientifique) in France.
  CNRS_PressLink, UGA_PressLink NRAO_PressLink, INAF_PressLink,

- "*Tracking the ice mantle history in the NGC 1333 IRAS 4 protostars*".
  De Simone M., Ceccarelli C., Codella C., Svoboda B.E., Chandler C. ,Bouvier M., Yamamoto S., Sakai N., Caselli P., Favre C., Loinard L., Lefloch B., Baobab Liu H., López-Sepulcre A., Pineda J.E., and Testi L.
  L'article est en cours de finalisation et il sera soumis à la *Astrophysical Journal Letters.*

B.2 Projets futurs

B.2.1 Contrainte de l'indice spectral d'opacité de la poussière β dans les protoétoiles IRAS 4A

La variation de la profondeur optique de la poussière en fonction de la fréquence, dans la gamme de longueurs d'onde NIR-millimétrique, peut être approximée par une loi de puissance (e.g., Hildebrand 1983):

$$\tau_\nu \propto \nu^\beta \tag{B.1}$$

où β est ce qu'on appelle l'indice spectral d'opacité de la poussière, et il est lié aux propriétés de la poussière. β dépend de la taille des grains de poussière, de leur composition chimique, de leur porosité, de leur géométrie et de la distribution de la taille des grains (e.g., Pollack et al. 1994; Draine 2006; Natta et al. 2007). En particulier, elle est largement sensible à la taille des grains, c'est-à-dire que les plus gros grains donnent des valeurs de β plus petites. Par exemple, indépendamment de toutes les incertitudes sur le modèle de poussière, les grains de poussière dont la taille est de l'ordre de 1 mm ou plus conduisent à des valeurs de β inférieures à 1 (Natta & Testi 2004).

Par conséquent, l'indice spectral d'opacité de la poussière change avec le stade évolutif des sources : les valeurs les plus élevées ont été mesurées vers les noyaux pré-stellaires avec $1 < \beta < 2.7$ (e.g., Shirley et al. 2011; Schnee et al. 2010; Sadavoy et al. 2013; Bracco et al. 2017), tandis que les valeurs les plus faibles ont été mesurées vers les proto-étoiles de classe II, hôtes de disques protoplanétaires, avec $0 < \beta < 1$ (e.g., Ricci et al. 2010a,b; Bracco et al. 2017; Tazzari et al. 2021). Les premières études des proto-étoiles de classe 0 et I ont trouvé des valeurs intermédiaires. $\beta \sim 1.7 - 2$ (Natta et al. 2007).

Cependant, des études plus récentes portant sur des proto-étoiles de classe 0 ont souvent trouvé des valeurs inférieures à 1, ce qui suggère que la croissance des grains pourrait déjà être à l'œuvre à ces stades précoces. (e.g., Jørgensen et al. 2007; Li et al. 2017; Galametz et al. 2019; Bouvier et al. 2021).

Généralement, la méthode utilisée pour dériver l'indice spectral de la poussière consiste à ajuster la SED (Spectral Energy Distribution) à différentes longueurs d'onde (du sub-mm au radio). En utilisant l'équation B.1 et sachant que la densité de flux F_ν est donnée par

$$F_\nu = B_\nu(T)(1 - e^{-\tau_\nu}) \, , \tag{B.2}$$

il est possible de relier l'indice spectral β à la densité de flux :

$$\nu^\beta = \ln(1 - F_\nu/B_\nu(T)) \, , \tag{B.3}$$

où $B_\nu(T)$ est le corps noir de la poussière à la température T.

En général, un bon échantillonnage de la SED depuis les bandes centimétriques jusqu'aux bandes submillimétriques permet d'ajuster simultanément la température de la poussière, l'opacité de la poussière et β.

Dans le cas où l'émission de poussière est optiquement mince (i.e., $\tau \ll 1$), et dans la limite de Rayleigh-Jeans ($h\nu/kT \ll 1$) l'équation B.2 peut être simplifiée en $F_\nu \propto \nu^\alpha$ où $\alpha = 2 + \beta$. Sur la base de ces hypothèses, il est possible de dériver β à partir d'observations à deux bandes de fréquence. Cependant, si l'on n'utilise que deux bandes de fréquences, la faible séparation dans la gamme de fréquences et les incertitudes des mesures de flux entraîneraient une grande incertitude dans la dérivation de β. De plus, les hypothèses d'épaisseur optique et de régime de Rayleigh-Jeans ne peuvent pas toujours être appliquées. Par exemple, les sources de classe 0 ont tendance à être fortement obscurcies, même à des longueurs d'onde (sub)millimétriques, de sorte que l'hypothèse de l'épaisseur optique ne tient pas. De plus, à de plus grandes longueurs d'onde, il peut y avoir une contamination de l'émission continue de la poussière, comme l'émission libre. Tous ces effets peuvent conduire à une sous-estimation de β, et donc à des prédictions incorrectes sur la taille des grains. (see, e.g., the discussion in Bouvier et al. 2021).

En ce qui concerne la source cible de ma thèse, IRAS 4A, l'indice spectral beta a été mesuré dans IRAS 4A2 pour être $\sim 1.2 - 1.7$, en utilisant la méthode d'ajustement SED (Jørgensen et al. 2007; Cox et al. 2015; Li et al. 2017). Je propose ici une autre méthode pour dériver l'indice spectral de la poussière β vers la classe 0 IRAS 4A1 et IRAS 4A2 : l'utilisation de l'émission de la raie CH_3OH à trois longueurs d'onde différentes (∼25, ∼143, et ∼206 GHz). En utilisant les observations VLA des raies du méthanol vers le système IRAS 4A, j'ai pu déduire l'opacité de la poussière à des longueurs d'onde mm. Plus précisément, en utilisant les observations du VLA à $\sim$ 25 GHz, j'ai pu dériver la densité et la température du gaz, la densité de la colonne de méthanol et la taille de l'émission, via une analyse LVG non-LTE sur plusieurs lignes de méthanol. En utilisant les conditions de gaz dérivées, j'ai prédit l'intensité théorique des lignes de méthanol à ∼143 GHz, où des observations précédentes ont été effectuées par Taquet et al. (2015). En comparant l'intensité prédite à ∼143 GHz avec la valeur observée, j'ai obtenu l'opacité de la poussière τ_ν dans IRAS 4A1 et IRAS 4A2 via l'équation de transfert radiatif standard :

$$I_\nu^{\rm obs} = I_\nu^{\rm pred} e^{-\tau_\nu}. \tag{B.4}$$

J'ai trouvé $\tau_{\rm 143GHz} \sim 0.3$ pour IRAS 4A2 et $\tau_{\rm 143GHz} > 1.6$ pour IRAS 4A1.

Dans le cadre du grand programme SOLIS, les raies du méthanol sont également détectées vers IRAS 4A2 à $\sim$ 206 GHz. Par conséquent, en utilisant la même méthode, il est possible de déduire l'opacité de la poussière à 206 GHz. En considérant que ν_1 = 143 GHz et ν_2 = 206 GHz, il est alors possible de déduire l'indice spectral de la poussière β comme :

$$\ln\left(\frac{\tau_{\nu_1}}{\tau_{\nu_1}}\right) = \beta \ln\left(\frac{\nu_1}{\nu_1}\right). \tag{B.5}$$

La valeur de β dérivée de cette manière sera une mesure assez directe de β, qui ne dépendra pas de l'approximation de Rayleigh-Jeans ou de l'émission libre.

B.2.2 VLA proposals

I. Diversité chimique des hot corinos : mythe ou réalité ?

Parmi les quelques hot corinos détectés, plusieurs sont des systèmes binaires avec des spectres moléculaires millimétriques très différents. Des exemples illustratifs sont IRAS 16293-2422 dans ρ-Oph, IRAS 4A dans Perseus, et CepE-mm dans Cepheus. IRAS 16293-2422 est composée de deux sources séparées par $\sim 5''$ (∼720 au) : la source A est plus faible en émission continue mm et plus brillante dans les raies iCOMs que la source B : (e.g., Caux et al. 2011;

Pineda et al. 2012; Jørgensen et al. 2016; Manigand et al. 2020). IRAS 4A est également un système binaire composé de IRAS 4A1 et IRAS 4A2, séparés par $\sim 1.''8$ (∼540 au) ; alors que le premier domine le continuum mm, seule la seconde montre des lignes iCOMs brillantes aux longueurs d'onde mm (Taquet et al. 2015; López-Sepulcre et al. 2017; De Simone et al. 2017). En revanche, le système binaire de masse intermédiaire CepE-mm montre un comportement différent par rapport à IRAS 4A et IRAS 16293-2422. En effet, la source qui domine l'émission continue mm, CepE-A, est celle qui montre un contenu chimique riche, alors que le compagnon CepE-B (séparé par $\sim 1.''7$) manque d'émission iCOMs (Ospina-Zamudio et al. 2018, 2019).

Pourquoi les objets coexistants semblent-ils radicalement différents dans leur composition chimique ? Un biais observationnel majeur pourrait être causé par l'opacité de la poussière qui pourrait être très élevée dans les sources de classe 0/I et absorber l'émission de la raie iCOMs. Alternativement, si la contribution de la poussière est négligeable, la source pourrait avoir une région hot corino qui est assez petite pour être diluée par le faisceau. Dans les deux cas, les deux composants du système binaire ne sont pas nécessairement chimiquement différents. Une dernière possibilité est que la source ne possède pas de région hot corino, et donc que la différence dans la composition chimique des deux sources est réelle.

Avec les observations du VLA aux longueurs d'onde centimétriques, où la poussière est plus probablement optiquement mince, (De Simone et al. 2020a) Je pourrais révéler un nouveau hot corino, caché par la poussière, vers IRAS 4A1 (voir Section 4.2). Le cas de l'IRAS 4A est-il unique en son genre ? Manquons-nous des hot corinos autour d'autres proto-étoiles de classe 0 à cause de la contribution de l'opacité de la poussière ?

Dans le cas de IRAS 4A (et probablement dans IRAS 16293) la poussière est responsable de la différence chimique observée aux longueurs d'onde mm. Cependant, le cas du système binaire CepE-mm est encore plus déroutant. En effet, dans CepE-mm, contrairement à IRAS 4A, la proto-étoile qui domine l'émission continue possède une région hot corino détectable aux longueurs d'onde mm, alors que la proto-étoile plus faible ne montre aucune émission iCOM. Par conséquent, la différenciation chimique dans les systèmes binaires CepE est-elle un mythe ou une réalité ? Tout d'abord, il est nécessaire d'exclure absolument l'effet d'opacité de la poussière en passant à des observations à haute résolution angulaire centimétrique avec le VLA.

A cette fin, j'ai proposé d'observer le système binaire Cep-E en suivant les mêmes observations réalisées vers IRAS 4A dans (De Simone et al. 2020a) avec le VLA en configuration C ($\sim 1''$ de résolution angulaire). J'ai ciblé plusieurs lignes de méthanol en bande K avec le VLA, pour évaluer si un hot corino est présent dans les deux composantes de Cep-E, et plusieurs lignes de NH_3 pour contraindre la température du gaz. En effet, les raies de l'ammoniac peuvent être utiles en cas de non-détection du méthanol, car elles pourraient aider à expliquer l'absence d'une région de hot corino si la température dérivée est inférieure aux 100 K attendus.

- Cette proposal a été soumise au semestre VLA 2021A. Elle a été approuvée avec *22 heures d'observation*. Les observations ont été réalisées en août-septembre 2021.

II. Suivre l'histoire du manteau de glace des bébés étoiles

La composition des manteaux de grains glacés est cruciale pour établir la diversité chimique observée dans les hot corinos de classe 0/I.

En utilisant des observations JVLA vers le système protobinaire IRAS4A, j'ai détecté plusieurs transitions de CH_3OH et NH_3. En effectuant une analyse multiligne non-LTE via le code LVG `grelvg` (Ceccarelli et al. 2003) j'ai pu dériver le rapport d'abondance NH_3/CH_3OH. En comparant les valeurs observées avec les prédictions théoriques du modèle astrochimique GRAINOBLE (Taquet et al. 2012b; Ceccarelli et al. 2018), j'ai pu contraindre les conditions du clump pré-collapse à une échelle de ∼70 au.

Afin de faire un pas de plus, je propose d'obtenir les mêmes observations vers un autre système binaire de classe 0, IRAS 2A, avec la configuration JVLA B (résolution angulaire de $\sim 0\farcs3$). IRAS 4A et IRAS 2A font toutes deux partie de la région de NGC 1333 qui est l'un des sites les plus actifs de formation d'étoiles en cours dans le voisinage du Soleil et qui est connu pour être fortement façonné par des événements externes qui pourraient avoir déclenché la formation d'étoiles : (e.g. Sandell & Knee 2001; Dhabal et al. 2018). Dans un travail récent, des preuves du clash d'une bulle en expansion avec le filament sud de NGC 1333, auquel appartiennent IRAS 4A et IRAS 2A, ont été rapportées (Dhabal et al. 2019). Cet affrontement pourrait avoir déclenché l'effondrement et, par conséquent, la formation des deux protoétoiles. Si elles ont été reliées par le même sort, IRAS 4A et IRAS 2A devraient avoir une histoire similaire de manteau de grains. Afin de vérifier ce scénario, nous proposons de mesurer le rapport d'abondance NH_3/CH_3OH dans IRAS 2A et de le comparer à celui mesuré vers les sources IRAS 4A.

Le système IRAS 2A a été initialement observé avec des observations mm à la fois mono-plateau et interférométriques (avec une résolution angulaire $\geq 0.''8$) révélant la présence d'un hot corino avec une taille déconvoluée estimée à $0.''4$ (Bottinelli et al. 2007; Maury et al. 2014b; Taquet et al. 2015; Coutens et al. 2015; De Simone et al. 2017). Ce n'est qu'en 2015 que Tobin et al. a imagé l'émission continue cm de IRAS 2A avec JVLA, révélant les deux sources binaires, VLA1 et VLA2 séparées de $\sim 0.''6$ (∼180 au, voir figure 4.8). Cependant, la complexité chimique des sources individuelles est encore inconnue car, jusqu'à présent, aucune observation de molécules complexes n'a été faite avec une résolution angulaire suffisante pour démêler les deux proto-étoiles. Dans cette perspective, les futures observations ALMA ou NOEMA avec une résolution angulaire $\leq 0.''5$, ciblant plusieurs molécules organiques complexes avec une large couverture spectrale, seront idéales pour caractériser complètement la composition chimique du système. Je propose ici de commencer leur caractérisation par l'observation du méthanol, la plus simple des iCOMS.

- Je prévois de soumettre cette proposition, pour 20 heures d'observation, au semestre 2023A du VLA en utilisant la configuration B (résolution angulaire de $0.''3$).

C

Synthèse de molécules organiques complexes

C.1 Contrainte des itinéraires de formation des iCOMs

Depuis la découverte de molécules organiques complexes interstellaires (iCOMs, molécules saturées contenant des hétéroatomes et au moins six atomes; Herbst & van Dishoeck 2009; Ceccarelli et al. 2017) dans des proto-étoiles de type solaire (Cazaux et al. 2003), la question de savoir si elles ont joué un rôle dans l'apparition de la vie sur Terre (et ailleurs dans l'Univers) a été soulevée. En particulier, les iCOMs pourraient avoir fourni les briques pour construire des molécules pré-biotiques.

Jusqu'à présent, environ 250 espèces ont été détectées dans le milieu interstellaire ou dans les coquilles circumstellaires: (CDMS; Müller et al. 2005; McGuire 2018, 2021). Pourtant, il n'existe pas de théorie fiable pouvant expliquer entièrement l'abondance observée dans les différents environnements où ces iCOMs sont détectés. De nos jours, deux paradigmes principaux sont invoqués (e.g., Herbst 2017) qui soutiennent que les iCOMs sont soit synthétisés à la surface des grains (e.g., Garrod & Herbst 2006; Garrod 2008; Jin & Garrod 2020) soit en phase gazeuse (e.g., Millar et al. 1991; Balucani et al. 2015; Skouteris et al. 2018). Comme point de départ, les deux voies ont la formation de molécules hydrogénées simples sur les manteaux des grains de poussière pendant la phase préstellaire. Déterminer laquelle des deux voies de synthèse des iCOMs est la plus efficace et où se forment les iCOMs n'est pas une tâche simple. De nombreuses méthodes ont été utilisées, de la comparaison des abondances mesurées des iCOMs dans les noyaux chauds/corinos avec les prédictions des modèles à leur fractionnement en deutérium mesuré (Turner 1990; Ceccarelli et al. 1998; Coutens et al. 2016; Skouteris et al. 2017, 2018; Jørgensen et al. 2018; Vazart et al. 2020).

Une autre méthode, qui s'est avérée très efficace, consiste à comparer les abondances de l'iCOMs vers les régions de jets de faible masse avec les prédictions du modèle (Codella et al. 2017, 2020a). Cette méthode présente l'avantage que les régions d'outflow choquées fournissent comme contrainte supplémentaire la dépendance temporelle. En effet, grâce aux observations interférométriques à haute résolution angulaire, il est possible de localiser l'émission iCOM dans une région particulière, et dans cette région, il est possible d'identifier un événement de choc qui correspond naturellement à un âge cinématique précis (Gueth et al. 1996; Podio et al. 2016).

Une fois le choc passé, la chimie du gaz choqué évolue avec le temps. Ainsi, selon le mécanisme de formation des iCOMs, leur abondance observée dans la phase gazeuse diffère.

Si les iCOMs se forment à la surface des grains, ils sont injectés dans la phase gazeuse juste après le passage du choc, de sorte que leur abondance dans la phase gazeuse va augmenter par bonds puis diminuer en étant détruits par des réactions en phase gazeuse ou gelés sur les manteaux des grains. Au contraire, si les iCOMs sont un produit de la phase gazeuse, ils se forment à partir d'espèces précurseurs de manteau de glace éjectées dans la phase gazeuse, et leur synthèse prend un certain temps. Cela signifie que leurs abondances vont augmenter dans quelques dizaines/milliers d'années (selon l'espèce) après le passage du choc, puis diminuer à cause des réactions ou de la congélation, comme ci-dessus. Par conséquent, la comparaison des abondances d'iCOM observées avec les prédictions du modèle fournit des contraintes fortes sur les voies de formation, car il est possible de faire la comparaison à un âge cinématique précis du choc.

Cette méthode a été appliquée avec succès au choc de l'outflow L1157-B1 pour contraindre la voie de formation du formamide par Codella et al. (2017). En effet, grâce aux observations interférométriques à haute résolution spatiale, les auteurs ont trouvé une différence dans la distribution spatiale entre l'émission d'acétaldéhyde et de formamide, et par conséquent, ils ont pu contraindre la formation de formamide comme étant due à des réactions en phase gazeuse. Ces conclusions s'appliquent uniquement à L1157-B1. Cependant, étant donné sa puissance, il est important d'appliquer la même méthode à d'autres iCOMs et à d'autres chocs protostellaires.

La détection des iCOMs dans les outflows interstellaires de faible masse a commencé par l'observation d'un seul plat vers une poignée d'objets : plusieurs iCOMs vers L1157-B1 (Arce et al. 2008; Lefloch et al. 2017), le formamide vers L1157-B2 (Mendoza et al. 2014), l'acétaldéhyde vers IRAS 2A et IRAS 4A (Holdship et al. 2019), et l'acétaldéhyde et l'éther diméthylique vers SMM4-W (Öberg et al. 2011b). Cependant, ces études n'ont pas pu démêler la distribution spatiale des iCOMS.

Afin d'appliquer la méthode expliquée ci-dessus, des observations interférométriques sont nécessaires et, jusqu'à présent, seul le flux sortant de L1157-B1 a été observé à une résolution angulaire suffisante pour démêler l'émission des iCOMs. À cette fin, j'ai utilisé des observations à haute résolution angulaire ($\sim 2''$) du système IRAS 4A, dans le cadre du programme NOEMA Seed Of Life (SOLIS) Large, pour explorer le contenu moléculaire de ses outflows.

Les recherches présentées dans cette section ont donné lieu à un article scientifique :

- "Seeds of Life in Space (SOLIS) X. Interstellar Complex Organic Molecules in the NGC 1333 IRAS 4A outflows "
  De Simone M., Codella C., Ceccarelli C., López-Sepulcre A., Witzel A., Neri R., Balucani N., Caselli P., Favre C., Fontani F., Lefloch B., Ospina-Zamudio J., Pineda J. E., and Taquet V.
  Publié dans *Astronomy and Astrophysics, 2020, 640, A75*.

C.2 Projets futurs

C.2.1 Voies de formation du formamide et de l'acétaldéhyde

Le formamide et l'acétaldéhyde sont deux iCOMs largement détectés dans les environnements interstellaires, tels que les hot corinos et les régions choquées (e.g., Cazaux et al. 2003; López-Sepulcre et al. 2015, 2017; Lefloch et al. 2017; López-Sepulcre et al. 2019; De Simone et al. 2020b; Codella et al. 2015a, 2017, 2020a). Cependant, leur voie de formation fait encore l'objet de débats : (e.g., Skouteris et al. 2017; Codella et al. 2017, 2020a; Rimola et al. 2018; Enrique-Romero et al. 2019, 2021).

Une voie de réaction possible pour le formamide implique la réaction en phase gazeuse entre le formaldéhyde (H_2CO) et le radical amidogène (NH_2), qui peut être formé à partir de l'ammoniac ou par la protonation/hydrogénation partielle de l'azote atomique: (e.g., Barone et al. 2015; Vazart et al. 2016; Skouteris et al. 2017). D'autre part, les observations astronomiques montrent une bonne corrélation linéaire entre l'acide isocyanique (HNCO) et le formamide (NH_2CHO), ce qui pourrait suggérer l'hydrogénation du HNCO sur la glace comme une voie de formation plausible du formamide. Cependant, il a été démontré que l'hydrogénation de HNCO sur une surface d'eau solide amorphe est un processus très lent: (Noble et al. 2015; Song & Kästner 2016). On a également pensé que le formamide se formait à la surface des grains par la réaction radicalaire NH_2 + HCO (e.g., Garrod 2008). Cependant, cette réaction est en concurrence avec la formation de NH_3 et de CO, le produit de l'extraction directe de H de HCO et NH_2. L'apparition de l'une ou l'autre voie dépend de l'orientation relative des radicaux en réaction et de la morphologie de la glace d'eau : (Rimola et al. 2018; Enrique-Romero et al. 2019, 2021, 2021b). Une autre possibilité est la réaction entre un radical CN en phase gazeuse avec des molécules d'eau appartenant au manteau de glace lorsque le premier se pose sur elles. Il s'agit d'une réaction à plusieurs étapes qui peut conduire au formamide grâce à la formation initiale d'une hémibondation entre le CN et l'eau, en supposant qu'il n'y ait pas de pertes d'énergie significatives dans le manteau de glace après chaque étape de la réaction (Rimola et al. 2018).

La formation d'acétaldéhyde en phase gazeuse peut se produire par deux réactions possibles: i) la réaction entre le radical éthyle (CH_3CH_2) avec l'oxygène atomique ; ii) la réaction entre l'éthanol (CH_3CH_3OH) avec OH et Cl et conduisant à la formation d'acétaldéhyde en phase gazeuse, et iii) la réaction entre l'éthanol (CH_3CH_3OH) avec OH et Cl et conduisant à la formation d'acétaldéhyde, d'acide formique et d'acide acétique ; (l'arbre généalogique de l'éthanol; Skouteris et al. 2018; Vazart et al. 2020). En outre, la réaction entre le méthanol CH_3OH et CH (Vasyunin et al. 2017) a été étudiée. Cependant, elle forme principalement du formaldéhyde et de l'éthylène et seulement une fraction négligeable d'acétaldéhyde (Vazart et al. 2020). En revanche, l'acétaldéhyde peut être formé sur le grain interstellaire par la réaction radicalaire entre CH_3 et HCO. Comme dans le cas du formamide, cette réaction entre en compétition avec la formation de CH_4 et de CO par absorption directe d'H (Enrique-Romero et al. 2019, 2020). En outre, une étude récente montre que la réaction peut ne pas se produire du tout, en fonction des caractéristiques de la surface de la glace (Enrique-Romero et al. 2021).

Une méthode qui s'est avérée efficace pour contraindre la voie de formation des iCOMs consiste à comparer les prédictions théoriques avec les abondances d'iCOMs mesurées dans les hot corinos. En particulier, le rapport de deutération des iCOMs a été utilisé avec succès

(Skouteris et al. 2017). En effet, le rapport de deutération dans différentes molécules pourrait fournir la séquence temporelle de leur formation et, éventuellement, des informations sur leur itinéraire de synthèse (e.g., Caselli & Ceccarelli 2012; Ceccarelli et al. 2014). Jusqu'à présent, le formamide deutéré n'a été détecté que vers une seule source, le hot corino IRAS16293-2422 B par Coutens et al. (2016). Ils ont trouvé des rapports d'abondance NH_2DCO/NH_2CHO et $NHDCHO/NH_2CHO$ similaires autour de $0,02-0,05$ et ont suggéré une formation de NH_2CHO à la surface des grains. En effet, compte tenu du pourcentage relativement faible de formamide deutéré par rapport au formaldéhyde, ils ont suggéré une préférence pour la synthèse sur glace, car les voies en phase gazeuse devraient surtout conserver le rapport de deutération des molécules parentes (NH_3 et H_2CO). Cependant, Skouteris et al. (2017) a par la suite effectué des calculs de chimie quantique montrant que les précurseurs et la deutération du formamide sont en parfait accord avec les observations de Coutens et al. (2016), soutenant la voie en phase gazeuse.

La même approche utilisée par Skouteris et al. (2017) pour contraindre la voie de formation du formamide peut être utilisée pour étudier la voie de formation d'autres iCOMs. À cette fin, je propose d'observer les formes deutérées de l'acétaldéhyde et du formamide dans le hot corino IRAS 4A2, en utilisant les données du grand programme ALMA FAUST. En effet, récemment, les réactions chimiques en phase gazeuse conduisant à l'acétaldéhyde, et à ses formes deutérées, ont été étudiées par des calculs de chimie quantique: (Vazart et al. 2020, 2021). De plus, les premiers spectres ALMA préliminaires vers IRAS 4A2 montrent que le CH_3CDO est bien détecté (voir figure 5.8).

Enfin, la même approche pourrait être réalisée pour le glycolaldéhyde dès que les résultats de calcul seront disponibles (Vazart et al. en préparation pour la formation en phase gazeuse, Enrique-Romero et al. en préparation pour la formation à la surface des grains).

D

Effets collatéraux

Les nuages moléculaires formant les étoiles de type solaire sont dominés par un réseau complexe de filaments qui sont largement reconnus comme jouant un rôle important dans le processus de formation des étoiles. En effet, la plupart des jeunes étoiles et des noyaux sont encastrés dans ces filaments : (e.g., Schneider & Elmegreen 1979; Goldsmith et al. 2008). Cette caractéristique est montrée comme étant omniprésente par les cartes à grande échelle de l'observatoire spatial Herchel et des satellites Planck (e.g., Molinari et al. 2010; Zari et al. 2016). Cependant, le processus exact régissant la formation de ces structures filamentaires et leur rôle spécifique dans le déclenchement de la formation d'étoiles sont encore débattus (e.g., Hennebelle & Inutsuka 2019; Robitaille et al. 2020). Outre la présence de champs magnétiques, un processus majeur de leur formation est la compression du gaz moléculaire par des déclencheurs externes, tels que les vents stellaires ou les restes de supernovae, les collisions nuage-nuage et les instabilités gravitationnelles (magnéto-)hydro-dynamiques (e.g., Padoan et al. 2001; Hennebelle 2013; Vázquez-Semadeni et al. 2019; Federrath et al. 2021).

Le nuage moléculaire NGC 1333 héberge un grand nombre de jeunes proto-étoiles associées à des structures filamentaires, probablement façonnées par des déclencheurs externes (e.g., Dhabal et al. 2019). Le filament sud est composé de multiples structures avec des vitesses systémiques et des gradients de vitesse distincts (e.g., Sandell & Knee 2001; Dhabal et al. 2018, 2019). Le système IRAS 4A est situé sur le côté ouest de ce filament. Dhabal et al. (2019) ont émis l'hypothèse que toute la partie sud-ouest de NGC 1333, englobant le filament où se trouve IRAS 4A, est due à une "cellule turbulente" en collision, un clash qui aurait pu déclencher la naissance des proto-étoiles. Cependant, aucune signature spécifique d'un clash, à savoir des chocs, n'a été rapportée jusqu'à présent, laissant sans réponse la question de savoir comment et où l'énergie de ce clash, si elle est réelle, est dispersée.

Dans le cadre du programme NOEMA Seed Of Life (SOLIS), des observations à haute résolution angulaire ($\sim 2''$) de la région à grande échelle ($\sim 60''$; $\sim$18000 au) entourant le système IRAS 4A ont été réalisées en ciblant le méthanol et le SiO. Ces deux espèces sont traditionnellement considérées comme l'un des, sinon le meilleur, traceurs des chocs, où l'on observe que leur abondance augmente radicalement de plusieurs ordres de grandeur : (e.g., Bachiller et al. 1998b, 2001; Arce et al. 2008; Codella et al. 2012; Lefloch et al. 2017; Codella et al. 2020a). L'abondance accrue de SiO est due à la pulvérisation des manteaux des grains et à l'éclatement des noyaux réfractaires des grains, ces deux processus libérant du SiO et du Si (qui est rapidement oxydé en SiO) dans la phase gazeuse : (e.g., Caselli et al. 1997; Schilke et al. 1997; Gusdorf et al. 2008a,b; Guillet et al. 2011). De même, on pense que le CH_3OH est principalement formé sur les surfaces froides des grains (e.g., Watanabe & Kouchi 2002; Rimola et al. 2014) et libéré dans la phase gazeuse par la pulvérisation du manteau des grains (e.g., Flower et al. 2010).

En utilisant les observations SOLIS, j'ai imagé l'émission de SiO et de CH_3OH dans la région IRAS 4A, découvrant la présence de caractéristiques particulières dans la partie sud de la carte. En effet, en plus de l'émission provenant des deux outflows IRAS 4A, trois structures filamentaires allongées ont été détectées au sud du centre de la proto-étoile. Elles montrent un profil spectral très étroit, avec un pic à la vitesse systémique du nuage, et elles ne semblent pas être connectées aux outflows.

En analysant l'émission dans ces structures, j'ai voulu comprendre : i) quelle est l'origine de ces structures, ii) quelle est la cause de la libération de CH_3OH et de SiO à partir des grains, et iii) si elles sont la signature du clash supposé par Dhabal et al. (2019).

Les recherches présentées dans cette section ont donné lieu à un article scientifique :

- "A train of shocks at 3000 au scale? Exploring the clash of an expanding bubble into the NGC 1333 IRAS 4 region. SOLIS XVI"
  De Simone M., Codella C., Ceccarelli C., López-Sepulcre A., Neri R., Rivera Ortiz P.R., Busquet G., Caselli P., Bianchi E., Fontani F., Lefloch B., Oya Y., and Pineda J.E.
  Accepté en *Monthly Notices of the Royal Astronomical Society*.

D.1 Projets futurs

D.1.1 SOFIA proposal

Au cours de mon doctorat et de mon activité de recherche, j'ai eu la possibilité d'interagir avec des chercheurs du NASA Ames Reseach Center dans le cadre d'une conférence internationale. A cette occasion, leur intérêt pour mes études sur les hot corinos et les discussions qui ont suivi ont conduit à un projet de collaboration intéressant, et à une proposition soumise à l'observatoire aéroporté SOFIA, décrite ci-dessous.

Teneur en eau dans les premiers stades des régions de formation de planètes

La présence d'eau sur une planète extraterrestre est une condition cruciale pour son habitabilité (Güdel et al. 2014). Cette petite molécule joue également un rôle important dans le processus de formation des étoiles, permettant aux nuages de s'effondrer en étoiles, agissant comme un refroidisseur de gaz majeur et aidant à la coagulation des grains de poussière glacés dans les planétésimaux et, finalement, les planètes. La mesure de la teneur en eau dans les sources astronomiques est une tâche très difficile, en raison de l'atmosphère terrestre. Les observations réalisées à l'aide de plusieurs instruments, tels que ISO, Spitzer et Herschel, ont montré que l'eau est très abondante dans les régions de formation d'étoiles ($\sim 10^{-4}$ par rapport à H_2 Whittet & Duley 1991; van Dishoeck et al. 2014; Boogert et al. 2015; van Dishoeck et al. 2021). Cependant, il est en grande partie gelé dans les manteaux glacés de poussière (e.g., Boogert et al. 2015), sauf dans les régions chaudes où les glaces d'eau se subliment (Ceccarelli et al. 2000a; Helmich et al. 1996; Coutens et al. 2014) ou dans les régions choquées où elles sont pulvérisées (Liseau et al. 1996; Snell et al. 2000; Nisini et al. 2010).

Dans les protoétoiles de type solaire, les régions sublimées par la glace d'eau sont les hot corinos ($\geq$100 K), denses ($\geq 10^7$ cm^{-3}) et compacts ($\leq$100 au) (Ceccarelli 2004). On les trouve autour des proto-étoiles de classe 0/I (10^{4-5} an ; Andre et al. 2000; De Simone et al. 2017; Bianchi et al. 2019b; Belloche et al. 2020). Des études récentes dans systèmes en formation de type solaire montrent que la formation des planètes commence relativement tôt, dès le stade de la classe I : (e.g., Harsono et al. 2018; Podio et al. 2020; Tychoniec et al. 2020; Sheehan et al. 2020; Segura-Cox et al. 2020). Les structures de lacunes et d'anneaux observées vers des disques protoplanétaires enchâssés dans des proto-étoiles de classe I ont été interprétées comme étant dues à la présence de jeunes planètes ou à leur formation imminente : (e.g., Isella et al. 2016; Andrews et al. 2018; Fedele et al. 2018; Long et al. 2019).

Cependant, l'abondance de l'eau dans ces régions est malheureusement mal connue. En effet, les quelques mesures effectuées avec ISO et Herschel dans les hot corinos ont été principalement limitées aux proto-étoiles de classe 0, trouvant de faibles abondances d'eau ($\sim 10^{-6}$) par rapport à la valeur attendue ($\sim 10^{-4}$) estimée dans les glaces (Ceccarelli et al. 1999, 2000a; Kristensen et al. 2010, 2012; Coutens et al. 2012; Visser et al. 2012). Il est important d'exclure que la faible abondance d'eau mesurée ne soit pas due à un biais d'observation. En effet, les observations ISO souffrent de la taille relativement importante du faisceau, de sorte que seules les lignes d'eau les plus brillantes ont pu être détectées et sont très probablement optiquement épaisses, ce qui en fait de piètres sondes pour les abondances d'eau supérieures à 10^{-6} (Ceccarelli et al. 2000a). De même, HERSCHEL n'a pu observer que des lignes d'eau basses, qui souffrent du même problème. Au contraire, une grande quantité d'eau deutérée (N(HDO)$\sim 4 \cdot 10^{17}$cm^{-2}) a été détectée dans le hot corino de classe I SVS13-A (voir Figure **??**), à l'aide d'observations IRAM 30m à un seul plat et d'observations interférométriques IRAM/-NOEMA dans les programmes ASAI et SOLIS Large, ce qui suggère la présence d'eau en abondance ($\sim 10^{-4}$) à cet endroit (Codella et al. 2016a).

SOFIA/EXES est actuellement la seule installation disponible qui offre une résolution spatiale et spectrale suffisante pour détecter l'émission de lignes d'eau provenant des hot corinos, à l'échelle de quelques secondes d'arc, avec une résolution spectrale de $\sim$5 km s^{-1}, et pour mesurer son abondance. En suivant les prédictions du modèle *ad hoc*, je propose d'observer plusieurs raies d'eau rotationnelles à 22,5-26,5 μm vers le seul hot corino de classe I où la preuve de la présence d'eau est jusqu'à présent connue, NGC 1333 SVS13-A. Les observations demandées permettront d'effectuer une analyse multi-lignes, en utilisant des modèles de transfert radiatif sophistiqués, afin de dériver les propriétés du hot corino SVS13-A, et l'abondance de l'eau. En d'autres termes, il sera possible de mesurer la quantité d'eau disponible dans les régions où les planètes commencent à se former. De plus, en combinant ces observations avec les observations HDO précédentes vers la même source, il sera possible de dériver le rapport de deutération et de le comparer avec celui mesuré dans les corps du système solaire (tels que les comètes et les météorites).

En résumé, la proposition se concentre sur la mesure de la teneur en eau dans la zone de formation des planètes lorsque le processus commence. Il s'agit d'un projet pilote qui fournira des indications précieuses pour comprendre le voyage de l'eau des proto-étoiles aux planètes, et qui servira de guide aux futures observations similaires du télescope spatial James Webb (JWST).

- Cette proposition a été soumise dans le cadre du cycle 9 de SOFIA. Elle a été approuvée avec *pour 4,6 heures d'observation et la mention Très bien.* Les observations seront probablement effectuées en janvier-février 2022.

E

Conclusions

E.1 The main conclusions of an unexpected journey

Le but ultime de cette thèse était de caractériser l'enrichissement moléculaire organique précoce des zones de formation de planètes dans les régions de formation d'étoiles de type solaire. En particulier, j'ai cherché à répondre à deux questions principales, celles rapportées dans la section 1.5.2 :

Q1 : Quelle est l'origine et la nature des hot corinos?

Q2 : Comment sont synthétisées ces molécules organiques complexes ?

Afin de répondre aux questions proposées, j'ai étudié le système binaire IRAS 4A et ses outflows en utilisant des observations interférométriques (sub-)mm et cm avec des installations de pointe, telles que l'IRAM-NOEMA et le VLA, et j'ai effectué l'analyse des lignes moléculaires.

Lorsque j'ai commencé ma thèse, le fait que IRAS 4A soit un système binaire avec des spectres moléculaires millimétriques très différents était connu depuis quelques années, et l'origine de cette différenciation spectrale était encore mystérieuse. En effet, puisque les deux protoétoiles proviennent du même nuage moléculaire et sont supposées être coexistantes, il était intriguant que seule l'une des deux soit entourée d'une région dense de molécules organiques complexes.

J'ai donc commencé à exploiter les nouvelles données NOEMA du grand programme SOLIS vers IRAS 4A. En particulier, la première étape a consisté à étudier la nature et l'origine de la différenciation spectrale entre 4A1 et 4A2. J'ai commencé à rechercher de nouveaux iCOMs pour compléter le recensement de la complexité moléculaire du hot corino connue IRAS 4A2 et pour rechercher par hasard une possible émission d'iCOMs dans les environs d'IRAS 4A1. Cependant, le voyage n'a pas suivi un chemin droit et propre mais a été plein de ramifications inattendues et intrigantes qui ont abouti à cette thèse.

E.1.1 Détermination de la voie de formation de l'acétaldéhyde

Pendant l'exploitation des données NOEMA-SOLIS dans le système binaire IRAS 4A, j'ai remarqué que l'émission de certains iCOMs n'est pas seulement compacte autour du hot corino IRAS 4A2, mais qu'elle trace aussi les deux flux bipolaires provenant des deux proto-étoiles centrales. Cette émission à grande échelle a attiré mon attention, et j'ai décidé de me concentrer sur la caractérisation chimique des outflows moléculaires. Des études interférométriques récentes sur la complexité moléculaire de L1157-B1 ont mis en évidence le rôle des régions choquées par jet dans les proto-étoiles de faible masse comme de parfaits laboratoires astrochimiques où contraindre la voie de formation des iCOMs (e.g., Codella et al. 2017). En effet, l'imagerie des iCOMs dans les régions choquées permet de différencier spatialement l'émission de différents iCOMs et d'utiliser la dépendance temporelle comme contrainte pour retrouver le chemin de formation des iCOMs. Cependant, cette méthodologie n'a été testée que dans L1157-B1, par conséquent, je l'ai employée sur les outflows IRAS 4A.

Grâce aux nouvelles observations à haute résolution de NOEMA-SOLIS, j'ai pu imager l'émission de plusieurs iCOMs dans les outflows émanant de IRAS 4A1 et 4A2 : méthanol, acétaldéhyde, éther diméthylique, et formamide. Les iCOMs détectés ne sont pas distribués de manière homogène dans les outflows : Le méthanol est répandu dans les deux outflows, l'acétaldéhyde n'est brillant que dans les lobes sud, et l'éther diméthylique et le formamide sont concentrés en quelques points compacts le long des outflows. La richesse moléculaire des outflows IRAS 4A était intrigante, étant le deuxième écoulement où l'émission iCOMs a été imagée à haute résolution angulaire, après L1157-B1. De plus, la ségrégation spatiale observée dans l'émission iCOMs méritait une étude plus approfondie. Par conséquent, en collaborant avec les chimistes et les modélisateurs de l'équipe DOC, j'ai pu comparer les abondances d'iCOMs observées dans différentes positions des deux outflows IRAS 4A avec les prédictions théoriques des modèles astrochimiques. Enfin, j'ai pu contraindre la voie de formation de l'acétaldéhyde dans les outflows comme un produit en phase gazeuse, formé par la réaction entre un radical éthyle et un atome d'oxygène. Notez qu'à l'époque, la réaction en phase gazeuse entre l'éthanol et OH conduisant à l'acétaldéhyde (the ethanol tree Skouteris et al. 2018) n'était pas prise en compte, car sa pertinence n'était pas claire (Vazart et al. 2020).

Ce travail a montré les forces de cette méthode pour contraindre les voies de formation des iCOMs et a mis en évidence que la dérivation des rapports d'abondance des iCOMs à partir des observations d'un seul plat peut être dangereuse, car elle ne permet pas de démêler la distribution spatiale des différents iCOMs.

E.1.2 Un choc imprévu qui anime le voyage

En étudiant l'émission de méthanol dans le gaz de l'outflows du système IRAS 4A avec les données NOEMA-SOLIS, j'ai découvert la présence d'une caractéristique particulière. Il existe une structure filamentaire presque perpendiculaire à l'outflow du système IRAS 4A1 et à $10''$ des proto-étoiles centrales. Elle présente un profil spectral très étroit qui culmine à la vitesse systémique du nuage. Il n'y avait aucune preuve que cette caractéristique, que j'ai appelée *finger*, soit liée à l'écoulement. J'ai donc essayé de découvrir son origine.

Étant donné que le méthanol est une espèce de surface de grain, il doit être libéré dans la phase gazeuse par un processus non thermique (tel qu'un choc) étant donné qu'il n'y a pas de sources chaudes dans l'environnement proche du doigt pour entraîner une désorption thermique. Le dispositif NOEMA-SOLIS couvrait également l'une des transitions du SiO, le traceur de choc le mieux connu. J'ai donc imagé la ligne SiO, et j'ai remarqué la présence de trois doigts équidistants et parallèles : celui du nord est le doigt tracé par le méthanol, et les deux autres, détectés uniquement dans SiO, avaient déjà été observés avec le VLA par Choi (2005), même si l'auteur n'a pas trouvé d'explication claire pour leur origine.

J'ai exploré diverses possibilités qui auraient pu conduire à la formation des doigts, et la plus plausible, soutenue par les abondances observées de méthanol et de SiO et la différenciation chimique des doigts, était un train de chocs.

La région de formation d'étoiles NGC 1333 qui abrite IRAS 4A est connue pour être fortement façonnée par des déclencheurs externes, tels que l'explosion d'une ou plusieurs supernovae dans le voisinage et d'autres formes d'activité stellaire. En particulier, il a été suggéré que le filament où se trouve IRAS 4A est le résultat du choc d'une bulle externe en expansion (Dhabal et al. 2019). La présence des doigts ainsi que l'analyse des émissions de méthanol et de SiO soutiennent ce scénario. Par conséquent, j'ai conclu que les doigts observés sont la signature du choc d'une bulle en expansion contre l'enveloppe d'IRAS 4A.

Ce travail a mis en évidence l'importance des observations de traceurs de chocs à haute résolution angulaire en arcsec pour aider à reconstruire l'histoire dynamique des régions de formation d'étoiles comme NGC 1333.

E.1.3 IRAS 4A1 et IRAS 4A2 : deux compagnons apparemment différents

Pendant mon doctorat, j'ai eu l'occasion de me rendre sur le site NRAO Socorro pour réduire les données VLA d'une proposition qui était un projet pilote visant à retrouver l'histoire du manteau de glace de deux sources représentatives de deux classes différentes d'objets, les hot corinos et les objets chauds à chaîne de carbone. Les molécules ciblées étaient l'ammoniac et le méthanol, car elles sont les principaux traceurs en phase gazeuse de la composition du manteau de glace. L'une des deux sources représentatives était le système IRAS 4A.

En réduisant les données, j'ai créé des images préliminaires de l'émission de méthanol vers IRAS 4A. J'ai immédiatement reconnu que l'émission était compacte et bien détectée sur les deux proto-étoiles avec des intensités similaires, contrairement à ce qui avait été trouvé jusqu'à présent aux longueurs d'onde mm dans les études précédentes. Emu par cette incroyable découverte, j'ai concentré mon attention sur l'émission de méthanol vers les deux proto-étoiles afin de comprendre si la poussière était le coupable de l'absorption de l'émission aux longueurs d'onde millimétriques et empêchait la détection de l'iCOMs vers IRAS 4A1. En effet, le méthanol est l'un des iCOMs les plus simples et les précurseurs de nombreuses molécules plus complexes, donc sa détection vers IRAS 4A1 est un signe de la présence d'une complexité chimique encore inconnue. J'ai analysé l'émission de méthanol via un code non LTE, confirmant qu'elle trace le gaz chaud et dense typique des hot corinos, et j'ai comparé les prédictions théoriques aux longueurs d'onde millimétriques avec les observations précédentes.

En conséquence, j'ai rapporté la première détection d'une région de hot corino autour de IRAS 4A1 et j'ai confirmé la supposition initiale : la poussière est le coupable qui cache le hot corino vers IRAS 4A1 et les observations aux longueurs d'onde centimétriques permettent de voir à travers l'épais voile de poussière. De plus, j'ai estimé l'effet de l'opacité de la poussière sur le hot corino connu IRAS 4A2. En effet, la poussière affecte l'émission de la raie millimétrique différemment dans les deux sources, avec une absorption complète dans le cas de IRAS 4A1 et une absorption partielle dans IRAS 4A2. Ceci soulève un avertissement important : Les abondances d'iCOMs dérivées aux longueurs d'onde millimétriques peuvent être fortement sous-estimées par l'absorption de la poussière.

La découverte, la nouveauté de la méthodologie utilisée et l'importance des observations centimétriques dans l'étude correcte des hot corinos ont donné lieu à un communiqué de presse en France par le biais du CNRS, aux États-Unis par le biais de la NRAO et en Italie par le biais de l'INAF.

Les observations de méthanol du VLA ont mis en évidence la présence d'un hot corino autour d'IRAS 4A1 mais elles ne peuvent pas soutenir l'hypothèse qu'une réelle différence chimique existe entre 4A1 et 4A2. A cette fin, je suis revenu à l'objectif initial de la proposition du VLA, et j'ai utilisé les observations VLA de l'ammoniac ainsi que celles du méthanol pour retrouver l'histoire du manteau de glace des deux proto-étoiles. En effet, l'abondance relative de ces deux molécules, qui sont des espèces de surface des grains, dépendrait principalement des conditions gazeuses du clump pré-collapse pendant leur formation dans la phase préstellaire. Si une réelle différenciation chimique existe, elle peut refléter une différence dans la composition du manteau de glace.

J'ai détecté une émission compacte d'ammoniac vers les deux proto-étoiles. J'ai ensuite comparé le rapport d'abondance de l'ammoniac par rapport au méthanol avec les prédictions des modèles astrochimiques dans lesquels les conditions de la phase préstellaire sont modifiées, à savoir la densité et la température du gaz et l'échelle de temps de la formation du manteau de glace. L'idée est que le rapport d'abondance observé reflète celui dans les manteaux de grains au moment de la sublimation de la glace. Avec cette méthode, j'ai pu contraindre les conditions gazeuses de l'amas pré-collision des deux proto-étoiles et mettre en évidence les différences possibles qui auraient pu conduire à des compositions chimiques différentes.

En résumé, ces études ont mis en évidence la grande importance, jusqu'alors non reconnue, des observations centimétriques dans l'étude correcte des hot corinos et dans la compréhension de leur origine et de leur nature.

E.1.4 Remarques finales

Au terme de ce parcours, il est important de comprendre quelle a été ma contribution aux questions auxquelles je souhaitais répondre (Q1 et Q2).

Q1 : En ce qui concerne la question ouverte de la nature et de l'origine des hot corinos, j'ai soulevé un avertissement important avec mes études. Les biais observationnels jouent un rôle énorme dans la caractérisation des hot corinos. En effet, le rôle de la poussière dans la dissimulation des hot corinos est plus important que ce que l'on pensait jusqu'à présent. Avec ce travail, j'ai ouvert la *boîte de Pandore*. En effet, j'ai montré comment les abondances des iCOMs estimées aux longueurs d'onde mm peuvent être fortement sous-estimées à cause de l'absorption de la poussière. Pour faire face à ce problème, j'ai utilisé des observations centimétriques pour étudier les raies moléculaires, afin i) d'estimer la contribution de l'opacité de la poussière aux longueurs d'onde millimétriques, et ii) de retrouver l'histoire du manteau de glace d'une proto-étoile de type solaire d'une manière indirecte. Ce travail ouvre la voie à de nouvelles observations avec les futures installations de longueurs d'onde centimétriques.

Q2: Regarding the open question of the iCOMs formation, I demonstrated how important is the close collaboration between observers, chemists, and modelers. Indeed, thanks to the different expertise, it was possible to efficiently exploit the observational data to constrain the formation route of acetaldehyde as a gas phase product in shocked regions.

This is just a first step toward the full comprehension of the general problem, and future works will help in completing the scenario.

F Perspectives

Dans le cadre de ma thèse, j'ai exploré certaines des principales questions ouvertes liées à l'enrichissement chimique des hot corinos, des régions de formation de planètes au stade précoce. J'ai fourni les premières pièces du grand puzzle qu'est l'image du hot corino. Cependant, il reste encore beaucoup à faire pour combler les lacunes et parvenir à une caractérisation complète.

Dans ce qui suit, je propose quelques études de suivi pour continuer le voyage que j'ai commencé il y a trois ans, divisé en une vue à court et à long terme.

F.1 Perspectives à court terme

F.1.1 La différenciation chimique des hot corino binaries

Une partie du travail que j'ai effectué au cours des trois dernières années porte sur l'origine de la différenciation chimique observée dans le système binaire IRAS 4A. J'ai utilisé des observations centimétriques pour i) comprendre le rôle de la poussière dans l'absorption des raies millimétriques iCOMs et ii) retrouver l'histoire du manteau de glace des deux proto-étoiles coéternelles. En particulier, j'ai montré que, dans le cas de IRAS 4A, la poussière est le protagoniste qui cache le hot corino vers la source de continuum millimétrique la plus brillante. Cependant, on peut se demander si le cas d'IRAS 4A est unique ou si d'autres hot corinos autour de proto-étoiles de classe 0 sont absents car leurs lignes iCOMs sont absorbées par la poussière. Je propose d'étudier plus avant si la poussière est responsable de la différenciation chimique observée dans les spectres à ondes millimétriques d'autres systèmes binaires.

- Parmi tous les systèmes binaires, le CepE-mm de classe 0 est un système particulier. La source de continuum millimétrique la plus brillante abrite une région hot corino, tandis que le compagnon plus faible ne présente pas d'émission iCOMs. Quel est le rôle de la poussière dans ce cas ? La différence chimique entre les deux proto-étoiles du système CepE-mm est-elle apparente ou réelle ? A cette fin, j'ai fait une proposition d'observation ciblant les raies du méthanol et de l'ammoniac à des longueurs d'onde cm vers le système CepE-mm avec l'interféromètre VLA. La proposition a été acceptée, et les données ont été observées en septembre 2021. Par conséquent, j'ai l'intention de réduire et d'analyser ces données et de les combiner avec les observations millimétriques obtenues dans le cadre du programme SOLIS Large afin de déterminer si la différenciation chimique dans CepE est réelle ou non.

- Un autre système binaire est NGC 1333 IRAS 2A. Il fait partie, avec IRAS 4A, du filament sud de la région de formation d'étoiles de Persée NGC 1333. Dans mon travail de thèse, j'ai rapporté des preuves du choc d'une bulle en expansion avec ce filament qui aurait pu déclencher l'effondrement et, par conséquent, la formation des deux systèmes protostellaires. Si les deux systèmes protostellaires sont liés par le même destin, IRAS 4A et IRAS 2A devraient avoir une histoire similaire de manteau de grains. Par conséquent, je prévois d'observer les raies du méthanol et de l'ammoniac avec le VLA à haute résolution angulaire pour résoudre le système binaire d'IRAS 2A, afin i) de retrouver l'histoire du manteau de glace des deux proto-étoiles et de la comparer à celle d'IRAS 4A, et ii) de faire une première caractérisation chimique des deux compagnons d'IRAS 2A en utilisant le méthanol, l'iCOM le plus simple. En effet, aucune observation des lignes iCOMs n'a été effectuée jusqu'à présent vers IRAS 2A avec une résolution angulaire suffisante pour résoudre les deux compagnons.
- Dans le cadre du suivi de ces propositions, j'aimerais construire une première grande étude de dizaines de hot corinos de type solaire observés à l'échelle de la formation des planètes afin de caractériser la diversité chimique des hot corinos et de fournir leur composition chimique réelle. J'utiliserais des observations centimétriques et millimétriques, en combinant les observations VLA, ALMA, et IRAM/NOEMA déjà en ma possession avec des données d'archives publiques et des propositions de suivi dédiées.
- Toutes les observations du méthanol effectuées à des longueurs d'onde centimétriques peuvent être combinées avec les précédentes à des longueurs d'onde millimétriques pour contraindre l'indice spectral de la poussière β. Ce facteur est largement sensible à la taille des grains, c'est-à-dire que les gros grains donnent de petites valeurs de β. Par conséquent, il est généralement utilisé pour retracer la croissance des grains. Typiquement, il est dérivé en ajustant la distribution de l'énergie spectrale à différentes longueurs d'onde (du sub-mm à la radio). Cependant, cette méthode dépend de plusieurs hypothèses. En utilisant les observations du méthanol à différentes longueurs d'onde (par exemple, 25 GHz, 143 GHz, 206 GHz), et en considérant qu'aux longueurs d'onde centimétriques la poussière est probablement optiquement mince, je propose de récupérer l'indice spectral de la poussière dans les sources de classe 0 d'une manière plus directe.
- Si la formation de la planète commence tôt, dans la phase de classe 0/I, il est important d'évaluer l'abondance de l'eau à ce stade. Cependant, elle est malheureusement peu contrainte, principalement en raison de biais observationnels. SOFIA/EXES est la seule installation disponible qui offre une résolution spatiale et spectrale suffisante pour détecter l'émission de la raie de l'eau dans les hot corinos et pour mesurer son abondance. Par conséquent, j'ai fait une proposition d'observation SOFIA pour observer les raies d'émission de l'eau à 22.5-26.5 μm vers le seul hot corino de classe I où la preuve de la présence d'eau est jusqu'à présent connue, SVS13-A. En effet, l'eau deutérée (HDO) a été détectée en émission compacte vers le hot corino de classe I SVS13-A avec des installations à une seule antenne et avec les données NOEMA/SOLIS.

F.1.2 Les parcours de formation de l'iCOMs

Dans mon travail de thèse, j'ai montré que la comparaison des abondances d'iCOMs vers les régions choquées par jet de faible masse avec les prédictions des modèles est une méthode puissante pour contraindre les routes de formation des iCOMs. Une autre méthode consiste à comparer les abondances d'iCOMs dans les hot corinos avec les prédictions théoriques. En particulier, le rapport de deutération des iCOMs a été utilisé avec succès à cette fin grâce aux nouveaux résultats des calculs de chimie quantique (Skouteris et al. 2017). Le rapport de deutération dans différentes molécules pourrait fournir la séquence temporelle de leur formation et, éventuellement, des informations sur leur itinéraire de synthèse.

Cependant, très peu de molécules organiques complexes deutérées ont été détectées, et seulement dans une cible, le hot corino IRAS 16293-2422 (Coutens et al. 2016; Manigand et al. 2020). Je propose d'observer la forme deutérée du formamide et de l'acétaldéhyde dans le hot corino IRAS 4A2, en utilisant les données obtenues dans le cadre du grand programme ALMA/FAUST. En utilisant les résultats de calcul pour le formamide par Skouteris et al. (2017) et l'acétaldéhyde par Vazart et al. (2020), je peux contraindre leur route de formation dans IRAS 4A2 et comparer les résultats avec ceux obtenus dans IRAS 16293-2422. De plus, la même méthodologie peut être appliquée au glycolaldéhyde une fois que les résultats de calcul seront disponibles (Vazart et al. et Enrique-Romero et al. en préparation, faisant tous deux partie du groupe DOC).

F.2 Perspectives à long terme

F.2.1 Une approche multi-longueurs d'onde pour dévoiler la nature des hot corinos

Une des conclusions principales de ma thèse est l'importance des observations centimétriques dans l'étude et la caractérisation correcte des hot corinos. En particulier, j'ai montré comment quantifier la contribution de l'opacité de la poussière dans l'absorption des lignes d'émission iCOMs dans les hot corinos et comment étudier indirectement la composition du manteau de glace en observant les principaux composants de la glace une fois libérés dans la phase gazeuse.

Historiquement, l'étude des hot corinos a été principalement réalisée à des longueurs d'onde (sub)millimétriques. Cela s'explique par le fait que les lignes d'émission rotationnelle les plus intenses des molécules organiques complexes prébiotiques se situent dans cette gamme. Des installations interférométriques de pointe comme ALMA et IRAM-NOEMA sont utilisées grâce à leur haute sensibilité et leur résolution angulaire.

Cependant, les hot corinos peuvent être riches en différentes iCOMs, plus ou moins complexes, dont l'émission peuple le spectre, apparaissant comme une *forêt* de lignes. Les spectres (sub-)mm riches en raies aux longueurs d'onde millimétriques seront alors affectés par deux problèmes principaux :

i) *L'opacité de la poussière.* Elle a un impact plus important en se déplaçant vers les fréquences plus élevées, et elle peut absorber les raies d'émission des iCOMs conduisant à une sous-estimation de leur densité de colonne. Finalement, elle peut absorber complètement les lignes d'émission des iCOMs qui cachent les hot corinos.

ii) *Confusion des raies.* En effet, la haute sensibilité des installations de pointe permet la détection d'espèces moins abondantes avec des transitions de faible intensité. Par conséquent, il y a une forte probabilité que les lignes observées soient confondues, considérant que, dans les hot corinos, les profils de lignes sont généralement de $\sim$3 km s^{-1}. Par conséquent, en dessous d'un certain seuil de limite de confusion, il sera impossible d'identifier les lignes et d'extraire des informations des spectres.

Pour surmonter ces problèmes, une possibilité est d'observer les hot corino à des longueurs d'onde centimétriques, puisque :

i) La poussière est plus probablement optiquement mince, de sorte que les hot corino cachés peuvent être révélés, comme dans le cas de IRAS 4A1. En outre, l'opacité de la poussière peut être estimée, et les abondances iCOMs dérivées aux longueurs d'onde millimétriques peuvent être corrigées.

ii) Il est possible d'étudier l'histoire du manteau de glace des proto-étoiles de type solaire grâce aux observations simultanées des traceurs critiques en phase gazeuse des principales espèces du manteau de glace (NH_3 et CH_3OH).

iii) La confusion des lignes est moins importante car le spectre est moins peuplé par la transition rotationnelle de molécules plus légères et plus petites.

iv) Il est possible d'observer des molécules plus lourdes et plus grandes car leur spectre de rotation est décalé vers les basses fréquences.

L'installation centimétrique interférométrique de pointe actuelle est le Very Large Array (VLA). La haute résolution angulaire fournie par les interféromètres est cruciale pour résoudre les hot corino, cartographier leur distribution et étudier leur cinématique.

Comme je l'ai montré dans cette thèse, le VLA est actuellement l'instrument le plus puissant pour étudier et caractériser les hot corino à des longueurs d'onde centimétriques. En effet, j'ai pu détecter l'émission de méthanol dans le cm avec une sensibilité suffisante ($S/N\sim10$) en utilisant un temps d'intégration raisonnable. Cependant, je n'ai pas pu détecter des molécules plus complexes, c'est-à-dire le formamide, le glycolaldéhyde, le formate de méthyle). Cela est dû au fait que leurs lignes d'émission, étant donné leurs faibles abondances, se situent en dessous du seuil de détection. Par conséquent, la détection de molécules plus complexes et moins abondantes que le méthanol et la réalisation d'un relevé spectral non biaisé avec une résolution spectrale suffisante et une grande largeur de bande restent un défi en termes de sensibilité.

Pour surmonter ces problèmes de sensibilité, deux nouvelles installations interférométriques centimétriques sont en cours de développement : ngVLA et SKA. Elles offriront une sensibilité et une résolution angulaire sans précédent. En outre, la mise à niveau de l'ALMA est prévue avec la bande 1 à venir.

En résumé, je pense que des observations millimétriques et centimétriques complémentaires sont nécessaires pour caractériser la nature des hot corinos.

Aux longueurs d'onde millimétriques, il est possible de détecter de petits iCOMS et d'étudier à travers eux la cinématique de la source.

Aux longueurs d'onde centimétriques, il est possible de rechercher des iCOMs plus grands et plus lourds et d'étudier leur distribution.

En complétant les observations millimétriques par des observations centimétriques, il est possible de quantifier la contribution de l'opacité de la poussière et de corriger les abondances des iCOMs estimées aux longueurs d'onde millimétriques par le facteur d'opacité. Enfin, il sera possible de détecter plusieurs transitions du même iCOM dans une large gamme d'énergies d'excitation afin d'obtenir une image complète de l'émission et de dériver fermement les conditions du gaz avec une analyse de transfert radiatif multi-lignes.

F.2.2 Futures installations pour l'étude des hot corinos

Pour surmonter les problèmes de sensibilité, de nouvelles installations centimétriques sont prévues :

- L'interféromètre Very Large Array (ngVLA ; https://ngvla.nrao.edu/) de nouvelle génération sera constitué de 244 antennes de 18 m de diamètre chacune, complétées par un réseau à ligne de base courte de 19 antennes de 6 m de diamètre chacune afin de fournir les lignes de base les plus courtes. Chaque antenne est équipée de récepteurs couvrant la gamme de fréquences de 1,2 − 50 GHz (21-0.6cm) et 70 − 116 GHz (4−2.6mm). Le réseau sera situé près du site actuel du VLA au Nouveau-Mexique, avec une station supplémentaire à ligne de base moyenne répartie en Arizona, au Texas et au Mexique, et un réseau à ligne de base longue à Washington, en Virginie occidentale, en Californie, en Iowa, au New Hampshire, à Hawaï, à Porto Rico, dans les îles Vierges américaines et au Canada. Les lignes de base étendues seront d'au moins plusieurs centaines de kilomètres, fournissant des échelles angulaires jusqu'à la milliarcseconde. En utilisant les lignes de base plus longues, séparément ou avec le réseau principal, il sera possible d'atteindre une résolution de 0,1 milliarcseconde. ngVLA sera environ 10 fois plus sensible que VLA et ALMA pour les observations de lignes spectrales et de continuum.
  En 2023, le premier prototype d'antenne sera livré sur le site du VLA, tandis que la construction du ngVLA devrait débuter en 2025, et la science précoce du ngVLA devrait commencer en 2029.

- Le Square Kilometer Array (SKA ; https://www.skatelescope.org/) sera composé de deux interféromètres, l'un en Afrique du Sud (Mid) et l'autre en Australie (Low), qui se complètent. SKA-Low couvrira la gamme de fréquences 50−350 MHz, et il se compose d'un réseau de 131072 antennes en forme d'arbre de Noël regroupées en 512 stations pouvant atteindre une résolution angulaire de $0\overset{\prime\prime}{.}3$. SKA-Mid couvrira la gamme de fréquences 350 MHz −15,4 GHz (avec un objectif de 24 GHz, et peut-être 50 GHz), et se compose de 197 antennes paraboliques pouvant atteindre une résolution angulaire de $3''$.
  SKA offrira une résolution angulaire de 40−2 milliarcsecondes à 0,5-10 GHz. Il aura une sensibilité aux sources ponctuelles de 4 à 20 fois supérieure à celle des installations actuelles de pointe et une vitesse de sondage 10 à 100 fois supérieure. La fin de la construction est prévue pour 2029.

- Le récepteur ALMA Bande 1 couvre la bande de fréquences 35−50 GHz (https://www.eso.org/public/usa/announcements/ann16044/). Il permettra à l'ALMA de combler le fossé entre la gamme mm/sub-mm et cm et, étant donné le rapport important de la bande passante disponible, il permet d'étudier une large gamme de régimes d'énergie.

Enfin, les prochaines installations IR d'une sensibilité sans précédent, comme le JWST et l'ELT, permettront de sonder les manteaux de glace à des stades plus évolués, comme les disques protoplanétaires. plus évolués, comme dans les disques protoplanétaires. Il sera alors possible de comparer la composition du manteau de glace des hot corinos de classe 0 avec celle des stades ultérieurs.

Je pense que ces futures installations, combinées aux installations actuelles, constitueront une percée dans l'étude de la complexité chimique des hot corinos. En effet, leur sensibilité et leur résolution angulaire sans précédent permettront de cibler des iCOMs plus complexes dans une gamme spectrale moins affectée par l'opacité de la poussière. De plus, il sera possible de construire de grands relevés d'objets ayant des caractéristiques différentes (par exemple, stade évolutif, environnement d'accueil, etc.) en utilisant une large bande passante.

Nous nous dirigeons vers une ère d'observation exceptionnelle. Je pense qu'il s'agit d'un avenir brillant pour l'astrochimie, plein de nouvelles découvertes et de nouveaux mystères intrigants à résoudre, dont je souhaite faire partie.

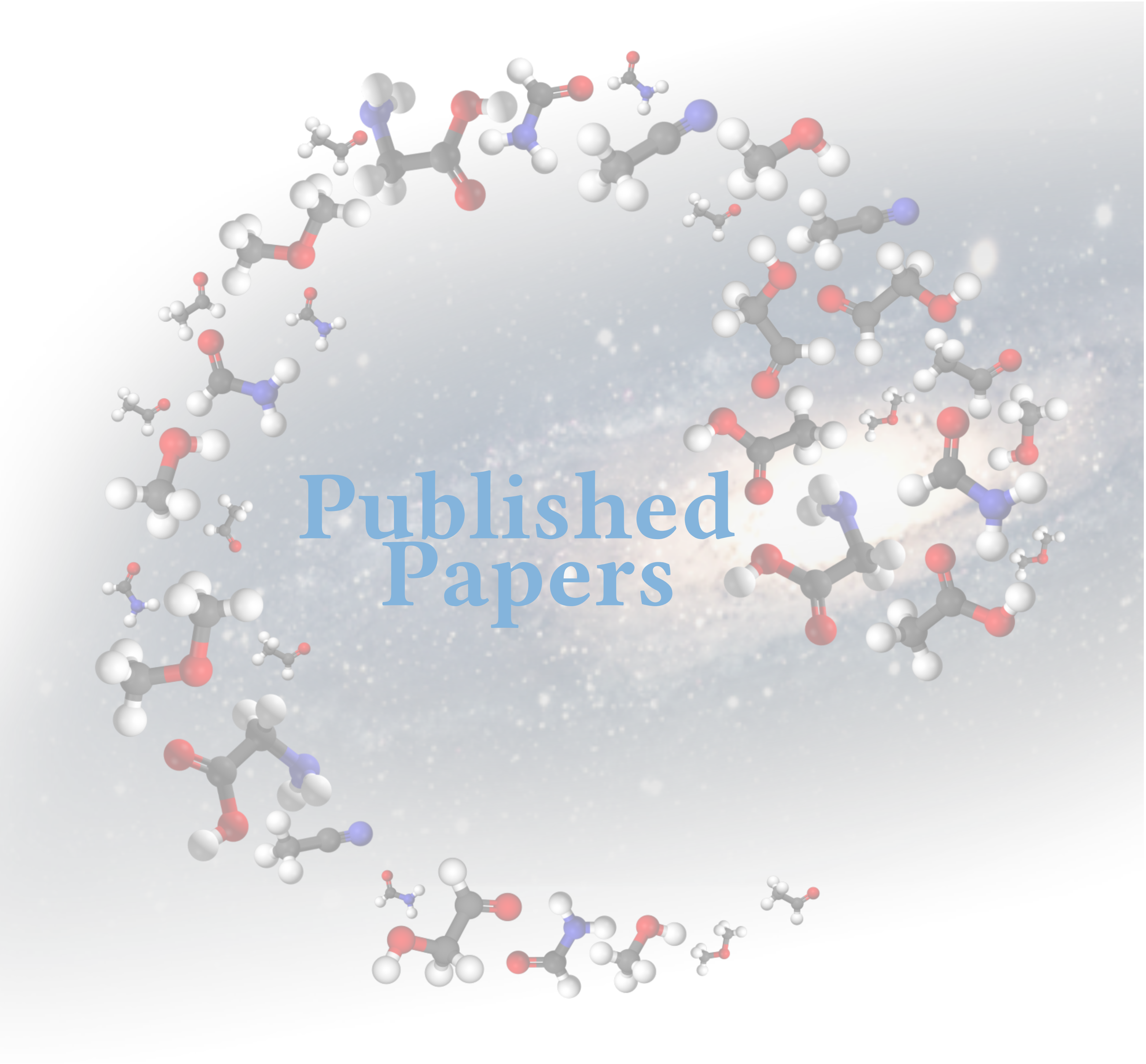

Published Papers

The Astrophysical Journal Letters, 896:L3 (8pp), 2020 June 10 https://doi.org/10.3847/2041-8213/ab8d41

Hot Corinos Chemical Diversity: Myth or Reality?

Marta De Simone[1], Cecilia Ceccarelli[1], Claudio Codella[1,2], Brian E. Svoboda[3,4], Claire Chandler[3], Mathilde Bouvier[1], Satoshi Yamamoto[5], Nami Sakai[6], Paola Caselli[7], Cecile Favre[1], Laurent Loinard[8], Bertrand Lefloch[1], Hauyu Baobab Liu[9], Ana López-Sepulcre[1,10], Jaime E. Pineda[7], Vianney Taquet[2], and Leonardo Testi[2,11,12]

[1] Univ. Grenoble Alpes, CNRS, IPAG, F-38000 Grenoble, France; marta.desimone@univ-grenoble-alpes.fr
[2] INAF, Osservatorio Astrofisico di Arcetri, Largo E. Fermi 5, I-50125 Firenze, Italy
[3] National Radio Astronomy Observatory,[13] 1003 Lopezville Road, Socorro, NM 87801, USA
[4] Steward Observatory, University of Arizona, 933 North Cherry Avenue, Tucson, AZ 85721, USA
[5] Department of Physics, The University of Tokyo, Bunkyo-ku, Tokyo 113-0033, Japan
[6] The Institute of Physical and Chemical Research (RIKEN), 2–1, Hirosawa, Wako-shi, Saitama 351-0198, Japan
[7] Max-Planck-Institut für extraterrestrische Physik (MPE), Giessenbachstrasse 1, D-85748 Garching, Germany
[8] Instituto de Radioastronomía y Astrofísica, Universidad Nacional Autónoma de México Apartado 58090, Morelia, Michoacán, Mexico
[9] Academia Sinica Institute of Astronomy and Astrophysics (ASIAA), No. 1, Section 4, Roosevelt Road, Taipei 10617, Taiwan
[10] Institut de Radioastronomie Millimétrique (IRAM), 300 rue de la Piscine, F-38400 Saint-Martin d'Hères, France
[11] ESO, Karl Schwarzchild Srt. 2, D-85478 Garching bei München, Germany
[12] Excellence Cluster Origins, Boltzmannstrasse 2, D-85748 Garching bei München, Germany

Received 2020 April 7; revised 2020 April 22; accepted 2020 April 25; published 2020 June 8

Abstract

After almost 20 years of hunting, only about a dozen hot corinos, hot regions enriched in interstellar complex organic molecules (iCOMs), are known. Of them, many are binary systems with the two components showing drastically different molecular spectra. Two obvious questions arise. Why are hot corinos so difficult to find and why do their binary components seem chemically different? The answer to both questions could be a high dust opacity that would hide the molecular lines. To test this hypothesis, we observed methanol lines at centimeter wavelengths, where dust opacity is negligible, using the Very Large Array interferometer. We targeted the NGC 1333 IRAS 4A binary system, for which one of the two components, 4A1, has a spectrum deprived of iCOMs lines when observed at millimeter wavelengths, while the other component, 4A2, is very rich in iCOMs. We found that centimeter methanol lines are similarly bright toward 4A1 and 4A2. Their non-LTE analysis indicates gas density and temperature ($\geqslant 2 \times 10^6$ cm^{-3} and 100–190 K), methanol column density ($\sim 10^{19}$ cm^{-2}), and extent ($\sim$35 au in radius) similar in 4A1 and 4A2, proving that both are hot corinos. Furthermore, the comparison with previous methanol line millimeter observations allows us to estimate the optical depth of the dust in front of 4A1 and 4A2, respectively. The obtained values explain the absence of iCOMs line emission toward 4A1 at millimeter wavelengths and indicate that the abundances toward 4A2 are underestimated by $\sim$30%. Therefore, centimeter observations are crucial for the correct study of hot corinos, their census, and their molecular abundances.

Unified Astronomy Thesaurus concepts: Interstellar medium (847); Protostars (1302); Star formation (1569); Chemical abundances (224); Astrochemistry (75)

1. Introduction

Interstellar complex organic molecules (iCOMs) are molecules detected in the interstellar medium containing carbon and at least six atoms (Herbst & van Dishoeck 2009; Ceccarelli et al. 2017). These molecules are of particular interest because they carry a substantial fraction of carbon that can be used for prebiotic chemistry (e.g., Caselli & Ceccarelli 2012).

In solar-like young Class 0 protostars, iCOMs are found in relatively large quantities toward the so-called hot corinos, which are compact ($\leqslant$100 au), hot ($\geqslant$100 K), and dense $\geqslant 10^7$ cm^{-3}) regions enriched in iCOMs at the center of the envelopes accreting the future star (Ceccarelli 2004; Ceccarelli et al. 2007; Caselli & Ceccarelli 2012).

The first hot corino was discovered in 2003 toward the Class 0 source IRAS 16293–2422 (e.g., Cazaux et al. 2003; Jørgensen et al. 2016; Manigand et al. 2020). Since then other Class 0 hot corinos have been discovered: NGC 1333 IRAS 4A (hereafter IRAS 4A; e.g., Bottinelli et al. 2004; Taquet et al. 2015; De Simone et al. 2017; López-Sepulcre et al. 2017; Sahu et al. 2019), NGC 1333 IRAS 2A, NGC 1333 IRAS 4B (e.g., Jørgensen et al. 2005; Bottinelli et al. 2007; Maury et al. 2014; De Simone et al. 2017), HH 212 (Codella et al. 2016; Bianchi et al. 2017; Lee et al. 2017, 2019), B335 (Imai et al. 2016), L483 (Oya et al. 2017; Jacobsen et al. 2019), Barnard1b-S (Marcelino et al. 2018), Ser-emb 1 (Martin-Domenech et al. 2019), and BHR71-IRS1 (Yang et al. 2020). Lately, a few more evolved Class I hot corinos were also discovered: NGC 1333 SVS13A (De Simone et al. 2017; Bianchi et al. 2019), B1a (Öberg et al. 2014), and Ser-emb 17 (Bergner et al. 2019). Therefore, after almost 20 years, only about a dozen hot corinos are known. Recent surveys concluded that $\sim$30% of low-mass Class 0/I protostars show emission from at least three iCOMs (De Simone et al. 2017; Belloche et al. 2020).

Most of the hot corinos cited above turn out to be binary systems when imaged at high angular resolution. This is in agreement with previous surveys that found that 40–60% of protostars are multiple systems (Maury et al. 2014; Tobin et al. 2016). Interestingly, with the first hot corino maps it became

---

[13] The National Radio Astronomy Observatory is a facility of the National Science Foundation operated under cooperative agreement by Associated Universities, Inc.

clear that the two objects in a given binary system can substantially differ in molecular complexity. Illustrative examples are provided by IRAS 16293–2422 and IRAS 4A (Jørgensen et al. 2016; López-Sepulcre et al. 2017). IRAS 16293–2422 is composed of two sources, A and B, separated by $5\overset{\prime\prime}{.}1$ (∼720 au), where source A, weaker in millimeter continuum emission, is brighter in iCOMs lines than source B (e.g., Caux et al. 2011; Pineda et al. 2012; Jørgensen et al. 2016; Manigand et al. 2020). IRAS 4A, located in the NGC 1333 region in the Perseus cloud at a distance of (299 ± 15) pc (Zucker et al. 2018), is also a binary system composed of IRAS 4A1 and IRAS 4A2 (hereafter 4A1 and 4A2), separated by $1\overset{\prime\prime}{.}8$ (∼540 au): while 4A1 is brighter in the millimeter continuum than 4A2, only 4A2 shows bright iCOMs lines (Taquet et al. 2015; De Simone et al. 2017; López-Sepulcre et al. 2017). However, not always the brightest millimeter continuum source in a binary system is the one weak iCOMs emission (see, e.g., Ospina-Zamudio et al. 2018).

In summary, despite two decades of hunting, only a dozen hot corinos are known so far. Of them, many are binary systems with the two components showing drastically different molecular spectra. Two related questions arise: (1) Why are hot corinos so difficult to find? While it is known that not all Class 0/I sources possess hot corinos (e.g., Sakai & Yamamoto 2013; Higuchi et al. 2018; Bouvier et al. 2020), observational biases might hamper their detection. (2) Why do coeval objects seem drastically different in their chemical composition? Is this a real difference or is it only/mostly due to observational biases?

A major observational bias could be caused by the dust opacity, which could be very high in Class 0/I sources, due to their high densities and, consequently, column densities (e.g., Miotello et al. 2014; Galván-Madrid et al. 2018; Galametz et al. 2019). If the effect of dust absorption is not negligible, there are three major consequences: (1) hot corinos may be difficult to detect in the millimeter (also) because of the high dust absorption of the iCOMs lines; (2) the molecular complexity diversity observed in binary system objects may reflect a difference in the front dust column density rather than a real chemical difference of the two objects; (3) the iCOM abundances in hot corinos could have been underestimated so far. In order to test this hypothesis, we targeted the IRAS 4A binary system, where the two objects show extremely different iCOM line spectra at millimeter wavelengths (see above), and carried out observations of several methanol lines, one of the simplest iCOMs, at centimeter wavelengths where the dust is optically thin.

2. Observations

The IRAS 4A system was observed at 1.3 cm using K-band receivers (18–26.5 GHz) of the Karl G. Jansky Very Large Array (VLA) in C-configuration (35–3400 m) on 2018 December 10 (project ID: VLA/18B-166). We targeted 10 CH_3OH lines, with frequencies from 24.9 to 26.4 GHz, upper level energies $E_{\rm up}$ from 36 to 175 K and Einstein coefficients A_{ij} in the range (0.5–1.1) × 10^{-7} s^{-1} (Table 1). The observed spectra were divided into eight spectral windows with ∼0.017 MHz (0.2 km s^{-1}) spectral resolution and ∼1″ (∼300 au at the distance of IRAS 4A) angular resolution. The observations were centered on 4A2, at $\alpha(\rm J2000) = 03^{\rm h}29^{\rm m}10\overset{\rm s}{.}43$, $\delta(J2000) = 31^\circ13'32\overset{\prime\prime}{.}1$. The flux calibrators were J0137+3309 and J0521+1638, while the bandpass and the gain ones were J0319+4130 and J0336+3218, respectively. The absolute flux calibration error is ⩽ 15%.[14]

The data reduction and cleaning process were performed using the CASA[15] package while data analysis and images were performed using the GILDAS[16] package. We obtained a continuum image by averaging line-free channels from all the spectral windows (Figure 1). We self-calibrated, in phase amplitude, using the line-free continuum channels and applied the solutions to both the continuum and molecular lines. The dynamic range, as defined by peak source flux over rms noise, was improved by 20% by the self-calibration. The final rms noise in the continuum image, 3 μJy beam^{-1}, is consistent with that reported by the VLA Exposure Time Calculator for a line-free continuum bandwidth of 4.5 GHz, 26 antennas, and an on-source integration time of 3 hr. The cube was subsequently continuum subtracted, smoothed to 1 km s^{-1} (∼0.08 MHz), and cleaned in CASA using a multiscale deconvolution[17] (scales = [0, 5, 15, 18, 25]) with natural weighting. The synthesized beams for each spectral window are reported in Table 1. The half power primary beam is ∼80″.

3. Results

3.1. Continuum Emission Map

Figure 1 reports the map of the continuum emission at 25 GHz. The two continuum peaks mark the two protostars, whose coordinates ($\alpha(\rm J2000) = 03^{\rm h}29^{\rm m}10\overset{\rm s}{.}536$, $\delta(J2000) = 31^\circ13'31\overset{\prime\prime}{.}07$ for 4A1, and $\alpha(\rm J2000) = 03^{\rm h}29^{\rm m}10\overset{\rm s}{.}43$, $\delta(J2000) = 31^\circ13'32\overset{\prime\prime}{.}1$ for 4A2) are consistent with those derived by Tobin et al. (2016) and López-Sepulcre et al. (2017) with higher angular resolution observations. Since the angular resolution of our observations (∼1″) is smaller than the separation between 4A1 and 4A2 ($1\overset{\prime\prime}{.}8$), they are clearly disentangled in our images, even if individually unresolved with the current resolution.

At centimeter wavelengths, 4A1 shows a brighter continuum emission (due to dust or free–free) than 4A2. The peak fluxes are (2.1 ± 0.3) mJy beam^{-1} and (0.47 ± 0.07) mJy beam^{-1} toward 4A1 and 4A2, respectively. Taking into account the slightly different wavelength (1.05 cm) and angular resolution (∼$0\overset{\prime\prime}{.}1$), these values are consistent with the ones measured by Tobin et al. (2016): (1.3 ± 0.2) mJy beam^{-1} for 4A1 and (0.38 ± 0.04) mJy beam^{-1} for 4A2.

3.2. Methanol Lines

All the targeted methanol lines are detected with a signal-to-noise ratio larger than 3 (Table 1). Their velocity-integrated spatial distribution is shown in Figure 1. The methanol emission peaks exactly toward the 4A1 and 4A2 continuum peaks, and it is well disentangled, even if unresolved at the current angular resolution, around the two protostars.

Figure 2 shows the 10 methanol line spectra, isolated and not contaminated by other species, extracted toward the 4A1 and

---

[14] https://science.nrao.edu/facilities/vla/docs/manuals/oss/performance/fdscale

[15] https://casa.nrao.edu/

[16] http://www.iram.fr/IRAMFR/GILDAS

[17] This technique is a scale-sensitive deconvolution algorithm efficient for images with complicated and extended spatial structures. In fact, it allows us to model the sky brightness as a linear combination of flux components of different scale sizes. The scale sizes are chosen following approximately the sizes of the dominant structures in the image and including the “0” scale to model the unresolved ones (see casadocs-deconvolution-algorithms).

Table 1
Spectral Parameters, Synthesized Beams, and Gaussian Fit Results of the CH_3OH Lines Extracted toward the 4A1 and 4A2 Continuum Peaks

Transition	Frequency[a] (GHz)	E_{up}[a] (K)	log A_{ij}[a]	Synthesized Beam maj × min (PA) ($'' \times ''$ (°))	IRAS 4A1 $\int T_B dV$[b] (K km s^{-1})	IRAS 4A1 V_{peak}[b] (km s^{-1})	IRAS 4A1 FWHM[b] (km s^{-1})	IRAS 4A1 rms[c] (K)	IRAS 4A2 $\int T_B dV$[b] (K km s^{-1})	IRAS 4A2 V_{peak}[b] (km s^{-1})	IRAS 4A2 FWHM[b] (km s^{-1})	IRAS 4A2 rms[c] (K)
3(2, 1)–3(1, 2) E	24.92871	36	−7.2	0.97 × 0.95 (−12)	17(4)	6.5(0.2)	2.7(1.2)	1.0	34(3)	6.8(0.2)	3.1(0.3)	0.9
4(2, 2)–4(1, 3) E	24.93347	45	−7.1	0.97 × 0.95 (−12)	23(3)	6.5(0.2)	3.7(0.5)	1.0	32(3)	6.9(0.2)	3.1(0.3)	0.9
2(2, 0)–2(1, 1) E	24.93438	29	−7.2	0.97 × 0.95 (−12)	19(3)	6.5(0.2)	3.3(0.6)	1.0	27(3)	6.9(0.2)	2.9(0.3)	0.9
5(2, 3)–5(1, 4) E	24.95908	57	−7.1	0.97 × 0.95 (−12)	19(3)	6.1(0.3)	4.2(0.9)	0.9	32(3)	6.8(0.2)	3.1(0.3)	0.9
6(2, 4)–6(1, 5) E	25.01812	71	−7.1	0.97 × 0.95 (−19)	19(3)	6.3(0.3)	3.5(0.6)	1.0	31(3)	6.7(0.1)	2.5(0.2)	1.0
7(2, 5)–7(1, 6) E	25.12487	87	−7.1	0.98 × 0.95 (−21)	20(2)	7.0(0.2)	3.2(0.5)	0.9	35(3)	6.8(0.2)	2.9(0.3)	1.2
8(2, 6)–8(1, 7) E	25.29442	106	−7.0	0.96 × 0.94 (−11)	13(3)	6.8(0.3)	3.4(0.9)	0.9	32(2)	6.8(0.1)	2.8(0.3)	0.9
9(2, 7)–9(1, 8) E	25.54140	127	−7.0	0.96 × 0.92 (−50)	18(2)	6.5(0.2)	2.7(0.5)	0.8	31(2)	6.9(0.1)	2.6(0.2)	0.9
10(2, 8)–10(1, 9) E	25.87827	150	−7.0	0.97 × 0.93 (−35)	20(2)	6.4(0.2)	3.2(0.5)	0.8	32(2)	6.9(0.1)	2.6(0.2)	0.8
11(2, 9)–11(1, 10) E	26.31312	175	−6.9	0.94 × 0.91 (−35)	24(4)	6.0(0.4)	4.9(0.9)	1.1	31(3)	6.8(0.1)	2.9(0.3)	0.9

Notes.

[a] Spectroscopic parameters by Xu et al. (2008) are from the Cologne Database for Molecular Spectroscopy (Müller et al. 2005).

[b] Results of the Gaussian fit algorithm.

[c] The rms is computed over each spectral window.

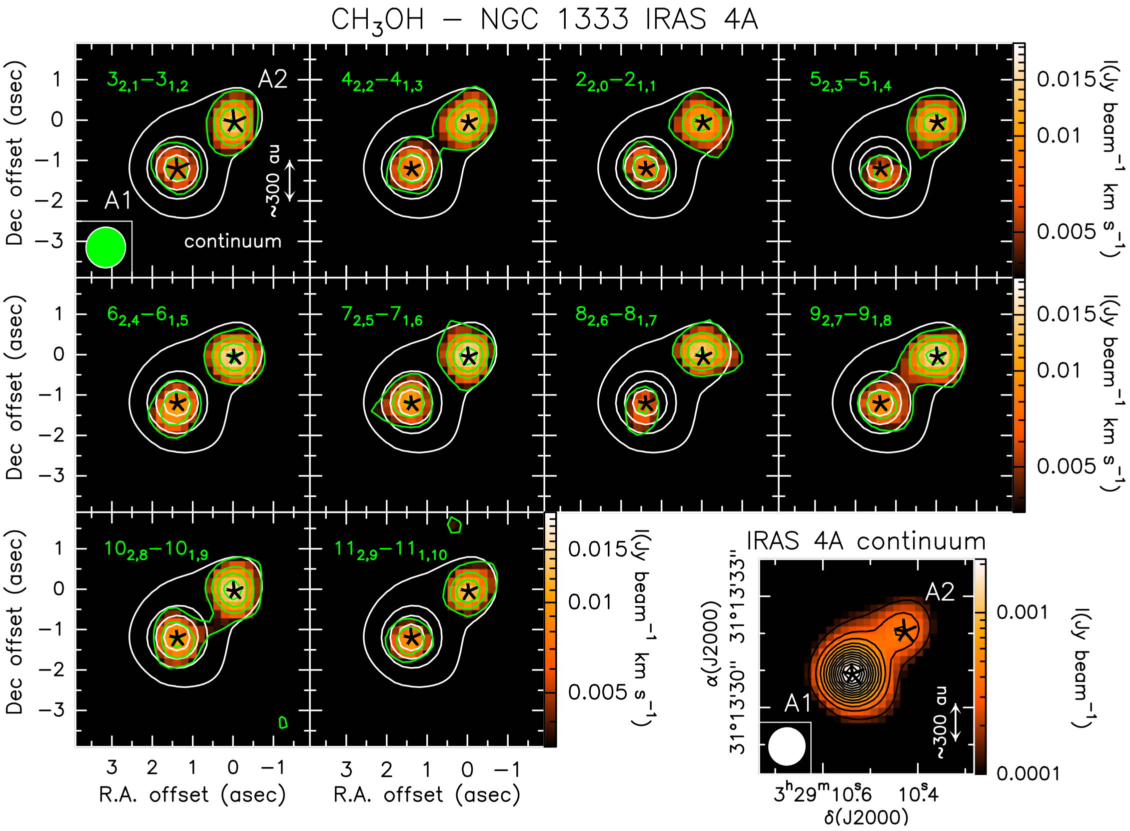

Figure 1. Bottom right panel: IRAS 4A continuum emission map at 25 GHz. First contour and steps correspond to $50\sigma_C$ ($\sigma_C = 3\ \mu$Jy beam^{-1}). Other panels: CH_3OH velocity-integrated maps toward IRAS 4A in color scale overlapped with the continuum (white) contours (from $50\sigma_C$ with steps of $170\sigma_C$). The emission is integrated from −2 to 2 km s^{-1} with respect to the v_{sys} (∼6.7 km s^{-1}). Methanol first contour (green) and steps correspond to 3σ ($\sigma = 1.2$ mJy beam^{-1} km s^{-1}). The transition of the imaged line is reported in each panel. The black stars show the 4A1 and 4A2 positions. Synthesized beams for continuum (white) and lines (green) are in the lower left corner.

4A2 continuum peaks. The lines are slightly brighter toward 4A2 than 4A1, whereas the linewidths are very similar (see also Table 1). We derived the velocity-integrated line intensities for each detected CH_3OH transition using a Gaussian fit, being the profile Gaussian-like. The fit results for both sources, namely the integrated emission ($\int T_b dV$), the linewidth (FWHM), the peak velocities (V_{peak}), and the rms computed for each spectral window, are reported in Table 1. The velocity peaks are consistent with the systemic velocity of the molecular envelope surrounding IRAS 4A (∼6.7 km s^{-1}; Choi 2001). The linewidths are between 3 and 4 km s^{-1} in agreement with those found by Taquet et al. (2015) and López-Sepulcre et al. (2017) toward 4A2 at millimeter wavelength.

In summary, our new VLA observations show a first clear important result: the detection of methanol emission toward 4A1, the protostar where previous millimeter observations showed no iCOMs emission (López-Sepulcre et al. 2017).

4. Centimeter versus Millimeter Observations: Dust Absorption Derivation

We compared our new centimeter observations of methanol lines with previous ones at 143–146 GHz in order to understand whether the dust absorption, more important at millimeter than at centimeter wavelengths, may explain the absence of iCOM millimeter line emission in 4A1 (López-Sepulcre et al. 2017). We first carried out a non-LTE analysis of the centimeter methanol lines from which we derived the gas temperature, density and CH_3OH column density toward 4A1 and 4A2 (Section 4.1). Then, using the same parameters, we predicted the methanol line intensities at 143–146 GHz, the frequency of the observations by Taquet et al. (2015; Section 4.2). Finally, we compared the predicted and measured millimeter line intensities and we attributed the difference to the absorption of the dust between us and the gas emitting methanol, via the usual equation:

$$I_\nu^{obs} = I_\nu^{pred} e^{-\tau_\nu} \tag{1}$$

in order to derive the dust optical depth toward 4A1 and 4A2, respectively (Section 4.3). Please note that the foreground dust opacity obtained by Equation (1) assumes that the absorbing dust fully covers the emitting gas area, which may not necessarily be the case. Yet, the derived attenuation of the methanol line intensities is still valid, even though it is only an average over the emitting gas area.

4.1. Non-LTE Analysis of the Centimeter Methanol Lines

To derive the physical properties of the gas emitting CH_3OH, namely gas temperature, density and methanol column density, we performed a non-LTE analysis using a Large Velocity Gradient (LVG) code (Ceccarelli et al. 2003). CH_3OH can be identified in A- and E-type due to the total spin (I) state of the hydrogen nuclei in the CH_3 group: A-type if the total spin function is symmetric ($I = 3/2$), E-type if

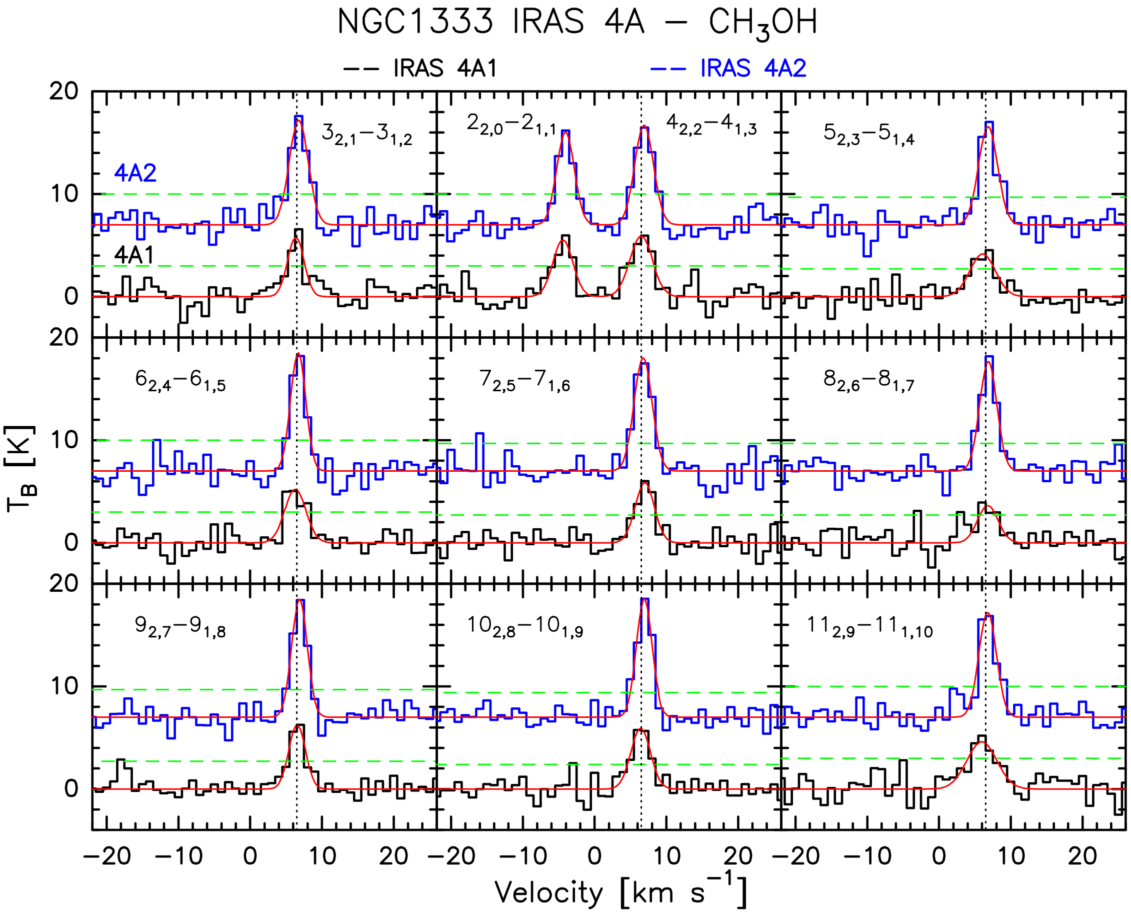

Figure 2. Methanol lines (marked in each panel) detected in the VLA *K*-band toward 4A1 (black) and 4A2 (blue). The horizontal green dashed lines show the 3σ level. The vertical dotted black lines report the v_{sys} (6.7 km s^{-1}). The red and magenta curves show the best Gaussian fits (see Table 1).

asymmetric ($I = 1/2$) (Rabli & Flower 2010). We used the collisional coefficients of both types of CH_3OH with para-H_2, computed by Rabli & Flower (2010) between 10 and 200 K for the first 256 levels and provided by the BASECOL database (Dubernet et al. 2013). We assumed a spherical geometry to compute the line escape probability (de Jong et al. 1980), the CH_3OH-A/CH_3OH-E ratio equal to 1, the H_2 ortho-to-para ratio equal to 3, and that the levels are populated by collisions and not by the absorption of the dust background photons whose contribution is very likely negligible due to the low values of the CH_3OH Einstein coefficients A_{ij}. Please note that the present LVG analysis only accounts for the line optical depth (to have also the dust τ in the methanol emitting region would require information on the structure of the region that we do not have, as the emission is unresolved).

We ran a large grid of models ($\geqslant$10,000) covering the frequency of the observed lines, a total (CH_3OH-A plus CH_3OH-E) column density N_{CH_3OH} from 2×10^{16} to 8×10^{19} cm^{-2}, a gas density n_{H_2} from 1×10^6 to 2×10^8 cm^{-3}, and a temperature T from 80 to 200 K. We then simultaneously fitted the measured CH_3OH-A and CH_3OH-E line intensities via comparison with those simulated by the LVG model, leaving N_{CH_3OH}, n_{H_2}, T, and the emitting size θ as free parameters. Following the observations, we assumed the linewidths equal to 3.5 km s^{-1} and 3.0 km s^{-1} for 4A1 and 4A2, respectively, and we included the calibration uncertainty (15%) in the observed intensities.

The best fit is obtained for a total CH_3OH column density $N_{CH_3OH} = 2.8 \times 10^{19}$ cm^{-2} with reduced chi-square $\chi^2_R = 0.6$ for 4A1 and $N_{CH_3OH} = 1 \times 10^{19}$ cm^{-2} with $\chi^2_R = 0.1$ for 4A2. All the observed lines are predicted to be optically thick and emitted by a source of 0$''$22 for 4A1 and 0$''$24 for 4A2 ($\sim$70 au) in diameter. Solutions with $N_{CH_3OH} \geqslant 1 \times 10^{18}$ cm^{-2} for 4A2 and $\geqslant 1 \times 10^{19}$ cm^{-2} for 4A1 are within 1σ of confidence level. Increasing the methanol column density, the χ^2_R decreases until it reaches a constant value for $N_{CH_3OH} \geqslant 1 \times 10^{19}$ cm^{-2} for 4A1 and $N_{CH_3OH} \geqslant 3 \times 10^{19}$ cm^{-2} for 4A2; this is because all the observed lines become optically thick ($\tau \sim$ 10–30 for 4A1, $\tau \sim$ 2–6 for 4A2) and, consequently, the emission becomes that of a blackbody. The results do not change assuming a linewidth ±0.5 km s^{-1} with respect to the chosen one.

Figure 3 shows, for both sources, the density-temperature χ^2 surface of the N_{CH_3OH} best fit. The gas temperature is (90–130) K for 4A1 and (120–190) K for 4A2, while for the gas density we obtained a lower limit of 2×10^6 cm^{-3} for 4A1 and 1.5×10^7 cm^{-3} for 4A2, which implies that the levels are LTE populated. The fit results are reported in Table 2. The derived n_{H_2} and T are consistent with those computed with the model summarized in Su et al. (2019) using our sizes.

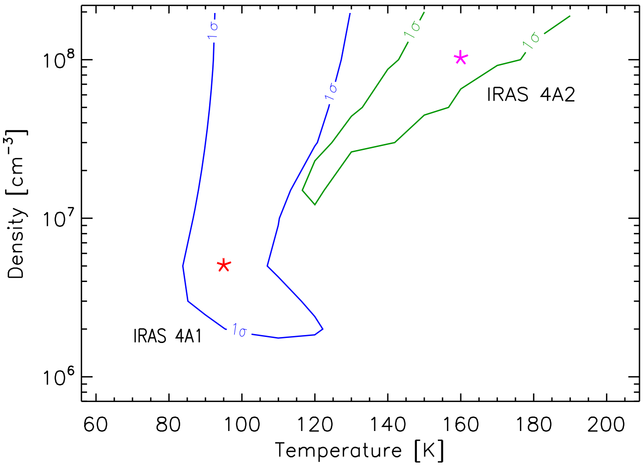

Figure 3. Density–temperature χ^2 contour plots. The contours represent 1σ confidence level contours for 4A1 (blue) and 4A2 (green), respectively, assuming the best-fit values of $N_{\mathrm{CH_3OH}}$ and θ in Table 2. The best-fit solutions are marked by the red (4A1) and magenta (4A2) asterisks.

4.2. Predictions of Millimeter Methanol Line Intensities

Adopting the 1σ range of gas temperature and density derived for 4A1 and 4A2 (Table 2), we ran a new grid of LVG models with the CH_3OH column density from 1×10^{18} to 8×10^{19} cm^{-2} at 143–146 GHz to predict the methanol line intensities observed by Taquet et al. (2015). We then used the CH_3OH $3_1 - 2_1$ A^+ line at 143.866 GHz, which provides the most stringent constraint to the dust optical depth, to compare the predicted intensity with that observed by Taquet et al. (2015). In the comparison, we took into account our LVG-derived source size and the angular resolution of the Taquet et al. (2015) observations. While for 4A2 we considered the line intensity quoted by Taquet et al. (2015), for 4A1, not having CH_3OH detection, we used the 3σ level of the Taquet et al. (2015) observations integrated over 3 km s^{-1} (average linewidth toward 4A1: see Section 3).

The 4A1 and 4A2 CH_3OH predicted and observed values are reported in Table 2. While the two intensities are similar toward 4A2, they differ by about a factor five toward 4A1.

4.3. Dust Absorption Toward 4A1 and 4A2

Assuming that the difference between the predicted and observed intensities is due to the (foreground) dust absorption and using Equation (1), we derived the dust optical depth at 143 GHz ($\tau_{\mathrm{dust}}^{143\mathrm{GHz}}$; Table 2). While $\tau_{\mathrm{dust}}^{143\mathrm{GHz}}$ toward 4A2 is small (~0.3), that toward 4A1 is large ($\geqslant$1.6) enough to attenuate the methanol line intensity by a factor $\geqslant$5. Therefore, the dust is affecting the millimeter line emission differently in the two sources.

5. Discussion

5.1. Is IRAS 4A1 a Hot Corino?

So far, only about a dozen hot corinos have been detected (Section 1) and the question arises whether this is because they are rare or because the searches have always been carried out at millimeter wavelengths, where dust could heavily absorb the line emission.

Our first result is that a source that was not supposed to be a hot corino based on millimeter observations, IRAS 4A1 (López-Sepulcre et al. 2017), indeed possesses a region with temperature $\geqslant$100 K (Section 3), namely the icy mantle sublimation one, and shows methanol emission (Section 3), the simplest of the iCOMs, when observed at centimeter wavelengths. According to its definition (Ceccarelli 2004), thus, IRAS 4A1 is a hot corino.

Although we cannot affirm that hot corinos are ubiquitous, it is clear that the searches at millimeter wavelengths may be heavily biased and that complementary centimeter observations are necessary to account for dust opacity and understand the occurrence of hot corinos.

5.2. 4A2 versus 4A1: Are They Chemically Different?

Unlike 4A2, no sign of iCOM millimeter emission was revealed toward 4A1 (Taquet et al. 2015; López-Sepulcre et al. 2017). Using ALMA observations at 250 GHz, López-Sepulcre et al. (2017) found that the iCOMs abundances toward 4A2 and 4A1 differ by more than a factor 17, with the largest values (~100) for $HCOOCH_3$ and CH_3CN.

The first question to answer is whether the chemical difference between the two coeval objects is real or due to a different absorption by the surrounding dust.

In Section 4.3, we found that τ_{dust} at 143 GHz toward 4A1 and 4A2 is $\geqslant$1.6 and 0.3, respectively (see Table 2). Using the dependence of τ_{dust} from the frequency ($\tau_{\nu_2}/\tau_{\nu_1} = (\nu_2/\nu_1)^{\beta}$) and assuming $\beta = 2$ (ISM value), the optical depth scaled at 250 GHz (frequency at which López-Sepulcre et al. 2017, derived the above iCOMs abundance ratios) is $\geqslant$4.9 for 4A1 and 0.9 for 4A2. Therefore, the different dust absorption toward 4A1 and 4A2 provides us, as a lower limit, a factor of 55 difference in their line intensities ($I^{\mathrm{A2}}/I^{\mathrm{A1}}$), comparable to the 4A2/4A1 iCOMs abundance ratios derived by López-Sepulcre et al. (2017). A large dust absorption was also suggested by the anomalous flattened continuum spectral index at 100–230 GHz (Li et al. 2017) and the 90° flipping of the linear polarization position angles observed at above and below 100 GHz frequencies (Ko et al. 2020).

Although we cannot exclude that a real chemical difference exists between 4A1 and 4A2, the observations so far available cannot support that hypothesis. Centimeter observations of other iCOMs than methanol are necessary to settle this issue. This conclusion may apply to other binary systems where an apparent chemical difference is observed using millimeter observations.

5.3. Are the iCOM Abundances in Hot Corinos Underestimated?

The dust absorption also affects the iCOM line intensities in 4A2. At 143 GHz τ_{dust} is 0.3, which leads to underestimate the iCOM abundances by about 30%. At higher frequencies, this factor becomes more important; e.g., at 250 GHz, where several hot corinos studies are carried out (see references in Section 1), the absorption factor would be 2.5, and at 350 GHz, frequency where the most sensitive iCOMs search has been carried out (e.g., Jørgensen et al. 2016), the absorption factor would be 6. This behavior also agrees with what has already been found in massive hot cores (e.g., Rivilla et al. 2017). Therefore, in order to derive reliable iCOM abundances, complementary centimeter observations are needed to estimate the dust absorption.

Table 2
Top: Best-fit Results and 1σ Confidence Level (range) from the Non-LTE LVG Analysis of the CH_3OH Lines toward 4A1 and 4A2

		IRAS 4A1		IRAS 4A2	
		LVG Results			
		Best Fit	Range	Best Fit	Range
$n(H_2)$	(cm^{-3})	5×10^6	$\geqslant 2 \times 10^6$	1×10^8	$\geqslant 1 \times 10^7$
T_{kin}	(K)	100	90–130	160	120–190
N_{CH_3OH}	(cm^{-2})	2.4×10^{19}	$\geqslant 1 \times 10^{19}$	1×10^{19}	$\geqslant 1 \times 10^{18}$
Source size	(″)	0.22	0.20-0.24	0.24	0.22–0.30
		Predictions versus Millimeter Observations			
$T_b dV_{pred}$	(K km s^{-1})	4.7(0.8)		9.1(1.2)	
$T_b dV_{obs}$	(K km s^{-1})	$\leqslant 0.9$		6.5(1.9)	
τ_{dust}^{143GHz}		$\geqslant 1.6$		0.3	

Note. Bottom: Comparison of the LVG model predictions with the Taquet et al. (2015) millimeter observations (see the text).

6. Conclusion

We carried out observations of methanol lines at centimeter wavelengths with the VLA interferometer toward the binary system IRAS 4A, where previous millimeter observations showed a possible chemical differentiation between the two objects. Specifically, while 4A2 showed iCOM line emission, 4A1 did not.

Our new observations detected 10 methanol lines in 4A1 and 4A2 with similar intensities. Using a non-LTE analysis and comparing with previous methanol millimeter observations, we showed that (1) 4A1 is a hot corino, (2) the lack of iCOMs detection toward 4A1 at millimeter wavelengths is caused by a large dust optical depth, and (3) the determination of the iCOMs abundances toward 4A2 via millimeter observations is slightly underestimated by the dust absorption.

Therefore, the difficulty in discovering new hot corinos could be because the searches have been carried out at (sub) millimeter wavelengths, where the dust absorption might not be negligible. The suspected different chemical nature of coeval objects of the same binary system needs also to be verified at centimeter wavelengths, as well as the iCOM abundances estimated from millimeter observations.

We conclude that centimeter observations of hot corinos are of paramount importance for their correct study. In the future, next generation instruments in the centimeter wavelength regime, such as ngVLA (McGuire et al. 2018) and SKA (Codella et al. 2015), could be the most efficient way to identify hot corinos and certainly the most appropriate facilities to study them.

We thank the referee P.T.P Ho for his fruitful comments and suggestions. This work has received funding from the European Research Council (ERC) under the European Union's Horizon 2020 research and innovation programme, for the Project "The Dawn of Organic Chemistry" (DOC), grant agreement No 741002. It was supported by the project PRIN-INAF 2016 The Cradle of Life–GENESIS-SKA (General Conditions in Early Planetary Systems for the rise of life with SKA), and partly supported by the Italian Ministero dell'Istruzione, Università e Ricerca, through the grant Progetti Premiali 2012–iALMA (CUP C52I13000140001). H.B.L. is supported by the Ministry of Science and Technology (MoST) of Taiwan (grant Nos. 108-2112-M-001-002-MY3). C.F. acknowledges support from the French National Research Agency in the framework of the Investissements d'Avenir program (ANR-15-IDEX-02), through the funding of the "Origin of Life" project of the Univ. Grenoble-Alpes.

ORCID iDs

Marta De Simone https://orcid.org/0000-0001-5659-0140
Cecilia Ceccarelli https://orcid.org/0000-0001-9664-6292
Claudio Codella https://orcid.org/0000-0003-1514-3074
Brian E. Svoboda https://orcid.org/0000-0002-8502-6431
Claire Chandler https://orcid.org/0000-0002-7570-5596
Mathilde Bouvier https://orcid.org/0000-0003-0167-0746
Satoshi Yamamoto https://orcid.org/0000-0002-9865-0970
Nami Sakai https://orcid.org/0000-0002-3297-4497
Paola Caselli https://orcid.org/0000-0003-1481-7911
Cecile Favre https://orcid.org/0000-0002-5789-6931
Laurent Loinard https://orcid.org/0000-0002-5635-3345
Bertrand Lefloch https://orcid.org/0000-0002-9397-3826
Hauyu Baobab Liu https://orcid.org/0000-0003-2300-2626
Ana López-Sepulcre https://orcid.org/0000-0002-6729-3640
Jaime E. Pineda https://orcid.org/0000-0002-3972-1978
Vianney Taquet https://orcid.org/0000-0003-0407-7489
Leonardo Testi https://orcid.org/0000-0003-1859-3070

References

Belloche, A., Maury, A. J., Maret, S., et al. 2020, A&A, 635, A198
Bergner, J. B., Martín-Doménech, R., Öberg, K. I., et al. 2019, ESC, 3, 1564
Bianchi, E., Codella, C., Ceccarelli, C., et al. 2017, A&A, 606, L7
Bianchi, E., Codella, C., Ceccarelli, C., et al. 2019, MNRAS, 483, 1850
Bottinelli, S., Ceccarelli, C., Lefloch, B., et al. 2004, ApJ, 615, 354
Bottinelli, S., Ceccarelli, C., Williams, J. P., & Lefloch, B. 2007, A&A, 463, 601
Bouvier, M., López-Sepulcre, A., Ceccarelli, C., et al. 2020, A&A, 636, A19
Caselli, P., & Ceccarelli, C. 2012, A&ARv, 20, 56
Caux, E., Kahane, C., Castets, A., et al. 2011, A&A, 532, A23
Cazaux, S., Tielens, A. G. G. M., Ceccarelli, C., et al. 2003, ApJL, 593, L51
Ceccarelli, C. 2004, in ASP Conf. Proc. 323, Star Formation in the Interstellar Medium: In Honor of David Hollenbach, Chris McKee and Frank Shu, ed. D. Johnstone et al. (San Francisco, CA: ASP), 195
Ceccarelli, C., Caselli, P., Fontani, F., et al. 2017, ApJ, 850, 176
Ceccarelli, C., Caselli, P., Herbst, E., Tielens, A. G. G. M., & Caux, E. 2007, in Protostars and Planets V, ed. B. Reipurth, D. Jewitt, & K. Keil (Tucson, AZ: Univ. Arizona Press), 47
Ceccarelli, C., Maret, S., Tielens, A. G. G. M., Castets, A., & Caux, E. 2003, A&A, 410, 587
Choi, M. 2001, ApJ, 553, 219
Codella, C., Ceccarelli, C., Cabrit, S., et al. 2016, A&A, 586, L3

Codella, C., Podio, L., Fontani, F., et al. 2015, Advancing Astrophysics with the Square Kilometre Array (AASKA14) (Sissa: POS), 123
de Jong, T., Boland, W., & Dalgarno, A. 1980, A&A, 91, 68
De Simone, M., Codella, C., Testi, L., et al. 2017, A&A, 599, A121
Dubernet, M.-L., Alexander, M. H., Ba, Y. A., et al. 2013, A&A, 553, A50
Galametz, M., Maury, A. J., Valdivia, V., et al. 2019, A&A, 632, A5
Galván-Madrid, R., Liu, H. B., Izquierdo, A. F., et al. 2018, ApJ, 868, 39
Herbst, E., & van Dishoeck, E. F. 2009, ARA&A, 47, 427
Higuchi, A. E., Sakai, N., Watanabe, Y., et al. 2018, ApJS, 236, 52
Imai, M., Sakai, N., Oya, Y., et al. 2016, ApJL, 830, L37
Jacobsen, Jørgensen, Jes, K., Di Francesco, James, et al. 2019, A&A, 629, A29
Jørgensen, J. K., Bourke, T. L., Myers, P. C., et al. 2005, ApJ, 632, 973
Jørgensen, J. K., van der Wiel, M. H. D., Coutens, A., et al. 2016, A&A, 595, A117
Ko, C.-L., Liu, H. B., Lai, S.-P., et al. 2020, ApJ, 889, 172
Lee, C.-F., Codella, C., Li, Z.-Y., & Liu, S.-Y. 2019, ApJ, 876, 63
Lee, C.-F., Li, Z.-Y., Ho, P. T. P., et al. 2017, ApJ, 843, 27
Li, J. I.-H., Liu, H. B., Hasegawa, Y., & Hirano, N. 2017, ApJ, 840, 72
López-Sepulcre, A., Sakai, N., Neri, R., et al. 2017, A&A, 606, A121
Manigand, S., Jørgensen, J. K., Calcutt, H., et al. 2020, A&A, 635, A48
Marcelino, N., Gerin, M., Cernicharo, J., et al. 2018, A&A, 620, A80
Martin-Domenech, R., Oberg, K. I., Bergner, J. B., & Jorgensen, J. K. 2019, ApJ, 880, 130
Maury, A. J., Belloche, A., André, P., et al. 2014, A&A, 563, L2
McGuire, B. A., Carroll, P. B., & Garrod, R. T. 2018, arXiv:1810.06586
Miotello, A., Testi, L., Lodato, G., et al. 2014, A&A, 567, A32
Müller, H. S. P., Schlöder, F., Stutzki, J., & Winnewisser, G. 2005, JMoSt, 742, 215
Öberg, K. I., Lauck, T., & Graninger, D. 2014, ApJ, 788, 68
Ospina-Zamudio, J., Lefloch, B., Ceccarelli, C., et al. 2018, A&A, 618, A145
Oya, Y., Sakai, N., Watanabe, Y., et al. 2017, ApJ, 837, 174
Pineda, J. E., Maury, A. J., Fuller, G. A., et al. 2012, A&A, 544, L7
Rabli, D., & Flower, D. R. 2010, MNRAS, 406, 95
Rivilla, V. M., Beltrán, M. T., Cesaroni, R., et al. 2017, A&A, 598, A59
Sahu, D., Liu, S.-Y., Su, Y.-N., et al. 2019, ApJ, 872, 196
Sakai, N., & Yamamoto, S. 2013, ChRv, 113, 8981
Su, Y.-N., Liu, S.-Y., Li, Z.-Y., et al. 2019, ApJ, 885, 98
Taquet, V., López-Sepulcre, A., Ceccarelli, C., et al. 2015, ApJ, 804, 81
Tobin, J. J., Looney, L. W., Li, Z.-Y., et al. 2016, ApJ, 818, 73
Xu, L.-H., Fisher, J., Lees, R., et al. 2008, JMoSp, 251, 305
Yang, Y.-L., Evans, N. J., II, Smith, A., et al. 2020, ApJ, 891, 61
Zucker, C., Schlafly, E. F., Speagle, J. S., et al. 2018, ApJ, 869, 83

A&A 640, A75 (2020)
https://doi.org/10.1051/0004-6361/201937004

Astronomy & Astrophysics

Seeds of Life in Space (SOLIS)

X. Interstellar complex organic molecules in the NGC 1333 IRAS 4A outflows[⋆]

M. De Simone[1], C. Codella[2,1], C. Ceccarelli[1], A. López-Sepulcre[3,1], A. Witzel[1], R. Neri[3], N. Balucani[4,1], P. Caselli[5], C. Favre[1], F. Fontani[2], B. Lefloch[1], J. Ospina-Zamudio[1], J. E. Pineda[5], and V. Taquet[2]

[1] Univ. Grenoble Alpes, CNRS, IPAG, 38000 Grenoble, France
e-mail: `marta.desimone@univ-grenoble-alpes.fr`
[2] INAF, Osservatorio Astrofisico di Arcetri, Largo E. Fermi 5, 50125 Firenze, Italy
[3] Institut de Radioastronomie Millimétrique (IRAM), 300 rue de la Piscine, 38400 Saint-Martin d'Hères, France
[4] Dipartimento di Chimica, Biologia e Biotecnologie, Università degli Studi di Perugia, Perugia 06123, Italy
[5] Max-Planck-Institut für extraterrestrische Physik (MPE), Giessenbachstrasse 1, 85748 Garching, Germany

Received 28 October 2019 / Accepted 12 June 2020

ABSTRACT

Context. The interstellar complex organic molecules (iCOMs) are C-bearing molecules containing at least six atoms; two main proposals for their formation are suggested: a direct formation in the icy mantle of the dust grains and formation through the reaction in gas phase of released grain mantle species. The shocked gas along outflows driven by low-mass protostars is a unique environment to study how the iCOMs can be formed as the composition of the dust mantles is sputtered into the gas phase.
Aims. The chemical richness in shocked material associated with low-mass protostellar outflows has been so far studied in the prototypical L1157 blue-shifted outflow to investigate the iCOM formation routes. To understand whether the case of L1157-B1 is unique, we imaged and studied the IRAS 4A outflows in the NGC 1333 star forming region.
Methods. We used the NOrthern Extended Millimeter Array interferometer as part of the IRAM Seeds Of Life in Space (SOLIS) Large Program to image the large-scale bipolar outflows driven by the IRAS 4A system in the 3 mm band, and we compared the observation with the GRAINOBLE+ astrochemical model.
Results. We report the first detection, in the IRAS 4A outflows, of several iCOMs: six lines of methanol (CH_3OH), eight of acetaldehyde (CH_3CHO), one of formamide (NH_2CHO), and four of dimethyl ether (CH_3OCH_3), all sampling upper excitation energy up to ~30 K. We found a significant chemical differentiation between the southeast outflow driven by the IRAS 4A1 protostar, showing a richer molecular content, and the north–southwest one driven by the IRAS 4A2 hot corino. The CH_3OH/CH_3CHO abundance ratio is lower by a factor of ~4 in the former; furthermore, the ratio in the IRAS 4A outflows is lower by a factor of ~10 with respect to the values found in different hot corinos.
Conclusions. After L1157-B1, the IRAS 4A outflow is now the second outflow to show an evident chemical complexity. Given that CH_3OH is a grain surface species, the astrochemical gas-phase model run with GRAINOBLE+ reproduced our observation assuming that acetaldehyde is formed mainly through the gas-phase reaction of the ethyl radical (CH_3CH_2) and atomic oxygen. Furthermore, the chemical differentiation between the two outflows suggests that the IRAS 4A1 outflow is likely younger than that of the IRAS 4A2. Further investigation is needed to constrain the age of the outflow. In addition, observation of even younger shocks are necessary. In order to provide strong constraints on the CH_3CHO formation mechanisms it would be interesting to observe CH_3CH_2, but given that its frequencies are not known, future spectroscopic studies on this species are needed.

Key words. astrochemistry – instrumentation: interferometers – stars: formation – ISM: jets and outflows – ISM: molecules – ISM: individual objects: NGC 1333 IRAS 4A

1. Introduction

Since the discovery of interstellar complex organic molecules (iCOMs[1], molecules containing carbon and at least six atoms: Herbst & van Dishoeck 2009; Ceccarelli et al. 2017) in solar-type protostars (Cazaux et al. 2003), the question whether they had a role in the appearance of life on Earth (and elsewhere in the Universe) has been raised. Although they are extremely small molecules compared to biotic molecules, iCOMs may have provided the bricks to build them. The presence of amino acids in meteorites and comets has certainly revived this possibility (e.g., Pizzarello et al. 2006; Elsila et al. 2009; Altwegg et al. 2016).

In addition to their possible role in the emergence of life, iCOMs represent a challenge for astrochemistry as their synthesis is all but obvious. Nowadays, two main paradigms are invoked (see, e.g., Herbst 2017) that argue that iCOMs are either synthesized on the grain surfaces (e.g., Garrod & Herbst 2006; Garrod 2008) or in the gas phase (e.g., Millar et al. 1991; Balucani et al. 2015; Skouteris et al. 2018). As a starting point, both pathways have the formation of simple hydrogenated molecules on dust grain mantles during the pre-stellar phase. Constraining which of the two ways to synthesize iCOMs is more efficient and where

---

[⋆] The reduced images are only available at the CDS via anonymous ftp to `cdsarc.u-strasbg.fr` (`130.79.128.5`) or via `http://cdsarc.u-strasbg.fr/viz-bin/cat/J/A+A/640/A75`

[1] We added "i" to the commonly used COMs acronym in order to be clear that these molecules are only complex in the interstellar context, contrary to what chemists consider complex in the terrestrial context.

the iCOMs form is not a simple task. Many methods have been used, from the comparison of the iCOM measured abundances in hot cores and hot corinos with model predictions to their measured deuterium fractionation (Turner 1990; Ceccarelli et al. 1998; Coutens et al. 2016; Skouteris et al. 2017; Jørgensen et al. 2018).

One method that turned out to be very efficient is to compare observations toward low-mass outflow shocks with model predictions (Codella et al. 2017). The advantage of this method is that the outflow shocks provide the time dependence as an additional constraint. Once the iCOM emission has been localized in a precise region (thanks to high spatial resolution observations), it is possible to identify in that region a shock event that corresponds naturally to a precise kinematical age (e.g., Gueth et al. 1996; Podio et al. 2016). After the passage of the shock, the chemistry in the shocked region evolves with time. Therefore, the comparison of observed iCOM abundances with model predictions provides strong constraints on the formation routes because it is possible to make the comparison at the precise kinematical shock age. This method was successfully applied in the L1157–B1 outflow shock to constrain the formation route of formamide. Thanks to interferometric high spatial resolution observations, Codella et al. (2017) found a difference in the spatial distribution between acetaldehyde and formamide emission, and consequently they were able to constrain the formamide formation as being due to gas-phase reactions. We note that these conclusions apply to L1157-B1 only. Given its power, it is important to apply the same method to other iCOMs and other protostellar shocks.

Unfortunately, there are very few observations of iCOMs in low-mass protostellar shocks. To our knowledge, iCOMs other than methanol have been detected only toward a handful of objects: several iCOMs toward L1157-B1 (Arce et al. 2008; Lefloch et al. 2017), formamide toward L1157-B2 (Mendoza et al. 2014), acetaldehyde toward IRAS 2A and IRAS 4A (Holdship et al. 2019), and acetaldehyde and dimethyl ether toward SMM4-W (Öberg et al. 2011). However, it is worth noting that all these works refer to single-dish observations at relatively low spatial angular resolution and are, by definition, unable to disentangle the different spatial distribution of iCOMs caused by the age of the shocks, so that the method described above cannot be used.

In this work, we present new high spatial observations toward the two outflows from IRAS 4A. This source is one of the targets of the Seeds Of Life In Space (SOLIS) Large Program (Ceccarelli et al. 2017) at the IRAM/NOrthern Extended Millimeter Array (NOEMA) interferometer, whose goal is to investigate iCOM chemistry during the earliest formation phases of solar-type stellar systems. The observations targeted three iCOMs in addition to methanol (CH_3OH): acetaldehyde (CH_3CHO), dimethyl ether (CH_3OCH_3), and formamide (NH_2CHO). All these iCOMs were detected in our data set. The detection of different iCOMs in the outflowing gas of IRAS 4A with high spatial resolution observations allows us to apply the method of model-observations comparison described above.

The article is organized as follows: we first give the IRAS 4A source background in Sect. 2, then present the observations in Sect. 3, and the results in Sect. 4; we derive the abundance ratios of the detected iCOMs in different positions of the IRAS 4A outflows in Sect. 5, and the model predictions to interpret them in Sect. 6; in Sect. 7 we discuss what our new observations imply, and finally in Sect. 8 we summarize our work.

2. IRAS 4A: source background

IRAS 4A is part of the multiple system IRAS 4, located at a distance of 299 ± 15 pc in the NGC 1333 region of the Perseus complex (Zucker et al. 2018). The system IRAS 4A is constituted of four objects: 4A, 4B, 4B′, and 4C (Lay et al. 1995; Looney et al. 2000; Smith et al. 2000; Di Francesco et al. 2001; Choi 2001). IRAS 4A is itself a binary system with two Class 0 objects, 4A1 and 4A2, separated by 1.″8 (~540 au; Looney et al. 2000; Santangelo et al. 2015; López-Sepulcre et al. 2017; Maury et al. 2019). At the millimeter wavelengths, 4A1 is three times brighter than 4A2. However, their respective luminosity is unknown since they are not resolved in the submillimeter to IR wavelengths where the luminosity peak lies. The bolometric luminosity of the whole IRAS 4A system is 9.1 $L_\odot$ (Kristensen et al. 2012; Karska et al. 2013).

IRAS 4A is the second hot corino ever discovered (Bottinelli et al. 2004), after IRAS 16293-2422 (Cazaux et al. 2003). Interferometric IRAM/PdBI (Plateau de Bure Interferometer, now evolved into NOEMA) observations later suggested that iCOM emission originates from 4A2 rather than 4A1 (Taquet et al. 2015; De Simone et al. 2017). More recently, López-Sepulcre et al. (2017) obtained high-resolution (~0.″5) ALMA images of IRAS 4A, and confirmed the huge contrast between 4A1 and 4A2: while 4A2 shows hot corino activity with enriched iCOM emission, no sign of iCOMs is detected in 4A1. López-Sepulcre et al. (2017) suggest that either 4A1 does not host a hot corino or, alternatively, the hot corino size is less than ~15 au (after scaling to 299 pc the distance adopted by López-Sepulcre et al. 2017), namely six times smaller than the 4A2 corino. However, thanks to recent observations at centimeter wavelengths performed with the *Jansky* Very Large Array (VLA), De Simone et al. (2020) have detected, for the first time, a clearly disentangled methanol emission toward both 4A1 and 4A2 revealing the 4A1 hot corino region that was obscured by the dust at millimeter wavelengths.

As for many Class 0 protostars, IRAS 4A is associated with a spectacular large-scale (a few arcminutes) bipolar outflow observed with several tracers, such as CO, SiO, SO, HCN (Blake et al. 1995; Lefloch et al. 1998; Choi 2005; Choi et al. 2011). Choi (2005) clearly traced the high-velocity component with SiO emission using VLA observations at 2″ spatial resolution. From their map it is possible to distinguish two different blue-shifted lobes toward the south and only one northern red-shifted lobe with a peculiar bending toward the northeast at 20″ from the protostars. Using IRAM/PdBI high spatial resolution observations (<1″), Santangelo et al. (2015) mapped the outflows at lower scale (~30″) with respect to the SiO map from Choi (2005). They traced different velocity components (from ~10 to ~60 km s $^{-1}$) using CO, SiO, and SO as tracers. With their study Santangelo et al. (2015) were able to clearly disentangle the two southern lobes, revealing a fast collimated jet associated with bright H_2 emission and driven by 4A1 (southeast lobe) and a slower and precessing jet driven by 4A2 (southwest lobe). Furthermore, the jets present different morphologies: the 4A2 jet shows a large spatial extent and an S-shaped pattern on small scales, probably due to jet precession; the 4A1 jet is faster, covers a smaller extent (~15″), and presents as C-shaped tilted toward the east of 4A1.

Thanks to a detailed study on sulfur species using interferometric observations, for the first time Taquet et al. (2020) were able to distinguish the outflow driven by 4A1 from the one driven by 4A2 also in the northern lobe.

The left panel of Fig. 1 summarizes the situation: it shows the distribution of the dust cores at large scale, traced by the

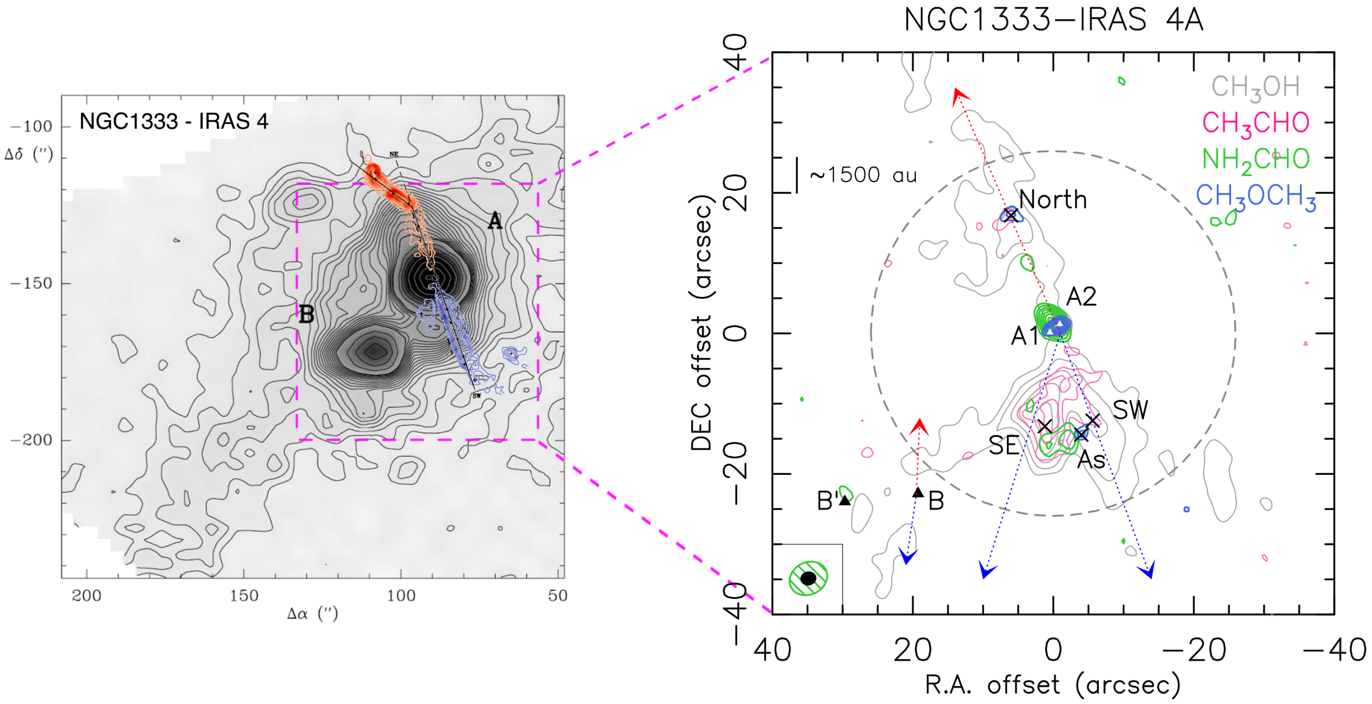

Fig. 1. *Left*: overlap of the contour map of the 1.25 mm continuum emission from NGC 1333 IRAS 4 region in Perseus, observed with the IRAM 30 m antenna (Lefloch et al. 1998), with the map of SiO line (VLA observations; Choi 2005). Axes offsets are in arcseconds from SVS 13 ($\alpha(2000) = 03^h29^m3^s.9$ and $\delta(2000) = 31°16'8''$). *Right*: zoomed-in image of the IRAS 4A system with NOEMA-SOLIS observations. Axes offsets are in arcseconds from IRAS 4A. A spatial separation of 5″ correspond to ~1500 au at a distance of 299 pc (Zucker et al. 2018). The white triangles give the position of the sources 4A1 and 4A2, while the black triangles give the position of the sources 4B and 4B′ (coordinates in Table 2). The black crosses give the analyzed positions in the outflows (SE, SW, North, and As; coordinates in Table 2). The dashed blue and red arrows indicate the direction of the blue- and red-shifted 4B outflow (from the HCN observations of Choi 2001) and of the 4A outflow. The contour map represents the iCOMs emission at 3 mm in the IRAS 4A outflows (this work). For all the iCOMs the contours start at 3σ with steps of 1σ, except for methanol whose contours have steps of 20σ. The emission distribution is the following: 1) methanol (CH_3OH in gray), integrated over the transitions $2_{0,2} - 1_{0,1}$ A, $2_{0,2} - 1_{0,1}$ E, and $2_{-1,2} - 1_{-1,1}$ E with σ = 75 mJy beam^{-1} km s^{-1}; 2) acetaldehyde (CH_3CHO, in magenta), here in the $5_{0,5} - 4_{0,4}$ A emission with σ = 11 mJy beam^{-1} km s^{-1}; 3) formamide (NH_2CHO, in green), $4_{1,4} - 3_{1,3}$ emission with σ = 10 mJy beam^{-1} km s^{-1}; dimethyl ether (CH_3OCH_3, in blue), $4_{1,4} - 3_{0,3}$ emission with σ = 9 mJy beam^{-1} km s^{-1}. The synthesized beams for the formamide line (green, ~4″) and for the other species (black, ~2″) are indicated in the lower left corner. The primary beam (~52″) is shown as a dashed gray circle.

Table 1. Characteristics of the SOLIS WideX backend setups.

Setup	Frequency range (GHz) [GHz]	Spectral resolution [km s^{-1}]	[MHz]	Spatial resolution [″]	[au] $^{(a)}$	Synthesized beam [″×″ (°)]	Primary beam [″]	[au] $^{(a)}$
1	80.8–84.4	7	2	4	~1200	4.5 × 3.5 (27)	61″.4	~2 × 10^4
3	95.5–99.5	6	2	4	~1200	2.2 × 1.9 (96)	59″.2	~2 × 10^4

Notes. $^{(a)}$Computed at the distance of the NGC 1333 region (~299 pc; Zucker et al. 2018).

continuum at 1.3 mm using the IRAM 30m (Lefloch et al. 1998), together with large-scale high-velocity outflow traced by the SiO (1-0) line using the VLA interferometer (Choi 2005).

3. Observations

IRAS 4A was observed with the IRAM/NOEMA interferometer during several tracks in June and September 2016. Two frequency setups were used, called 1 and 3 in Ceccarelli et al. (2017, Table 4), centered at ~82 and ~97 GHz, respectively. The array was used in configurations D and C with baselines from 15 m to 304 m for Setup 3 and from 16 to 240 m for Setup 1. Here, we present the data obtained using the WideX backend, whose characteristics are summarized in Table 1.

The phase center is on the IRAS 4A1 source, whose coordinates are listed in Table 2. The bandpass was calibrated on 3C454.3 and 3C84, while the flux was calibrated using MWC349 and LKHA101. The calibration of phase and amplitude was done observing 0333+321. The system temperatures typically ranged between 50 and 200 K. The calibration error associated with the absolute flux is ≤15%. The data were reduced using the packages CLIC and MAPPING of the GILDAS[2] software collection. The data were self-calibrated in phase only; the self-calibration solutions were applied to the data spectral cube, which was then cleaned. A continuum map (see Fig. 2) was obtained by averaging line-free channels from the self-calibrated data. The resulting synthesized beam is 2″.2 × 1″.9 (PA = 96°), for Setup 3, and

---

[2] `http://www.iram.fr/IRAMFR/GILDAS`

Table 2. Coordinates of the protostars (see also Choi 2001; Di Francesco et al. 2001; López-Sepulcre et al. 2017; Maury et al. 2019) and the analyzed emission peaks (chosen from methanol and dimethyl ether emission, see text) in the outflows.

Position	α(2000)	δ(2000)
4A1	$03^{\rm h}29^{\rm m}10\overset{\rm s}{.}536$	$31°13'31\overset{\prime\prime}{.}07$
4A2	$03^{\rm h}29^{\rm m}10\overset{\rm s}{.}428$	$31°13'32\overset{\prime\prime}{.}27$
4B	$03^{\rm h}29^{\rm m}12\overset{\rm s}{.}000$	$31°13'08\overset{\prime\prime}{.}10$
4B′	$03^{\rm h}29^{\rm m}12\overset{\rm s}{.}813$	$31°13'06\overset{\prime\prime}{.}97$
SE peak	$03^{\rm h}29^{\rm m}10\overset{\rm s}{.}591$	$31°13'17\overset{\prime\prime}{.}53$
SW peak	$03^{\rm h}29^{\rm m}10\overset{\rm s}{.}061$	$31°13'18\overset{\prime\prime}{.}61$
North peak	$03^{\rm h}29^{\rm m}10\overset{\rm s}{.}966$	$31°13'47\overset{\prime\prime}{.}87$
As region	$03^{\rm h}29^{\rm m}10\overset{\rm s}{.}184$	$31°13'16\overset{\prime\prime}{.}62$

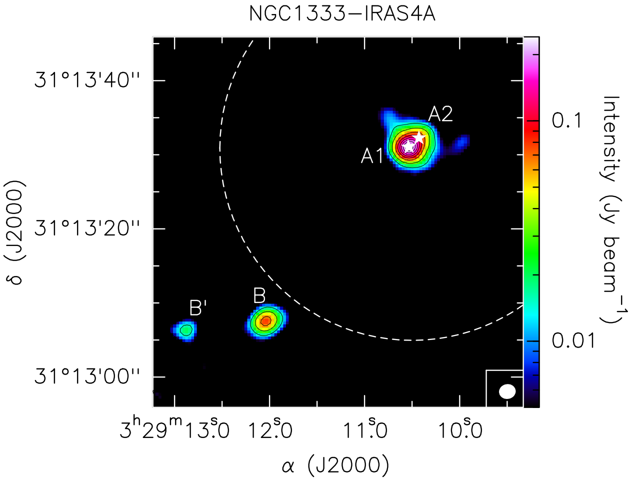

Fig. 2. Dust continuum emission maps of IRAS 4A at 95.85–99.45 GHz (Setup 3, see Table 1). Contours start at 3σ and increase by steps of 20σ, with σ = 1.5 mJy beam^{-1}. The synthesized beam (~2″) is represented in white in the lower right corner of the panel, the primary beam (~52″) is shown with a dashed white circle. The millimeter continuum sources in the field are labeled following the nomenclature used by Choi (2001) for 4A1 and 4A2 and Di Francesco et al. (2001) for B and B′.

$4\overset{\prime\prime}{.}5 \times 3\overset{\prime\prime}{.}5$ (PA = 27°) for Setup 1. The half-power primary beam is $59\overset{\prime\prime}{.}2$ and $61\overset{\prime\prime}{.}4$ for Setup 3 and Setup 1, respectively.

4. Results

4.1. Dust continuum emission

Figure 2 shows the map of the dust continuum emission at 3 mm, whose emission peaks at the position of 4A1 and 4A2. As expected, the two sources are not disentangled as the angular resolution of ~ 2″ is too close to their angular separation (~$1\overset{\prime\prime}{.}8$; Sect. 3). In addition, the two protostars IRAS 4B and IRAS 4B′ were detected (e.g., Looney et al. 2000; Choi 2001; Di Francesco et al. 2001; Maury et al. 2019), even if they were located outside the primary beam of our observations (~52″). The coordinates of all the four protostars are reported in Table 2.

The root mean square (RMS) noise level is 1.5 mJy beam^{-1} and the peak flux toward IRAS 4A1+4A2 is 240 ± 40 mJy beam^{-1}. Taking the error on the measured flux into account and considering the slightly different wavelength (2.7 mm) and angular resolution (~$1\overset{\prime\prime}{.}2$) of the observations, this flux value is consistent with the value found by López-Sepulcre et al. (2017). The uncertainties in the flux measurements include the amplitude calibration error (~15%) that dominates the RMS.

4.2. Line emission: maps

The present observations allow us to image both 4A1 and 4A2 and their molecular outflows. The study of the molecular content around the 4A1 and 4A2 protostars is beyond the scope of the present paper. Instead, we focus here on the molecular composition of the outflows.

Several lines from methanol (CH_3OH), acetaldehyde (CH_3CHO), dimethyl ether (CH_3OCH_3), and formamide (NH_2CHO) were detected along the outflows with a signal-to-noise ratio (S/N) higher than 3. Table 3 lists the detected lines with their spectroscopic properties. In Setup 3 we detected six lines of methanol that cover a range of upper level energy ($E_{\rm up}$) from 7 to 28 K; eight lines of acetaldehyde with $E_{\rm up}$ between 13 and 23 K; and four lines of dimethyl ether, blended together and all with $E_{\rm up}$ = 10 K. In Setup 1 we detected one line of formamide with $E_{\rm up}$ of 28 K.

Figure 1 shows the distribution of the line emission of the four detected iCOMs. To obtain the methanol map we integrated from −36 to 36 km s^{-1} with respect to the systematic velocity of the source (~6.5 km s^{-1}), for acetaldehyde between −15 to 15 km s^{-1}, while for formamide and dimethyl ether we integrated from −9 km to 9 km s^{-1}. First, the methanol emission is extended (~ 1′) and covers the lobes of the two outflows from the two protostars: north (North) and southwest (SW) lobes of the outflow from 4A2, and the southeast (SE) lobe from 4A1. Second, acetaldehyde emission is less extended than the methanol one (~15″) and it is bright toward the southern lobes, especially toward the SE one. The dimethyl ether emission is not resolved being less than the beam size (2″) in two positions, in the North lobe and in the region As (named by Ceccarelli et al. 2017) where the SE and SW lobes seem to cross. Finally, formamide emission is also compact (~6″) and is located around the As position (see also Ceccarelli et al. 2017). The same iCOMs are also detected in the central protostars (4A1+4A2); we note that the methanol and acetaldehyde emission is not visible in Fig. 1 because it is hidden by the dimethyl ether and formamide contours. Figure 1 clearly shows a first important result: the evidence of a spatial segregation between the different iCOMs due to the fact that their emission covers different outflow regions.

4.3. Line emission: spectra and intensities

In order to do a quantitative analysis, we extracted the spectra from different positions of the three lobes where both methanol and acetaldehyde emit. The first two selected positions correspond to the emission peaks of methanol in the two southern lobes, SE and SW, while the last selected position corresponds to the emission peak of dimethyl ether in the northern lobe, North (Fig. 1). A fourth position is the one where formamide and dimethyl ether emit, called As. The spectra extracted at the pixels corresponding to the four positions are shown in Fig. 3. It is immediately evident that the SE position is richer and brighter in iCOMs when compared to the others (SW, North, and As).

We then derived the velocity-integrated line intensities of each detected transition using a Gaussian fit, obtained with the CLASS package of the GILDAS software. All the lines used for the analysis are not contaminated by other species and are well isolated. For instance, three of the six detected methanol lines, namely $2_{-1,2}$–$1_{-1,1}$ E ($E_{\rm up}$ = 13 K), $2_{0,2}$–$1_{0,1}$ A ($E_{\rm up}$ = 7 K), and

Table 3. Spectral parameters and fit results of the detected iCOM emission lines observed using the NOEMA WideX backend toward the IRAS 4A outflow peaks (see text and Table 2).

Transition	Spectral parameters			Outflow SE			Outflow SW			Outflow North			Region As [a]		
	Frequency [b] [GHz]	E_{up} [b] [K]	$\log A_{ij}$ [b]	Area [c] [K km s^{-1}]	T_{peak} [K]	RMS [d] [mK]	Area [c] [K km s^{-1}]	T_{peak} [K]	RMS [d] [mK]	Area [c] [K km s^{-1}]	T_{peak} [K]	RMS [d] [mK]	Area [c] [K km s^{-1}]	T_{peak} [K]	RMS [d] [mK]
							CH_3OH								
$2_{1,2}$–$1_{1,1}$ A	95.91431	21.4	−5.6	17.1(0.9)	1.4	20	2.7(0.3)	0.4	20	5.1(0.5)	0.4	20	≤0.5	≤0.05	30
$2_{-1,2}$–$1_{-1,1}$ E [e]	96.73936	12.5	−4.6												
$2_{0,2}$–$1_{0,1}$ A [e]	96.74138	6.9	−5.6	199 (4)	12	20	69(4)	5	30	48(4)	3	20	37(1)	2.5	30
$2_{0,2}$–$1_{0,1}$ E [e]	96.74454	20.1	−5.5												
$2_{1,1}$–$1_{1,0}$ E	96.75550	28.0	−5.5	11.2(0.3)	0.9	20	2.0(0.2)	0.3	30	3.2(0.3)	0.2	20			
$2_{1,1}$–$1_{1,0}$ A	97.58280	21.6	−5.6	21.5(0.2)	1.9	20	2.5(0.3)	0.3	30	4.4(0.3)	0.4	30	≤0.5	≤0.05	30
							CH_3CHO								
$5_{0,5}$–$4_{0,4}$ E	95.94744	13.9	−4.5	3.9(0.2)	0.4	20	≤0.6	≤0.06	20	0.8(0.4)	0.1	20	≤0.5	≤0.05	30
$5_{0,5}$–$4_{0,4}$ A	95.96346	13.8	−4.5	3.7(0.3)	0.4	20	1.7(0.4)	0.1	20	1.3(0.5)	0.1	20	≤0.5	≤0.05	30
$5_{2,4}$–$4_{2,3}$ A	96.27425	22.9	−4.6	1.1(0.4)	0.1	30	0.7(0.3)	0.07	20	1.0(0.2)	0.1	30	0.5(0.3)	0.1	20
$5_{2,4}$–$4_{2,3}$ E	96.42561	22.9	−4.6	1.1(0.2)	0.2	30	≤0.7	≤0.07	20	0.8(0.3)	0.06	30	≤0.3	≤0.03	20
$5_{2,3}$–$4_{2,2}$ E	96.47552	23.0	−4.6	0.8(0.2)	0.1	20	≤0.7	≤0.07	20	≤0.8	≤0.08	30	≤0.3	≤0.03	20
$5_{2,3}$–$4_{2,2}$ A	96.63266	23.0	−4.6	1.5(0.3)	0.1	20	≤0.7	≤0.07	20	≤0.8	≤0.08	30	≤0.3	≤0.03	20
$5_{1,4}$–$4_{1,3}$ E	98.86331	16.7	−4.5	2.3(0.4)	0.2	20	1.6(0.8)	0.1	20	2.1(0.5)	0.2	30	2.8(0.6)	0.1	20
$5_{1,4}$–$4_{1,3}$ A	98.90094	16.5	−4.5	2.5(0.5)	0.2	20	≤0.6	≤0.06	20	1.9(0.3)	0.2	30	2.0 (0.3)	0.1	20
							CH_3OCH_3								
$4_{1,4}$–$3_{0,3}$ EA [e]	99.32443	10.2	−5.3	≤0.2	≤0.02	15	≤0.3	≤0.03	15	2.1(0.3)	0.12	15	1.8(0.5)	0.09	15
$4_{1,4}$–$3_{0,3}$ AE [e]	99.32443	10.2	−5.3												
$4_{1,4}$ - $3_{0,3}$ EE [e]	99.32521	10.2	−5.3												
$4_{1,4}$–$3_{0,3}$ AA [e]	99.32607	10.2	−5.3												
							NH_2CHO [f]								
$4_{1,4}$–$3_{1,3}$	81.69354	12.8	−4.5	≤0.2	≤0.02	7	≤0.1	≤0.01	7	≤0.06	≤0.006	7	0.4(0.1)	0.04	10

Notes. [a]Region where formamide and dimethyl ether emits (Ceccarelli et al. 2017). [b]Frequencies and spectroscopic parameters are retrieved from the JPL (Jet Propulsion Laboratory; Pickett et al. 1998) molecular database and from the CDMS (Cologne Database for Molecular Spectroscopy; Müller et al. 2005): for CH_3OH by Xu et al. (2008), for CH_3CHO by Kleiner et al. (1996), for CH_3CHO_3 by Neustock et al. (1990), for NH_2CHO by Kirchhoff et al. (1973). Upper level energies refer to the ground state of each symmetry. [c]Mean velocity–integrated line flux over the whole velocity emission range from the spectra extracted at the CH_3CHO and CH_3OH transitions at each outflow peaks (see Table 2). In case of non–detection we report the 3σ limit. The lines are centered at ~3 km s^{-1}, ~1 km s^{-1}, ~11 km s^{-1} for outflow SE, SW and North respectively, in agreement with the expected outflow velocity (Santangelo et al. 2015) given the WideX channel resolution (~6 km s^{-1}). [d]The rms is computed over a 200 km s^{-1} band around each line. [e]These lines are blended together at the WideX resolution (~2 MHz), therefore they are not used for the non-LTE analysis. [f]From Setup 1.

$2_{0,2}$–$1_{0,1}$ E (E_{up} = 21 K), are blended together at the WideX resolution (~2 MHz); therefore, they were not used in the analysis described in the next section. Table 3 reports the fit results; in the case of non-detection, the 3σ limit is reported.

5. Derivation of the column densities and abundance ratios

5.1. Methanol and acetaldehyde

We used the detected lines of methanol and acetaldehyde to estimate their column densities in the four positions of Table 2. We used the standard rotational diagram method (Goldsmith & Langer 1999), which assumes local thermodynamic equilibrium (LTE) and optically thin line emission. We checked a posteriori that the latter assumption is valid. Also, because the map in Fig. 1 shows that the emission is more extended with respect to the observation beam, we did not apply a dilution factor. The used error bar of each data point includes the spectral RMS and the calibration error (~15%).

Figure 4 shows the rotational diagrams of methanol and acetaldehyde in the SE, SW, and North positions (Table 2), and Table 4 lists the fitted values. In the As position, we could not build a rotational diagram for either of the two species as not enough lines were detected. In this case we obtained an estimate of their column density by assuming a rotational temperature ranging from 10 to 30 K, a range that includes the temperatures found in the other positions (SE, SW, and North). If no line was detected we used the 3σ limit.

To compute the methanol over acetaldehyde abundance ratios, quoted in Table 4, we adopted the assumptions that the lines emitted by the two species come from the same region, and therefore possess the same rotational temperature T_{rot}. Under these two assumptions the column density ratio R of the two species is obtained by taking the column density N_x of each species at the same rotational temperature T_{rot}, namely $R = N_1(T_{rot})/N_2(T_{rot})$. The error bar δR is then obtained by computing R at the smallest and largest T_{rot} of the two species. For example, in the Outflow SE the derived T_{rot} is equal to (11 ± 3) K and (9 ± 2) K in methanol and acetaldehyde, respectively;

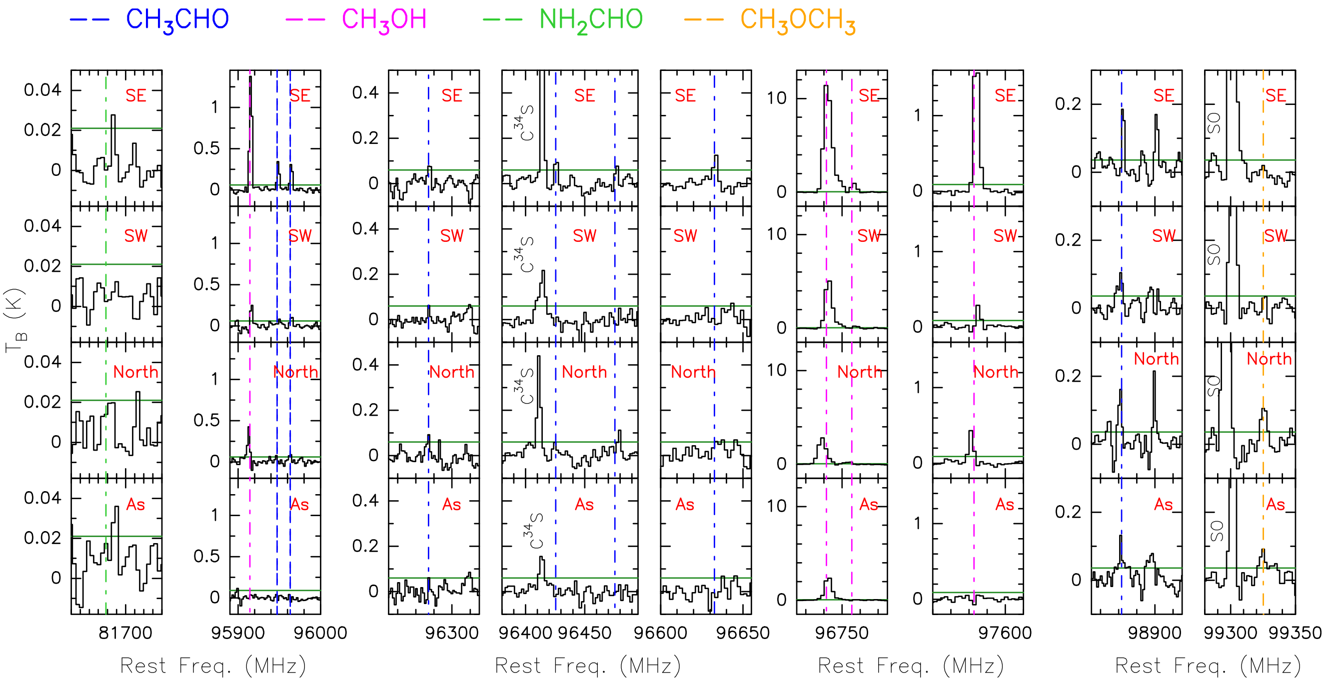

Fig. 3. Spectra toward the four positions along the outflows of IRAS 4A listed in Table 2. The horizontal green lines represent the 3σ levels (reported in Table 3); the vertical dashed lines in blue and magenta represent the rest frequency of acetaldehyde and methanol lines, respectively. The rest frequency corresponds to the protostar Local Standard of Rest (LSR) velocity (6.5 km s^{-1}).

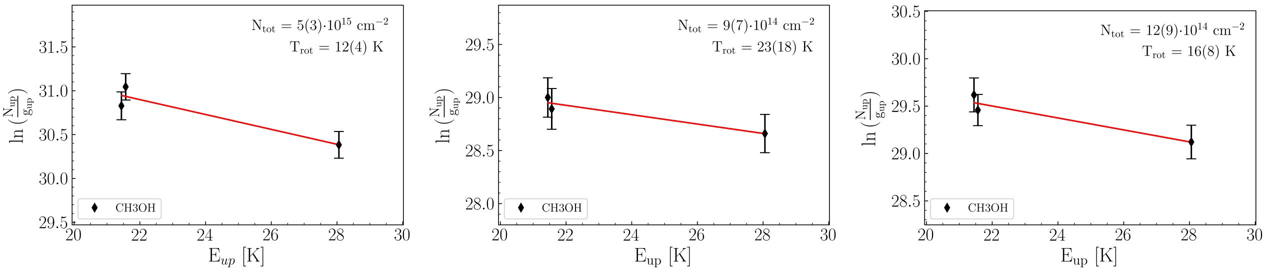

Outflow SE Outflow SW Outflow North

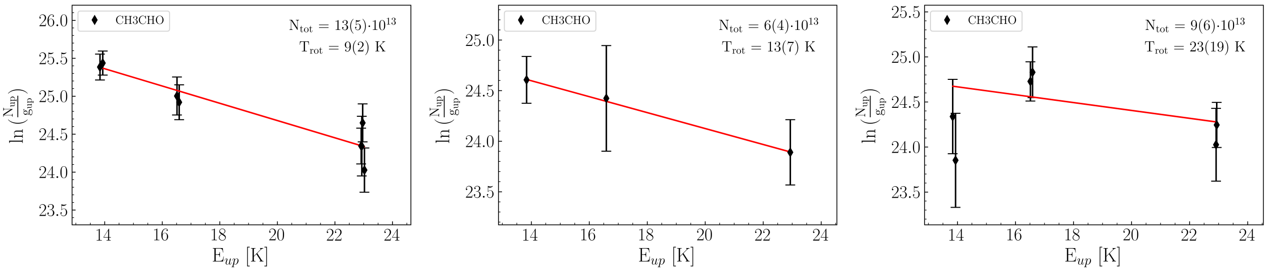

Fig. 4. *Upper panels*: rotational diagrams of methanol (CH_3OH) in outflow SE, SW, and North (*from left to right*). *Lower panels*: rotational diagrams of acetaldehyde (CH_3CHO) in outflow SE, SW, and North. The parameters $N_{\rm up}$, $g_{\rm up}$, and $E_{\rm up}$ are the column density, the degeneracy, and the energy of the upper level. The error bars on $\ln(N_{\rm up}/g_{\rm up})$ are computed by taking the calibration error on the integrated flux (15%) into account. The red lines represent the best fits.

therefore, to estimate the error δR we computed $R(T_{\rm rot})$ at 7 and 14 K. We note that the method described above allows us to reduce the error bar in the abundance ratio because the calibration uncertainty, which enters in the column density estimate of each species, cancels out when considering the column density of two species derived with the same observation data set.

For methanol, we obtain a column density $N_{\rm CH_3OH} \simeq 9-50 \times 10^{14}$ cm^{-2} and a rotational temperature $T_{\rm CH_3OH}$ between 11 and 23 K. For acetaldehyde, we obtain $N_{\rm CH_3CHO} \simeq 0.6{-}1.3 \times 10^{14}$ cm^{-2} and $T_{\rm CH_3CHO}$ between 9 and 23 K. Their abundance ratios vary from 10–20 to ~44 in the three lobes; more precisely, the SE lobe is the one with the largest CH_3OH/CH_3CHO abundance ratio. In As we only derive a lower limit to the CH_3OH/CH_3CHO abundance ratio of ≥20. We note that our observations provide different values of the CH_3OH/CH_3CHO abundance ratio compared to those previously derived by

Table 4. Results of the LTE analysis with the rotational diagrams for each outflow peak, using the observation with the NOEMA WideX backend.

Molecule			Outflow SE	Outflow SW	Outflow North	Region As [a]	L1157-B1[b]
CH_3OH	N_{tot}	$[10^{14}$ cm$^{-2}]$	50(30)	9(7)	12(9)	5-15	130(30)
	T_{rot}	[K]	11(3)	23(18)	18(8)	10–30 [c]	10.0(1.1)
CH_3CHO	N_{tot}	$[10^{14}$ cm$^{-2}]$	1.3(0.5)	0.6(0.4)	0.9(0.6)	≤(0.25–0.5)	0.7(0.3)
	T_{rot}	[K]	9(2)	13(7)	23(19)	10–30 [c]	8(1)
CH_3OCH_3	N_{tot}	$[10^{14}$ cm$^{-2}]$	≤0.5	≤0.7	1.6(0.7)	1.0(0.4)	3
	T_{rot}	[K]	11	16	19	10–30 [c]	9
NH_2CHO	N_{tot}	$[10^{14}$ cm$^{-2}]$	≤0.02	≤0.02	≤0.02	0.03(0.02)	–
	T_{rot}	[K]	11	16	19	10–30 [c]	–
$\frac{CH_3OH}{CH_3CHO}$ [d]			44(5)	11(3)	17(3)	≥20	190(60)

Notes. In the last row are shown the values of the abundance ratio of methanol to acetaldehyde for each outflow peak. [a]Region where formamide and dimethyl ether emit (Ceccarelli et al. 2017). [b]From Codella et al. (2020) based on interferometric observations. [c]Fixed rotational temperature used to derive a range of possible N_{tot}. [d]Abundance ratio computed dividing the best fit column densities derived assuming that the two species are tracing the same gas with the same properties (see text).

Holdship et al. (2019, ~300) toward the south and north lobes of the IRAS 4A outflows via single-dish observations. We attribute this difference to the fact that the single-dish observations of IRAS 4A by Holdship et al. (2019) include emission from a much larger region (including some from the central protostars) with respect to that probed by the present SOLIS observations. Moreover Holdship et al. (2019) do not explicitly derive the emitting size, even though they minimize with respect to this parameter; since the maximization is done independently for each species, their column density ratio has a relatively large intrinsic uncertainty. Therefore, the interferometric images allow us to minimize the risk of mixing different gas components (typical of shocked regions).

The abundance ratio analysis confirms what we can see from the emission maps (Fig. 1), namely that the methanol and acetaldehyde emission (and their relative abundance) is quite different in the SE lobe with respect to the SW and North lobes. We note that the difference cannot be attributed to excitation effects, having the methanol and acetaldehyde lines with similar upper level energies (E_{up} from 7 to 28 K), similar Einstein coefficients ($A_{ij} \sim 10^{-5}$ s^{-1}), and comparable derived temperatures, within the measurement errors.

To summarize, the SW and North lobes have a relatively low CH_3OH/CH_3CHO abundance ratio (8–20), whereas the SW lobe presents a ratio at least two times higher (~44). Since the SW and North lobes belong to the same outflow emanating from 4A2 and the SE lobe traces the outflow emanating from 4A1, it seems reasonable to attribute the observed difference to an intrinsic difference in the two outflows. We explore this hypothesis in the next section with the help of an astrochemical model.

5.2. Dimethyl ether and formamide

Regarding formamide and dimethyl ether, we detected only one line at most of the latter and four lines (blended at the WideX resolution, ~2 MHz) of the former in any position (see Table 3). For this reason, we did not carry out the rotational diagram analysis as we did for the other iCOMs. Furthermore, while formamide is marginally resolved at the As position, dimethyl ether is not resolved in any outflow peaks (see Fig. 1). If detected, we derived the column densities using the integrated area of the $4_{1,4}$–$3_{1,3}$ line for formamide and the blended ones for dimethyl ether, assuming fixed rotational temperatures. As for methanol and acetaldehyde, we used 11, 16, and 19 K for SE, SW, and North, respectively, and 10–30 for As. If not detected, an upper limit on the column density is derived considering the 3σ limit of the spectra and using the above rotational temperatures. The derived values are reported in Table 4.

6. Astrochemical modeling

We ran our model GRAINOBLE+ in order to reproduce the observations and understand what could be the cause of the observed difference in the CH_3OH/CH_3CHO abundance ratio in the different lobes of the IRAS 4A outflows.

There is solid evidence (observational, theoretical, and experimental) that methanol is synthesized on the grain surfaces via the hydrogenation of iced CO by the successive addition of H atoms (Boogert et al. 2015; Tielens & Hagen 1982; Watanabe & Kouchi 2002). On the contrary, the acetaldehyde formation route is less clear, and the two paths, formation in the gas phase or on the grain surfaces, are still debated. Specifically, grain surface models predict that CH_3CHO could be formed through the combination of the two radicals CH_3 and HCO (previously formed by photodissociation of methanol and formaldehyde, respectively) on the surface of the grains (Garrod & Herbst 2006). However, recent quantum chemistry computation by Enrique-Romero et al. (2016, 2019) show that alternative channels leading back to the two simple species CH_4 and CO are competitive. Conversely, the gas-phase models claims that acetaldehyde formation could occur by the oxidation of hydrocarbons (formed previously on the grain mantles via hydrogenation of carbon chains; Charnley et al. 1992; Charnley 2004). In particular, the injection from grain mantles of ethane (C_2H_6) is expected to drive CH_3CH_2 that will then react in the gas phase with atomic oxygen, giving CH_3CHO (Charnley 2004). The crucial reaction is therefore

$$CH_3CH_2 + O \rightarrow CH_3CHO + H. \qquad (1)$$

Following these two possibilities, we ran a grid of astrochemical models in order to reproduce our observations and to understand the possible cause of the difference in the observed CH_3OH/CH_3CHO values in the two IRAS 4A outflows.

6.1. Model description

GRAINOBLE+ is a gas-grain model simulating the chemical evolution of gas and ices. It is the upgraded version of GRAINOBLE, initially developed by Taquet et al. (2012a); in particular, it is re-coded and improved in terms of computational efficiency and treatment of processes. The GRAINOBLE+ version[3] allows an easy incorporation of many complicated processes that occur in the gas and on the grain surfaces. The code can carry out an easy implementation of evolution of physical conditions of a cloud with a given time-dependent physical profile. Additionally, the new code allows a distribution of size for the grains, multilayer formation of the grain ice mantle, growth and depletion of the ice, and desorption.

In this work we used a chemical network of 522 species and 7785 reactions based on the KIDA database[4], which has been updated from various recent works (e.g., Loison et al. 2014; Balucani et al. 2015; Skouteris et al. 2017, 2018).

In order to simulate the passage of a shock in IRAS 4A, we employed the gas-phase mode of GRAINOBLE+. The simulation follows two steps: (1) a cold molecular gas phase at 10 K and $2 \times 10^4 \mathrm{cm}^{-3}$ H-nuclei density (n_H); (2) a post-shock gas phase where density and temperature suddenly jump to 2×10^6 cm^{-3} and 70 K. In other words, the second phase inherits the evolved chemical composition of the cloud from the cold phase[5]. Additionally, the gas is infused by species that were formerly synthesized in ice mantles due to the grain sputtering caused by the shock passage.

It is possible that before reaching the temperature of 70 K, the shocked gas passes through a short initial phase with high temperature. However, this phase unlikely affects the results reported in the next section because there are no known gas-phase reactions with activation barriers that form acetaldehyde. This is confirmed by models taking into account the temperature evolution in the shocked gas (e.g., Nesterenok 2018; Burkhardt et al. 2019).

We do not have precise estimates of the density and temperature in the positions where we derived the CH_3OH/CH_3CHO abundance ratio. However, the values derived at positions close to those selected here via a non-LTE analysis of observed SO_2 lines (Taquet et al. 2020) are similar to those adopted in our modeling. We assumed that the cosmic ray ionization rate is the same as toward L1157-B1 ($\zeta = 3 \times 10^{-16}$ s^{-1}; Podio et al. 2014) and that the abundance of the injected species are also similar to the values adopted for L1157–B1 (see Table B1 of Codella et al. 2017), listed in Table 5.

We ran series of models to compare the observed CH_3OH/CH_3CHO abundance ratio with the predicted ratio, and to understand what the ratio depends on. We start exploring the gas-phase formation route of acetaldehyde assuming that its formation is dominated by reaction (1) in the passage of shock. Oxygen is much more abundant than the injected ethyl radical in the post-shock phase; therefore, CH_3CH_2 is the bottleneck of the rate of the reaction (1).

First, we ran a grid of 169 models with different injected abundances at the beginning of the shocked phase for ethyl radical (CH_3CH_2) and methanol in the ranges $[4 \times 10^{-9}, 4 \times 10^{-7}]$ and $[4 \times 10^{-8}, 4 \times 10^{-6}]$, respectively. The methanol abundance range was chosen in order to include the observed values in the hot corinos and in the protostellar shocks (the L1157-B1 outflow in particular); the ethyl radical range was chosen in order to match our observed CH_3OH/CH_3CHO abundance ratio. The results are shown in Fig. 5 and described in the next section.

Table 5. Injected abundances (with respect to H-nuclei) into the gas phase at the second step of the model.

Molecules	Injected abundances (/H)
CO_2	3×10^{-5}
H_2O	2×10^{-4}
OCS	2×10^{-6}
H_2CO	1×10^{-6}
NH_3	2×10^{-5}

Notes. These values are based on previous observations toward L1157-B1 (Codella et al. 2017).

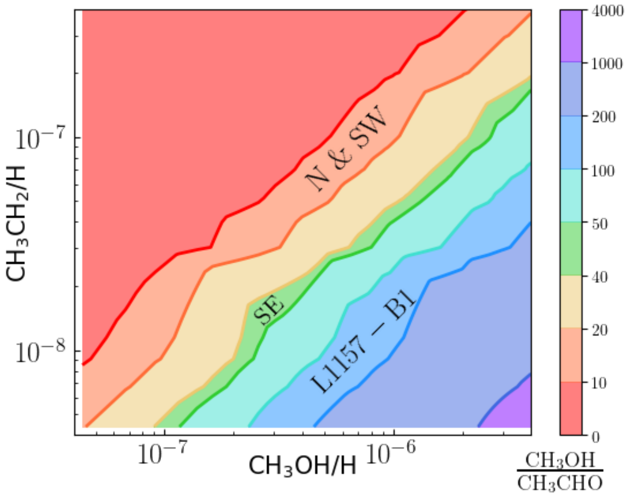

Fig. 5. Contour map of the CH_3OH/CH_3CHO abundance ratio at 1000 yr after the start of the shock passage. The *x*- and *y*-axis are the injected abundances of methanol $[4 \times 10^{-8}, 4 \times 10^{-6}]$ and the parent molecule of acetaldehyde, ethyl radical CH_3CH_2 $[4 \times 10^{-9}, 4 \times 10^{-7}]$, respectively. The measured methanol to acetaldehyde abundance ratio of the North and SW outflows (8−20) fall in the orange band, and that of SE (38−50) in the green band; the L1157-B1 value (130−250) is covered by the blue band (Codella et al. 2020).

Second, we studied the influence of the density and cosmic ray ionization rate ζ on the chemical evolution, and how the CH_3OH and CH_3CHO abundances and their relative ratio depend on the time after the shock passage. We note that protostellar shocks could be local accelerators of cosmic ray protons (Padovani et al. 2016), and therefore in this work ζ is an unknown parameter. We then ran two additional models. In the first we decrease the chosen n_H density value to 2×10^5 cm^{-3}; in the second we decrease the chosen cosmic ray ionization rate value to $\zeta = 3 \times 10^{-17}$ s^{-1} for the post-shock phase. The injected abundances of methanol is 3×10^{-6} and for the ethyl radical it is 3×10^{-7} in both cases. These values are chosen such that the models reproduce the observed CH_3OH/CH_3CHO abundance ratios for the SW and North lobes (8-20) at 1000 yr (orange band in Fig. 5) and for the SE lobe as well. The results are shown in Fig. 6 and described in the next section.

Finally, we ran a model with the assumption that acetaldehyde is synthesized on the ice mantles and injected directly into the gas phase at the passage of the shock.

---

[3] A detailed description of the GRAINOBLE+ model will be presented in a forthcoming dedicated article.

[4] `http://kida.obs.u-bordeaux1.fr`

[5] We do not compute the grain mantle composition as it is treated as a parameter in the following analysis.

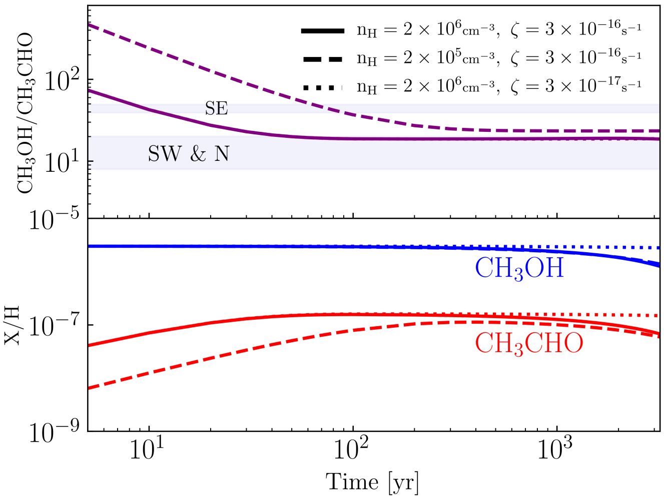

Fig. 6. Time evolution of abundances of methanol in blue and acetaldehyde in red (*bottom*) and their ratios in purple (*top*) for the same injected methanol abundance, 3×10^{-6}, and ethyl radical value, 3×10^{-7}. The different line styles correspond to models run with different conditions, as reported in the upper panel legend. The CH_3OH/CH_3CHO abundance ratio is constant if both species are directly injected from the grain mantles (see text).

6.2. Model results

Figure 5 shows the contour map of the CH_3OH/CH_3CHO abundance ratio at 1000 yr after the shock passage as a function of the injected methanol and ethyl radical, assuming that acetaldehyde is entirely synthesized in the gas phase. We note that the chosen age (1000 yr) is approximately the same magnitude as the kinematical age of L1157-B1 (Podio et al. 2016; Codella et al. 2017) and, likely, IRAS 4A outflows. First, the figure shows that there is a linear dependence of the CH_3OH/CH_3CHO abundance ratio on the injected methanol abundance and on the ethyl radical abundance in the range explored in our simulations. Second, reasonable values of methanol and ethyl radical abundance can reproduce the observed values in the four IRAS 4A outflow positions that we studied (Table 2).

In Fig. 6, we show the evolution of methanol and acetaldehyde abundance as a function of the time after the shock passage, for different densities n_H and cosmic ray ionization rates ζ. Given that methanol is a grain surface product, even by varying n_H or ζ, the injected abundance remains constant in the early stages of the shock up to $\sim 2 \times 10^3$ yr. The time evolution of acetaldehyde in the early stages is different from that of methanol; while the latter remains constant, acetaldehyde abundance increases soon after the shock passage. This is expected since we assumed that acetaldehyde is a gas phase product and its evolution is dominated by the formation through ethyl radical reaction (1). Furthermore, the time evolution of acetaldehyde in the post-shock phase is influenced by variation of n_H or ζ. Lower density slows down the formation rate of acetaldehyde in the early stages; this is due the fact that in lower density gas the ion abundance is higher. Therefore, the contribution of destruction rates is higher in the evolution. Similar to methanol, a lower cosmic ray ionization rate does not affect the early stages.

Finally, we ran a model in which acetaldehyde is synthesized on the icy dust surfaces and injected directly into the gas phase. Therefore, in the model the species injected into the gas phase right after the shock is no longer the ethyl radical but acetaldehyde, whose abundance is chosen to be equal to the observed one. Therefore, the gas-phase production of acetaldehyde is, in this case, negligible. As for methanol, the abundance of acetaldehyde, now injected from grains, remains constant up to $\sim 2\times10^3$ yr when the destruction by ions (H_3O^+ in this specific case) becomes dominant. Therefore, the difference in the abundance of acetaldehyde between the gas- and grain-synthesized models is only within the first 200 yr of the shocked phase, when acetaldehyde takes time to be formed by the reactions between ethyl radical with atomic oxygen.

7. Discussion

7.1. Two IRAS 4A outflows

Our new SOLIS observations show that the two outflows emanating from 4A1 and 4A2, previously identified by Choi (2005) and Santangelo et al. (2015) via simple molecules (SiO, CO, and SO), are enriched with methanol all across the three (visible) lobes. Conversely, acetaldehyde is spread only over the southern lobes and is concentrated in a compact spot in the northern one. Therefore, a first conclusion of this work is that in the protostellar post-shock regions there is the release in gas phase of methanol, previously formed on the grain surfaces, and the production of acetaldehyde. The statistics are very poor for the moment, with the two IRAS 4A outflows and the L1157–B1 outflow in which acetaldehyde is detected with interferometric observations (Codella et al. 2015, 2017, 2020).

For the IRAS 4A outflows, the SE lobe is richer in both methanol and acetaldehyde, specifically the outflow emanating from 4A1. We note that this is the opposite behavior with respect to the SiO emission, which is instead brighter along the 4A2 outflow (Choi 2005). This anti-correlation with SiO is also seen in other (simple) molecules, such as NH_3, H_2CO, and HCN by Choi et al. (2011). As Choi et al. (2011) suggested, it could be due to a different strength of the shock (the sputtering of Si could require different shock velocities with respect to the other molecules) or to SiO tracing different physical conditions with respect to the other molecules. For example, SiO could trace the jet, while the other molecules could have originated in the gas entrained by the jet (e.g., Bachiller et al. 1998; Ospina-Zamudio et al. 2018, 2019). Linked with this, the different spatial distribution between SiO and other species, could be due to time-evolution effects, namely different ages of the shocks, as previously observed in other outflows (e.g., Castets et al. 2001). We discuss this point further in the next section.

Finally, the origin of the iCOMs emission in the As position is not clear. It does not seem to be clearly associated with any of the two southern lobes, but rather with the point where they intersect. That would imply that additional shocks can occur at the interface of the swept-up cavities opened up by the jets. Higher spatial resolution observations are needed to confirm or reject this hypothesis.

7.2. CH_3OH/CH_3CHO abundance in IRAS 4A1 and 4A2 outflows

In Sect. 5 we measured the methanol to acetaldehyde abundance ratio toward the three positions of the two IRAS 4A outflows, in the North, SW, and SE lobes (Table 4). While the North and SW lobes have a similar values, between 8 and 20 (considering the error bars), the SE lobe has higher CH_3OH/CH_3CHO, 38–50. In other words, the methanol to acetaldehyde abundance ratio is about two times higher in the outflow emanating from 4A1 with respect to that from 4A2. In this section we try to understand the origin of this difference, keeping in mind that while methanol is a past grain-surface product, acetaldehyde can either be itself a past grain-surface or a gas-phase product.

One easy possible explanation then of the CH_3OH/CH_3CHO difference is that the grain mantle composition is different in the two outflows. However, this seems unlikely because, on the one hand, no gradient in the ratio is seen between the North and SW lobes of the 4A2 outflow; moreover, the SW and SE lobes are very close in space, closer than the two 4A2 outflow positions where we estimated the CH_3OH/CH_3CHO abundance ratio. Therefore, although we cannot totally exclude it, it seems to us that the different grain composition is an improbable explanation.

If acetaldehyde is synthesized by the gas-phase reaction (1), there are more possibilities than a different grain mantle composition. As shown by the modeling in Sect. 6, a lower density or a younger age of the 4A1 outflow with respect to 4A2 would explain the observed CH_3OH/CH_3CHO difference. Specifically, if the two outflows are very young and 4A1 is younger than about 200 yr, then this would explain why its ratio is higher than the 4A2 value (see Fig. 6).

Unfortunately, our observations did not have enough methanol lines to allow a meaningful non-LTE analysis to derive the volume density, so we do not know if the density in the 4A1 outflow is lower than in the 4A2 outflow. With a non-LTE analysis on SO_2, Taquet et al. (2020) suggest that there is no significant difference in density between the outflow driven by 4A1 and that from 4A2. On the other hand, assuming a typical shock velocity of 100 $km\,s^{-1}$, we estimate a kinematical age of ~200 yr for the 4A1 outflow which has a very short extent; this seems to support the younger age of 4A1 hypothesis. Furthermore, Santangelo et al. (2015), using high spatial resolution observations of CO, SiO, and SO, showed that the 4A1 jet is faster than the 4A2 one; this, combined with the smaller spatial extension again supports the hypothesis that the 4A1 outflow is younger than that of 4A2. In favor of a different age for the two outflows there is also the observed chemical differentiation between the two driving sources: 4A1 is bright in the continuum but lacks iCOM line emission, exactly the opposite of 4A2 (e.g., López-Sepulcre et al. 2017). One of the possible explanations for this situation is the smaller hot corino size, which could also imply a younger age of 4A1, and this agrees with the younger age of its outflow as well.

In summary, the different CH_3OH/CH_3CHO abundance ratio measured in the 4A1 and 4A2 outflows is unlikely caused by a different grain mantle composition of the two outflows because the more extended 4A2 outflow shows no significant variation in this ratio on a scale of about 6000 au. On the contrary, the observed CH_3OH/CH_3CHO abundance ratio is consistent with the scenario in which (i) the 4A1 outflow is younger (and consequently faster) than the 4A2 outflow and (ii) in both outflows acetaldehyde is synthesized in the gas phase. The major reaction is between atomic oxygen and ethyl radical. The gas-phase synthesis hypothesis also agrees with theoretical quantum chemistry studies (Enrique-Romero et al. 2016, 2019). Thus, although terrestrial laboratory experiments show that acetaldehyde can be formed on the surfaces of dust grains (e.g., Bennett et al. 2005a,b; Öberg et al. 2009), our results provide evidence that the gas-phase formation route cannot be neglected, and actually appears to be the dominant process in the IRAS 4A outflows. We note that these conclusions are robust as they depend very little on the details of the modeling being based on known reactions in the gas phase.

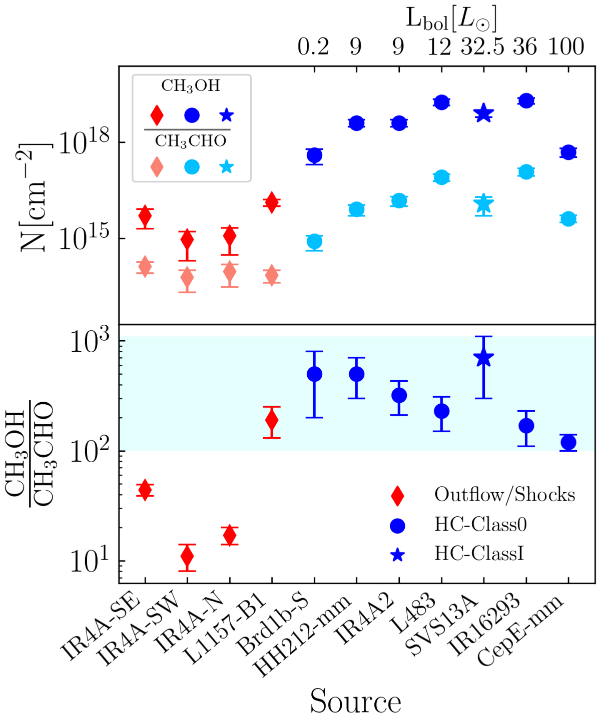

Fig. 7. Abundance ratios of CH_3OH to CH_3CHO (*bottom panel*) and the CH_3OH and CH_3CHO column density (*upper panel*) compared to different sources whose emitting size has been estimated via interferometric observations: the values in the outflows of IRAS 4A (this paper), in the outflow of L1157-B1 (Codella et al. 2020), the Class I source SVS 13A (Bianchi et al. 2019), and the Class 0 sources, in decreasing order of bolometric luminosity: Barnard1b-S (Marcelino et al. 2018), HH212-mm (Bianchi et al. 2017; Codella et al. 2020), IRAS 4A2 (Taquet et al. 2015; López-Sepulcre et al. 2017), L483 (Jacobsen et al. 2019), IRAS 16293-2422B (Jørgensen et al. 2016), CepE-mm (Ospina-Zamudio et al. 2018). The outflow values are shown in red (pink for CH_3CHO), the hot corinos in blue (cyan for CH_3CHO), using diamonds for the outflows, dots for Class 0 sources, and stars for the Class I sources. The cyan band represents the area in which the hot corino values fall.

7.3. Comparison with other solar-type objects

Figure 7 shows the methanol to acetaldehyde abundance ratio in the IRAS 4A outflows, compared with the values measured in other low and intermediate star forming regions for which the emitting size as been estimated via interferometric observations: the L1157-B1 molecular shock and seven hot corinos.

First, the IRAS 4A outflows have a much lower value for CH_3OH/CH_3CHO with respect to the L1157–B1 value (130–250), reliably measured by Codella et al. (2020). Following the discussion of the previous section, this could be due to a difference in the composition of the grain mantles, to a lower density, or to a younger age of the 4A outflows with respect to the L1157-B1 value. At present, we do not have enough information to support or rule out any of the three possibilities; a more accurate analysis of the IRAS 4A outflows is needed. Obviously, having more information of one key actor, the abundance of ethyl radical in these outflows, could shed more light on why the two outflow systems are different.

Finally, the same difference observed between the IRAS 4A and L1157 outflows, if not larger, is observed with respect to the values measured in Class 0 and I hot corinos (Marcelino et al. 2018; Bianchi et al. 2017, 2019; Taquet et al. 2015; López-Sepulcre et al. 2017; Jacobsen et al. 2019; Jørgensen et al. 2016; Codella et al. 2020; Ospina-Zamudio et al. 2018).

In Fig. 7, we ordered the hot corinos according to their increasing bolometric luminosity $L_{\rm bol}$, keeping in mind that the measure of $L_{\rm bol}$ is relatively uncertain. It is possible to note an interesting trend: in the Class 0 hot corinos, the CH_3OH/CH_3CHO abundance ratio decreases with increasing $L_{\rm bol}$. Our modeling (Sect. 6) is not directly applicable to the hot corino case for two main reasons: 1) the hot corino density ($n_H \sim 10^7 cm^{-3}$) is higher than those used in our model (Figs. 6 and 2) there is continuous injection of the infalling material toward the center. Having said that, it seems improbable that the behavior shown in Fig. 7 has something to do with a time effect. In the hot corino conditions (higher density and low cosmic ionization rate) the synthesis in the gas phase is fast during the first decades, while the destruction by molecular ions is slow in the later stages ($\geq 10^5$ yr), leading to a CH_3OH/CH_3CHO abundance ratio that is almost constant.

On the contrary, a possible interpretation is that higher luminosity corresponds to larger hot corino sizes (namely larger regions with a dust temperature ≥100 K; Ceccarelli et al. 2007) and, assuming a central peaked density distribution, regions with lower densities. Since methanol is produced during the pre-stellar phase by hydrogenation of frozen CO (Taquet et al. 2012b; Vasyunin et al. 2017), a higher density will bring a greater methanol abundance; acetaldehyde, on the other hand, could be either a past grain-surface or a present-day gas-phase product (see Sect. 6). Therefore, the decreasing CH_3OH/CH_3CHO abundance ratio could indicate that while methanol abundance decreases with density, acetaldehyde or its gas-phase precursors do not. We note that these conclusions have to be taken with caution as the errors on the hot corinos bolometric luminosity are relatively large, but they are worth a deeper study.

8. Conclusions

In this work we reported new observations using the IRAM/NOEMA interferometer in the context of the SOLIS Large Program, and the detection of several iCOMs in the two outflows emanating from IRAS 4A1 and 4A2: methanol, acetaldehyde, dimethyl ether, and formamide. This is the second ever outflow system, after the solar-type protostellar L1157 outflow, where multiple iCOMs have been detected using interferometers. Our main conclusions are the following:

- As in the case of L1157-B1 (Codella et al. 2017), iCOMs are not homogeneously distributed across the IRAS 4A outflows: methanol is more widespread over the two outflows, while acetaldehyde emission is only bright in the southern lobes, and dimethyl ether and formamide are concentrated in a spot at the (apparent) interface between the southern lobes of the 4A1 and 4A2 outflows. We therefore advise that derivation of iCOM abundance ratios from single-dish observations could be hazardous.
- The measured methanol to acetaldehyde abundance ratio is twice as large in the 4A1 outflow with respect to that in the 4A2 outflow; the comparison between these results with model predictions suggests that 1) the 4A1 outflow is younger than the 4A2 one and 2) acetaldehyde is synthesized in the gas phase by the reaction of atomic oxygen with ethyl radical. Alternatively, the grain mantle distribution might vary widely on small scales, which seems unlikely since the larger scale 4A2 outflow shows a similar CH_3OH/CH_3CHO value in two distant points of the southern and northern lobes.
- Considering the CH_3OH/CH_3CHO abundance ratio, the two IRAS 4A outflows show a sharp difference with respect to the L1157-B1 outflow. This may indicate that either the grain mantles or the gas volume densities are very different in the two regions. Additional observations are necessary to better constrain the reason of the observed difference.
- The methanol to acetaldehyde abundance ratio in the solar-type hot corinos is at least ten times higher than in the IRAS 4A outflows, again pointing to different grain mantle composition or densities. Interestingly, we note that CH_3OH/CH_3CHO tentatively decreases with increasing bolometric luminosity of the Class 0 hot corino; a possible reason could be the larger sizes of the hot corinos.

Acknowledgements. We are very grateful to all the IRAM staff, whose dedication allowed us to carry out the SOLIS project. This project has received funding from: (i) the European Research Council (ERC) under the European Union's Horizon 2020 research and innovation programme, for the Project "The Dawn of Organic Chemistry" (DOC), grant agreement No 741002. (ii) This work has been supported by the project PRIN-INAF 2016 The Cradle of Life - GENESIS-SKA (General Conditions in Early Planetary Systems for the rise of life with SKA). V.T. acknowledges the financial support from the European Union's Horizon 2020 research and innovation programme under the Marie Sklodowska-Curie grant agreement n. 664931. C.F. acknowledges support from the French National Research Agency in the framework of the Investissements d'Avenir program (ANR-15- IDEX-02), through the funding of the "Origin of Life" project of the Univ. Grenoble-Alpes

References

Altwegg, K., Balsiger, H., Bar-Nun, A., et al. 2016, Sci. Adv., 2, e1600285
Arce, H. G., Santiago-García, J., Jørgensen, J. K., Tafalla, M., & Bachiller, R. 2008, ApJ, 681, L21
Bachiller, R., Guilloteau, S., Gueth, F., et al. 1998, A&A, 339, L49
Balucani, N., Ceccarelli, C., & Taquet, V. 2015, MNRAS, 449, L16
Bennett, C. J., Jamieson, C. S., Osamura, Y., & Kaiser, R. I. 2005a, ApJ, 624, 1097
Bennett, C. J., Osamura, Y., Lebar, M. D., & Kaiser, R. I. 2005b, ApJ, 634, 698
Bianchi, E., Codella, C., Ceccarelli, C., et al. 2017, A&A, 606, L7
Bianchi, E., Codella, C., Ceccarelli, C., et al. 2019, MNRAS, 483, 1850
Blake, G. A., Sandell, G., van Dishoeck, E. F., et al. 1995, ApJ, 441, 689
Boogert, A. C. A., Gerakines, P. A., & Whittet, D. C. B. 2015, ARA&A, 53, 541
Bottinelli, S., Ceccarelli, C., Lefloch, B., et al. 2004, ApJ, 615, 354
Burkhardt, A. M., Shingledecker, C. N., Le Gal, R., et al. 2019, ApJ, 881, 32
Castets, A., Ceccarelli, C., Loinard, L., Caux, E., & Lefloch, B. 2001, A&A, 375, 40
Cazaux, S., Tielens, A. G. G. M., Ceccarelli, C., et al. 2003, ApJ, 593, L51
Ceccarelli, C., Castets, A., Loinard, L., Caux, E., & Tielens, A. G. G. M. 1998, A&A, 338, L43
Ceccarelli, C., Caselli, P., Herbst, E., Tielens, A. G. G. M., & Caux, E. 2007, Protostars and Planets V (Tucson, AZ: University of Arizona Press), 47
Ceccarelli, C., Caselli, P., Fontani, F., et al. 2017, ApJ, 850, 176
Charnley, S. B. 2004, Adv. Space Res., 33, 23
Charnley, S. B., Tielens, A. G. G. M., & Millar, T. J. 1992, ApJ, 399, L71
Choi, M. 2001, ApJ, 553, 219
Choi, M. 2005, ApJ, 630, 976
Choi, M., Kang, M., Tatematsu, K., Lee, J.-E., & Park, G. 2011, PASJ, 63, 1281
Codella, C., Fontani, F., Ceccarelli, C., et al. 2015, MNRAS, 449, L11
Codella, C., Ceccarelli, C., Caselli, P., et al. 2017, A&A, 605, L3
Codella, C., Ceccarelli, C., Bianchi, E., et al. 2020, A&A, 635, A17
Coutens, A., Jørgensen, J. K., van der Wiel, M. H. D., et al. 2016, A&A, 590, L6
De Simone, M., Codella, C., Testi, L., et al. 2017, A&A, 599, A121
De Simone, M., Ceccarelli, C., Codella, C., et al. 2020, ApJ, 896, L3
Di Francesco, J., Myers, P. C., Wilner, D. J., Ohashi, N., & Mardones, D. 2001, ApJ, 562, 770
Elsila, J. E., Glavin, D. P., & Dworkin, J. P. 2009, Meteorit. Planet. Sci., 44, 1323
Enrique-Romero, J., Rimola, A., Ceccarelli, C., & Balucani, N. 2016, MNRAS, 459, L6

Enrique-Romero, J., Rimola, A., Ceccarelli, C., et al. 2019, ACS Earth Space Chem., 3, 2158
Garrod, R. T. 2008, A&A, 491, 239
Garrod, R. T., & Herbst, E. 2006, A&A, 457, 927
Goldsmith, P. F., & Langer, W. D. 1999, ApJ, 517, 209
Gueth, F., Guilloteau, S., & Bachiller, R. 1996, A&A, 307, 891
Herbst, E. 2017, Int. Rev. Phys. Chem., 36, 287
Herbst, E., & van Dishoeck, E. F. 2009, ARA&A, 47, 427
Holdship, J., Viti, S., Codella, C., et al. 2019, ApJ, 880, 138
Jacobsen, S. K., Jørgensen, J. K., Di Francesco, J., et al. 2019, A&A, 629, A29
Jørgensen, J. K., van der Wiel, M. H. D., Coutens, A., et al. 2016, A&A, 595, A117
Jørgensen, J. K., Müller, H. S. P., Calcutt, H., et al. 2018, A&A, 620, A170
Karska, A., Herczeg, G. J., van Dishoeck, E. F., et al. 2013, A&A, 552, A141
Kirchhoff, W. H., Johnson, D. R., & Lovas, F. J. 1973, J. Phys. Chem. Ref. Data, 2, 1
Kleiner, I., Lovas, F. J., & Godefroid, M. 1996, J. Phys. Chem. Ref. Data, 25, 1113
Kristensen, L. E., van Dishoeck, E. F., Bergin, E. A., et al. 2012, A&A, 542, A8
Lay, O. P., Carlstrom, J. E., & Hills, R. E. 1995, ApJ, 452, L73
Lefloch, B., Castets, A., Cernicharo, J., Langer, W. D., & Zylka, R. 1998, A&A, 334, 269
Lefloch, B., Ceccarelli, C., Codella, C., et al. 2017, MNRAS, 469, L73
Loison, J.-C., Wakelam, V., & Hickson, K. M. 2014, MNRAS, 443, 398
Looney, L. W., Mundy, L. G., & Welch, W. J. 2000, ApJ, 529, 477
López-Sepulcre, A., Sakai, N., Neri, R., et al. 2017, A&A, 606, A121
Marcelino, N., Gerin, M., Cernicharo, J., et al. 2018, A&A, 620, A80
Maury, A. J., André, P., Testi, L., et al. 2019, A&A, 621, A76
Mendoza, E., Lefloch, B., López-Sepulcre, A., et al. 2014, MNRAS, 445, 151
Millar, T. J., Herbst, E., & Charnley, S. B. 1991, ApJ, 369, 147
Müller, H. S. P., Schlöder, F., Stutzki, J., & Winnewisser, G. 2005, J. Mol. Struct., 742, 215
Nesterenok, A. V. 2018, Astrophys. Space Sci., 363, 151
Neustock, W., Guarnieri, A., Demaison, J., & Wlodarczak, G. 1990, Z. Naturforsch. A, 45, 702
Öberg, K. I., Garrod, R. T., van Dishoeck, E. F., & Linnartz, H. 2009, A&A, 504, 891
Öberg, K. I., van der Marel, N., Kristensen, L. E., & van Dishoeck, E. F. 2011, ApJ, 740, 14
Ospina-Zamudio, J., Lefloch, B., Ceccarelli, C., et al. 2018, A&A, 618, A145
Ospina-Zamudio, J., Lefloch, B., Favre, C., et al. 2019, MNRAS, 490, 2679
Padovani, M., Marcowith, A., Hennebelle, P., & Ferrière, K. 2016, A&A, 590, A8
Pickett, H. M., Poynter, R. L., Cohen, E. A., et al. 1998, J. Quant. Spectr. Rad. Transf., 60, 883
Pizzarello, S., Cooper, G. W., & Flynn, G. J. 2006, Meteorites and the Early Solar System II (Tucson, AZ: University of Arizona Press), 625
Podio, L., Lefloch, B., Ceccarelli, C., Codella, C., & Bachiller, R. 2014, A&A, 565, A64
Podio, L., Codella, C., Gueth, F., et al. 2016, A&A, 593, L4
Santangelo, G., Codella, C., Cabrit, S., et al. 2015, A&A, 584, A126
Skouteris, D., Vazart, F., Ceccarelli, C., et al. 2017, MNRAS, 468, L1
Skouteris, D., Balucani, N., Ceccarelli, C., et al. 2018, ApJ, 854, 135
Smith, K. W., Bonnell, I. A., Emerson, J. P., & Jenness, T. 2000, MNRAS, 319, 991
Taquet, V., Ceccarelli, C., & Kahane, C. 2012a, A&A, 538, A42
Taquet, V., Ceccarelli, C., & Kahane, C. 2012b, ApJ, 748, L3
Taquet, V., López-Sepulcre, A., Ceccarelli, C., et al. 2015, ApJ, 804, 81
Taquet, V., Codella, C., De Simone, M., et al. 2020, A&A, 637, A63
Tielens, A. G. G. M., & Hagen, W. 1982, A&A, 114, 245
Turner, B. E. 1990, ApJ, 362, L29
Vasyunin, A. I., Caselli, P., Dulieu, F., & Jiménez-Serra, I. 2017, ApJ, 842, 33
Watanabe, N., & Kouchi, A. 2002, ApJ, 571, L173
Xu, L.-H., Fisher, J., Lees, R., et al. 2008, J. Mol. Spectr., 251, 305
Zucker, C., Schlafly, E. F., Speagle, J. S., et al. 2018, ApJ, 869, 83

MNRAS **000**, 1–14 (2021) Preprint 6 January 2022 Compiled using MNRAS LaTeX style file v3.0

A train of shocks at 3000 au scale?
Exploring the clash of an expanding bubble into the NGC 1333 IRAS 4 region. SOLIS XVI

Marta De Simone,[1,2]★ Claudio Codella,[2,1] Cecilia Ceccarelli,[1] Ana López-Sepulcre,[3,1] Roberto Neri,[3] Pedro Ruben Rivera-Ortiz,[1] Gemma Busquet,[1] Paola Caselli,[4] Eleonora Bianchi,[1,2] Francesco Fontani,[2,4] Bertrand Lefloch,[1] Yoko Oya,[5] and Jaime E. Pineda[4]

[1]*Univ. Grenoble Alpes, CNRS, IPAG, 38000 Grenoble, France*
[2]*INAF, Osservatorio Astrofisico di Arcetri, Largo E. Fermi 5, 50125 Firenze, Italy*
[3]*Institut de Radioastronomie Millimétrique (IRAM), 300 rue de la Piscine, 38400 Saint-Martin d'Hères, France*
[4]*Max-Planck-Institut für extraterrestrische Physik (MPE), Giessenbachstrasse 1, 85748 Garching, Germany*
[5]*Department of Physics, The University of Tokyo, Bunkyo-ku, Tokyo 113-0033, Japan*

Accepted —. Received —; in original form —

ABSTRACT

There is evidence that the star formation process is linked to the intricate net of filaments in molecular clouds, which may be also due to gas compression from external triggers. We studied the southern region of the Perseus NGC 1333 molecular cloud, known to be heavily shaped by similar external triggers, to shed light on the process that perturbed the filament where the Class 0 IRAS4 protostars lie. We use new IRAM-NOEMA observations of SiO and CH_3OH, both known to trace violent events as shocks, toward IRAS 4A as part of the Large Program Seeds Of Life in Space (SOLIS). We detected three parallel elongated (>6000 au) structures, called fingers, with narrow line profiles ($\sim$1.5 km s^{-1}) peaked at the cloud systemic velocity, tracing gas with high density (5–20$\times10^5$ cm^{-3}) and high temperature (80–160 K). They are chemically different, with the northern finger traced by both SiO and CH_3OH ([CH_3OH]/[SiO]$\sim$160–300), while the other two only by SiO ([CH_3OH]/[SiO]$\leq$ 40). Among various possibilities, a train of three shocks, distanced by $\geq$5000 yr, would be consistent with the observations if a substantial fraction of silicon, frozen onto the grain mantles, is released by the shocks. We suggest that the shock train is due to an expanding gas bubble, coming behind NGC 1333 from the southwest and clashing against the filament, where IRAS 4A lies. Finally, we propose a solution to the two-decades long debate on the nature and origin of the widespread narrow SiO emission observed in the south part of NGC 1333, namely that it is due to unresolved trains of shocks.

Key words: Stars: formation – ISM: abundances – ISM: molecules – ISM: bubbles – ISM: individual objects: IRAS 4A

1 INTRODUCTION

Molecular clouds forming Solar-type stars are characterized by an intricate net of filaments which are widely accepted to play an important role in the star formation process. Indeed most of the young stars and cores in low-mass star forming regions are embedded in filaments of gas and dust which dominate the cloud structure (e.g., Schneider & Elmegreen 1979; Ungerechts & Thaddeus 1987; Goldsmith et al. 2008), a characteristic shown to be ubiquitous by the large scale maps of the Herschel Space Observatory and Planck satellites (e.g., Molinari et al. 2010; André et al. 2010, 2014; Zari et al. 2016). Some of the most prominent cloud filaments actually are collections of velocity-coherent fibers that can become gravitationally unstable and fragment into chains of cores (Hacar et al. 2013, 2017; Tafalla & Hacar 2015; Henshaw et al. 2016, 2017; Sokolov et al. 2019, 2020; Chen et al. 2020). However, the exact process ruling the formation of these filamentary structures and their specific role in triggering star formation are still debated (e.g., Hennebelle & Inutsuka 2019; Robitaille et al. 2020). A major process in their shaping, in addition to the presence of magnetic fields, is the compression of the molecular gas by external triggers, such as ionization/shock fronts around OB stars or supernovae remnants, cloud-cloud collisions, and (magneto-)hydro-dynamical gravitational instabilities (e.g., Padoan et al. 2001; Hennebelle 2013; Vázquez-Semadeni et al. 2019; Federrath et al. 2021).

All these external triggers leave signatures at different scales, from parsec to sub-parsec, observed with specific molecular shocks tracers (e.g., Jiménez-Serra et al. 2010; Berné et al. 2010; Dumas et al. 2014; Cosentino et al. 2018, 2019, 2020). SiO and CH_3OH are traditionally considered among the best tracers of such shocks, where their abundance is observed to drastically increase by several orders of magnitude (e.g., Bachiller et al. 1998, 2001; Arce et al. 2008; Codella et al. 2012; Lefloch et al. 2017; Codella et al. 2020). The SiO enhanced abundance is due to the sputtering of the grain mantles and shattering of the grain refractory cores, both processes releasing SiO and Si (which is quickly oxidized in SiO) into the gas-phase

---

★ E-mail: marta.desimone@univ-grenoble-alpes.fr

Table 1. Spectroscopic parameters and line Gaussian-fit results of CH_3OH and SiO lines observed toward the selected positions (1a, 1b and 2) on the IRAS 4A fingers shown in Fig. 2).

Spectroscopic parameters						Gaussian-fit results				
Setup[a]	Transition	Frequency[b] [GHz]	E_{up}^{b} [K]	$\log A_{ul}^{b}$ [s^{-1}]	Finger[c] position	Integrated Area [K km s^{-1}]	v_{peak} [km s^{-1}]	FWHM [km s^{-1}]	T_{peak} [K]	rms [mK]
					CH_3OH					
6-HR	$5_{1,5}$–$4_{0,4}$ E	84.5212	40	-5.7	1a	25.6(0.3)	6.50(0.01)	1.37(0.02)	17.6	300
					1b	35.3(0.2)	6.30(0.01)	1.40(0.01)	23.7	300
					2a	-	-	-	$\leq 0.9^{d}$	300
3-HR	$2_{-1,2}$–$1_{-1,1}$ E	96.7394	13	-5.6	1a	4.8(0.1)	6.40(0.02)	1.60(0.03)	2.8	60
					1b	8.0(0.1)	6.30(0.01)	1.60(0.02)	4.7	60
					2a	-	-	-	$\leq 0.2^{d}$	60
3-HR	$2_{0,2}$–$1_{0,1}$ A	96.7414	7	-5.5	1a	4.8(0.1)	6.20(0.02)	1.46(0.03)	3.1	60
					1b	8.8(0.1)	6.10(0.01)	1.60(0.02)	5.2	60
					2a	-	-	-	$\leq 0.2^{d}$	60
3-HR	$2_{0,2}$–$1_{0,1}$ E	96.7445	21	-5.5	1a	3.5(0.1)	6.10(0.02)	1.66(0.05)	1.9	60
					1b	4.6(0.1)	6.00(0.03)	1.70(0.02)	2.6	60
					2a	-	-	-	$\leq 0.2^{d}$	60
3-HR	$2_{1,1}$–$1_{1,0}$ E	96.7555	28	-5.6	1a	1.9(0.1)	6.40(0.03)	1.55(0.08)	1.2	60
					1b	1.8(0.1)	6.20(0.03)	1.6(0.1)	1.1	60
					2a	-	-	-	$\leq 0.2^{d}$	60
					SiO					
6-LR	2-1	86.8469	6	-4.5	1a	5.6(0.4)	7.3(0.5)	6.9(0.3)	0.8	40
					1b	5.7(0.4)	8.6(0.4)	6.9(0.2)	0.8	40
					2a	6.4(0.3)	8.3(0.5)	6.9(0.8)	0.9	40

[a] HR: High resolution (Δv∼0.5 and 0.2 km s^{-1} for setup 3 and 6, respectively); LR: Low resolution (Δv∼6 km s^{-1} in both setups).
[b] Frequencies and spectroscopic parameters are taken from Xu et al. (2008) and Müller et al. (2013) and retrieved from the CDMS (Cologne Database for Molecular Spectroscopy: Müller et al. 2005) database. Upper level energies E_{up} refer to the ground state of each symmetry. $\log A_{ul}$ are the logarithmic spontaneous emission coefficients.
[c] Selected position on the IRAS 4A fingers (see text and Fig. 2).
[d] 3σ limit for non-detection.

(e.g., Caselli et al. 1997; Schilke et al. 1997; Gusdorf et al. 2008a,b; Guillet et al. 2011). Likewise, CH_3OH is believed to be prevalently formed on the cold grain surfaces (e.g., Watanabe & Kouchi 2002; Rimola et al. 2014) and released into the gas-phase by the grain mantle sputtering (e.g., Flower et al. 2010).

Perseus is one of the molecular clouds in the vicinity of our Sun that is believed to have been formed and shaped by external triggers, such as the explosion of one or more supernovae and other forms of stellar feedback activity. For example, new 3D dust extinction maps obtained by GAIA support this hypothesis (see e.g., Zucker et al. 2021; Bialy et al. 2021). One of the most active sites of ongoing star formation in Perseus is NGC 1333 in the Perseus molecular cloud complex (∼300 pc; Zucker et al. 2018). This region hosts a large number of young stars and protostars associated with filamentary structures, and it displays a complex network of fibers characterized by a high degree of internal fragmentation with typically three to four cores per fiber (Hacar et al. 2017).

Recent observations produced large scale maps of the magnetic field in NGC 1333, helping in understanding their role in the star formation process (e.g., Doi et al. 2020). For all these reasons, NGC 1333 is one of the best regions to study the connection between filaments, magnetic fields, external triggers, and star formation.

More specifically, this article focuses on the southern filament of NGC 1333, which is composed of multiple structures with distinct systemic velocities and velocity gradients (e.g., Sandell & Knee 2001; Dhabal et al. 2018, 2019). The famous IRAS 4A system, a protostellar binary which drives two large-scale molecular outflows, is located on the west side of the filament (Choi 2005; Santangelo et al. 2015; De Simone et al. 2020; Taquet et al. 2020; Chuang et al. 2021). The filament joins an arc-like structure on the west which hosts other young protostars (the SVS13 and IRAS 2 systems). In a recent study, Dhabal et al. (2019) hypothesized that the entire southwest region of NGC 1333, encompassing the filament where IRAS 4A lie, is due to a colliding "turbulent cell", a clash that triggered the birth of the above-mentioned protostars. However, no specific signatures of a clash, namely shocks, have been reported so far, leaving unanswered how and where the energy of this clash, if real, is dispersed.

To answer this question, we analyzed new high spatial resolution (∼ 600 au) observations of CH_3OH and SiO toward IRAS 4A, obtained in the context of the IRAM-NOEMA Large Program SOLIS[1] (Seeds Of Life In Space; Ceccarelli et al. 2017). Our goal is to search for specific signatures of the clash event and to gain a more detailed insight into what happened and why.

The article is organized as follows. In Sects. 2 and 3, we described the observations and the results, respectively. In Sect. 4, we analyze

---

[1] `https://solis.osug.fr/`

the physical and chemical properties of the observed structures. In Sect. 5, we discuss the implication of our analysis and in Sect. 6 we summarise our conclusions.

2 OBSERVATIONS

The IRAS 4A system was observed at 3mm with the IRAM NOEMA (NOrthern Extended Millimeter Array) interferometer[2] within the SOLIS project[1]. Part of the data was already published in De Simone et al. (2020). For the present study, we used the observations obtained with two setups, hereinafter called 3 and 6, during several tracks (18.6 hrs for setup 3 in June, September, and October 2016 and 6.8 hrs for setup 6 in March 2018).

Setup 3 was observed with the WideX correlator at 95.5-99.5 GHz and with ~2 MHz (~6 km s^{-1}) spectral resolution, plus four narrow spectral windows with ~0.16 MHz (~0.5 km s^{-1}) spectral resolution. Setup 6 was observed using the PolyFiX correlator[3] at 80.4-88.1 GHz (lower sideband, LSB) and 95.9-103.6 GHz (upper sideband, USB) with ~2 MHz (~6 km s^{-1}) spectral resolution, plus 64 narrow spectral windows with ~0.06 MHz (~0.2 km s^{-1}) spectral resolution.

The NOEMA array was used in configurations DC (baselines 15-304 m) and AC (64-704 m) for setup 3 and 6, respectively. The phase center was on IRAS 4A1, at coordinates αJ2000 = $03^h29^m10.''5$, δJ2000 = +31° 13′ 30.″9.

The bandpass was calibrated on 3C454.3 and 3C84, the absolute flux was fixed by observing MWC349, LKHA101, and the gains in phase and amplitude were set on 0333+321. The final uncertainty on the absolute flux scale is ≤ 15%. The phase rms was ≤ 50° and ~ 10-20° and the typical precipitable water vapor (pwv) was 4-15 mm and 1-30 mm for setup 3 and 6, respectively. The system temperature was 50-200 K for both setups.

The data were reduced using the GILDAS[4] software collection. The continuum map was obtained by averaging line-free channels and self-calibrating the data. The self-calibration solutions were then applied to the spectral cubes, which were subsequently cleaned using natural weighting. The resulting synthesised beams are 2.″2×1.″9 (P.A.=96°) and 2.″05×1.″12 (P.A.=11°) and the half power primary beams are 59.″2 and 61.″2 for setups 3 and 6, respectively.

3 RESULTS

We detected five CH_3OH and one SiO lines, listed in Table 1 with their spectroscopic parameters. Figure 1 shows the spatial distribution of the CH_3OH and SiO line emission in two different velocity ranges: around the systemic velocity V_{sys} (~ 6.7 km s^{-1}) and at High-Velocity (HV), at about ±7 km s^{-1} from the systemic velocity and over a velocity interval of about Δv~ 6 km s^{-1} (see caption for details). Two major components appear in the figure: the two outflows associated with A1 and A2, especially visible in the HV maps, and two filamentary structures at the systemic velocity, which we will refer to as "fingers" in the following.

3.1 Outflows emission

The emission from the IRAS 4A outflows detected by SOLIS in different molecular lines has been presented already and discussed by Taquet et al. (2020) (S-bearing species) and De Simone et al. (2020) (interstellar Complex Organic Molecules). The Fig. 1 methanol emission map is in general agreement with those two studies and, being not the focus of this paper, will not be discussed further.

3.2 Fingers emission

The high resolution spectra of the five methanol lines (Fig. 1) show that the elongated structures are characterized by narrow lines (FWHM~1.5 km s^{-1}) centered at the systemic velocity V_{sys} (see below). Their filamentary morphology is better highlighted in Fig. 2, where the CH_3OH and SiO narrow-line emission is shown over a larger field of view. Based on Fig. 2 and the spectral profile described above, we identified three fingers:
Finger1, traced by CH_3OH and SiO, is the northern one;
Finger2, traced only by SiO, is 10″ south and parallel to Finger1;
Finger3, traced only by SiO, is an additional 10″ south and, again parallel to Finger1.
While Finger2 and Finger3, detected only in SiO (2-1), are perfectly in agreement with the SiO (1-0) VLA observations by Choi (2005), Finger1 was never detected before and it is traced by both CH_3OH and SiO. It is worth emphasizing that the three fingers are each separated by about 10″ (~ 3000 au) and are parallel to each other. Note also that Finger2 and Finger3 seem to be connected to each other by an almost vertical structure, but it is very likely that this connecting structure is tracing the outflowing material from IRAS 4A2.

In order to understand the nature of the three fingers, we selected three positions along Finger1 and Finger2 to carry out a non-LTE analysis to derive the gas temperature and density and the column density of CH_3OH and SiO, respectively (see Section 4.1)[5]. The three positions (two - 1a and 1b - toward Finger1 and one - 2a - toward Finger2), are shown in Fig. 2 and their coordinates are reported in Table 2. These positions were selected because they show the brightest CH_3OH and SiO emission in the fingers and are outside the outflows emission region in order to minimize the contamination from the latter. Figure 1 shows the CH_3OH and SiO spectra extracted from Finger1a, as an example.

In each of the three selected positions, we extracted the spectra of CH_3OH and SiO and derived the velocity-integrated line intensities of each detected transition using a Gaussian fit with the GILDAS-CLASS package. The fit results, namely the integrated emission (T_bdV), the linewidth (FWHM), the peak velocities (V_{peak}), and the rms computed for each spectral window, are reported in Table 1. As mentioned above, the methanol lines observed with the high resolution narrow bands have an average linewidth of about 1.5 km s^{-1}. Unfortunately, for SiO we are limited by the PolyFiX low spectral resolution (~ 6 km s^{-1}). However, from the VLA observations, Choi (2005) estimated a similar linewidth (~1.5 km s^{-1}) for the SiO narrow component. It is worth noticing that, while the methanol emission drastically changes from one finger to another, the integrated SiO emission derived at points Finger1a, Finger1b, and Finger2a is almost constant. We will comment the implications of this characteristics in Sect. 4.

Finally, we searched for the presence of other molecules in the

---

[2] `https://www.iram-institute.org/EN/noema-project.php`
[3] `https://www.iram.fr/IRAMFR/GILDAS/doc/html/noema-intro-html/node6.html`
[4] `http://www.iram.fr/IRAMFR/GILDAS`

[5] Note that since Finger3 is outside the primary beam we did not carry the analysis there.

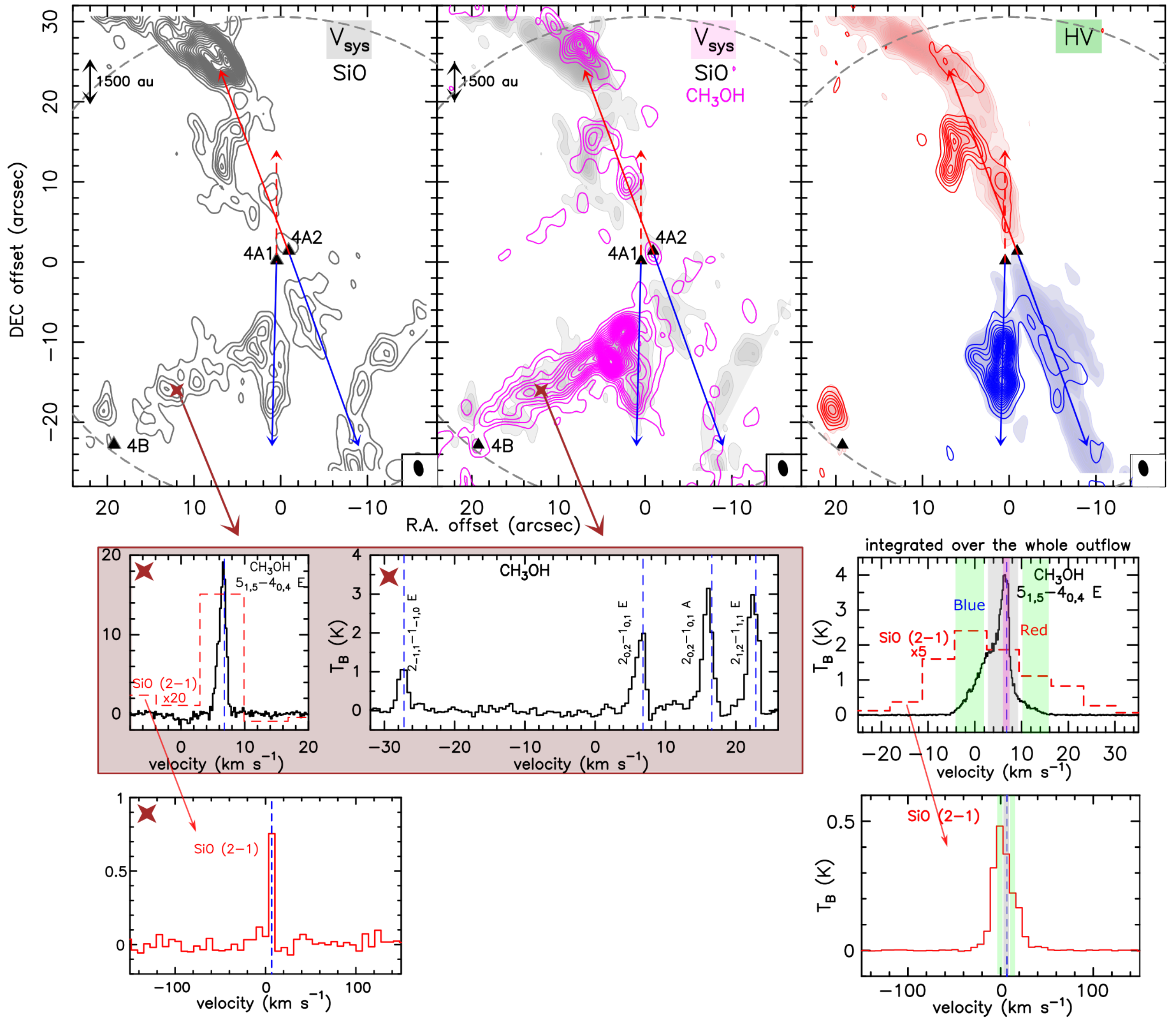

Figure 1. *Upper panels:* Velocity-integrated maps of CH_3OH $5_{1,5}$-$4_{0,4}$ E (coloured contours) and SiO 2-1 (gray contours and shaded colors) of the NGC 1333 IRAS 4 system. The three protostellar sources in the field are marked by black triangles. Jet directions are indicated by blue and red arrows following Choi (2005) and Santangelo et al. (2015). The primary beam ($\sim 62''$) is shown by the grey dashed circle and the synthesized beam ($\sim 1\farcs5$) is shown in the lower right corner of the panels. Upper left panel: SiO emission at the systemic velocity channel, with first contours and steps of 3σ (σ=1 mJy beam^{-1} km s^{-1}). Upper middle panel: CH_3OH Emission integrated from 5.8 to 7.8 km s^{-1} around the systemic velocity, with first contours and steps of 3σ (σ=15 mJy beam^{-1} km s^{-1}). Upper right panel: CH_3OH Blue- and red-shifted high velocity (HV) emission integrated from -4 to 2.4 km s^{-1} (blue) and 9.6 to 16 km s^{-1} (red) with first contours and steps of 3σ ($\sigma_{\rm blue}$=35 mJy beam^{-1} km s^{-1} and $\sigma_{\rm red}$=13 mJy beam^{-1} km s^{-1}). *Lower panels:* CH_3OH (in black) and SiO (in red) spectra extracted at the Finger1a position with offset ($-12''$, $+16''$) marked by a brown cross (see text). To compare with CH_3OH the SiO spectra is overlapped in dashed red magnified by a factor of 20. The map integrated ranges are shown as colored bands on the spectra of SiO (in red) and CH_3OH (in black overlapped, for comparison, with SiO in dashed red magnified by a factor of 5) integrated over the whole outflow in the lower right panels.

fingers' positions and only found faint emission of HC_3N (11-10), which appears to be associated with Finger1.

4 PHYSICAL AND CHEMICAL PROPERTIES OF THE FINGERS

4.1 Physical properties

The detection of five CH_3OH transitions allowed us to perform a non-LTE analysis via our in-home Large Velocity Gradient (LVG) code `grelvg` adapted from Ceccarelli et al. (2003).

CH_3OH has two nuclear-spin isomers, A-type (symmetric) and

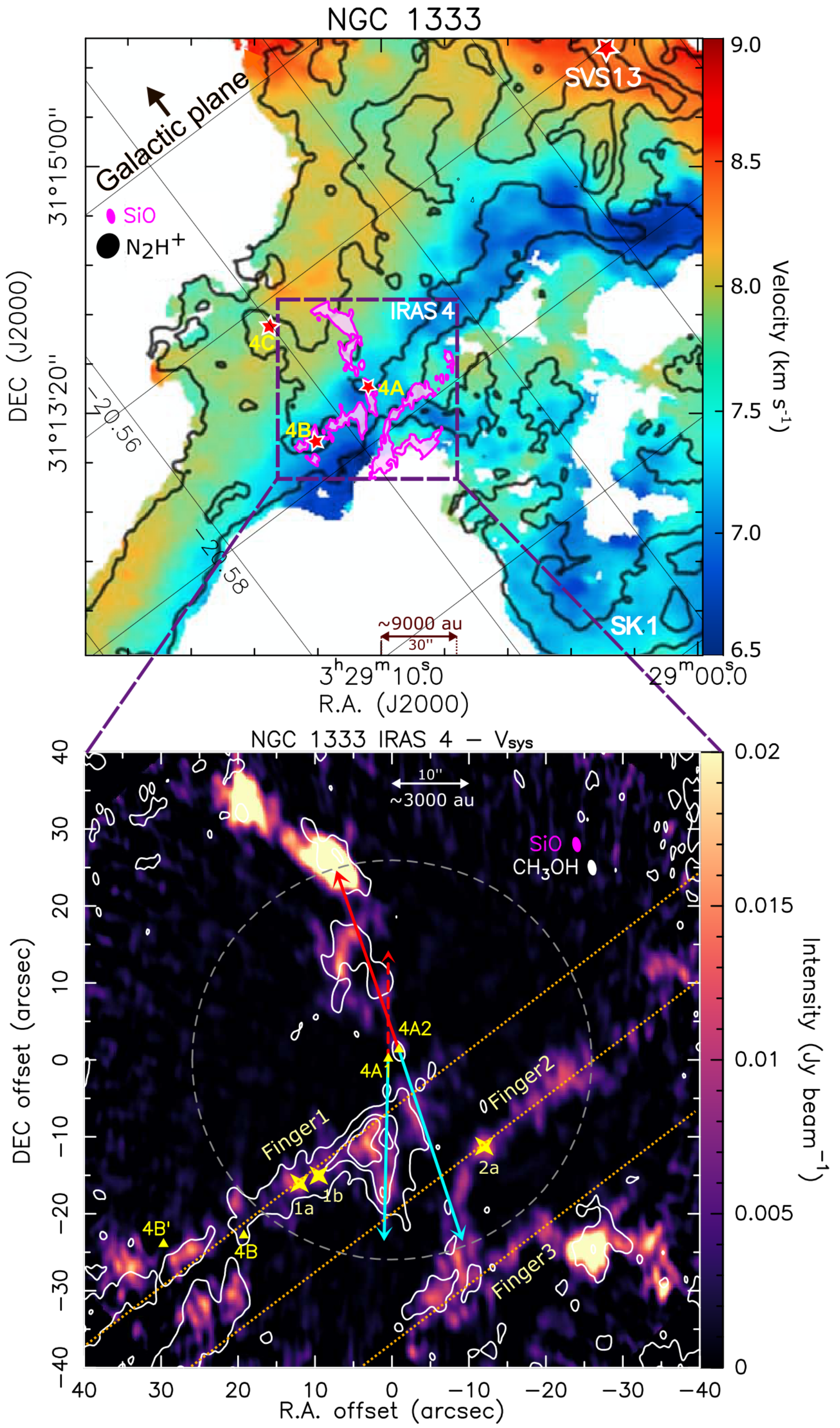

Figure 2. Emission of the fingers detected by NOEMA-SOLIS in the CH_3OH and SiO shown at a large scale. *Upper panel*: Overlap of the N_2H^+ (1-0) line-of-sight velocity map of the southern-east part of NGC 1333 from CARMA observations (adapted from Fig. 17 of Dhabal et al. 2019) with the SiO emission from NOEMA-SOLIS observations (this work) shown as 3σ contours. The internal grid is in Galactic coordinates. The red stars mark the position of IRAS 4A, 4B, 4C, and SVS13. The synthesized beams ($\sim 1\farcs5$ for SiO and $\sim 3\farcs5$ for N_2H^+) are in the upper left corner. *Bottom panel*: Zoomed-in map of the IRAS 4A system with SiO (colour scale, 3σ= 3 mJy beam^{-1}) and CH_3OH (white contours starting at 3σ with steps of 15σ, σ=30 mJy beam^{-1}) emission integrated in a range of ~6 km s^{-1} around the $v_{\rm lsr}$ ($\sim$ 6.7 km s^{-1}). The yellow triangles indicate the sources 4A1, 4A2, 4B and 4B′. The synthesized beams ($\sim 1\farcs5$) are in the upper right corner, while the primary beam (~61″) is a dashed white circle. The yellow crosses mark the fingers positions where we carried out a non-LTE analysis of the methanol lines. Orange lines show the direction of the three fingers (Finger1, traced by CH_3OH and SiO; Finger2 and Finger3 traced by SiO only) and are parallel to the Galactic plane.

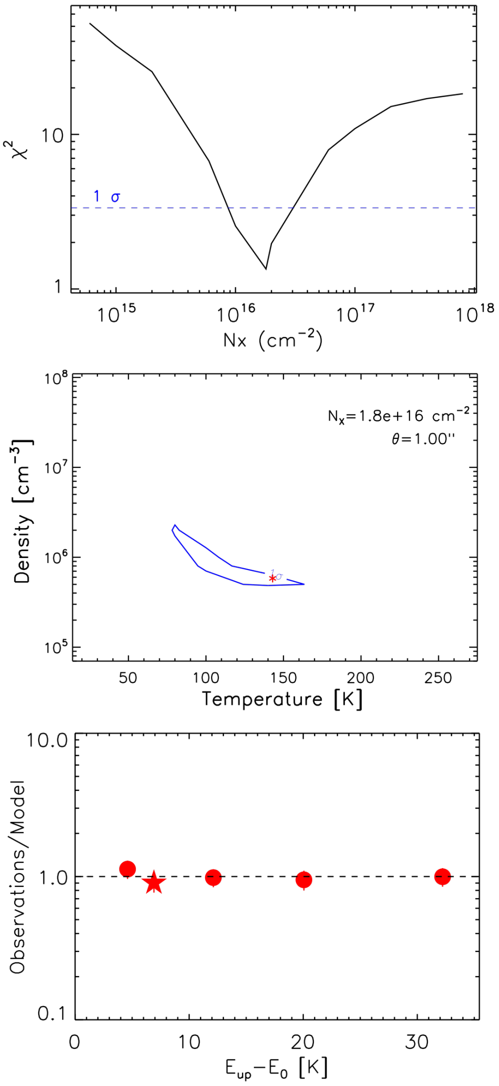

Figure 3. Results of the non-LTE analysis of CH_3OH at the Finger1a position (see Table 2) using the `grelvg` code. *Top*: χ^2-column density N(CH_3OH) plot. The dashed blue line represents the 1σ confidence level. *Middle*: Density-Temperature χ^2 contour plot. The contour represents 1σ confidence level, assuming the best fit values of N(CH_3OH) and θ (upper right corner). The best fit solution is marked by the red asterisk. *Bottom*: Ratio between the observed line intensities (circles for E-type and stars for A-type) with those predicted by the best fit model as a function of line upper-level energy E_{up}.

Table 2. 1σ Confidence Level (range) from the Non-LTE LVG Analysis of the CH_3OH lines toward the three selected positions in the Fingers (marked as yellow crosses in Fig. 2).

Species	N(X) [cm^{-2}]	n_{H_2} [cm^{-3}]	T_{gas} [K]	size [arcsec]
		Finger1a -offset (+12″, -16″)		
CH_3OH	$(8-30)\times10^{15}$	$(5-20)\times10^{5}$	80-160	0.6-1.5
SiO	$(5-10)\times10^{13}$	″	″	″
[CH_3OH]/[SiO]	160-300			
		Finger1b - offset (+9.5″, -15″)		
CH_3OH	$(4-12)\times10^{15}$	$(2-3)\times10^{5}$	130-210	1.5-2.5
SiO	$(2-5)\times10^{13}$	″	″	″
[CH_3OH]/[SiO]	200-240			
		Finger2a - offset (-12″, -11.2″)		
CH_3OH^a	$\leq1.6\times10^{15}$	$(5-20)\times10^{5}$ ^{a}	80-210 ^{a}	1-2 ^{a}
SiO	$(4-15)\times10^{13}$	″	″	″
[CH_3OH]/[SiO]	$\leq$40			

^{a} Assumed the same gas condition (n_{H_2} and T_{gas}) of the Finger1.

E-type (asymmetric), differentiated by the total spin state of the hydrogen nuclei in the CH_3 group (Rabli & Flower 2010). We used the collisional coefficients of both CH_3OH isomers with para-H_2, computed by Rabli & Flower (2010) between 10 and 200 K for the first 256 levels and provided by the BASECOL database (Dubernet et al. 2013). We assumed the CH_3OH-A/CH_3OH-E ratio equal to 1. A semi-infinite slab geometry was used to compute the line escape probability as a function of the line optical depth.

We ran a large grid of models (≥ 5000) covering a total methanol (A-type plus E-type) column density N(CH_3OH) from 6×10^{14} to 8×10^{17} cm^{-2}, a gas H_2 density n_{H_2} from 3×10^5 to 6×10^6 cm^{-3}, sampled in logaritmic scale, and a gas temperature T from 20 to 200 K. We then simultaneously fitted the measured CH_3OH-A and CH_3OH-E line intensities by comparing them with those predicted by the `grelvg` model, leaving N(CH_3OH), n_{H_2}, T, and the emitting size θ as free parameters. Following the observations, we assumed the linewidth equal to 1.5 km s^{-1} (see Table 1), and we included the flux calibration uncertainty (15%) to the observed intensities errors.

The best fit in the Finger1a position is obtained for a total column density N(CH_3OH)=1.8×10^{16} cm^{-2}, gas density n_{H_2}=5×10^5 cm^{-3}, gas temperature T=140 K and emitting size of ∼ 1″ with reduced χ^2_R=1.3 (see Figure 3). The values within the 1σ confidence level are reported in Table 2. To explore the gas conditions along the Finger1, we repeated the analysis described above in position 1b still finding high gas temperature and density (see Table 2). The derived emitting sizes represent the best-fit 2D-Gaussian FWHM[6], and suggest that the fingers may have a clumpy structure, not resolved by our ~600 au spatial resolution.

To derive the SiO column density in the three positions we run `grelvg` for a range of N(SiO) from 5×10^{12} to 1×10^{15} cm^{-2} assuming the same gas temperature, density and emitting size as those found in Finger1a (Table 2). We then best fitted the measured SiO line intensities via comparison with those simulated by `grelvg` leaving only N(SiO) as a free parameter. The same procedure was adopted to estimate the upper limit of the CH_3OH column density in Finger2a. The results of the non-LTE analysis carried out toward the three positions are summarised in Table 2.

In order to assess the impact of assuming that the gas conditions derived for CH_3OH are also valid for SiO, we estimated the SiO column density by combining our NOEMA observations with the VLA observation by Choi (2005). We performed a LTE analysis using the SiO 2-1 and SiO 1-0 integrated emission in Finger2a deriving a SiO column density of $(30\pm7\times10^{12}$ cm^{-2}, which is consistent with the SiO column density derived above following our assumption (see Table 2). In other words, even if the gas conditions in Finger1 and

---

[6] In fitting the observations with the LVG theoretical predictions, we considered three possibilities for the filling factor, depending on the shape of the emitting region: i) a 2D circular Gaussian shape, ii) an infinite finger-like shape with a resolved transverse size, and iii) emitting size larger than the synthesised beam. The best fit by far was obtained with the 2D circular Gaussian shape.

Finger2 are not exactly the same, the observed abundance ratio of the two species is consistent, within the error bars, with what we computed. Additionally, in order to investigate the non detection of SiO in Finger1 in the maps of Choi (2005), we computed the predicted intensity ratio of the SiO 2-1 (target of our NOEMA observations) with respect to the SiO 1-0 (target of the VLA observations of Choi 2005) using the non-LTE LVG `grelvg` code. We found that the predicted SiO 2-1/1-0 line ratio varies from 6.5 to 13 in the range of gas density and temperature derived in Finger1 with our analysis (Table 2). Considering the various uncertainties, in particular on the column density in Finger1 and Finger2 (which are assumed to be the same but can be also a factor ~2 different), there is no contradiction with the fact that there is no SiO detection in Finger1 with the VLA observations by Choi (2005).

4.2 Chemical properties

From the computations of the previous subsection, we can estimate the CH_3OH and SiO abundances in Finger1 as follows. In Finger1, assuming that the finger depth is equal to the linear diameter of the methanol emitting region ($\sim 0.6-1.5''$ equivalent to $\sim 180-450$ au: see Tab. 2) and considering the derived gas density range ($\sim 5-20\times10^5$ cm^{-3}: see Tab. 2), we obtained the H_2 column density N(H_2) range equal to $\sim 1.4-14\times10^{21}$ cm^{-2}. Using the derived CH_3OH column density range ($\sim 8-30\times10^{15}$ cm^{-2}: Tab. 2), we then estimate a methanol abundance [CH_3OH]/[H_2] range of $0.6-22\times10^{-6}$. Likewise, the SiO abundance [SiO]/[H_2] range is estimated to be 0.4–7.4 $\times 10^{-8}$. The SiO abundance is then lower than that measured in the IRAS4A jets, 3–4 $\times 10^{-7}$ by Santangelo et al. (2015).

From the derivation of the CH_3OH and SiO column densities in Finger1 and Finger2 of the previous subsection, the [CH_3OH]/[SiO] ratio is 160–300 in Finger1 and ≤40 in Finger2 (see Tab. 2). There seems to be a difference in the chemical composition of Finger1 and Finger2, at least regarding CH_3OH and SiO, with Finger1 enriched in methanol with respect to Finger2.

5 DISCUSSION

5.1 Summary of the fingers properties

In the previous sections, we have shown that the new SOLIS maps, coupled with older VLA maps, reveal the presence of three filamentary structures, extended more than about 6000 au in the major axis (i.e. $\geq 20''$) and unresolved in the minor one, namely ≤450 au (Fig. 2 and Tab. 2). These structures, which we named "fingers", are approximately aligned in the direction of the galactic plane and to the large scale magnetic field observed by Planck (Planck Collaboration et al. 2020), but approximately perpendicular to the local magnetic field (e.g. Doi et al. 2020, ; see their Fig. 4) and the SE filament where IRAS 4A lies. The three fingers are regularly spaced by about ∼ 3000 au (i.e. $\sim 10''$). Finally, they are almost perpendicular (certainly not parallel) to the outflows emanating from IRAS 4A1 and 4A2, even though they seem connected with them in some way: Finger1 starts midway at the edge of the south lobe of the 4A1 outflow and extends east of it, Finger2 starts midway at the edge of the south lobe of the 4A2 outflow and extends west of it, and Finger3 starts at the visible south end of the 4A2 outflow and extends west of it.

Using the detected multiple methanol lines, we carried out a non-LTE analysis that provided stringent constraints to the temperature and density of the gas in Finger1 (Section 4.1; Tab. 2). The derived temperature, 80–160 K, is definitively larger than that in the surrounding envelope gas, estimated to be smaller than ∼12 K (Jørgensen et al. 2002; Maret et al. 2005). In other words, Finger1 is too far away from the IRAS 4A for its gas to be heated by the protostar radiation, so that a non-thermal process must be responsible for the observed large temperature.

In the same vein, the measured SiO enhanced abundance $4-7.4\times10^{-8}$ (Section 4.2) points to a non-thermal process capable of extracting silicon from the grains (see Introduction and Section 5.3). Likewise, methanol in Finger1, with an abundance of $0.6-22\times10^{-6}$, suggests a similar non-thermal process capable to extract it from the grain mantles.

There are not many possible non-thermal processes capable to create the observed linear and almost periodic structures with enhanced gas temperature and capable to increase the SiO and methanol abundances. To our best knowledge, only two processes could a priori reproduce the observed properties of the fingers in NGC 1333 IRAS 4A: hydro-dynamical Kelvin-Helmholtz instabilities and shocks. In the following, we will discuss in detail these two possibilities.

5.2 Do the IRAS 4A fingers trace Kelvin-Helmholtz instabilities?

Hydro-dynamical instabilities (HDI) are known to play a major role in shaping the morphology of the ISM, in particular in modifying the superficial structure of molecular clouds via Rayleigh-Taylor, Kelvin-Helmholtz, and self-gravity instabilities. All these processes can generate long and narrow streams of material (Hunter et al. 1997; Coughlin & Nixon 2020). Among them, the Kelvin-Helmholtz instability (KHI) occurs at the interface of two fluids of different densities in relative shear motion and it is characterized by a wavelike periodic structure. Such instabilities have been invoked to explain the periodic filamentary structures observed in Orion (Berné et al. 2010; Berné & Matsumoto 2012) and Taurus (Heyer et al. 2016). Following the approach by Berné et al. (2010), we explored if the development of a KHI is possible and in what conditions, and if it can reproduce the gas properties of the IRAS 4A fingers, assuming that the insulating layer (i.e., the interface between the two fluids) is infinitely thin.

5.2.1 Method

First, the maximum spatial wavelength λ_{KH} of the KHI is connected to the physical conditions in which the instability occurs. Specifically, the value of λ_{KH} depends on the acceleration due to self-gravity g_{cl} and on the density n_{cl} of the first cloud, and the relative velocity v_f and density n_f of the second cloud, which we will call “flowing cloud”, as follows:

$$\lambda_{KH} = \frac{2\pi}{g_{cl}} v_f^2 \frac{n_f}{n_{cl}} \tag{1}$$

where we used g_{cl}=π Gμ m$_H$ N$_H$ and which gives 1×10^{-11}m s^{-2} assuming N$_H$ equal to 1.2×10^{21} cm^{-2} (from our analysis, see Section 4.2). On the other hand, the growth rate ω_{KH} for a Kelvin Helmholtz instability depends on the velocity v_f and density n_f of the flowing cloud as follows:

$$\omega^2_{KH} = \frac{k^2 v_f^2 n_f n_{cl}}{(n_f + n_{cl})^2}\,, \tag{2}$$

where k is the spatial wavenumber. If the KHI is responsible for the IRAS 4A fingers, their spatial separation sets a lower limit to λ_{KH}

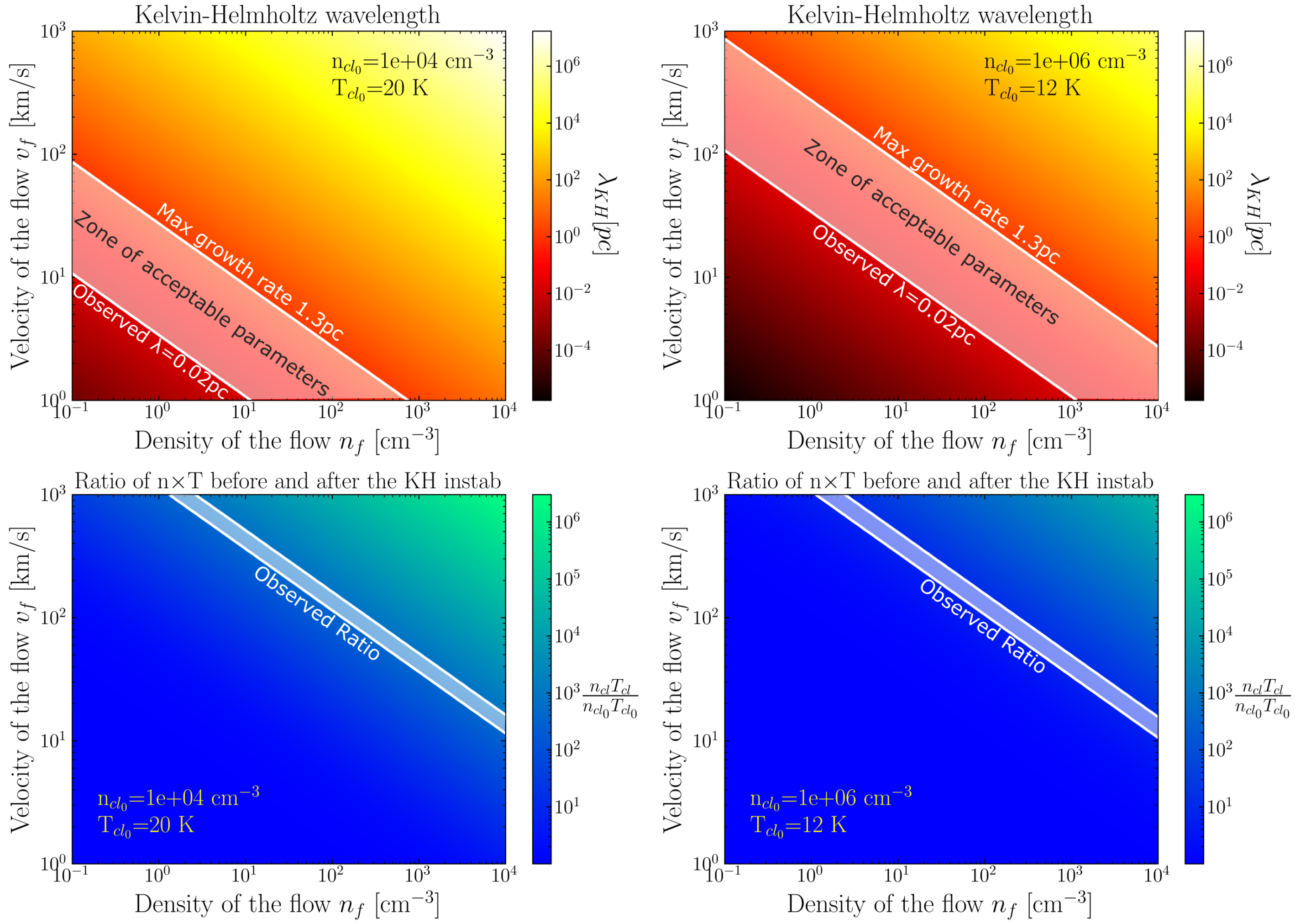

Figure 4. *Top:* Evolution of the Kelvin-Helmholtz wavelength for the observed molecular cloud as a function of density (n_f) and velocity of the flowing gas (v_f). The white continuous lines represent the observational constraints that set the zone (shadowed white) of physically acceptable values for n_f and v_f that allow a Kelvin-Helmholtz instability to exist. The condition assumed for the cloud before the interaction are reported in the upper right corner. *Bottom:* Ratio of the density temperature product before and after the KH instability as a function of density (n_f) and velocity of the flowing gas (v_f). The shadowed white zone represents the observed ratio. The conditions assumed for the cloud before the interaction are given in the lower left corner.

equal to ~0.02 pc at the distance of NGC 1333 (and assuming a face-on orientation). Likewise, the widths of the lines that trace the fingers set an upper limit to ω_{KH} of about 8×10^5 yrs^{-1}.

Second, we estimated how the temperature and density of the cloud would change in the region of KHI growth. As the first assumption, we considered the two interacting fluids in hydrostatic equilibrium so that the pressure of the flow and the cloud before the interaction is the same (P_{f0}=P_{cl_0}). This is a standard assumption since the fluids previously were not mixed. When the instability starts to grow, the thermal pressure and the ram pressure of the flow interact with the instability so that:

$$P_{cl} = P_{cl_0} + \mu m_H n_f (\mathrm{v}_f \cos\theta)^2 \,, \tag{3}$$

where θ is the angle between the flow and the instability. Assuming that the vertical amplitude is unlikely to be larger than λ, the angle between the instability interface and the flow is at most θ=45°, and considering the ideal equation of state (P=nk_BT, where k_B is the Boltzmann's constant) we can rewrite Eq. 3 to link the density and temperature before (n_{cl_0} and T_{cl_0}) and after (n_{cl} and T_{cl}) the KHI emergence, respectively, as follows:

$$\frac{n_{cl}T_{cl}}{n_{cl_0}T_{cl_0}} = \frac{m_H n_f \mathrm{v}_f^2}{2 n_{cl_0} k_B T_{cl_0}} + 1 \,, \tag{4}$$

We considered two cases: i) the interaction occurs in the cloud, where the gas density is 10^4 cm^{-3} and the temperature is 20 K (i.e. the same assumptions of Berné et al. 2010); ii) the interaction takes place inside the IRAS 4A envelope, at ≥3000 au from the center (where the first finger is located in the 2D projection), where the gas temperature and density are estimated to be ≤ 12 K and ≤ 10^6 cm^{-3} (Jørgensen et al. 2002; Maret et al. 2005).

5.2.2 Results

Figure 4 shows the results of our calculations. Specifically, it displays the evolution of the KHI wavelength (Eq. 1) and the density-temperature ratio before and after the KHI (Eq. 4), using a grid of possible values for the velocity and density of the flowing cloud (v_f from 1 to 10^3 km s^{-1}and n_f from 0.1 to 10^4 cm^{-3}), and for the

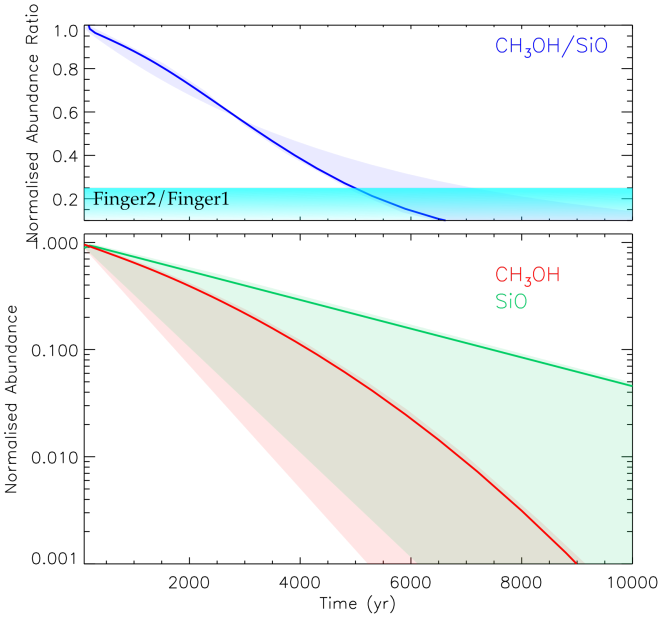

Figure 5. Predicted chemical evolution of methanol (red lines) and SiO (green lines) once injected into the gas phase by the passage of a shock. The solid lines show the predictions using the non-LTE best fit (Section 4.1), namely ∼ 140 K and $\sim 5 \times 10^5$ cm^{-3}. The shadowed area represents the range of predictions obtained using the limits on the gas density and temperature derived by the non-LTE analysis and listed in Table 2. *Bottom panel:* Abundances normalized to 1 as a function of time. *Top panel:* Normalised [CH_3OH]/[SiO] abundance ratio as a function of time. The horizontal band represents the range of normalized abundance ratio observed in Finger2 with respect to that observed in Finger1.

two cases described above (KHI occurring in the cloud or IRAS 4A envelope). Whatever are the conditions of the flowing gas, Fig. 4 demonstrates that KHI can not explain at the same time the observed fingers separation and the observed local increase of density and temperature in the cloud.

Finally, in addition to the difficulty to reproduce the observed fingers separation and enhanced gas density and temperature, KHI can not explain the presence of CH_3OH and SiO in the gas. Since no sputtering or shattering are expected to play a major role in KHI, the only way for them to release CH_3OH and SiO from the grains is via thermal evaporation of their volatile mantles. However, although the gas cools down slowly via line emission, the dust would cool down very rapidly and probably would never reach the temperature necessary for the grain mantle to sublimate.

In summary, KHI does not seem able to explain the observed properties of the IRAS 4A fingers.

5.3 Do the IRAS 4A fingers trace a train of shocks?

Shocks are omnipresent in the ISM, at various scales and in various objects, playing a major role in its thermal and physical structure. In particular, for decades young forming stars are known to be the source of energetic ejections of material which causes shocks when they encounter the quiescent surrounding matter (e.g., Lada 1985). In these shocks, the gas and density temperature, as well as both SiO and methanol abundances are enhanced (e.g., Bachiller et al. 1998, 2001; Arce et al. 2008; Codella et al. 2012; Lefloch et al. 2017; Codella et al. 2020). The quantitative details depend on the type of shock, jump (J) or continuous (C) when it is in presence of a magnetic field, the pre-shocked gas properties and velocity of the shock (e.g., Hollenbach & McKee 1979; Draine & McKee 1993). In the following, we discuss whether the observed properties of the fingers can be accounted for by shocks.

5.3.1 The shock hypothesis

The analysis of the relative abundances of CH_3OH and SiO shows a clear difference in the chemical composition of Finger1 and Finger2, with Finger1 enriched in methanol with respect to Finger2 by more than a factor four. As mentioned in the Introduction, methanol can not be produced by gas-phase reactions in the measured quantity (Geppert et al. 2006), while it is easily formed on the grain mantle surfaces by the hydrogenation of frozen CO (e.g., Tielens & Hagen 1982; Watanabe & Kouchi 2002; Rimola et al. 2014) during the prestellar cold phase (e.g., Caselli & Ceccarelli 2012). Therefore, the gaseous methanol observed in Finger1 must have been extracted from the grain mantles and injected into the gas phase. A similar argument applies to the observed gaseous SiO. The abundance of Si is extremely low in molecular clouds ($\leq 10^{-12}$; Ziurys et al. 1989; Requena-Torres et al. 2007) because it is trapped in the refractory and, to a lesser extent, in the volatile components of interstellar grains (Jenkins 2009), but it becomes very abundant in the gas where it is extracted from the grains, such as in shocks. In summary, the gaseous SiO and CH_3OH observed toward the three fingers must originate by their injection from the interstellar grains. This implies two possible explanations of the observed different [CH_3OH]/[SiO] abundance ratio: either (1) the two species are injected from the grains with a different abundance ratio in the different fingers or (2) they are injected from the grains with the same abundance ratio but the latter changes in time because of chemical processes occurring in the gas phase. In the following, we investigate whether the relative and absolute abundances can be reproduced by shocks with properties appropriate for the IRAS 4A fingers (the details of these properties will be described in the following discussion).

5.3.2 Chemical modeling of the measured [CH_3OH]/[SiO] abundance ratio: time constraints on the shock passage

To quantify the SiO and methanol abundance evolution after their injection into the gas phase and whether it could explain the measured [CH_3OH]/[SiO] ratio, we ran an astrochemical model and compared the predictions with the observations in the three fingers. To this end, we used the time-dependent gas-phase code MyNahoon, which is a modified version of the publicly available code Nahoon[7] (Wakelam et al. 2012), in which we added the accretion of gaseous species into the grain mantles (but no chemistry is computed on the grain surfaces). To describe the injection of SiO and CH_3OH in the gas-phase, we adopted a two-step procedure, as follows (see also Codella et al. 2017; Codella et al. 2020; De Simone et al. 2020).

Step 1: We first compute the chemical composition of the gas during the phase preceding the ejection phenomenon. For this, we assumed the steady-state composition of a molecular cloud at 10 K with a H_2 density of 2×10^4 cm^{-3}, cosmic-ray ionization rate of 3×10^{-17} s^{-1}, visual extinction of 20 mag, and initial elemental abundances as those adopted by Agúndez & Wakelam (2013, their Table 3).

Step 2: We increase the gas temperature, density, and gaseous abundance of the major components of the grain mantle to simulate their

---

[7] `http://kida.astrophy.u-bordeaux.fr/codes.html`

injection into the gas-phase due to the passage of the shock, while the other species abundance results from Step 1. The gas temperature and H_2 density are those found by the non-LTE LVG modeling in the Finger1a (Table 2). The abundances of the species injected into the gas phase are assumed to be those measured by IR observations of the interstellar dust ices in similar regions (Boogert et al. 2015): 2×10^{-4} for H_2O; 3×10^{-5} for CO_2, CO and CH_4; 2×10^{-5} for CH_3OH and NH_3, where the abundances are with respect to the H-nuclei. The SiO abundance is assumed to be 200 times smaller than CH_3OH, namely 1×10^{-7}.
Results: The evolution of the SiO and CH_3OH abundances and their ratio are shown in Fig. 5. Using the best fit of the non-LTE analysis (Section 4.1 and Table 2), namely $\sim$ 140 K and $\sim 5 \times 10^5$ cm^{-3}, once methanol is ejected into the gas phase, its abundance decreases by a factor of 10 after 4000 yr mainly due to the reaction with OH (Shannon et al. 2013), while SiO remains in the gas phase longer (decreasing by a factor of 10 in abundance around 7000 yr because of the freeze-out into the grains). This basic result holds also for relatively different abundances of SiO and CH_3OH, with a ten times abundance decrease of methanol in 2000 yr or more and of SiO in 3000 yr or more. More important in the context of understanding what happened, for their normalized ratio being as that observed in Finger1 and Finger2 the difference in age of the two shocks should be larger than about 5000 yr (Fig. 5, top panel). In other words, if the same relative quantity of CH_3OH and SiO has been injected into the gas phase by the passage of two shocks, at Finger1 and Finger2 respectively, the shock in Finger1 is younger more than 5000 yr compared to that in Finger2. However, if the relative initial abundance ratio is different by a factor two, then the the time between two shocks can be different, namely 2000 yr if Finger2 has an initial abundance ratio higher than Finger1 and 10^4 yr in the opposite case.

5.3.3 *Shock modeling of the SiO injection: constraints on the shock velocity*

Since more than two decades models have predicted that the SiO abundance is highly enhanced in high velocity ($\geq$ 25 km/s) shocks, where the grains are shattered and/or sputtered and silicon is liberated into the gas-phase where it undergoes reactions leading to the SiO formation (e.g. Draine et al. 1983; Flower & Pineau des Forets 1994; Caselli et al. 1997; Schilke et al. 1997). In lower velocity shocks, Si or SiO previously frozen onto the grain mantles are predicted to be injected into the gas-phase by the sputtering of the mantles because of the ions-neutral drift velocity (Gusdorf et al. 2008b; Jiménez-Serra et al. 2008; Lesaffre et al. 2013; Nguyen-Luong et al. 2013). Relevant for the case of the Fingers, the above models predict that shocks with velocities lower than about 10 km s^{-1} are not strong enough to liberate Si or SiO from the frozen mantles (see, e.g. Nguyen-Luong et al. 2013).

Nonetheless, it is worth emphasizing that these conclusions critically depend on the assumed frozen-SiO sputtering threshold energy, a parameter which is poorly constrained and which enters as an exponential factor in the equations (e.g. Barlow 1978; Flower & Pineau des Forets 1994). For example, Nguyen-Luong et al. (2013) used the Paris-Durham shock code[8] where the SiO sputtering threshold energy is 1900 K (in the original version of the code it was instead assumed to be 2500 K: Barlow 1978; Flower & Pineau des Forets 1994). We ran the Paris-Durham shock code to simulate the conditions found in the Fingers, described above. If the SiO sputtering threshold energy is 1200 K instead of 1900 K, SiO is predicted to be injected from the mantles into the gas-phase already at 7 km s^{-1} with a predicted SiO column density consistent with what we observe in the Fingers.

However, it is important to emphasize that the above constraints have to be taken with a grain of salt and not at face value. Therefore, giving the large uncertainty linked to the SiO sputtering threshold, which enters in an exponential term in the equations, one may speculate that shocks with velocities larger than about 7 km s^{-1} can reproduce the observations.

5.3.4 *Shock velocity and inclination angle*

Using the time between Finger1 and Finger2 shock passage derived in Section 5.3.2, we can provide an approximation of the shock velocity:

$$\mathrm{v} = \frac{s_\perp}{\sin\theta} \frac{1}{\mathrm{time}} \tag{5}$$

where $s_\perp$ is the projected separation among the fingers and it is about 3000 au, and θ is the angle of the shock propagation with respect to the line of sight.

The lower limit to the shock velocity so to be able to release enough SiO into the gas-phase, reported in Section 5.3.3, provides an upper limit to the inclination angle, which depends on the shock passage time. Taking v$\geq$ 10 km s^{-1} gives $\theta \leq$15, 25 and 45 degrees for 10^4, 5000 and 2000 yr, respectively. In the case of lower SiO sputtering threshold, v$\geq$ 7 km s^{-1} corresponds to $\theta \leq$15, 25 and 90 degrees for 10^4, 5000 and 2000 yr, respectively. Note that, if the time is 2000 yr, no solutions exist for a velocity lower then 7 km s^{-1}, for any θ.

5.4 IRAS 4A fingers: the signature of the clash of an expanding bubble

As briefly mentioned in the Introduction, at a large scale, the NGC 1333 region is constituted by several filaments, of which the southeast one (SE) runs parallel to our Fingers (Dhabal et al. 2019). This SE filament is characterized by two substructures running parallel to each other with two distinct systemic velocities, +7.5 km s^{-1} and +8.2 km s^{-1}, respectively, with the western one blue-shifted with respect to the eastern (Dhabal et al. 2018). The gas in the arch-like structure west of the SE filament has approximately the same velocity as the western substructure of the SE filament, namely +6.5 km s^{-1}. This arch-like structure traces the borders of a large cavity (see Fig. 2), to the north and west of which lie the protostellar systems of IRAS2, SVS13, and IRAS4 and to the south the SK1 system. Dhabal et al. (2019) suggested that this region represents the gas compressed by a “turbulent cell” moving from the south and clashing against the NGC 1333 cloud. Always according to Dhabal et al. (2019), this clash could have formed the SE filament and triggered the formation of the IRAS2, SVS13, and IRAS4 protostars.

The new detection of the train of shocks in the IRAS 4A region allows us to put some constraints to this hypothesis.

First, the presence of a train of three shocks in IRAS 4A suggests that the turbulent cell is the result of an expanding bubble, which caused three different shock events, as schematically shown in Fig. 6. If the proposed bubble, coming from the southeast and moving toward the IRAS 4A main cloud from behind, continuously expands, it can create a series of shocks as the ones described in Sects. 5.1 and 5.3.

---

[8] The Paris-Durham shock code is publicly available at `https://ism.obspm.fr/shock.html`

Following the discussion done in Section 5.3 to explain the observed SiO column density we propose that the expanding velocity of the bubble has to be at least 7 km s^{-1}.

Incidentally, this would not be the first case reported in the literature of a train of shocks caused by the clashing of an expanding bubble into a quiescent dense molecular cloud. It has been observed, for example, in at least two other cases, both associated with supernovae remnants (SRN). Dumas et al. (2014) detected two parallel filamentary structures in SiO toward a cloud next to the SRN W51C and attributed them to the passage of the SNR primary shock. Similarly, Cosentino et al. (2019) reported the presence of two parallel shocks, probed by SiO, toward SNR W44, caused by the interaction of the expanding SNR bubble into the infrared dark cloud G034.77-00.55.

On the contrary, the origin of the expanding bubble clashing toward NGC 1333 is not obvious. As Dhabal et al. (2019) already pointed out, there are no known nearby ionizing stars, SNRs, or Hɪɪ regions that could be responsible for it. Using CO isotopologues, Arce et al. (2011) presented a complete mapping of shells and bubbles in the Perseus molecular cloud. Among them, southeast of IRAS 4A, there is the so-called CPS 2 shell with ∼ 6′ of radius and whose origin is unknown. However, CPS2 is located 24′ away from the IRAS 4A fingers, so it does not seem to be a good candidate. On the other hand, our Galaxy is populated with very large (tens of degrees) loops, arcs, spurs, and filaments visible at different wavelengths (e.g., X-rays, microwaves, synchrotron emission). The most famous are the so-called Loop I, II, III, and IV, probably old ($\sim 10^5 - 10^6$ yr) nearby supernova (SN) remnants (Berkhuijsen et al. 1971; Vidal et al. 2015; Dickinson 2018). The NGC 1333 molecular complex lies at the edge of Loop II (called also Cetus arc; Large et al. 1962), an expanding bubble of ∼ 90° of diameter and centered at galactic longitude −100° and latitude 30°. Hence, Loop II could be a possible candidate for the proposed expanding bubble.

5.5 Traces of other clashes in NGC 1333

Previous single-dish observations have shown the presence of extended SiO emission, with a narrow (FWHM<1.5 km s^{-1}) line profile at ambient velocity, in the region encompassing SVS13 and IRAS 4A (Lefloch et al. 1998; Codella et al. 1999). The origin of this emission was debated but no clear consensus was reached. For example, the hypothesis of fossil shocks connected with the outflows from the protostars was evoked, although no definite answer was found. The three fingers discovered by SOLIS can help to elucidate the origin of this large-scale SiO narrow emission.

Figure 7 shows the overlap of the line-of-sight N_2H^+ line-of-sight velocity map by Dhabal et al. (2019) of the southern NGC 1333 filaments with the large-scale SiO narrow emission by Lefloch et al. (1998) and the three fingers discovered by SOLIS in the present work. The large-scale SiO narrow emission extends from southeast of SVS13A to southwest of IRAS 4A, and it seems to be composed of two parts, or lobes, that have different orientations. In the northern lobe, the SiO emission is elongated in the direction northeast-west while, in the southern lobe, the emission runs in the direction northwest-southeast. The SOLIS fingers lie at the northern limit of the southern lobe and they are pretty much parallel to the observed large-scale SiO emission. As discussed in Sect. 5.4, we propose that the SOLIS fingers are due to shocks caused by the interaction of an expanding bubble coming from southeast behind the NGC 1333 SE filament, where IRAS 4A lies. It is tempting to hypothesize that the southern lobe of the SiO emission observed by Lefloch et al. (1998) is an ensemble of small-scale shocks, like the ones traced by the SOLIS fingers, caused by older bubble expansion events. Our prediction, therefore, is that the SiO emission of the southern lobe will break up in multiple parallel small-scale shocks if observed with interferometers like NOEMA. If this is true, the frequency and chemical composition of these hypothetical shocks may add stringent constraints on the phenomenon and expansion velocity of the bubble clashing against NGC 1333 from the southeast.

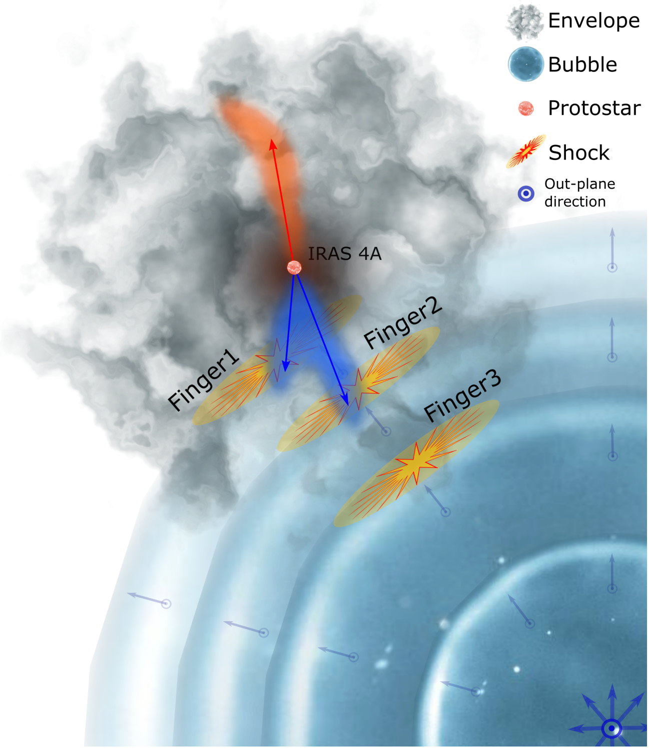

Figure 6. Cartoon model of the IRAS 4A region, illustrating the outflowing system inside the envelope and the proposed expanding bubble. The size of the bubble increases with time, and each circle in the figure represents the bubble at subsequent times: the largest circle represents the last expansion that caused the shock at the origin of Finger1. In the cartoon, the bubble is farther from us in the line of sight than the IRAS 4A main cloud and it is moving toward it. The three orange regions represent the collision zones, in which the observed three fingers are formed.

A similar possibility could apply to the northern SiO lobe: it could be an ensemble of multiple parallel small-scale shocks unresolved by the single-dish observations of Lefloch et al. (1998) and Codella et al. (1999). However, in this case, since the SiO emission orientation is almost perpendicular to that of the southern lobe, the shocks would be caused by another bubble clashing from the northwest and expanding toward the region encompassing SVS13-A from the front (being that region red-shifted in the N_2H^+ velocity map). We searched for SiO and methanol fingers around SVS13-A using the SOLIS observations toward this source, but we could not find any. Interestingly, however, the region encompassed by the SOLIS observations, in this case, lies in an area where Lefloch et al. (1998) and Codella et al. (1999) did not detect the SiO narrow emission, slightly north to where it appears.

Finally, the comparison of the large-scale SiO narrow emission map and the local magnetic field (Figure 4 and 6 in Doi et al. 2020) presents an intriguing feature (see Figure 7). The change in orientation observed in the two SiO lobes seems to be correlated with a change in the orientation of the magnetic field. Specifically, in both cases, the magnetic field is almost parallel to the direction

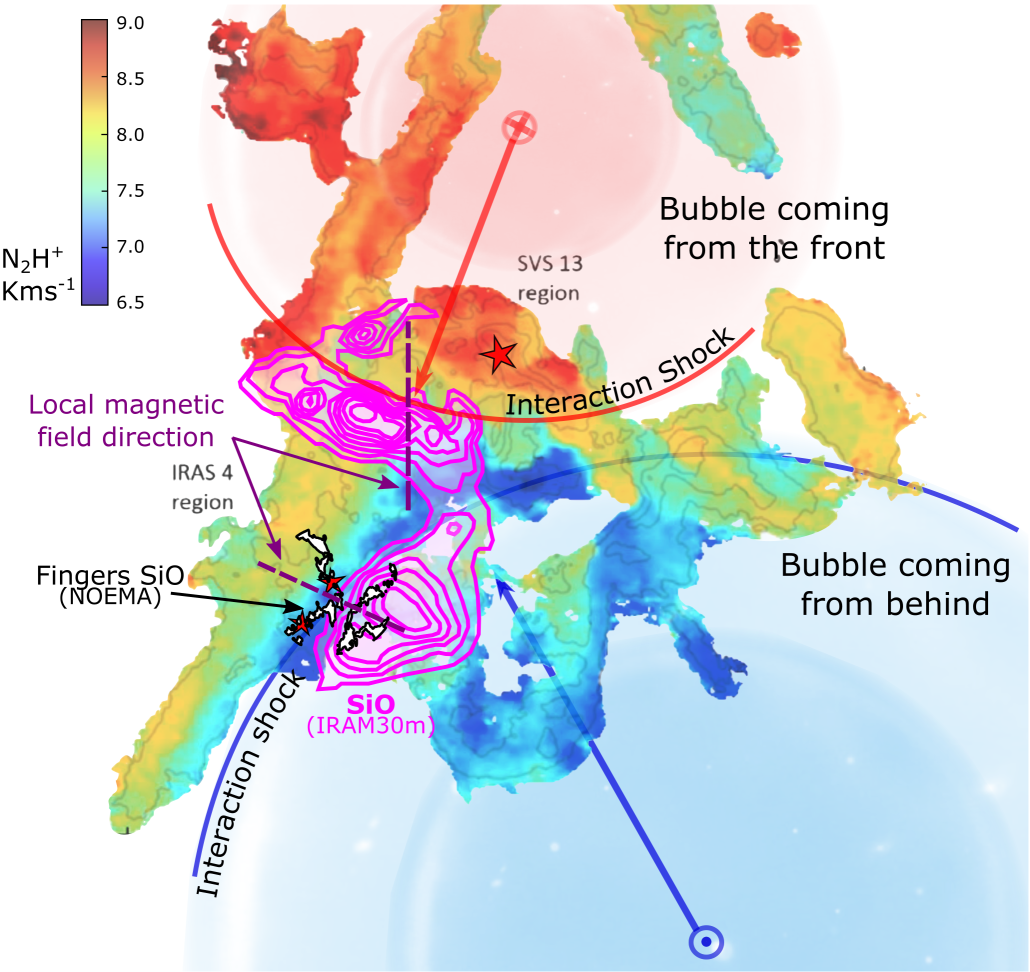

Figure 7. Large-scale view of the NGC 1333 filament. Overlap of the N_2H^+ line-of-sight velocity map by Dhabal et al. (2019) in color with the IRAM-30m SiO large scale ambient component emission by Lefloch et al. (1998) in magenta contours and the IRAS 4A fingers detected in SiO with the SOLIS/NOEMA observations of the present work in black contours. The purple dashed lines represent the local magnetic field direction from Doi et al. (2020). The red stars mark the SVS13, IRAS 4A, and IRAS 4B protostars. The solid blue and red lines represent the interaction of the expanding bubbles: the red one is expanding from the northwest direction toward the SVS13 cloud from the front, and the blue one is expanding from the southwest direction toward the IRAS 4A cloud from behind.

of the shocks, and almost perpendicular to the fingers/filamentary emission.

6 CONCLUSIONS

We report CH_3OH and SiO IRAM-NOEMA high spatial resolution ($\sim 1\farcs5$; $\sim$ 450 au) observations in the direction of NGC 1333 IRAS 4A, obtained in the context of the Large Program SOLIS.

The observations reveal the presence of three elongated filamentary structures traced by SiO and CH_3OH $\sim$ 10″ (~3000 au) south from the protostar center. They are characterized by narrow (FWHM~1.5 km s^{-1}) lines peaked at the systemic velocity of the cloud. These structures, which we called fingers, are parallel to each other, extended for more than about 6000 au, approximately equispaced by about 3000 au, and almost perpendicular to the two outflows arising from IRAS 4A and the SE filament where IRAS 4A lies.

The non-LTE analysis of the methanol lines in the northern finger indicates that the gas has a high density (5–20 $\times 10^5$ cm^{-3}) and high temperature (80–160 K), much larger than that expected if the gas was heated by the central protostar. The three detected fingers are chemically different, with the northern one traced by both SiO and CH_3OH and the southern two only by SiO. The CH_3OH over SiO abundance ratio is 160–300 in the northern finger, while it is $\leq$ 40 in the southern one. Both the measured temperature and enhanced SiO and CH_3OH abundances point to a non-thermal process responsible for them.

Given their quasi-periodicity and morphology, we considered the possibility that the fingers trace a Kelvin-Helmholtz instability occurring at the interface of the NGC 1333 IRAS4 region and a less dense cloud sliding from south to north. However, this hypothesis can not reproduce the observed properties of the fingers.

We then considered the possibility that the three fingers represent a train of three shocks. This hypothesis agrees with the observed physical and chemical properties of the fingers, and provides constraints on when the shocks occurred, with an interval of at least 5000 yr between the youngest northern finger and the next southern one.

Previous studies had already shown that the NGC 1333 is a region heavily shaped by the dynamical interaction of internal outflows and external bubbles with the quiescent molecular cloud. In particular, previous large-scale maps of gas distribution and velocities in the IRAS 4A region already suggested the presence of a “turbulent cell” pushing toward the NGC 1333 IRAS4 from behind and coming from the south. The newly detected fingers provide support to this hypothesis, considering that the turbulent cell is the result of an expanding bubble, which caused three different shock events, with an expanding velocity of at least 7 km s^{-1}.

Finally, we suggest that the widespread narrow SiO emission observed toward the NGC 1333 IRAS 4 and SVS 13 region with single-dish observations in the late 90s is due to unresolved trains of shocks like the SOLIS fingers. These shocks would be the signature of the interaction of the bubble giving rise to the IRAS 4A fingers in the south and of another bubble pushing from the north toward SVS 13. We predict, therefore, that large-scale high-spatial resolution mosaics of SiO and other shock-related species can help to fully reconstruct the dynamical history of NGC 1333 and, consequently, provide precious constraints to the relevant theories and models.

ACKNOWLEDGMENTS

We thank the referee P. Goldsmith for the fruitful comments and suggestions. We are very grateful to all the IRAM staff, whose dedication allowed us to carry out the SOLIS project. We warmly acknowledge fruitful discussion with Prof. Lucio Piccirillo and Dr. Geoffroy Lesur, as well as with Dr. Antoine Gusdorf on the shock models. Some of the computations presented in this paper were performed using the GRICAD infrastructure (`https://gricad.univ-grenoble-alpes.fr`), which is partly supported by the Equip@Meso project (reference ANR-10-EQPX-29-01) of the programme Investissements d'Avenir supervised by the Agence Nationale pour la Recherche. This project has received funding within the European Union's Horizon 2020 research and innovation programme from the European Research Council (ERC) for the project "The Dawn of Organic Chemistry" (DOC), grant agreement No 741002, and from the Marie Sklodowska-Curie for the project "Astro-Chemical Origin" (ACO), grant agreement No 811312. C. Codella acknowledges the project PRIN-INAF 2016 The Cradle of Life - GENESIS-SKA (General Conditions in Early Planetary Systems for the rise of life with SKA).

DATA AVAILABILITY

The data underlying this article are part of the IRAM-NOEMA SOLIS Large program and they will be publicly available on the IRAM archive at the end of the proprietary period (`https://www.iram-institute.org/EN/content-page-240-7-158-240-0-0.html`).

REFERENCES

Agúndez M., Wakelam V., 2013, Chemical Reviews, 113, 8710

André P., et al., 2010, A&A, 518, L102

André P., Di Francesco J., Ward-Thompson D., Inutsuka S. I., Pudritz R. E., Pineda J. E., 2014, in Beuther H., Klessen R. S., Dullemond C. P., Henning T., eds, Protostars and Planets VI. p. 27 (`arXiv:1312.6232`), doi:10.2458/azu_uapress_9780816531240-ch002

Arce H. G., Santiago-García J., Jørgensen J. K., Tafalla M., Bachiller R., 2008, The Astrophysical Journal Letters, 681, L21

Arce H. G., Borkin M. A., Goodman A. A., Pineda J. E., Beaumont C. N., 2011, ApJ, 742, 105

Bachiller R., Guilloteau S., Gueth F., Tafalla M., Dutrey A., Codella C., Castets A., 1998, Astronomy and Astrophysics, 339, L49

Bachiller R., Pérez Gutiérrez M., Kumar M. S. N., Tafalla M., 2001, Astronomy and Astrophysics, 372, 899

Barlow M. J., 1978, MNRAS, 183, 367

Berkhuijsen E. M., Haslam C. G. T., Salter C. J., 1971, A&A, 14, 252

Berné O., Matsumoto Y., 2012, ApJ, 761, L4

Berné O., Marcelino N., Cernicharo J., 2010, Nature, 466, 947

Bialy S., et al., 2021, ApJ, 919, L5

Boogert A. C. A., Gerakines P. A., Whittet D. C. B., 2015, Annual Review of Astronomy and Astrophysics, 53, 541

Caselli P., Ceccarelli C., 2012, Astronomy and Astrophysics Review, 20, 56

Caselli P., Hartquist T. W., Havnes O., 1997, Astronomy and Astrophysics, 322, 296

Ceccarelli C., Maret S., Tielens A. G. G. M., Castets A., Caux E., 2003, Astronomy & Astrophysics, 410, 587

Ceccarelli C., et al., 2017, The Astrophysical Journal, 850, 176

Chen M. C.-Y., et al., 2020, ApJ, 891, 84

Choi M., 2005, The Astrophysical Journal, 630, 976

Chuang C.-Y., Aso Y., Hirano N., Hirano S., Machida M. N., 2021, arXiv e-prints, p. arXiv:2105.04224

Codella C., Bachiller R., Reipurth B., 1999, Astronomy and Astrophysics, 343, 585

Codella C., et al., 2012, The Astrophysical Journal, 757, L9

Codella C., et al., 2017, Astronomy and Astrophysics, 605, L3

Codella C., et al., 2020, A&A, 635, A17

Cosentino G., et al., 2018, MNRAS, 474, 3760

Cosentino G., et al., 2019, ApJ, 881, L42

Cosentino G., et al., 2020, MNRAS, 499, 1666

Coughlin E. R., Nixon C. J., 2020, ApJS, 247, 51

De Simone M., et al., 2020, A&A, 640, A75

Dhabal A., Mundy L. G., Rizzo M. J., Storm S., Teuben P., 2018, ApJ, 853, 169

Dhabal A., Mundy L. G., Chen C.-y., Teuben P., Storm S., 2019, ApJ, 876, 108

Dickinson C., 2018, Galaxies, 6, 56

Doi Y., et al., 2020, ApJ, 899, 28

Draine B. T., McKee C. F., 1993, ARA&A, 31, 373

Draine B. T., Roberge W. G., Dalgarno A., 1983, ApJ, 264, 485

Dubernet M.-L., et al., 2013, Astronomy and Astrophysics, 553, A50

Dumas G., Vaupré S., Ceccarelli C., Hily-Blant P., Dubus G., Montmerle T., Gabici S., 2014, ApJ, 786, L24

Federrath C., Klessen R. S., Iapichino L., Beattie J. R., 2021, Nature Astronomy, 5, 365

Flower D. R., Pineau des Forets G., 1994, MNRAS, 268, 724

Flower D. R., Pineau des Forêts G., Rabli D., 2010, MNRAS, 409, 29

Geppert W. D., et al., 2006, Faraday Discussions, 133, 177

Goldsmith P. F., Heyer M., Narayanan G., Snell R., Li D., Brunt C., 2008, ApJ, 680, 428

Guillet V., Pineau Des Forêts G., Jones A. P., 2011, A&A, 527, A123

Gusdorf A., Cabrit S., Flower D. R., Pineau Des Forêts G., 2008a, A&A, 482, 809

Gusdorf A., Pineau Des Forêts G., Cabrit S., Flower D. R., 2008b, A&A, 490, 695

Hacar A., Tafalla M., Kauffmann J., Kovács A., 2013, A&A, 554, A55

Hacar A., Tafalla M., Alves J., 2017, A&A, 606, A123

Hennebelle P., 2013, A&A, 556, A153

Hennebelle P., Inutsuka S.-i., 2019, Frontiers in Astronomy and Space Sciences, 6, 5

Henshaw J. D., Longmore S. N., Kruijssen J. M. D., 2016, MNRAS, 463, L122

Henshaw J. D., et al., 2017, MNRAS, 464, L31

Heyer M., Goldsmith P. F., Yıldız U. A., Snell R. L., Falgarone E., Pineda J. L., 2016, MNRAS, 461, 3918

Hollenbach D., McKee C. F., 1979, ApJS, 41, 555

Hunter James H. J., Whitaker R. W., Lovelace R. V. E., 1997, ApJ, 482, 852

Jenkins E. B., 2009, ApJ, 700, 1299

Jiménez-Serra I., Caselli P., Martín-Pintado J., Hartquist T. W., 2008, A&A, 482, 549

Jiménez-Serra I., Caselli P., Tan J. C., Hernandez A. K., Fontani F., Butler M. J., van Loo S., 2010, MNRAS, 406, 187

Jørgensen J. K., Schöier F. L., van Dishoeck E. F., 2002, A&A, 389, 908

Lada C. J., 1985, ARA&A, 23, 267

Large M. I., Quigley M. J. S., Haslam C. G. T., 1962, MNRAS, 124, 405

Lefloch B., Castets A., Cernicharo J., Loinard L., 1998, The Astrophysical Journal, 504, L109

Lefloch B., Ceccarelli C., Codella C., Favre C., Podio L., Vastel C., Viti S., Bachiller R., 2017, Monthly Notices of the Royal Astronomical Society, 469, L73

Lesaffre P., Pineau des Forêts G., Godard B., Guillard P., Boulanger F., Falgarone E., 2013, A&A, 550, A106

Maret S., Ceccarelli C., Tielens A. G. G. M., Caux E., Lefloch B., Faure A., Castets A., Flower D. R., 2005, A&A, 442, 527

Molinari S., et al., 2010, A&A, 518, L100

Müller H. S. P., Schlöder F., Stutzki J., Winnewisser G., 2005, Journal of Molecular Structure, 742, 215

Müller H. S. P., Spezzano S., Bizzocchi L., Gottlieb C. A., Degli Esposti C., McCarthy M. C., 2013, Journal of Physical Chemistry A, 117

Nguyen-Luong Q., et al., 2013, ApJ, 775, 88

Padoan P., Juvela M., Goodman A. A., Nordlund Å., 2001, ApJ, 553, 227

Planck Collaboration et al., 2020, A&A, 641, A12

Rabli D., Flower D. R., 2010, Monthly Notices of the Royal Astronomical Society, 406, 95

Requena-Torres M. A., Marcelino N., Jiménez-Serra I., Martín-Pintado J., Martín S., Mauersberger R., 2007, The Astrophysical Journal Letters, 655, L37

Rimola A., Taquet V., Ugliengo P., Balucani N., Ceccarelli C., 2014, Astronomy and Astrophysics, 572, A70

Robitaille J. F., Abdeldayem A., Joncour I., Moraux E., Motte F., Lesaffre P., Khalil A., 2020, A&A, 641, A138

Sandell G., Knee L. B. G., 2001, ApJ, 546, L49

Santangelo G., et al., 2015, Astronomy and Astrophysics, 584, A126

Schilke P., Walmsley C. M., Pineau des Forets G., Flower D. R., 1997, A&A, 321, 293

Schneider S., Elmegreen B. G., 1979, ApJS, 41, 87

Shannon R. J., Blitz M. A., Goddard A., Heard D. E., 2013, Nature Chemistry, 5, 745

Sokolov V., et al., 2019, ApJ, 872, 30

Sokolov V., Pineda J. E., Buchner J., Caselli P., 2020, ApJ, 892, L32

Tafalla M., Hacar A., 2015, A&A, 574, A104

Taquet V., et al., 2020, A&A, 637, A63

Tielens A. G. G. M., Hagen W., 1982, Astronomy and Astrophysics, 114, 245

Ungerechts H., Thaddeus P., 1987, ApJS, 63, 645

Vázquez-Semadeni E., Palau A., Ballesteros-Paredes J., Gómez G. C., Zamora-Avilés M., 2019, MNRAS, 490, 3061

Vidal M., Dickinson C., Davies R. D., Leahy J. P., 2015, MNRAS, 452, 656

Wakelam V., et al., 2012, ApJS, 199, 21

Watanabe N., Kouchi A., 2002, The Astrophysical Journal, 571, L173

Xu L.-H., et al., 2008, Journal of Molecular Spectroscopy, 251, 305

Zari E., Lombardi M., Alves J., Lada C. J., Bouy H., 2016, A&A, 587, A106

Ziurys L. M., Snell R. L., Dickman R. L., 1989, The Astrophysical Journal, 341, 857

Zucker C., Schlafly E. F., Speagle J. S., Green G. M., Portillo S. K. N., Finkbeiner D. P., Goodman A. A., 2018, The Astrophysical Journal, 869, 83

Zucker C., et al., 2021, ApJ, 919, 35

This paper has been typeset from a TEX/LATEX file prepared by the author.

Submitted Papers

(Or close to be submitted)

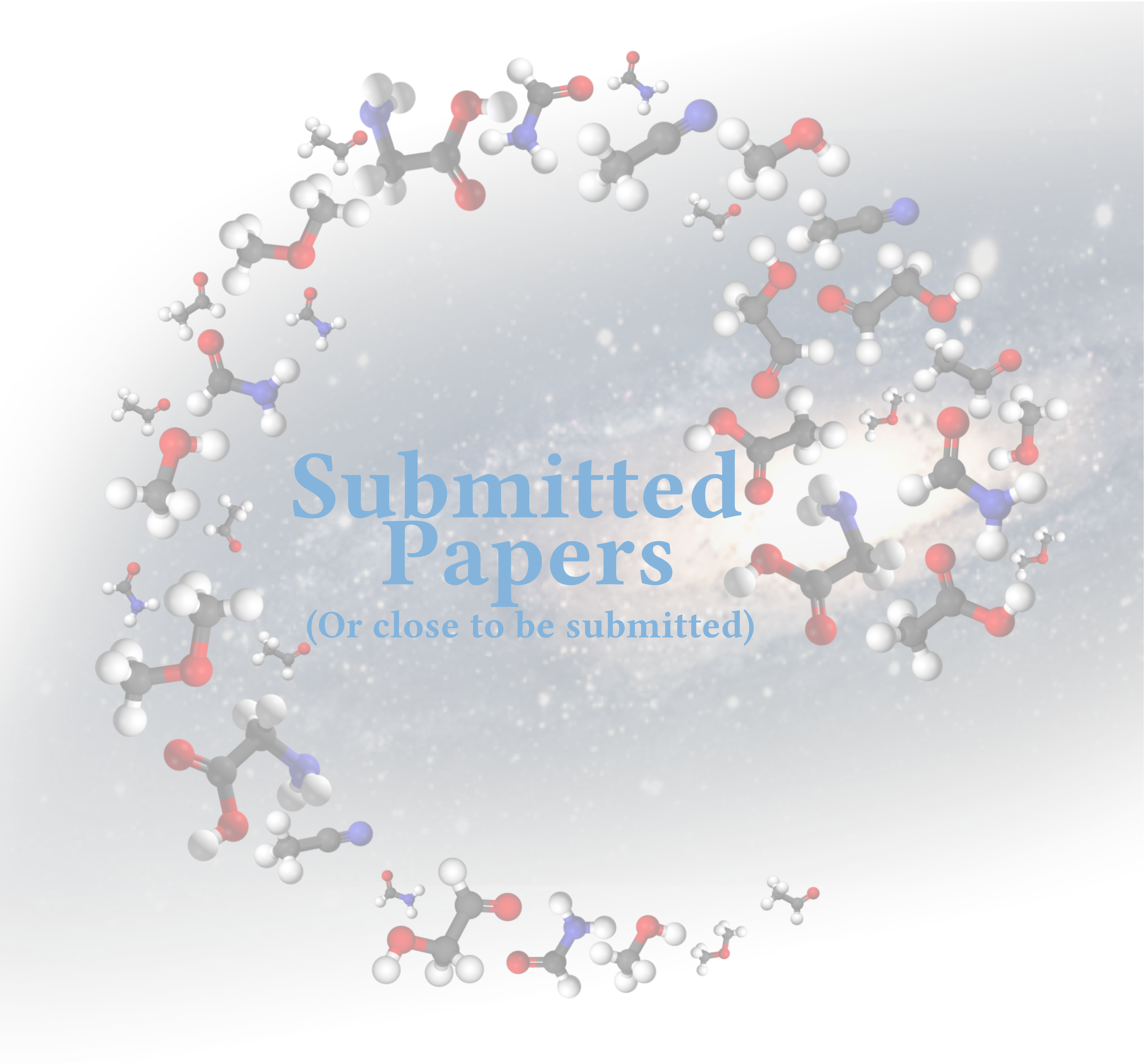

To be submitted…

Draft version December 2, 2021
Typeset using LaTeX **twocolumn** style in AASTeX63

Tracking the ice mantle history in the Solar-type Protostars of NGC 1333 IRAS 4

Marta De Simone,[1,2] Cecilia Ceccarelli,[1] Claudio Codella,[2,1] Brian E. Svoboda,[3,4] Claire Chandler,[3] Mathilde Bouvier,[1]
Satoshi Yamamoto,[5] Nami Sakai,[6] Paola Caselli,[7] Cecile Favre,[1] Laurent Loinard,[8] Bertrand Lefloch,[1] Hauyu Baobab Liu,[9]
Ana López-Sepulcre,[10,1] Jaime E. Pineda,[7] and Leonardo Testi[11,2,12]

[1] *Univ. Grenoble Alpes, CNRS, IPAG, 38000 Grenoble, France*
[2] *INAF, Osservatorio Astrofisico di Arcetri, Largo E. Fermi 5, 50125 Firenze, Italy*
[3] *National Radio Astronomy Observatory*[a]*, 1003 Lopezville Rd, Socorro, NM 87801, USA*
[4] *Steward Observatory, University of Arizona, 933 North Cherry Avenue, Tucson, AZ 85721, USA*
[5] *Department of Physics, The University of Tokyo, Bunkyo-ku, Tokyo 113-0033, Japan*
[6] *The Institute of Physical and Chemical Research (RIKEN), 2-1, Hirosawa, Wako-shi, Saitama 351-0198, Japan*
[7] *Max-Planck-Institut für extraterrestrische Physik (MPE), Giessenbachstrasse 1, 85748 Garching, Germany*
[8] *Instituto de Radioastronomía y Astrofísica, Universidad Nacional Autónoma de México Apartado 58090, Morelia, Michoacán, Mexico*
[9] *Academia Sinica Institute of Astronomy and Astrophysics (ASIAA), No. 1, Section 4, Roosevelt Road, Taipei 10617, Taiwan*
[10] *Institut de Radioastronomie Millimétrique (IRAM), 300 rue de la Piscine, 38400 Saint-Martin d'Hères, France*
[11] *ESO, Karl Schwarzchild Srt. 2, 85478 Garching bei München, Germany*
[12] *Excellence Cluster Origins, Boltzmannstrasse 2, D-85748 Garching bei München, Germany*

(Received –; Revised –; Accepted –)

Submitted to ApJL

ABSTRACT

Keywords: Stars: formation — ISM: abundances — ISM: molecules — ISM: individual objects: IRAS4A

1. INTRODUCTION

The thousands exoplanets discovered so far (e.g., http://exoplanet.eu/) provide clear evidence of the incredible variety of planetary systems, different from each other and from our Solar System. In order to understand the origin of such diversity, it is crucial to characterize the early stages (Class 0/I protostellar objects, $10^4 - 10^5$ yr; Andre et al. 2000) of the formation of a planetary system. To study the diversity of these early stages , a powerful observational diagnostic tool is their chemical composition (Ceccarelli et al. 2007; Sakai & Yamamoto 2013). Indeed, the chemical complexity in star-forming regions starts at the very beginning of the process, during the pre-collapse phase. At this stage, icy mantles form on interstellar grains and grow rich of hydrogenated species. Then, during the warm protostellar phase, the ice mantle species are released in the gas phase through ice mantle sublimation (forming the so-called hot corinos[1]) (e.g., Caselli & Ceccarelli 2012; Öberg & Bergin 2021). Therefore, the composition of the icy mantles is crucial in establishing the observed chemical diversity.

Infrared (IR) absorption observations towards Solar-type protostars have shown that the icy mantles major components are H_2O, CO, CO_2, CH_4, NH_3, CH_3OH and other species with lower abundances (Bottinelli et al. 2010; Öberg et al. 2011; Boogert et al. 2015). However, these observations can only be obtained toward sources with enough bright IR continuum emission, making it very difficult to characterize the ice mantles of deeply embedded protostars, and even more of prestellar cores. Another possibility is to observe the icy mantles major components once they are released into the gas phase during the hot corino phase. In this context, NH_3 and CH_3OH are the best, if not the only, major components of the mantle composition that can be studied with ground-based telescopes. Indeed, they are the only easily observable tracers as CO is often optically thick and confused with the

Corresponding author: Marta De Simone
marta.desimone@univ-grenoble-alpes.fr

---

[a] The National Radio Astronomy Observatory is a facility of the National Science Foundation operated under cooperative agreement by Associated Universities, Inc.

[1] Hot corinos are compact (<100 au), hot (≥100 K) and dense ($n_{H_2} \geq 10^7$ cm^{-3}) regions (e.g., Ceccarelli 2004), enriched in interstellar Complex Organic Molecules (iCOMs; Herbst & Van Dishoeck 2009; Ceccarelli et al. 2017).

surrounding cloud, CO_2 and CH_4 do not have dipole moments, and H_2O observations are hampered by the terrestrial atmosphere. Since NH_3 and CH_3OH are grain surface products (Watanabe & Kouchi 2002; Fuchs et al. 2009; Rimola et al. 2014; Song & Kästner 2017), their abundance ratio only depends on the mantle formation history (e.g., time, density, and temperature of the pre-collapse clump; Taquet et al. 2012; Cuppen et al. 2017; Aikawa et al. 2020). Additionally, both molecules are key participants in the formation of more complex N- and O-bearing molecules

In this Letter we investigate the icy mantle composition, through the relative abundance of NH_3 and CH_3OH, of a set of Class 0 hot corinos in the inner 300 au region where planets will eventually form. In particular we targeted three sources in the Perseus NGC 1333 region (distant (299 ± 15) pc Zucker et al. 2018): the Class 0 protobinary system IRAS 4A, composed by IRAS 4A1 and IRAS 4A2 (hereafter 4A1 and 4A2) separated by 1.8″ (~540 au), and IRAS 4B (hereafter 4B) located ~ 30″ south-east of IRAS 4A. All the three sources have a hot corino region (Taquet et al. 2015; López-Sepulcre et al. 2017; De Simone et al. 2017, 2020; Sakai et al. 2006; Bottinelli et al. 2007; De Simone et al. 2017).

2. OBSERVATIONS

The data used for this work are the VLA observations in K-band described in De Simone et al. (2020) (project ID: 18B-166). In summary, we targeted ten CH_3OH and five NH_3 lines, with frequencies from 23.8 to 26.4 GHz and upper level energies (E_{up}) from 36 to 175 K for CH_3OH and from 24 to 640 K for NH_3 (see Table 1). The observed lines were associated to 13 spectral windows with ~0.017 MHz (~0.2 km s^{-1}) spectral resolution and 1″ (~ 300 au at the distance of IRAS 4A; Zucker et al. 2018) angular resolution. The absolute flux calibration error is ≤15%[2]. Data reduction and cleaning process were performed using the CASA[3] package while data analysis and images were performed using the GILDAS[4] package. Further details can be found in De Simone et al. (2020). The cubes, self-calibrated and continuum subtracted, were smoothed to 1 km s^{-1} (~0.08 MHz). The synthesized beams for each spectral window are reported in Table 1. The half power primary beam is ~ 80″.

3. RESULTS

3.1. *Maps and Spectra*

Figure 1 reports the velocity-integrated map of the five NH_3 lines, for the three targeted sources (4A1, 4A2, and 4B), and of ten CH_3OH lines for 4B (as the CH_3OH maps for 4A1 and 4A2 are reported in De Simone et al. 2020), overlapped with the 25 GHz continuum emission. The emission of both species peaks at the continuum position of the sources, with coordinates $\alpha(J2000) = 03^{h}29^{m}10^{s}.536$, $\delta(J2000) = 31^{\circ}13'31''.07$ for 4A1, $03^{h}29^{m}10^{s}.43$, $31^{\circ}13'32''.1$ for 4A2, and $03^{h}29^{m}12^{s}.02$, $31^{\circ}13'07''.9$ for 4B. Additionally, even if unresolved at the current angular resolution, the emission of NH_3 around the binaries 4A1 and 4A2 is well disentangled around the two protostars.

Figure 2 shows the spectra of all the targeted lines extracted at the continuum peak of the sources (the CH_3OH spectra for 4A1 and 4A2 are reported in De Simone et al. 2020). We derived the velocity-integrated line intensities for each transition using for CH_3OH a Gaussian fit, while for NH_3 we used a Hyperfine fit since we were able to spectrally resolve the hyperfine structure. The Hyperfine fit is taking into account the hyperfine structure of ammonia assuming: i) the same excitation temperature for all the components of the multiplet, ii) Gaussian distribution of velocity, iii) the lines have the same width, and iv) the multiplet components do not overlap. The fits results are reported in Table 1. In the case of NH_3, the integrated emission is computed as the sum of the integrated area of the main and the satellite hyperfine components. The velocity peaks are consistent with the systemic velocity of the cloud hosting IRAS 4A1, 4A2 and 4B (~ 6.7 km s^{-1}; Choi 2001). In summary, we detected multiple lines of ammonia and methanol in the three Class 0 hot corinos, IRAS 4A1, 4A2 and 4B, at small scale (~ 1″) around the central region.

3.2. *Column density estimation*

Thanks to the detection of several lines of NH_3 and CH_3OH covering a large range of upper level energies (see Table 1) we could perform a multi-line analysis to derive the abundance ratio of these two species. More specifically, we performed a non-LTE analysis via our in-home Large Velocity Gradient (LVG) code `grelvg` originally developed by Ceccarelli et al. (2003). The collisional coefficients of CH_3OH (both A-type and E-type; Rabli & Flower 2010) and NH_3 with para-H_2 are taken from the BASECOL database (Dubernet et al. 2013). They are computed between 10 and 200 K by Rabli & Flower (2010) for the first 256 levels of CH_3OH and by Bouhafs et al. (2017) for the lowest 17 and 34 rotation-inversion levels of ortho- and para-NH_3. We assumed the CH_3OH A-type/E-type ratio equal to 1 and the NH_3 ortho-to-para ratio equal to 2. For both NH_3 and CH_3OH we assumed a semi-infinite slab geometry to compute the line escape probability as a function of the line optical depth, and the H_2 ortho-to-para ratio equal to 3.

Methodology: We first performed the LVG analysis to the methanol lines, in order to better constrain the gas con-

---

[2] https://science.nrao.edu/facilities/vla/docs/manuals/oss/performance/fdscale

[3] https://www.casa.nrao.edu/

[4] http://www.iram.fr/IRAMFR/GILDAS

Table 1. Spectral parameters, synthesized beams and the Gaussian and Hyperfine fit results for the CH_3OH and NH_3 lines, respectively, extracted toward the IRAS 41A, 4A2 and 4B continuum peak.

Transition	Frequency$^{(a)}$	$E_{up}^{(a)}$	$\log A_{ij}^{(a)}$	Synthesized Beam maj × min (PA)	Source $\int T_B dV$	V^b_{peak}	FWHM^b	RMS
	[GHz]	[K]		[″×″ (°)]	[K km s^{-1}]	[km s^{-1}]	[km s^{-1}]	[K]
CH_3OH					IRAS 4B			
3(2,1)-3(1,2) E	24.92871	36	-7.2	0.97×0.95 (-12)	17(2)	+6.9(0.1)	1.5(0.2)	1.2
4(2,2)-4(1,3) E	24.93347	45	-7.1	0.97×0.95 (-12)	21(3)	+6.9(0.2)	2.2(0.4)	1.2
2(2,0)-2(1,1) E	24.93438	29	-7.2	0.97×0.95 (-12)	17(3)	+6.9(0.2)	2.3(0.4)	1.2
5(2,3)-5(1,4) E	24.95908	57	-7.1	0.97×0.95 (-12)	17(2)	+6.8(0.1)	1.5(0.2)	1.2
6(2,4)-6(1,5) E	25.01812	71	-7.1	0.97×0.95 (-19)	21(3)	+6.9(0.2)	2.3(0.5)	1.4
7(2,5)-7(1,6) E	25.12487	87	-7.1	0.98×0.95 (-21)	19(2)	+6.8(0.1)	1.7(0.2)	1.5
8(2,6)-8(1,7) E	25.29442	106	-7.0	0.96×0.94 (-11)	19(2)	+6.9(0.1)	1.9(0.3)	1.2
9(2,7)-9(1,8) E	25.54140	127	-7.0	0.96×0.92 (-50)	22(3)	+6.8(0.1)	1.8(0.3)	1.4
10(2,8)-10(1,9) E	25.87827	150	-7.0	0.97×0.93 (-35)	16(2)	+7.1(0.1)	1.9(0.3)	1.1
11(2,9)-11(1,10) E	26.31312	175	-6.9	0.94×0.91 (-35)	14(2)	+6.6(0.2)	1.4(0.5)	1.4
NH_3					IRAS 4B			
3-3	23.87013	124	-6.6	1.00×0.95 $(+6)$	64(8)	7.2(0.2)	1.7(0.5)	1.5
4-4	24.13942	201	-6.5	0.99×0.94 (-2)	41(7)	7.1(0.1)	1.7(0.1)	1.4
5-5	24.53299	296	-6.5	0.99×0.95 (-3)	39(7)	6.6(0.4)	2.5(0.7)	1.4
6-6	25.05602	409	-6.5	0.97×0.95 (-18)	37(7)	6.1(0.2)	1.7(0.4)	1.4
7-7	25.71518	639	-6.4	0.96×0.92 (-45)	27(7)	6.9(0.3)	1.7(0.1)	1.4
NH_3					IRAS 4A2			
3-3	23.87013	124	-6.6	1.00×0.95 $(+6)$	169(20)	+6.9(0.1)	2.3(0.1)	1.3
4-4	24.13942	201	-6.5	0.99×0.94 (-2)	89(14)	+6.9(0.1)	1.8(0.1)	1.2
5-5	24.53299	296	-6.5	0.99×0.95 (-3)	54(14)	+6.9(0.1)	1.7(0.2)	1.2
6-6	25.05602	409	-6.5	0.97×0.95 (-18)	62(11)	+6.5(0.1)	2.3(0.1)	1.1
7-7	25.71518	639	-6.4	0.96×0.92 (-45)	40(8)	+7.1(0.1)	1.8(0.1)	1.0
NH_3					IRAS 4A1			
3-3	23.87013	124	-6.6	1.00×0.95 $(+6)$	121(16)	+6.4(0.1)	2.7(0.2)	1.3
4-4	24.13942	201	-6.5	0.99×0.94 (-2)	90(13)	+6.5(0.1)	1.9(0.1)	1.0
5-5	24.53299	296	-6.5	0.99×0.95 (-3)	87(12)	+6.4(0.1)	2.5(001	1.0
6-6	25.05602	409	-6.5	0.97×0.95 (-18)	87(11)	+6.7(0.1)	2.9(0.2)	1.1
7-7	25.71518	639	-6.4	0.96×0.92 (-45)	46(9)	+6.4(0.1)	1.9(0.2)	1.1

[a] Spectroscopic parameters are by Xu et al. (2008) from the CDMS (Cologne Database for Molecular Spectroscopy; Müller et al. 2005) molecular database for CH_3OH and Yu et al. (2010) from the JPL (Pickett et al. 1998, Jet Propulsion Laboratory) catalog for NH_3.

[b] The spectral resolution is 1 km s^{-1}.

ditions, namely gas density and temperature, and to derive the CH_3OH column density and emitting size. Assuming that NH_3 is tracing the same gas as CH_3OH, we performed the LVG analysis to the NH_3 lines in order to derive the NH_3 column density considering the source size, the gas density and temperature ranges derived for CH_3OH. Finally, we computed the NH_3/CH_3OH abundance ratio.

Methanol line analysis: The methanol line analysis for IRAS 4A1 and IRAS 4A2 is reported in De Simone et al. (2020). We carried out a similar analysis for IRAS 4B. Indeed, we ran a large grid of models (~ 70000) covering the frequency of the observed CH_3OH lines, a total (A-type plus E-type) column density N_{CH_3OH} from 2×10^{16} to 16×10^{19} cm^{-2}, a gas density n_{H_2} from 1×10^7 to 1×10^9 cm^{-3}, and a temperature T from 60 to 200 K. We simultaneously fit the measured CH_3OH line intensities, for IRAS 4B, via comparison with those simulated by the LVG model, leaving N_{CH_3OH}, n_{H_2}, T and the emitting size θ as free parameters. Following the observations, we assumed a linewidth equal to 2 km s^{-1} and we included the calibration uncertainty (15%) in the observed intensities. The best fit is obtained for a total CH_3OH

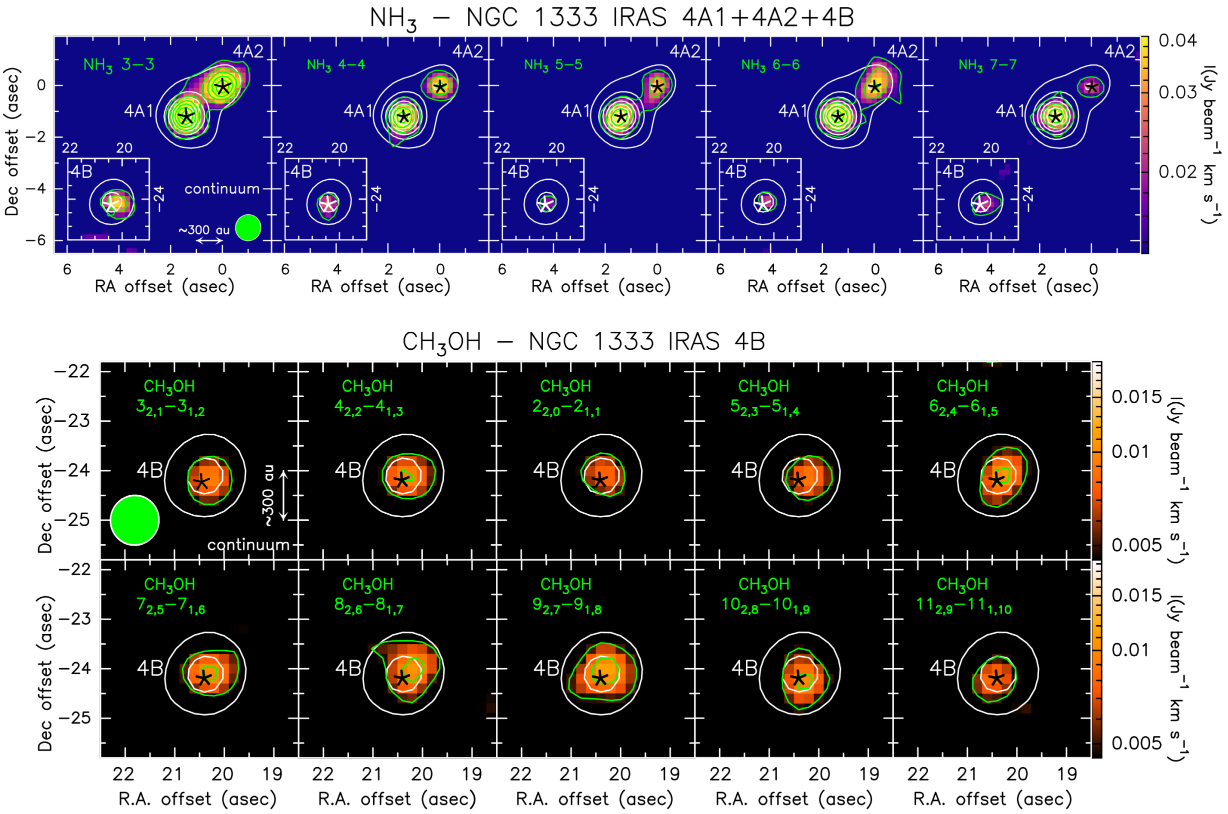

Figure 1. *Top panels*: NH_3 velocity-integrated maps toward IRAS 4A1, 4A2, and 4B in color scale, overlapped with the continuum white contours (from 50σ with steps of 100σ). The emission is integrated from −30 to −11 km s^{-1}, −3 to +15 km s^{-1}, and +25 to +43 km s^{-1}, in order to include the main and the satellite hyperfine components. NH_3 first contour and steps (in green) correspond to 3σ (σ=4.4 mJy beam^{-1}). *Bottom panels:* CH_3OH velocity-integrated maps toward IRAS 4B in color scale overlapped with the continuum white contours (from 50σ with steps of 100σ). The emission is integrated from −2 to +2 km s^{-1} with respect to the v_{sys} (∼ +6.7 km s^{-1} Choi 2001). Methanol first contour and steps (in green) correspond to 3σ (σ=1.6 mJy beam^{-1} km s^{-1}). The CH_3OH maps for IRAS 4A1 and IRAS 4A2 are reported in De Simone et al. (2020). The transition of the imaged line is reported in each panel. The black stars show protostars positions. Synthesised beams for continuum (white) and lines (green) are in the lower left corner.

column density $N_{CH_3OH}=1.4\times10^{18}$ cm^{-2}, with a reduced chi-square χ^2_R=0.4, emitted by a source of $0\farcs24-0\farcs40$. Solutions with $N_{CH_3OH} \geq 1\times10^{18}$ cm^{-2} are within 1σ of confidence level. The χ^2_R decreases, increasing the CH_3OH column density, until a constant value, as all the observed lines become optically thick (τ = 1.5 − 3) and, consequently, the emission is that of a black body. The gas density and temperature, the CH_3OH column density and emitting size for IRAS 4A1, 4A2 and 4B are reported in Table 2.

Ammonia line analysis: We then considered the source size, the gas density and temperature derived by the methanol line analysis and ran a grid of models (∼ 5000) with these parameters to fit the observed ammonia lines for the three sources, leaving as free parameter the ammonia column density.

Following the observations we assumed a linewidth of 12, 10, 9 km s^{-1}, for 4A1, 4A2, and 4B, respectively. The assumed linewidth is computed as the one derived from the Hyperfine fitting (Table 1) multiplied by the number of components (main plus satellites). The best fit is obtained for N_{NH_3} = 1.4×10^{18} cm^{-2} with χ^2_R=0.4 for 4A1, 2×10^{18} cm^{-2} with χ^2_R=1.1 for 4A2, and 1.6×10^{18} cm^{-2} with χ^2_R=1.4 for 4B. The N_{NH_3} 1σ confidence level range is reported in Table 2. Some of the observed lines are quite optically thick (∼20-40), while the majority of the NH_3 lines have opacity between 0.4 and 4. The lines that are optically thin (≤1) allowed us to constrain the column density.

Abundance ratios: Finally, we computed the NH_3/CH_3OH abundance ratio, using the column densities derived from the LVG analysis described above. The derived values are ≥ 0.5, ≥ 3, and ≥ 15, for 4A1, 4A2 and 4B (Table

Table 2. Results of the non-LTE LVG analysis of the CH_3OH and NH_3 lines toward IRAS 4A1, 4A2 and 4B using the `grelvg` code. The reported values for gas density (n_{H_2}) and temperature (T_{kin}), source size, species column densities and their abundance ratio, are the 1σ confidence level.

		IRAS 4A1	IRAS 4A2	IRAS 4B
n_{H_2}	[cm^{-3}]	$\geq 2\times10^6$	$\geq 10^7$	$\geq 2\times10^7$
T_{kin}	[K]	100-120	130-160	110-130
N_{CH_3OH}	[cm^{-2}]	$\geq 10^{19}$	$\geq 10^{18}$	$\geq 10^{18}$
N_{NH_3}	[cm^{-2}]	$(1.2\text{-}5)\times10^{18}$	$(0.6\text{-}3)\times10^{18}$	$(0.3\text{-}15)\times10^{18}$
size[a]	["]	0.20-0.24	0.22-0.24	0.24-0.26
NH_3/CH_3OH	-	≤ 0.5	≤ 3	≤ 15

[a] The reported range for the source size is constrained from both CH_3OH and NH_3 analysis.

2). They are all upper limits as the derived CH_3OH column density is a lower limit.

4. DISCUSSION

4.1. *Astrochemical modelling*

We used the astrochemical model `GRAINOBLE` (Taquet et al. 2012; Taquet et al. 2013). Briefly, this is a time-dependent grain-gas chemistry code that computes the layered grain mantles structure. The model adopted here follows the one used in Ceccarelli et al. (2018). For further details on the processes included in the model (such us accretion, diffusion, surface, and desorption) please refer to Ceccarelli et al. (2018). For the reactions occurring in the gas phase, we used the KIDA 2014 network; (http://kida.obs.u-bordeaux1.fr; Wakelam et al. 2015), updated with the reactions described in Loison et al. (2014); Balucani et al. (2015); Skouteris et al. (2017, 2018); Codella et al. (2020). The reactions on the grain surface leading to formaldehyde, methanol and water are described in Taquet et al. (2013). The hydrogenation of C and N that leads to methane (CH_4), ammonia (NH_3), respectively, have been added.

We assumed that the H number density of the molecular cloud, n_H is constant, and an average grain radius of 0.1 μm^2, typical of the galactic ISM grains (e.g., Jones et al. 2013). The gas and dust are assumed to be thermally coupled, and the abundances of the elements in the gas phase are the one reported in Table 2 by Ceccarelli et al. (2018).

We started with a partially atomic cloud, i.e. all the elements are in atomic form except for hydrogen that is assumed to be in molecular form. The cloud chemical composition is left to evolve with time for 10^7 yr. The `GRAINOBLE` code follows the chemical evolution of each grain mantle layer, therefore it provides the composition of each layer as the mantle grows. The mantle is formed of approximately 100 layers.

4.2. *Observations vs model predictions*

The NH_3 and CH_3OH relative abundance depends on the pre-collapse clump temperature and density, and the ice mantle formation timescale. Figure 3 reports the theoretical predictions of the abundance ratio between ammonia and methanol as a function of time for several temperatures (8,9,12,15,18,20 K) and H density ((0.2, 2, 20)$\times10^5$ cm^{-3}).

The NH_3/CH_3OH abundance ratio decreases with time, as methanol starts to form after ammonia. The first layers of the grain mantle are mostly composed of the hydrogenated forms of C and N, namely methane and ammonia. When the C and N atoms land on the grain, they undergo hydrogenation, which is a fast process since it does not have energy barriers. Then, the gaseous abundance of both C and N drops and CO and N_2 form. Later on, the gaseous CO freezes out into the mantles, and the methanol is efficiently formed through its hydrogenation.

Increasing the cloud temperature, the mantle growth is slower and the mantles have less layers becoming thinner (see Figure 1 in Ceccarelli et al. 2018). As a consequence of the increasing temperature, the hydrogenation processes are reduced as the residence time in the mantle of H and O atoms, as well as of CO molecules, decreases, so that the hydrogenation and oxidation processes are reduced. Additionally, if the dust temperature becomes larger than its sublimation temperature (approximately 20–30 K) CO cannot remain frozen on the surface. Therefore, increasing the temperature, the methanol abundance decreases and consequently the NH_3/CH_3OH ratio increases (see Figure 3).

On the other hand, increasing the n_H density, the species accretion on the grain mantles is faster, as the accretion rate is directly proportional to the grain number density [5]. Therefore, the formation of hydrogenated species occurs earlier and, consequently, the predicted curves move towards shorter timescales when the gas density increases.

Figure 3 reports also, as colored bands, the NH_3/CH_3OH ratio observed and computed toward the prostostars 4A1, 4A2, and 4B. Comparing the observed values with the model predictions we can constrain the pre-collapse clump conditions.

The main results are: i) we can exclude per-collapse clump temperature higher than 18 K, as they cannot reproduce the observed values; ii) More precisely, the upper limits are T≤18 K for IRAS 4B, T≤12–15 K for IRAS 4A2, and T≤8 K for IRAS 4A1; iii) The stringent upper limit on the abundance ratio computed toward IRAS 4A1 allows us to constrain, besides the pre-collapse clump temperature (T≤8 K), the gas density (around 10^5 cm^{-3}) and the ice mantle formation timescale (5–9$\times10^5$ yr).

---

[5] A species x with mass m_x can accrete from the gas to the grain surfaces with an accretion rate $k_{acc} = S_x \pi a^2 n_{grain} v_x$, where S_x is the species sticking probability, a the (average) grain radius, n_{grain} the grain number density, and v_x the velocity of the gaseous species ($v_x = (2 k_b T_{gas}/m_x)^{1/2}$).

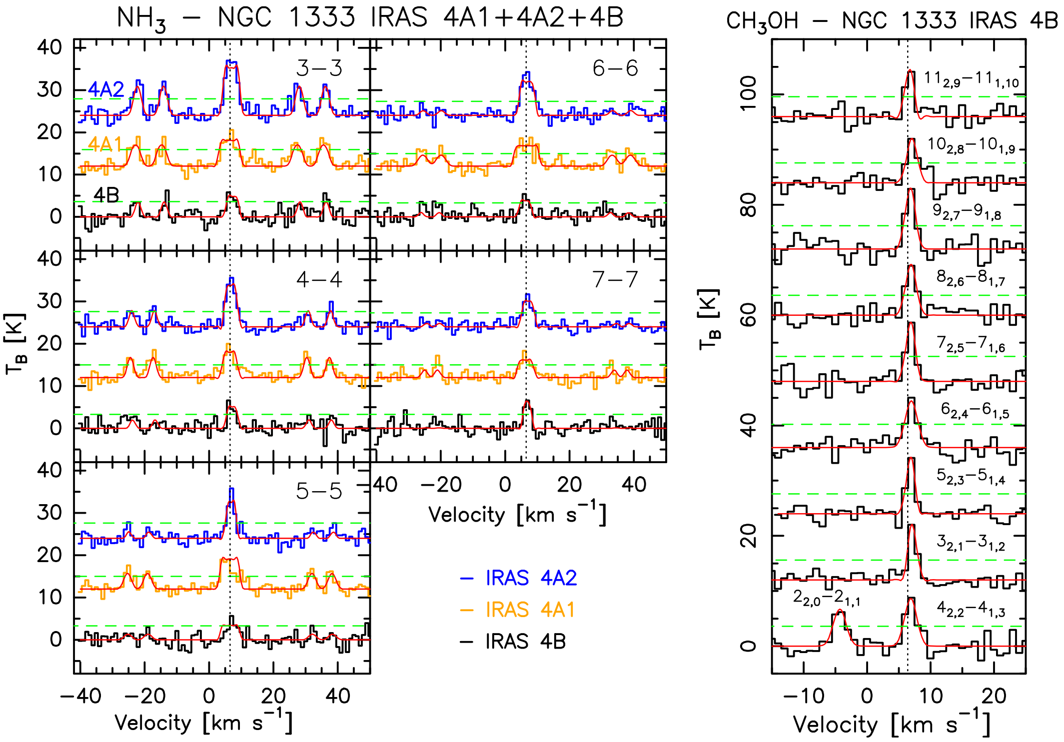

Figure 2. *Left panels:* NH_3 lines (marked in each panel) detected toward the continuum peak of IRAS 4B (black), 4A1 (orange), 4A2 (blue). The red curves show the best hyperfine fits. Each spectrum is shifted on 12 K from the previous one. *Right panel:* CH_3OH lines (marked on each spectrum) detected in the VLA K-band toward 4B. The red curves show the best Gaussian fits. Each spectrum is shifted on 12 K from the previous one. The vertical dotted black lines report the v_{sys} (6.7 km s^{-1}) and the horizontal green dashed lines show the 3σ level.

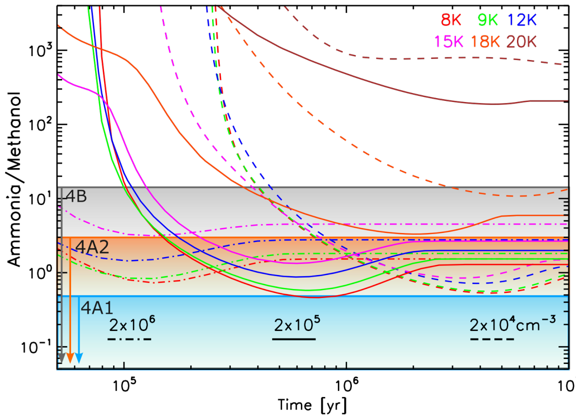

Figure 3. Theoretical predictions of NH_3/CH_3OH versus time for several temperatures (8, 9, 12, 15, 18, 20 K) and H density ($(0.2, 2, 20)\times10^5$ cm^{-3}), obtained with the `GRAINOBLE` code, following the model described in Ceccarelli et al. (2018). The grey, orange and blue bands represent the NH_3/CH_3OH values derived in 4B, 4A2 and 4A1, respectively.

In summary, we could retrieve information on the early stages of the formation of the three protostars. In particular, we showed which conditions of the pre-collapse clump would lead to a different ice mantle history.

5. CONCLUSIONS

We carried out observations of ammonia and methanol lines at cm wavelengths with the VLA interferometer toward three protostars in the NGC 1333 region (IRAS 4A1, IRAS 4A2, and IRAS 4B), in order to retrieve the ice mantle history of these objects.

We detected 10 methanol lines and 5 ammonia lines with compact emission around the targeted protostars. Using a non-LTE LVG analysis we could retrieve the NH_3/CH_3OH abundance ratio. We compared the observed abundance ratio with astrochemical models that predict the evolution of NH_3/CH_3OH with varying the pre-collapse clump conditions, namely gas density and temperature, and ice mantle formation timescale. We could constrain the gas temperature for all the three protostars, and the gas density and formation timescale for IRAS 4A1.

These results show how powerful is this method in retrieving the ice mantle history of Solar-type protostars without being biased by the dust opacity. Indeed, following the conclusion by De Simone et al. (2020), centimetere-wave observations are crucial for the correct study of hot corinos, and more in general for protostars. Indeed, with interferometric observations at centimeter wavelengths it is possible to get rid of the dust contribution (that can be important in the embedded protostellar phase) and to observe simultaneously and at planet formation scales the two major grain components NH_3 and CH_3OH, whose relative abundance, being grain surface species, will mainly depend on the gas conditions during their formation in the prestellar phase.

This is just a first step, and more observations are needed, in particular towards other star forming regions, possibly associated with different initial conditions. Additionally, these observations are an important testbed for future results that can be obtained with the next generation instruments in the centimeter wavelength regime such as ngVLA (McGuire et al. 2018) and SKA (Codella et al. 2015).

ACKNOWLEDGMENTS

This work has received funding from the European Research Council (ERC) under the European Union's Horizon 2020 research and innovation programme, for the Project "The Dawn of Organic Chemistry" (DOC), grant agreement No 741002.

REFERENCES

Aikawa, Y., Furuya, K., Yamamoto, S., & Sakai, N. 2020, ApJ, 897, 110, doi: 10.3847/1538-4357/ab994a

Andre, P., Ward-Thompson, D., & Barsony, M. 2000, PPIV, 59. http://adsabs.harvard.edu/abs/2000prpl.conf...59A

Balucani, N., Ceccarelli, C., & Taquet, V. 2015, MNRAS, 449, L16, doi: 10.1093/mnrasl/slv009

Boogert, A. C. A., Gerakines, P. A., & Whittet, D. C. B. 2015, Ann. Rev. A&A, 53, 541, doi: 10.1146/annurev-astro-082214-122348

Bottinelli, S., Ceccarelli, C., Williams, J. P., & Lefloch, B. 2007, A&A, 463, 601, doi: 10.1051/0004-6361:20065139

Bottinelli, S., Boogert, A. C. A., Bouwman, J., et al. 2010, The Astrophysical Journal, 718, 1100, doi: 10.1088/0004-637X/718/2/1100

Bouhafs, N., Rist, C., Daniel, F., et al. 2017, MNRAS, 470, 2204, doi: 10.1093/mnras/stx1331

Caselli, P., & Ceccarelli, C. 2012, A&A Rv, 20, 56, doi: 10.1007/s00159-012-0056-x

Ceccarelli, C. 2004, in ASPC, Vol. 323, 195

Ceccarelli, C., Caselli, P., Herbst, E., Tielens, A. G. G. M., & Caux, E. 2007, PPV, 47. http://adsabs.harvard.edu/abs/2007prpl.conf...47C

Ceccarelli, C., Maret, S., Tielens, A. G. G. M., Castets, A., & Caux, E. 2003, A&A, 410, 587, doi: 10.1051/0004-6361:20031243

Ceccarelli, C., Viti, S., Balucani, N., & Taquet, V. 2018, MNRAS, 476, 1371, doi: 10.1093/mnras/sty313

Ceccarelli, C., Caselli, P., Fontani, F., et al. 2017, ApJ, 850, 176, doi: 10.3847/1538-4357/aa961d

Choi, M. 2001, ApJ, 553, 219, doi: 10.1086/320657

Codella, C., Podio, L., Fontani, F., et al. 2015, Advancing Astrophysics with the Square Kilometre Array (AASKA14), 123. http://adsabs.harvard.edu/abs/2015aska.confE.123C

Codella, C., Ceccarelli, C., Bianchi, E., et al. 2020, arXiv e-prints, 2001, arXiv:2001.00217. http://adsabs.harvard.edu/abs/2020arXiv200100217C

Cuppen, H. M., Walsh, C., Lamberts, T., et al. 2017, SSRev, 212, 1, doi: 10.1007/s11214-016-0319-3

De Simone, M., Codella, C., Testi, L., et al. 2017, A&A, 599, A121, doi: 10.1051/0004-6361/201630049

De Simone, M., Ceccarelli, C., Codella, C., et al. 2020, ApJL, 896, L3, doi: 10.3847/2041-8213/ab8d41

Dubernet, M.-L., Alexander, M. H., Ba, Y. A., et al. 2013, A&A, 553, A50, doi: 10.1051/0004-6361/201220630

Fuchs, G. W., Cuppen, H. M., Ioppolo, S., et al. 2009, A&A, 505, 629, doi: 10.1051/0004-6361/200810784

Herbst, E., & Van Dishoeck, E. 2009, ARA&A, 47, 427, doi: 10.1146/annurev-astro-082708-101654

Jones, A. P., Fanciullo, L., Köhler, M., et al. 2013, A&A, 558, A62, doi: 10.1051/0004-6361/201321686

Loison, J.-C., Wakelam, V., & Hickson, K. M. 2014, MNRAS, 443, 398, doi: 10.1093/mnras/stu1089

López-Sepulcre, A., Sakai, N., Neri, R., et al. 2017, A&A, 606, A121, doi: 10.1051/0004-6361/201630334

McGuire, B. A., Carroll, P. B., & Garrod, R. T. 2018, arXiv e-prints, 1810, arXiv:1810.06586. http://adsabs.harvard.edu/abs/2018arXiv181006586M

Müller, H. S. P., Schlöder, F., Stutzki, J., & Winnewisser, G. 2005, Journal of Molecular Structure, 742, 215, doi: 10.1016/j.molstruc.2005.01.027

Öberg, K. I., & Bergin, E. A. 2021, PhR, 893, 1, doi: 10.1016/j.physrep.2020.09.004

Pickett, H. M., Poynter, R. L., Cohen, E. A., et al. 1998, Journal of Quantitative Spectroscopy and Radiative Transfer, 60, 883, doi: 10.1016/S0022-4073(98)00091-0

Rabli, D., & Flower, D. R. 2010, MNRAS, 406, 95, doi: 10.1111/j.1365-2966.2010.16671.x

Rimola, A., Taquet, V., Ugliengo, P., Balucani, N., & Ceccarelli, C. 2014, A&A, 572, A70, doi: 10.1051/0004-6361/201424046

Sakai, N., Sakai, T., & Yamamoto, S. 2006, PASJ, 58, L15, doi: 10.1093/pasj/58.1.L15

Sakai, N., & Yamamoto, S. 2013, Chem. Rev., 113, 8981, doi: 10.1021/cr4001308

Skouteris, D., Balucani, N., Ceccarelli, C., et al. 2018, ApJ, 854, 135, doi: 10.3847/1538-4357/aaa41e

Skouteris, D., Vazart, F., Ceccarelli, C., et al. 2017, MNRAS, 468, L1, doi: 10.1093/mnrasl/slx012

Song, L., & Kästner, J. 2017, ApJ, 850, 118, doi: 10.3847/1538-4357/aa943e

Taquet, V., Ceccarelli, C., & Kahane, C. 2012, A&A, 538, A42, doi: 10.1051/0004-6361/201117802

Taquet, V., López-Sepulcre, A., Ceccarelli, C., et al. 2015, ApJ, 804, 81, doi: 10.1088/0004-637X/804/2/81

Taquet, V., Peters, P. S., Kahane, C., et al. 2013, A&A, 550, A127, doi: 10.1051/0004-6361/201220084

Wakelam, V., Loison, J. C., Herbst, E., et al. 2015, ApJS, 217, 20, doi: 10.1088/0067-0049/217/2/20

Watanabe, N., & Kouchi, A. 2002, ApJ, 571, L173, doi: 10.1086/341412

Xu, L.-H., Fisher, J., Lees, R., et al. 2008, Journal of Molecular Spectroscopy, 251, 305

Yu, S., Pearson, J. C., Drouin, B. J., et al. 2010, The Journal of Chemical Physics, 133, 174317, doi: 10.1063/1.3499911

Zucker, C., Schlafly, E. F., Speagle, J. S., et al. 2018, ApJ, 869, 83, doi: 10.3847/1538-4357/aae97c

Öberg, K. I., Boogert, A. C. A., Pontoppidan, K. M., et al. 2011, The Astrophysical Journal, 740, 109, doi: 10.1088/0004-637X/740/2/109

Observational Proposals

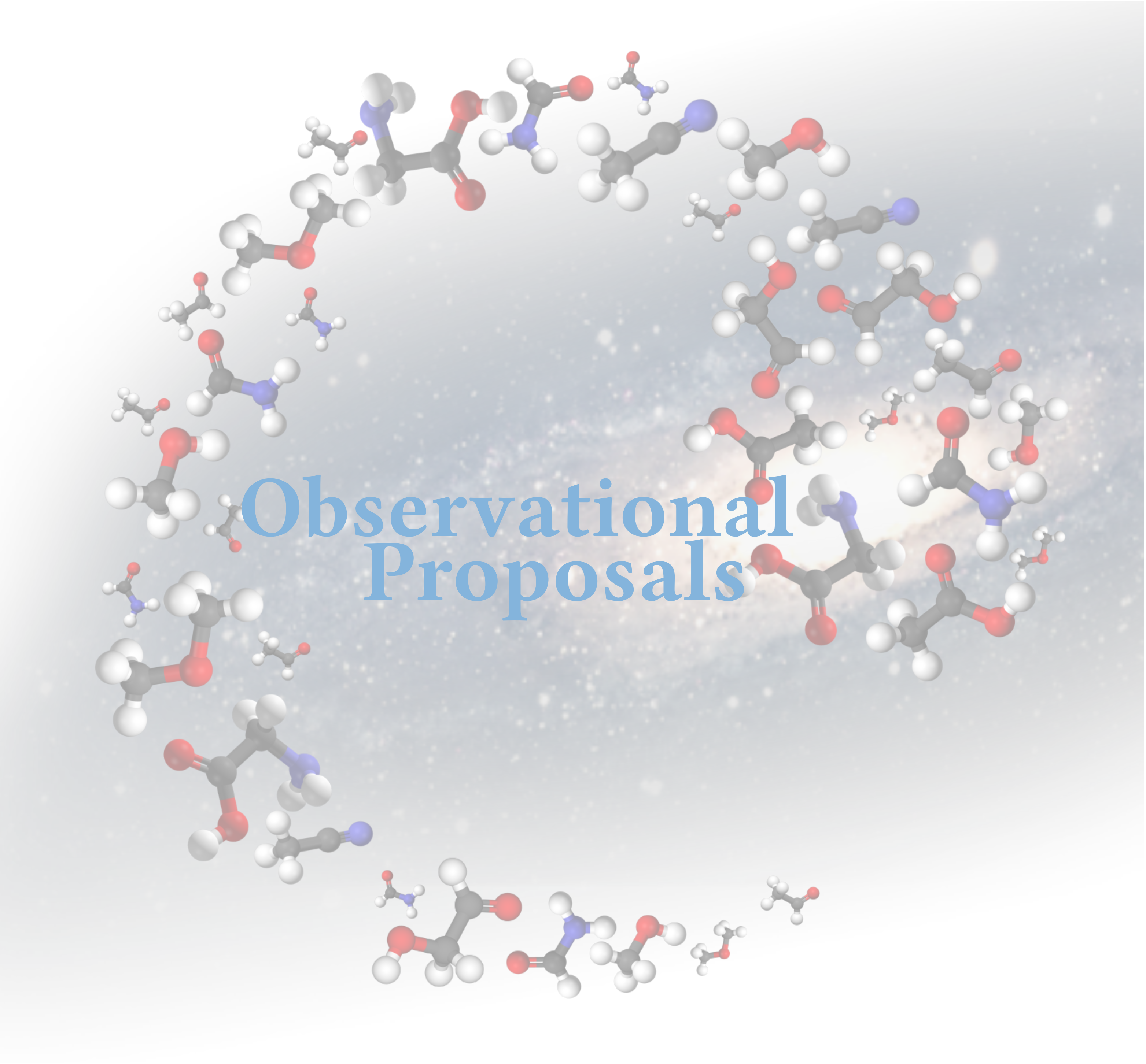

Observing Application

Date:	
Proposal ID:	VLA/2020-06-007
PI:	Marta De Simone
Type:	Regular
Category:	Star Formation
Total time:	22.0

Hot Corinos chemical diversity: myth or reality?

Abstract:

After almost 20 years of hunting, only a dozen hot corinos-- compact, hot (T>100 K), dense (nH2>10^7 cm^(-3)) regions enriched in interstellar Complex Organic Molecules (iCOMs)--are known. Of them, many are binary systems with the two components showing drastically different molecular spectra at (sub-)mm wavelengths. Does this difference correspond to a real chemical difference in two coeval objects or is it just an artifact? Indeed, dust could be responsible for the iCOMs line absorption, if it is opaque enough, as is the case in IRAS4A (De Simone et al. 2020). Therefore, only observations at radio frequencies, where the dust continuum is optically thin, can reveal the real nature of protostellar binary systems. Following up on our previous successful VLA observations of IRAS4A (De Simone et al. 2020), we propose here to study the binary system CepE-mm, which represents a different case with respect to IRAS4A: of the two components, CepE-A and CepE-B (separated by 1.7"), only the former, bright in mm continuum, has a detected hot corino. To confirm a real chemical differentiation, we propose to observe CepE-mm in the methanol lines in the K band with C-configuration (0.9" angular resolution).

Authors:

Name	Institution	Email	Status
De Simone, Marta	Grenoble Alpes, Université	marta.desimone@univ-grenoble-alpes.fr	
Codella, Claudio	Istituto Nazionale di Astrofisica	codella@arcetri.astro.it	
Ceccarelli, Cecilia	Grenoble Alpes, Université	cecilia.ceccarelli@univ-grenoble-alpes.fr	
Chandler, Claire	National Radio Astronomy Observatory	cchandle@nrao.edu	
Bouvier, Mathilde	Grenoble Alpes, Université	mathilde.bouvier@univ-grenoble-alpes.fr	Graduating: N/A Thesis: false
Lopez-Sepulcre, Ana	Institut de Radio Astronomique Millimétrique	lopez@iram.fr	
Schutzer, André	Grenoble Alpes, Université	andre.schutzer@univ-grenoble-alpes.fr	Graduating: 2022 Thesis: false
Lefloch, Bertrand	Grenoble Alpes, Université	bertrand.lefloch@univ-grenoble-alpes.fr	
Svoboda, Brian	National Radio Astronomy Observatory	brian.e.svoboda@gmail.com	
Sakai, Nami	Riken's institute & centers	nami.sakai@riken.jp	
Yamamoto, Satoshi	Tokyo, University of	yamamoto@phys.s.u-tokyo.ac.jp	
Loinard, Laurent	México, Universidad Nacional Autónoma de	l.loinard@crya.unam.mx	

Principal Investigator: Marta De Simone
Contact: Marta De Simone
Telephone: +33 (0)4 0456520897

Observing Application

Date: Aug 02, 2021
Proposal ID: VLA/22A-162
Legacy ID: AD865
PI: Marta De Simone
Type: Regular
Category: Star Formation
Total time: 20.0

Tracing the ice mantle history of baby stars

Abstract:

To understand the origin of the diversity observed in the numerous exoplanetary systems, it is crucial to characterize the early stages of their formation. The best-known representatives of these stages are the Solar-like Class 0 protostars, which are likely to retain detailed information on the initial conditions of the process. Such diversity can probably be caused by the different history of these objects, namely a different composition of the grain mantles, which were formed in the previous prestellar core phase. Indeed, the icy mantles are sublimated in the central hot region of protostars, defining the chemical composition of the forming planetary system. To quantify this effect, we propose to target the critical tracers of the ice mantle composition, ammonia and methanol, in the VLA K-band, toward the Class 0 binary system IRAS 2A. Being well-known grain surface products, the evolution of their abundances only depends on the mantle formation history. Only high angular resolution observations at radio wavelengths where it is possible to observe several methanol and ammonia transitions, and where additionally the dust continuum is optically thin, allow retrieving the IRAS 2A ice mantle history, constraining the pre-collapse clump temperature, density, and ice mantle formation time scale.

Authors:

Name	Institution	Email	Status
De Simone, Marta	Grenoble Alpes, UniversitÃ©	marta.desimone@univ-grenoble-alpes.fr	
Ceccarelli, Cecilia	Grenoble Alpes, UniversitÃ©	cecilia.ceccarelli@univ-grenoble-alpes.fr	
Codella, Claudio	Istituto Nazionale di Astrofisica	claudio.codella@inaf.it	
Chandler, Claire	National Radio Astronomy Observatory	cchandle@nrao.edu	
Svoboda, Brian	National Radio Astronomy Observatory	brian.e.svoboda@gmail.com	
Busquet, Gemma	Grenoble Alpes, UniversitÃ©	gemma.busquet@univ-grenoble-alpes.fr	
Lopez-Sepulcre, Ana	Institut de Radio Astronomique MillimÃ©trique	lopez@iram.fr	
Bouvier, Mathilde	Grenoble Alpes, UniversitÃ©	mathilde.bouvier@univ-grenoble-alpes.fr	Graduating: N/A Thesis: false
Lefloch, Bertrand	Grenoble Alpes, UniversitÃ©	bertrand.lefloch@univ-grenoble-alpes.fr	
Schutzer, AndrÃ©	Grenoble Alpes, UniversitÃ©	andre.schutzer@univ-grenoble-alpes.fr	Graduating: 2022 Thesis: false
Sakai, Nami	Riken's institute & centers	nami.sakai@riken.jp	
Yamamoto, Satoshi	Tokyo, University of	yamamoto@phys.s.u-tokyo.ac.jp	
Loinard, Laurent	MÃ©xico, Universidad Nacional AutÃ³noma de	l.loinard@crya.unam.mx	

SOFIA PROPOSAL

Water content in the early stages of planet-forming regions

Principal Investigator: Dr. Marta De Simone
University of Grenoble
France
Telephone:
Contact Email: marta.desimone@univ-grenoble-alpes.fr

Scientific Category: STAR FORMATION
Scientific Keywords: CHEMICAL ABUNDANCES,EMISSION LINES,STAR FORMATION,YOUNG STARS AND PROTOSTELLAR OBJECTS

Abstract

The presence of water on an extraterrestrial planet is a crucial condition for its habitability. This small molecule also plays an important role in the star formation process allowing clouds to collapse into stars acting as a major gas coolant and helping the coagulation of icy dust grains in planetesimals and, eventually, planets.
Although very abundant in star forming regions, water is mostly frozen, except in warm enough zones, where water ices sublimate and becomes observable via its rotational lines. In Solar-type protostars, the water-ice-sublimated regions are called hot corinos. The abundance of water there, and more specifically in the Class I protostars where planets start to form, is unfortunately poorly known.
SOFIA/EXES is currently the only available facility that provides sufficient spatial and spectral resolution to detect water line emission originated in hot corinos and to measure its abundance. Following ad hope model predictions, we propose to observe several rotational water lines at 22.5-26.5 micron toward the only Class I hot corino where evidence of water presence is so far known, NGC 1333 SVS13-A.
The requested observations will allow us to perform a multi-line analysis, using sophisticated radiative transfer models, in order to derive the SVS13-A hot corino properties, and the water abundance. In other words, it will be possible to measure how much water is available in regions where planets start to form.

Investigators:

	Investigator	Institution	Email
PI	Dr. Marta De Simone	University of Grenoble	marta.desimone@univ-grenoble-alpes.fr
CoI	Dr. Cecilia Ceccarelli	Institut de Planetologie et d'Astrophysique de Grenoble	cecilia.ceccarelli@univ-grenoble-alpes.fr
CoI	Dr. Claudio Codella	INAF Florence	codella@arcetri.astro.it
CoI	Dr. Eleonora Bianchi	University of Grenoble	eleonora.bianchi@univ-grenoble-alpes.fr
CoI	Dr. Curtis DeWitt	USRA	cdewitt@usra.edu
CoI	Dr. Sarah Nickerson	NASA Ames Research Center/BAERI	nickerson@baeri.org
CoI	Dr. Naseem Rangwala	NASA Ames Research Center	naseem.rangwala@nasa.gov

Number of investigators: 7

DCS account name : marta.desimone@univ-grenoble-alpes.fr
TAC Queue: US
Regular Observation requested.

Related Proposals

Status of SOFIA Observations in the Last Two Years

Special Instructions

Instruments Requested:

Instrument	Observing Time (hr)
EXES	4.6

Total observing time requested = 4.6 hours

Bibliography

Agúndez, M., Marcelino, N., Tercero, B., et al. 2021, Astronomy and Astrophysics, 649, L4

Agúndez, M. & Wakelam, V. 2013, Chemical Reviews, 113, 8710

Aikawa, Y., Cataldi, G., Yamato, Y., et al. 2021, The Astrophysical Journal Supplement Series, 257, 13

Aikawa, Y., Furuya, K., Yamamoto, S., & Sakai, N. 2020, The Astrophysical Journal, 897, 110

Aikawa, Y., Momose, M., Thi, W.-F., et al. 2003, Publications of the Astronomical Society of Japan, 55, 11

Aikawa, Y. & Nomura, H. 2006, The Astrophysical Journal, 642, 1152

Aikawa, Y., van Zadelhoff, G. J., van Dishoeck, E. F., & Herbst, E. 2002, Astronomy and Astrophysics, 386, 622

Akimkin, V., Zhukovska, S., Wiebe, D., et al. 2013, The Astrophysical Journal, 766, 8

Altwegg, K., Balsiger, H., Bar-Nun, A., et al. 2016, Science Advances, 2

Alves, J. F., Lada, C. J., & Lada, E. A. 2001, Nature, 409, 159

Andersson, B.-G., Lazarian, A., & Vaillancourt, J. E. 2015, Annual Review of Astronomy and Astrophysics, 53, 501

Andre, P., Ward-Thompson, D., & Barsony, M. 1993, The Astrophysical Journal, 406, 122

Andre, P., Ward-Thompson, D., & Barsony, M. 2000, Protostars and Planets IV

Andre, P., Ward-Thompson, D., & Motte, F. 1996, Astronomy and Astrophysics, 314, 625

Andrews, S. M., Huang, J., Pérez, L. M., et al. 2018, The Astrophysical Journal Letters, 869, L41

Andrews, S. M. & Williams, J. P. 2007, The Astrophysical Journal, 659, 705

André, P. 2002, EAS Publications Series, 3, 1

André, P., Di Francesco, J., Ward-Thompson, D., et al. 2014, Protostars and Planets VI, 27

André, P., Men'shchikov, A., Bontemps, S., et al. 2010, Astronomy and Astrophysics, 518, L102

Arce, H. G., Borkin, M. A., Goodman, A. A., Pineda, J. E., & Beaumont, C. N. 2011, The Astrophysical Journal, 742, 105

Arce, H. G., Santiago-García, J., Jørgensen, J. K., Tafalla, M., & Bachiller, R. 2008, The Astrophysical Journal Letters, 681, L21

Arce, H. G. & Sargent, A. I. 2006, The Astrophysical Journal, 646, 1070

Arce, H. G., Shepherd, D., Gueth, F., et al. 2007, Protostars and Planets V

Aresu, G., Meijerink, R., Kamp, I., et al. 2012, Astronomy and Astrophysics, 547, A69

Ascenzi, D., Cernuto, A., Balucani, N., et al. 2019, Astronomy and Astrophysics, 625, A72

Avison, A. & George, S. J. 2012, European Journal of Physics, 34, 7

Ayouz, M. A., Yuen, C. H., Balucani, N., et al. 2019, Monthly Notices of the Royal Astronomical Society, 490, 1325

Bachiller, R. 1996, Annual Review of Astronomy and Astrophysics, 34, 111

Bachiller, R. & Cernicharo, J. 1986, Astronomy and Astrophysics, 166, 283

Bachiller, R., Codella, C., Colomer, F., Liechti, S., & Walmsley, C. M. 1998a, Astronomy and Astrophysics, 335, 266

Bachiller, R., Gueth, F., Guilloteau, S., Tafalla, M., & Dutrey, A. 2000, Astronomy and Astrophysics, 362, L33

Bachiller, R., Guilloteau, S., Gueth, F., et al. 1998b, Astronomy and Astrophysics, 339, L49

Bachiller, R., Liechti, S., Walmsley, C. M., & Colomer, F. 1995, Astronomy and Astrophysics, 295, L51

Bachiller, R., Martin-Pintado, J., & Fuente, A. 1991, Astronomy and Astrophysics, 243, L21

Bachiller, R. & Pérez Gutiérrez, M. 1997, The Astrophysical Journal, 487, L93

Bachiller, R., Pérez Gutiérrez, M., Kumar, M. S. N., & Tafalla, M. 2001, Astronomy and Astrophysics, 372, 899

Bacmann, A., Lefloch, B., Ceccarelli, C., et al. 2002, Astronomy and Astrophysics, 389, L6

Bacmann, A., Lefloch, B., Ceccarelli, C., et al. 2003, The Astrophysical Journal, 585, L55

Bacmann, A., Taquet, V., Faure, A., Kahane, C., & Ceccarelli, C. 2012, Astronomy and Astrophysics, 541, L12

Bally, J., Devine, D., & Reipurth, B. 1996, The Astrophysical Journal, 473, L49

Bally, J., Reipurth, B., & Davis, C. J. 2007, Protostars and Planets V

Bally, J., Walawender, J., Johnstone, D., Kirk, H., & Goodman, A. 2008, Handbook of Star Forming Regions, Volume I, 308

Balucani, N., Ceccarelli, C., & Taquet, V. 2015, Monthly Notices of the Royal Astronomical Society, 449, L16

Balucani, N., Leonori, F., Bergeat, A., Petrucci, R., & Casavecchia, P. 2011, Physical Chemistry Chemical Physics, 13, 8322

Balucani, N., Skouteris, D., Ceccarelli, C., et al. 2018, Molecular Astrophysics, 13, 30

Barlow, M. J. 1978, Monthly Notices of the Royal Astronomical Society, 183, 367

Barnard, E. E. 1907, The Astrophysical Journal, 25, 218

Barnard, E. E. 1910, The Astrophysical Journal, 31, 8

Barone, V., Latouche, C., Skouteris, D., et al. 2015, Monthly Notices of the Royal Astronomical Society, 453, L31

Belloche, A., Maury, A. J., Maret, S., et al. 2020, Astronomy and Astrophysics, 635, A198

Bennett, C. J., Jamieson, C. S., Osamura, Y., & Kaiser, R. I. 2005a, The Astrophysical Journal, 624, 1097

Bennett, C. J., Osamura, Y., Lebar, M. D., & Kaiser, R. I. 2005b, The Astrophysical Journal, 634, 698

Bergin, E. A., Aikawa, Y., Blake, G. A., & van Dishoeck, E. F. 2007, Protostars and Planets V

Bergin, E. A., Alves, J., Huard, T., & Lada, C. J. 2002, The Astrophysical Journal, 570, L101

Bergin, E. A., Hogerheijde, M. R., Brinch, C., et al. 2010, Astronomy and Astrophysics, 521, L33

Bergin, E. A. & Langer, W. D. 1997, The Astrophysical Journal, 486, 316

Bergin, E. A. & Tafalla, M. 2007, Annual Review of Astronomy and Astrophysics, 45, 339

Bergner, J. B., Guzmán, V. G., Öberg, K. I., Loomis, R. A., & Pegues, J. 2018, The Astrophysical Journal, 857, 69

Bergner, J. B., Martín-Doménech, R., Öberg, K. I., et al. 2019, ACS Earth and Space Chemistry, 3, 1564

Berkhuijsen, E. M., Haslam, C. G. T., & Salter, C. J. 1971, Astronomy and Astrophysics, 14, 252

Berné, O., Marcelino, N., & Cernicharo, J. 2010, Nature, 466, 947

Berné, O. & Matsumoto, Y. 2012, The Astrophysical Journal, 761, L4

Bialy, S., Zucker, C., Goodman, A., et al. 2021, The Astrophysical Journal, 919, L5

Bianchi, E., Ceccarelli, C., Codella, C., et al. 2019a, ACS Earth and Space Chemistry, 3, 2659

Bianchi, E., Chandler, C. J., Ceccarelli, C., et al. 2020, Monthly Notices of the Royal Astronomical Society

Bianchi, E., Codella, C., Ceccarelli, C., et al. 2017, Astronomy and Astrophysics, 606, L7

Bianchi, E., Codella, C., Ceccarelli, C., et al. 2019b, Monthly Notices of the Royal Astronomical Society, 483, 1850

Birnstiel, T., Andrews, S. M., & Ercolano, B. 2012, Astronomy and Astrophysics, 544, A79

Bisschop, S. E., Fraser, H. J., Öberg, K. I., van Dishoeck, E. F., & Schlemmer, S. 2006, Astronomy and Astrophysics, 449, 1297

Bizzocchi, L., Caselli, P., Spezzano, S., & Leonardo, E. 2014, Astronomy & Astrophysics, 569, A27

Bjerkeli, P., van der Wiel, M. H. D., Harsono, D., Ramsey, J. P., & Jørgensen, J. K. 2016, Nature, 540, 406

Blake, G. A., Sandell, G., van Dishoeck, E. F., et al. 1995, The Astrophysical Journal, 441, 689

Blake, G. A., Sutton, E. C., Masson, C. R., & Phillips, T. G. 1987, The Astrophysical Journal, 315, 621

Bohlin, R. C., Savage, B. D., & Drake, J. F. 1978, The Astrophysical Journal, 224, 132

Bontemps, S., Andre, P., Terebey, S., & Cabrit, S. 1996, Astronomy and Astrophysics, 311, 858

Boogert, A. C. A., Gerakines, P. A., & Whittet, D. C. B. 2015, Annual Review of Astronomy and Astrophysics, 53, 541

Booth, A. S., Walsh, C., Terwisscha van Scheltinga, J., et al. 2021, Nature Astronomy, 5, 684

Born, M. & Wolf, E. 1999, Principles of Optics: Electromagnetic Theory of Propagation, Interference and Diffraction of Light, 7th edn. (Cambridge University Press)

Bottinelli, S., Boogert, A. C. A., Bouwman, J., et al. 2010, The Astrophysical Journal, 718, 1100

Bottinelli, S., Ceccarelli, C., Lefloch, B., et al. 2004a, The Astrophysical Journal, 615, 354

Bottinelli, S., Ceccarelli, C., Neri, R., et al. 2004b, The Astrophysical Journal Letters, 617, L69

Bottinelli, S., Ceccarelli, C., Williams, J. P., & Lefloch, B. 2007, Astronomy and Astrophysics, 463, 601

Bouhafs, N., Rist, C., Daniel, F., et al. 2017, Monthly Notices of the Royal Astronomical Society, 470, 2204

Bouvier, M., Ceccarelli, C., López-Sepulcre, A., et al. 2022, The Astrophysical Journal, 929, 10

Bouvier, M., López-Sepulcre, A., Ceccarelli, C., et al. 2020, Astronomy & Astrophysics, 636, A19

Bouvier, M., López-Sepulcre, A., Ceccarelli, C., et al. 2021, Astronomy and Astrophysics, 653, A117

Bracco, A., Palmeirim, P., André, P., et al. 2017, Astronomy and Astrophysics, 604, A52

Burkhardt, A. M., Shingledecker, C. N., Le Gal, R., et al. 2019, The Astrophysical Journal, 881, 32

Canosa, A., Goulay, F., Sims, I. R., & Rowe, B. R. 2008, Low Temperatures and Cold Molecules, Imperial College Press, 55

Carruthers, G. R. 1970, The Astrophysical Journal, 161, L81

Casavecchia, P., Leonori, F., Balucani, N., et al. 2009, Physical Chemistry Chemical Physics, 11, 46

Caselli, P. & Ceccarelli, C. 2012, Astronomy and Astrophysics Review, 20, 56

Caselli, P., Hartquist, T. W., & Havnes, O. 1997, Astronomy and Astrophysics, 322, 296

Caselli, P., Hasegawa, T. I., & Herbst, E. 1993, The Astrophysical Journal, 408, 548

Caselli, P., Keto, E., Bergin, E. A., et al. 2012, The Astrophysical Journal, 759, L37

Caselli, P., van der Tak, F. F. S., Ceccarelli, C., & Bacmann, A. 2003, Astronomy and Astrophysics, 403, L37

Caselli, P., Walmsley, C. M., Tafalla, M., Dore, L., & Myers, P. C. 1999, The Astrophysical Journal, 523, L165

Caselli, P., Walmsley, C. M., Terzieva, R., & Herbst, E. 1998, The Astrophysical Journal, 499, 234

Castets, A., Ceccarelli, C., Loinard, L., Caux, E., & Lefloch, B. 2001, Astronomy and Astrophysics, 375, 40

Cataldi, G., Yamato, Y., Aikawa, Y., et al. 2021, The Astrophysical Journal Supplement Series, 257, 10

Caux, E., Kahane, C., Castets, A., et al. 2011, Astronomy and Astrophysics, 532, A23

Cazaux, S., Tielens, A. G. G. M., Ceccarelli, C., et al. 2003, The Astrophysical Journal, 593, L51

Ceccarelli, C. 2004, ASP Conference Proceedings, 323, 195

Ceccarelli, C., Caselli, P., Bockelée-Morvan, D., et al. 2014, Protostars and Planets VI, 859

Ceccarelli, C., Caselli, P., Fontani, F., et al. 2017, The Astrophysical Journal, 850, 176

Ceccarelli, C., Caselli, P., Herbst, E., Tielens, A. G. G. M., & Caux, E. 2007, Protostars and Planets V, 47

Ceccarelli, C., Castets, A., Caux, E., et al. 2000a, Astronomy and Astrophysics, 355, 1129

Ceccarelli, C., Castets, A., Loinard, L., Caux, E., & Tielens, A. G. G. M. 1998, Astronomy and Astrophysics, 338, L43

Ceccarelli, C., Caux, E., Loinard, L., et al. 1999, Astronomy and Astrophysics, 342, L21

Ceccarelli, C. & Dominik, C. 2006, Philosophical Transactions of the Royal Society of London Series A, 364, 3091

Ceccarelli, C., Dominik, C., Caux, E., Lefloch, B., & Caselli, P. 2005, The Astrophysical Journal, 631, L81

Ceccarelli, C., Hollenbach, D. J., & Tielens, A. G. G. M. 1996, The Astrophysical Journal, 471, 400

Ceccarelli, C., Loinard, L., Castets, A., Tielens, A. G. G. M., & Caux, E. 2000b, Astronomy and Astrophysics, 357, L9

Ceccarelli, C., Loinard, L., Castets, A., et al. 2001, Astronomy and Astrophysics, 372, 998

Ceccarelli, C., Maret, S., Tielens, A. G. G. M., Castets, A., & Caux, E. 2003, Astronomy and Astrophysics, 410, 587

Ceccarelli, C., Viti, S., Balucani, N., & Taquet, V. 2018, Monthly Notices of the Royal Astronomical Society, 476, 1371

Cernicharo, J., Agúndez, M., Cabezas, C., et al. 2021a, Astronomy and Astrophysics, 649, L15

Cernicharo, J., Agúndez, M., Kaiser, R. I., et al. 2021b, Astronomy and Astrophysics, 652, L9

Cernicharo, J., Marcelino, N., Roueff, E., et al. 2012, The Astrophysical Journal Letters, 759, L43

Cernis, K. 1990, Astrophysics and Space Science, 166, 315

Chacón-Tanarro, A., Caselli, P., Bizzocchi, L., et al. 2019, Astronomy and Astrophysics, 622, A141

Chahine, L., López-Sepulcre, A., Neri, R., et al. 2022, Astronomy and Astrophysics, 657, A78

Chapillon, E., Dutrey, A., Guilloteau, S., et al. 2012a, The Astrophysical Journal, 756, 58

Chapillon, E., Guilloteau, S., Dutrey, A., Piétu, V., & Guélin, M. 2012b, Astronomy & Astrophysics, 537, A60

Charnley, S. B. 2004, Advances in Space Research, 33, 23

Charnley, S. B., Tielens, A. G. G. M., & Millar, T. J. 1992, The Astrophysical Journal, 399, L71

Chen, M. C.-Y., Di Francesco, J., Rosolowsky, E., et al. 2020, The Astrophysical Journal, 891, 84

Choi, M. 2001, The Astrophysical Journal, 553, 219

Choi, M. 2005, The Astrophysical Journal, 630, 976

Choi, M., Kang, M., Tatematsu, K., Lee, J.-E., & Park, G. 2011, Publications of the Astronomical Society of Japan, 63, 1281

Choi, M., Panis, J.-F., & Evans, II, N. J. 1999, The Astrophysical Journal Supplement Series, 122, 519

Chuang, C.-Y., Aso, Y., Hirano, N., Hirano, S., & Machida, M. N. 2021, The Astrophysical Journal, 916, 82

Cieza, L. A., Casassus, S., Tobin, J., et al. 2016, Nature, 535, 258

Clark, B. G. 1980, Astronomy and Astrophysics, 89, 377

Cleeves, L. I., Bergin, E. A., Alexander, C. M. O. D., et al. 2014, Science, 345, 1590

Cleeves, L. I., Bergin, E. A., Qi, C., Adams, F. C., & Öberg, K. I. 2015, The Astrophysical Journal, 799, 204

Codella, C., Bachiller, R., Benedettini, M., et al. 2005, Monthly Notices of the Royal Astronomical Society, 361, 244

Codella, C., Bachiller, R., & Reipurth, B. 1999, Astronomy and Astrophysics, 343, 585

Codella, C., Benedettini, M., Beltrán, M. T., et al. 2009, Astronomy and Astrophysics, 507, L25

Codella, C., Ceccarelli, C., Bianchi, E., et al. 2020a, Astronomy and Astrophysics, 635, A17

Codella, C., Ceccarelli, C., Bianchi, E., et al. 2016a, Monthly Notices of the Royal Astronomical Society, 462, L75

Codella, C., Ceccarelli, C., Cabrit, S., et al. 2016b, Astronomy and Astrophysics, 586, L3

Codella, C., Ceccarelli, C., Caselli, P., et al. 2017, Astronomy and Astrophysics, 605, L3

Codella, C., Ceccarelli, C., Lefloch, B., et al. 2012, The Astrophysical Journal, 757, L9

Codella, C., Fontani, F., Ceccarelli, C., et al. 2015a, Monthly Notices of the Royal Astronomical Society, 449, L11

Codella, C., Podio, L., Fontani, F., et al. 2015b, Proceedings of Advancing Astrophysics with the Square Kilometre Array (AASKA14)

Codella, C., Podio, L., Garufi, A., et al. 2020b, Astronomy & Astrophysics, 644, A120

Collaboration, P., Aghanim, N., Akrami, Y., et al. 2020, Astronomy and Astrophysics, 641, A12

Cosentino, G., Jiménez-Serra, I., Caselli, P., et al. 2019, The Astrophysical Journal, 881, L42

Cosentino, G., Jiménez-Serra, I., Henshaw, J. D., et al. 2018, Monthly Notices of the Royal Astronomical Society, 474, 3760

Cosentino, G., Jiménez-Serra, I., Henshaw, J. D., et al. 2020, Monthly Notices of the Royal Astronomical Society, 499, 1666

Coughlin, E. R. & Nixon, C. J. 2020, The Astrophysical Journal Supplement Series, 247, 51

Coutens, A., Jørgensen, J. K., van der Wiel, M. H. D., et al. 2016, Astronomy and Astrophysics, 590, L6

Coutens, A., Persson, M. V., Jørgensen, J. K., Wampfler, S. F., & Lykke, J. M. 2015, Astronomy and Astrophysics, 576, A5

Coutens, A., Vastel, C., Caux, E., et al. 2012, Astronomy and Astrophysics, 539, A132

Coutens, A., Vastel, C., Hincelin, U., et al. 2014, Monthly Notices of the Royal Astronomical Society, 445, 1299

Cox, E. G., Harris, R. J., Looney, L. W., et al. 2015, The Astrophysical Journal, 814, L28

Crapsi, A., Caselli, P., Walmsley, M. C., & Tafalla, M. 2007, Astronomy and Astrophysics, 470, 221

Cuppen, H. M., Walsh, C., Lamberts, T., et al. 2017, Space Science Reviews, 212, 1

De Duve, C. 2011, Philosophical Transactions of the Royal Society of London Series A, 369, 620

De Jong, T., Boland, W., & Dalgarno, A. 1980, Astronomy and Astrophysics, 91, 68

De Jong, T., Chu, S., & Dalgarno, A. 1975, The Astrophysical Journal, 199, 69

De Simone, M., Ceccarelli, C., Codella, C., et al. 2020a, The Astrophysical Journal Letters, 896, L3

De Simone, M., Codella, C., Ceccarelli, C., et al. 2022, Monthly Notices of the Royal Astronomical Society, 512, 5214

De Simone, M., Codella, C., Ceccarelli, C., et al. 2020b, Astronomy and Astrophysics, 640, A75

De Simone, M., Codella, C., Testi, L., et al. 2017, Astronomy and Astrophysics, 599, A121

Desert, F.-X., Boulanger, F., & Puget, J. L. 1990, Astronomy and Astrophysics, 500, 313

Dhabal, A., Mundy, L. G., Chen, C.-y., Teuben, P., & Storm, S. 2019, The Astrophysical Journal, 876, 108

Dhabal, A., Mundy, L. G., Rizzo, M. J., Storm, S., & Teuben, P. 2018, The Astrophysical Journal, 853, 169

Di Francesco, J., Myers, P. C., Wilner, D. J., Ohashi, N., & Mardones, D. 2001, The Astrophysical Journal, 562, 770

Dickinson, C. 2018, Galaxies, 6, 56

Doi, Y., Hasegawa, T., Furuya, R. S., et al. 2020, The Astrophysical Journal, 899, 28

Draine, B. T. 2003, Annual Review of Astronomy and Astrophysics, 41, 241

Draine, B. T. 2006, The Astrophysical Journal, 636, 1114

Draine, B. T. 2011, Princeton University Press

Draine, B. T. & McKee, C. F. 1993, Annual Review of Astronomy and Astrophysics, 31, 373

Drozdovskaya, M. N., van Dishoeck, E. F., Jørgensen, J. K., et al. 2018, Monthly Notices of the Royal Astronomical Society, 476, 4949

Drozdovskaya, M. N., van Dishoeck, E. F., Rubin, M., Jørgensen, J. K., & Altwegg, K. 2019, Monthly Notices of the Royal Astronomical Society, 490, 50

Dubernet, M.-L., Alexander, M. H., Ba, Y. A., et al. 2013, Astronomy & Astrophysics, 553, A50

Duchêne, G., McCabe, C., Ghez, A. M., & Macintosh, B. A. 2004, The Astrophysical Journal, 606, 969

Duley, W. W. & Williams, D. A. 1993, Monthly Notices of the Royal Astronomical Society, 260, 37

Dullemond, C. P. & Dominik, C. 2004, Astronomy and Astrophysics, v.421, p.1075-1086 (2004), 421, 1075

Dullemond, C. P., Hollenbach, D., Kamp, I., & D'Alessio, P. 2007, Protostars and Planets V

Dumas, G., Vaupré, S., Ceccarelli, C., et al. 2014, The Astrophysical Journal, 786, L24

Dunham, M. M., Stutz, A. M., Allen, L. E., et al. 2014, Protostars and Planets VI, 195

Dunham, Jr., T. 1937, Publications of the Astronomical Society of the Pacific, 49, 26

Dutrey, A., Guilloteau, S., & Guelin, M. 1997, Astronomy and Astrophysics, 317, L55

Dutrey, A., Semenov, D., Chapillon, E., et al. 2014, Protostars and Planets VI, 317

Dutrey, A., Wakelam, V., Boehler, Y., et al. 2011, Astronomy and Astrophysics, 535, A104

Einstein, A. 1916, Deutsche Physikalische Gesellschaft, 18, 318

Elitzur, M. 1992, Astrophysics and Space Science Library, 170

Elsila, J. E., Glavin, D. P., & Dworkin, J. P. 2009, Meteoritics and Planetary Science, 44, 1323

Enoch, M. L., Evans, II, N. J., Sargent, A. I., & Glenn, J. 2009, The Astrophysical Journal, 692, 973

Enoch, M. L., Young, K. E., Glenn, J., et al. 2006, The Astrophysical Journal, 638, 293

Enrique-Romero, J., Ceccarelli, C., Rimola, A., et al. 2021, Astronomy and Astrophysics, 655, A9

Enrique-Romero, J., Rimola, A., Ceccarelli, C., & Balucani, N. 2016, Monthly Notices of the Royal Astronomical Society, 459, L6

Enrique-Romero, J., Rimola, A., Ceccarelli, C., et al. 2019, ACS Earth and Space Chemistry, vol. 3, issue 10, pp. 2158-2170, 3, 2158

Enrique-Romero, J., Álvarez Barcia, S., Kolb, F. J., et al. 2020, Monthly Notices of the Royal Astronomical Society, 493, 2523

Ercolano, B., Clarke, C. J., & Drake, J. J. 2009, The Astrophysical Journal, 699, 1639

Evans, II, N. J., Dunham, M. M., Jørgensen, J. K., et al. 2009, The Astrophysical Journal Supplement Series, 181, 321

Favre, C., Fedele, D., Semenov, D., et al. 2018, The Astrophysical Journal Letters, 862, L2

Fedele, D. & Favre, C. 2020, Astronomy and Astrophysics, 638, A110

Fedele, D., Tazzari, M., Booth, R., et al. 2018, Astronomy and Astrophysics, 610, A24

Federrath, C., Klessen, R. S., Iapichino, L., & Beattie, J. R. 2021, Nature Astronomy, 5, 365

Ferrero, S., Zamirri, L., Ceccarelli, C., et al. 2020, The Astrophysical Journal, 904, 11

Flower, D. R. & Pineau des Forets, G. 1994, Monthly Notices of the Royal Astronomical Society, 268, 724

Flower, D. R., Pineau des Forêts, G., & Rabli, D. 2010, Monthly Notices of the Royal Astronomical Society, 409, 29

Frank, A., Ray, T. P., Cabrit, S., et al. 2014, Protostars and Planets VI, 451

Franz, R., Picogna, G., Ercolano, B., & Birnstiel, T. 2020, Astronomy and Astrophysics, 635, A53

Fuchs, G. W., Cuppen, H. M., Ioppolo, S., et al. 2009, Astronomy and Astrophysics, 505, 629

Fukui, Y., Iwata, T., Mizuno, A., Bally, J., & Lane, A. P. 1993, Protostars and Planets III

Furlan, E., Fischer, W. J., Ali, B., et al. 2016, The Astrophysical Journal Supplement Series, 224, 5

Gaensler, B. M., Madsen, G. J., Chatterjee, S., & Mao, S. A. 2008, Astronomical Society of Australia, 25, 184

Galametz, M., Maury, A. J., Valdivia, V., et al. 2019, Astronomy and Astrophysics, 632, A5

Galván-Madrid, R., Liu, H. B., Izquierdo, A. F., et al. 2018, The Astrophysical Journal, 868, 39

Garrod, R. T. 2008, Astronomy and Astrophysics, 491, 239

Garrod, R. T. & Herbst, E. 2006, Astronomy and Astrophysics, 457, 927

Garrod, R. T., Wakelam, V., & Herbst, E. 2007, Astronomy and Astrophysics, 467, 1103

Geppert, W. D., Hamberg, M., Thomas, R. D., et al. 2006, Faraday Discussions, 133, 177

Geppert, W. D., Hellberg, F., Österdahl, F., et al. 2005, Astrochemistry: Recent Successes and Current Challenges, 231, 117

Goldsmith, P. F., Heyer, M., Narayanan, G., et al. 2008, The Astrophysical Journal, 680, 428

Goldsmith, P. F. & Langer, W. D. 1999, The Astrophysical Journal, 517, 209

Gordon, M. A. & Sorochenko, R. L. 2002, Astrophysics and Space Science Library, 282

Greaves, J. S. & Rice, W. K. M. 2011, Monthly Notices of the Royal Astronomical Society, 412, L88

Gredel, R. 1996, Astronomy and Astrophysics, 305, 582

Gredel, R., Lepp, S., Dalgarno, A., & Herbst, E. 1989, The Astrophysical Journal, 347, 289

Greenhill, L. J., Gwinn, C. R., Schwartz, C., Moran, J. M., & Diamond, P. J. 1998, Nature, 396, 650

Gueth, F., Guilloteau, S., & Bachiller, R. 1996, Astronomy and Astrophysics, 307, 891

Guidi, G., Tazzari, M., Testi, L., et al. 2016, Astronomy and Astrophysics, 588, A112

Guillet, V., Pineau Des Forêts, G., & Jones, A. P. 2011, Astronomy and Astrophysics, 527, A123

Guilloteau, S., Dutrey, A., Wakelam, V., et al. 2012, Astronomy and Astrophysics, 548, A70

Guilloteau, S., Piétu, V., Dutrey, A., & Guélin, M. 2006, Astronomy and Astrophysics, 448, L5

Guilloteau, S., Reboussin, L., Dutrey, A., et al. 2016, Astronomy and Astrophysics, 592, A124

Gusdorf, A., Cabrit, S., Flower, D. R., & Pineau Des Forêts, G. 2008a, Astronomy and Astrophysics, 482, 809

Gusdorf, A., Pineau Des Forêts, G., Cabrit, S., & Flower, D. R. 2008b, Astronomy and Astrophysics, 490, 695

Gutermuth, R. A., Myers, P. C., Megeath, S. T., et al. 2008, The Astrophysical Journal, 674, 336

Güdel, M., Dvorak, R., Erkaev, N., et al. 2014, Protostars and Planets VI, 883

Hacar, A., Tafalla, M., & Alves, J. 2017, Astronomy and Astrophysics, 606, A123

Hacar, A., Tafalla, M., Kauffmann, J., & Kovács, A. 2013, Astronomy and Astrophysics, 554, A55

Hagen, W., Allamandola, L. J., & Greenberg, J. M. 1979, Astrophysics and Space Science, 65, 215

Haro, G. 1952, The Astrophysical Journal, 115, 572

Harsono, D., Bjerkeli, P., van der Wiel, M. H. D., et al. 2018, Nature Astronomy, 2, 646

Hartigan, P., Curiel, S., & Raymond, J. 1989, The Astrophysical Journal, 347, L31

Haschick, A. D., Moran, J. M., Rodriguez, L. F., et al. 1980, The Astrophysical Journal, 237, 26

Hatchell, J., Richer, J. S., Fuller, G. A., et al. 2005, Astronomy and Astrophysics, 440, 151

Helled, R. & Morbidelli, A. 2021, in Planet Formation ("Big questions in exoplanetary science", Bristol: IOP Publishing Ltd)

Helmich, F. P., van Dishoeck, E. F., Black, J. H., et al. 1996, Astronomy and Astrophysics, 315, L173

Hennebelle, P. 2013, Astronomy & Astrophysics, 556, A153

Hennebelle, P. & Inutsuka, S.-i. 2019, Frontiers in Astronomy and Space Sciences, 6, 5

Henning, T., Semenov, D., Guilloteau, S., et al. 2010, The Astrophysical Journal, 714, 1511

Henshaw, J. D., Jiménez-Serra, I., Longmore, S. N., et al. 2017, Monthly Notices of the Royal Astronomical Society, 464, L31

Henshaw, J. D., Longmore, S. N., & Kruijssen, J. M. D. 2016, Monthly Notices of the Royal Astronomical Society, 463, L122

Herbig, G. H. 1951, The Astrophysical Journal, 113, 697

Herbig, G. H. & Jones, B. F. 1983, The Astronomical Journal, 88, 1040

Herbst, E. 2017, International Reviews in Physical Chemistry, 36, 287

Herbst, E. & van Dishoeck, E. F. 2009, Annual Review of Astronomy and Astrophysics, 47, 427

Heyer, M., Goldsmith, P. F., Yıldız, U. A., et al. 2016, Monthly Notices of the Royal Astronomical Society, 461, 3918

Higuchi, A. E., Sakai, N., Watanabe, Y., et al. 2018, The Astrophysical Journal Supplement Series, 236, 52

Hildebrand, R. H. 1983, Quarterly Journal of the Royal Astronomical Society, 24, 267

Hiraoka, K., Sato, T., Sato, S., et al. 2002, The Astrophysical Journal, 577, 265

Hogerheijde, M. R., Bergin, E. A., Brinch, C., et al. 2011, Science, 334, 338

Holdship, J., Viti, S., Codella, C., et al. 2019, The Astrophysical Journal, 880, 138

Hollenbach, D. & McKee, C. F. 1979, The Astrophysical Journal Supplement Series, 41, 555

Horn, A., Møllendal, H., Sekiguchi, O., et al. 2004, The Astrophysical Journal, 611, 605

Hsu, S.-Y., Liu, S.-Y., Liu, T., et al. 2020, The Astrophysical Journal, 898, 107

Huang, J., Öberg, K. I., Qi, C., et al. 2017, The Astrophysical Journal, 835, 231

Hunter, Jr., J. H., Whitaker, R. W., & Lovelace, R. V. E. 1997, The Astrophysical Journal, 482, 852

Högbom, J. A. 1974, Astronomy and Astrophysics Supplement Series, 15, 417

Ilee, J. D., Walsh, C., Booth, A. S., et al. 2021, The Astrophysical Journal Supplement Series, 257, 9

Imai, M., Sakai, N., Oya, Y., et al. 2016, The Astrophysical Journal Letters, 830, L37

Ioppolo, S., van Boheemen, Y., Cuppen, H. M., van Dishoeck, E. F., & Linnartz, H. 2011, Monthly Notices of the Royal Astronomical Society, 413, 2281

Isella, A., Guidi, G., Testi, L., et al. 2016, Physical Review Letters, 117, 251101

Jaber, A. A., Ceccarelli, C., Kahane, C., & Caux, E. 2014, The Astrophysical Journal, 791, 29

Jacobsen, S. K., Jørgensen, J. K., Di Francesco, J., et al. 2019, Astronomy and Astrophysics, 629, A29

Jenkins, E. B. 2009, The Astrophysical Journal, 700, 1299

Jenkins, E. B. 2013, The Astrophysical Journal, 764, 25

Jennings, R. E., Cameron, D. H. M., Cudlip, W., & Hirst, C. J. 1987, Monthly Notices of the Royal Astronomical Society, 226, 461

Jiménez, E., Ballesteros, B., Canosa, A., et al. 2015, Review of Scientific Instruments, 86

Jiménez-Serra, I., Caselli, P., Tan, J. C., et al. 2010, Monthly Notices of the Royal Astronomical Society, 406, 187

Jiménez-Serra, I., Vasyunin, A. I., Caselli, P., et al. 2016, The Astrophysical Journal Letters, 830, L6

Jiménez-Serra, I., Vasyunin, A. I., Spezzano, S., et al. 2021, The Astrophysical Journal, 917, 44

Jin, M. & Garrod, R. T. 2020, The Astrophysical Journal Supplement Series, 249, 26

Johansen, A., Blum, J., Tanaka, H., et al. 2014, Protostars and Planets VI

Johnson, J. A. 2019, Science, 363, 474

Jones, A. P., Fanciullo, L., Köhler, M., et al. 2013, Astronomy and Astrophysics, 558, A62

Jørgensen, J. K., Bourke, T. L., Myers, P. C., et al. 2007, The Astrophysical Journal, 659, 479

Jørgensen, J. K., Bourke, T. L., Myers, P. C., et al. 2005, The Astrophysical Journal, 632, 973

Jørgensen, J. K., Harvey, P. M., Evans, II, N. J., et al. 2006, The Astrophysical Journal, 645, 1246

Jørgensen, J. K., Hogerheijde, M. R., van Dishoeck, E. F., Blake, G. A., & Schöier, F. L. 2004, Astronomy and Astrophysics, 413, 993

Jørgensen, J. K., Johnstone, D., Kirk, H., et al. 2008, The Astrophysical Journal, 683, 822

Jørgensen, J. K., Müller, H. S. P., Calcutt, H., et al. 2018, Astronomy and Astrophysics, 620, A170

Jørgensen, J. K., Schöier, F. L., & van Dishoeck, E. F. 2002, Astronomy and Astrophysics, 389, 908

Jørgensen, J. K., van der Wiel, M. H. D., Coutens, A., et al. 2016, Astronomy and Astrophysics, 595, A117

Kalvāns, J. 2021, The Astrophysical Journal, 910, 54

Karska, A., Herczeg, G. J., van Dishoeck, E. F., et al. 2013, Astronomy and Astrophysics, 552, A141

Kennedy, G. M. & Kenyon, S. J. 2008, The Astrophysical Journal, 673, 502

Keto, E. & Caselli, P. 2010, Monthly Notices of the Royal Astronomical Society, 402, 1625

Keto, E., Caselli, P., & Rawlings, J. 2015, Monthly Notices of the Royal Astronomical Society, 446, 3731

Kirchhoff, W. H., Johnson, D. R., & Lovas, F. J. 1973, Journal of Physical and Chemical Reference Data, 2, 1

Kirk, H., Johnstone, D., & Di Francesco, J. 2006, The Astrophysical Journal, 646, 1009

Kirk, H., Johnstone, D., & Tafalla, M. 2007, The Astrophysical Journal, 668, 1042

Kleiner, I., Lovas, F. J., & Godefroid, M. 1996, Journal of Physical and Chemical Reference Data, 25, 1113

Klessen, R. S. & Glover, S. C. O. 2016, Saas-Fee Advanced Course, Springer, 43, 85

Knee, L. B. G. & Sandell, G. 2000, Astronomy and Astrophysics, 361, 671

Ko, C.-L., Liu, H. B., Lai, S.-P., et al. 2020, The Astrophysical Journal, 889, 172

Konigl, A. & Pudritz, R. E. 2000, Protostars and Planets IV

Kristensen, L. E., van Dishoeck, E. F., Bergin, E. A., et al. 2012, Astronomy and Astrophysics, 542, A8

Kristensen, L. E., Visser, R., van Dishoeck, E. F., et al. 2010, Astronomy and Astrophysics, 521, L30

Kuan, Y.-J., Huang, H.-C., Charnley, S. B., et al. 2004, The Astrophysical Journal, 616, L27

Kurtz, S., Cesaroni, R., Churchwell, E., Hofner, P., & Walmsley, C. M. 2000, Protostars and Planets IV

Lada, C. J. 1985, Annual Review of Astronomy and Astrophysics, 23, 267

Lada, C. J. 1987, IAU Symposium,, 115, 1

Lada, C. J., Alves, J., & Lada, E. A. 1996, The Astronomical Journal, 111, 1964

Lada, E. A. & Lada, C. J. 1995, The Astronomical Journal, 109, 1682

Ladd, E. F., Lada, E. A., & Myers, P. C. 1993, The Astrophysical Journal, 410, 168

Lamberts, T., Markmeyer, M. N., Kolb, F. J., & Kästner, J. 2019, ACS Earth and Space Chemistry, 3, 958

Large, M. I., Quigley, M. J. S., & Haslam, C. G. T. 1962, Monthly Notices of the Royal Astronomical Society, 124, 405

Lay, O. P., Carlstrom, J. E., & Hills, R. E. 1995, The Astrophysical Journal, 452, L73

Le Gal, R., Öberg, K. I., Loomis, R. A., Pegues, J., & Bergner, J. B. 2019, The Astrophysical Journal, 876, 72

Lee, C.-F. 2020, Astronomy and Astrophysics Review, 28, 1

Lee, C.-F., Codella, C., Li, Z.-Y., & Liu, S.-Y. 2019a, The Astrophysical Journal, 876, 63

Lee, C.-F., Ho, P. T. P., Li, Z.-Y., et al. 2017a, Nature Astronomy, 1, 0152

Lee, C.-F., Li, Z.-Y., Codella, C., et al. 2018, The Astrophysical Journal, 856, 14

Lee, C.-F., Li, Z.-Y., Ho, P. T. P., et al. 2017b, The Astrophysical Journal, 843, 27

Lee, C.-F., Mundy, L. G., Reipurth, B., Ostriker, E. C., & Stone, J. M. 2000, The Astrophysical Journal, 542, 925

Lee, C.-F., Stone, J. M., Ostriker, E. C., & Mundy, L. G. 2001, The Astrophysical Journal, 557, 429

Lee, C. W. & Myers, P. C. 2011, The Astrophysical Journal, 734, 60

Lee, J.-E., Lee, S., Baek, G., et al. 2019b, Nature Astronomy, 3, 314

Lefloch, B., Bachiller, R., Ceccarelli, C., et al. 2018, Monthly Notices of the Royal Astronomical Society, 477, 4792

Lefloch, B., Castets, A., Cernicharo, J., Langer, W. D., & Zylka, R. 1998a, Astronomy and Astrophysics, 334, 269

Lefloch, B., Castets, A., Cernicharo, J., & Loinard, L. 1998b, The Astrophysical Journal, 504, L109

Lefloch, B., Ceccarelli, C., Codella, C., et al. 2017, Monthly Notices of the Royal Astronomical Society, 469, L73

Leger, A., Jura, M., & Omont, A. 1985, Astronomy and Astrophysics, 144, 147

Lesaffre, P., Pineau des Forêts, G., Godard, B., et al. 2013, Astronomy and Astrophysics, 550, A106

Li, J. I.-H., Liu, H. B., Hasegawa, Y., & Hirano, N. 2017, The Astrophysical Journal, 840, 72

Ligterink, N. F. W., Calcutt, H., Coutens, A., et al. 2018a, Astronomy & Astrophysics, 619, A28

Ligterink, N. F. W., Terwisscha van Scheltinga, J., Taquet, V., et al. 2018b, Monthly Notices of the Royal Astronomical Society, 480, 3628

Linnartz, H., Ioppolo, S., & Fedoseev, G. 2015, International Reviews in Physical Chemistry, 34, 205

Liseau, R., Ceccarelli, C., Larsson, B., et al. 1996, Astronomy and Astrophysics, 315, L181

Loinard, L., Castets, A., Ceccarelli, C., et al. 2000, Astronomy and Astrophysics, 359, 1169

Loison, J.-C., Wakelam, V., & Hickson, K. M. 2014, Monthly Notices of the Royal Astronomical Society, 443, 398

Long, F., Herczeg, G. J., Harsono, D., et al. 2019, The Astrophysical Journal, 882, 49

Looney, L. W., Mundy, L. G., & Welch, W. J. 2000, The Astrophysical Journal, 529, 477

López-Sepulcre, A., Balucani, N., Ceccarelli, C., et al. 2019, ACS Earth and Space Chemistry, 3, 2122

López-Sepulcre, A., Jaber, A. A., Mendoza, E., et al. 2015, Monthly Notices of the Royal Astronomical Society, 449, 2438

López-Sepulcre, A., Sakai, N., Neri, R., et al. 2017, Astronomy and Astrophysics, 606, A121

Manara, C. F., Morbidelli, A., & Guillot, T. 2018, Astronomy & Astrophysics, 618, L3

Manigand, S., Calcutt, H., Jørgensen, J. K., et al. 2019, Astronomy and Astrophysics, 623, A69

Manigand, S., Jørgensen, J. K., Calcutt, H., et al. 2020, Astronomy and Astrophysics, 635, A48

Marcelino, N., Gerin, M., Cernicharo, J., et al. 2018, Astronomy and Astrophysics, 620, A80

Maret, S., Ceccarelli, C., Caux, E., Tielens, A. G. G. M., & Castets, A. 2002, Astronomy and Astrophysics, 395, 573

Maret, S., Ceccarelli, C., Caux, E., et al. 2004, Astronomy and Astrophysics, 416, 577

Maret, S., Ceccarelli, C., Tielens, A. G. G. M., et al. 2005, Astronomy and Astrophysics, 442, 527

Markwick, A. J., Ilgner, M., Millar, T. J., & Henning, T. 2002, Astronomy and Astrophysics, v.385, p.632-646 (2002), 385, 632

Marois, C., Zuckerman, B., Konopacky, Q. M., Macintosh, B., & Barman, T. 2010, Nature, 468, 1080

Martín-Doménech, R., Bergner, J. B., Öberg, K. I., et al. 2021, The Astrophysical Journal, 923, 155

Martin-Domenech, R., Oberg, K. I., Bergner, J. B., & Jorgensen, J. K. 2019, The Astrophysical Journal, 880, 130

Martin-Pintado, J., Bachiller, R., & Fuente, A. 1992, Astronomy and Astrophysics, Vol. 254, p. 315-326 (1992), 254, 315

Martín-Doménech, R., Öberg, K. I., & Rajappan, M. 2020, The Astrophysical Journal, 894, 98

Maury, A. J., André, P., Maret, S., et al. 2014a, Astrophysics and Space Science Proceedings, 233

Maury, A. J., André, P., Testi, L., et al. 2019, Astronomy and Astrophysics, 621, A76

Maury, A. J., Belloche, A., André, P., et al. 2014b, Astronomy and Astrophysics, 563, L2

McElroy, D., Walsh, C., Markwick, A. J., et al. 2013, Astronomy and Astrophysics, 550, A36

McGuire, B. A. 2018, The Astrophysical Journal Supplement Series, 239, 17

McGuire, B. A. 2021, Accepted for publication in the Astrophysical Journal Supplements

McGuire, B. A., Burkhardt, A. M., Loomis, R. A., et al. 2020, The Astrophysical Journal, 900, L10

McGuire, B. A., Carroll, P. B., & Garrod, R. T. 2018, ASP Monograph Series

McKellar, A. 1940, Publications of the Astronomical Society of the Pacific, 52, 187

Mendoza, E., Lefloch, B., López-Sepulcre, A., et al. 2014, Monthly Notices of the Royal Astronomical Society, 445, 151

Mihalas, D. 1978, Stellar atmospheres (San Francisco: W.H. Freeman, 1978)

Millar, T. J., Herbst, E., & Charnley, S. B. 1991, The Astrophysical Journal, 369, 147

Minissale, M. & Dulieu, F. 2014, Journal of Chemical Physics, 141, 014304

Minissale, M., Dulieu, F., Cazaux, S., & Hocuk, S. 2016, Astronomy & Astrophysics, 585, A24

Miotello, A., Testi, L., Lodato, G., et al. 2014, Astronomy and Astrophysics, 567, A32

Molinari, S., Bally, J., Glover, S., et al. 2014, Protostars and Planets VI

Molinari, S., Ceccarelli, C., White, G. J., et al. 1999, The Astrophysical Journal, 521, L71

Molinari, S., Noriega-Crespo, A., Ceccarelli, C., et al. 2000, The Astrophysical Journal, 538, 698

Molinari, S., Swinyard, B., Bally, J., et al. 2010, Astronomy and Astrophysics, 518, L100

Mottram, J. C., van Dishoeck, E. F., Kristensen, L. E., et al. 2017, Astronomy & Astrophysics, 600, A99

Muench, A. A., Lada, C. J., Luhman, K. L., Muzerolle, J., & Young, E. 2007, The Astronomical Journal, 134, 411

Mundy, L. G., McMullin, J. P., Grossman, A. W., & Sandell, G. 1993, Icarus, 106, 11

Murakawa, K., Tamura, M., & Nagata, T. 2000, The Astrophysical Journal Supplement Series, 128, 603

Myers, P. C. & Ladd, E. F. 1993, The Astrophysical Journal, 413, L47

Müller, H. S. P., Belloche, A., Xu, L.-H., et al. 2016, Astronomy and Astrophysics, 587, A92

Müller, H. S. P., Schlöder, F., Stutzki, J., & Winnewisser, G. 2005, Journal of Molecular Structure, 742, 215

Müller, H. S. P., Spezzano, S., Bizzocchi, L., et al. 2013, Journal of Physical Chemistry A, 117

Najita, J. R. & Kenyon, S. J. 2014, Monthly Notices of the Royal Astronomical Society, 445, 3315

Natta, A. & Testi, L. 2004, Astronomical Society of the Pacific, 2004, 323, 279

Natta, A., Testi, L., Calvet, N., et al. 2007, Protostars and Planets V

Nesterenok, A. V. 2018, Astrophysics and Space Science, 363, 151

Neufeld, D. A., Melnick, G. J., Sonnentrucker, P., et al. 2006, The Astrophysical Journal, 649, 816

Neustock, W., Guarnieri, A., Demaison, J., & Wlodarczak, G. 1990, Zeitschrift Naturforschung Teil A, 45, 702

Nguyen, H., Dawson, J. R., Miville-Deschênes, M. A., et al. 2018a, The Astrophysical Journal, 862, 49

Nguyen, T., Baouche, S., Congiu, E., et al. 2018b, Astronomy and Astrophysics, 619, A111

Nguyen-Luong, Q., Motte, F., Carlhoff, P., et al. 2013, The Astrophysical Journal, 775, 88

Nisini, B., Benedettini, M., Codella, C., et al. 2010, Astronomy and Astrophysics, 518, L120

Nisini, B., Codella, C., Giannini, T., et al. 2007, Astronomy and Astrophysics, 462, 163

Noble, J. A., Theule, P., Congiu, E., et al. 2015, Astronomy & Astrophysics, 576, A91

Noriega-Crespo, A., Cotera, A., Young, E., & Chen, H. 2002, The Astrophysical Journal, 580, 959

Ocaña, A. J., Blázquez, S., Potapov, A., et al. 2019, Physical Chemistry Chemical Physics, 21, 6942

Ospina-Zamudio, J., Lefloch, B., Ceccarelli, C., et al. 2018, Astronomy and Astrophysics, 618, A145

Ospina-Zamudio, J., Lefloch, B., Favre, C., et al. 2019, Monthly Notices of the Royal Astronomical Society, 490, 2679

Osterbrock, D. E. 1958, Publications of the Astronomical Society of the Pacific, 70, 399

Osterbrock, D. E. 1974, Astrophysics of gaseous nebulae (A Series of Books in Astronomy and Astrophysics, Freeman)

Oya, Y., Sakai, N., Watanabe, Y., et al. 2017, The Astrophysical Journal, 837, 174

Padoan, P., Juvela, M., Goodman, A. A., & Nordlund, A. 2001, The Astrophysical Journal, 553, 227

Padovani, M., Marcowith, A., Hennebelle, P., & Ferrière, K. 2016, Astronomy and Astrophysics, 590, A8

Pagani, L., Pardo, J.-R., Apponi, A. J., Bacmann, A., & Cabrit, S. 2005, Astronomy and Astrophysics, 429, 181

Pantaleone, S., Enrique-Romero, J., Ceccarelli, C., et al. 2021, The Astrophysical Journal, 917, 49

Pantaleone, S., Enrique-Romero, J., Ceccarelli, C., et al. 2020, The Astrophysical Journal, 897, 56

Parise, B., Belloche, A., Leurini, S., et al. 2006a, Astronomy and Astrophysics, 454, L79

Parise, B., Castets, A., Herbst, E., et al. 2004, Astronomy and Astrophysics, 416, 159

Parise, B., Ceccarelli, C., Tielens, A. G. G. M., et al. 2006b, Astronomy and Astrophysics, Volume 453, Issue 3, July III 2006, pp.949-958, 453, 949

Parise, B., Ceccarelli, C., Tielens, A. G. G. M., et al. 2002, Astronomy and Astrophysics, 393, L49

Phuong, N. T., Chapillon, E., Majumdar, L., et al. 2018, Astronomy and Astrophysics, 616, L5

Phuong, N. T., Dutrey, A., Chapillon, E., et al. 2021, Astronomy and Astrophysics, 653, L5

Pickett, H. M., Poynter, R. L., Cohen, E. A., et al. 1998, Journal of Quantitative Spectroscopy and Radiative Transfer, 60, 883

Pineda, J. E., Maury, A. J., Fuller, G. A., et al. 2012, Astronomy and Astrophysics, 544, L7

Pizzarello, S., Cooper, G. W., & Flynn, G. J. 2006, Meteorites and the Early Solar System II, 625

Podio, L., Codella, C., Gueth, F., et al. 2016, Astronomy and Astrophysics, 593, L4

Podio, L., Garufi, A., Codella, C., et al. 2020, Astronomy and Astrophysics, 644, A119

Podio, L., Lefloch, B., Ceccarelli, C., Codella, C., & Bachiller, R. 2014, Astronomy and Astrophysics, 565, A64

Pollack, J. B., Hollenbach, D., Beckwith, S., et al. 1994, The Astrophysical Journal, 421, 615

Pontoppidan, K. M. 2006, Astronomy and Astrophysics, 453, L47

Pontoppidan, K. M., van Dishoeck, E. F., & Dartois, E. 2004, Astronomy and Astrophysics, 426, 925

Punanova, A., Caselli, P., Feng, S., et al. 2018, The Astrophysical Journal, 855, 112

Qi, C., Wilner, D. J., Aikawa, Y., Blake, G. A., & Hogerheijde, M. R. 2008, The Astrophysical Journal, 681, 1396

Qi, C., Öberg, K. I., Andrews, S. M., et al. 2015, The Astrophysical Journal, 813, 128

Qi, C., Öberg, K. I., & Wilner, D. J. 2013, The Astrophysical Journal, 765, 34

Quillen, A. C., Thorndike, S. L., Cunningham, A., et al. 2005, The Astrophysical Journal, 632, 941

Rabli, D. & Flower, D. R. 2010, Monthly Notices of the Royal Astronomical Society, 406, 95

Racine, R. 1968, The Astronomical Journal, 73, 233

Rank, D. M., Townes, C. H., & Welch, W. J. 1971, Science, 174, 1083

Rayleigh. 1879, The London, Edinburgh, and Dublin Philosophical Magazine and Journal of Science, 8, 261

Rebull, L. M., Stapelfeldt, K. R., Evans, II, N. J., et al. 2007, The Astrophysical Journal Supplement Series, 171, 447

Redman, M. P., Rawlings, J. M. C., Nutter, D. J., Ward-Thompson, D., & Williams, D. A. 2002, Monthly Notices of the Royal Astronomical Society, 337, L17

Reipurth, B., Chini, R., Krugel, E., Kreysa, E., & Sievers, A. 1993, Astronomy and Astrophysics, 273, 221

Reipurth, B., Rodríguez, L. F., Anglada, G., & Bally, J. 2002, The Astronomical Journal, 124, 1045

Requena-Torres, M. A., Marcelino, N., Jiménez-Serra, I., et al. 2007, The Astrophysical Journal Letters, 655, L37

Ricci, L., Testi, L., Natta, A., & Brooks, K. J. 2010a, Astronomy and Astrophysics, 521, A66

Ricci, L., Testi, L., Natta, A., et al. 2010b, Astronomy and Astrophysics, 512, A15

Rimola, A., Skouteris, D., Balucani, N., et al. 2018, ACS Earth and Space Chemistry, 2, 720

Rimola, A., Taquet, V., Ugliengo, P., Balucani, N., & Ceccarelli, C. 2014, Astronomy and Astrophysics, 572, A70

Rivilla, V. M., Beltrán, M. T., Cesaroni, R., et al. 2017, Astronomy & Astrophysics, 598, A59

Roberts, H., Fuller, G. A., Millar, T. J., Hatchell, J., & Buckle, J. V. 2002, Planetary and Space Science, 50, 1173

Roberts, H., Herbst, E., & Millar, T. J. 2003, The Astrophysical Journal, 591, L41

Robitaille, J.-F., Abdeldayem, A., Joncour, I., et al. 2020, Astronomy and Astrophysics, 641, A138

Rodriguez, L. F., Anglada, G., & Curiel, S. 1999, The Astrophysical Journal Supplement Series, 125, 427

Rogerson, J. B., Spitzer, L., Drake, J. F., et al. 1973, The Astrophysical Journal, 181, L97

Ruaud, M., Loison, J. C., Hickson, K. M., et al. 2015, Monthly Notices of the Royal Astronomical Society, 447, 4004

Rubin, R. H., Swenson, Jr., G. W., Benson, R. C., Tigelaar, H. L., & Flygare, W. H. 1971, The Astrophysical Journal Letters, 169, L39

Rybicki, G. B. & Lightman, A. P. 1986, Radiative Processes in Astrophysics (Wiley-VCH)

Sadavoy, S. I., Di Francesco, J., André, P., et al. 2014, The Astrophysical Journal, 787, L18

Sadavoy, S. I., Di Francesco, J., Johnstone, D., et al. 2013, The Astrophysical Journal, 767, 126

Sahu, D., Liu, S.-Y., Su, Y.-N., et al. 2019, The Astrophysical Journal, 872, 196

Sakai, N., Sakai, T., Hirota, T., & Yamamoto, S. 2008, The Astrophysical Journal, 672, 371

Sakai, N., Sakai, T., & Yamamoto, S. 2006, Publications of the Astronomical Society of Japan, 58, L15

Sakai, N. & Yamamoto, S. 2013, Chemical Reviews, 113, 8981

Salinas, V. N., Hogerheijde, M. R., Mathews, G. S., et al. 2017, Astronomy & Astrophysics, 606, A125

Sanchis, E., Testi, L., Natta, A., et al. 2020, Astronomy and Astrophysics, 633, A114

Sandell, G., Aspin, C., Duncan, W. D., Russell, A. P. G., & Robson, E. I. 1991, The Astrophysical Journal, 376, L17

Sandell, G. & Knee, L. B. G. 2001, The Astrophysical Journal, 546, L49

Santangelo, G., Codella, C., Cabrit, S., et al. 2015, Astronomy and Astrophysics, 584, A126

Schilke, P., Walmsley, C. M., Pineau des Forets, G., & Flower, D. R. 1997, Astronomy and Astrophysics, 321, 293

Schisano, E., Molinari, S., Elia, D., et al. 2020, Monthly Notices of the Royal Astronomical Society, 492, 5420

Schnee, S., Enoch, M., Noriega-Crespo, A., et al. 2010, The Astrophysical Journal, 708, 127

Schneider, S. & Elmegreen, B. G. 1979, The Astrophysical Journal Supplement Series, 41, 87

Schreel, K., Schleipen, J., Eppink, A., & Meulen, J. J. t. 1993, Journal of Chemical Physics, 99, 8713

Schwab, F. R. & Cotton, W. D. 1983, The Astronomical Journal, 88, 688

Schwartz, R. D. 1975, The Astrophysical Journal, 195, 631

Scibelli, S. & Shirley, Y. 2020, The Astrophysical Journal, 891, 73

Scibelli, S., Shirley, Y., Vasyunin, A., & Launhardt, R. 2021, Monthly Notices of the Royal Astronomical Society, 504, 5754

Scoville, N. Z. & Solomon, P. M. 1974, The Astrophysical Journal, 187, L67

Seale, J. P. & Looney, L. W. 2008, The Astrophysical Journal, 675, 427

Segura-Cox, D. M., Schmiedeke, A., Pineda, J. E., et al. 2020, Nature, 586, 228

Shannon, R. J., Blitz, M. A., Goddard, A., & Heard, D. E. 2013, Nature Chemistry, 5, 745

Shannon, R. J., Caravan, R. L., Blitz, M. A., & Heard, D. E. 2014, Physical Chemistry Chemical Physics, 16, 3466

Sheehan, P. D., Tobin, J. J., Federman, S., Megeath, S. T., & Looney, L. W. 2020, The Astrophysical Journal, 902, 141

Shen, C. J., Greenberg, J. M., Schutte, W. A., & van Dishoeck, E. F. 2004, Astronomy and Astrophysics, 415, 203

Shirley, Y. L., Huard, T. L., Pontoppidan, K. M., et al. 2011, The Astrophysical Journal, 728, 143

Shu, F. H., Adams, F. C., & Lizano, S. 1987, Annual Review Astronomy and Astrophysics, 25, 23

Shull, J. M. & van Steenberg, M. E. 1985, The Astrophysical Journal, 294, 599

Sims, I. R., Queffelec, J. L., Defrance, A., et al. 1994, Journal of Chemical Physics, 100, 4229

Skouteris, D., Balucani, N., Ceccarelli, C., et al. 2019, Monthly Notices of the Royal Astronomical Society, 482, 3567

Skouteris, D., Balucani, N., Ceccarelli, C., et al. 2018, The Astrophysical Journal, 854, 135

Skouteris, D., Vazart, F., Ceccarelli, C., et al. 2017, Monthly Notices of the Royal Astronomical Society, 468, L1

Sleiman, C., El Dib, G., Talbi, D., & Canosa, A. 2018, ACS Earth and Space Chemistry, 2, 1047

Smith, I. W. & Rowe, B. R. 2000, Accounts of Chemical Research, 33, 261

Smith, I. W. M., Herbst, E., & Chang, Q. 2004, Monthly Notices of the Royal Astronomical Society, 350, 323

Smith, K. W., Bonnell, I. A., Emerson, J. P., & Jenness, T. 2000, Monthly Notices of the Royal Astronomical Society, 319, 991

Snell, R. L., Howe, J. E., Ashby, M. L. N., et al. 2000, The Astrophysical Journal Letters, 539, L101

Snell, R. L., Loren, R. B., & Plambeck, R. L. 1980, The Astrophysical Journal, 239, L17

Snow, T. P. & McCall, B. J. 2006, Annual Review of Astronomy and Astrophysics, 44, 367

Sobolev, V. V. 1957, Soviet Astronomy, 1, 678

Sobolev, V. V. 1960, Moving envelopes of stars (Cambridge: Harvard University Press, 1960)

Sokolov, V., Pineda, J. E., Buchner, J., & Caselli, P. 2020, The Astrophysical Journal, 892, L32

Sokolov, V., Wang, K., Pineda, J. E., et al. 2019, The Astrophysical Journal, 872, 30

Song, L. & Kästner, J. 2016, Physical Chemistry Chemical Physics, 18, 29278

Song, L. & Kästner, J. 2017, The Astrophysical Journal, 850, 118

Stahler, S. W. & Palla, F. 2005, The Formation of Stars (Wiley-VCH)

Strazzulla, G., Calcagno, L., & Foti, G. 1983, Monthly Notices of the Royal Astronomical Society, 204, 59P

Strom, S. E., Grasdalen, G. L., & Strom, K. M. 1974, The Astrophysical Journal, 191, 111

Strom, S. E., Vrba, F. J., & Strom, K. M. 1976, The Astronomical Journal, 81, 314

Su, Y.-N., Liu, S.-Y., Li, Z.-Y., et al. 2019, The Astrophysical Journal, 885, 98

Sugimura, M., Yamaguchi, T., Sakai, T., et al. 2011, Publications of the Astronomical Society of Japan, 63, 459

Swings, P. & Rosenfeld, L. 1937, The Astrophysical Journal, 86, 483

Tafalla, M., Bachiller, R., Lefloch, B., et al. 2015, Astronomy and Astrophysics, 573, L2

Tafalla, M. & Hacar, A. 2015, Astronomy and Astrophysics, 574, A104

Tafalla, M., Myers, P. C., Caselli, P., & Walmsley, C. M. 2004, Astronomy and Astrophysics, 416, 191

Tafalla, M., Santiago-García, J., Myers, P. C., et al. 2006, Astronomy and Astrophysics, 455, 577

Takahashi, T., Silk, J., & Hollenbach, D. J. 1983, The Astrophysical Journal, 275, 145

Taquet, V., Ceccarelli, C., & Kahane, C. 2012a, The Astrophysical Journal, 748, L3

Taquet, V., Ceccarelli, C., & Kahane, C. 2012b, Astronomy and Astrophysics, 538, A42

Taquet, V., Codella, C., De Simone, M., et al. 2020, Astronomy and Astrophysics, 637, A63

Taquet, V., López-Sepulcre, A., Ceccarelli, C., et al. 2015, The Astrophysical Journal, 804, 81

Taquet, V., Peters, P. S., Kahane, C., et al. 2013, Astronomy & Astrophysics, 550, A127

Taquet, V., Wirström, E. S., & Charnley, S. B. 2016, The Astrophysical Journal, 821, 46

Tazzari, M., Testi, L., Natta, A., et al. 2021, Monthly Notices of the Royal Astronomical Society, 506, 5117

Ter Meulen, J. J. 1997, IAU Symposium, 178, 241

Testi, L., Birnstiel, T., Ricci, L., et al. 2014, Protostars and Planets VI, 339

Testi, L., Natta, A., Scholz, A., et al. 2016, Asronomy & Astrophysics, 593, A111

Tielens, A. G. G. M. 2005, The Physics and Chemistry of the Interstellar Medium (Cambridge University Press)

Tielens, A. G. G. M. 2013, Reviews of Modern Physics, 85, 1021

Tielens, A. G. G. M. & Allamandola, L. J. 1987, Interstellar Processes, 134, 397

Tielens, A. G. G. M. & Hagen, W. 1982, Astronomy and Astrophysics, 114, 245

Tobin, J. J., Dunham, M. M., Looney, L. W., et al. 2015, The Astrophysical Journal, 798, 61

Tobin, J. J., Looney, L. W., Li, Z.-Y., et al. 2016, The Astrophysical Journal, 818, 73

Tobin, J. J., Megeath, S. T., van't Hoff, M., et al. 2019, The Astrophysical Journal, 886, 6

Trumpler, R. J. 1930, Publications of the Astronomical Society of the Pacific, 42, 214

Turner, B. E. 1990, The Astrophysical Journal, 362, L29

Turner, N. J., Fromang, S., Gammie, C., et al. 2014, Protostars and Planets VI

Tychoniec, L., Manara, C. F., Rosotti, G. P., et al. 2020, Astronomy and Astrophysics, 640, A19

Ungerechts, H. & Thaddeus, P. 1987, The Astrophysical Journal Supplement Series, 63, 645

van den Bergh, S. 1966, The Astronomical Journal, 71, 990

van der Tak, F. F. S. 2004, International Astronomical Union Symposium, 221, 59

van Dishoeck, E. F., Bergin, E. A., Lis, D. C., & Lunine, J. I. 2014, Protostars and Planets VI, 835

van Dishoeck, E. F., Kristensen, L. E., Mottram, J. C., et al. 2021, Astronomy and Astrophysics, 648, A24

van Dishoeck, E. F., Thi, W.-F., & van Zadelhoff, G.-J. 2003, Astronomy and Astrophysics, 400, L1

van 't Hoff, M. L. R., Tobin, J. J., Trapman, L., et al. 2018, The Astrophysical Journal, 864, L23

Vastel, C., Caselli, P., Ceccarelli, C., et al. 2006, The Astrophysical Journal, 645, 1198

Vastel, C., Ceccarelli, C., Lefloch, B., & Bachiller, R. 2014, The Astrophysical Journal Letters, 795, L2

Vastel, C., Phillips, T. G., Ceccarelli, C., & Pearson, J. 2003, The Astrophysical Journal, 593, L97

Vasyunin, A. I., Caselli, P., Dulieu, F., & Jiménez-Serra, I. 2017, The Astrophysical Journal, 842, 33

Vasyunin, A. I. & Herbst, E. 2013, The Astrophysical Journal, 769, 34

Vasyunin, A. I., Wiebe, D. S., Birnstiel, T., et al. 2011, The Astrophysical Journal, 727, 76

Vazart, F., Calderini, D., Puzzarini, C., Skouteris, D., & Barone, V. 2016, Journal of Chemical Theory and Computation, 12, 5385

Vazart, F., Ceccarelli, C., Balucani, N., Bianchi, E., & Skouteris, D. 2020, Monthly Notices of the Royal Astronomical Society, 499, 5547

Vazart, F., Latouche, C., Skouteris, D., Balucani, N., & Barone, V. 2015, The Astrophysical Journal, 810, 111

Vidal, M., Dickinson, C., Davies, R. D., & Leahy, J. P. 2015, Monthly Notices of the Royal Astronomical Society, 452, 656

Vigren, E., Kamińska, M., Hamberg, M., et al. 2007, Phys. Chem. Chem. Phys., 9, 2856

Visser, R., Kristensen, L. E., Bruderer, S., et al. 2012, Astronomy and Astrophysics, 537, A55

Vázquez-Semadeni, E., Palau, A., Ballesteros-Paredes, J., Gómez, G. C., & Zamora-Avilés, M. 2019, Monthly Notices of the Royal Astronomical Society, 490, 3061

Wakelam, V., Dartois, E., Chabot, M., et al. 2021, Astronomy and Astrophysics, 652, A63

Wakelam, V., Herbst, E., Loison, J.-C., et al. 2012, The Astrophysical Journal Supplement Series, 199, 21

Wakelam, V., Loison, J. C., Herbst, E., et al. 2015, The Astrophysical Journal Supplement Series, 217, 20

Walawender, J., Bally, J., Francesco, J. D., Jørgensen, J., & Getman, K. 2008, Handbook of Star Forming Regions, Volume I, 346

Walawender, J., Bally, J., & Reipurth, B. 2005, The Astronomical Journal, 129, 2308

Walmsley, C. M., Flower, D. R., & Pineau des Forêts, G. 2004, Astronomy and Astrophysics, 418, 1035

Walsh, A. J., Bourke, T. L., & Myers, P. C. 2006, The Astrophysical Journal, 637, 860

Walsh, A. J., Myers, P. C., Di Francesco, J., et al. 2007, The Astrophysical Journal, 655, 958

Walsh, C., Loomis, R. A., Öberg, K. I., et al. 2016, The Astrophysical Journal Letters, 823, L10

Walsh, C., Millar, T. J., Nomura, H., et al. 2014, Astronomy and Astrophysics, 563, A33

Ward-Thompson, D., Motte, F., & Andre, P. 1999, Monthly Notices of the Royal Astronomical Society, 305, 143

Warin, S., Castets, A., Langer, W. D., Wilson, R. W., & Pagani, L. 1996, Astronomy and Astrophysics, 306, 935

Watanabe, N. & Kouchi, A. 2002, The Astrophysical Journal, 571, L173

Watson, W. D. 1974, The Astrophysical Journal, 188, 35

Weinreb, S., Barrett, A. H., Meeks, M. L., & Henry, J. C. 1963, Nature, 200, 829

Whittet, D. C. B. 2003, Dust in the galactic environment (Institute of Physics (IOP) Publishing, 2003)

Whittet, D. C. B. & Duley, W. W. 1991, Astronomy and Astrophysics Review, 2, 167

Wilson, T., Rohlfs, K., & Huettemeister, S. 2009, Tools of Radio Astronomy, 5th edn., Astronomy and Astrophysics Library (Berlin Heidelberg: Springer-Verlag)

Wolfire, M. G., McKee, C. F., Hollenbach, D., & Tielens, A. G. G. M. 2003, The Astrophysical Journal, 587, 278

Wu, Y., Wei, Y., Zhao, M., et al. 2004, Astronomy and Astrophysics, v.426, p.503-515 (2004), 426, 503

Wyatt, M. C. 2018, in Handbook of Exoplanets, ed. H. J. Deeg & J. A. Belmonte (Cham: Springer International Publishing), 2543–2568

Xu, L.-H., Fisher, J., Lees, R. M., et al. 2008, Journal of Molecular Spectroscopy, 251, 305

Yamaguchi, T., Takano, S., Watanabe, Y., et al. 2012, Publications of the Astronomical Society of Japan, 64, 105

Yamamoto, S. 2017, Introduction to Astrochemistry: Chemical Evolution from Interstellar Clouds to Star and Planet Formation (Springer Japan)

Yang, Y.-L., Evans, II, N. J., Smith, A., et al. 2020, The Astrophysical Journal, 891, 61

Yang, Y.-L., Sakai, N., Zhang, Y., et al. 2021, The Astrophysical Journal, 910, 20

Young, K. E., Young, C. H., Lai, S.-P., Dunham, M. M., & Evans, II, N. J. 2015, The Astronomical Journal, 150, 40

Yu, S., Pearson, J. C., Drouin, B. J., et al. 2010, The Journal of Chemical Physics, 133, 174317

Zari, E., Lombardi, M., Alves, J., Lada, C. J., & Bouy, H. 2016, Astronomy & Astrophysics, 587, A106

Ziurys, L. M., Snell, R. L., & Dickman, R. L. 1989, The Astrophysical Journal, 341, 857

Zucker, C., Goodman, A., Alves, J., et al. 2021, The Astrophysical Journal, 919, 35

Zucker, C., Schlafly, E. F., Speagle, J. S., et al. 2018, The Astrophysical Journal, 869, 83

Öberg, K. I. & Bergin, E. A. 2021, Physics Reports, 893, 1

Öberg, K. I., Boogert, A. C. A., Pontoppidan, K. M., et al. 2011a, The Astrophysical Journal, 740, 109

Öberg, K. I., Bottinelli, S., Jørgensen, J. K., & van Dishoeck, E. F. 2010, The Astrophysical Journal, 716, 825

Öberg, K. I., Garrod, R. T., van Dishoeck, E. F., & Linnartz, H. 2009, Astronomy and Astrophysics, 504, 891

Öberg, K. I., Guzmán, V. V., Furuya, K., et al. 2015, Nature, 520, 198

Öberg, K. I., Guzmán, V. V., Merchantz, C. J., et al. 2017, The Astrophysical Journal, 839, 43

Öberg, K. I., Lauck, T., & Graninger, D. 2014, The Astrophysical Journal, 788, 68

Öberg, K. I., Qi, C., Wilner, D. J., & Hogerheijde, M. R. 2012, The Astrophysical Journal, 749, 162

Öberg, K. I., van Broekhuizen, F., Fraser, H. J., et al. 2005, The Astrophysical Journal, 621, L33

Öberg, K. I., van der Marel, N., Kristensen, L. E., & van Dishoeck, E. F. 2011b, The Astrophysical Journal, 740, 14

Acknowledgments

Everything started in a warm and calm summer day in Florence, when I received an unexpected email while preparing the last exams of my Master degree. Cecilia Ceccarelli was offering me the opportunity to join her new group at IPAG as a PhD student. I felt honored and excited to start this new experience and now, that is almost done, I am grateful and proud to have started this path that allowed me to grow up personally and professionally. These last years have been incredibly eventful, fulls of ups and downs, of bad and good moments and of gratifications, and, most importantly, full of people who have accompanied me on this journey, supported me, and pushed me to go beyond my limits.

First of all, a heartfelt and proper thanks goes to those who have supervised my work, who have supported and sustained me from the beginning, who have transmitted and taught me so much both from a scientific and human point of view: Cecilia, a great person and a great dreamer; thank you for your enthusiasm for every little thing, your perseverance and your encouragement. You pushed me beyond my limits, always asking for that little bit more that I could not see. Thank you for believing in me, and supporting me, for understanding my needs even before I did, and for always being there for me in the joyful and dark times. Claudio, an exceptional person; thank you for having supported me, for your esteem towards me since the first day we met. You have seen me grow, and you have been an integral part of my growth. Thank you for your timing, for understanding me and for being able to calm me down in every situation. Working with the two of you is stimulating and fun, and above all, it is like being at home, in a second traveling family.

The experience in France and at IPAG was interesting. I was lucky to be in an international group full of other students and post docs. Thanks to them it was easier to face the first difficulties related to the language barrier. A special thank to Eleonora, for her availability and friendship, for hosting me the first days, for helping me looking for a house, and for all the advice on the work and personal side. To Fanny for her help with the bank. To Mathilde for being a great office mate and travel companion, and for escorting me along the roads of New Mexico. To Ana, for all her help and encouraging words. To Joan for lightening things up, for the hiking and bike rides, and for much more. To the friends I met along the way: Jolantha, Pedro, Junko, Aina, Ricardo, Simon, Lorenzo, Luca and Panta, we spent very nice evenings and activities. To the other members of the DOC & ACO team: Marie, Juan, Cecile, Layal, André, Bertrand, Gemma, Arezu.

I thank the funding agency that has made this thesis possible: the European Reserch Council for the European Union's Horizon 2020 research and innovation programme project "The Dawn of Organic Chemistry" (DOC, grant agreement No 741002), and its PI (C. Ceccarelli) for have build this amazing and high-level project. Being part of this project, and of several observational Large Programs, allowed me to build international collaborations, and to interact with many great scientists as Nadia Balucani, Albert Rimola, Serena Viti, Paola Caselli, Claire Chandler, Leonardo Testi, Satoshi Yamamoto, Piero Ugliengo, Daniela Ascenzi, Charlotte Vastel, and many more, enriching my scientific baggage.

I would like to thank also the referees of this thesis manuscript, Rafael Bachiller and Sergio Molinari, for the time they dedicated to read the manuscript and for the advices and the good words they had for me. I am very grateful to the other members of the jury, Claire Chandler, Linda Podio, Pierre Beck, Leonardo Testi and Paola Caselli, for accepting to be part of this jury.

Finally, the most important and heartfelt thanks goes to my family, for always supporting me and for their strength in managing the distance between us.

Ringraziamenti

Tutto è iniziato in una calda e tranquilla giornata estiva a Firenze, quando ho ricevuto una mail inaspettata mentre preparavo gli ultimi esami della mia laurea magistrale. Cecilia Ceccarelli mi stava offrendo l'opportunità di unirmi al suo nuovo gruppo ad IPAG come studentessa di dottorato. Mi sono sentita onorata ed eccitata di iniziare questa nuova esperienza e ora, che è quasi finita, sono grata e orgogliosa di aver iniziato questo percorso che mi ha permesso di crescere personalmente e professionalmente. Questi ultimi anni sono stati incredibilmente movimentati, pieni di alti e bassi, di momenti brutti e buoni e di gratificazioni, e, soprattutto, pieni di persone che mi hanno accompagnato in questo viaggio, sostenuto e spinto ad andare oltre i miei limiti.

Prima di tutto, un sentito e doveroso ringraziamento va a coloro che hanno supervisionato il mio lavoro, che mi hanno supportato e sostenuto fin dall'inizio, che mi hanno trasmesso e insegnato tanto sia dal punto di vista scientifico che umano: Cecilia, una grande persona e una grande sognatrice; grazie per il tuo entusiasmo su ogni piccola cosa, la tua perseveranza e il tuo incoraggiamento. Mi hai spinto oltre i miei limiti, chiedendo sempre quel poco di più che non riuscivo a vedere. Grazie per aver creduto in me e per avermi sostenuto, per aver capito i miei bisogni prima di me e per esserci sempre stata nei momenti gioiosi e in quelli bui. Claudio, una persona eccezionale; grazie per avermi sembre supportata, per la tua stima nei miei confronti sia dal primo giorno che ci siamo conosciuti. Mi hai visto crescere, e sei stato parte integrante della mia crescita. Grazie per il tuo tempismo, per capirmi e per sapermi tranquillizzare in ogni situazione. Lavorare con voi due é stimolante e divertente, e soprattutto é come sentirsi a casa, in una seconda famiglia itinerante.

L'esperienza in Francia e ad IPAG é stata interessante. Sono stata fortunata ad essere in un gruppo internazionale pieno di altri studenti e post doc. Grazie a loro é stato più semplice affrontare le prime difficoltà legate alla barriera linguistica. Un grazie speciale ad Eleonora, per la sua disponibilità e amicizia, per avermi ospitato i primi giorni, per avermi aiutato a cercare casa, e per tutti i consigli sul lavoro e sul lato personale. A Fanny per il suo aiuto con la banca. A Mathilde per essere stata un ottima compagna di ufficio e di viaggio e per avermi scorrazzato lungo le strade del New Mexico. Ad Ana, per tutto il suo aiuto e le sue parole incoraggianti. A Joan per aver alleggerito il tutto, per i trekking e i giri in bici, e per tanto altro. A gli altri amici incontrati in tutto il percorso: Jolantha, Pedro, Junko, Aina, Ricardo, Simon, Lorenzo and Stefano, abbiamo trascorso belle serate insieme. Agli altri membri del DOC & ACO team: Marie, Juan, Cecile, Layal, André, Bertrand, Gemma, Arezu.

Ringrazio l'agenzia di finanziamento che ha reso possibile questa tesi: l'European Reserch Council per il programma di ricerca e innovazione dell'Unione Europea Horizon 2020 "The Dawn of Organic Chemistry" (DOC, grant agreement No 741002), e il suo PI (C. Ceccarelli) per aver costruito questo progetto incredibile e di alto livello. Far parte di questo progetto, e di diversi Large Programs osservativi, mi ha permesso di costruire collaborazioni internazionali, di interagire con molti grandi scienziati come Nadia Balucani, Albert Rimola, Serena Viti, Paola Caselli, Claire Chandler, Leonardo Testi, Satoshi Yamamoto, Piero Ugliengo, Daniela Ascenzi, Charlotte Vastel, e molti altri, arricchendo il mio bagaglio scientifico.

Vorrei ringraziare anche i referee di questa tesi, Rafael Bachiller e Sergio Molinari, per il tempo che hanno dedicato alla lettura della tesi e per i consigli e le buone parole che hanno avuto per me. Sono molto grata agli altri membri della giuria, Claire Chandler, Linda Podio, Pierre Beck, Leonardo Testi e Paola Caselli, per aver accettato di far parte di questa giuria.

Infine, il più importante e sentito ringraziamento va alla mia famiglia, per supportarmi sempre e per la loro forza nel riuscire a gestire la distanza che ci separa.